Experimental Investigation of Polyurethane Electrospun Nanofibers Mat for Nanobiomedical Device----Relationship between Mechanical Property and Thickness

Xin Li[1], Wenzhong Lou[1]*, Rongchang Song[1]

National Key Laboratory of Mechatronics Engineering and Control,

Beijing Institute of Technology, Beijing 100081,China

Abstract — **Electrospinning is a method to produce polymer fibers from solution with diameters ranging from 100 to 500 nm. Pure Polyurethane was electrospun from solution to produce an isotropic fiber mat. The mechanical behavior such as stress-strain curve and maximum load during fracture of the mat was characterized by uniaxial tensile tests. Scanning electron microscopy was used to characterize the electrospun material. Finite Element Analysis method is utilized to simulate stress distribution. The experimental result shows that the maximum load increases when the thickness increases.**

Keywords — ***Electrospinning; nanofibers; tensile testing; mechanical properties; polyurethane; FEA analysis***

I. INTRODUCTION

Electrospinning[1],as Fig. 1 shows, is the most widely used method to fabricate membrane with nonwoven nano fibers for nanobiomedical application. It is reported by numerous researchers for its application as artificial tissue/skin, as well as the base to nurture stem cells[2,3]. For all these application and the promising future of Electrospinning application, increasing number of research is undertaken for 20 years since 1990s. During the assembly process with other micro/nano device, the membrane should have a relatively good performance to withstand tensile strength, otherwise it could easily be damaged. Currently, there is a limited number work on the mechanical properties of electrospun nanofibers mat. [4, 5].

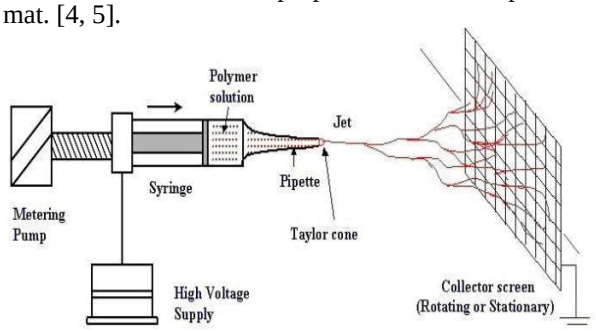

Fig 1, The electrospinning set up.

In this study, the experiment is carried out to visualize the relationship between tensile strength and the thickness of membrane in order to build a foundation for future researcher for more valuable research in the nanobiomedical area. The experiment result is analyzed with FEM method. Further recommendation is presented in the paper.

II. EXPERIMENTAL STUDY

Thermoplastic Polyurethane (PU) elastomer were dissolved in a mixture of THF and DMF (60/40, v/v) at room temperature to a fixed weight concentration of 18%. After Electrospinning, five samples,as figure 2 shows, of fiber mat produced were dried to remove the residual solvent. Each PU solution prepared was poured in a 20-ml syringe attached to a capillary tip of about 1mm diameter. An alligator style clip was used to charge the syringe tip, and solution with flow rate of 0.050ml/min was electrospun onto a grounded collector wrapped with Aluminum foil. The distance between the capillary tip and the grounded collector is 20cm. The electric field was set to 18KV generated by a high-voltage power supply.

Fig 2, Five Electrospun nanofiber mats with different thickness

As Fig. 1 shows, tensile testing with grip system was carried out using an Instron micro-functional mechanical tester.

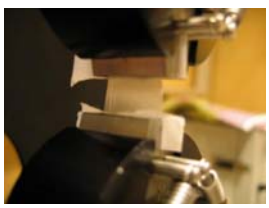

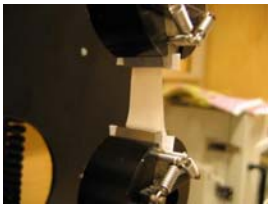

Fig 3, the electrospun nanofibers has elastic property

III, RESULTS AND DISCUSSION

For 5 samples with different thickness, as shown in Figure 4, maximum stress strain, load are summarized in Table 1. In the test sample, except the thickness, the dimension of length and width remains the same.

**Contact author: Wenzhong LOU(1969-), Ph.D. National Key laboratory of Mechatronics Engineering and Control, Beijing Institute of Technology, main research is involved in Microsystems integration.*

Tel: 008610-68912750 E-mail: louwz@bit.edu.cn

TABLE 1: EXPERIMENTAL RESULT SUMMARY

Thickness (micron)	**Max stress MPa**	**Max strain**	**Maximum load L (N)**
2.89	16.55405	1.726204	0.161761
3.6	12.19649	1.21584	0.225976
8.6	11.28568	1.69146	0.35766
37	1.67193	1.580181	0.25479
43	2.83089	1.567605	0.50771

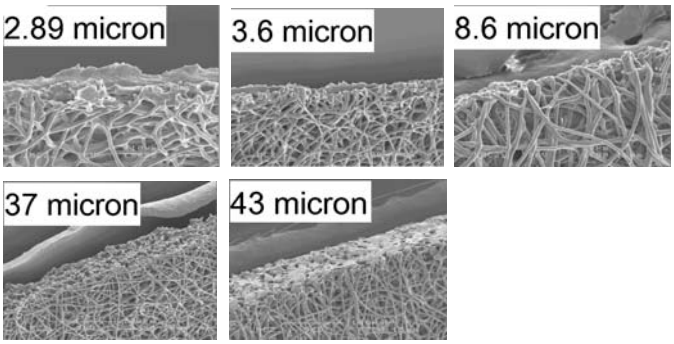

Fig 4, SEM pictures of samples with 5 different thicknesses

To be specific, the detailed data is listed under to illustrate the relationship between mechanical property and thickness one by one. The 1st sample's thickness is 2.89 micron, while the width is 19.00 millimeter, and the length is 5.00 millimeter. According to Figure 5, the maximum load when the fiber mat is torn apart is 0.161761 N. The maximum extension is 18.47712millimeter. The maximum stress is 16.55205MPa. The maximum strain is 1.726204. The Young's modulus is calculated to be 9.589857MPa, with the strain rate 0.013700/s.

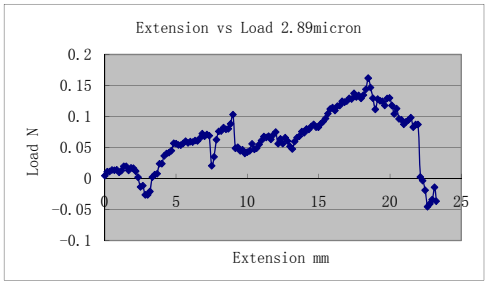

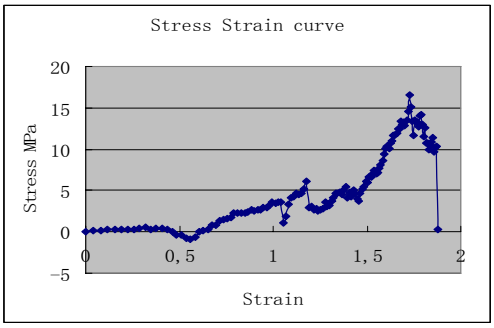

Fig 5, Stress Strain Extension and Maximum load when thickness is 2.89micron

The 2nd sample's thickness is 3.6 micron, with the width 19,00 millimeter and length 5.00 millimeter. According to Figure 6, the maximum load when the fiber mat is torn apart is 0.225976N. The maximum extension is 9.658874 millimeter. The maximum stress is 12.19649MPa, and maximum strain is 1.21584. The Young's modulus is 10.031328MPa, with the strain rate 0.009573/s.

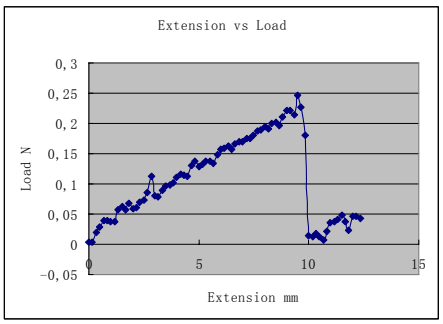

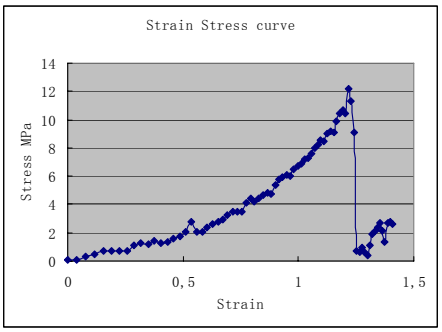

Fig 6, Stress Strain Extension and Maximum load when thickness is 3.6 micron

The 3rd sample's thickness is 8.6 micron, with the width 19.00 millimeter and length 5.00 millimeter. According to Figure 7, the maximum load when the fiber mat is torn apart is 0.35766N. The maximum extension is 22.137 millimeter. The maximum stress is 11.28568MPa, and maximum strain is 1.69146. The Young's modulus is 6.672153MPa, with the strain rate 0.012717/s.

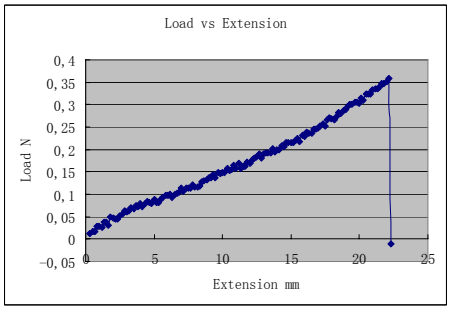

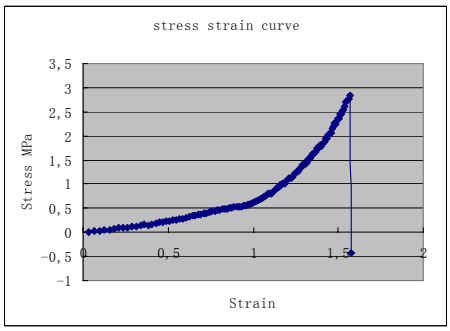

Fig 7, Stress Strain Extension and Maximum load when thickness is 8.6 micron

The 4th sample's thickness is 37.0 micron, with the width 19.00 millimeter and length 5.00 millimeter. According to Figure 8, the maximum load when the fiber mat is torn apart is 0.25479N. The maximum extension is 23.135millimeter. The maximum stress is 1.67193MPa, and maximum strain is

1.580181. The Young's modulus is 1.058062MPa, with the strain rate 0.011368/s.

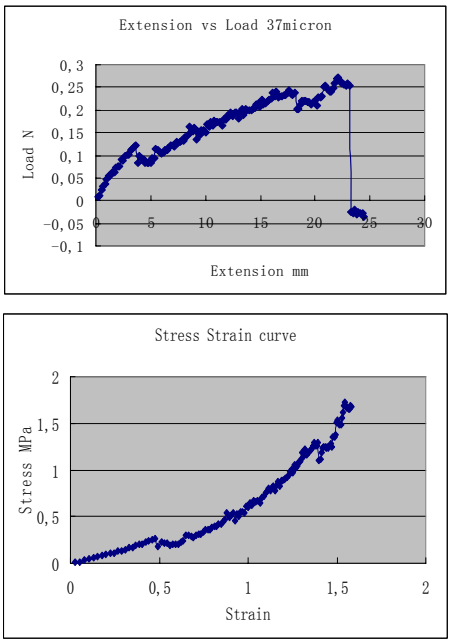

Fig 8, Stress Strain Extension and Maximum load when thickness is 37.0 micron

The 5th sample's thickness is 43.0 micron, with the width 19.00 millimeter and length 5.00 millimeter. According to Figure 9, the maximum load when the fiber mat is torn apart is 0.50771N. The maximum extension is 18.97575millimeter. The maximum stress is 2.83089MPa, and maximum strain is 1.567605. The Young's modulus is 1.805869MPa, with the strain rate 0.013750/s.

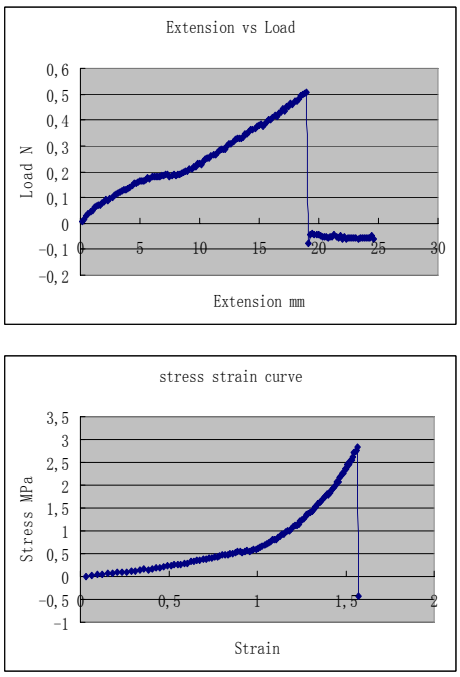

Fig 9, Stress Strain Extension and Maximum load when thickness is 43.0 micron

Figure 10 and Figure 11 shows the relationship between mechanical properties of electrospun nanofibers mat and the thicknesses. Although the thickness of the mat increases, it does not affect the maximum strain. The reason could be due to the fact that mat is fabricated with the same material and same procedure. It is possible to manufacture the mat with lower volume of solution, but can still gain sample with similar elongation property. However, the maximum load is in direct proportion to the increase of mat's thickness. The phenomena that, at the break point, the maximum stress is in inverse proportion to the thickness augment, is caused by the fact that the scale of sample's cross-section area aggrandizes in a relatively larger extent to that of maximum load.

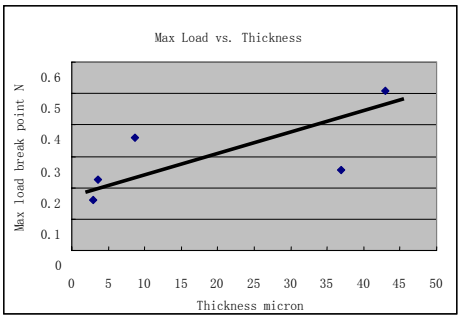

Fig 10, Relation between thickness and Maximum Load at breakpoint

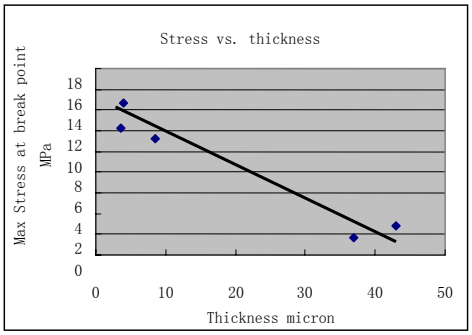

Fig 11, Relation between thickness and Maximum stress at breakpoint

IV. FINITE ELEMENT ANALYSIS

By the FEA method, the fiber is modeled and simulated with software MSC.Patran/Marc according to the tensile test. The material constitutive model of fiber is described as elastic, plastic and failure. For the simulation involves non-linear of material, the simulation is conducted by implicit arithmetic. The dimensions of fiber section are 19 mm×5 mm, and the thickness is 0.0086 mm. The up edge of section is exerted a 0.357 N magnitude tensile force, and the down edge of section is fixed, which is similar to the test. The results are presented as figure 12 shows.

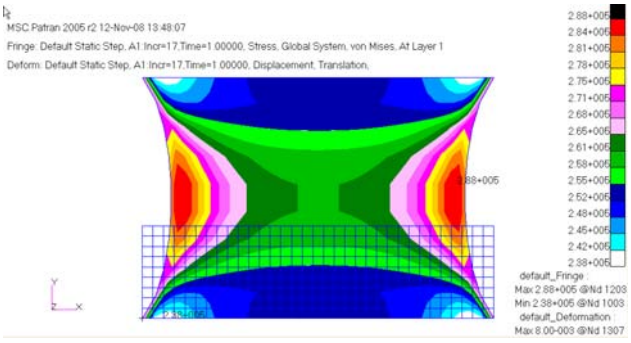

Fig 12, the globe stress of fiber section (meshed rectangle area is the original dimension of sample with thickness of 8.6 micron)

V, SUMMARY

Pure polyurethane solution is electrospun and 5 samples with different thickness were collected. Scanning electron microscopy was used to determine the thickness of samples. The relationship between the thickness and the mechanical properties of electrospun nanofibers mat of polyurethane has

been investigated with tensile testing. FEM simulation is performed to simulate the distribution of stress when the sample is elongated. The experimental result shows that the maximum load increases when the thickness increases. Thus, in order to get more robust and reliable nanofibers mat, it is recommended to increase its thickness to an optimum dimension to fulfill the requirement of potential application. In the future study, more compatible materials will be investigated in our group and the experimental discovery will be updated.

REFERENCES

[1], A. Formhals US patent, 1-975-504, 1934
[2], R. Dersch, et."Electrospinning of Nanofibres: Towards New Techniques, Functions, and Applications" Aust.J. Chem 2007,60, 719-728
[3], Boland, E. D.; Matthews, J. A.; Pawlowski, K. J.; Simpson, D. G.; Wnek, G. E.; Bowlin, G. L. Front. Biosci. 2004, 9, 1422.
[4], A. Pedicini, R. J. Farris "Mechanical behavior of electrospun polyurethane" Polymer 44 (2003) 6857–6862
[5], K. H.. Lee,et "Mechanical Behavior of Electrospun Fiber Mats of Polyurethane Polyblends" J Polym Sci: 1256+1262, 2003

PHOTON BUDGET ANALYSIS FOR A NOVEL FLUORESCENCE LIFETIME IMAGING MICROSCOPY SYSTEM WITH A MODULATED ELECTRON-MULTIPLIED ALL-SOLID-STATE CAMERA

Q. Zhao[1], I. T. Young[1], J. G. S. de Jong[2]*
[1]Department of Imaging Science & Technology, Lorentzweg 1
Delft University of Technology, 2628 CJ Delft, The Netherlands
[2]Lambert Instruments, Oosteinde 16, 9301 ZP Roden, The Netherlands
[*]E-mail: qiaole.zhao@tudelft.nl

Abstract— In this paper, a novel fluorescence lifetime imaging microscopy system is proposed that uses a modulated, electron-multiplied, all-solid-state camera (MEM-FLIM). This camera will eliminate the need for an image intensifier through the use of an application-specific charge coupled device (CCD) design. We are designing and building a CCD image sensor that can be modulated at the pixel level and that will have an electron multiplication feature to provide high sensitivity at low-light levels. The proposed design has advantages such as better signal-to-noise ratio (SNR), less geometric distortion, better resolution and low cost. It will be employed in both fluorescence lifetime imaging microscopy (FLIM) and, hopefully, in other biological and medical applications. We describe here the characteristic of our system and present a photon budget analysis for MEM-FLIM. This photon budget is important in order to understand the constraints which will be encountered in design and fabrication of our system.

Index Terms— modulated electron-multiplied all-solid-state camera for fluorescence lifetime imaging microscopy (MEM-FLIM), charge coupled device (CCD), signal-to-noise ratio (SNR), photon budget

I. INTRODUCTION

The fluorescence lifetime is the *average* time that a fluorophore remains in an excited state prior its return to the ground state after excitation by a photon of a shorter wavelength [1]. When the fluorophore returns to its ground state, a photon of a longer wavelength is emitted, as depicted in Fig. 1. Fluorescence lifetime imaging microscopy (FLIM) is a well-established and intrinsically quantitative tool to image the lifetime of fluorescence molecules, not only the fluorescence intensity. Unlike the intensity, the lifetime is independent of fluorophore concentration and light path length, and thus environmental properties, such as pH, Ca^{++}, or O_2 levels, of biomolecules can be investigated [2].

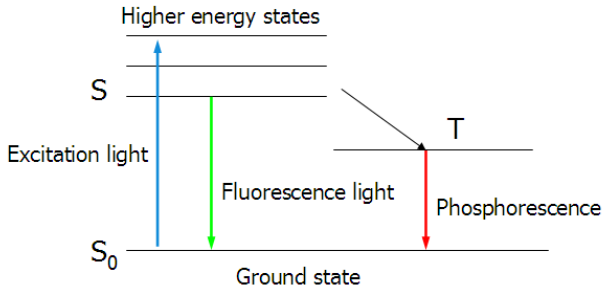

Figure 1. Jablonski diagram illustrating the fluorescence process.

II. THEORY

Fig. 2 shows a conventional frequency-domain FLIM system, which requires a sinusoidally modulated light source and a sinusoidally modulated detector to calculate the lifetime from the phase change and modulation depth change between the excitation and emission signals. The lifetime can be calculated using (1) and/or (2):

$$\tau_o = \frac{1}{2\pi f_o}\tan(\Delta\varphi) \quad (1)$$

$$\tau_o = \frac{1}{2\pi f_o}\sqrt{\frac{1}{m^2}-1} \quad (2)$$

in which, $\Delta\Phi$ is the phase change, f_0 the modulation frequency, and m the relative modulation depth of the emission signal compared to the excitation signal.

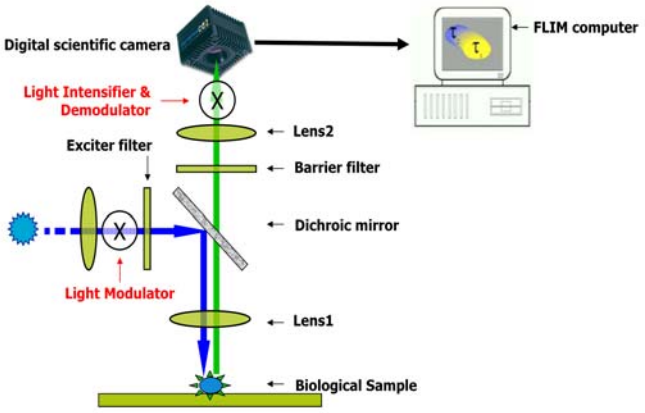

Figure 2. Schematic of a conventional, frequency-domain fluorescence lifetime microscope (FLIM).

Fig. 3 shows the proposed MEM-FLIM camera. By eliminating the light intensifier and modulating the pixel directly, the full duty cycle of the silicon sensor can be utilized. The gain of the camera is readily tunable in real time via a software interface. The electron-multiplied register enables weak signals to be amplified before any readout noise is added by the readout amplifier.

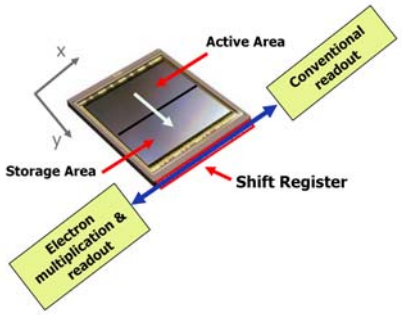

Figure 3. Schematic of the proposed modulated electron-multiplied, all-solid-state camera sensor.

III. RESULTS AND DISCUSSION

A. From Emission to Detection

We assume that the total number of photons that a single fluorescence molecule can emit before photodestruction occurs is n_{emit}. The directions which these photons travel can be divided into two major parts: direction in the upper half-plane, and in the lower half-plane, as shown in Fig. 4. The photons which travel towards the lower half-plane will never have the chance to reach the lens. The photons which have the chance to reach and be captured by the lens (n_{tolens}) are at most half of the total photons emitted by the molecule:

$$n_{tolens} = \frac{1}{2} n_{emit} \tag{3}$$

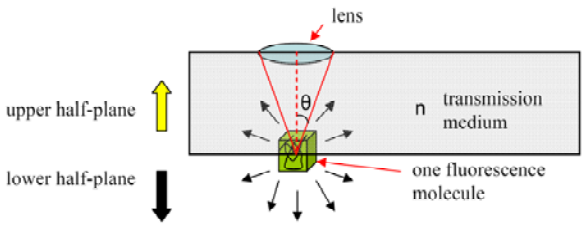

Figure 4. Illustration of the directions of photons emitted by the fluorescence molecule and that portion captured by the objective lens.

The numerical aperture (NA) represents the light collection ability of a lens, which is described as:

$$NA = n \bullet \sin\theta \tag{4}$$

in which θ is the acceptance angle of the lens, and n the index of refraction of medium through which the light must travel to reach the lens.

So θ can be described using NA and n as:

$$\theta = \arcsin\left(\frac{NA}{n}\right) \tag{5}$$

When θ equals to $\pi/2$, the lens will capture all the photons traveling towards the lens in the upper half-plane. The photon amount n_{lens} for the lens with an angle of θ can be calculated:

$$n_{lens} = \frac{\theta}{\pi/2} \bullet n_{tolens} = \frac{2\theta}{\pi} \bullet \frac{1}{2} n_{emit} = \frac{\theta}{\pi} n_{emit} = \frac{n_{emit}}{\pi} \arcsin\left(\frac{NA}{n}\right) \tag{6}$$

The photon capture efficiency ε of the lens is described in (7), and Fig. 5 shows the photon capture efficiencies using different mediums such as air (n = 1.0), water (n = 1.33) and oil (n = 1.51).

$$\varepsilon = \frac{n_{lens}}{n_{emit}} = \frac{1}{\pi} \arcsin\left(\frac{NA}{n}\right) \tag{7}$$

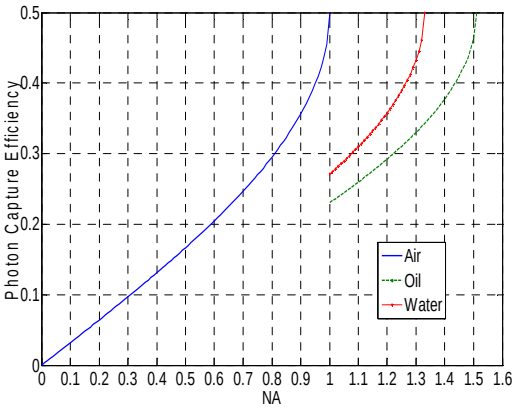

Figure 5. Photon capture efficiency: the photons captured by the lens compared to the photon emitted by the fluorescence molecules. If the medium through which the light must travel to reach the lens is air, n = 1, 0 ≤ NA ≤ 1; if water is used as the medium, n = 1.33, NA > 1; and if immersion oil is used, n = 1.51[3], NA > 1.

It is assumed that the transmission efficiency of the first lens, the dichroic mirror, the barrier filter, and the second lens are τ_{lens1}, τ_D, τ_B and τ_{lens2}, respectively. When the transmission coefficient of the camera window is τ_w, the fill factor is F, and the quantum efficiency is $\eta(\lambda)$, the photo-electrons which can be actually used by the camera will be n_e:

$$n_e = (\tau_{lens1}\tau_D\tau_B\tau_{lens2}\tau_w F\eta)\left(\frac{n_{emit}}{\pi}\right)\arcsin\left(\frac{NA}{n}\right) \tag{8}$$

Assuming the limiting case of Poisson noise, the SNR is given by:

$$SNR = \frac{\text{average}}{\text{std. deviation}} = \frac{\mu}{\sigma} = \frac{< n_e >}{\sqrt{< n_e >}} = \sqrt{< n_e >} \tag{9}$$

With g [ADU/e] as the electronic gain, the conversion of photo-electrons to A/D converter units N [ADU] is described by $N = g \bullet n_e$. $<N> = g<n_e>$, $\sigma(N) = g\,(<n_e>)^{1/2}$, so the SNR

remains the same. The ADC conversion factor does not reduce the fundamental SNR, but only the observed grey level dynamic range.

Using these equations, the photo-electrons which can be ultimately used by the MEM-FLIM can be calculated. We assume, for example, a NA = 1.4 objective lens with oil as the medium for which the index of refraction is n = 1.51. The quantum efficiency which depends on the wavelength is about $\eta(\lambda)$ = 35% when the wavelength is chosen to be 510 nm. We assume the fill factor F = 40%, the transmission efficiency of the dichroic mirror is τ_D = 90%, and that of the barrier filter is τ_B = 95% [4]. We assume the transmission of both lenses and the camera window are $\tau_{lens1} = \tau_{lens2} = \tau_w$ = 100% and the total number of photons that a single fluorescence molecule can emit is $n_{emit} \approx 30{,}000$. Then using (8), approximately 1357 photo-electrons can be obtained by the camera. The SNR before ADC conversion will be SNR = 1357/ $(1357)^{1/2} \approx$ 37:1. With an electronic gain for the camera of g = 0.126 [ADU/e^-] [5], the SNR as discussed above is still 37:1.

B. From Excitation to Emission

A comparable photon budget involving the light source required to excite a fluorescence sample is presented below to assist in choosing a suitable light source for MEM-FLIM.

Assuming we have an $a \times a$ pixels camera, the pixel size of the camera is b[m], and the magnification of the camera is M. Then the volume of the voxel we have at the specimen will approximately be V:

$$V \approx \left(\frac{b}{M}\right)^3 \quad [\mathrm{m}^3] \tag{10}$$

Assume there are m molecules per voxel. The fluorescence molecule concentration c will then be:

$$c = \frac{m}{\mathrm{N_A} \bullet V} = \frac{m}{\mathrm{N_A} \bullet \left(\frac{b}{M}\right)^3} \quad [\mathrm{mol/m}^3] \tag{11}$$

in which, $\mathrm{N_A}$ is Avogadro constant:

$$\mathrm{N_A} \approx 6.022 \times 10^{23} \ \mathrm{mol}^{-1}$$

We can collect a maximum of $n_{emit} \cdot m$ photons per voxel before bleaching. Allowing r recordings, n_{rec} photons can be used per recording as a maximum:

$$n_{rec} = \frac{n_{emit} \bullet m}{r} \tag{12}$$

As shown in Fig. 6, the absorbance over 1 voxel pathlength will be A, which is calculated in (10), when the fluorescence molecule has a molar extinction coefficient of ε [m^2/mol],

$$A = \varepsilon \bullet \frac{b}{M} \bullet c = \varepsilon \bullet \frac{b}{M} \bullet \frac{m}{\mathrm{N_A} \bullet \left(\frac{b}{M}\right)^3} = \frac{\varepsilon m M^2}{\mathrm{N_A} b^2} \tag{13}$$

We assume that excitation photons are $n_0(\lambda_{ex})$, the photons after absorption are $n_1(\lambda_{ex})$.

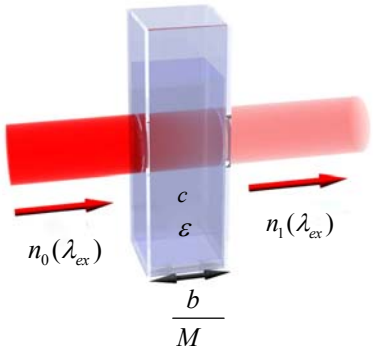

Figure 6. Absorbance over 1 voxel pathlength.

According to the Beer-Lambert law, we can calculate the photon amount ($n_0(\lambda_{ex})$) needed for excitation per voxel per recording:

$$\begin{cases} A = -\log_{10} \dfrac{n_1(\lambda_{ex})}{n_0(\lambda_{ex})} \\ n_1(\lambda_{ex}) = n_0(\lambda_{ex}) - n_{absorb}(\lambda_{ex}) \end{cases} \tag{14}$$

In which, $n_{absorb}(\lambda_{ex}) = n_{rec} = n_{emit} \bullet m / r$, then $n_0(\lambda_{ex})$ can be calculated below, which means we need $n_0(\lambda_{ex})$ excitation photon to obtain n_{absorb} absorbed excitation photons:

$$n_0(\lambda_{ex}) = \frac{1}{1-10^{-A}} \bullet \frac{m n_{emit}}{r} = \frac{m n_{emit}}{r\left(1-10^{-\frac{\varepsilon m M^2}{\mathrm{N_A} b^2}}\right)} \tag{15}$$

As shown in Fig. 2, the reflection efficiency of the dichroic mirror R_D, the transmission efficiency of the exciter filter τ_{EF}, and the transmission efficiency of the lens in the excitation path τ_{lens0} should also be considered. So the photons we need from the light source to get $n_0(\lambda_{ex})$ will be $n_{0source}$:

$$n_{0source} = \frac{n_0(\lambda_{ex})}{R_D \tau_{EF} \tau_{lens0}} = \frac{m n_{emit}}{r R_D \tau_{EF} \tau_{lens0}\left(1-10^{-\frac{\varepsilon m M^2}{\mathrm{N_A} b^2}}\right)} \tag{16}$$

If one recording takes T seconds, the maximum photons we have per second for illumination of the entire field of view, n_i:

$$n_i = \frac{a^2 n_{0source}}{T} = \frac{a^2 m n_{emit}}{R_D \tau_{EF} \tau_{lens0} r T \left(1 - 10^{-\frac{\varepsilon m M^2}{N_A b^2}}\right)} \quad (17)$$

If the light from the light source is of E_{ex} [J per photon], then with a power of the light source at W, the entire sample can be excited. The calculation of W is:

$$W = E_{ex} \bullet n_i = \frac{a^2 m n_{emit} E_{ex}}{R_D \tau_{EF} \tau_{lens0} r T \left(1 - 10^{-\frac{\varepsilon m M^2}{N_A b^2}}\right)} \quad (18)$$

For example, the total number of photons that a single EGFP fluorescence molecule can emit before photodestruction occurs is $n_{emit} \approx 30000$. Assume we have an $a \times a = 512 \times 512$ pixels camera, the pixel size of the camera is $b = 25 \times 10^{-6}$ [m], and the magnification of the microscope is $M = 100$. Assume there are $m = 10$ molecules per voxel. Then we have voxels of $(25 \times 10^{-6} / 100)^3 = 1.5625 \times 10^{-20}$ m^3. The fluorescence molecule concentration is then approximately $c = 1$ μM ($10 / 1.5625 \times 10^{-20} / N_a \approx 1 \times 10^{-3}$ mol/m^3 $= 1 \times 10^{-6}$ M). Allowing $r = 5$ recordings, $n_{rec} = 60000$ photons per recording can be used as a maximum.

EGFP [6] has a molar extinction coefficient of $\varepsilon = 55{,}000$ $M^{-1}cm^{-1}$. Absorbance $A = \varepsilon \cdot (b/M) \cdot c = 5.5 \times 10^4 \times 250 \times 10^{-7} \times 1 \times 10^{-6} = 1.375 \times 10^{-6}$ over 1 voxel pathlength. Using (11), we get:

$$\begin{cases} A = -\log_{10} \dfrac{n_1(\lambda_{ex})}{n_0(\lambda_{ex})} \\ n_1(\lambda_{ex}) = n_0(\lambda_{ex}) - 60000 \end{cases}$$

Solving the above equations, we find that $n_0(\lambda_{ex}) = 1.895 \times 10^{10}$ excitation photons per voxel per recording are needed to get 60,000 absorbed excitation photons.

We assume that the reflection efficiency of the dichroic mirror is $R_D = 95\%$, the transmission efficiency of the exciter filter is $\tau_{EF} = 95\%$ [4], and the transmission efficiency of the lens in the excitation path is $\tau_{lens0} = 100\%$. So the photons we need from the light source will be 2.100×10^{10}:

$$n_{0source} = \frac{n_0(\lambda_{ex})}{R_D \tau_{EF} \tau_{lens0}} = \frac{1.895 \times 10^{10}}{95\% \times 95\% \times 100\%} = 2.100 \times 10^{10}$$

If a recording takes 1 second, we have a maximum of $512 \times 512 \times 2.100 \times 10^{10} = 5.505 \times 10^{15}$ photons per second for illumination of the entire field of view. This means a perfect light source at 488 nm ($= 4.071 \times 10^{-19}$ J per photon) with a power of 2.2 mW is needed for excitation of the entire sample.

IV. CONCLUSION

In conclusion, our MEM-FLIM design eliminates the need for an image intensifier through the use of a high-quality application-specific CCD design. The proposed MEM-FLIM has the various advantages: (1) there is no need for high voltage source, (2) the entire signal is used during demodulation, (3) spatial resolution is limited only by optics and pixel dimensions, (4) there is no geometric distortion, and (5) it is compact and low cost. A quantitative analysis has been done concerning the photon budget in the proposed method which provides a helpful tool for design and fabrication of the proposed system.

REFERENCES

[1] J. Siegel et al., "Studying Biological Tissue with Fluorescence Lifetime Imaging: Microscopy, Endoscopy, and Complex decay Profiles," *Applied Optics*, 42, 2995-3004, 2003.

[2] A. Squire, P. J. Verveer and P. I. H. Bastiaens, "Multiple Frequency Fluorescence Lifetime Microscopy," *Journal of Microscopy*, 197, 136-149, 2000.

[3] http://www.microscopyu.com/tutorials/java/objectives/immersion/.

[4] http://www.semrock.com/Catalog/SetDetails.aspx?SetBasePartID=11.

[5] J. C. Mullikin, L. J. van Vliet, H. Netten, F. R. Boddeke, G. van der Feltz and I. T. Young, "Methods for CCD Camera Characterization," in: H. C. Titus, A. Waks (eds), SPIE vol. 2173, "Image Acquisition and Scientific Imaging Systems," 73-74, 1994.

[6] http://en.wikipedia.org/wiki/Green_fluorescent_protein.

Word Count: 1958

1A1-5

A Portable Electronic Nose System with Chemiresistor Sensors to Detect and Distinguish Chemical Warfare Agents

L.C. Wang[1], K.T. Tang[2,*], C.T. Kuo[3], C.L. Ho[4], S.R. Lin[4], Yuh Sung[4], C.P. Chang[5]

[1]*Department of Materials Science and Engineering, National Chiao Tung University, Taiwan*
[2]*Department of Electrical Engineering, National Tsing Hua University, Taiwan*
[3]*Institutes of Materials and Systems Engineering, Ming Dao University, Taiwan*
[4]*Physical Chemistry Section, Chung-Shan Institute of Science & Technology, Taiwan*
[5] *Department of Applied Chemistry &Materials Science, Chung Cheng Institute of Technology, National Defense University, Taiwan*

***Abstract* — Electronic nose has been studied as a means to realize artificial olfaction. Currently there are still only relatively large electronic nose "instruments", since the signal manipulation and classification are still done by a personal computer or a laptop. A portable electronic nose system based on hand-held machine has been developed by using the vapor detection array made of carbon black–polymer composites and the sensor circuit.**

In an effort to make a portable electronic nose, we used thin-film chemical sensors based on carbon black polymer nanocomposite to reliably detect chemical warfare agents. The use of FPGA to replace the PC has also been studied. The eNose system was exposed to dimethyl-methylphosphonate (DMMP) and DCMin part per million (ppm) concentration levels. DMMP and DCM were considered as stimulants of nerve agent-sarin, incapacitating agent-BZ gases, respectively.

Keywords —***Electronic nose, chemiresistor, chemical warfare agents (CWA)***

I. INTRODUCTION

Gas sensing and identification have found many applications, including indoor air quality monitoring, medical treatment and health care, security, food quality control [1…3], environment quality control [4, 5], diagnosis [6… 9], medical products, military applications, hazardous gas detection, etc. There is a need for an alternative method for gas sensing and recognition other than human beings. Researches for artificial olfaction have come a long way from the earliest mechanical nose by Moncrieff in 1961 [10] to today's electronic nose devices. Although several products are commercially available at present, there are additional needs for E-Nose system small enough to be carried or hand-held by an individual person [11]. Inspired by biology, the electronic nose uses an array of sensors to perform the task of odor sensing and classification. Since 1990, researches have been going on with several different kinds of electronic nose sensors, including conductivity sensors, piezoelectric sensors, MOSFETs, optical sensors, and spectrometry-based sensing methods. In this project, carbon-black conducting polymers are used as the sensors [12…16]. The sensitivity can reach the ppm range, the interfacing circuitry is relatively simple, and the response time can be as short as within 100ms depending on the polymer and the odor of interest. The greatest drawback of the conducting polymer sensor may be that it is too sensitive to humidity. For this reason, the interfacing circuitry must include an adaptation circuit that is capable of adapting to the background odor, responding to quick changes, and tuning out the variations with long time constants. Over the past 40 years, there have been efforts to build commercial electronic nose instruments with the size of a desktop, laptop, or palmtop. One of the reasons for these eNoses to be large in size is to perform odor signal manipulation and classification with the demanding computing power of CPU due to the complexity of the algorithms. But in many applications, an electronic nose may just be responsible for performing a relatively simple task, so it does not require a very complicated algorithm, and the demand of CPU with high computing power can be eased. Thus a portable electronic nose may be viable.

For this purpose, instead of using the PC, we report the use of FPGA on the fabrication of portable E-Nose system composed of a miniaturized sensor array, electrical and mechanical hardware, and data acquisition and pattern recognition software. This report also includes the test result of our FPGA eNose system.

II. EXPERIMENT

A. Single gas sensor array chip

Fig. 1(a) shows the sensor array chip fabricated by the photo mask process. This sensor chip has 12 independent sensing elements integrated on one single silicon substrate. Ten sensor array chips are fabricated on 4 in. Si wafer through the batch process. Fig. 1(b) shows one sensor array chip obtained by sawing the wafer. The array chip has the size of 100 mm ×30 mm. Each sensing element contains the square membrane with the area of 10mm×10mm in order to minimize heat loss into Si substrate.

B. Sensor Array

The carbon-black conducting polymer sensors used in our system are provided by Chung-Shan Institute of Science and Technology. According to the linear solvation energy relationship (LSER), eight polymers are selected as shown in Table I. The choices of different polymers for the sensor arrays are to enhance the capability of recognizing different odors. To

This project was funded by the National Science Council of Taiwan, under Contract No. NSC 97-2220-E-007-036 and Chung-Shan Institute of Science and Technology, under Contract No. CSIST-808-V110.

Contact author: for questions of this project please contact* ***kttang@ee.nthu.edu.tw.*

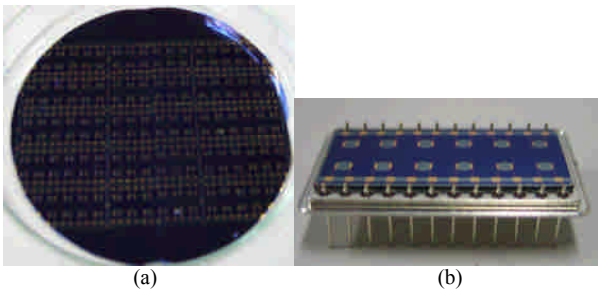

(a) (b)

Figure 1. The photos of sensor array

TABLE I. POLYMER MATERIALS USED IN THE ARRAY

Sensor No.	Sensor no. Polymer material
1	Poly(ethylene oxide)(PEO)
2	Ethyl cellulose(EC)
3	Poly(4-vinylphenol-co-methyl methacrylate)(PVCMM)
4	Polyethyleneimine(PEI)
5	Poly(vinylpropinoate)(PVPR)
6	Poly(epichlorhydrin)(PECH)
7	Poly(isobutylene)(PIB)
8	75%-phenyl-25%-methylpolysiloxane(OV25)

fabricate these sensors, polymers are dissolved in the solution, and then suitable percentage of conducting carbon-black is added to the solution. Uniform dispersion is achieved by magnetic stir and ultrasonic oscillation. Next, uniformly mixed composite material is injected with HPLC syringe onto the chip. Dissolvent is removed by 24-hour baking in the vacuum oven, and then the composite membrane material is formed.

C. *Experimental Setup*

Figure 2 shows the experimental setup used to characterize the sensing volatile organic compounds (VOCs) properties of the sensor devices. To perform the experiments, the sensor device is placed in a glass chamber. The gas under test is produced by a standard air generator (AID360). The organic solvent of the testing gas sits inside the diffusion tube of the standard air generator under room temperature. A constant heater is used to increase the temperature in the tube to cause the organic solvent to evaporate. By the time the whole system

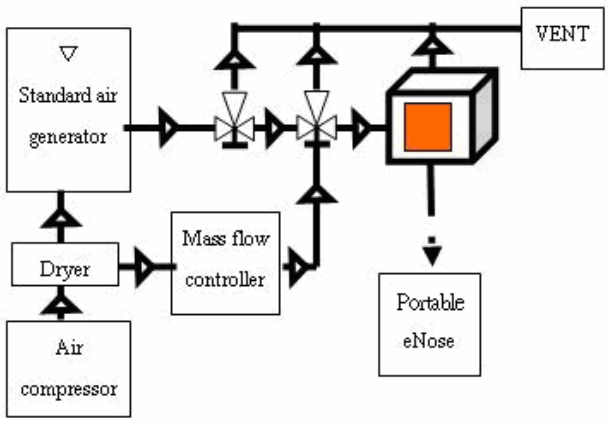

Figure 2. Experimental setup of the eNose system

reaches a steady state of temperature and flow rate, a testing gas with stable concentration can be achieved. By theory, the diffusion rate can be controlled by setting the temperature, and the air concentration can be accurately calculated by measuring the weight loss of the organic solvent. The testing gas is carried out by a steady air coming from the air compressor. The gas flow rate is controlled by the mass flow controller. The testing air is then infused into the glass chamber, where the array of the sensors sits. After completing the experiment, dry air is again used to purge the chamber. The output electric resistance of the sensors was measured by an electric resistance counter with the signals addressed by a multiplexer switch unit. The sensor array is wired to our eNose system outside the chamber to perform signal manipulation and odor classification. For each test, the testing air is infused into the chamber for 1800 seconds (absorption), and then dry air is infused for another 1800 seconds (desorption).

D. *Sensor Interface Circuitry*

Since the fabrication process of sensor cannot be easily controlled, the resistance of the sensor may vary from 10 kΩ to more than 1 MΩ. Thus an auto-adjustable biasing for the sensor is required. In addition, the sensor drifts with background odor, temperature variation, water vapor, etc. Thus the sensor interface circuitry must work in a way to respond to quick changes while tuning out long time constant variation, just like the biological nose. Then R_{max} / R_b information is extracted and converted into digital statistics through an A/D for further computation, storage, analysis, and recognition in the FPGA. A circuit implementation is in Fig. 3.

III. RESULTS AND DISCUSSION

A. *Result of gas sensing experiments*

To understand the absorption and desorption phenomenon of gas sensors, in this experiment the fabricated sensor device was placed inside the sealed chamber filled with chemical vapors of different concentrations produced by standard gas

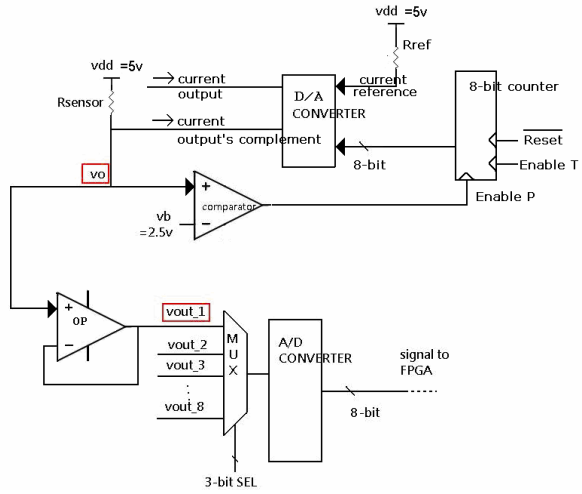

Figure 3. The circuits implemented in the sensor interface circuitry

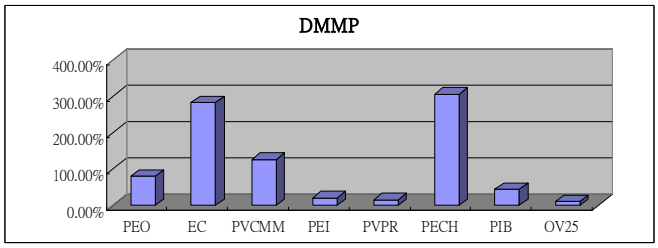

Figure 4. Bar chart of chemical warfare agent stimulant DMMP vs. the sensitivities of eight different polymer sensor membranes

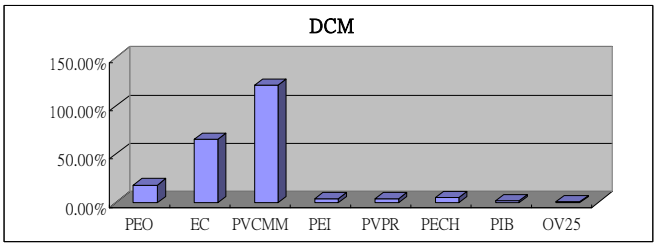

Figure 6. Bar chart of chemical warfare agent stimulant DCM vs. the sensitivities of eight different polymer sensor membranes

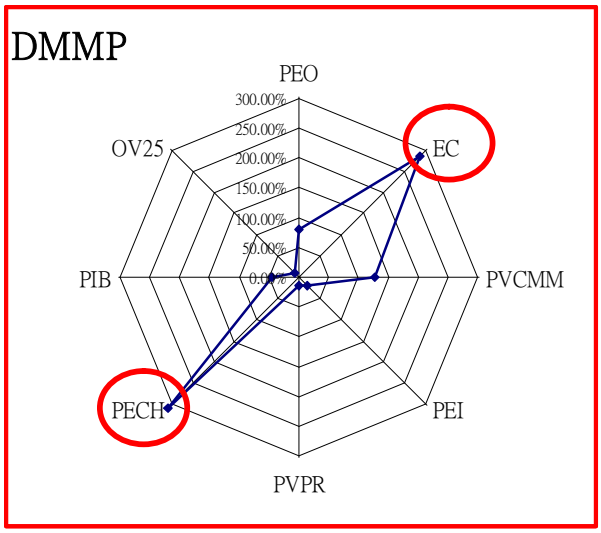

Figure 5. Radar chart of chemical warfare agent stimulant DMMP vs. the sensitivities of eight different polymer sensor membranes

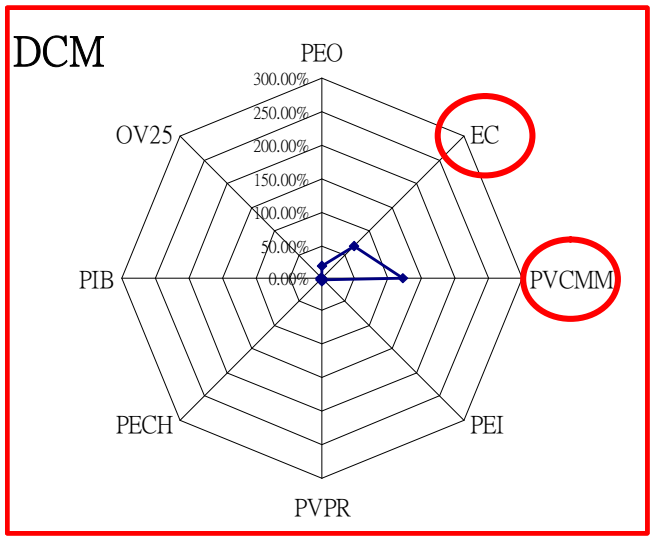

Figure 7. Radar chart of chemical warfare agent stimulant DCM vs. the sensitivities of eight different polymer sensor membranes

generator. The device was connected to the precise digital meter outside the sealed chamber through silver wires for the purpose of continuous monitoring of varying resistance. Once the resistance value became stable, the gas absorption experiment would be conducted for 1800 seconds. We should be able to observe the rise of resistance due to the absorption of gas molecules by polymer sensor membrane. Then dry air was infused into the chamber for 1800 seconds for conducting gas desorption experiment, and it should be observed that resistance dropped to original baseline. This procedure of gas absorption and desorption experiments would be repeated 3 times. Based on the experimental results we can compose bar charts and radar charts of sensor results of 3 kinds of chemical warfare agents stimulants and 8 kinds of polymer sensor membranes. (As shown in Fig. 4-9) From the bar charts we can tell that EC and PECH show greater response with respect to DMMP detection; EC and PVCMM show greater response with respect to DCM detection; PEO、EC and PVCMM show greater response with respect to AN detection. These results show that the 8 kinds of polymers selected by LSER formula are highly capable of distinguishing these three special gases. Plus, the pattern responses of these three kinds of chemical warfare agents' stimulants on radar charts are very different from each other. Choosing an appropriate sensor channel for initial gas classification is proved to be very helpful for following classification experiments. In addition, the response time is found to be very fast: the rise time of ~30 s and the decay time of ~60 s, where the rise and the decay time is defined by the time needed for the signal to reach 90% of the peak maximum and to reduced to 10% of the peak maximum, respectively.

B. The use of Principal Component Analysis to identify all kinds of gases

We use two major approaches to conduct gas classification in this research. The first approach is to use principal component analysis for calculation on PC or Laptop. The second approach is to use FPGA circuits to conduct direct classification to avoid the need for other computer equipments and to reach our eventual goal of reducing the size of the overall sensor system. We already know that eventually we will have to deal with the choice of channel characteristics in the research of designing multi-channel sensor array. The principal component analysis method can change many correlated channels (variables) into fewer numbers of independent linear combination variables. This way we can maximize the component variance obtained through linear combination, and allow the tested gas to show maximum difference among channels of different components. If we analyze the experimental results of three different chemical

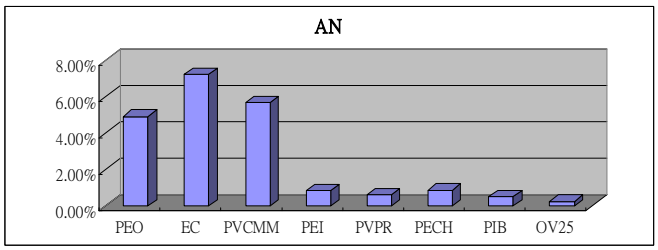

Figure 8. Bar chart of chemical warfare agent stimulant AN vs. the sensitivities of eight different polymer sensor membranes

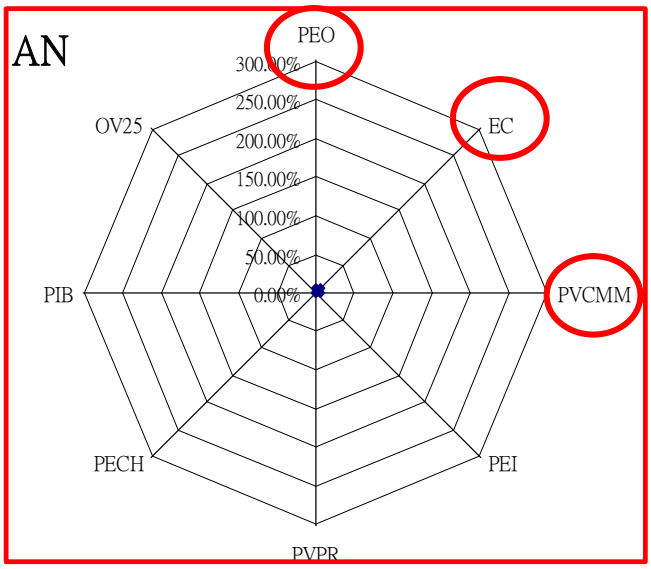

Figure 9. Radar chart of chemical warfare agent stimulant AN vs. the sensitivities of eight different polymer sensor membranes

warfare agents stimulants vs. eight different polymer membranes through principle component analysis method, as shown in Fig. 10, the results fall on different locations on the coordinates that are far apart. Therefore, the successful classification is easily confirmed by simply glancing at the plots obtained by PCA analysis. Fig. 10 show the recognition boundaries of the three stimulates in PCA plots displayed with the two main principal axes of PC1 and PC2. They clearly demonstrate that the two liquors have well-defined boundaries.

C. The use of FPGA system

By forming an array of sensors, a signal vector containing information about the odor is obtained. This signal vector is then sent to FPGA for signal processing. In our FPGA eNose system, we use the Altera DE2 Board (Type DK-DE2-2C35N/UN-0A) to perform the designed tasks. Altera DE2 uses Verilog and runs simulation under the ModelSim environment. There are four tasks that the FPGA is designed to perform.

1) Steady State Detection: The signal vector is constantly sent to FPGA, thus the first function of the steady state detection block is to recognize whether or not there is an odor coming in. This is achieved by scanning the sensor signal throughout the array and comparing it with a threshold. As

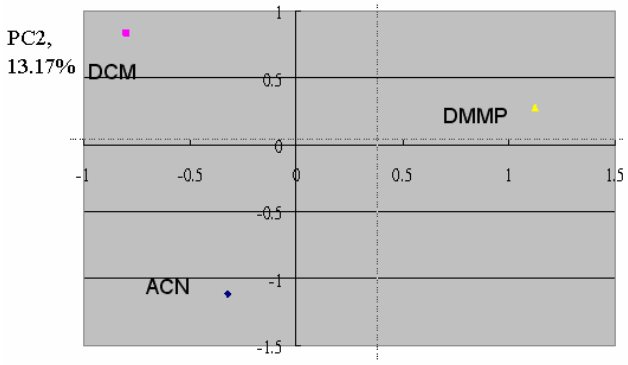

Figure 10. The analysis of three chemical warfare agents stimulants through principle component analysis method

long as one of the channels in the array exceeds the threshold, the system should recognize it as an odor coming in and activate all the circuits. Once the system activates all the circuits, the steady state detection block must detect when the sensor responses reach equilibrium. This is done by monitoring the sensor signals throughout the array with respect to its previous state. If all the sensor signals do not change for a fixed time, the system should report steady-state and go to the next step.

2) Normalization: The signal vector must be normalized before further processing since the odor concentration is usually unknown. It has been reported that the sensor response is linearly proportional to the vapor concentration [17]. There are many ways to perform normalization, for example, Euclidean distance normalization; city-blocks distance normalization, maximum normalization, etc. In our FPGA eNose system, we adopt the Euclidean distance normalization.

3) Learning State: If the FPGA eNose system is in the learning state, the normalized signal vector is stored in the memory as data vector.

4) Classifying State: If the FPGA eNose system is in the classifying state, the normalized signal vector is compared with all the data vectors in the memory, and classification is performed. There are many algorithms for classification, for example, nearest neighbor, SVM, PCA, DFA, etc. We implement the nearest neighbor classifier in our FPGA eNose because of its simplicity and good performance for odors that do not have very similar patterns. After the classification is done, the FPGA will demonstrate the result on the LED display. After the odor signatures of DCM and DMMP are recorded in the memory, the eNose FPGA system is switched into its classifying state. In the experiment, the system is tested 6 times. For the six tests, the FPGA eNose system was capable of recognizing both DCM and DMMP.

IV. CONCLUSIONS

Most of the researches regarding eNose system are limited to developing a gas sensor system controlled by PC or PDA. In our research we successfully used FPGA circuits to replace

fore-mentioned control instruments and successfully completed the experiments of detection and classification of three special gases. This can be very helpful to following development of integrated gas sensing circuit chip with the "system-on-chip" design.

ACKNOWLEDGMENT

The authors would like to acknowledge the support of the National Science Council of Taiwan, under Contract No. NSC 97-2220-E-007-036. We also acknowledge the support of the Chung-Shan Institute of Science and Technology, under Contract No. CSIST-808-V110. We also thank the National Chip Implementation Center for technical support.

REFERENCES

[1] E. Llobet, E. L. Hines, J. W. Gardner, and S. Franco, "Non-destructive banana ripeness determination using a neural network-based electronic nose," in Measurement Science and Technology, vol. 10, 1999, pp. 538–547.

[2] E. L. Hines, E. Llobet, and J. W. Gardner, "Neural network based electronic nose for apple ripeness determination",in Electronics Letters, vol. 35, 1999, pp. 821–822.

[3] C. Di Natale, A. Macagnano, E. Martinelli, R. Paolesse, E. Proietti, and A. D'Amico, "The Evaluation of Quality of Post-harvest Oranges and Apples by Means of an Electronic Nose", in Sensors and Actuators, vol. B78, 2001, pp. 26–31.

[4] J. W. Gardner, H. W. Shin, E. L. Hines, and C. S. Dow, "An electronic nose system for monitoring the quality of potable water", in Sensors and Actuators, vol. B69, 2000, pp. 336–341.

[5] H. W. Shin, E. Llobet, J. W. Gardner, E. L. Hines, and C. S. Dow, "Classification of the strain and growth phase of cyanobacteria in potable water using an electronic nose system", in IEE Proceedings-Science Measurement and Technology, vol. 147(4), 2000, pp. 158–164.

[6] J. W. Gardner, M. Craven, C. Dow, and E. L. Hines, "The prediction of bacteria type and culture growth phase by an electronic nose with a multi-layer perception network", in Measurement Science and Technology, vol. 9, 1998, pp. 120–127.

[7] J. W. Gardner, E. L. Hines, F. Molinier, P. N. Bartlett, and T. T. Mottram, "Prediction of health of dairy cattle from breath samples using neural network with parametric model of dynamic response of array of semiconducting gas sensors", in IEE Proceedings-Science Measurement and Technology, vol. 146(2), 1999, pp. 102–106.

[8] J. W. Gardner, H. W. Shin, and E. L. Hines, "An electronic nose system to diagnose illness", in Sensors and Actuators, vol. B70, 2000, pp. 19–24.

[9] Y. –J. Lin, H. –R. Guo, Y. –H. Chang, M. –T. Kao, H. –H. Wang, and R. –I Hong, "Application of the Electronic Nose for Uremia Diagnosis", in Sensors and Actuators B vol. 76, 2001, pp. 177–180.

[10] R. W. Moncrieff, "An instrument for measuring and classifying odours", in J. Appl. Physiol., vol. 16, 1961, pp. 742.

[11] H. T. Chueh, J. V. Hatfield, "A real-time data acquisition system for a hand-held electronic nose (H2EN)", Sens. Actuators B 83 (2002) 262–269.

[12] T. C. Pearce, J. W. Gardner, S. Friel, P. N. Bartlett, and N. Blair, "Electronic nose for monitoring the flavour of beers", in Analyst, vol. 118, 1993, pp. 371–377.

[13] K. C. Persaud, "Electronic gas and odour detectors that mimic chemoreception in animals", in Trends Anal. Chem., vol. 11, 1992, pp. 61–67.

[14] J. M. Slater, J. Paynter, and E. J. Watt, "Multi-layer conducting polymer gas sensor arrays for olfactory sensing", in Analyst, vol. 118, 1993, pp. 379–384.

[15] M. S. Freund, and N. S. Lewis, "A chemically diverse conducting polymer-based electronic nose", in Proc. Natl. Acad. Sci., vol. 92, 1995, pp. 2652.

[16] Y.S. Kim, S. C. Ha, Yoonseok Yang, Y. J. Kim, S. M. Cho, H. Yang, Y. T. Kim, "Portable electronic nose system based on the carbon black–polymer composite sensor array", Sensors and Actuators B 108 (2005) 285–291

[17] Doleman, B.J.; Lonergan, M.C.; Severin, E.J.; Vaid, T.P.; Lewis, N.S. Anal. Chem. 1998, 70, 4177.

1A1-6

Measurement of blood pressure using magnetic method of blood pulse acquisition

Chee Teck Phua[1] Gaëlle Lissorgues[2]

[1]*School of Engineering (Electronics), Nanyang Polytechnic, Singapore*

[2]*ESIEE – ESYCOM , University Paris Est, France*

***Abstract* — Current cuffless method of Arterial Blood Pressure (ABP) measurements can be continuously calculated from pulse wave velocity and the Pulse Transit Time (PTT). PTT is usually recorded as the time delay from the R wave of Electrocardiographic (ECG) signal to the upstroke of a peripheral pulse wave signal measured using Photoplethysmographic (PPG) sensors or alternatively from the sound of Phonocardiographic (PCG) signal. This paper proposes an alternative novel method of measuring the magnetic disturbance, using a Giant-Magneto-Resistance (GMR) based sensor, created by blood flow in a uniform magnetic field for peripheral pulse wave signal measurements allowing an optical independent measurement system for ABP. The magnetic disturbance created by blood flow in a uniform magnetic field allows for the sensing of the peripheral pulse wave... Measurements were done on 10 subjects aged between 22 to 25 years old where the ABP measured using the PTT correlates well within 8% error with respect to the Mean Arterial blood Pressure (MAP) measured from commercially available cuff based automated ABP measurement devices.**

Keywords — ***blood pressure, blood flow, biomagnetic, magnetic disturbance***

I. INTRODUCTION

Blood pressure measurement devices have become increasingly popular during the last decade as prices of these measurement devices have sunk to an appropriate level for ordinary consumers. The incorporation of automatic measurement features and ease of use have also contributed to the growing popularity of blood pressure measurement devices as a lifestyle device. However, such measurements devices are typically cuff based and based on indirect Blood Pressure (BP) measuring method using the detection of Korotkov-sounds. This method had been used for more than 100 years and has two major deficiencies. Firstly, the cuff grossly affects the measured parameter. Secondly, the method determines the blood pressure only at a single point of time. Oscillometric methods, applied in automatic home BP-meters, apart from the aforementioned inadequacies, has also a built-in uncertainty, where it empirically calculates the systolic and diastolic values from the measured mean pressure.

Tonometry is, however, a very different approach. Although a pressure is applied to the artery to press it against the bone, the pressure is not as strong as to completely occlude the artery. Rather, the pressure is maintained at a level that counteracts the circumferential tension of the arterial wall. Therefore, it is sometimes named the "vascular unloading" technique [1]. Since Tonometry is to be applied to the peripheral circulation, an algorithm is often used to estimate arterial BP from the recorded pressure.

Although these automatic BP meters can provide objective BP readings, all of them, like the conventional mercury sphygmomanometer, incorporate the use of a cuff in their working principles. In addition, the size of the cuff must not be too small since overestimation of BP by using an inappropriate small cuff has been well documented [2]. This renders the reduction of size, cost and power consumption in these devices difficult. Moreover, the occlusion of the artery increases the workload of the heart and causes circulatory interference at the measurement site. Therefore, they are not preferred for situations that require frequent measurements.. Compared to the cuff-based approaches, a cuff-less technique would be more desirable [3].

Researchers have long reported that Pulse Transit Time (PTT) is directly related to ABP and can be used as an index for the beat-to-beat BP estimation [4]-[6]. Typical PTT is the measured using the time difference between the R-wave peak of Electrocardiogram (ECG) and maximum slope of the finger Photoplethysmogram (PPG) as shown in Figure 1. However, the use of the finger PPG will require continuous optical contact with the skin on the finger and is restrictive for daily activities as the finger is covered.

In this paper, the magnetic method of blood pulse acquisition [8] is explored. The Giant-Magneto-Resistance (GMR) based sensor was applied on the wrist in place of the finger PPG. The peripheral pulse wave is sensed and used to compute the ABP. The objective in this approach is to provide the basis for the development of devices that are capable of continuous blood pressure acquisition, which is unrestrictive and allows for daily activities of the monitored subjects.

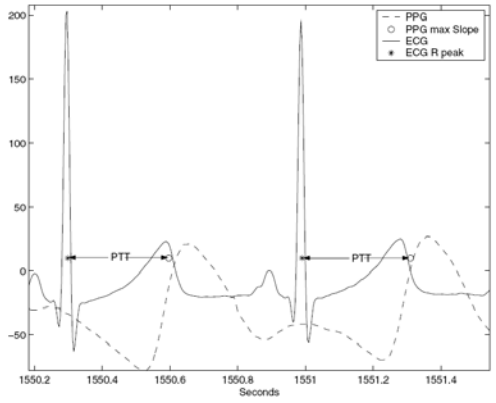

Figure 1. Illstration of PTT Definition [6]

II. EXPERIMENTAL SETUP

A. ABP measurement using oscillometric based BP meter

There are many commercially available cuff based blood pressure monitoring devices which are designed for lifestyle applications. In this experimental setup, the OMRON Intellisense Blood Pressure Monitor - Arm Model IA1/IA1B is used for acquisition of blood pressure. The setup is typically as shown in Figure 2.

Using this setup, 10 young volunteers, aged between 22 to 25 years are recruited as test subjects for this experiment. The blood pressure measured results are shown in Table I. The Systolic (SYS) and Diastolic (DIA) pressure can be associated to the heart activities that occur during heart contraction, the blood pressure in the artery increases from diastolic to systolic blood pressure. The difference between these pressures is called pulse pressure. Normal blood pressure occurs when the systolic pressure is less than 130 mmHg and diastolic blood pressure is less than 80 mmHg for adults [11].

Mean arterial pressure (MAP) is the mean pressure over one cardiac cycle. Using equation (1) [9], the MAP can be calculated. This is also tabulated in Table I and is the parameter used for comparison with other measurements for BP, reported in the next section.

$$MAP = P_{DIA} + \left(\frac{P_{SYS} - P_{DIA}}{3}\right) \quad (1)$$

where PDIA = Diastolic pressure in mmHg
PSYS = Systolic pressure in mmHg

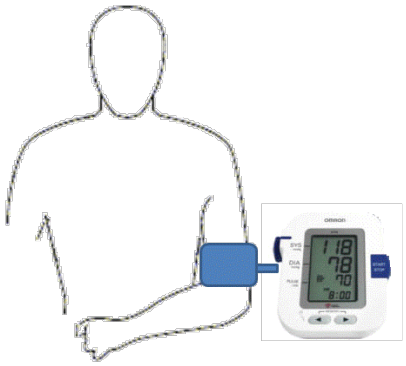

Figure 2. Experiment setup using OMRON Intellisense Blood Pressure Monitor - Arm Model IA1/IA1B

Name	SYS (mmHg)	DIA (mmHg)	PULSE/min	MAP (mmHg)
Subject 1	130	65	75	86.66666667
Subject 2	110	67	62	81.33333333
Subject 3	116	69	45	84.66666667
Subject 4	132	71	64	91.33333333
Subject 5	97	65	82	75.66666667
Subject 6	113	73	85	86.33333333
Subject 7	112	74	74	86.66666667
Subject 8	161	90	88	113.6666667
Subject 9	129	81	59	97
Subject 10	104	63	78	76.66666667

TABLE I. TABULATED BP-METER MEASUREMENTS WITH CALCULATED MAP

B. ECG and MMSB measurements

The alternative and new experiment for acquisition of blood pressure is based on the magnetic method of pulse acquisition using MMSB [8]. The experimental setup is shown in Figure 3. Here, the signals from the ECG electrodes and the MMSB are concurrently sampled and processed using the gTEC USBAmp. The data from these two channels are post-processed using a MATLAB Simulink model (see Figure 4). The typical waveform obtained from the Simulink model is shown in Figure 5.

Using equation (2) obtained from reference [7], the MAP is estimated based on PTT (Figure 5), the distance d (Figure 6) and the relative height h (Figure 3).

$$BP = \frac{1}{0.7}\left(\frac{1}{2}\rho\frac{d^2}{PTT^2} + \rho g h\right) \quad (2)$$

where BP = blood pressure or MAP
ρ = density of blood, 1035 kg/m^3
g = 9.81m/s^2
h = height difference between heart and wrist
d = distance from heart to wrist
PTT = Pulse transit time

As may be noted from Figure 5, the PTT is measured from the peak of the R-wave to the maximum slope of the MMSB signal. These values are tabulated in Table II for each of the ten volunteer subjects.

In addition, the arterial loop distance d between the heart and the wrist (where the MMSB signal is acquired) is also measured as illustrated in Figure 5 and tabulated in Table II.

The relative height parameter, h, (Figure 3) that appears in equation (2), ranges between 7cm to 9cm for all the subjects in this experiment. As such, the mean value h = 8cm is adopted for all ten subjects.

It is to be noted that all the measurements were done while the subject is in a sitting position with their arm rested on their upper leg. The subject volunteers for these measurements happened to be of similar build and height. There would be inaccuracies in fixing h as a constant. This can however be overcome by taking measurements at the level of the heart and at two other differential relative heights. These measurements would be sufficient to characterize the linear dependence of the hydrostatic pressure due to h on MAP.

The computations for MAP as per equation (2), based on the above considerations for d, h and PTT measurements, are tabulated in Table II.

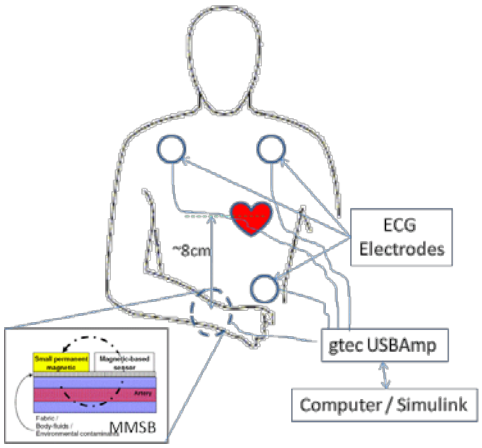

Figure 3. Experimental setup used for PTT measurements using MMSB and ECG

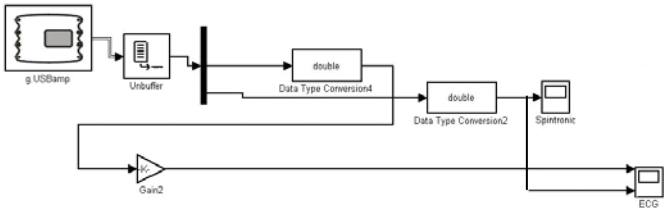

Figure 4. MATLAB Simulink model for data acquisition from gtec USBAmp

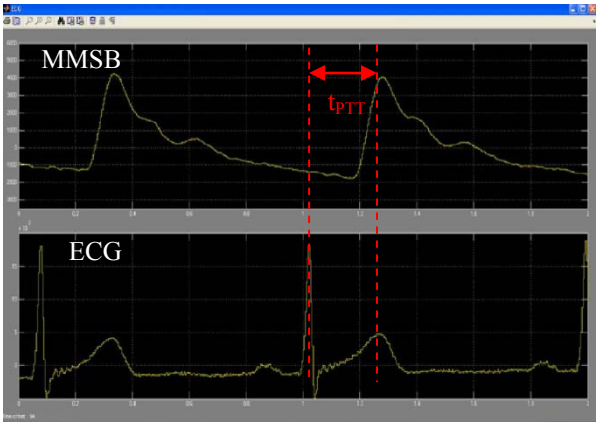

Figure 5. Waveform for ECG and MMSB signal with PTT measurement

Figure 6. Illustrations of distance measurements from heart to wrist

Name	Distance from heart to wrist (cm)	Pulse Transit Time (sec)	Estimated MAP (mmHg)
Subject 1	81	0.22	83.88583005
Subject 2	75	0.21	79.44521816
Subject 3	77	0.215	79.84059794
Subject 4	85	0.225	87.85578776
Subject 5	75	0.225	70.32759618
Subject 6	74	0.19	92.83262885
Subject 7	78	0.2	93.06015432
Subject 8	71	0.17	105.4439198
Subject 9	84	0.21	97.44151752
Subject 10	77.5	0.23	71.67449735

TABLE II. MEASUREMENT RESULTS FOR DISTANCE FROM HEART TO WRIST AND PTT WITH MAP ESTIMATED USING MEASURED DATA

III. RESULTS AND DISCUSSIONS

The measured MAP (using the classical BP-meter, Table I) and the estimated MAP (MMSB) from Table II are compared and tabulated in Table III. A plot of the tabulated results is also shown in Figure 7 to illustrate the coherent trend in the signal acquired for the two MAP plots.

The percentage difference between measured (BP-meter) and estimated (MMSB) MAP as observed from Table III is seen to be less than 8%.

The difference in MAP data can be attributed to the assignment of h as a constant. The uncertainty contributed for each of the variables in (1) is shown in (3), where h is a variable, and in (4), where h is a constant. Uncertainty with h as a variable:

$$\frac{\Delta MAP}{MAP} = \sqrt{\left(\left[2\frac{\Delta d}{d}\right]^2 + \left[2\frac{\Delta PTT}{PTT}\right]^2 + \left[\frac{\Delta h}{h}\right]^2\right)} \quad (3)$$

Uncertainty with h as a constant:

$$\frac{\Delta MAP}{MAP} = \sqrt{\left(\left[2\frac{\Delta d}{d}\right]^2 + \left[2\frac{\Delta PTT}{PTT}\right]^2\right)} \quad (4)$$

Assuming each of the variable $\frac{\Delta d}{d}$, $\frac{\Delta PTT}{PTT}$ and $\frac{\Delta h}{h}$ has equal contributions to the uncertainty of MAP, the unaccounted uncertainty of selecting h as a constant can contribute up to 6% of the MAP values obtained using PTT measurements from MMSB waveform.

Therefore, the results obtained from these experiments have provided sufficient evidence that the use of MMSB in place of PPG for PTT measurements is feasible.

Name	MAP (mmHg)	Estimated MAP (mmHg)	% Difference between measured and estimated MAP
Subject 1	86.66666667	83.88583005	-3.21%
Subject 2	81.33333333	79.44521816	-2.32%
Subject 3	84.66666667	79.84059794	-5.70%
Subject 4	91.33333333	87.85578776	-3.81%
Subject 5	75.66666667	70.32759618	-7.06%
Subject 6	86.33333333	92.83262885	7.53%
Subject 7	86.66666667	93.06015432	7.38%
Subject 8	113.6666667	105.4439198	-7.23%
Subject 9	97	97.44151752	0.46%
Subject 10	76.66666667	71.67449735	-6.51%

TABLE III. TABULATED RESULTS FOR MEASURED MAP USING BP METER WITH ESTIMATED MAP USING PTT MEASUREMENTS

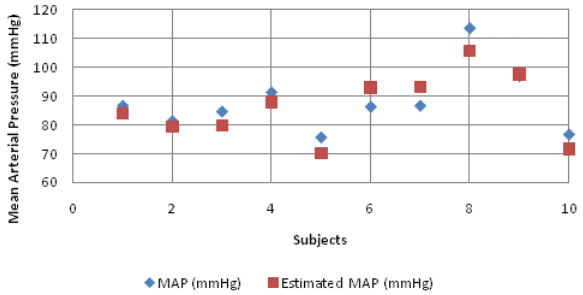

Figure 7. Plot of MAP and Estimated MAP using PTT measured from MMSB and ECG measurements

IV. CONCLUSION

The application of MMSB to acquire PTT at the wrist of monitored subjects, in place of the PPG at the finger, should be more convenient for the continuous monitoring of physiological signs such as the blood pressure. The result of such an acquisition is qualitatively and quantitatively assessed using the waveform (Figure 5) and the computation of MAP as shown in Table III and Figure 7.

From the waveform (Figure 5), the ease of identifying the measurable PTT value with respect to PPG method is illustrated. In addition, the measured and calculated MAP data using PTT obtained using MMSB shows good correlations with errors of less than 8% with respect to the measurements obtained from the use of the classical BP-meter.

With the successful completion of MMSB for measurement of blood pulse transit time, further work will focus on the development of wearable devices based on MMSB for heart rate and relaxation analysis.

ACKNOWLEDGMENT

The authors would like to thank Nanyang Polytechnic of Singapore and ESIEE, France for the opportunity to work on this development. In particular, the authors would like to express their gratitude to the School of Engineering (Electronics), Nanyang Polytechnic (Singapore) for the usage of facilities that supported this work.

REFERENCES

[1] J. Penáz, "Photo-electric measurement of blood pressure, volume and flow in the finger," Digest of the 10-th Int. Conf. on Medical and Biol. Eng., pp. 104, 1973.

[2] The Sixth Report of the Joint National Committee on Prevention, Detection, Evaluation, and Treatment of High Blood Pressure. National Institutes of Health, the U.S.A., Publication No. 98-4080, Nov. 1997.

[3] C.C.Y. Poon and Y.T. Zhang, "Cuff-less and noninvasive measurements of arterial blood pressure by pulse transit time," in Proc. 27th Annu. Int. Conf. IEEE Engineering in Medicine and Biology Society, Shanghai, P.R.C., 1-4 Sept., pp. 5877-5880, 2005.

[4] B. Gribbon, A. Steptoe and P. Sleight, "Pulse wave velocity as a measure of blood pressure change," Psychophysiology, vol 13, pp. 36-90, 1976.

[5] L. A. Geddes, M. H. Voelz, C. F. Babbs, J. D. Bourland and W. A. Tacker, "Pulse transit time as an indicator of arterial blood pressure," Psychophysiology, vol. 18; pp.71-74, 1981.

[6] W. Chen, T. Kobayashi, S . Ichikawa, Y. Takeuchi and T. Togawa, "Continuous estimation of systolic blood pressure using the pulse arrival time and intermittent calibration," Med. & Bio. Eng. Computing, vol. 38, pp. 569 -574.

[7] Parry Fung, Guy Dumont, Craig Ries, Chris Mott, Mark Ansermino, "Continuous Noninvasive Blood Pressure Measurement by Pulse Transit Time", Proceedings of the 26th Annual International Conference of the IEEE EMBS, Sept 1-5, 2004.

[8] Chee Teck Phua, Gaëlle Lissorgues, Bruno Mercier, "Noninvasive acquisition of Blood Pulse using magnetic disturbance technique", International Conference on BioMedical Engineering (ICBME2008)

[9] Yinbo Liu, Y.T. Zhang, "Pulse Transit Time and Arterial Blood Pressure at Different Vertical Wrist Positions", ITAB 2006

[10] J. Keener and J. Sneyd, Mathmatical Physiology. New York, USA: Springer-Verlag, 1998.

[11] Bates B (1995) A Guide to Physical Examination, 6th edition, J.B. Lippingcott Company, Philadelphia, USA.

2A1-2

Fast DNA Hybridization Chip by Controling Temperature and Velocity of Nucleic Acids

Yung-Chiang Chung[1], Yu-Cheng Lin[2], Wei-Chieh Liao[1], Po-Wen Chen[1], Fong-Jian Sie[1], and Chia-Ming Hu[1]

[1]*Graduate School of Mechanical-Electro Engineering, Ming Chi University of Technology, Taiwan*
[2]*Department of Engineering Science, National Cheng Kung University, Taiwan*

***Abstract* — We demonstrate that the efficiency of DNA hybridization could be improved by introducing elevated temperature in the hot region and higher velocities in the cold region of a microfluidic chip. Compared with the conventional methods, this hybridization microchip was shown to increase the hybridization signal 4.6-fold within 30 minutes using a 1.4 kb target DNA as the test material. The increase in fluorescence intensity was apparent when the temperature was higher than 82°C, and the fluorescence intensity reached an asymptotic value as T > 90°C. A mathematical model was proposed to relate the fluorescence intensity of DNA hybridization with the temperature of hot region and the velocity of cold region. Based on these results, the new hybridization chip with the processes of temperature and velocity differences will provide additional efficiency in DNA detection.**

***Keywords* —hybridization, temperature, velocity, microfluid**

I. INTRODUCTION

DNA hybridization has become a commonly used technique in DNA sequencing and analysis [1-3]. Various methods have been reported for decreasing the nucleic acid hybridization time in the past few years. The hybridization rates were enhanced by using high-density arrays [4], electric field [5], and chemically improving methods including volume exclusion agents or precipitating reagents [6]. Previously, we demonstrated that the effect of extensional strain rate was larger than that of velocity on the hybridization reaction [7]. A lateral convective flow past the chip surface was induced, thus reducing the analysis time to 10 to 30 minutes [8]. Various hybridization detection methods to amplify the hybridization signals and reduce the hybridization time had been reported, including the electrochemical approaches to nucleic acid detection [9, 10], labeling of DNA with metal nanoparticles [11] and the mediated catalytic oxidation of guanine in DNA strands [12, 13]. A fiber-optic DNA microarray using microsphere-immobilized oligonucleotide probes was developed, and the hybridization time reached a plateau after 30 minutes [14]. Redox polymer mediator and DNA probe sequences on gold electrodes could eliminate nonspecific interaction, and the sensor response increased linearly with increasing concentration of target DNA [15]. Magnetic nanoparticles were applied in electrochemical detection, and could be used to control the DNA hybridization process [16]. The simultaneous multicolor array hybridization of eight samples provided a 4-fold increase in throughput over standard two-color assays [17].

II. METHOD AND DESIGN

Two factors are used to affect the DNA hybridization. The first factor is increasing the velocity of the target DNA, the second factor is increasing the temperature of the target mixture in the hot (denature) region, as shown in Figure 1. The long target molecules, oligonucleotide or single-stranded DNA, may coil up due to the intra-molecular bonds. Here, the elevated temperature (T) was introduced to break the intra-molecular bonds of the targets prior to the hybridization process. The probes are located along the channel in the cold (hybridization) region. If the temperature is higher than some critical value, it will cause the DNA intra-molecular bonds to break. Thus, the devices were designed to generate different temperatures in the hot region and velocities in the cold region along the channel to test the hybridization efficiencies.

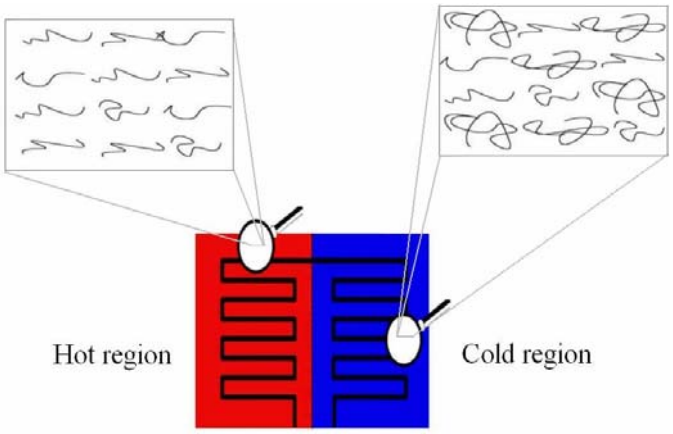

Figure 1. Mechanism of DNA stretch caused by the high temperature.

The hybridization chip included a glass slide with probes and a micro-reactor with flow channels, as shown in Figure 2. The distances between heater route turns were placed uniformly in the micro-heater. The temperature of the cold (hybridization) region was set to be 42°C, and the temperatures of the hot (denature) region were set to be different values varying from 42°C to 94°C. The hybridization reaction region was designed as a channel shape to avoid bubble generation. There was a uniform channel with the width of 500 μm and the depth of 300 μm in the device. The channel was fabricated by CNC engraving and milling machine. The channel design of the device with the probe locations is also shown in Figure 2(a). A structure of the micro-reactor was used to get the different temperatures in the cold and hot regions, shown in Figures 2(b). The heater and sensor in the micro-reactor were designed at the

backside of the channel. The trench in the bottom glass slide that was near the heater and sensor could decrease heat transfer path length. The distance between probe positions in each column was the same, and the diameter of each probe was 300 μm.

The substrate of the micro-reactor was Pyrex 7740 glass, and the fabrication process of the micro-reactor is sequential. First, the photoresist was used as sacrificial layer. Second, the heater and sensor were patterned using exposure and development. Third, 20 nm chromium and 200 nm platinum were sequentially sputtered. Fourth, the lift-off process was used to remove the sacrificial layer and unwanted parts. The temperature coefficient of resistance (TCR) relation of the micro-heater was nearly a straight line (R-square = 0.93) with a slope of 25 ohm/°C. Finally, the probe-spotted glass and the micro-reactor with flow channel were clamped by a clip to form the device.

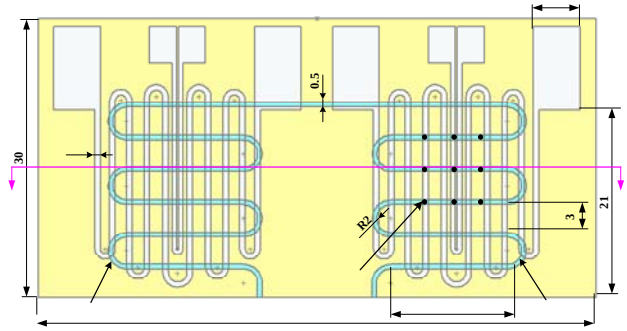

Figure 2. (a) Layout of the hybridization chip, the dots on the channel are the locations of probes, (b) Schematic drawing of the cross-section A-A' in (a). (unit: mm)

A pneumatic pump controlling system [18] was connected to the device and generated the oscillations of the sample solution. The solution flowing processes from hot region (T_2) to cold region (T_1) are schematically illustrated in Figure 3. First, the solution remained in the hot region for 1 min, Figure 3(a), after it reached the chosen temperature. A chosen temperature in the hot region represented an independent experiment. Second, the solution was pumped to the cold region, as shown in Figure 3(b). Third, the solution was actuated back and forth for 2 min at a bulk flow velocity by a pump for hybridization in the cold region, shown in Figure 3(c) and (d), and it would not move to the hot region in this time (2 min). The results were almost the same when the time was more than 1 min, so the conditions were chosen. It was the first cycle, and the used time was about 3 min. After that, the solution was pumped to the hot region and remained there for 1 min, and then was actuated to the cold region, and flowed forward and backward for 2 min again. It was the second cycle. Finally, it totally repeated 15 cycles, so the hybridization time was about 30 min. This was referred to the control condition when the flow condition was static and the temperature of the sample solution was always 42°C. In this study, the bulk flow velocities in the cold region were set to be different values, varying from 0 cm/s to 3.0 cm/s.

After the hybridization, the results needed to be analyzed qualitatively and quantitatively. A scanner (ScanArray 4000, GSI Lumonics, USA) was used to scan and analyze the hybridization results, which are shown in the images and fluorescence intensities.

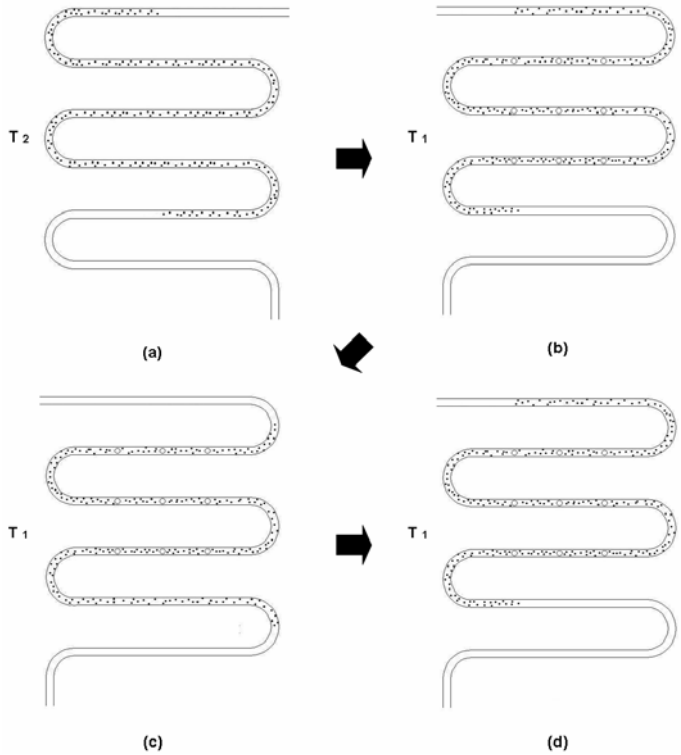

Figure 3. Schematic diagram of the solution flowing processes from the hot region (T_2) to the cold region (T_1): (a) the solution staying in the hot region, (b) the solution reaching the cold region, (c) to (d) the solution flowing back and forth in the cold region. The (a)-(d) are the steps for each cycle.

III. ANALYSIS AND RESULTS

The fluorescence images of the hybridization experiments are shown in Figure 4. In Figure 4(a), the differences in the fluorescence images among nine probe positions at T = 42°C were very small, so the uniformity of the nine probe positions was good. For comparing easily, the images of the middle three probe positions at different temperatures were chosen, as shown in Figure 4(b). In Figure 4(b), the differences in the fluorescence images between T = 82 and 94 °C were fairly apparent. The images between T = 62 and 82 °C could be distinguished, but the differences were not apparent. Higher temperatures in the hot region resulted in brighter fluorescence images in the cold region.

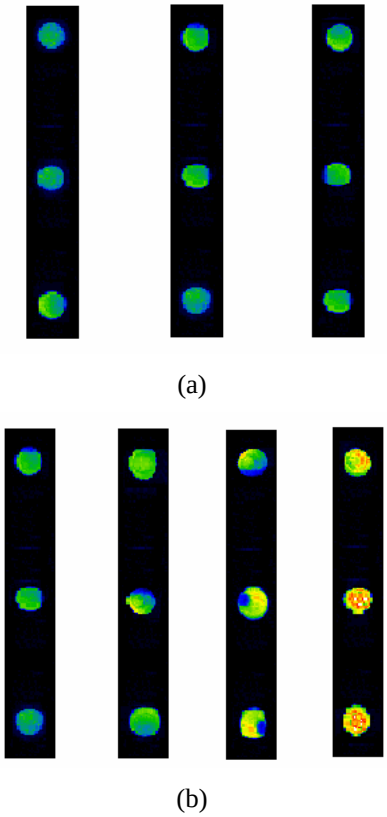

(a)

(b)

Figure 4. Images of hybridization experiments after 30-minute hybridization: (a) nine probes at T = 42°C, (b) middle line probes at u= 0.5 cm/s in the cold region and T = 42, 62, 82, 94°C in the hot region, respectively.

The fluorescence intensity distributions of the cold region at bulk flow velocity u = 0, 0.5, 1.0, 1.5, 2.0 cm/s in the cold region, respectively, and different temperatures in the hot region are shown in Figure 5. The hybridization fluorescence intensity in the cold region increased gradually as increasing temperature in the hot region. The tendency was similar except that the values were different. In these conditions, the fluorescence intensity increased sharply when the temperature was higher than 80°C. The changing values of the fluorescence intensity did not increase linearly as that of the temperatures. One point worth noticing was that the higher the velocity was, the higher the fluorescence intensity would be. These results illustrated that the temperature could enhance the hybridization efficiency and played an important role in enhancing hybridization. And it provided powerful evidence to our hypothesis that the effect of temperature on the hybridization was comparative to that of velocity.

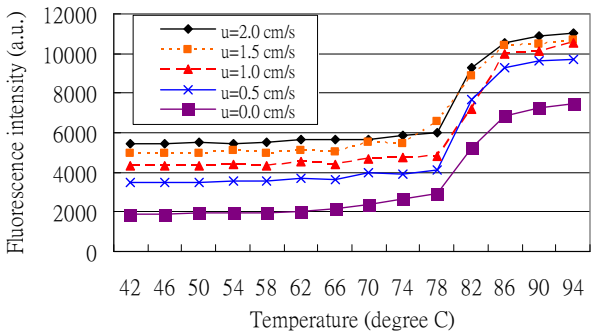

Figure 5. Comparison of fluorescence intensity after 30-minute hybridization at different hot-region temperatures and u = 0, 0.5, 1, 1.5, 2 cm/s in the cold region.

The fluorescence intensity distributions of the cold region at different velocities in the cold region are shown in Figure 6. One can see that the fluorescence intensity increased gradually when the velocities increased, and the tendency was similar as increasing temperatures except for the different values. Higher velocities in the cold region resulted in higher fluorescence intensities. The changing values of the fluorescence intensity per degree ($\Delta F / \Delta T$) did not increase linearly as that of the velocities, and the curve shared a little similarity with the square root function. From the results shown in Figures 5 and 6, it was evident that both the temperature in the hot (denature) region and velocity in the cold (hybridization) region could improve the hybridization efficiency.

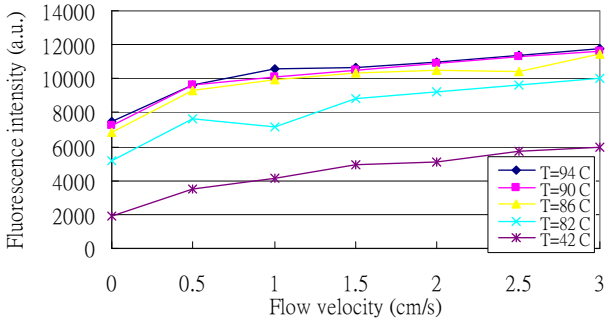

Figure 6. Comparison of fluorescence intensity after 30-minute hybridization at different velocities in the cold region and T = 82, 86, 90, 94°C in the hot region.

A mathematical model was proposed to relate the fluorescence intensity (F) with the hot-region temperature (T) and the cold region velocity (u):

$$F = 2798\, u^{1/2} + 3245 \tanh [0.132\, (T-81.8)] + 5056 \qquad (1)$$

The curvy plane of predicted fluorescence intensities described by Equation (1) is shown in Figure 7. The changing tendency of predicted fluorescence intensities can be seen. The predicted fluorescence intensities were smaller than 5000 when the bulk flow velocity in the cold region was smaller than 1 cm/s and the hot-region temperature was smaller than 70°C. And the predicted fluorescence intensities were larger than 10000 when the cold-region bulk flow velocity was larger than 1.4 cm/s and the hot-region temperature was larger than 86°C.

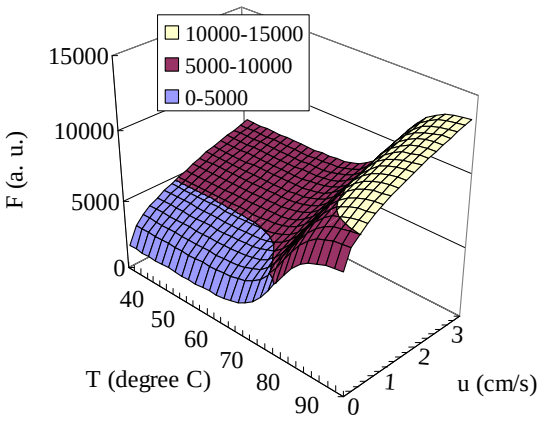

Figure 7. Fluorescence intensity (F) distribution predicted by Equation (2) as function of the hot-region temperature (T) and cold-region bulk flow velocity (u).

The relationships between predicted and experimental fluorescence intensities of DNA hybridization are shown in Figure 8. Good correlation between experimental data and predicted data by Equation (1) was obtained. Thus, Equation (1) can be used to predict the fluorescence intensity of nucleic acid hybridization, which is especially useful in the range of hot-region temperature and cold-region bulk flow velocity in this research. It provides useful information for designing DNA hybridization chips.

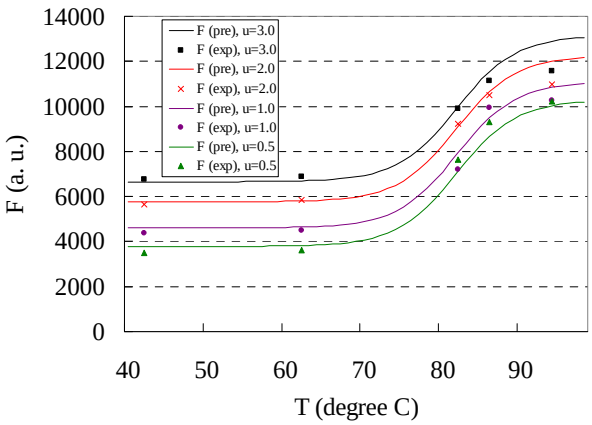

Figure 8. Comparison of predicted and experimental fluorescence intensities.

REFERENCES

[1] R. Drmanac, S. Drmanac, Z. Strezoska, T. Paunesku, I. Labat, M. Zeremski, J. Snoddy, W. K. Funkhouser, B. Koop, L. Hood, R. Crkvenjakov, DNA sequence determination by hybridization: a strategy for efficient large-scale sequencing, Science 260 (1993) 1649-1652.

[2] A. C. Pease, D. Solas, E. J. Sullivan, M. T. Cronin, C. P. Holmes, S. P. A. Fodor, Light-generated oligonucleotide arrays for rapid DNA sequence analysis, Proc. Natl. Acad. Sci. U. S. A. 91 (1994) 5022-5026.

[3] M. Schena, D. Shalon, R. W. Davis, P. O. Brown, Quantitative monitoring of gene expression patterns with a complementary DNA microarray, Science 270 (1995) 467-470.

[4] M. Chee, R. Yang, E. Hubbell, A. Berno, X. C. Huang, D. Stern, J. Winkler, D. J. Lockhart, M. S. Morris, S. P. A. Fodor, Accessing genetic information with high-density DNA arrays, Science 274 (1996) 610-614.

[5] R. G. Sosnowski, E. Tu, W. F. Butler, J. P. O'Connell, M. J. Heller, Rapid determination of single base mismatch mutations in DNA hybrids by direct electric field control, Proc. Natl. Acad. Sci. U. S. A. 94 (1997) 1119-1123.

[6] C. R. Petrie, L. M. Rutledge, J. R. Morgan, Chemical promotion of nucleic acid hybridization, U.S. Patent No. 5,853,986, issued in December 1998.

[7] Y. C. Chung, Y. C. Lin, Y. L. Hsu, W. N. T. Chang, M. Z. Shiu, The effect of velocity and extensional strain rate on enhancing DNA hybridization, J. Micromech. Microeng., **14**, pp. 1376-1383, (2004).

[8] K. Pappaert, J. Vanderhoeven, P. Van Hummelen, B. Dutta, D. Clicq, G. V. Baron, Enhancement of DNA micro-array analysis using a shear-driven micro-channel flow system, J. Chromatogr. A 1014 (2003) 1-9.

[9] D. O. Ariksoysal, H. Karadeniz, A. Erdem, A. Sengonul, A. A. Sayiner, M. Ozsoz, Label-free electrochemical hybridization genosensor for the detection of hepatitis B virus genotype on the development of lamivudine resistance, Anal. Chem. 77 (2005) 4908-4917.

[10] C. A. Marquette, M. F. Lawrence, L. J. Blum, DNA covalent immobilization onto screen-printed electrode networks for direct label-free hybridization detection of p53 sequences, Anal. Chem. 78 (2006) 959-964.

[11] Z. L. Zhang, D. W. Pang, H. Yuan, R. X. Cai, H .D. Abruna, Electrochemical DNA sensing based on gold nanoparticle amplification, Anal. Bioanal. Chem. 381 (2005) 833-838.

[12] I .V. Yang, H. H. Thorp, Modification of indium tin oxide electrodes with repeat polynucleotides: electrochemical detection of trinucleotide repeat expansion, Anal. Chem. 73 (2001) 5316-5322.

[13] G. Marchand, C. Delattre, R. Campagnolo, P. Pouteau, F. Ginot, Electrical detection of DNA hybridization based on enzymatic accumulation confined in nanodroplets, Anal. Chem. 77 (2005) 5189-5195.

[14] S. Ahn, and D. R. Walt, Detection of Salmonella spp. using microsphere-based, fiber-optic DNA microarrays, Anal. Chem., **77**, pp. 5041-5047, (2005).

[15] P. Kavanagh, D. Leech, Redox polymer and probe DNA tethered to gold electrodes for enzyme-amplified amperometric detection of DNA hybridization, Anal. Chem. 78 (2006) 2710-2716.

[16] X. Zhu, K. Han, G. Li, Magnetic nanoparticles applied in electrochemical detection of controllable DNA hybridization, Anal. Chem., **78**, 2447-2449 (2006).

[17] J. R. E. Shepard, Polychromatic microarrays: simultaneous multicolor array hybridization of eight samples, Anal. Chem., **78**, pp. 2478-2486, (2006).

[18] Y. C. Chung, B. J. Wen, Y. C. Lin, Optimal fuzzy sliding-mode control for bio-microfluidic manipulation, Control Engineering Practice, accepted, will be published in 2007. .

Continuous Monitoring of Histamine Release from Single KU-812 Cell with an Electrochemical Cellular Chip

Kuei-Yui Lai[1,2], Ching-Yu Chang[1], Tsung-Che Chou[2], Hsien-Chang Chang[1,*]

[1]*Institute of Biomedical Engineering, National Cheng Kung University, Tainan, Taiwan, ROC*

[2]*Industrial Technology Research Institute South, Microsystems Technology center, Tainan, Taiwan, ROC*

***Abstract* — In this study, we developed an electrochemical cellular chip for continuous monitoring of histamine release at single cell level. The cells were individually accommodated and stabilized inside a microwell electrode (MWE), and then the released histamine was electrochemically detected by the MWE. We employed KU-812 cells (ECACC no. 90071807) as a cell model, and a spiked amperogram was observed in accordance to the exocytotic event of histamine release. In our experiment, the investigated cells were stimulated with high K^+ solution which increases a cytosolic Ca^{2+} influx. The amperograms (+0.6 V *vs.* Ag/AgCl) of single KU-812 cell with and without stimulation were compared, and an amperogram with higher spiked current were found in high K^+ solution. Our result shows that a feasible application for the cell secretion measurement by using this device.**

Keywords* — *single-cell analysis, microwell electrodes, histamine

I. INTRODUCTION

Single cell detection provides a powerful technique for exocytosis research. The exocytotic event of an individual cell can be monitored either by using fluorescent probes or ultramicroelectrode (UME). Amperometric detection which places a UME on the cell surface was suggested as a preferred technique for cell release detection. However, the fabrication and manipulation of UME to approach a selected cell is laborious; thus, an improved method for single cell electrochemical measurement is desired. Many single cell manipulating techniques [1-3] based on gravity, hydraulic and electrokinetic forces were developed to allocate single cell on a specific position. Consequently, the laborious operation in amperometry could be improved by integrating the single cell manipulation technique on an electrochemical chip.

Histamine which will cause allergic inflammatory reaction is the principal ingredients of mast cell granules. The histamine level in human serum was suggested as an indicator of allergic response. In physiological condition, histamine is synthesized from histidine by histidine decarboxylase (HDC), and it also can be oxidized on the electrode surface at a suitable potential [4]. Besides primary mast cells, KU-812 (ECACC no. 90071807) which is a human basophilic derived cell line was usually employed as a model for histamine release study [5-6]. The exocytotic activity can be stimulated by high K^+ solution or calcium ionophore (A23187) by increasing the Ca^{2+} influx of cytoplasm [7]. In this work, we developed a microwell electrode (ϕ=30 μm, depth=25 μm) to accommodate KU-812 cells by gravity for exocytosis measurement. MWE was sequentially constructed with gold electrode, SU-8 sheet, adhesive tape and ITO cover. We found a low flow velocity area (LFVA) at the bottom of MWE which can stabilized the trapped cell in a continuous flow.

[1]Institute of Biomedical Engineering, National Cheng Kung University, Tainan 701,
[2]Industrial Technology Research Institute South, Microsystems Technology center, Tainan, Taiwan, ROC,
*Taiwan, Laboratory, No.1, Daxue Rd., East Dist., Tainan City 701, Taiwan (R.O.C.)
(phone: 886-6-275-7575#63426; email: **hcchang@mail.ncku.edu.tw**).

II. MATERIAL AND METHOD

A. REAGENTS AND SOLUTIONS

SU-8 negative photoresist sheet (thickness=25 μm) and SU-8 developer were supplied from Nippon Kayaku (Tokyo, Japan). Positive g-line photoresist (S1818) and S1818 developer were obtained from Center for Micro/Nano Science and Technology (Tainan, Taiwan). Dulbecco's Phosphate Bufferd Saline (PBS) without calcium chloride and magnesium chloride and RPMI 1640 (+ L-Glutamine) were purchased from Invitrogen (Carlsbad, CA). CHI 705B electrochemical analyzer was purchased from CH Instrument (TX, USA). Ferricyanide ($(K_3Fe(CN)_6)$) was purchased from Uni-Onward Co. (Tainan, Taiwan). Histamine dihyfrochloride minimum 99% (TLC) was purchased from Sigma (USA). High K^+ solution used for cell stimulation was prepared as the receipt (PBS, 145 mM KCl, 10 mM $CaCl_2$, 1 mM $MgCl_2$, pH=7.3~7.4).

B. CHIP FABRICATION

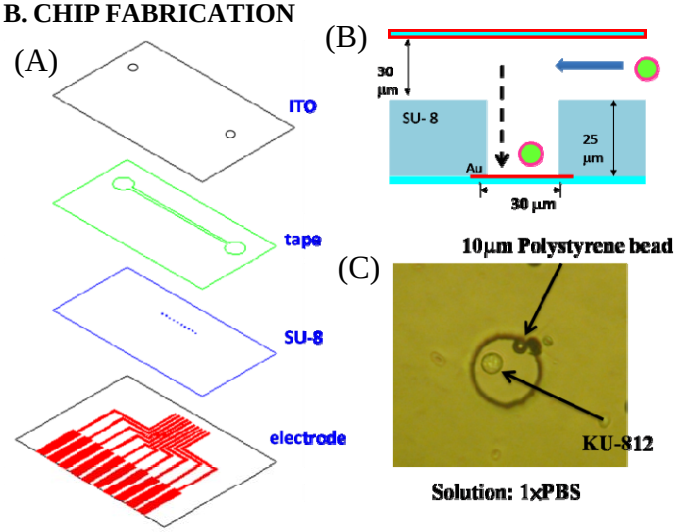

Fig. 1 (A) Exploring drawings of the proposed device (B) Schematic drawing of the proposed MWE (ϕ=30 μm, depth=25 μm). Cells can be accommodated by gravity. (C) A polystyrene bead (ϕ=10 μm) and single KU-812 cell were manipulated inside a MWE.

The exploding drawings and cross section of the proposed device was described as Fig.1. Titanium (30 nm) and gold (150 nm) was deposited on a glass slide by a physical deposition process, Titanium makes as connection layer among the gold and glass slide, and then the electrode patterns were transferred from a mask by a photolithography procedure. Next, a SU-8 sheet (25 μm) was attached on the electrode and firmly rolled to squeeze the encapsulated bubble. After, pre-bake (65°C /3 min, 95°C/5 min) and UV expose 40 sec (250 mJ/cm^2), the microwell structure was developed in

SU-8 developer for 3 min. A hard-bake (180°C, 30 min) process was performed to stabilize the structure. A double-sides adhesive tape was used as a space between electrode slide and the ITO cover, and then the flow channel (0.2 mm in width) can be defined by the tape. All compartments were cleaned by oxygen plasma for 5 min before assembly. A bare ITO glass was bounded onto microwell electrode through the channel defined tape. The microwells were carefully aligned within flow channel.

C. CELL PREPARATION AND TREATMENT

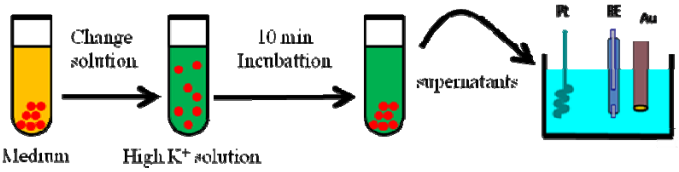

Fig. 2 Procedure for the electrochemical detection of histamine release from (A) KU-812 cells (6×10^8 cells/mL), voltage start from 0 to +0.8 V, scan rate is 50 mV/sec).

KU-812 was used as a model for the investigation of histamine exocytosis. The exocytosis of KU-812 can be induced by the calcium ionophore (A23187) and other chemicals like high K^+ solution, which can cause an increase of the Ca^{2+} influx. KU-812 cells were cultured with RPMI-1640 medium (10% fetal bovine serum, FBS) in an incubator (5% CO_2, 37°C) before use. For the cell experiments, we used high K^+ solution to stimulate KU-812. Cells were changed the medium into high K^+ solution, and then incubated with high K^+ solution for 10 min in an incubator. After that, collected the supernatants and analyzed by a voltammogram (started from 0 to +0.8 V and finally back to 0 V, scan rate is 50 mV/sec). Fig. 2 shows the procedure for the electrochemical detection of histamine release from KU-812 cells (6×10^8 cells/mL) after the stimulus of high K^+ solution.

D. SINGLE CELL MEASUREMENT

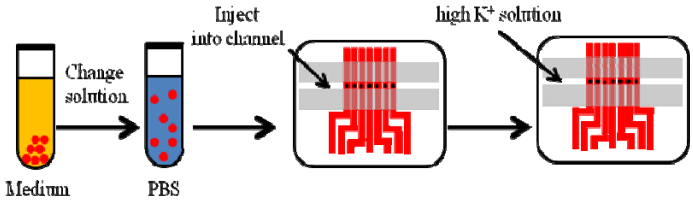

Fig. 3 Procedure for the electrochemical detection of histamine release from single KU-812 cell after the stimulus of high K^+ solution (+0.6 V vs.Ag/AgCl).

In on-chip measurement, to confirm the histamine release, the cells were incubated in RPMI-1640 medium. Then cells solution was spun (1000 rpm, 10 min) and washed with PBS solution before measurement, the conductivity of cell suspension was checked to be 1.5 S/m. Next, we injected cells solution into channel and trapped a cell into an MWE. After that, changed the PBS solution into high K^+ solution to stimulate the trapped cell 10 min, and then an amperometry (+0.6 V vs.Ag/AgCl) was conducted to monitor the histamine exocytosis. Fig. 3 shows the procedure for the electrochemical detection of histamine release from single KU-812 cell after the stimulus of high K^+ solution.

III. RESULT AND DISCCUSION

A. A LFVA AT THE BOTTOM OF MICROWELL

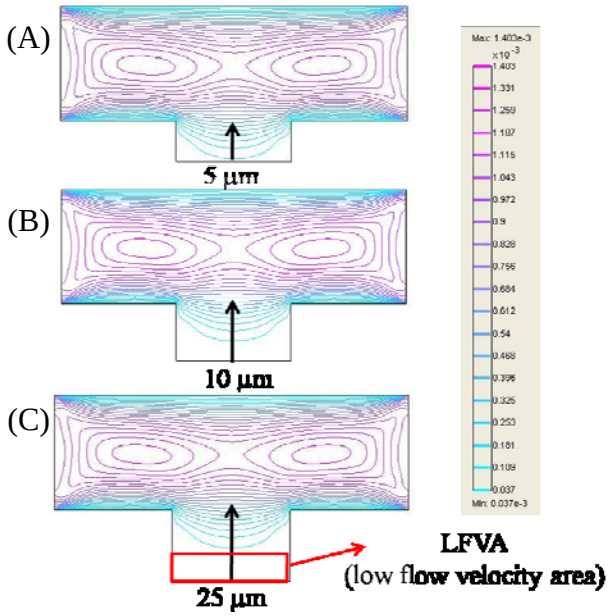

Fig. 4 Simulation of flow field inside the MWE, flow velocity inside a microwell, ϕ=30 μm with (A) 5 μm (B) 10 μm (C) 25 μm well depth. The flow velocity of each channel was set as 1 mm/sec. The contour lines indicate the isovelocity according to the simulation results.

The microwell was designed to provide a shield space in a continuous flow. The flow velocity in a microwell was simulated by COMSOL Multiphysics 3.4a software (CA, USA) to estimate the optimal geometry design of microwell. 2D geometry used for simulation experiment was assigned as Fig. 4, where the channel height was 25 μm and channel length was 100 μm respectively. Microwell (ϕ=30 μm) with different depths (5, 10 and 25 μm) were placed under main channel respectively. The boundary conditions were set as no-slip for all boundaries except for the inlets and outlets of channels. The inlet (left boundary) of flow channel was set to be constant flow velocity (1 mm/sec), and outlet (right one) was normal flow with zero pressure. The incompressible Navier-Stoke system of fluidic dynamic module was selected as the model. The flow velocity at central of each microwell were acquired from the simulation result and plotted against the distance from bottom of microwell. A low flow velocity area (LFVA) was found at the bottom of MWE, which can provide a shield for the trapped cell.

B. VALIDATION OF MWE CHARACTERISTICS

The effective area of MWE was checked by performing a voltammogram in 5 mM ferricyanide ($K_3Fe(CN)_6$,) solution. The measurement was performed as a two-electrode configuration by setting Ag/AgCl electrode as the reference/counter electrode. The applied voltage started from +0.5 to 0 V and finally back to +0.5 V, scan rate is 20 mV/sec. Fig. 3 shows the voltammograms of MWE in 5 mM $K_3Fe(CN)_6$. With the known $K_3Fe(CN)_6$ concentration, diffusion coefficient and MWE depth, the diameter of MWE can be estimated by the measured steady-state current. Therefore, we regard the MWE as an ideal inlaid UME.

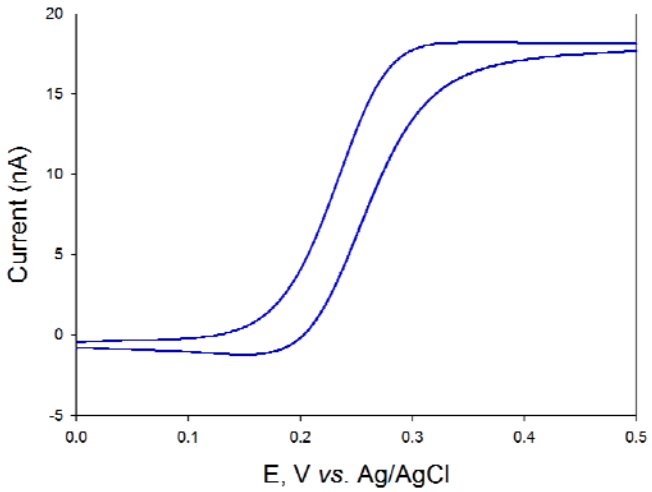

Fig. 5 Voltammograms (20 mV/sec) of a microwell electrode (ϕ=30 μm) in 5 mM ferricyanide ($K_3Fe(CN)_6$), voltage start from +0.5 to 0 V.

C. ELECTROCHEMICAL BEHAVIOR OF HISTAMINE

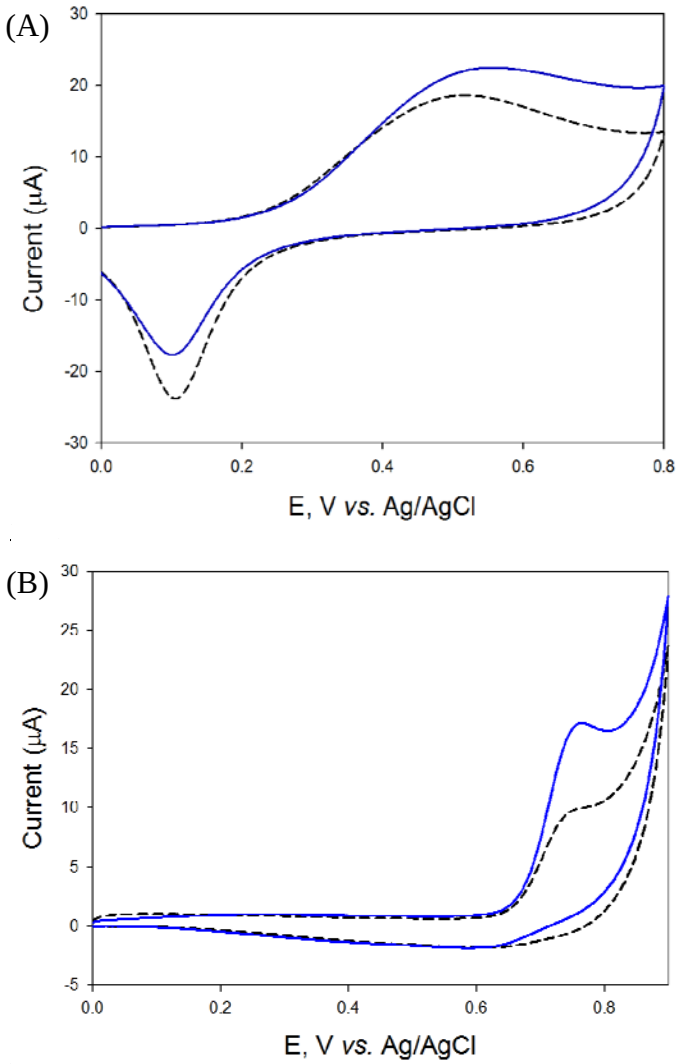

Fig. 6 (A) Voltammograms (50 mV/sec) of a rod Au electrode (ϕ=3 mm) in 0.1 M NaOH with (solid line) and without (dashed line) histamine (10 mM). (B) Voltammograms (50 mV/sec) of a rod Au electrode (ϕ=3 mm) in high K^+ solution with (solid line) and without (dashed line) histamine (10 mM).

The electrochemical characteristic of histamine was investigated based on cyclic voltammogram (CV) with a gold electrode in NaOH (pH=13). But NaOH is not a suitable environment for cell detection, pH=7.2~7.4 is better. High K^+ solution (pH=7.3~7.4) was employed to active the exocytisis of KU-812. Before measuring exocytisis of KU-812, we must confirm the electrochemical characteristic of histamine first. Based on the voltammograms, the histamine was investigated in 0.1 M NaOH and high K^+ solution (see Fig. 4). Since the oxidized histamine will contaminate the electrode surface, the rod electrode was polished with alumina powder before each measurement. The applied voltage started from 0 to +0.8 V and finally back to 0 V for 0.1 M NaOH and started from 0 to +0.9 V for high K^+ solution at 50 mV/sec. Similar voltammograms were found in both solution that with and without histamine. However, elevated oxidation peaks were observed at +0.6~ 0.7 V in 10 mM histamine in both solution, even no obvious oxidation peaks at +0.6 V in high K^+ solution. We was still suggested to the histamine oxidation.

D. CELL PREPARATION AND TREATMENT

Fig. 7 shows the voltammograms (50 mV/sec) of a rod Au electrode (ϕ=3 mm) in high K^+ solution and cell solution was stimulated 10 min by high K^+ solution (line a). Compared with 10 mM histamine in high K^+ solution (line b) and cell supernatants was stimulated by high K^+ solution (line c), elevated oxidation peaks were observed at +0.6 ~ 0.7 V in both solution. We suggested that the event was histamine oxidation on the Au electrode surface and the histamine release attributed to the activated KU-812.

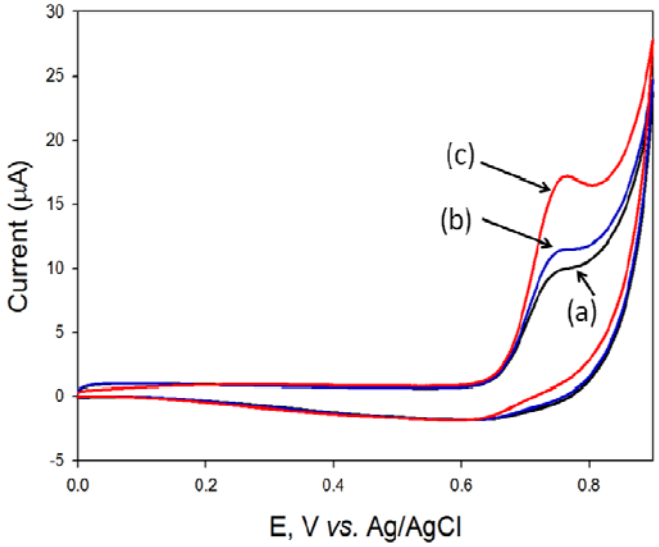

Fig. 7 Voltammograms (50 mV/sec) of a rod Au electrode (ϕ=3 mm) in cell supernatants was stimulated 10 min by high K^+ solution (line b) and high K^+ solution (line a) and histamine (10 mM) in high K^+ solution (line c).

D. SINGLE CELL MEASUREMENT

The cells solution (~6×10^8 cells/mL) was dipped on the MWE chip inlet and allowed to flow through the channel automatically. The channel was washed several times with the physiological buffer in which the experiments were to be performed. Cells were introduced into the flow channel and allowed them to descend inside the MWE after the channel flow is stopped. With the protection of LFVA, the cell can be

accommodated inside the MWE for electrochemical measurement. After single cell manipulation, we change the PBS solution into high K^+ solution to introduced into the flow channel to stimulate the trapped cell inside a MWE. Since the response current was small (several nA), two-electrodes configuration was employed for electrochemical measurements. The Ag/AgCl reference electrode can be immersed in the inlet reservoir. Amperometry (+0.6 V *vs.* Ag/AgCl) was performed sequentially for the single KU-812 cell. Both Fig. 6 and Fig. 7 shows the histamine oxidation current at +0.6~0.7 V compared to without histamine in 0.1 M NaOH and cells solution was stimulated by high K^+ solution. In the single cell experiment, an individual KU-812 cell which was accommodated and stabilized inside the microwell was evaluated in high K^+ solution. The electrode area was partially occupied by the cell, cell's attachment might contribute some charging current, but we could still observed the spiked current on amperograms.

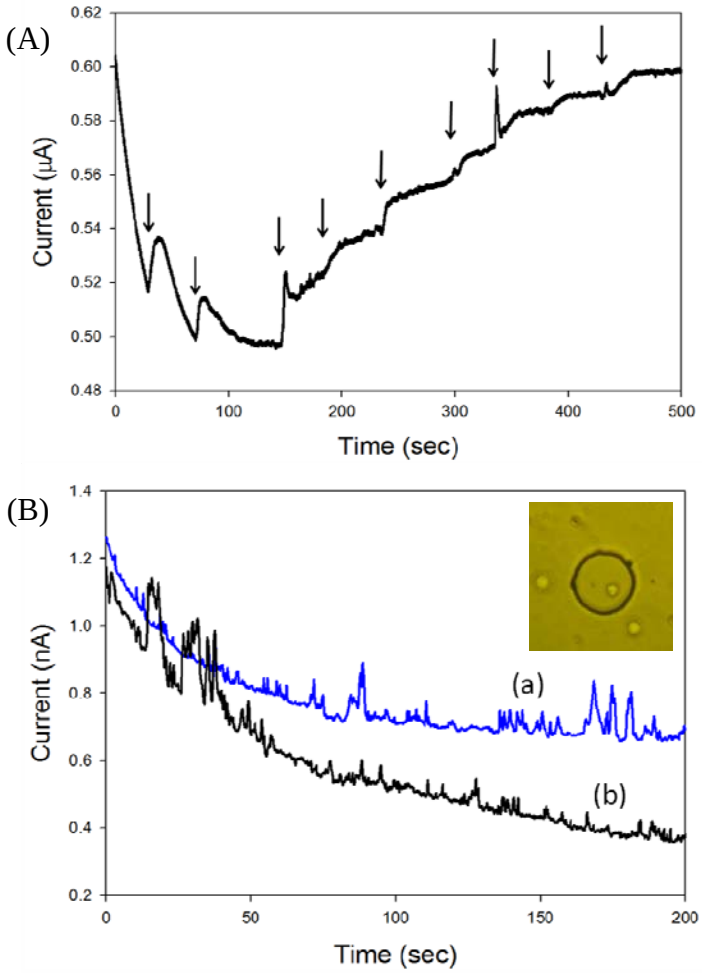

Fig. 8 (A) Titration amperograms of histamine (10 mM) in 2 mL NaOH (0.1 M) working solution. The arrows represents 10 μL for each titration. (B)

Fig. 8 (A) shows the amperograms (+0.6 V) of adding 10 μL histamine (10 mM) to 2 mL NaOH (0.1 M) per 40 sec. A stepwise current response was observed in accordance to histamine addition. Fig. 7 (B) shows the amperograms of the same trapped cell measured in PBS and high K^+ solution, respectively. The spiked currents were suggested to the oxidation of released histamine. The smaller spiked current was considered to the noise signal which might be attributed to the fluctuation of the trapped cell. However, a larger spikes which might probably contributed by the released histamine were found in the amperogram after the stimulus of high K^+ solution. A higher and fluctuated current was observed in single KU-812 cell detection after stimulation; however, no obvious difference for the normal cell case. Because cell secretion is a kind of exocytotic mechanism, histamine concentration will vary according to the secretion activity. Moreover, histamine will spontaneously diffuse out as concentration gradients, and the concentration of histamine is not equilibrium. Due to cell heterogeneity, sometimes we cannot observe the fluctuation even in the single cell experiment, because the trapped cells have probably already died.

IV. CONCLUSION

Both advantages of active and passive traps are integrated in the proposed chip. The investigated cell can be stabilized within the MWE for electrochemical detection. Histamine was detected with Au electrode in different solutions, and a better current response was found in NaOH solution. However, a oxidation current still can be observed in high K^+ solution, which can be used for living cell detection. A spiked amperogram was recorded in an activated KU-812 cell, and the spike current was suggested to the exocytotic events. The proposed device demonstrated a capability for single cell analysis. This techniques presented here may be helpful for single cell array manipulation and electrochemical measurement for cell biological studies.

V. REFERENCE

[1] A. Khademhosseini, R. Langer, J. Borenstein, and J. P. Vacanti, "Microscale technologies for tissue engineering and biology," *Proc Natl Acad Sci U S A*, vol. 103, pp. 2480-2487, 2006.

[2] P. S. Dittrich, K. Tachikawa, and A. Manz, "Micro Total Analysis Systems. Latest Advancements and Trends," Anal Chem, vol. 78, pp. 3887-3907, 2006.

[3] M. Deutsch, A. Deutsch, O. Shirihai, I. Hurevich, E. Afrimzon, Y. Shafran, and N. Zurgil, "A novel miniature cell retainer for correlative high-content analysis of individual untethered non-adherent cells," Lab Chip, vol. 6, pp. 995-1000, 2006.

[4] R. S. Zeiger, F. J. Twarog,H. R. Colten, "Histamine release from human granulocytes," J.Exp Med, vol. 144, pp. 1049-1061, 1976.

[5] M. Hosoda, M. Yamaya, T. Suzuki, N. Kamanaka, K. Sekizawa, J. H. Butterfield, T. Watanabe, H. Nishimura, H. Sasaki, "Effects of rhinovirus infection on histamine and cytokine production by cell lines from human mast cells and basophils," J Immunol, vol. 169, pp. 1482-1491, 2002.

[6] T. Toyo'oka, "Separation assay of histamine and its metabolites in biological specimens," Biomed. Chromatogr. vol. 22, pp. 919-930, 2008.

[7] Y. Fujimura, D. Umeda, Y. Kiuohara, Y. Sunada, K. Yamada, H. Tachibana, "The involvement of the 67 kDa laminin receptor-mediated modulation of cytoskeleton in the degranulation inhibition induced by epigallocatechin-3-O-gallate," Biochem Biophys Res Common, vol. 348, pp. 524-531,2006.

2A1-5

Electroosmotic Flow in Dielectrophoresis-Formed Microchannel

Hao-Yu Hu[1], Cheng-Yeh Huang[1], Wensyang Hsu[1], and Shih-Kang Fan[2*]

[1]*Department of Mechanical Engineering, National Chiao Tung University, Taiwan, R.O.C.*
[2]*Institute of Nanotechnology, National Chiao Tung University, Taiwan, R.O.C.*

***Abstract*—We have demonstrated the electroosmotic flow (EOF) pumping in a dielectrophoresis (DEP)-formed virtual microchannel by applying a DC electric field across the microchannel. The geometry of wall-less virtual microchannel was determined by the electrode patterns. A test device with single-layer electrode on both top and bottom plates are prepared by photolithography to generate an appropriate electric field and form a virtual channel on the chip. Neutral fluorescent polystyrene beads are used to indicate the velocity of EOF. Liquid pumping at the velocity of 219.39 μm/s is achieved when the applied DC electric field is 26.67 V/cm.**

Keywords — ***Dielectrophoresis, Electroosmosis, Pumping, Virtual channel***

I. INTRODUCTION

Electroosmotic flow (EOF) has been widely applied to generate liquid pumping in microchannels [1]. In this paper, we have demonstrated EOF in a wall-less microchannel defined by dielectrophoresis (DEP) [2]. First, a virtual microchannel is formed when we apply an AC electric field between parallel plates. This non-uniform AC electric field draws the liquid with high dielectric constant (*e.q.* ε_{water}=78) to occupy the electrode instead of air (ε_{air}=1). After the virtual microchannel is formed, a DC electric field is then applied to generate EOF and continuous pump the liquid in the virtual microchannel. The presented integration of EOF and DEP would pump liquids in reconfigurable DEP-formed microchannel.

Regulating liquids by DEP was first demonstrated by coplanar electrodes on an open surface [2]. Recently, manipulating liquid between parallel plates using DEP has also been reported [3, 4]. In the latter case, DEP drives and deforms the liquid to fit the region of the strong electric field between electrodes. Thus, the patterned electrodes establish desirable electric fields to generate virtual microchannels. However, after the strong electric field is entirely occupied by the liquid, the pumping behavior stops immediately. Alternatively, applying an electric field along a tube causes a plug flow by EOF [5]. Here we employ two perpendicular electric fields: an AC field for virtual channel and a DC field for EOF, in order to generate EOF in a DEP-formed virtual microchannel.

II. PRINCIPLE

A. DEP

The DEP force between draws the liquid with a higher dielectric constant towards the strong electric field region filled with a surrounding medium (air or oil) as shown in Fig. 1(a).

* *Contacting Author: Prof. Shih-Kang Fan, Institute of Nanotechnology, National Chiao Tung University (NCTU), Address: 1001 University Road, Hsinchu, Taiwan 300, ROC, (Tel:+886-3-571-2121 #55813, Fax: +886-3-5729912, mail:* ***skfan@mail.nctu.edu.tw****.).*

(a)

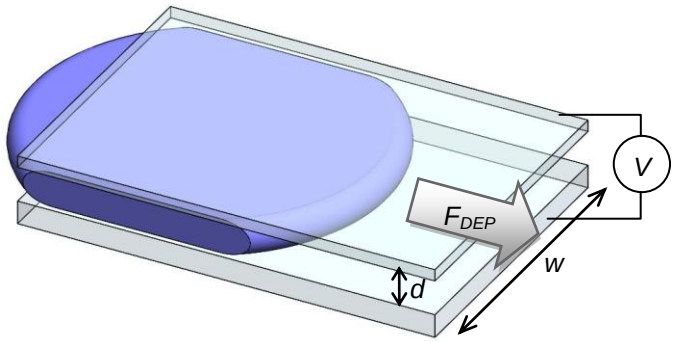

(b)

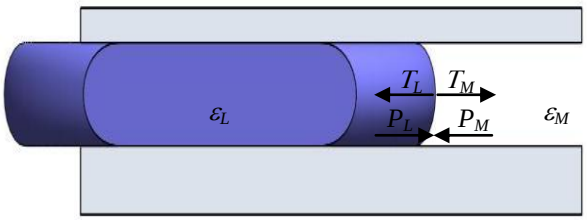

Figure 1. DEP phenomenon between parallel electrode plates.

According to Maxwell stress tensor in the electric field, the relation between Maxwell stress tensor, dielectric material and electric field can be expressed by Eq. 1.

$$T = -\frac{1}{2}\varepsilon_0 \varepsilon E^2 , \tag{1}$$

where T is the Maxwell stress tensor, ε_0 is the permittivity of vacuum, ε is the relative permittivity of the material, and E is the amplitude of the electric field.

In the equilibrium state, the forces per area at the interface shown in Fig. 1(b) can be expressed as:

$$T_L - P_L = T_M - P_M , \tag{2}$$

where T_L, P_L, T_M and P_M are the Maxell stress tensor of the liquid, pressure of the liquid, Maxell stress tensor of the medium, and the pressure of the medium, respectively. The pressure at the interface can be expressed by:

$$P = \frac{F}{wd}, \quad (3)$$

where w and d are the width of the electrode and the distance between the electrodes shown in Fig. 1(a).

Therefore, from Eq. (1) to (3), the DEP force can be derived as:

$$F_{DEP} = \frac{1}{2d}\varepsilon_0(\varepsilon_L - \varepsilon_M)wV^2, \quad (4)$$

where F_{DEP}, ε_L, ε_M, and V are the DEP force, relative permittivity of the liquid, relative permittivity of the medium, and the applied voltage, respectively. The DEP force is induced from the different permittivity of two materials within an electric field. Moreover, the higher the difference of the permittivity is, the larger the DEP force becomes, even in the same electric field strength. With the DEP force, a liquid column is drawn into the device and forms a wall-less virtual channel. The dimension of the channel is determined by the electrodes and the distance between electrodes on the parallel plates.

B. EOF

The EOF phenomenon is a kind of bulk flow which is commonly found in fused silica (SiO_2) capillary tube. The interior wall of the dried fused silica capillary contains the silanol (Si-OH) group. When the surface of the interior wall is exposed to the solution whose pH value is higher than 2, the silanol group will ionize to be the negatively charged silanoate ($Si\text{-}O^-$) group. This negatively charged silanoate layer makes cations to adsorb onto the capillary interior wall and establishes an electric double layer (EDL). EDL includes a stern layer and a mobile layer as shown Fig. 2(a). When a DC electric field is applied along the channel, the mobile layer tends to migrate to the direction of the cathode. Due to the bulk flow mechanism of EOF, the flow profile is flat (plug flow) as shown in Fig. 2(b) rather than parabolic caused by a pressure-driven laminar flow as shown in Fig. 2(c).

The velocity of EOF can be expressed as:

$$u_{EO} = \mu_{EO}E \quad (5)$$

where u_{EO}, μ_{EO}, and E are the velocity, the mobility and the electric field strength of the EOF, respectively. Moreover, depending on the polarities of the surface charge, the EOF phenomenon exists in capillaries made of other materials. In this paper, the device is treated by Teflon coating to be hydrophobic. It is found that the liquid was pumped from the anode to the cathode, meaning the channel surface was negatively charged caused by ion adsorption [5]. Based on the EOF studies, capillary electrophoresis would be possible by the proposed liquid manipulation mechanism. Here we utilize DEP force to create a virtual channel and further apply a DC electric field along the channel to induce EOF within the virtual channel.

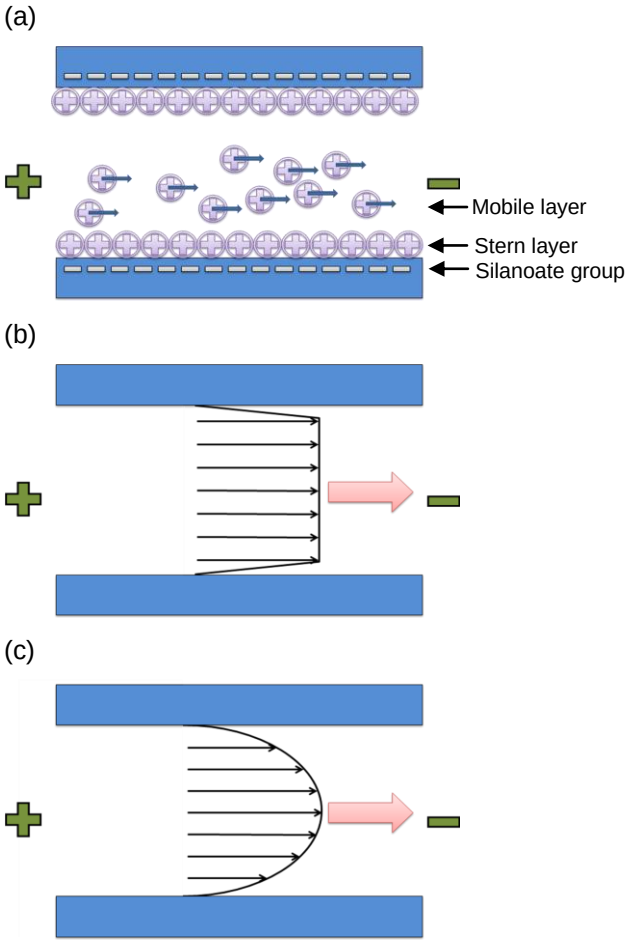

Figure 2. The schematics of EOF. (a) Silanoate group is a negatively charged surface between the interface of the fused silica and the buffer. (b) An EOF profile shows a plug-flow. (c) A pressure-driven laminar flow shows a parabolic profile.

III. EXPERIMENT

In this paper, we replace the fused silica capillary with ITO glass plates. We build a DEP-formed virtual microchannel by applying a proper AC electric field between the ITO electrodes. As can be seen in Fig. 3, the device is a sandwich structure consisting of liquid, dielectric layers, hydrophobic layers, and ITO glass plates. The thickness and sheet resistance of the ITO layer are 500 nm and 10 ohm/□, respectively. The DEP and EOF electrodes on the bottom plate (Fig. 3(a)) are first patterned by photolithography and wet etching processes. The patterned electrodes are subsequently covered by a dielectric layer (MicroChem SU8-2002 photoresist, 1 μm) and a hydrophobic coating (DuPont Teflon AF 1600, 55 nm). The ITO layer on the top plate was not patterned and coated by Parylene and Teflon layers. The Parylene coating is achieved by a vapor deposition process which can cover the entire plate. Because the liquid reservoirs are placed at the edges of the top plate, conformally-deposited Parylene is necessary to prevent

the top ITO electrode from electrolysis. The device configuration is shown in Fig. 3(a)-(c). The liquids are manipulated between the parallel ITO glass plates as shown in Fig. 3(b) and (c).

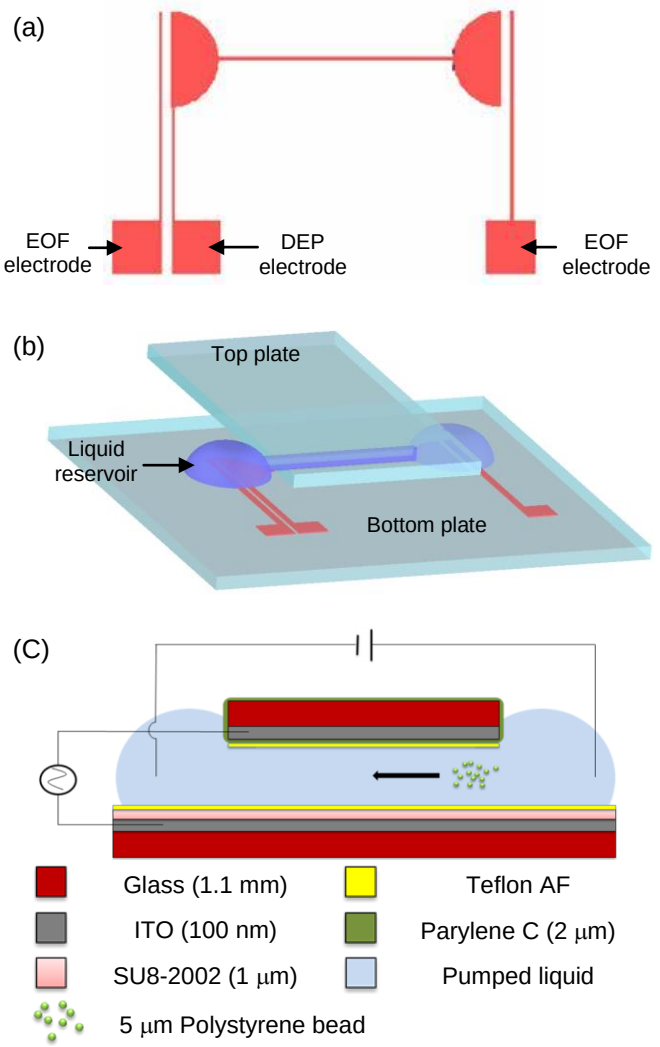

Figure 3. The device configuration. (a) Top view: the DEP and EOF electrode designs on the bottom plate. (b) Assembly of the device. By applying an AC field between the plates, a virtual microchannel was formed. (c) Liquid pumping by EOF was achieved by applying a DC field along the microchannel between the reservoirs.

A. *Virtual channel forming*

As mention above, a wall-less virtual channel is formed by DEP force. DEP provides a pressure difference between the pumped liquid and the medium. When voltage is applied between the DEP electrode on the bottom plate and the blank ITO electrode on the top plate, the non-uniform electric field would draw the liquid by DEP. As shown in Fig. 4, when a 72 Vrms and 100 kHz signal was applied, the liquid containing 20 mM borax and 5 mM sodium dodecyl sulfate (SDS) was pumped in the virtual microchannel. The liquid was pumped from the right reservoir (Fig. 4(b)) to the left reservoir (Fig. 4(d)) in 108 s. The dimensions of the DEP-formed microchannel were 500 μm in width, 3 cm in length, and 25 μm in height. The width and length were determined by the bottom DEP electrode, while the height was defined by the spacer between the plates. A double side tape was utilized to be a spacer.

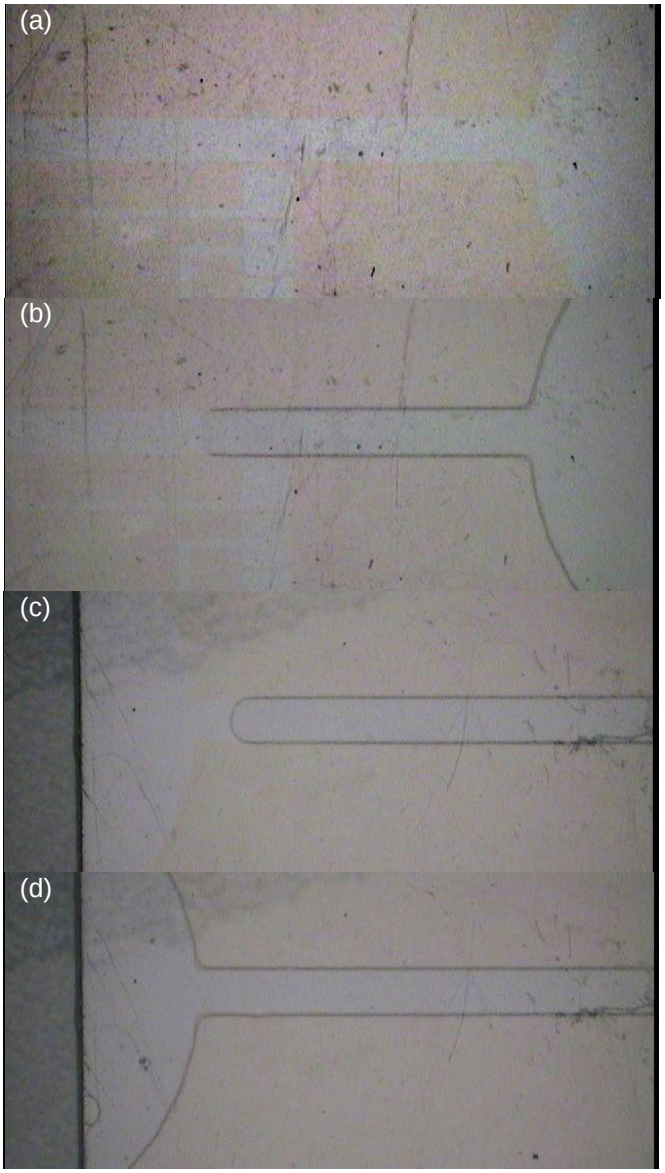

Figure 4. Virtual microchannel formation by DEP. (a) Initial condition with no liquid injected. (b) Voltage application between plates to draw liquid in the DEP-formed microchannel. (c) Liquid approached to another reservoir. (d) Microchannel established between two reservoirs.

B. *EOF pumping*

5 μm neutral fluorescent polystyrene beads are added in the pumped liquid to observe the EOF in the DEP-formed microchannel. After the microchannel is established by DEP, another DC electric field is applied along the microchannel between the two reservoirs. The 10 cSt silicone oil is used as the filler medium around the pumped liquid to prevent possible evaporation [6] and increase the stability of the microchannel.

As shown in Fig. 3 (c), an AC signal is applied to maintain the microchannel, while a DC voltage is applied to pump the liquid. A fluorescence microscopy is utilized to observe the migration of neutral fluorescent polystyrene beads through an appropriate filter (excitation: 510-550 nm, emission: >590 nm). The EOF velocity is measured by analyzing the recorded video frames (Fig. 5) every 20 V from 0 V to 100 V.

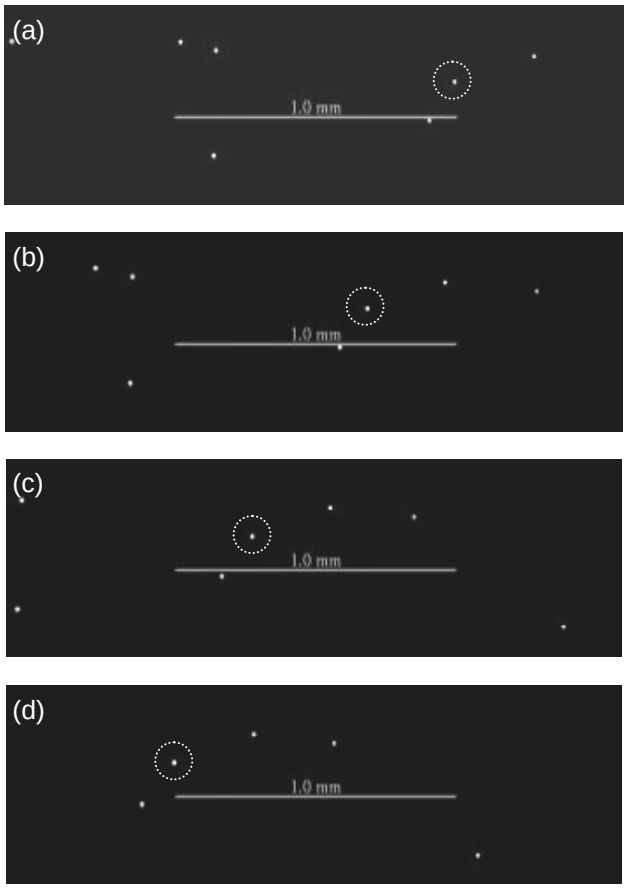

Figure 5. Microscopic photographs of the EOF velocity test. (a) Initial state at t = 0 s. (b) t = 9.66 s. The marked neutral fluorescent polystyrene bead is moved along the EOF. (c) t = 21.62 s. (d) t = 29.69 s. The observed particle migrated for 1 mm (scale bar length).

IV. Result and Discussion

From the recorded video, particles migrated from right to left and the positions between particles were nearly fixed (Fig. 5). This result indicated EOF in DEP-formed microchannel still remained a uniform plug flow. The measured EOF velocities in a DEP-formed virtual microchannel are plotted in Fig. 6. Each experimental data was averaged from five measurements using image analyses. The velocity increased when the DC voltage increased until it saturates at 80 V. Before saturation, the EOF velocity can be adjusted by simply tuning the applied DC electric filed. A maximum velocity of EOF was 219.39 μm/s when the DC electric field was 26.67 V/cm.

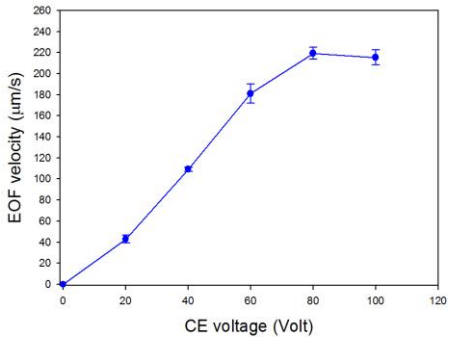

Figure 6. EOF velocity plotted against the applied DC voltage along the virtual microchannel maintained by an 80 Vrms and 100 kHz signal. The liquid containing 20 mM borax and 5 mM SDS was continuously pumped by the DC voltage application from the anode to the cathode. The velocity was increased until it saturated at 80 V.

We suspect the saturation of EOF velocity was caused by joule heating from the applied DC electric field. A heated buffer started to evaporate and caused uncertainties of the EOF pumping.

V. Conclusion

In this paper, we demonstrated liquid pumping in a wall-less virtual channel. The virtual microchannel was formed by applying an AC electric field between the electrodes on the parallel plates to generate DEP, while liquid pumping was obtained EOF through applying a DC electric field across the established virtual microchannel. The EOF pumping velocity was investigated under different DC electric fields. The presented wall-less virtual channel provides flexibility of microchannel networks by proper voltage application on desired electrode patterns.

Reference

[1] R. B. M. Schasfoort, S. Schlautmann, J. Hendrikse, and A. van den Berg "Field-Effect Flow Control for Microfabricated Fluidic Networks," Science, vol. 286, pp. 942-945, 1999.

[2] T. B. Jones, "Liquid dielectrophoresis on the microscale," Journal of Electrostatics, vol. 51-52, pp. 290-299, 2001.

[3] S.-K. Fan, W.-J. Chen, T.-H. Lin, T.-T. Wang and Y.-C. Lin, "Reconfigurable liquid pumping in electric-field-defined virtual microchannels by dielectrophoresis," Lab on a Chip, vol. 9, pp. 1590-1595, 2009.

[4] Y.-C. Lin, K.-C. Chuang, T.-T. Wang, C.-P. Chiu and S.-K. Fan, "Integrated Digital and Analog Microfluidics by EWOD and LDEP," in Digest Tech. Papers Int. Conf. on IEEE Nano/Micro Engineered and Molecular Systems, Zhuhai, China, Jan. 2006, pp.1414-1417.

[5] C. Werner, U. Konig, A. Augsburg, C. Arnhold, H. Korber, R. Zimmermann and H. J. Jacobasch "Electrokinetic surface characterization of biomedical polymers—a survey," Colloids Surface A: Physicochemical and Engineering Aspects, vol. 159, pp. 519-529, 1999.

[6] M. G. Pollack, A. D. Shenderov and R. B. Fair, "Electrowetting-based Actuation of Droplets for Integrated Microfluidics," Lab on a Chip, vol. 2, pp. 96–101, 2002.

Test on Acoustic Resonance Characteristic of PTFE Micro/Nano-aperture Membrane for Nanobiomedical Application

Wanfeng Lin[1,2]*,Wenzhong Lou [1] ,Xin Li[1], Jing Xu[3]

[1]* *National Key Laboratory of Mechatronics Engineering and Control, Beijing Institute of Technology, Beijing 100081, China*

[2]*Department of Physics, Air Force Aviation University, Changchun 130022, China*

[3]*School of Science, Changchun Institute of Technology, Changchun 130012, China*

***Abstract* — This study investigate the potential biomedical application of micro/nano-aperture membrane fabricated with Polytetrafluoroethylene (PTFE). Experimental work is carried out to examine the membrane's sound transmission /absorption characteristics under the condition of different aperture diameter, thickness and cavity depth of tube. It is discovered that when there is no air layer besides the tested membrane, sound transmission is not affected. When there is sound layer, it is resonant sound absorption. In the frequency range of 100-1500Hz, it is low frequency high rate sound transmission zone. In the frequency range of 1500Hz-6300Hz, it is high frequency resonant sound absorption. It is found that PTFE as a fine sound transmission material as well as a fine sound absorption material. The original test provides a solid evidence for further research and modeling of sound transmission theory.**

Keywords — ***Sound Transmission Characteristic ↫ PTFE Micro-aperture Membrane ↫ Resonant Sound Absorption ↫ Sound transmission***

I. INTRODUCTION

In the nanobiomedical area, sound ultrasonic therapy is widely used as a main source to detect abnormal tissue and tumor cells. In the conventional method, micro acoustic sensors and generator [1,2] is widely used and the protection layer is composed mostly by woven metal wires with micro-aperture on it. It is discovered that the method is relatively unreliable, because micro dust particle and micro liquid drop can easily contaminate the inner acoustic and sensor and generator thus cause dysfunction in the long term. In this study, it is proposed with a novel fabricated micro/nano aperture membrane to solve the above mentioned potential problems. In order to make sure the micro/nano membrane is biocompatible, PTFE membrane [3] is selected as the main function material for its excellent performance, e.g. high/low temperature endurance, corrosive endurance, dielectric performance, low friction coefficient, etc.

II EXPERIMENTAL STUDY

PTFE micro-aperture membrane is made of bidirectional drawing fluorin plastic [4], as Fig. 1 shows. From scanning electron microscopy photo, it is found that the surface of PTFE takes on net structure whereas micro-aperture membrane takes on ellipse shape, as Fig. 2 shows. It is estimated that there are 10^{9}-10^{14} PTFE micro-apertures per square meter with limited grades of 10^{-6}-10^{-7}m.

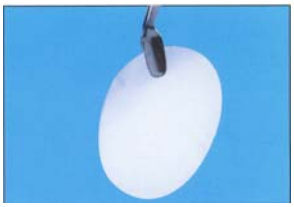

Fig 1. Photo of PTFE Membrane Fig 2. SEM of PTFE Membrane

After fabricating the membrane, three samples of different parameters are selected to be measured in the testing system. The parameters including aperture diameter, thickness, density of aperture, and sample size are shown in Table 1.

TABLE 1, PTFE MEMBRANE PARAMETERS

Index Number	PTFE 1	PTFE 2	PTFE 3
Aperture diameter(μm)	0.22	0.45	0.80
Thickness(μm)	150	150	150
Density of Aperture (%)	82	83	86
Shape	Wafer	Wafer	Wafer
Length, Width(mm)	60,30	60,30	60,30

The testing system to measure sound transmission loss in shown in Fig. 3.

Fig 3. Transmission Loss Test System

When sound wave diffuses onto material, some is reflected, the other is absorbed. The other parts include sound energy that transforms to heat energy and vibration energy, and sound energy that transmits through the material. Base on mechanism of sound absorption, material is divided to lacunaris structure and sympathetic vibration material. Mechanism of sound absorption is as follows: Diffusing to aperture, sound wave causes vibration of air, so part of sound energy transforms to heat energy. Generally, sound absorption advances with the number of aperture increasing and the degree of communication among apertures rising.

III EXPERIMENTAL RESULTS AND DISCUSSION

3.1 Sound Absorption Measurement

Sound transmission mechanism [5, 6] is the phenomenon occurs when sound wave travels from one medium and to

This project was funded. Funding:B3320080127&9140A050A0309BQ0152

**Contact author: Wanfeng Lin(1979-). Master of Science Student, Beijing Institute of Technology. Contact: linwanfeng@126.com.*

another. Sound energy will be separated into three parts, first part of the energy is reflected or dispersed, second part is absorbed by the medium, which transformed into heat energy and vibration energy, the third part of the energy is perforated through the medium to the other side. For the sound wave energy, except the energy that is reflected, the other part of energy can be considered as marginal absorption.

3.1.1 Sound Absorption Measurement Characteristic

The experimental result, as Fig. 4 shows, gives the sound absorption characteristic of material with aperture diameter of 0.22μm without cavity in the backside. The figure shows that the sound absorption performance is extremely weak. All the sound energy is reflected back in all the frequency range. Plus, when the frequency increases, the sound absorption coefficient does not have a profound change. It is in the frequency range from 3000 to 4000 Hz that sound absorption coefficient reach its maximum value, which is 0.2. The reason for this phenomenon is the material thickness is as low as 150μm. On the other hand, the relative greater aperture ratio under the condition of low membrane thickness is also one of the reasons that make the sound absorption coefficient low.

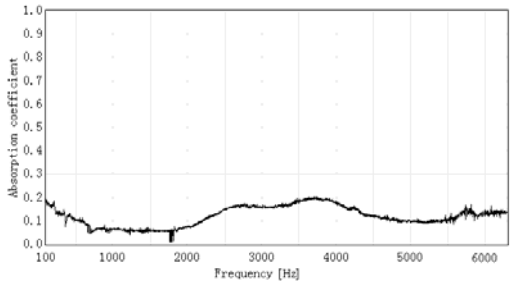

Fig 4. The curve of absorption coefficient with aperture diameter of 0.22μm

In order to make a proper mathematical model to better analyze the sound transmission phenomenon of micro aperture membrane, an assumption is made here. We assume that the micro aperture membrane is composed of many thin rigid hollow tubes attached to each other. In the same time, the sticky effect and thermal exchange effect is considered to make a more practical theoretical sound transmission model.

Concerning on the micro aperture medium filled with air, it is treated it as rigid materials, thus the incidence impedance is

$$z = z_2 / j \tan k_2 L \text{ [7]} \tag{1}$$

where L is the thickness of membrane(tube length in the model). k_2 is the wave number, z_2 is the characteristic impedance ratio.

$$k_2 = \frac{\omega}{c_0}[\tau(\omega)\beta(\omega)]^{\frac{1}{2}}$$
$$z_2 = \frac{S}{\sigma}[\tau(\omega)/\beta(\omega)]^{\frac{1}{2}} \tag{2}$$

where S is the area of the material, σ is aperture degree,c_0 is the sound speed in the air, τ (ω) is dynamic change degree function of micro aperture material.

$$\tau(\omega) = \tau_\infty - \frac{j\eta\sigma}{\eta_0\rho_0\omega}\left\{1 + j\frac{4\eta_0^2\tau_\infty^2\rho_0\omega}{\eta\Lambda^2\sigma^2}\right\}^{\frac{1}{2}} \tag{3}$$

β(ω) is the air dynamic compression degree function for micro aperture material.

$$\beta(\omega) = \gamma - (\gamma - 1)\left[1 - \frac{j\eta\sigma}{\rho_0\eta_0' P_r\omega}\left(1 + \frac{4j\rho_0\eta_0'^2 P_r\omega}{\Lambda'^2\sigma^2\eta}\right)^{\frac{1}{2}}\right]^{-1} \tag{4}$$

After calculation, the incidence impedance Z can be put in equation (5) to get sound absorption coefficient.

$$\alpha = \frac{4\,\mathrm{Re}(z)}{(1 + \mathrm{Re}(z))^2 + (\mathrm{Im}(z))^2} \tag{5}$$

where α is the sound absorption coefficient.

After take the parameters of PTFE micro aperture membrane in equation 5, MATLAB is used to plot the sound absorption coefficient in the α-*f* curve, as shown in Fig. 5 where *f* is frequency.

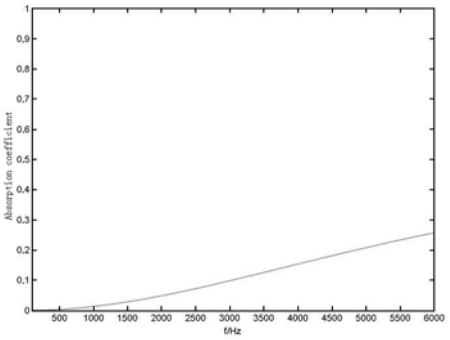

Fig 5 Theoretical sound absorption coefficient α -*f* curve

Compare Fig. 4 and Fig. 5, it is discovered that the two curves is in the similar range, although the difference between peak point and sound absorption coefficient in low frequency range is relatively high. The reason is that in the theoretical modeling, the PTFE material is assumed to be composed of a collection of large amount of rigid hollow tube, while in reality, it is elastic material. So its elastic modulus is relatively low, and the inner impedance is relatively high. For this reason, it creates an elastic sound absorption effect [8]. In addition, the aperture structure in PTFE material is not regular. Plus, there are many agglomerations inside the PTFE material, as shown in Fig. 1.So it makes the experimental results, in peak point and in low frequency range, different from theoretical calculation. On the whole, the theoretical curve correlates with the experimental results approximately.

3.1.2 The relationship between thickness and sound absorption coefficient

The thickness of the air layer behind the sound absorption material has dramatic effect on sound absorption performance. Fig. 6 shows that, adding air layer behind the material can increase the average sound absorption performance. For most of the cases, it is resonated sound absorption. When the thickness of the sound layer increases, the maximum sound absorption coefficient moves to lower frequency band. The band is also broadening. However, when it reaches certain value, the maximum point starts to decrease.

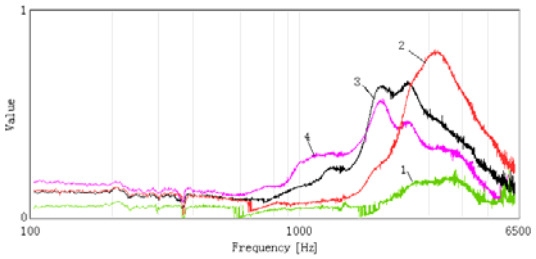

d=0.45μm 1.D=0cm 2.D=1cm 3.D=2cm 4.D=3cm

Fig 6. Connection between Absorption Coefficient and Depth of Cavum

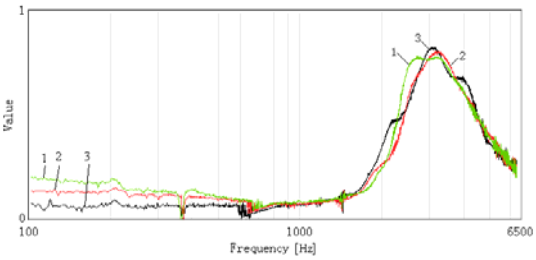

D=1cm 1.d=0.22μm 2.d=0.45μm 3.d=0.8μm

Fig 7. Connection between Absorption Coefficient and Aperture Diameter

Fig.7 shows that when the aperture is decreasing，the resonate absorption maximum value is decreasing. Under the frequency of 1000 Hz, the sound absorption coefficient is increasing when the aperture diameter is decreasing. The improvement of sound absorption performance is due to the fact that when aperture is decreasing, the material density is increasing. Also, the material aperture ratio is another impact factor that cannot be ignored. Because for multi perforated material, it is difficult to define the relationship among aperture diameter, aperture ratio and density, so it is possible for the existence of deviation between theoretical calculation and experimental result. In a word, in order to get a better sound absorption performance based on specific application, it is recommended to balance the aperture diameter and aperture ratio.

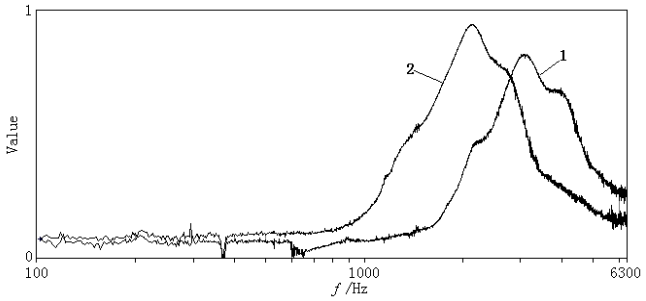

d=0.8μm D=1cm 1.t=150μm 2.t=450μm

Fig8. Connection between sound absorption characteristic and thickness of material

Since the enlargement of material thickness may increase the sound resistance, the material thickness affects the sound absorption performance to a large extent. As figure 8 shows, when the thickness is increasing, the high frequency sound absorption performance increases dramatically. The average sound absorption coefficient increases, resonant sound absorption increases, sound absorption frequency band broadens, and moves to the lower frequency area.

3.2 Sound isolation measurement

In order to describe the inherent sound isolation performance of the material, the sound transmission loss measurement is used to test. Sound transmission loss(TL) is defined as ratio of sound energy between before material and behind the material: $R = 10lg(E_i / E_t)$ [6] .E_i is energy of incident sound wave, E_t is transmission sound wave.

3.2.1 Sound isolation characteristic

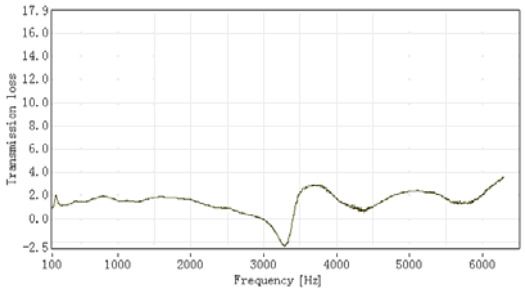

Fig 9. The curve of transmission loss with aperture diameter 0.22μm

Fig. 9 shows that, less than 3000Hz, the TL is less than 2dB. TL fluctuates after 3500Hz, and the biggest value is less than 4dB. The reason is that aperture diameter of PTFE micro aperture membrane is small and the thickness is low. The distance is small from membrane to the center. The aperture tube is connected to the air, and it keeps thermo static. Heat conduct execute quickly when sound ware spears through the tube, so it can be treated as isothermal state. Thus the sound speed is $c = c_0 a/2 \times \sqrt{\rho_0 \omega / \gamma \eta}$ [6], it is smaller than the sound velocity in the space without boundary. The density is lower than usual material, and ratio f cavity can reaches 80%, and density is small. The accumulate effect is that characteristic impedance is similar to that value of air, so that most of the wave energy can enter the material. Plus, it is known that the sound transmission loss from the material itself is very small, and most of the energy is transmit to the opposite side of the material, thus makes it fine sound transmission material.

3.2.2 The relationship between sound isolation and aperture diameter

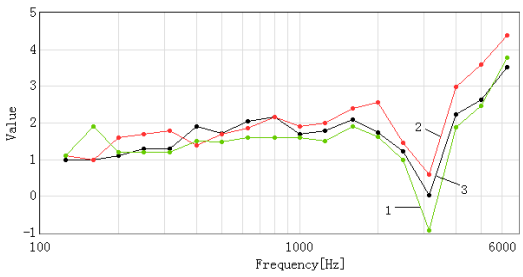

1.d=0.22μm 2.d=0.45μm 3.d=0.80μm

Fig 10: Connection between TL and aperture diameter

As shown in Fig.10, the shape of three curves is approximately the same. The transmission loss of PTFE micro-aperture membrane whose aperture diameter is 0.22um is lowest. The aperture diameter with 0.8um ranks the middle .The aperture diameter with 0.45um is the highest. The reason is that there is a balance between aperture diameter and the density of cavity, so for different application, it is recommended to analyze their ratio.

3.2.3 The relationship between sound isolation and material thickness

As shown in Fig. 11 the TL increases when thickness increases. The high frequency increase more than low frequency. The resonant frequency of sound isolation lowers, and sound isolation curve remains the same. Therefore, when it is used as sound transmission material, it is better to decrease the thickness.

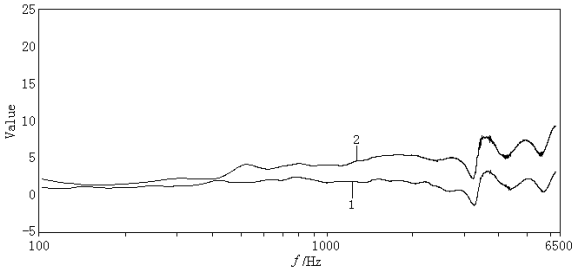

d=0.80m 1.t=150μm 2.t=450μm

Fig 11: Connection between Transmission Loss and thickness of material

IV.SUMMARY AND FUTURE WORK

PTFE micro aperture membrane has similar characteristic impedance as the air, which ensures that the sound wave can go through the material. With a thorough investigation of PTFE micro/nano aperture membrane, it is discovered that in the frequency range of 100Hz-1500Hz, the material reveal well sound transmission characteristic. In the frequency range of 1500Hz-6300Hz, it is reveal resonant sound absorption characteristic. Thus, it can be utilized in both as fine sound transmission material and fine sound absorption material in different frequency range as protective layer for acoustic sensors and generators. The future work, the membrane will be doped with hydrophobic nano-particle, thus inherit waterproof and dustproof feature for even more wide range of potential biomedical applications.

REFERENCES

[1] Zhang Chaoqian, Lou Wenzhong,Qiao Jie. Application of Microphone in Sound Collection System for Aircraft in Low Altitude[J]・CHINESE JOURNAL OF SENSORS AND ACTUATORS, 2006,19(5):2276-2282

[2] Ci Gang、Zheng Shuqin. Manufacture and application of PTFE Micro-aperture Membrane[C] //Zhu Chao.Metallurgical Environmental Protection: National bag filter and filter technology exchange conference proceedings.Kunming: THE CHINESE SOCIETY FOR METALS,2004,c: 43-44.

[3] Liu Xiaosong,Lou Wenzhong. Measurement of Acoustic Performance of PTFE Microporous Membrane [J]. NANOTECHNOLOGY AND PRECISION ENGINEERING , 2008,6(2)：85-88.

[4] Kang Yong,Yao Peng,Kong Xinjun. Study on Preparation of a New Compound Micro-membrane Filter Media [J]・CHEMICAL INDUSTRY AND ENGINEERING PROGRESS,2003,22(6):606-609.

[5] Sun Guangrong. Material and structure of sound absorption[J]. ART SCIENCE AND TECHNOL・2001,(3):12-17.

[6]HeLin,Zhu Haichao.Acoustic Theory and Application [M].Beijing:Science Press,2006:77**,** 168

[7],Ma Dayou. Fundamental Theory of Modern Acoustics Science[M]. Beijing:Science Press,2005:66-67

[8] Du Gonghuan, Zhu Zhemin, Fundamentals of Acoustic[M]. Nanjing:Nanjing University Press, 2006: 464-472.

2A2-2

Two-Photon-Excited Fluorescence Enhanced by Metal Nanoparticles: the Effect of Nonradiative Energy Transfer

Zhenling Yang , Yanqiang Yang *

Center for Condensed Matter Science and Technology, Harbin Institute of Technology, China

***Abstract* — Two-photon-excited fluorescence (TPEF) enhancement of a semiconductor quantum dot (SQD) adsorbed on a Au nanoparticle (NP) was investigated theoretically. Surface plasmon resonance (SPR) enhancement of the exciting light and radiative rate of the SQD, and nonradiative energy transfer (NRET) from SQD to Au NP were taken into account. Compared to the unitary enhancement factor obtained from considering SPR enhancement only, TPEF enhancement factor puts up dispersive property and greatly shrinks, even more than 90 percents in special conditions. It was indicated that the peak and the valley of the TPEF enhancement curve are not consistent with the peaks of positive SPR enhancement curve and negative NRET rate curve. By tuning SPR of the Au NP to the exciting light wavelength, larger enhancement of TPEF was observed. All these should be attributed to the effect of nonradiative energy transfer from SQDs to Au NPs.**

Keywords — ***Metal nanoparticle, Nonradiative energy transfer, Surface plasmon resonance, Two-photon-excited fluorescence***

I. INTRODUCTION

Two-photon-excited fluorescence (TPEF) is a third order nonlinear optical process, whose excitation probability scales quadratically with the incident light, confining it to the proximate vicinity of the focal plane of a focused beam. Therefor the spatial resolution is observably increased [1], which induced widely applications of TPEF in confocal imaging [2,3,4]. Composite systems based on metal nanoparticles (NPs) represent opportunities to enhance optical responses, such as surface-enhanced Raman scattering [5], second harmonic generation [6]. More recently metal NPs has been applied to TPEF due to the tremendous electric field enhancement at the surface plasmon resonance (SPR) [7,8,9,10,11,12]. More than two order of magnitudes of enhancements have been reported. However, nonradiative energy transfer from fluorophore to metal NPs should be taken into account at appropriate surface distance and special spectral rang [13,14].

In order to have a better understanding of metal NPs assisted TPEF, we present a theoretical study of TPEF enhancement in a composite system combined with Au NPs and semiconductor quantum dots (SQDs). SQDs are considered to have large multiphoton absorption cross section and have thus been the focus of material research for multiphoton fluorescence imaging [2,15]. SQDs adsorb on the surface of Au NPs with 1nm surface distance controlled by biolinkers. The radius of SQD was supposed to be 2nm. SPR enhancement of the exciting light and radiative rate of the SQD, and nonradiative energy transfer from SQD to Au NP were taken into account. SPR property can be changed by changing metal NPs' size, shape and medium dielectric constant [16,17], and in this letter, the SPR enhancement effect was changed through changing the size of Au NP and medium dielectric constants. Dispersive curve of TPEF enhancement factor was obtained. By tuning SPR of the Au NP to the exciting light wavelength, larger enhancement of TPEF was observed. All these should be attributed to the effect of nonradiative energy transfer from SQDs to Au NPs.

II. FORMALISM

TPEF intensity should be generally expressed by the following expression when $I_0 \beta D \ll 1$ [18],

$$I_{fluo} \propto \Phi I_0^{\,2} \beta D \tag{1}$$

Where $\Phi = \gamma_{rad} / (\gamma_{rad} + \gamma_{nonrad})$ is quantum yield of the fluorophore and I_0 , β , D are the incident light intensity, two photon absorption coefficient and the thickness of the sample, respectively. It is known that the incident light and the radiative rate of fluorophore can be modified strongly in the presence of metal NPs

$$I = P(\omega_0) I_0 \text{ and } \gamma_{rad} = P(\omega) \gamma_{rad}^{\,0}$$

Where I_0 and $\gamma_{rad}^{\,0}$ are the incident intensity and radiative rate of the fluorophore in the absence of the metal NPs, ω and ω_0 are emission and incident laser frequencies. $P(\omega)$ is the electromagnetic-field enhancement factor, which can be obtained by solving Laplace equation describing the potential distribution around a conductor sphere in uniform electric field.

$$P(\omega) = \left| 1 + 2 \frac{\varepsilon_m - \varepsilon_0}{\varepsilon_m + 2\varepsilon_0} \left(\frac{R_0}{R} \right)^3 \right|^2 \tag{2}$$

Where ε_m and ε_0 are the dielectric constants of metal NP and medium respectively. R_0 and R are the radius of metal NP and the distance to the center of sphere. We use the following formula to describe the nonradiative energy transfer rate at emission wavelength λ [14]

*Contact author:yqyang**@hit.edu.cn.***

$$\frac{\gamma_{et}(\lambda)}{\gamma_{rad}{}^{0}(\lambda)} = \frac{6}{R^6} R_0^3 \left(\frac{\lambda}{2\pi}\right)^3 \cdot \frac{1}{\varepsilon_0^{2.5}} \mathrm{Im}[\frac{\varepsilon_m(\lambda)-\varepsilon_0}{\varepsilon_m(\lambda)+2\varepsilon_0}] \quad (3)$$

In our composite system described above, TPEF intensity should be expressed by the following expression

$$I_{fluo}{}^{*}(\omega) \propto \frac{P(\omega)\gamma_{rad}{}^{0} P^2(\omega_0) I_0{}^2(\omega_0)\beta D}{\gamma_{nonrad} + P(\omega)\gamma_{rad}{}^{0} + \gamma_{et}} \quad (4)$$

and the enhancement factor of TPEF is

$$A(\omega) = P^2(\omega_0)\frac{P(\omega)}{P(\omega) + \gamma_{et}/\gamma_{rad}{}^{0}} \quad (5)$$

When the quantum yield of the SQD $\Phi \approx 1$, $P^2(\omega_0)$ is the TPEF enhancement factor when SPR effect is considered only. Here the dielectric constants of Au NPs we used was given by Johnson and Christy in 1972 [19]. Three hundreds dielectric constants of Au in three hundreds incident light wavelength from 400nm to 850nm were obtained by interpolating to the polynomial fit of the dielectric constants given by Johnson and Christy, in order to getting smooth curves.

III. RESULTS AND DISCUSSION

It is supposed that the composite system described above is excited by 800nm femtosecond laser. The medium dielectric constant can be changed in different solvent and polymer, and here we considered three discretionary constants.

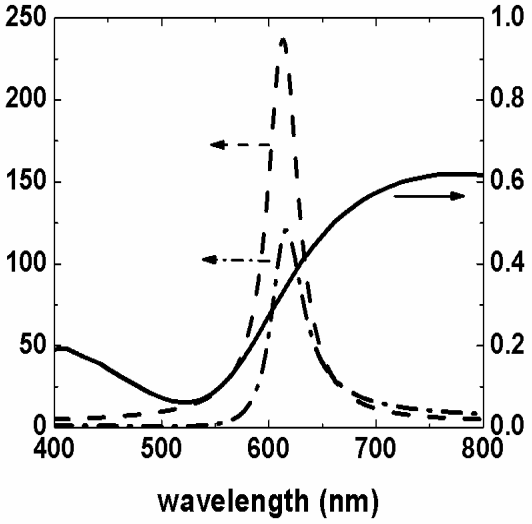

Figure 1. $P(\omega)$ (dash dot), $\gamma_{et}/\gamma_{rad}{}^{0}$ (dash)and $A(\omega)/P^2(\omega_0)$ (solid) of the composite system combined with a 10nm Au NP and a 2nm SQD with 1nm surface distance, excited by 800nm femtosecond laser. The medium dielectric constant is 5.

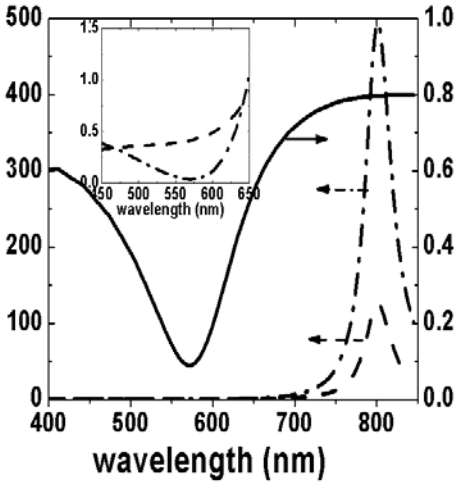

Figure 2. $P(\omega)$ (dash dot), $\gamma_{et}/\gamma_{rad}{}^{0}$ (dash)and $A(\omega)/P^2(\omega_0)$ (solid) of the composite system combined with a 10nm Au NP and a 2nm SQD with 1nm surface distance, excited by 800nm femtosecond laser. The medium dielectric constant is 12. The insert figure is $P(\omega)$ and $\gamma_{et}/\gamma_{rad}{}^{0}$ from 450nm to 650nm to manifest the origin of the solid curve clearly.

Electromagnetic field enhancement factor $P(\omega)$, nonradiative energy transfer rate/ intrinsic radiative rate of SQDs $\gamma_{et}/\gamma_{rad}{}^{0}$ and TPEF enhancement factor $A(\omega)/P^2(\omega_0)$ of the composite system containing a 10nm Au NP are given by

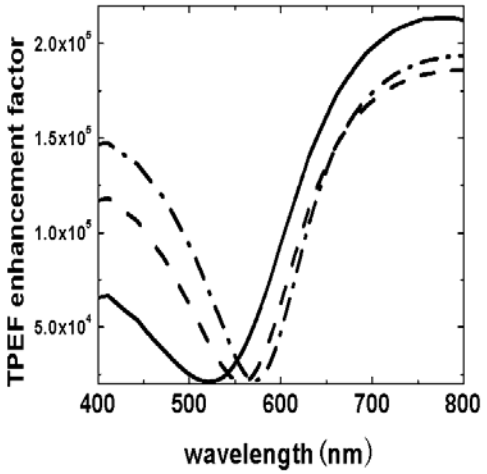

Figure 3. The TPEF enhancement factor of the composite system combined with a 10nm Au NP and a 2nm SQD with 1nm surface distance, excited by 800nm femtosecond laser. The medium dielectric constants are 5 (solid), 10 (dash) and 12 (dash dot). The solid curve was multiplied by 5000, while the dash one was multiplied by 50 for better comparing.

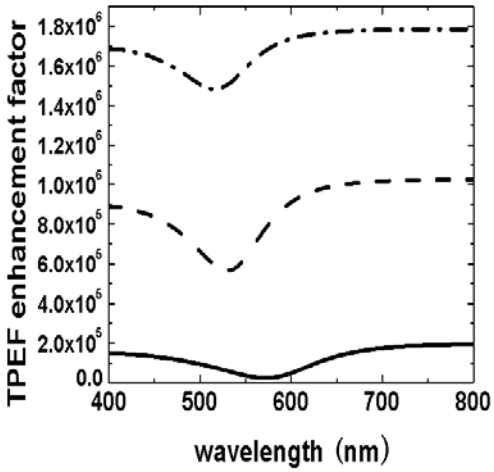

Figure 4. The TPEF enhancement factor A of the composite system combined with different size of Au NP and a 2nm SQD and 1nm surface distance, excited by 800nm femtosecond laser. The size of Au NP is 10nm (solid), 20nm (dash) and 30nm (dash dot). The medium dielectric constant is 12.

Fig. 1, and the medium dielectric constant is 5. More than 40% of enhancement factor is reduced compared to $P^2(\omega_0)$, even 90% for 520nm emission wavelength. It is not as we anticipated that the minimum the TPEF enhancement factor appears in the region bluer than the maximum of nonradiative energy transfer rate, which is more obviously revealed in Fig. 2 when the medium dielectric constant is 12. The varieties of the peak and valley positions of TPEF enhancement curve are induced by taking nonradiative energy transfer from SQDs to Au NPs into account. The key to understanding the dispersion properties of these curves and the bluer phenomena comes from recognizing the permittivity of Au varies with wavelength, and the dispersion of TPEF enhancement factor will induce a distortion of TPEF line shape. By tuning the SPR peak to the exciting wavelength region (Fig. 2), enhancement greater than 4 orders of magnitudes is acquired, and the vale of the curve shows a red shift, which is more obviously revealed in Fig. 3. When the SPR peak is tuned to the exciting region by changing the medium dielectric constant, the enhancement factor of the exciting light becomes greater, at the same time nonradiative energy transfer is deeply suppressed, which results in the greater enhancement of TPEF and the red shift of the vale. In Fig. 4, TPEF enhancement factor increases with increasing the size of Au NP, and the vale of enhancement curve shows a blue shift, because the near filed enhancement increases while nonradiative energy transfer decreases with increasing the size, without any peak position shift in the same medium dielectric constant, which results from utilizing bulk material permittivity of Au.

IV. CONCLUSION

In summary, TPEF enhancement of a composite system combined with a Au NP and a SQD was investigated theoretically. Surface plasmon resonance (SPR) enhancement of the exciting light and radiative rate of the SQD, and nonradiative energy transfer from SQD to Au NP were taken into account. Compared to the unitary enhancement factor obtained from considering SPR enhancement only, TPEF enhancement factor puts up dispersive property and greatly shrinks, even more than 90 percents in special conditions. It is indicated that the peak and the valley of the TPEF enhancement curve are not consistent with the peaks of positive SPR enhancement curve and negative NRET rate curve. Through changing the size of Au NP and the medium dielectric constant, SPR peak position and intensity of Au NPs were tuned, resulting in a greater than 4 orders of magnitudes enhancement of the TPEF. These results should be attributed to the effects of SPR enhancement and nonradiative energy transfer from SQD to Au NP. People can tune SPR by changing size and shape of metal NPs, to achieve enhancing SPR effect and minishing nonradiative energy transfer effect. This will promote metal NPs more widely used in TPEF.

REFERENCES

[1] W. Denk, J. H. Strickler and W. W. Webb, “Two-photon laser scanning fluorescence microscopy,” Science, vol. 248, pp. 73–76, April 1990.

[2] D. R. Larson, W. R. Zipfel, R. M. Williams, S. W. Clark, M. P. Bruchez, F. W. Wise and W. W. Webb, “Water-Soluble Quantum Dots for Multiphoton Fluorescence Imaging in Vivo,” Science, vol. 300, pp. 1434–1436, May 2003

[3] J. M. Squirrel, D. L. Wokosin, J. G. White and B. D. Bavister, “Long-term two photon fluorescence imaging of mammalian embryos without compromising viability,” Nat. Biotechnol. vol. 17, pp. 763–767, Aug. 1999

[4] R. H. Kohler, J. Cao, W. R. Zipfel, W. W. Webb, and M. R. Hansen, “Exchange of Protein Molecules Through Connections Between Higher Plant Plastids,” Science, vol. 276, pp. 2039–2042, June 1997

[5] S. Nie and S. R. Emory, “Probing Single Molecules and Single Nanoparticles by Surface-Enhanced Raman Scattering,” Science, vol. 275, pp. 1102–1106, Feb. 1997

[6] C. K. Chen and A. R. B. de Castro and Y. R. Shen, “Surface-Enhanced Second-Harmonic Generation,” Phys. Rev. Lett., vol. 46, pp. 145–148, Jan. 1981

[7] H. Kano and S. Kawata, “Two-photon-excited fluorescence enhanced by a surface plasmon,” Opt. Lett., vol. 21, pp. 1848–1850, Nov. 1996

[8] E. J. Sanchez, L. Novotny, and X. S. Xie, “Near-field fluorescence microscopy based on two-photon excitation with metal tip,” Phys. Rev. Lett., vol. 82, pp. 4014–4017, May 1999

[9] I. Gryczynski, J. Malicka, Y. Shen, Z. Gryczynski, and J. R. Lakowicz, “Multiphoton excitation of fluorescence near metallic particles: Enhanced and localized excitation,” J.Phys. Chem. B, vol. 106, pp. 2191–2195, Mar. 2002

[10] Y. Shen, J. Swiatkiewicz, T.-C. Lin, P. Markowicz, and P. N. Prasad, “Near-field probing surface plasmon enhancement effect on two-photon emission,” J.Phys. Chem. B, vol. 106, pp. 4040–4042, Apr. 2002

[11] W. Wenseleers, F. Stellacci, T. Meyer-Friedrichsen, T. Mangel, C. A.Bauer, S. J. K. Pond, S. R. Marder, and J. W. Perry, “Five Orders-of-Magnitude Enhancement of Two-Photon Absorption for Dyes on Silver Nanoparticle Fractal Clusters,” J.Phys. Chem. B, vol. 106, pp. 6853–6963, Jul. 2002

[12] I. Cohanoschi and F. E. Hernandez, “Surface Plasmon Enhancement of Two- and Three-Photon Absorption of Hoechst 33 258 Dye in Activated Gold Colloid Solution,” J.Phys. Chem. B, vol. 109, pp. 14506–14512, Aug. 2005

[13] S. Bhowmick and S. Saini and V. B. Shenoy and B. Bagchi, “Resonance energy transfer from a fluorescent dye to a metal nanoparticle,” J. Chem. Phys., vol. 125, pp. 181102, Nov. 2006

[14] A. O. Govorov, G. W. Bryant, W. Zhang, T. Skeini, J. Lee, N. A. Kotov, J. M. Slocik and R. R. Naik, “Exciton-Plasmon Interaction and Hybrid Excitons in Semiconductor-Metal Nanoparticle Assemblies,” Nano Lett., vol. 6, pp. 984-994, Apr. 2006

[15] X. Michalet, F. F. Pinaud, L. A. Bentolila, J. M. Tsay, S. Doose, J. J. Li, G. Sundaresan, A. M. Wu, S. S. Gambhir, and S. Weiss, “Quantum dots for live cells, in vivo imaging, and diagnostics,” Science, vol. 307, pp. 538–544, Jan. 2005

[16] S. Link, and M. A. EI-Sayed, “Size and temperature dependence of the plasmon absorption of colloidal gold nanoparticles,” J.Phys. Chem. B, vol. 103, pp. 4212–4217, May 1999

[17] S. Link, M. B. Mohamed, and M. A. El-Sayed, “Simulation of the optical absorption spectra of gold nanorods as a function of their aspect ratio and the effect of the medium dielectric constant,” J.Phys. Chem. B, vol. 103, pp. 3073–3077, Apr. 1999

[18] G. S. He, L. S. Tan, Q. D. Zheng and P. N. Prasad, “Multiphoton absorbing materials: molecular designs, characterizations, and applications,” Chem. Rev. , vol. 108, pp. 1245–1330, Apr. 2008

[19] P. B. Johnson, R. W. Christy, “Optical Constants of the Noble Metals,” Phys. Rev. B, vol. 6, pp. 4370–4379, Jul. 1972

2A2-5

Micro Integrated Laser Doppler Blood Flow sensor and its Application to Dehydration Prevention

Hirofumi Nogami[1,*], Wataru Iwasaki[1], Fumio Matsuoka[1], Kazuyoshi Akase[1], Yoshinori Kimura[1,2], Atushi Onoe[2], Eiji Higurashi[3], Satoshi Takeuchi[4], Makiko Kido[4], Masutaka Furue[4] and Renshi Sawada[5]

[1]*Graduate School of Systems Life Sciences, Kyushu University, Fukuoka, Japan*
[2]*Corporate Research and Development Laboratories, Pioneer Corporation, Saitama, Japan*
[3]*Reseach center for Advanced Science and Technology, The University of Tokyo, Tokyo, Japan*
[4]*Department of Dermatology, Graduate School of Medical Sciences, Kyushu University, Fukuoka, Japan*
[5]*Department of Mechanical Engineering, Kyushu University, Fukuoka, Japan*

***Abstract* — Using Micro Electro Mechanical Systems (MEMS) technologies, we have developed the world's smallest, lightest, and least power-consuming integrated laser Doppler blood flow sensor. Unlikely commercial optical fiber type blood flow instruments, the structure of our sensor need not optical fiber, which is also invulnerable to any movements of the person wearing it. Therefore our sensor enables stable measurement the person raising an arm with our sensor attached to a finger-tip (arm-raising test). In this paper, we present a new structure of an integrated laser Doppler blood flow sensor and its application to dehydration prevention using our sensor and arm-raising test.**

Keywords — ***Laser Doppler Blood Flowmeter, Micro Electro Mechanical Systems, arm-raising test, dehydration prevention***

I. INTRODUCTION

Laser Doppler blood flow measuring devices have been studied for many years because they enable noninvasive examination of microcirculation [1], and detection of physiological information. However, conventional and commercial optical fiber-type blood flow instruments cannot be used in daily life and the application of those is limited. Since the entire instruments are large and heavy, and the power consumption is also high. Further, the optical fiber is vulnerable to vibration or movement, and the output signal is easily affected by the movements of the person using it. To solve these challenges, we previously developed an integrated laser Doppler blood flow sensor chip consisted of only a laser diode (LD), a photodiode (PD), a polyimide waveguide and a silicon cap on the same silicon substrate (2 mm × 3 mm) [3]. In addition, our blood flow sensor having the chip (a MEMS blood flow sensor) can see use in a wide range of applications such as systemic sclerosis diagnosis using an arm-raising test [4] and monitoring alcohol consumption to prevent drinking and driving [5]. And new application is to prevent dehydration of a person in daily life. Since dehydration is suffered from by plenty of people and severe dehydration can cause disturbed consciousness, remarkable hyperglycemia and remarkable hyperosmolarity. By not drinking enough water, an elderly person may become dehydrated and susceptible to brain infarction.

This paper describes a new structure of the sensor chip which enables wafer-level packaging to improve productivity. We also evaluate means to detect dehydration of a person using our MEMS blood flow sensor.

II. BLOOD FLOW MEASUREMENT PRINCIPLE

Fig.1 shows a schematic of blood flow measurement principle. The laser beam from a laser diode (LD) is emitted into the skin tissue and scattered by it. The backscattered light from the body tissue is detected on a photodiode (PD). The backscattered light is of two kinds: Doppler-shifted light caused by moving particles (mainly red blood cells of the capillary and arteriole) and non-Doppler-shifted light scattered by static tissue. The light is interfered at the PD, and intensity modulations, which are related to blood velocity, are observed on the PD. The power spectrum of these intensity modulations includes random characteristics of the velocity vector of blood perfusion in the cutaneous vessel. In such a case, the blood flow is indicated by following formula [6].

$$\langle\omega\rangle = \omega\int P(\omega)d\omega \qquad (1)$$

The blood flow is proportional to the averaged velocity times the concentration of Doppler scattering particles, which is statistically-derived flow. $P(\omega)$ is the power spectrum of the frequency distribution, and $\langle\omega\rangle$ is the first moment of the power spectrum of the frequency distribution. We use $\langle\omega\rangle$ as the statistically-derived blood flow value.

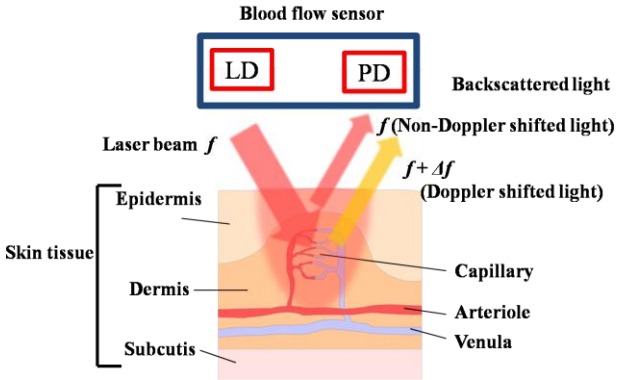

Fig.1 Schematic of blood flow measurement principle

*Hirofumi N. is with the Microsystems & Bioengineering Lab, Graduate School of Systems Life Sciences, Kyushu Univ. 744, Motooka, Nishi-ku, Fukuoka-city 819-0395, Japan (phone:+82-92-802-3241;fax:+81-92-802-3241;e-mail:nogami@nano-micro.mech.kyushu-u.ac.jp).

III. MICRO INTEGRATED SENSOR CHIP AND THE BLOOD FLOW SENSOR

A. *New structure of an integrated blood flow sensor chip*

Fig.2 (a) and (b) show schematic of a new structure of an integrated blood flow sensor chip. The new structure enables wafer level packaging because it is sealed tightly by covering the cavity structure of the bottom silicon plate with the upper silicon plate. Two cavities of the bottom silicon plate are created using anisotropic silicon etching to mount a LD chip and a PD chip. The LD chip is a distributed feed-back bragg-reflector LD (DFB-LD) chip with a wavelength of 1310 nm, and the PD is an InGaAs type PD. This bottom silicon plate reflects the laser beam emitted from the LD chip vertically to the silicon plate by means of a micromirror formed by depositing gold onto the silicon(111)facet. Therefore, the upper silicon plate can serve to seal the two cavities of the bottom silicon plate, which enables production of a wafer level package. In addition, the upper silicon plate has a silicon microlens, which collimates the reflected laser beam [7].

B. *Our MEMS blood flow sensor having an integrated blood sensor chip*

Fig.3 shows a photograph of our blood flow sensor consisting of the electric circuit box and the probe (MEMS blood flow sensor). The probe has an integrated blood flow sensor chip, which is 5.6 x 12.0 x 17.5 mm and weighs 3 g. The size of the electric circuit box with a display monitor and a rechargeable battery is 47.0 x 65.0 x 19.0 mm and it weighs 67 g. The detected signals of the probe are sent to the closely connected the electric circuit box. The electric circuit box can send the signals directly to a notebook PC using a wireless transmitter, which enables continuous monitoring in any situation.

The output signals of the MEMS blood flow senor were compared to those of a commercial fiber-type instrument. Fig. 4 (a) shows a photograph of the fiber-type instrument and the MEMS blood flow sensor attached to finger-tips. In this condition, the person was waving his hand and the blood flow

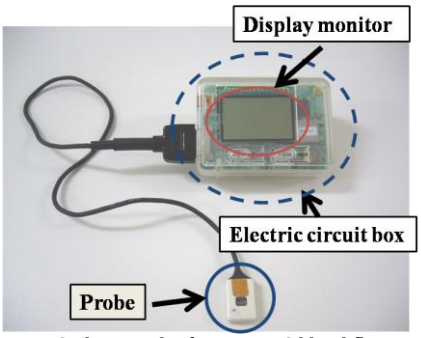

Fig. 3 Photograph of our MEMS blood flow sensor

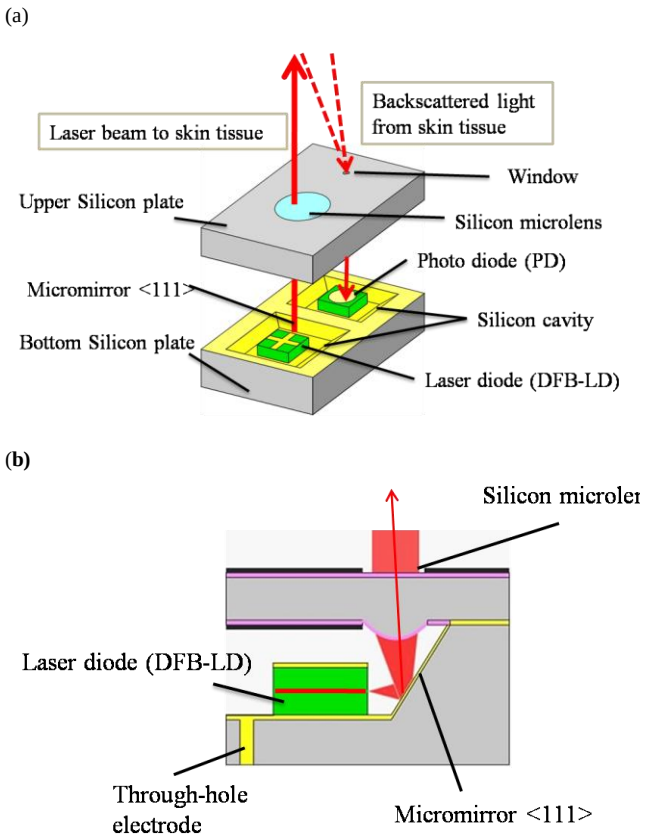

Fig.2 Schematic view (a) and cross sectional-view (b) of a new structure of an integrated blood flow sensor.

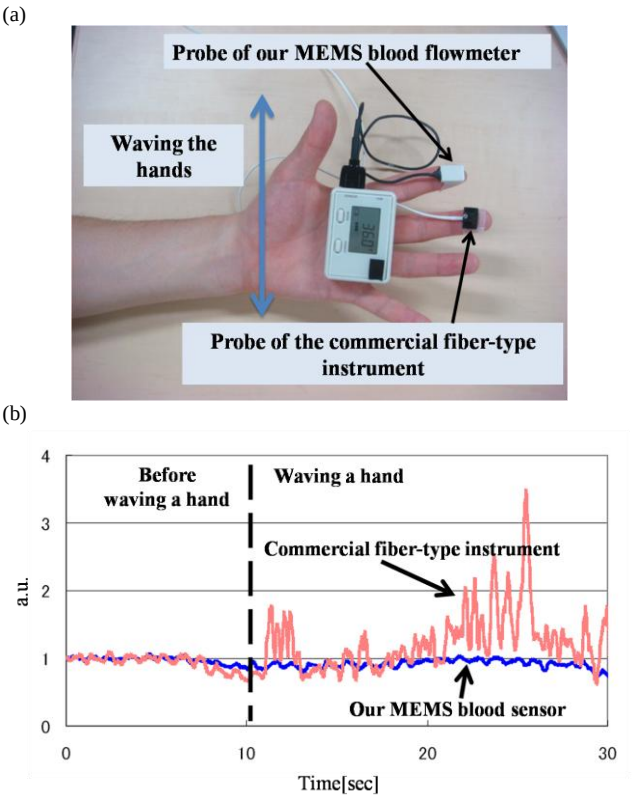

Fig.4 Our MEMS blood flow sensor and the commercial fiber-type instrument were attached to the finger-tips (a), and they simultaneously measured finger-tips blood flow when the person was waving the hand (b).

was simultaneously measured by both the MEMS blood flow sensor and the fiber-type instrument (Fig.4 (b)). Before waving his hand, both the MEMS blood flow sensor and the fiber-type instrument could measure the blood flow. While the person was waving his hand, the MEMS blood flow sensor could measure the blood flow, but the fiber-type instrument couldn't measure the blood flow as the output signals were affected by the vibration and movement of the optical fiber. Therefore, the MEMS blood flow sensor was able to take stable measurements even when the subject being measured was moving freely, than when compared to a conventional instrument.

IV. Experiment

A. Dehydration and examinees

The examinees were nine males (mean age 23.0, range 21 – 27; mean weight 61.4 kg, range 55.9 – 69.4). Mild dehydration is defined as a 2% to 4% loss of body weight, and it can be recovered by drinking water. The purpose of this paper was to detect mild dehydration state, and the dehydration ratio was equivalent to a 2% loss of their body weight (mean dehydration ratio 2.5%, range 2.0 – 3.3). The examinee became dehydrated by sweating in a sauna. Dehydration state was set as the examinee's state three hours after he left the sauna. Non-dehydration state was set as the examinee's state before he entered the sauna. The dehydration ratio was calculated from the body weight measured using a scale.

B. Arm-raising test using our MEMS blood flow sensor

Fig.5 (a) shows a photograph of the arm-raising test using our MEMS blood flow sensor. The arm-raising test had the person raise his arm with our MEMS blood flow sensor attached to his finger-tip and could obtain more physiological information than by measuring in a static condition. It is one of the tolerance tests, which can obtain more physiological information than by measuring a static condition. Therefore, inadequate blood flow caused by dehydration was considered to be detected when using this arm-raising test. The arm-raising test was done in non-dehydration and dehydration states. When the arm-raising test was done, the room temperature was controlled from 24˚C to 26˚C and the finger-tip temperature of an examinee was over 28 ˚C.

The four parameters calculated from the blood flow of the arm-raising test are considered to change greatly between dehydration and non-dehydration states (Fig.5 (b)). Mean blood flow (MBF) is the average of blood flow value before arm-raising. Minimum inclination (MI) is the lowest value of difference blood flow value per half a second, they are within 2 seconds when the examinee raised the arm. Recovery rate (RR) is the difference value between the minimum blood flow value within 10 seconds when the examinee raised the arm and the average blood flow value for 15 seconds the time of the minimum blood flow. Mean amplitude (MA) is the average of ten pulse wave amplitudes after 10 seconds when the examinee was raising the arm.

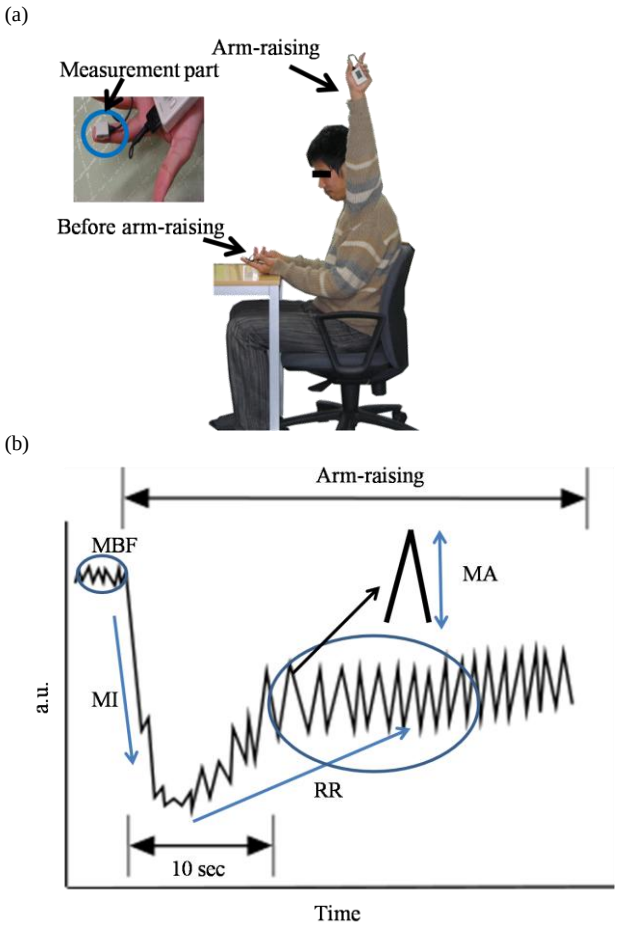

Fig.5 *A photograph of the arm-raising test using our MEMS blood flow sensor(a), and how we calculated 4 parameters from the blood flow data of the arm-raising test(b).* Mean blood flow (MBF) is the average of blood flow value before arm-raising. Minimum inclination (MI) is the lowest value of difference blood flow value per half a second, they are within 2 seconds when the examinee raised the arm. Recovery rate (RR) is the difference value between the minimum blood flow value within 10 seconds when the examinee raised the arm and the average blood flow value for 15 seconds the time of the minimum blood flow. Mean amplitude (MA) is the average of ten pulse wave amplitudes after 10 seconds when the examinee was raising the arm.

Data were presented as the mean ± standard deviation. The statistical difference was determined by a two-side paired *t* test. A difference of $p < 0.05$ was considered significant.

V. Result

A. New integrated blood flow sensor

Fig.6 (a) and (b) show an overview of photograph of a new integrated blood flow sensor chip. The size of a new integrated blood flow sensor chip was 2.0 x 2.7 x 0.9 mm. The upper silicon microlens was made by etching using reflowed photosensitive resist as the etchant mask, and the lower four electrode pads were connected to the four through-hole electrodes (Fig.6 (a)). Two cavities were created using anisotropic silicon etching, and the DFB-LD chip and PD chip were mounted on a silicon cavity. To reflect laser beam from

(a)

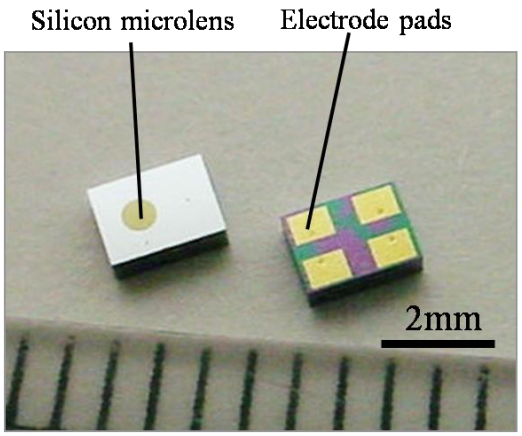

(b)

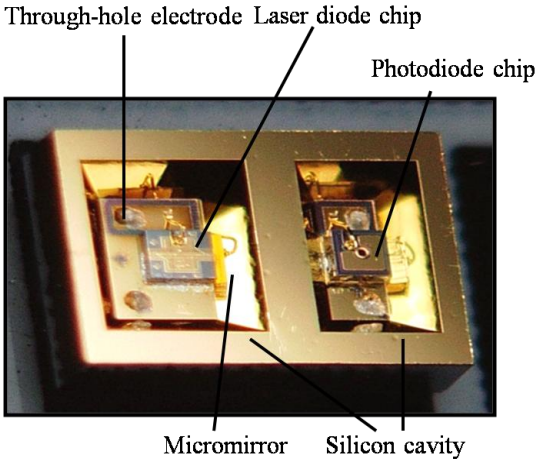

Fig.6 Photographs of the new MEMS blood flow sensor chip. (a) Overview of top side and back side. (b) Silicon cavity after laser diode and photodiode were bonded

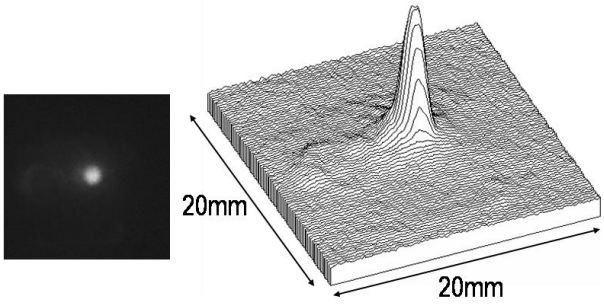

Fig.7 Laser beam profile emmeted from a new integrated blood flow sensor

the DFB-LD chip, gold was deposited on the silicon(111)facet. In addition, an anti-reflection (AR) coating composed of a single layer of SiO2 applied to both the silicon microlens and the laser emission window also reduce the surface reflection loss. As a result, the beam profile was collected and the laser beam loss was low (Fig.7).

B The arm-raising test

Fig.8 shows typical results of the blood flow data for both non-dehydration and dehydration states in the arm-raising test using our MEMS blood flow sensor. Each of the 2 parameters (MBF and RR) of dehydration was visibly lower than those of non-dehydration (Fig.8 (a)). The MA of dehydration was lower than that of non-dehydration (Fig.8 (b)). However, MI was not changed between dehydration and non-dehydration.

Fig.9 shows the 4 parameters in the 9 examinees. The MBF was found to be lower in 6 of 9 examinees with dehydration state than in those with non-dehydration state. However, there was no statistical difference in MBF in this study. (MBF: non-dehydration 47.3 ± 10.1 vs. dehydration 42.9±10.9; P = 0.314.) The experiment showed that the MI was lower in 7 of 9 examinees with dehydration state than in those with non-dehydration state. However, there was no statistical difference in MI (MI: non-dehydration −17.6±7.24 vs. dehydration −20.5±5.40; P = 0.218). The results showed that the RR was lower with 9 in 9 examinees with dehydration state than in those with non-dehydration state. There was statistical

(a)

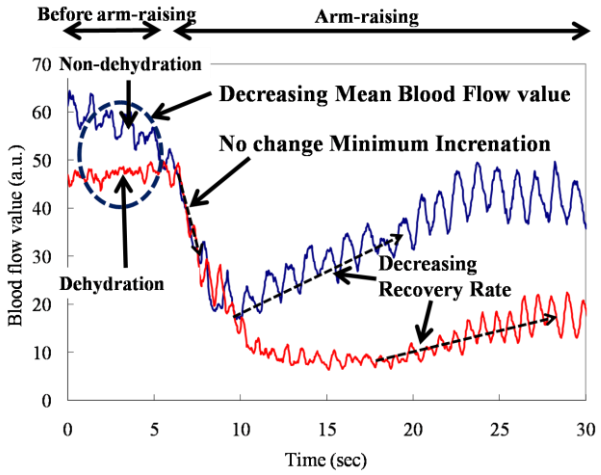

(b)

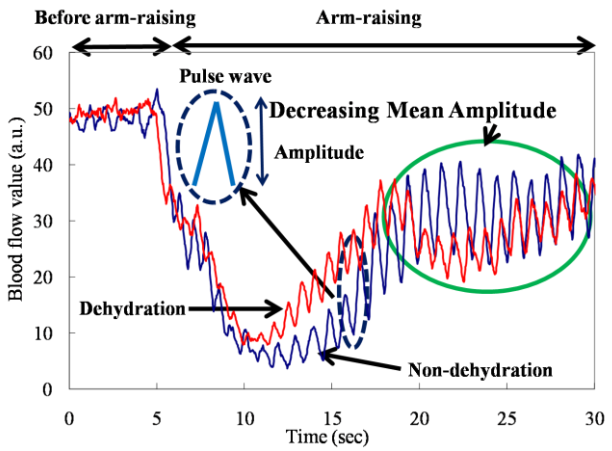

Fig. 8 Typical results of the examinee of both non-dehydration states and dehydration state. Both the mean blood flow value and the recovery rate were visibly different between dehydration and non-dehydration states (a). The mean amplitudes of pulse wave were largely different between

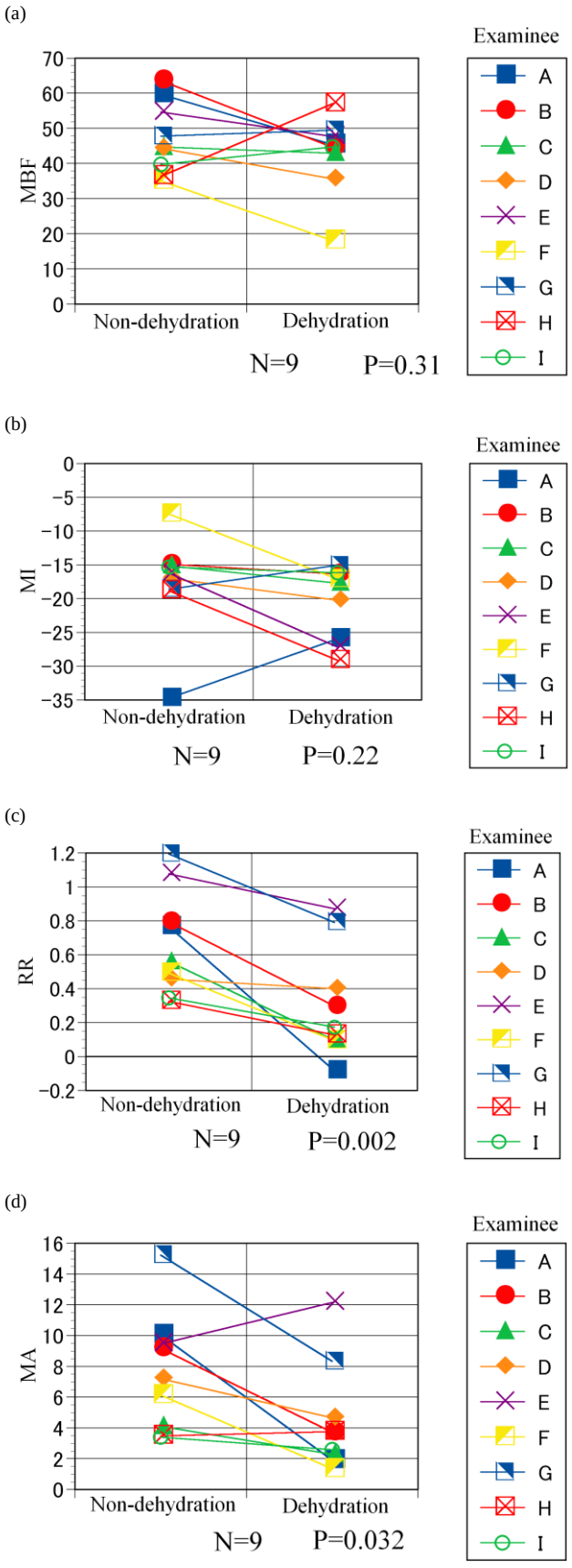

Fig.9 Four parameters compared in non-dehydration and dehydration states. Mean blood flow (MBF) is the average of blood flow value before arm-raising. (a) Minimum inclination (MI) is the lowest value of difference blood flow value per half a second, they are within 2 seconds when the examinee raised the arm. (b) Recovery rate (RR) is the difference value between the minimum blood flow value within 10 seconds when the examinee raised the arm and the average blood flow value for 15 seconds the time of the minimum blood flow. (c) Mean amplitude (MA) is the average of ten pulse wave amplitudes after 10 seconds when the examinee was raising the arm.(d)

dehydration 0.307±0.327; P = 0.00186). The MA was lower with 7 in 9 examinees with dehydration state than in those with non-dehydration state. There was statistical difference in MA (MA: non-dehydration 7.56±3.86 vs. dehydration 4.53±3.53; P = 0.0322). In this study, both the RR and the MA were more effective parameters for detecting dehydration because both RR and MA had statistical differences between dehydration and non-dehydration. In particular, RR was the most effective parameter for detecting dehydration as the RR was lower with 9 in 9 examinees with dehydration state than in those with non-dehydration state.

VI. Conclusion

We have successfully developed a laser Doppler integrated blood flow sensor chip. The new structure of an integrated blood flow sensor chip enabled wafer-level packaging, and its laser loss is low. Our MEMS blood flow sensor can be carried as it is very small, light and low power-consuming. And it can stably measure even the person waving the hand with it attached to a finger-tip.

The arm-raising test using our MEMS blood sensor confirmed that it could detect dehydration when the person's loss of water was 2% of the body weight. Two parameters (RR and MA) of dehydration were significantly lower than those of non-dehydration.

In this study, dehydration was set at when the examinee lost about 2% water of a body weight. To further aid in preventing dehydration, in our next experiments dehydration will be set at when the examinee loses less than 2% waster of a body weight. In the future, we will achieve a new portable device utilizing the arm-raising test for preventing dehydration.

References

[1] M. D. Stern, "In vivo evaluation of microcirculation by coherent light scattering," in Nature, vol.254, London, 1975, pp. 1906-1909.

[2] T.P Newson, A. Obeid, R.S. Wolton, D. Boggett and P. Rolfe, "Laser Doppler velocimetry: the problem of fibre movement artefact," J. Biomed Eng., vol.9, pp.169-172, 1987.

[3] E. Higurashi, R. Sawada, and Takahiro Ito, "An Integrated Laser Blood Flowmeter " .Jounal of Lightwave Technology, Vol21, No.3 March 2003, pp 591-595

[4] M. Kido, S. Takeuchi, S. Hayashida, K. Urabe, R. Sawada* and M. Furue : "Assessment of abnormal blood flow and efficacy of treatment in patients with systemic sclerosis using a newly developed microwireless laser Doppler flowmeter and arm-raising test", Blitish journal of dermatology(1951), Vol.157, No.4, pp.690-697(2007).

[5] W. Iwasaki, Y. Kimura, A. Onoe, H. Nogami "Micro Integrated Laser Doppler Blood Flow Sensor and its Application for the Monitoring of Alcohol Consumption", IEE J. 25th Sensor Symposium on sensors, Micromachines, and Applied Systems, No.55, pp641-644, 2008.

[6] R. Bonner and R. Nossal : “Model for laser Doppler measurement of blood flow in tissue”, Apple. Opt., Vol.20, No.12, pp.2097-2107(1981)

[7] Kimura, A. Onoe, E. Higurashi, and R. Sawada “Low-power Consumption Integrated Laser Doppler Blood Flowmeter with a Built-in Silicon Microlens,”IEEE/LEOS International Conference on Optical MEMS & Nanophotonics 2008, Freiburg, Germany (August 2008)

2A2-6

Study on Wafer-Level Packaging and Electrochemical Characterization of Planar AgCl Micro Reference Electrode

I-Yu Huang [1,*], Chia-Hsu Hsieh[1], Chi-Chih Chu[2]

[1] *Department of Electrical Engineering, Nation Sun Yat-sen University, Kaohsiung, Taiwan.*
[2] *Advanced Semiconductor Engineering Inc., Kaohsiung, Taiwan.*

***Abstract* — This study proposes a novel chip-level packaged planar Ti/Pd/Ag/AgCl/KCl-gel micro reference electrode for the electrochemical and biomedical sensing applications. The miniaturized reference electrode is constructed by two wafers ("Ti/Pd/Ag/AgCl quasi reference electrode wafer" and "KCl-gel cap sealing wafer") and with a total dimension of only 9 mm (L) × 6 mm (W) × 1 mm (H), hundredfold less than the commercial Ag/AgCl reference electrode (OD = 12 mm). Many excellent characteristics were demonstrated by the optimized encapsulated solid-state micro reference electrode, including a very stable cell potential (5 mV drift voltage in 30,000 s), an approximately zero offset-voltage, a very low impedance (<1.50 kΩ) and phase shift (<8.98 º) at normal operation frequency range (0~1 kHz), and a low electro-chemical noise spectrum.**

Keywords — ***Chip-level packaging; Drift and offset voltage; Impedance and phase shift; Micro reference electrode; Noise analysis; Reproducibility***

I. INTRODUCTION

The development of stable and reliable solid-state micro reference electrodes (μREs) could lead to great advances in the practical applications of electrochemical and biomedical microsensors or micro-total analytical system (μTAS). The planar μREs not only facilitated the use of microsensors, but also brought out the advantages of small testing sample volume, all solid-state rugged structure and significant reduction of device physical size.

D. Harame was the first to integrate a silver/silver chloride (Ag/AgCl) structure on the ion-sensitive field-effect transistor (ISFET) chip [1]. In electrochemical or biomedical sensing microsystems, Ag/AgCl thin-film reference electrodes (REs), without any internal reference electrolyte, are often referred as "quasi-reference electrodes (QREs)". However, these QREs are susceptible to changing activity of its primary ion (e.g. $a(Cl^-)$ in Ag/AgCl system) and the existence of interference [2]. Another approach was attempted and devoted to miniaturizing the macroscopic mature liquid-junction RE, yet preserving its basic structure and operational principle. For instance, the "silicon-based planar μREs" with miniaturized liquid-junction were designed to encapsulate the Ag/AgCl electrode in a separate compartment filled with internal reference electrolyte of constant Cl^- activity [3−8]. On the other hand, various non-silicon-based (e.g. conventional glass-tube-based and PDMS-based) miniaturized reference electrodes (MREs) have been continuously developed in the last decade and performed very good electrochemical characteristics [9−17]. The physical size of MREs is about tenfold more than that of μREs and their fabrication processes are not compatible with the silicon-based microfabrication technology, which limits their integration with electronic circuits and the development of system-on-a-chip (SOC). Furthermore, many researches are incorporating the liquid-filled μRE, solid-state QRE and μRE as an integrated part of the ISFET chip fabricated by IC technology and micromachining [5,18−19]. However, to seal a small volume of the saturated KCl electrolyte is still a challenge to mass production fabrication.

In 1998, H. Suzuki and his co-workers utilized a polyimide adhesive layer and a gold backbone structure to improve the durability of the thin-film Ag/AgCl RE [20−22]. The polyimide layer covers the entire surface of Ag layer and makes the AgCl layer grown laterally from the periphery of the patterned Ag electrode. They reported that their electrodes could provide a stable potential for approximately 8 h. On the other hand, our previous researches reported an all solid-state unpackaged planar Ti/Pd/Ag/AgCl/KCl-gel μRE with a very high stable potential (drift voltage < 1 mV over 30 min), very small offset voltage (0.45 mV) and near insensitive to various pH values and Cl- concentrations (less than 2 mV variation over pH4 to pH10 and less than 0.25 mV over KCl concentration ranging from 0.1 M to 0.6 M) [2,19]. However, the potential stability of the unpackaged Ti/Pd/Ag/AgCl/KCl-gel μRE degraded after it was in operation for more than 1 h, since the Cl^- ions of the saturated KCl-gel would diffuse gradually to the sample solution. In addition, no impedance, phase shift and electrochemical noise analysis results of the multi-layered μREs were investigated in our previous studies [2,18−19].

To seal effectively the agarose-stabilized KCl-gel layer and simultaneously reserve a miniature liquid-junction of the planar Ag/AgCl μRE, a novel chip-level packaging technique was developed in this study. Two wafers were used in this research, one referred as the "KCl-gel cap sealing wafer" (with a micromachined KCl-gel filling cavity and a micro liquid-junction aperture) and another wafer denoted as the "Ti/Pd/Ag/AgCl QRE wafer". With a view of practical applications, many important electrochemical characteristics of the chip-level packaged Ti/Pd/Ag/AgCl/KCl-gel μREs were investigated and discussed in the following sections, including the potential stability and offset voltage, A.C. impedance, phase shift, and electrochemical noise spectrum [23−34].

II. EXPERIMENTS

**Contact author:* *I-Yu Huang is with the Department of Electrical Engineering, Nation Sun Yat-sen University; No. 70, Lienhai Rd., Kaohsiung 80424, Taiwan, R.O.C. (phone: +886-7-5252000 ext. 4163; fax: +886-7-5254163; e-mail: iyuhuang@mail.nsysu.edu.tw)*

A. *Fabrication of "Ti/Pd/Ag/AgCl QRE Wafer"*

An ideal RE should provide a stable and accurate electrochemical potential as the measurement reference in the electrochemical or biomedical sensing systems. It is therefore important for the potential of a RE to be constant and invariant with solution composition during the operation time. The behavior of these REs is of critical importance for a reliable response of the entire sensor system. Properties such as the potential drift (long-term stability), offset voltage, corrosion resistance, A.C. impedance and phase shift, noise spectrum and reproducibility are usually evaluated for a RE. To integrate an all solid-state RE with microsensors, the electrode needs to adhere well to the surface of microsensors chip, which usually is a silicon dioxide insulation passivation layer. A thin film Ti/Pd/Ag/AgCl QRE is developed in this work, where the titanium layer is used to improve surface adhesion and the palladium layer is to passivate and protect the titanium from oxidation and corrosion [1−2,18−19,25].

In the fabrication of the QRE, integrated circuit processing technology and lift-off techniques were utilized to deposit and pattern the multilayer metals. The Ti/Pd (60 nm/60 nm) layer was first E-gun evaporated in sequence without breaking the vacuum to avoid the oxidation of the titanium film, and then an Ag layer was DC-sputtered onto the Ti/Pd layer. The thickness of the Ag layer needs to be thick enough for not completely being chlorinated into AgCl during electrochemical chlorination, yet not to be too thick to avoid cracks in the film. 4 μm-thick Ag layer was found reasonably well in our studies.

All the chlorination of silver electrodes were carried out electrochemically in a 0.1 M HCl (J. T. Baker) solution by applying either a constant voltage of 1.0 V or a constant current of several tenths of mA. It was found that chlorination proceeded better and had a higher yield when performed under galvanostatic conditions, rather than potentiostatic ones. Therefore, the chlorination of the silver surface was accomplished by the constant current mode. To avoid any noise perturbation resulting from the contact with peripheral sidewall of the silicon wafer and the chlorination solution during the chlorination of the front side Ag electrode, a single-side contact setup, as shown in Fig. 1(a), was developed for the chlorination process. In the setup, the wafer is designed as a part of the chlorination container; only the front surface containing the Ti/Pd/Ag electrodes is exposed to the chlorination solution. During the chlorination, the Si/SiO2/Ti/Pd/Ag wafer is acting as the working electrode (WE) and a large-area Pt mesh is as the RE and counter electrode (CE) of the commercial potentiostat/galvanostat (Autolab, PGSTATS30, USA).

As shown in Table I, four different chlorination conditions were adopted in this work for performance investigation and optimization of the planar Ag/AgCl electrodes. As reported in previous literatures, factors that affect the electrode adhesion during the chlorination process are the average grain size and pore density in the AgCl thin film [2, 19]. This research kept the thickness of Ti/Pd/Ag multilayer of the four μRE wafers to60 nm/60 nm/4 μm and varied the chlorination current

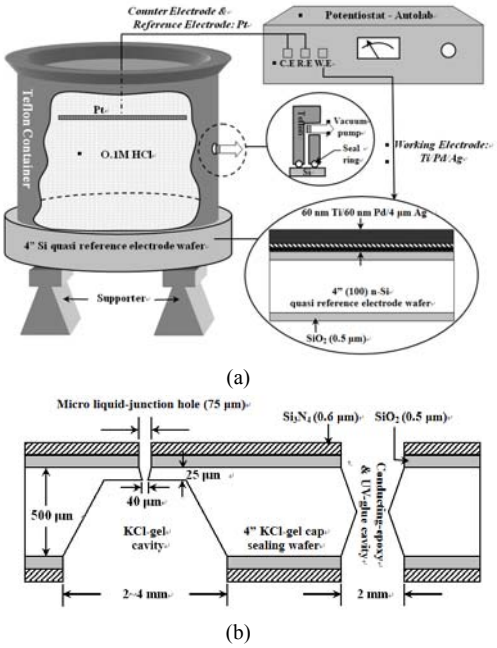

Fig. 1 (a) single-side contact setup and (b) cross-sectional diagram of the KCl-gel cap sealing wafer.

TABLE I.

THE AVERAGE THICKNESS, GRAIN SIZE AND PORE DENSITY OF AgCl LAYERS OBTAINED UNDER FOUR DIFFERENT CHLORINATION CONDITIONS.

Chip No.	Chlorination Recipe		Ag/AgCl Average Thickness (nm)	AgCl grain size (μm)	Average pole density ($1/\mu m^2$)
	Current density (mA/cm^2)	Time (Min)			
1	1	3.5	3430/850	0.4−2.0	0.1
2	1	10	3140/1570	0.4−2.0	0.02
3	3	3.5	1710/2430	0.6−3.0	0
4	3	10	0/2780	0.6−3.5	0

density (1 and 3 mA/cm^2) and time durations (3.5 min and 10 min).

B. *Fabrication of "KCl-gel cap sealing wafer"*

The cross-sectional diagram of the KCl-gel cap sealing wafer was displayed in Fig. 1(b). The two bulk-micromachined silicon cavities are designed for the conducting-epoxy/UV-glue encapsulated electrical conduction wire and the KCl-gel cap sealing, respectively. A micro liquid-junction aperture designed in such wafer can provide a good separation between sample solution and KCl-gel and reduce the diffusion of Cl^- ion from the saturated KCl-gel into the solution. After the top-side and bottom-side silicon nitride (0.6μm-thick) and dioxide (0.5μm-thick) patterned, the wafer was etched anisotropically in 30 wt% KOH solution (Kanto Chemical) at 80 ºC to form the silicon cavities and liquid-junction apertures. To improve the structural rigidity and enhance the fabrication yield of the KCl-gel cap sealing wafer, this study did not etch through the silicon wafer using KOH solution and retained a 25 μm-thick silicon membrane in the

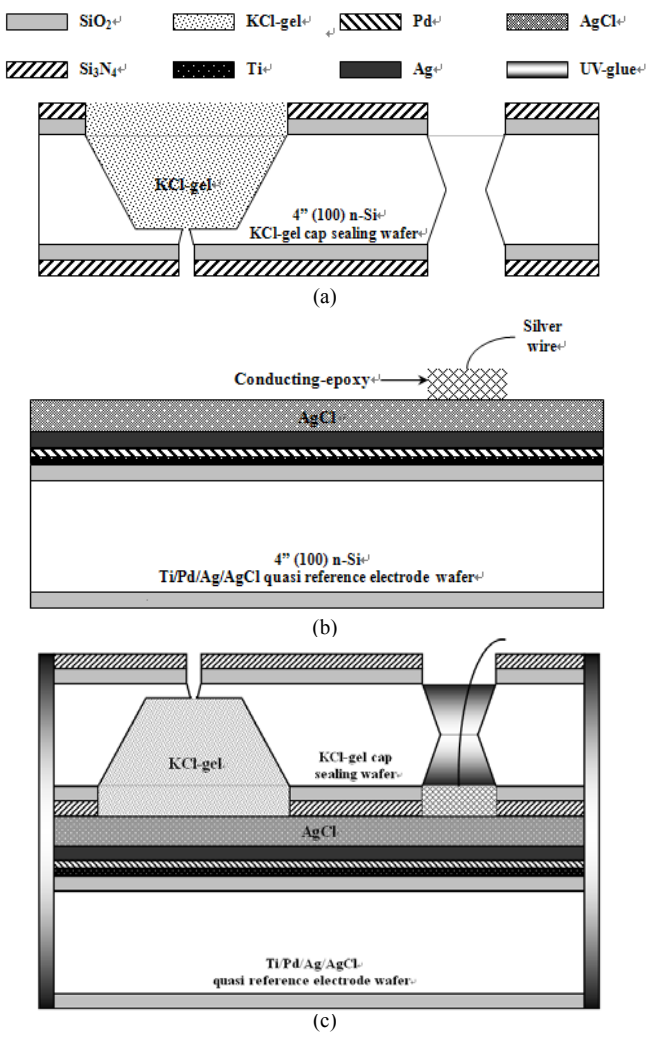

Fig. 2 The main process steps; (a) KCl-gel cap sealing wafer (b) quasi reference electrode wafer and (c) chip-level packaged planar Ti/Pd/Ag/AgCl/KCl-gel micro reference electrode.

top-side of the KCl-gel filling cavity. This study designs three different window size of the KCl-gel trapezoid cavity (2 mm × 2 mm, 3 mm × 3 mm and 4 mm × 4 mm) for the investigation of the KCl-gel reservoir size effect, and the corresponding KCl-gel injection volume of these cavities are 1.33, 3.39 and 6.40 μL, respectively. However, the dimension of liquid-junction aperture is fixed to 75μm × 75μm and the window size of conducting-epoxy/UV-glue sandglass-shape cavity on the both sides of wafer is kept constant at 2 mm × 2 mm.

C. Fabrication of "chip-level packaged planar Ti/Pd/Ag/AgCl/KCl-gel μRE"

To enhance the endurance of the Ti/Pd/Ag/AgCl QRE against the contamination caused by sample solution and to improve its ability to provide a constant reference potential free from the effects of changing Cl^- ion concentration, an agarose-supported KCl-gel membrane was employed. The KCl-gel membrane not only bridges ionically between AgCl layer and sample solution but also supplies a stable and sufficient Cl^- concentration to the AgCl/KCl-gel/sample

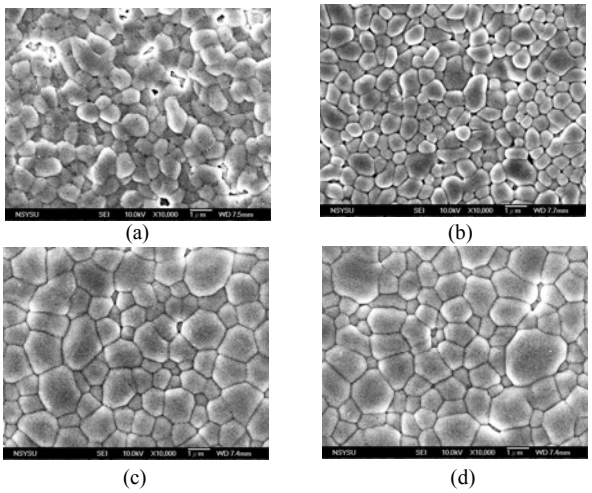

Fig. 3 The SEM photographs of Ti/Pd/Ag/AgCl Electrode; (a) current density = 1000 μm/cm^2, time = 3.5 min (b) 1000 μm/cm^2, 10 min (c) 3000 μm / cm^2, 3.5 min and (d) 3000 μm/cm^2, 10 min.

solution interfaces to achieve a stable junction potential. In our experiments, the 2 wt% agarose powder (SeaKem LE agarose, BMA) was dissolved in the saturated 3M KCl (Kanto Chemical) solution heated at agarose melting temperature (150 °C) and mixed thoroughly, then cooled the solution to gelling temperature (60−70 °C) prior to dispense into the "KCl-gel filling cavity" as shown in Fig. 2(a) by syringe method.

Figure 2(b) depicts the process of providing electrical connection to the Ti/Pd/Ag/AgCl QRE, including the conducting-epoxy layer (ABLEBOND 2100A) dispensing and silver wire (AWG30, Ling Chun Enterprise) binding. The temperature and time of curing the coated conducting-epoxy are 150 °C and 1 h. Finally, as Fig. 2(c) shows, a commercial UV-glue (Kyoritsu Chemical) was used to seal and bond the KCl-gel filled chip and the wire connected Ti/Pd/Ag/AgCl chip in an UV exposure system (LINTEC RAD2000). The dimensions of the two chips are big enough to be manually aligned and assembled on the microscope working stage. To avoid any melting and vaporization of KCl-gel, the curing temperature of UV-glue was controlled under 25−30 °C. The fabrication yield of the sealing and packaging processes mentioned above is about 45% in a lab environment and the total dimension of the implemented chip-level packaged planar Ti/Pd/Ag/AgCl/KCl-gel μRE module is equal to 9 mm (L) × 6 mm (W) × 1 mm (H), which is about 250 times less than the traditional commercial Ag/AgCl RE (OD = 12 mm, Length = 120 mm).

III. Results And Discussion

A. Grain size and pores density inspection of the AgCl layer

Figures 3(a)−(d) show the SEM surface micrographs of the AgCl layer chlorinated under four different chlorination conditions as listed in Table I. It was observed that the AgCl thin films have the same granular morphology but with various grain sizes and pore densities. The current density of chlorination is the key parameter which can affect manifestly the size of the AgCl grains; however, the chlorination time

only shows minor influence on the AgCl grain size. On the other hand, the pores density of AgCl films decreased with the chlorination current density and chlorination time. Adjusting these two parameters, a great range of AgCl grain size ranging from 0.4 μm to 3.5 μm and pores density ranging from zero to 0.1 per μm^2 were obtained. Our results show that larger grains (No. 4 chip in Table I) have poorer adhesion due to the exhausted silver layer, and higher pore-density (No. 1 chip in Table 1) causing larger potential variation and drift. It also appears that the grain size and pore density depend on the chlorination current density and time.Define abbreviations and acronyms the first time they are used in the text, even after they have been defined in the abstract. Abbreviations such as IEEE, SI, MKS, CGS, sc, dc, and rms do not have to be defined. Do not use abbreviations in the title or heads unless they are unavoidable.

The porosity of the AgCl layer can have a large influence on the impedance of the μREs and the higher porosity in the top AgCl layer results in the higher possibility of direct exposing the underlying Ag layer to the KCl-gel solid-state electrolyte, which would cause interference noise by redox reactions. To avoid this situation, the electrochemically chlorinated AgCl layer must contain no gross pores. Although a pore free film can be achieved as shown in Figs. 3(c) and (d), the AgCl layer of Fig. 3(d) has poor adhesion since the 4 μm-thick silver layer has completely chlorinated to silver chloride and this resulted peeling off and lost the normal function of Ag/AgCl μRE. The experimental results suggested that the optimum galvanostatic condition of chlorination was around 600 mC cm^{-2} (1 mA/cm^2 × 10 min or 3 mA/cm^2 × 3.5 min). Such process condition could achieve an AgCl layer having its grain size well controlled about 0.4−3.0 μm and has nearly zero porosity as observed in Figs. 3(b) and (c).

B. Potentiometric analysis of the unpackaged and chip-level packaged planar Ti/Pd/Ag/AgCl/KCl-gel μREs

The potential stabilities of the unpackaged planar Ti/Pd/Ag/AgCl QRE, chip-level packaged and unpackaged planar Ti/Pd/Ag/AgCl/KCl-gel μREs were characterized by the potentiometric analysis. The analysis was accomplished by measuring the open circuit potential (OCP) utilizing two-electrode system in 0.01 M KCl aqueous solution at 25 °C over 30,000 s. In order to test the performance of our fabricated electrodes using as reference electrodes, the fabricated electrodes were the RE and the commercial Ag/AgCl electrode was the WE in our OCP measurement assembling.

Figure 4(a) presents the OCP variations of an unpackaged planar Ti/Pd/Ag/AgCl QRE, an unpackaged planar Ti/Pd/Ag/AgCl/KCl-gel μRE and a commercial Ag/AgCl RE in 30,000 seconds testing time. The measured potential drift of the planarTi/Pd/Ag/AgCl QRE (6 mV in 30,000 s) is approximately equal to that of the commercial Ag/AgCl RE (11 mV in 30,000 s); however, the planar Ti/Pd/Ag/AgCl QRE has a higher offset-voltage (about -124 mV) much larger than that of a commercial Ag/AgCl RE (about -5 mV). It is clear that adding the KCl-gel salt-bridge layer can substantially reduce the offset-voltage of the planar Ti/Pd/Ag/AgCl QRE

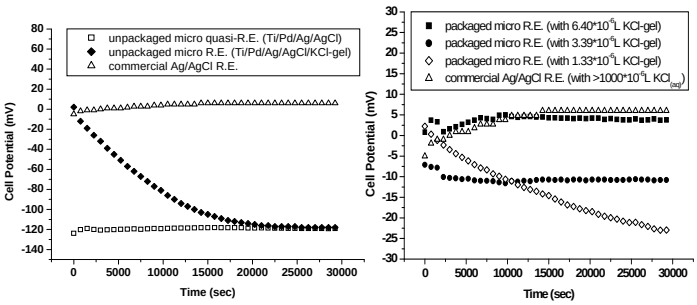

(a) (b)

Fig. 4 the potentiometric analysis; (a) unpackaged micro quasi reference electrode with coated and without coated KCl-gel (b) packaged micro reference electrode with different KCl volumes.

from -124 mV to 2 mV. However, the open circuit potential of the unpackaged planar Ti/Pd/Ag/AgCl/KCl-gel μRE degraded gradually with the operational time and approached the OCP level of micro Ti/Pd/Ag/AgCl QRE at about 400 minutes later. The Cl^- ions of the unsealed saturated KCl-gel will diffuse slowly into the sample solution, resulting in an unstable interface potential. The following Nernst Eq. (2) based on the half reaction (1) can explain the above-mentioned phenomenon. That is, any change of the Cl- ion activity could alter the potential of RE.

$$AgCl + e^- \rightarrow Ag + Cl^- \quad (1)$$

$$E = E^0 - (RT/F)\ ln\ a_{Cl^-} \quad (2)$$

Where E^0 is the standard electrochemical potential, R is the universal gas constant, T is the absolute temperature, F is the Faraday's constant and a_{Cl^-} is the activity of Cl^- ion. The Cl^- ion diffused from the internal filled saturated KCl-gel into the sample solution due to the high concentration gradient of Cl^- ion between these two electrolytes. The leaching out of the Cl^- ion from KCl-gel caused the electrochemical potential moved to the more negative value.

Figure 4(b) shows the OCP variations of three chip-level packaged planar Ti/Pd/Ag/AgCl/KCl-gel μREs with different KCl-gel volumes compared with a commercial Ag/AgCl RE. As shown in Table II, the chip-level packaged μREs have very small offset-voltage (-7−2 mV) and potential drift (4−25 mV) since the "KCl-gel cap sealing wafer" can protect and keep effectively a nearly constant chloride ion concentration of the filled KCl-gel. Very small cell potential drift (4−5 mV) can be obtained in the packaged μREs with 6.40 and 3.39 μL KCl-gel. Obviously the volume of filled and sealed KCl-gel has little influence on the potential drift and offset-voltage of the chip-level packaged planar μREs if the volume is sufficiently large. However, as shown in Fig. 4(b), insufficient saturated KCl-gel reservoir (e.g. 1.33 μL) results in a higher potential drift since the supply of Cl^- ion is relatively limited.

C. Impedance and phase shift of the chip-level packaged planar Ti/Pd/Ag/AgCl/KCl-gel μREs

The impedances of μREs are determined by the resistance of their isolation junction (liquid junction aperture) which separates the internal filled KCl aqueous or KCl-gel from the sample electrolyte. We have built up a three-electrode electrochemical cell to measure the impedance and phase shift of three chip-level packaged Ti/Pd/Ag/AgCl/KCl-gel μREs at

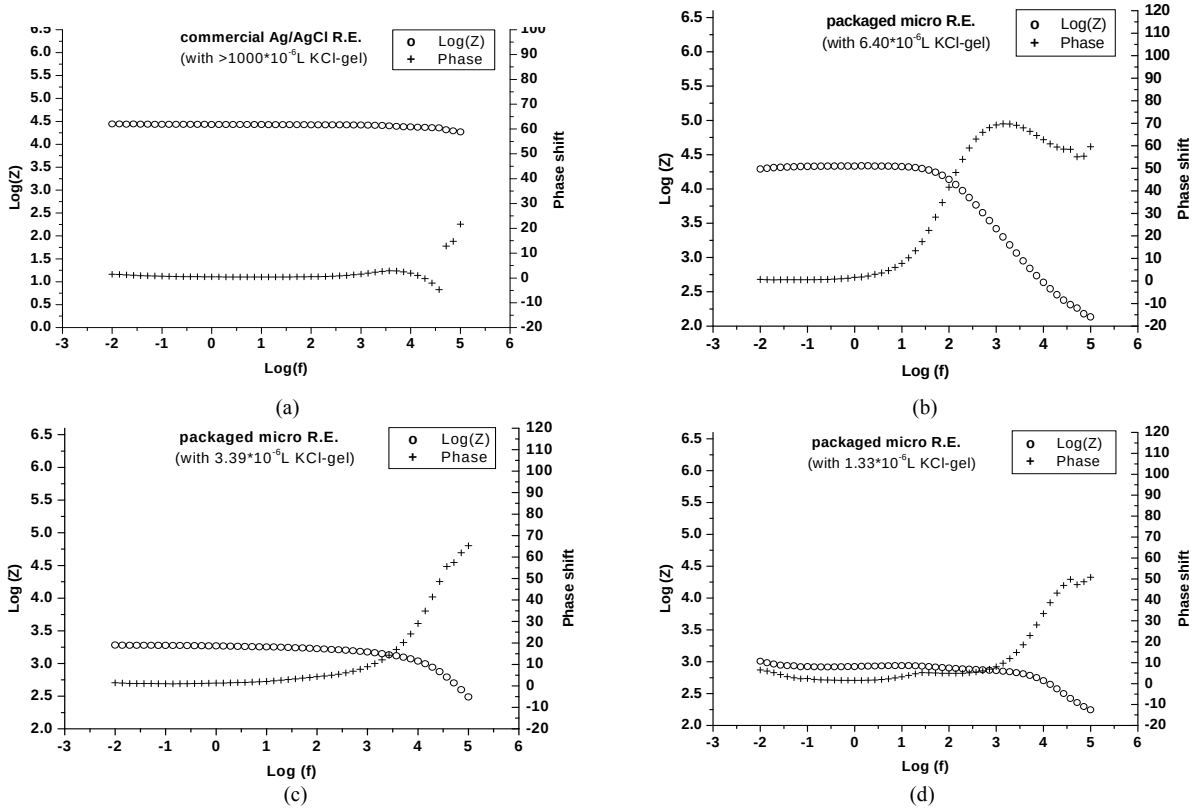

Fig. 5 The impedance and phase shift analysis; (a) commercial Ag/AgCl reference electrode and packaged micro reference electrode with (b) 6.40 µL KCl-gel (c) 3.39µL KCl-gel (d) 1.33 µL KCl-gel.

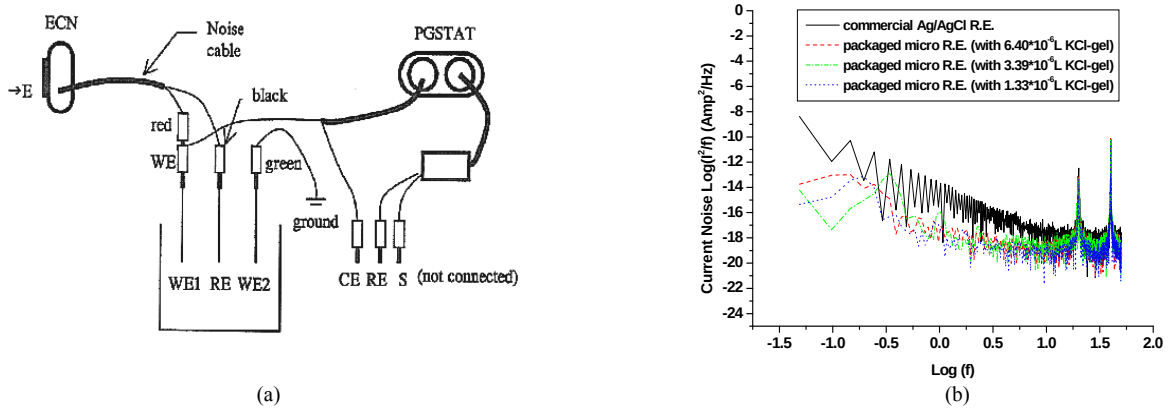

Fig. 6 (a) Electrochemical noise measurements (b) noise spectrums of the chip-level packaged planar micro reference electrodes

25 °C. The three-electrode cell is composed of a WE (that is our µRE), a platinum CE and a commercial Ag/AgCl RE. The measured absolute value of the impedances and phase shifts are plotted as a function of frequency in two different plots giving a Bode plot, as shown in Figs. 5(a)−(d) respectively. The scanning frequency of the small amplitude sinusoidal excitation signal is ranging from 0.01 Hz to 100 kHz. It is observed that an apparent phase shift occurs at high frequencies due to the oscillation of the system.

The phase shift represents the feedback needed for the electrochemical system stability. The phase shift effect would be more significant as the reference impedance rises. Fig. 5(a) displays the impedance and phase shift measured at 1 kHz of the commercial Ag/AgCl RE are about 26.30 kΩ and 1.57º. The impedance of the chip-level packaged planar Ti/Pd/Ag/AgCl/KCl-gel µREs measured at 1 kHz are about 0.73−2.62 kΩ, smaller than that of the commercial Ag/AgCl RE. It is known, a slow diffusion of the filled solution through this junction is necessary for proper electrode operation. Unfortunately, slower diffusion flow requires a more restricted flow path, so the resistance of electrolyte in the path will increase. However, small impedance of RE represents little compensation potential is required for the WE and CE. So there is a fundamental tradeoff between electrode impedance and leakage rate.

In addition, the Bode plots of these packaged µREs

demonstrated a nearly zero degree phase shift can be achieved. Once the frequency increased more than 1 kHz, the electrolyte resistance effect appeared in all of the packaged planar μREs since the influence of electron transfer and the capacitance effect could not be neglected. It is obvious that the phase shift effect is negligible at lower frequencies, however, it becomes more significant at higher frequencies. The commercial macro RE has very small phase shift over the whole range of testing frequency (0.01 Hz to 100 kHz). The packaged μREs with 1.33 and 3.39 μL KCl-gel can provide a small phase shift (8.06º and 8.98º, respectively) as the operating frequency is kept constant at 1 kHz. In contrast, the packaged μREs with 6.40 μL KCl-gel has very large phase shift (69.26º) at 1 kHz and it can provide a small phase shift (less than 10º) only when the frequency is smaller than 10 Hz, hence, it is inconvenient for the applications.

D. Electrochemical noise spectrum of the chip-level packaged planar Ti/Pd/Ag/AgCl/KCl-gel μREs

Electrochemical noise measurements were performed in a three-electrode set-up as shown in Fig. 6(a) with a sampling solution of 0.1M KCl. In such configuration, the counter electrode, reference electrode and secondary working electrode cables of the potentio/galvanostat are not connected to any point of the electrochemical noise measuring system. The implemented Ti/Pd/Ag/AgCl μRE functioned as a first working electrode (WE1) connected with the WE cable of the potentio/galvanostat and the red cable of the noise cable. A commercial RE was employed in this set-up to provide a stable reference potential and it is connected to the black cable of the noise cable. A mesh type Pt electrode was used to serve as a secondary working electrode (WE2) which is connected to the ground of the potentio/galvanostat through the green cable. It is sampled at the frequency of 100 Hz for 20.48 s and the detected power spectral densities for current (PSDI) of the chip-level packaged planar Ti/Pd/Ag/AgCl/KCl-gel μREs and the commercial Ag/AgCl RE are shown in Fig. 6(b).

IV. CONCLUSION

This work presents a MEMS-based chip-level packaging method to reduce the potential drift, the offset voltage, and the noise spectrum of the planar Ti/Pd/Ag/AgCl/KCl-gel μRE for long-term electrochemical or biomedical sensing applications. A bulk-micromachined KCl-gel cap sealing silicon wafer with a micro liquid-junction aperture was designed to effectively reduce the diffusion of Cl^- ion from the sealed saturated KCl-gel into the test solution. This study also measured and compared three different sizes of KCl-gel filled trapezoid cavities (with 1.33, 3.39 and 6.40 μL volumes, respectively) for the design optimization of the packaged μRE. Compared relative to the commercial Ag/AgCl RE, the optimized encapsulated μRE (has 3.39 μL KCl-gel and a total dimension of only about 9 mm (L) × 6 mm (W) × 1 mm (H)) has demonstrated many excellent characteristics. Including a very stable cell potential (drift voltage equals 5 mV in 30,000 s), an approximately zero offset-voltage (-7 mV), a very low impedance (1.50 kΩ) and phase-shift (8.98º) at 1 kHz operation frequency, a very small double-layer capacitance (0.04 μF), and a low noise spectrum.

ACKNOWLEDGEMENT

The authors would like to thank the National Science Council of the Republic of China, Taiwan, for financially supporting this research under Contracts No. NSC 92-2212-E-110-020. The authors are indebted to the National Nano Device Laboratories (NDL)-South Branch in Taiwan for their assistance in providing the access to their processing facilities.

REFERENCES

[1] D. Harame, J. Shott, J. Plummer and J. Meindl, "An implantable ion sensor transducer," *Tech. Dig. 1981 IEEE International Electron Devices Meeting*, Washington, USA, pp. 467-470, 1981.

[2] I.-Y. Huang and R.-S. Huang, "Fabrication and characterization of a new planar solid-state reference electrode for ISFET sensors," *Thin Solid Films* 406, pp. 255-261, 2002.

[3] W.H. Ko, *Implantable Sensors for Closed-Loop Prosthetic Systems*, Chap. 4, Futura Publishing, New York, 1985.

[4] O. Prohaska, P. Goiser, A. Jackomowicz, F. Kohl and F. Olcaytug, "Miniaturized chamber-type electrochemical cells for medical application," *Proc. 2nd International Meeting on Chemical Sensors*, Bordeaux, France, pp. 652-655, 1986.

[5] R.L. Smith and D.C. Scott, "An integrated sensor for electrochemical measurements," *IEEE Trans. Biomed. Eng.* BME-33, 1986, pp. 83-90.

[6] S. Yee, H. Jin and L.K.C. Lam, "Miniature liquid junction reference electrode with micromachined silicon cavity," *Sens. Actuators*, 15, pp. 337-345, 1988.

[7] A. Van Den Berg, A. Grisel, H.H. Van Den Vlekkert and N.F. De Rooij, "A micro-volume open liquid-junction reference electrode for pH–ISFETs," *Sens. Actuators B: Chem.* 1, pp. 425-432, 1990.

[8] K. Eine, S. Kjelstrup, K. Nagy and K. Syverud, "Towards a solid state reference electrode," *Sens. Actuators B: Chem.* 44, pp. 381-388, 1997.

[9] D. Desmond, B. Lane, J. Alderman, J.D. Glennon, D. Diamond and D.W.M. Arrigan, "Evaluation of miniaturised solid state reference electrodes on a silicon based component," *Sens. Actuators B: Chem.* 44, pp. 389-396, 1997.

[10] M. Ciobanu, J.P. Wilburn, N.I. Buss, P. Ditavong and D.A. Lowy, "Miniaturized reference electrodes based on Ag/AgiX internal reference elements. I. manufacturing and performance," *Electroanalysis* 14, pp. 989-997, 2002.

[11] M. Ciobanu, J.P. Wilburn and D.A. Lowy, "Miniaturized reference electrodes. II. use in corrosive, biological, and organic media," *Electroanalysis* 16, pp. 1351-1358, 2004.

[12] J.P. Wilburn, M. Ciobanu, N.I. Buss, D.R. Franceschetti and D.A. Lowy, "Miniaturized reference electrodes with stainless steel internal reference elements," *Anal. Chim. Acta* 511, pp. 83-89, 2004.

[13] J.P. Wilburn, M. Ciobanu and D.A. Lowy, "Characterization of acrylic hydrogels by open circuit potential monitoring," *J. Appl. Electrochem.* 34, pp. 729-734, 2004.

[14] A. Kisiel, H. Marcisz, A. Michalska and K. Maksymiuk, "All-solid-state reference electrodes based on conducting polymers," *Analyst* 130, pp. 1655-1662, 2005.

[15] S.K. Kim, H. Lim, T.D. Chung and H.C. Kim, "A miniaturized electrochemical system with a novel polyelectrolyte reference electrode and its application to thin layer electroanalysis," *Sens. Actuators B: Chem.* 115, pp. 212-219, 2006.

[16] J. Ghilane, P. Hapiot and A.J. Bard, "Metal/Polypyrrole quasi-reference electrode for voltammetry in nonaqueous and aqueous solutions," *Anal. Chem.* 78, pp. 6868-6872, 2006.

[17] J.-H. Han, S. Park, H. Boo, H.C. Kim, J. Nho and T.D. Chung, "Solid-state reference electrode based on electrodeposited nanoporous platinum for microchip," *Electroanalysis* 19, pp. 786-792, 2007.

[18] I.-Y. Huang and R.-S. Huang, "A pH Sensor with Integrated Planar Reference Electrode," *Tech. Dig. 10th International Conference on Solid-State Sensors and Actuators (Transducers'99)*, Sendai, Japan, pp. 644-647, 1999.

[19] I.-Y. Huang, R.-S. Huang and L.-H. Lo, "Improvement of integrated

Ag/AgCl thin-film electrodes by KCl-gel coating for ISFET applications," *Sens. Actuators B: Chem.* 94, pp. 53-64, 2003.
[20] H. Suzuki, A. Hiratsuka, S. Sasaki and I. Karube, "Problems associated with the thin-film Ag/AgCl reference electrode and a novel structure with improved durability," *Sens. Actuators B: Chem.* 46, pp. 104-113, 1998.
[21] H. Suzuki, T. Hirakawa, S. Sasaki and I. Karube, "Micromachined liquid-junction Ag/AgCl reference electrode," *Sens. Actuators B:* Chem. 46, pp. 146-154, 1998.
[22] H. Suzuki, H. Ozawa, S. Sasaki and I. Karube, "A novel thin-film Ag/AgClanode structure for microfabricated Clark-type oxygen electrode," Sens. Actuators B: Chem. 53, pp. 140-146, 1998.
[23] Delahay and Paul, The Electrical Double Layer and Electrode Kinetics, Interscience, New York, 1965.
[24] M.G. Fontana, Corrosion Engineering, McGraw-Hill, New York, 1986.
[25] M. Lambrechts, J. Suls and W. Sansen, "Corrosion Resistance of Silver Thin Film Layers for Planar Voltammetric Sensors," Proc. 2nd International Meeting on Chemical Sensors, Bordeaux, France, pp. 572-575, 1986.
[26] M. Steyaert, M. Lambrechts and W. Sansen, "Noise power spectrum density analysis of planar Ag/AgCl electrodes," Sens. Actuators, 12, pp. 185-192, 1987.
[27] J.R. MacDonald, Impedance spectroscopy - emphasizing solid materials and systems, John Wiley & Sons, New York, 1987.
[28] F. Mansfeld, S. Lin, Y.C. Chen and H. Shih, "Minimization of high-frequency phase shifts in impedance measurements," J. Electrochem. Soc.: Electrochem. Sci. Tech. 135, pp. 906-908, 1998.
[29] J.G. Webster, Electrical Impedance Tomography, Adam Hilger, Bristol, UK, 1990.
[30] M. Noel and K. I. Vasu, Cyclic Voltammetry and the Frontiers of Electrochemistry, Aspect Publications, London, 1990.
[31] E. Gileadi, Electrode Kinetics, VCH Publisher, New-York, 1993.
[32] A.J. Bard and L.R. Faulkner, Electrochemical Methods Fundamentals and Applications, John Wiley & Sons, New-York, 2001.
[33] A. Aballe and F. Huet, "Noise resistance applied to corrosion measurements: VI. partition of the current fluctuations between the electrodes," J. Electrochem. Soc. 149, pp. B89-B96, 2002.
[34] C. Gabrielli, F. Huet and R.P. Nogueira, "Electrochemical noise measurements of coalescence and gas-oscillator phenomena on gas-evolving electrodes," J. Electrochem. Soc. 149, pp. E71-E77, 2002.

3A1-6

Raman Based Nanoparticle Labels for Bioassays

Philip Drake*, Hong-Wen Chang, and Yuh-Jiuan Lin

Medical Electronics and Device Technology Centre, Industrial Technology Research Institute, Hsinchu, Taiwan

***Abstract*— 4-Mercaptobenzoic acid coated gold nanoparticles were used as Raman based labels in a standard immunoassay for mouse IgG. The Au nanoparticles used had a diameter of 51 ± 2 nm and were synthesised by the citrate reduction method. Dynamic light scattering and TEM image analysis were used to characterise the nanoparticles. The SERS spectra was recorded on an EZRaman desk-top spectrometer operating with a 670 nm laser, 22mW output and a 0.30 NA focusing lens. For the immunoassay results the Raman signal intensity was recorded at 1071 cm^{-1}. This gave a linear correlation to the mouse IgG concentration of slope $1.5Exp^{13}$ counts per mole, giving an estimated detection limit of 0.1 femtomoles.**

Keywords — Gold, Immunoassay, Label, Nanoparticle, Raman

I. Introduction

Surface enhanced Raman spectroscopy (SERS) has been used as an analytical tool for many years.[1,2] SERS active particles have been successfully employed as labels or probes in chemical assays,[3] immunoassays, [4-6] and DNA detection, [7,8] with the SERS peak intensity being correlated to the concentration of target species. The work presented here details the synthesis and application of Raman labels based on 4-mercaptobenzoic acid (MBA) coated AuNPs.

SERS was first discovered in 1974 by Fleischmann *et al.* [9] when they recorded intense Raman signals from pyridine absorbed on roughened silver electrodes. Latter, several papers concluded that these intense signals could not be accounted for by conventional Raman theory and suggested an enhancement mechanism was taking place at the metal surface increasing the scattering intensity from each adsorbed pyridine molecule. [10,11] Since then many papers have documented this surface enhancement effect and several theories have been proposed to account for it. A number of excellent review article cover this historical and theoretical development in detail. [12-14]

In SERS experiments the surface plasmon resonance (SPR) adsorption of the metal nanoparticle (NP) overlaps with the excitation laser used. This overlap greatly enhances the Raman signal from molecules located on the NP surface and makes SERS one of the most sensitive forms of spectroscopy available. SERS has even been used for single molecule detection. [15,16] The large enhancement factors observed in SERS experiments has been attributed to two factors, chemical enhancement and electromagnetic enhancement. Chemical enhancement results from charge transfer from the molecule to the metal surface or *visa versa*. [17] Electromagnetic enhancement results from the localized SPR associated with the metal NP, this greatly enhances the electromagnetic field at the surface of the NP. [18]

The Raman labels developed here are based on MBA coated AuNPs. The MBA provides the intense Raman signal enhanced by the AuNP. The labels are used in a similar way to conventional fluorescent labels. When an excitation laser is directed onto the NPs Raman scattered photons are emitted with a characteristic spectra. The intensity of the spectra can then be correlated with the concentration of the target species. As an example of their use a standard sandwich assay was performed based on mouse IgG as the target and antimouse IgG labelled with the MBA-AuNPs.

II. Experimental

The AuNPs were synthesised following the citrate reduction method.[19,20] This is one of the most commonly used syntheses for hydrophilic AuNPs. [21] Small AuNPs particles were made first and used as seed particles to grow the final larger AuNPs.

Small AuNP seed particles were synthesised by citrate reduction. Trisodium citrate (50 mg) was dissolved in distilled water (5 ml) to produce a 1% solution. This was added to a refluxing solution of hydrogen tetrachloroaurate (20 mg) in distilled water (50 mL). The resulting solution went through a colour change to deep red/purple. The heat was removed after refluxing for 30 minutes. The UV-Vis spectrum for the solution was recorded from 300 nm to 900 nm and showed the characteristic surface plasmon resonance peak at wavelength 517 nm. TEM image analysis gave a NP diameter of 12.2 ± 0.8 nm.

Large AuNP were synthesised by seed particle growth with citrate reduction. Hydrogen tetrachloroaurate solution (0.5 mL, 11mM solution) was added to distilled water (32 mL) and brought to reflux with a condenser fitted. The seed solution from the above small AuNP synthesis was added to this (0.3 mL) followed closely by trisodium citrate solution (0.17 mL of 1% solution). The solution started to change to a blue colour after 30 seconds and a red colour after 1 minute. After 10 minutes the

This project was funded by the Ministry of Economic Affairs (MOEA), Taiwan, for funding this work..

**Contact author:* Philip Drake, Medical Electronics and Device Technology Center, Industrail Technology Reserach Institute, Hsinchu, Taiwan (phone: +886 35912609; fax: +886 35912444; e-mail: pldrake@itri.org.tw).

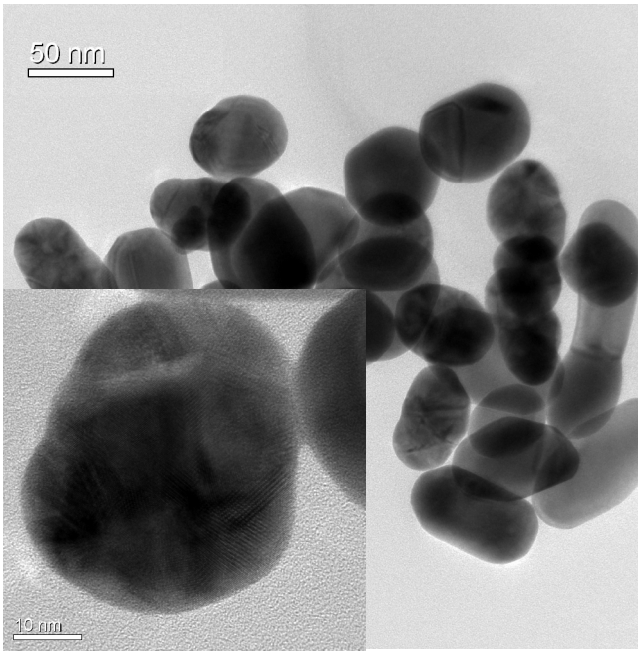

Figure 1: TEM image of the large AuNPs scale bar for main image is 50 nm. Incept shows a close-up of a single NP scale bar equals 10 nm

heat was removed and the solution allowed to cool with stirring. The UV-Vis spectrum for the solution was recorded from 300 nm to 900 nm and showed the characteristic surface plasmon resonance peak at wavelength 535 nm. TEM image analysis gave a NP diameter of 51 ± 2 nm. The large AuNPs were mixed with MBA (50 mg) dissolved in 5 ml of ammonia (1 moldm^{-3}). A representative TEM image can be seen in figure 1, the inset shows a close-up of a single AuNP. Figure 2 shows the dynamic light scattering (DLS) data.

The desktop Raman spectrometer was an EZRaman-L system purchased from Enwave Optronics operating with a 670 nm laser, 22mW measured output and a 0.30 NA focusing lens. The SERS spectra of the liquid samples were recoded using the desk-top system. The final solution (0.2ml) was diluted with water (0.8 ml) and placed in the liquid sample holder. The holder held the sample so that the laser focus point fell in the centre of the solution. The laser exits the 105 μm diameter waveguide and passes through a collimation lens giving a beam width of 0.25 cm. The beam then passes through a lens with a focus length of 0.7 cm giving a spot diameter of 100 μm at is focus point. With this set-up the laser effectively illuminates and collects a signal from a volume of 6.9 nL within the sample.

Immunoassays were performed as follows. The AuNPs were coated with goat derived anti-mouse IgG F_{ab} following standard 1-ethyl-3-(3-dimethylaminopropyl) carbodiimide (EDC) methods. Au coated glass slides were activated with the homo-bifunctional cross linker 3,3´ dithiobis [sulfosuccinimidylpropionate] (DTSSP). After 24 hours the slides were then exposed to 28 μl of a solution of rabbit derived

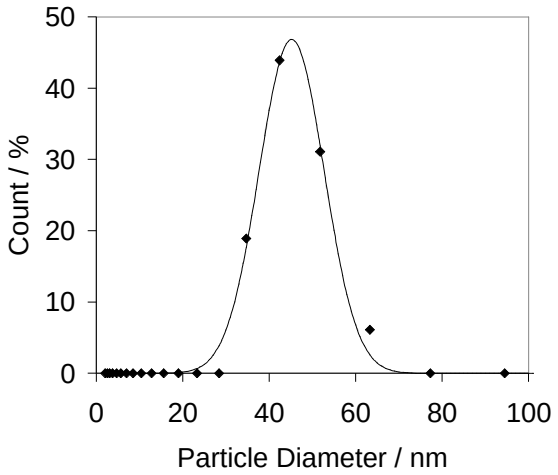

Figure 2: Results from the dynamic light scattering (DLS) measurements on the AuNPs with a Gaussian fit to the data

anti-mouse IgG F_c (90 μgml^{-1}) in borate buffer (50 mM). The slides were exposed to different concentrations of mouse IgG (100 μl) and developed with 100 μl of the AuNP labels coated with goat derived anti-mouse IgG F_{ab}. The SERS spectrum was recorded from the slide surface by focusing the laser spot on the slide surface. The height of the laser mounting was adjusted so that the signal collected was maximised.

III. Discussion

After synthesising the AuNPs the optimal condition for producing the most intense SERS spectra from MBA was investigated. The MBA was mixed with the freshly prepared large AuNPs and the SERS spectra recorded. This showed the characteristic double peaks at about 1075 cm^{-1} and 1587 cm^{-1}. The SERS spectra are dominated by these two peaks. These can be assigned to the ν_{8a} and ν_{12} aromatic ring vibrations respectively.[22] The other obvious peak in the SERS spectra appears at 1419 cm^{-1}. This can be assigned to the ν_s(COO-) band.[22] An example of the SERS spectra can be seen in figure 3.

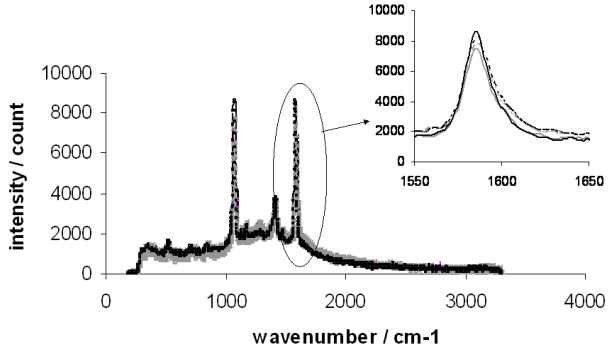

Figure 3: The SERS spectra from the MBA-AuNPs showing the signal reproducibility. The spectra were recorded for two different AuNP samples both

immediately after synthesis and two months after synthesis. The insert shows a close up of the 1580 cm^{-1} peak.

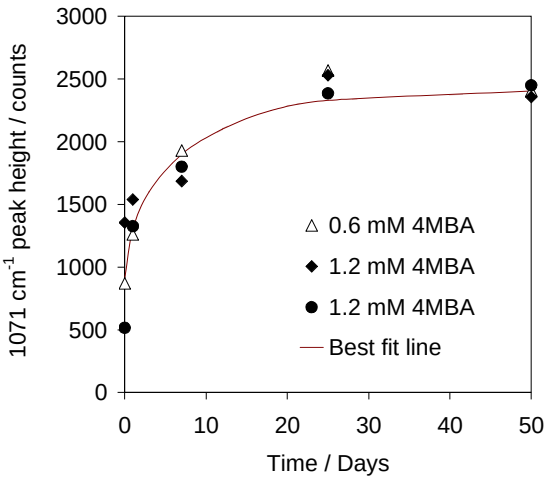

Figure 4: Showing the development of the SERS signal from the MBA-AuNP system. Two different concentrations were used and the higher concentration repeated. The best-fit line was added buy hand for guidance only.

However, it was noted that the spectra increased in intensity over time even though no further MBA was added to the solution. It can be seen in figure 4 that the MBA SERS spectra took several weeks to fully develop. This is surprising as the formation of thiol based self-assembled monolyers on Au surfaces are thought to develop over a period of several minutes and to be fully formed after several hours. After mixing a set ratio of MBA:AuNPs it took around 14-21 days for the SERS signal to maximise. After this time the signal was remarkably stabile. Figure 4 shows the SERS spectra for two samples made on different occasions each recorded as synthesised and two months after synthesising. The variation in signal strength between all four spectra was less than 10 %. For the immunoassay procedure the MBA-AuNPs were coated with goat derived anti-mouse IgG F_{ab} following standard EDC methods. After the coating the ν_s(COO-) band at 1419 cm^{-1} had greatly reduced in intensity confirming that the antibodies had been successfully coupled to the carboxylic acid giving an amide link. Glass microscope slides were then coated with rabbit derived anti-mouse IgG F_c. This acts as the capture antibody and binds to mouse IgG at a different location to the goat derived anti-mouse IgG F_{ab}. The coated slides were exposed to different concentrations of mouse IgG and finally washed with equal amounts of antibody coated MBA-AuNPs. When used in the sandwich assay the MBA-AuNPs produced an intense SERS signal from the surface of the glass microscope slides. The signal strength was directly proportional to the concentration of mouse IgG used during the procedure. See figure 5. The control experiments missing the mouse IgG, the capture IgG or the label IgG all gave no signal. The mouse IgG was placed over an area of 1 cm^2. Since the laser has a spot size of 100μm diameter it is estimated that the signal for the lowest concentration of mouse IgG was associated with less than 0.1 femtomoles of IgG.

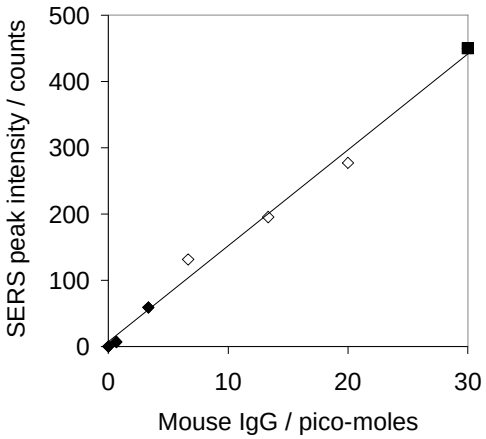

Figure 5: Showing the results of the mouse IgG immunoassay employing MBA-AuNP labels. The three different sets of data, black diamonds, white diamonds and black squares, were recorded from three different experiments on different days.

REFERENCES

[1] K. T. Carron, B. J. Kennedy, Anal. Chem., 1995, 67, 3353-3356
[2] S. Xu, X. Ji, W. Xu, B. Zhao, X. Dou, Y. Bai, Y. Ozaki, J. Biomed. Opt., 2005, 10(3), 031112, 1-12
[3] P. D. Enlow, M. Buncick, R. J. Warmack, T. Vo-Dinh, Anal. Chem., 1986, 58, 1119-1123
[4] J. D. Driskell, K. M. Kwarta, R. J. Lipert, M. D. Porter, Anal. Chem., 2005, 77, 19, 6147-6154
[5] S. Xu, X. Ji, W. Xu, X. Li, L. Wang, Y. Bai, B. Zhao, Y. Ozaki, Analyst, 2004, 129, 63-68
[6] D. S. Grubisha, R. J. Lipert, H. Y. Park, J. Driskell, M. D. Porter, Anal. Chem., 2003, 75, 5936-5943
[7] K. Faulds, L. Stewart, W. E. Smith, D. Graham, Talanta, 2005, 67, 667-671
[8] K. Faulds, W. E. Smith, D. Graham, Analyst, 2005, 130, 1125-1131
[9] M. Fleischmann, P. J. Hendra, A. J. McQuillan, Chem. Phys. Lett., 1974, 26, 163
[10] M. G. Albrecht, J. A. Creighton, J. Am. Chem. Soc., 1977, 99, 5215
[11] D. L. Jeanmaire, R. P. Van Duyne, J. Electroanal. Chem., 1977, 84, 1
[12] A. Campion, P. Kambhampati, Chem. Soc. Rev., 1998, 27, 241-250
[13] A. Otto, I. Mrozek, H. Grabhorn, W. Akemann, J. Phys. Condens. Matter, 1992, 4, 1143-1212
[14] M. Moskovits, Rev. Mod. Phys., 1985, 57, 783-826
[15] Z. Zhou, G. Wang, Z. Xu, Appl. Phys. Lett., 2006, 88, 034104
[16] S. Nie, S. R. Emory, Science, 1997, 275, 21, 1102-1106
[17] P. Kambhampati, C. M. Child, M. C. Foster, A. Campion, J. Chem. Phys., 1998, 108, 5013-5026
[18] M. J. Weaver, S. Zou, H. Y. H. Chan, Anal. Chem., 2000, 72, 38A-47A
[19] P. C. Lee, D. Meisel, J. Phys. Chem., 1982, 86, 3391-3395
[20] K. C. Grabar, R. G. Freeman, M. B. Hommer, M. J. Natan, Anal. Chem., 1995, 67, 735-743
[21] K. R. Brown, D. G. Walter, M. J. Natan, Chem. Mater., 2000, 12, 306-313
[22] A. Michota, J. Bukowska, J. Raman Spectrosc., 2003, 34, 21-25

3A1-2

An Intelligent Flow Sensr System with Zero Drift Selt Calibration Function

Ziqiang Dong[#], Qing-An Huang[*], Ming Qin, Guangping Shen
Key Laboratory of MEMS of Ministry of Education, Southeast University, Nanjing, China

***Abstract* — A double operation modes intelligent flow sensor system with zero drift self calibration function is reported in this paper. In order to improve the sensitivity and the stability, the sensor chip was fabricated on ceramic substrate, and using lift off process to pattern the heater and sensing detectors. The heating and sensing elements are Ti/Pt resistors and with the temperature coefficient is 3050ppm, Ti layer was introduced to improve the adhesion between Pt layer and the front surface of ceramic substrate. Direct Chip Attach(DCA) packaging was adopted to protect the chip and the circuits below it. The Constant Temperature Difference(CTD) control mode is introduced to detect high velocity flow, while calorimetric operation mode is used for low flow velocity measurement. The sensor is designed to operate in the two modes at the same time, and their outputs are detected by a Micro Controller Unit(MCU). Because the calorimetric control mode presents low zero point drift, it is used to calibrate the zero point of CTD control mode. The intelligent sensor system was tested in flow tunnel, if the calorimetric control mode shows the flow velocity less than 20m/s, the MCU computes the difference of the two modes outputs and gets a calibration voltage to change the zero point of the CTD control mode. When the calorimetric control mode shows the flow velocity higher than 20m/s, the last calibration zero point of the CTD control mode is considered as a accurate value. After calibration, the relative error of flow velocity measurement is less than 5% from 0m/s to 60m/s.**

Keywords — ***double modes, flow speed, self calibration, intelligent sensor system***

I. INTRODUCTION

In the field of biomedical applications, flow always should be measured for real time monitoring and real time control. Up to now, many techniques have been devised to measure flow velocity and its direction, the 2-D solid thermal flow sensor is accepted as a promising technology because of its fabrication simplicity and stable characteristic. Meanwhile, IC industry has developed for half a century, the fabrication processes of silicon have been greatly matured, many institutes and companies choose silicon as the substrate material to fabricate thermal flow sensor. Such as that AFP van Putten proposed the first integrated silicon anemometer in 1974[1]. Because of the high thermal conductivity of silicon substrate, the flow sensor has a relatively low sensitivity. While S.Kim[2] and Battles[3] fabricated micro membranes and bridges as the sensing parts using anisotropic etching of silicon substrate from backside or front side in order to improve the sensitivity of sensors. But the reliability of the fragile structures usually is low, and the post-processes such as packaging can easily destroy them.

Ceramic is a ideally material for packaging thermal wind sensor. On the one hand, ceramic has the ability to transfer heat from sensor chip to air flow, on the other hand it can protect the sensing parts from contaminating and been damaged. In order to achieve high performance and reliability, a flow sensor fabricated on the ceramic substrate using single lift-off process was proposed in this paper. As shown in Fig.1, the dimension of sensor chip is 4mm×4mm, and the valid structure area is 3mm×3mm. Heater R_h and detector R_S, which have the same temperature, located in the center of chip, are introduced to operate in Constant Temperature Difference(CTD) control mode[4]. Two detection elements include eight detectors are fabricated surrounding the R_h and R_S, the distance of one element to the center of chip is 380μm and the other is 950μm. The two elements are used for the operating of calorimetric control mode. The resistances of R_h and R_S are about 150Ω, while the resistances of eight detectors are 1K.

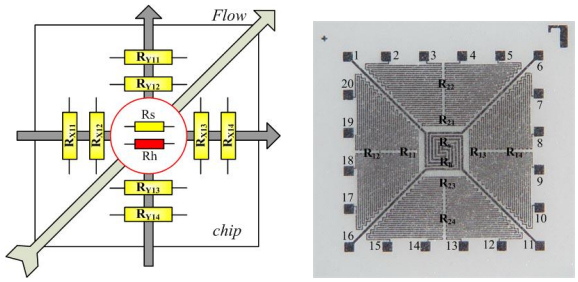

Figure 1. Schematic structure of the chip and its micro-photograph.

The sensor operated in CTD control mode can keep a better sensitivity than operated in the calorimetric control mode at the measurement of high flow velocity, but usually the error caused by zero point drift is unacceptable. The principle of calorimetric control mode is to detect the temperature difference of the chip surface, its error induced by zero point drift is much lower than the CTD control mode. In order to achieve high sensitivity and reduce the error in the measurement of high flow velocity, the calorimetric control mode is used as a rule to calibrate the zero point of CTD control mode in this paper. The CTD control mode is used to measure the flow velocity higher than 20m/s, while the calorimetric control mode is used to measure the flow velocity less than 20m/s and calibrate the zero point of CTD control mode.

II. FABRICATION AND PACKAGING

A. Fabrication

The proposed sensor was fabricated on ceramic substrate, which thickness is only 300μm, using single lift-off process to pattern heater and detectors. Firstly, photoresist was spin-coated on the front side surface of the ceramic substrate, and patterned to expose the area where the resistors was located.

Identify applicable sponsor/s here. *This project was funded by the Natural Science Foundation of China (Project code: 90607002).*

Contact author: for fabrication aspects of this project please contact* ***hqa@seu.edu.cn.*

#Contact author: for microrobotic aspects of this project please contact ***zqdong1982@163.com.***

Secondly, 1000Å Ti and 2000Å Pt were sputtered, the Ti layer was introduced to improve the adhesion between Pt layer and the front surface of ceramic substrate. Thirdly, using lift off process to remove those Ti/Pt layers above the photoresist, and finally leaving the Ti/Pt resistors on the front side surface of ceramic substrate. The two sides of this ceramic substrate were polished in order to guarantee the resistance congruence of those resistors.

B. Packaging

The sensor chip adopts Direct Chip Attach(DCA) packaging[5], and the packaging structure is shown in Fig. 2. One requirement of the chip packaging is to guarantee most of the heat produced by heater R_h been transferred to the air flow, the other requirement is that the sensor resistors and the circuits bellow the ceramic chip have a well environment isolation. The front surface of the chip, which the resistors were located on, was glued to a FR4 PCB board, where there is a 3.2mm×3.2mm slotted window in the board center, in order to expose the Au Pad on the front side surface of the chip. Then, ultrasonic wire bonding machine was used to achieve electrical connection between the sensor chip and FR4 PCB. Finally, the bonding wires were protected by bonding glue. The backside surface of the sensor chip was the sensing surface directly contacted with the air flow.

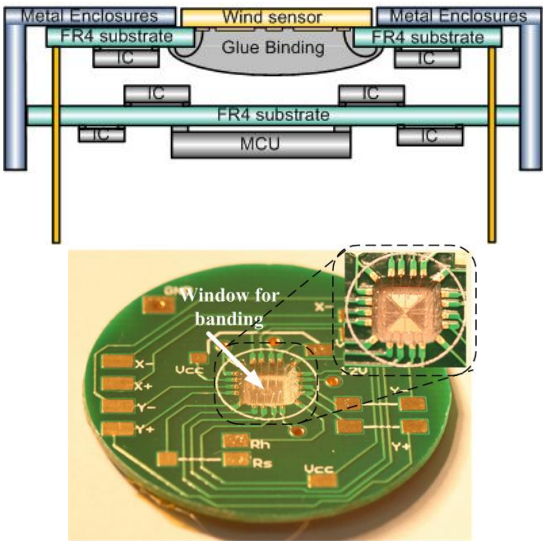

Figure 2. Schematic structure of the chip packaging and the photograph of the sensor chip after bonding.

III. MODES CONTROL AND OPERATION PRINCIPLE

Thermal flow sensors can be divided into two main categories: CTD control anemometers and calorimetric flow sensors[6]. The CTD control mode is based on the measurement of total thermal dissipation induced by the thermal convection between the sensor hot surface and the air flow. The calorimetric control mode detects the temperature difference between upstream detectors and downstream detectors on the backside surface of sensor chip to respond the change of air flow, while the temperature difference is the asymmetric thermal distribution at the surface of chip caused by the air convection. Commonly, the CTD control mode can keep a acceptable sensitivity at high air flow speed, but usually the error caused by zero drift is unacceptable. The calorimetric control mode has the ability to restrain the effect of zero point drift largely but the sensitivity at high air flow speed is poor. In order to keep better sensitivity and low zero point drift in full scale testing, the sensor system is designed to operate in the two modes at the same time. Fig. 3 shows the block diagram for control, detecting and calibration of the two control modes.

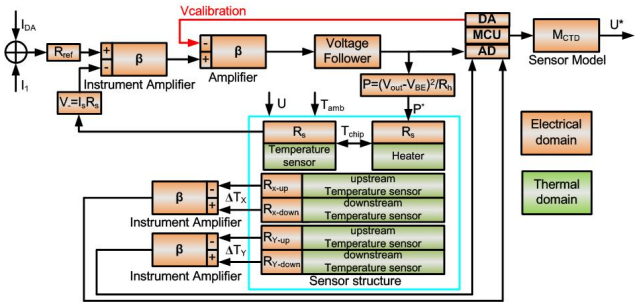

Figure 3. CTD and calorimetric control mode for measurement and calibration

A. CTD control mode

Through adjusting the power drop on the heater R_h, the CTD control mode is used to keep the temperature of chip higher than the temperature of external air flow a constant value, δT. Firstly, the CTD control mode detects the imbalance value ΔV of its sensing electrical bridge, which represents the temperature change of the sensor chip induced by thermal convection with external air flow. And then, this mode exports a signal to change the voltage drop on the heater R_h, to change the heating power of it, in order to keep the constant temperature difference, δT. Therefore the power drop on the heater R_h is proportion to the velocity of external air flow. According to the thermal boundary theory of heated plate, the convection coefficient can be express as :

$$h = 0.664 k_f \alpha^{-1/3} \nu^{-1/6} L^{-1/2} U^{1/2} \tag{1}$$

Where U, k_f, ν and α are the velocity, the thermal conductivity, the kinematic viscosity, and the thermal diffusivity of the air flow, respectively. The total heating power of the sensor chip can be expressed as :

$$P_{tot} = P_{cond} + P_{conv} = \left(\lambda L^2 + 0.664 \frac{k_f L^{3/2}}{\alpha^{1/3} \nu^{1/6}} U^{1/2} \right) \Delta T \tag{2}$$

where P_{tot} is the total power dissipated of the sensor chip, it can be divide into two terms, thermal conduction and thermal convection respectively. λ is the thermal coefficient of the sensor. $\Delta T = T_{sensor} - T_{ambient}$ is the overheat with respect to ambient temperature $T_{ambient}$. The thermal flow sensor obeys the King's law, which is denoted as :

$$P_{tot} = \left(A + B U^{0.5} \right) \Delta T \tag{3}$$

where $A = \lambda L^2$ and $B = 0.664 k_f \alpha^{-1/3} \nu^{-1/6} L^{-1/2}$ can be calibrated by flow tunnel experiments.

B. *Calorimetric control mode*

The calorimetric control mode can measure flow velocity and flow direction simultaneously by detecting the temperature difference of upstream detectors and downstream detectors. The temperature gradient on the chip surface can be decomposed to two terms which depend on flow velocity and flow direction, respectively. The flow velocity and flow direction can be expressed as:

$$F(U) = \delta T / \Delta T = c \frac{k_f L}{k_c D} \left(L^2 / \mu\alpha\right)^{1/3} \sqrt{U} \qquad (4)$$

$$G(\phi) = \cos(\phi) \qquad (5)$$

where the δT is the temperature difference at the edges of the chip, K_c is the thermal conductivity of the sensor materials, L is the dimensions of the chip and D is the thickness of the chip. When the velocity of air flow is zero, a symmetrical temperature distribution is achieved by thermal conduction through the sensor chip as well as the surrounding air. The temperature of the upstream detectors and downstream detectors is equal, so the output of the calorimetric control mode is none. When the speed of air flow is not zero, the symmetrical temperature distribution will be broken, and bring a temperature gradient in the chip surface, which will scale up with the increase of the velocity of air flow until saturated. In this paper, two full bridge circuits included eight detectors, worked in calorimetric control mode were used to perform the role to measure flow velocity and flow direction. For optimizing the measuring range and sensitivity, one of the special design is that the distance of the eight detectors to the center of chip is different, four detectors are 380μm and others are 950μm.

C. *Intelligent flow sensor system*

As shown in Fig. 4, the CTD control circuit can be divided into three parts.

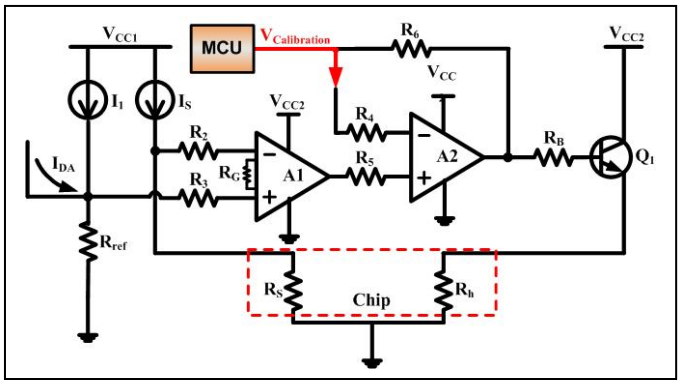

Figure 4. The CTD control circuit for flow velocity measuring and zer point drift calibration.

Current source element is used to sensing the temperature variation of the chip surface, and transfer the temperature variation to a voltage signal. A1 is an instrument amplifier and A2 is an operational amplifier, they are used to amplify the voltage signal. Meanwhile, the A2 is used to calibrate zero point drift caused by the fluctuation of ambient temperature. The last element in the circuit is to drive the heater R_h to keep the temperature of the chip higher than the ambient temperature a constant temperature, δT, which can be changed by setting the original voltage drop on the heater R_h by changing the current I_{DA}.

The CTD control has the ability to measure a very high speed air flow, and keep an acceptable sensitivity meanwhile. By it usually suffer from the zero drift, which bring in unacceptable errors of measurement.

The calorimetric control mode has high sensitivity in measuring the low speed air flow, and cannot be used if the velocity of air flow extend 30m/s commonly, but this mode hardly any zero drift. The intelligent flow sensor system was tested in the flow tunnel for velocity and direction testing. The characters of the two modes are shown in Fig.5, and the flow direction testing is shown in Fig.6.

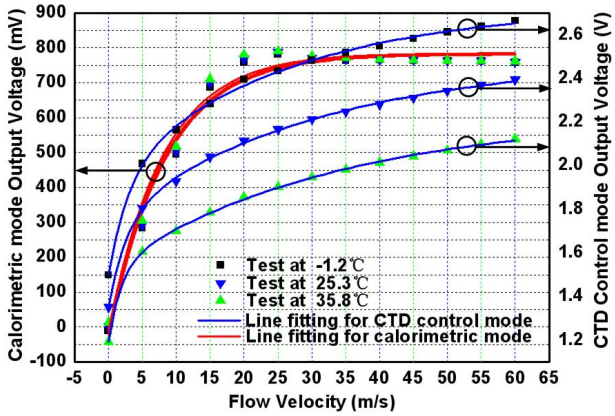

Figure 5. Flow velocity test for the CTD control mode and calorimetric mode at different ambient temperature.

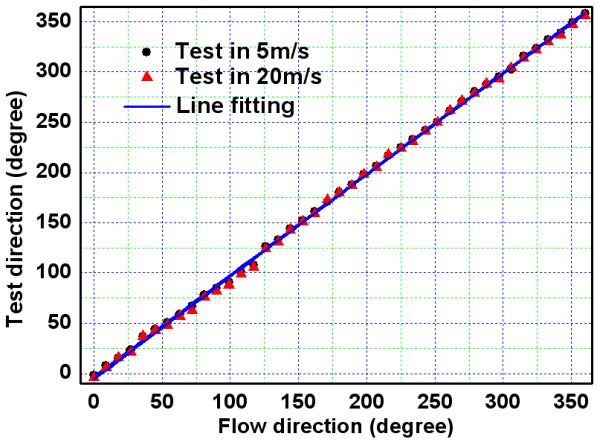

Figure 6. Flow direction test in 5m/s and 20m/s, respectively

The intelligent flow sensor system adopts a MCU as the center of process control, signal collecting and signal processing. If the calorimetric control mode shows the flow velocity less than 20m/s, the MCU computes the difference of

the two modes outputs and gets a calibration signal to change the positive voltage of A2 and finally calibrates the zero-point of the CTD control mode. When the calorimetric control mode shows the flow velocity higher than 20m/s, the last calibration zero-point of the CTD control mode is considered as a accurate value and the calorimetric control mode enter into a sleep mode. After calibrating, its relative error of flow velocity measurement is less than 5% from 0m/s to 60m/s. Fig.7 shows the result of flow sensor system measured in wild environment in 22 hours continuously.

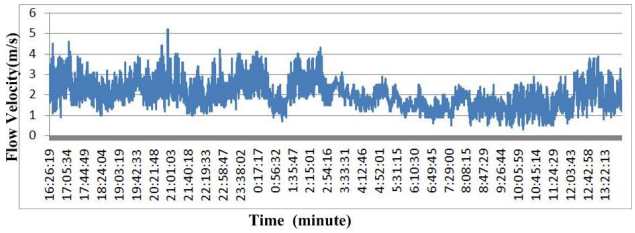

Figure 7. Flow sensor system measurement in wild environment continuously in 22 hours.

IV. CONCLUSION

An intelligent flow sensor system with zero drift self-calibration function was proposed in this paper. The sensor chip was fabricated on the ceramic substrate using single lift off process. The heating and sensing parts are Ti/Pt resistors and located symmetrically on the front side of the chip, and the backside surface of the chip act as the role to sense the change of air flow. The sensor structure was design to work in the CTD control mode and the calorimetric control mode at the same time. The calorimetric control mode plays the role to measure the air flow which velocity is lower than 20m/s and calibrate the zero point of the CTD control mode simultaneously. The CTD control mode is to measure the air flow which velocity is higher than 20m/s. After testing in the flow tunnel, the measurement range is extended to 60m/s and the relative error is less than 5% in the full measurement range.

ACKNOWLEDGMENT

Project supported by Natural Science Foundation of China under Contract No. 90607002.

REFERENCES

[1] G. Eason, B. Noble, and I. N. Sneddon, “On certain integrals of Lipschitz-Hankel type involving products of Bessel functions,” Phil. Trans. Roy. Soc. London, vol. A247, pp. 529–551, April 1955.

[2] Kim S, Kim S, Kim Y, etal, A circular-type thermal flow direction sensor free from temperature compensation, Sensors and Actuators A p.64-68 (2003).

[3] Moser D, Baltes H, A high sensitivity CMOS gas flow sensor on a thin dielectric membrane, Sensors and Actuators A ,p.37 33–37 (1993).

[4] Oudheusden BW, Silicon flow sensors. Control Theory and Applications, IEE Proceedings p.373-380 (1988).

[5] G. Shen, J. Wu, H. Zhang, M. Qin, and Q. Huang, Direct Chip Attachment (DCA) Packaging of a 2-D Thermal Flow Sensor, Electronic Packaging Technology, 2007. ICEPT 2007. 8th International Conference on, pp. 1-3, 2007.

[6] M. Elwenspoek, “Thermal Flow Micro Sensors”, in Semiconductor Conference,1999. CAS '99 Proceedings 1999 International, Sinaia, Romania, 1999, pp.423-435.

3A1-3

Impedance Spectroscopy of Chicken Infectious Laryngotracheitis Virus Based on Atomic Force Microscopy

Michael B. Schulte*[1], Zhuxin Dong[1], Steve Tung[1], Jin-Woo Kim[#2], Uche Wejinya[1], Hyung-Mo Moon[2], and Byung-Whi Kong[3]

[1]*Department of Mechanical Engineering, University of Arkansas, Fayetteville, Arkansas, United States of America*

[2]*Department of Biological and Agricultural Engineering, University of Arkansas, Fayetteville, Arkansas, United States of America*

[3]*Department of Poultry Science and Center of Excellence for Poultry Science, University of Arkansas, Fayetteville, Arkansas, United States of America*

Abstract — **The AC impedance spectroscopy of Chicken Infectious Laryngotracheitis Virus (ILTV, *gallid herpesvirus 1*) was measured using atomic force microscopy (AFM). The result indicates a 30% difference in the absolute impedance values between the control and virus samples within a 10-65 kHz frequency range. Using an equivalent circuit of the systems and an electrical curve fitting program, the data shows the average capacitance of a single virus particle is approximately 6 nF. Based on a similar analysis of the electrical properties of polystyrene beads, the overall dielectric constant of the ILTV was determined to be approximately 2.4.**

Keywords — ***AC impedance spectroscopy, ILTV, AFM, Equivelent cuircut, Dielectric constant, Polystyrene bead, Micro-electro-mechanical systems (MEMS), Total analysis system (TAS).***

I. Introduction

Over the passed few years, virus detection techniques are becoming increasingly important due to frequent occurrence of new pathogenic virus strains. At present, the means of virus detection and classification involve extensive serological procedures. These tests, such as ELISA and immune-fluorescent assay, include collecting a sample of bodily fluids to be analyzed [1]. The extensiveness of these techniques creates the need for a more generalized testing apparatus. The engineering research is to create easier and cheaper ways to analyze the physical condition of a living organism. Much has been improved in the MEMS and the TAS industry. The alternate means to detect pathogens with electrical signals using mechanical structures are being developed swiftly.

An alternative approach in detecting viruses can be through the material properties of a virus. As seen from previous work, shown in Figure 1, an AFM can be used to successfully scan and nanoindent viruses for the purpose of extracting the mechanical properties of individual virus particles [2]. In the present study the electrical properties of an ILTV particle was characterized by a similar AFM based technique. The electrical properties of the ILTV were examined to better understand the means to detect their presence within an organism. In an attempt to classify the ILTV's electrical properties, a virus will be analyzed through impedance spectroscopy and the properties will be determined. The ILTV is one of the most contagious viruses that can cause severe health problems in chicken flocks, which can lead to financial losses within the poultry industry. It is hypothesized that the viral electrical properties can be used to specifically identify ILTV through impedance spectroscopy. Confirmation of the hypothesis will be a breakthrough in the detection, classification, and isolation of ILTV.

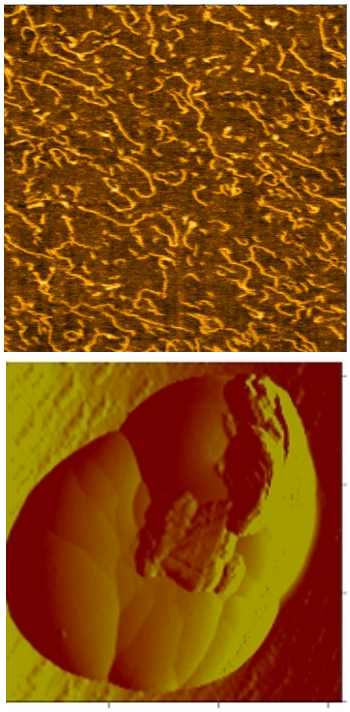

Figure 1: AFM based analysis of biomolecules. Topography of 3000 bp dsDNA ladders; and Nanoindented Avian Influenza Virus.

II. Materials and Methods

A. Virus Sample Preperation

Infectious laryngotracheitis virus (ILTV; *gallid herpesvirus 1*) is a member of large *Herpesviridae* family. United States Department of Agriculture (USDA) reference strain of ILTV was purchased from the National Veterinary Services Laboratory (NVSL; Ames, IA). The stock ILTV titer, which is defined as plaque forming unit per milliliter (pfu/ml), was 10^5 pfu/ml. Generally, one pfu titer consists of 10^3-10^7 numbers of individual virus particles (termed as virion), thus total virion numbers for ILTV stock estimate approximately 10^8-10^{12} virions/ml. For both the inactivation and the fixation of ILTV,

Michael B. Schulte is a Masters Candidate in the Department of Mechanical Engineering at the University of Arkansas in Fayetteville, AR, USA.

*Contact author: for all aspects of this project, please contact Michael B. Schulte by e-mail: mschult@uark.edu; and/or call: 1-479-414-3886.

#Contact author: for bioprocess aspects of this project, please contact by e-mail: jwkim@uark.edu.

200 µl ILTV stock was mixed with paraformaldehyde to become a 4% concentration. To verify the virus inactivation, ILTV in 4% paraformaldehyde was infected to cultured cells and the plaque formation was monitored for the virus propagation. The inactivated viral samples were used in this study after being confirmed that no live ILTV propagation was observed.

10X dilutions of the inactivated stock virus samples were prepared using DI water. Each virus sample contained a 100 µl drop of solution on an indium tin oxide (ITO) surface. The sample was then allowed to dry in environmental condition in a biological fume hood.

B. Electrical Setup

In this experiment, an Agilent 5500 AFM was used. The AFM software provides a Current Sensing (CSAFM) function under contact mode. This mode allowed the electrical connection for the impedance analyzer. CSAFM requires a special 10˚ nose cone containing a pre-amp. A bias voltage is applied to the sample and set at zero to keep the cantilever as a virtual ground. A current sensing conductive AFM probe tip on a 10 µm scanner was put into the AFM. The Cr/Pt plated, silicon tip of R < 25 nm and kc of 0.2+50% N/m (Budget Sensors) with a resonant frequency of 13 kHz was used for the AC impedance measurements.

Since the impedance analyzer needs a closed circuit for the frequency sweep, wires were bonded to the nose cone's spring that holds the cantilever and to the sample's conductive surface. The sample surface has a 1500 Å conductive ITO layer that completes the closed circuit when the tip is in contact mode.

C. Impedance Measurement

Within the closed circuit an AC frequency was applied and the absolute impedance of the system can be recorded. Impedance is a measurement involving the opposition to a sinusoidal alternating current. It is composed of the resistance and reactance of a dielectric material and can be measured by the complex addition of the two. In figure 2 the θ represents the phase angle of the impedance. With a value for both impedance and phase angle one can calculate the resistive and reactive quantities with use of (1). These values are essential to determining a correlation between material properties and impedance.

$$R = Z\cos(\theta)$$
$$X = Z\sin(\theta) \qquad 1$$

Where: R=Resistance; X=Reactance.

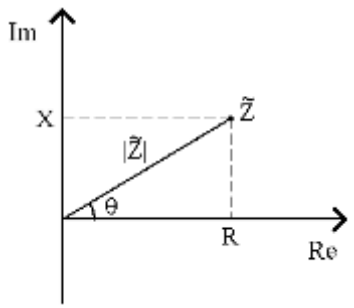

Figure 2: Impedance Measurement, Z=R+jX

To characterize the electrical properties the absolute impedance and phase angle values were obtained using an external impedance analyzer (HP 4192A) connected through the AFM tip. Data were recorded in the frequency range of 10 kHz to 1 MHz at increments of 10 kHz, all at 1VAC. Figure 3 shows the schematic of the virus-AFM-impedance analyzer experimental setup. This set-up was used to collect all the virus characterization data. National Instruments computer software, LabView, was used to decode a general purpose interface bus (GPIB). This card is used as the electrical interaction from the impedance analyzer to a computer. A downloadable program from LabView's website was used to read the GPIB card from the impedance analyzer.

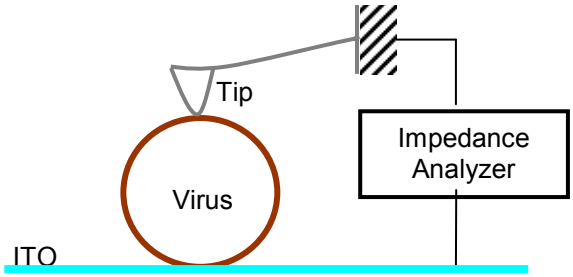

Figure 3: Schematic of the Experimental Setup.

D. Equivelent Cuircut and ZView

After the impedance spectrums were recorded the data were then converted into the resistance and reactance parts of impedance and plotted with a computer software program (ZView). The software creates a curve-fit of the collected data with a circuit model and calculates the model's components (Figure 5) to determine the virus capacitance values [3].

Figure 4: Equivalent Circuit Model without Virus.

R1: Instrument Resistance
CPE: Constant Phase Element of Instrument and Surrounding

Figure 5: Equivalent Circuit Model.

C1: Capacitance of Virus

As seen in MacCuspie's article, ZView is a strong program to calculate the components of an equivalent circuit. The program was downloaded from an online source and installed to be ready to use. The program has equivalent circuits pre programmed as well as an option to create a circuit. ZView also allows for impedance data to be inserted, as a text file in resistance and capacitance versus frequency form, into a plot. There are curve fitting options to allow an equivalent circuit to be fit to the plot. The circuit component can be made constant or variable; and the variable elements are then calculated.

E. Virus Dielectric Constant Measurement

First, the instrument resistance and constant phase elements had to be calculated. If the virus capacitor is said to be a short, the ZView program can calculate these two components. Data was recorded without the presence of a virus. Figure 3 then will be changed to have the tip touching the ITO substrate, closing the circuit. This then gives the electrical circuit shown in figure 4. The data was then used to calculate the two unknown components of the equivalent circuit. Second, the impedance data of the virus was plotted in ZView. Now the equivalent circuit of figure 5 is set up in the ZView program. The two now known components of the circuit are set as constants and the curve fit only considers the circuit change of the added capacitor, the virus. The capacitance of the virus was then known as well.

The impedance of the polystyrene beads was initially measure to find the capacitance. This was then compared with previous calculated and verified results. If the result is equivalent to other researchers, then the techniques used by the authors can be validated. Polystyrene nanobeads of similar size (200nm diameter) to the ILTV were used as the reference sample. The polystyrene bead is known to have a dielectric value approximately 2.6 [4]. Knowing this value as well as calculating the capacitance value of the bead, a reference capacitance can then be determined with (2) [5].

$$\varepsilon_r = \frac{C_x}{C_0} \qquad 2$$

Where: ε_r =Dielectric Constant; C_x =Known Capacitance; C_0 =Reference Capacitance.

III. EXPERIMENTAL RESULTS

Figure 6 is a topographical image of the nanobead and virus samples, as well as the substrate used as a control to compute the circuit resistor and CPE elements. Each image was within the ILTV size range of previous studies, 200 nm. Figure 7 represents the average absolute impedance spectrum based on multiple experimental runs. The control, ITO, is shown possessing lower impedance values throughout all frequency ranges. As expected the capacitance values of the bead, buffer, and virus cause an increase in absolute impedance of the system. It can also be observed that the absolute impedance values of the virus are different from that of the PS beads.

Taking data of the virus was then performed by the techniques used in finding the bead data. Once the absolute impedance was converted into the reactive and resistive parts, the data was inserted into ZView, plotted, and fit to the equivalent circuit shown in figure 5. Using the equivalent circuit model the capacitance values of the bead, buffer control, and virus are calculated and shown in Figure 8. It is evident that the bead capacitance and the virus capacitance vary. The capacitance values for the bead came out to be 6.5 nF, whereas the virus was 6 nF. The slight deviation can best be expressed as an electrical properties difference, and therefore is the most likely cause for the variance.

The result from an AC impedance spectroscopy shows a 27% difference between the ITO control and bead absolute impedance values. Likewise the difference between the ITO control and virus absolute impedance values is 30%. Using the experimental values of the reference capacitance, based on the bead data, the dielectric constant of the ILTV was calculated. The values from the experimental impedance spectra gave a dielectric constant of the ILTV to be ~2.4; whereas, that of the PS nanobead is ~2.6 [4].

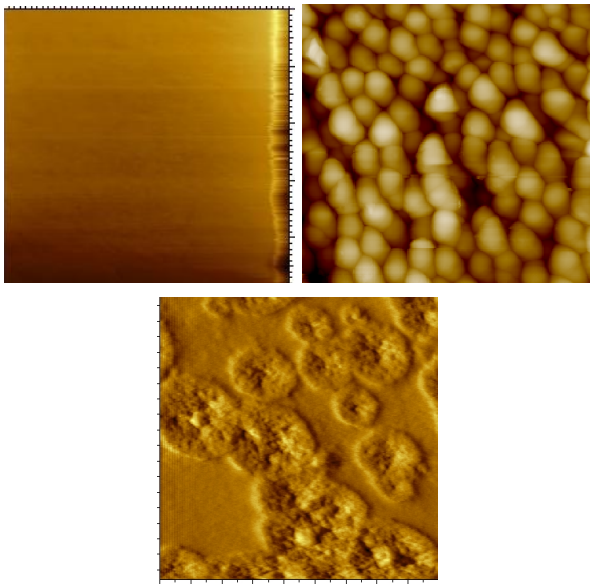

Figure 6: Topographical Images for Substrate (top left); Nanobeads (top right); and ILTV (bottom).

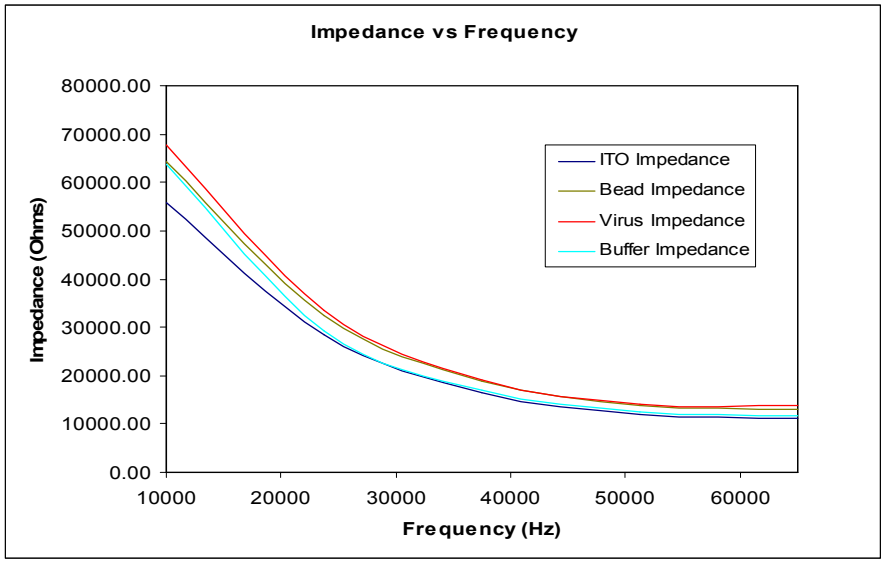

Figure 7: Bead-Virus-Substrates Impedance versus Frequency Spectra.

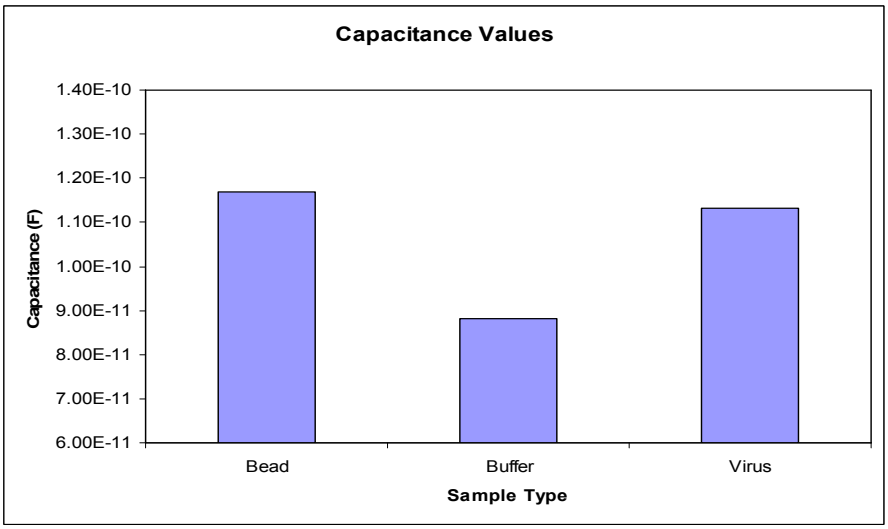

Figure 8: Capacitance versus Sample Type.

IV. Conclusions

With known differences between the ILTV and the control properties, an electrical detection of ILTV scheme can be based off an impedance spectrum of a chicken's bodily fluid. A TAS will be created with the impedance spectroscopy theory discussed in this paper. Further research on other detection schemes will ultimately be the deciding factor whether or not an impedance spectroscopy, based on the dielectric properties of the material, system will be utilized.

The ILTV will soon be able to be detected and isolated within a chicken flock before further contamination occurs. Finally, providing a quicker and easier detection technique will give overall financial gain to the poultry industry.

References

[1] Nester, Eugene W., et al. *Microbiology, A human Perspective, 5th Edition*. McGraw Hill Companies Inc., New York, NY. 2007.

[2] Rokadia, Husein, et al. "Characterization of Avian Influenza Virus Subtypes using Atomic Force Microscopy." IEEE Nano 2009.

[3] MacCuspie, Robert I., et al. "Comparison of Electrical Properties of Viruses Studied by AC Capacitance Scanning Probe Microscopy." JACS Articles, 12/20/2007.

[4] Lee, Sang-Wook, et al. "Determination of Dielectric Constant of Dielectric Particles Using Negative Dielectrophoresis." 1996 IEEE Annual Report.

[5] Jackson, John David. *Classical Electrodynamics, 3rd edition.* 1998. New York: Wiley.

3A1-4

Nanoparticle Induced DNA Damage

Thomas Prevenslik

Discovery Bay, Hong Kong, China

***Abstract* — DNA damage induced by nanoparticles (NPs) is now considered to mimic that by conventional ionizing radiation, and therefore it is reasonable to hypothesize the NPs somehow produce electromagnetic (EM) radiations, at least at ultraviolet (UV) levels. In fact, ionizing radiation from NPs at UV levels is consistent with the theory of QED induced EM radiation. QED stands for quantum electrodynamics. By this theory, fine NPs (< 100 nm) absorb low frequency thermal kT energy in collisions with solution molecules only to be induced by QED to be frequency up-converted to the EM frequency of the NP, usually beyond the UV. But the quasi-bound EM confinement allows the UV to leak from the NP, thereby providing a significant antibacterial agent in food processing, reducing infections in burn treatment, sunscreen skin lotions, and treating cancer tumors. However, there is a darkside. Over the past decade, experiments have shown NPs to produce the reactive oxygen species (ROS) of hydroxyl radicals that cause apoptosis/cell death and single and double strand breaks in the DNA. What enables the NPs to function as an antibacterial agent while posing a health risk is the remarkable fact NPs provide a low level source of continuous UV radiation. DNA damage leads to the increased risk of producing cancer, the health risk of which suggests the regulation of NPs in commercial applications.**

Keywords — cancer, DNA, nanoparticles, QED

I. Introduction

DNA damage by <100 nm NPs is now [1] considered to mimic the same pathways as by conventional sources of ionizing radiation. The most reasonable hypothesis is the NPs are somehow producing their own ionizing radiation at least at UV levels, albeit at low intensity.

NPs producing low level ionizing radiation is consistent with the theory of QED induced EM radiation [2]. By this theory, NPs nearby the walls of a biological cell produce at least UV radiation upon absorbing kT energy of colliding extra cellular solution molecules. Even though the UV intensity is low, DNA damage by single strand (SS) and double strand (DS) breaks may occur directly by photolysis or indirectly by forming the hydroxyl radical.

Currently, the NP oxidative stress mechanism based on the surface area of < 100 nm NPs is thought to govern DNA damage. However, experimental data [1, 3-15] over the past few decades has placed this paradigm in question.

II. Purpose

The purpose of this paper is to show QED induced EM radiation in NPs produces EM radiation beyond UV levels that directly or indirectly cause SS and DS breaks in the DNA culminating with the conjecture that natural and man-made NPs are indeed the most likely source of ALL cancers.

III. Background

DNA damage caused by ionizing radiation from NPs has been cited in numerous publications. Only limited background relative to the DNA damage hypothesis by NPs is presented.

A. EM Energies

EM energies necessary to directly damage the DNA require at least photolysis at UV levels. The DNA ionization potential [3] varies from 7.5 to 10 eV. Breaking SS and DS in dry DNA requires EM radiation [4] having energies above a threshold of 7 eV. The number of DS breaks then increases monotonically to about 12 eV and then remains constant.

The indirect ionizing radiation pathway relies on photolysis to form hydroxyl radicals in the extra and intracellular water [5] that causes SS and DS breaks by chemical reaction. The EM radiation need only exceed 5.2 eV to break the H-OH bond, and therefore the indirect pathway is more likely to cause DNA damage than by the direct path. The hydroxyl radical is a significant oxidative mechanism suggesting the NP oxidative stress paradigm in part finds basis in the hydroxyl radical.

B. NP Induced Oxidative Stress Paradigm and Problems

In the 1990's, evidence that α-quartz particles (Min-U-Sil) having a mean diameter of 5 microns were capable [6] of inducing oxidation damage of biological systems. However, it is likely that some <100 nm NPs were included with the Min-U-Sil particles. In silicosis, the induced hemolysis from ROS upon the interaction of silica particles with red blood cell membranes was attributed to the formation of hydrogen peroxide on the particle surface that upon reaction with metal ions by the Fenton reaction produced the hydroxyl radical. Indeed, hydrogen peroxide was detected [7] by ESR in aqueous suspensions of quartz particles. However, the source of hydrogen peroxide that produced the hydroxyl radical has never been conclusively identified.

In 2003, the NP oxidative stress paradigm as a measure of forming ROS was [8] correlated with the surface area of <100 nm NPs, although the mechanism by which the hydroxyl radicals and hydrogen peroxide form was not defined. Instead, the toxicology of air pollution was based on polycyclic aromatic hydrocarbons (PAH) particles as the most damaging to the DNA. However, there was difficulty with this paradigm because ESR comparisons [9] of the coarse $PM_{2.3\text{-}10}$ particulate produced a greater number of hydroxyl radicals than the fine $PM_{<2.5}$ particulate.

Similar problems were found [10] with the NP oxidative stress paradigm in 2006. Ambient and manufactured NPs were investigated with regard to the biological consequences of ROS production. Ambient particulate collected from the Los

Thomas Prevenslik is a retired American living in Hong Kong and Berlin.
Contact author: nanoqed@gmail.com.
URL Reference: www.nanoqed.org

Angeles basin having diameters about 1500 nm and NH2–PS spheres 1000 nm in diameter showed the clearest evidence of toxicity compared to 100 to 300 nm NPs. Also in 2006, pulmonary studies were conducted on rats using a wide range of α-quartz NPs [11] that showed about the same toxicity for 10-20 nm synthetic and 300-700 nm (Min-U-Sil) NPs. DNA damage was attributed to surface activity.

In 2008, DNA damage [12] by silver NPs widely used as antimicrobial agents was studied. Bare 25 nm silver NPs while were coated with polysaccharide to an overall diameter of 80 nm. More severe DNA damage comprising DS breaks and apoptosis/cell death was found with the larger coated NPs. Similarly, otherwise inert gold NPs were not only found [13] to generate free radicals, but also scavenge the NP)s. Absent NPs other than naturally present [14] in ex vivo human skin, the free radical production with VIS (400-700 nm) light and NIR (700-1600 nm) radiation is difficult to explain as neither VIS and NIR light are not ionizing radiations.

C. *Modified NPIinducedOxidativeStress Paradigm*

Observations [9-12] suggest the NP oxidative stress paradigm that correlates DNA damage with the area of <100 nm NPs should be modified to account for the greater DNA damage from larger 300-1400 nm NPs. By QED induced EM radiation, the NPs < 100 are the source of ionizing radiation induced DNA damage.

But if so, how is the greater DNA damage from larger NPs reconciled?

In this paper, the NP induced oxidative stress paradigm is modified to consider only the <100 nm NPs that accompany the large 300-1400 nm particulate. The larger NPs should not be viewed as the correlation to DNA damage, but rather as means of converting the kT energy in collisions from surrounding molecules to NIR that is subsequently enhances the collision induced UV radiation from the <100 nm NPs

D. *QED Induced Radiations*

Ionizing radiation from NPs based on QED induced EM radiation [2] was proposed [15, 16] as an alternative to the heating mechanism thought to cause cancer necrosis in photodynamic therapy (PDT). Previously, gold NPs attached to cancer tumors were thought destroyed by high temperatures upon the absorption of NIR laser irradiation However, conservation of the absorbed laser photon does not proceed by temperature increase of the NP, but rather by the emission of EM radiation at its EM confinement frequency, typically beyond the UV. By this theory, the UV radiation causes cancer necrosis – not high temperature.

Similar to the necrosis of cancer cells with NPs irradiated with NIR lasers, conservation of absorbed EM energy in nanostructures proceeds by UV or higher EM radiation emission by QED induced radiations. The nanostructure need not be a NP, but may be a thin film under Joule heating, or the excitation of the higher quantum states of a molecule irradiated by multiphoton infrared photons, or nanocatalysts inducing chemical reactions from the kT energy of colliding molecules in the surroundings.

QED induced EM radiation is applicable anytime nanostructures absorb EM radiation from lasers, Joule heating, or the kT thermal energy in collisions from surrounding molecules – none of which may be conserved by an increase in temperature as illustrated for NPs in Fig. 1.

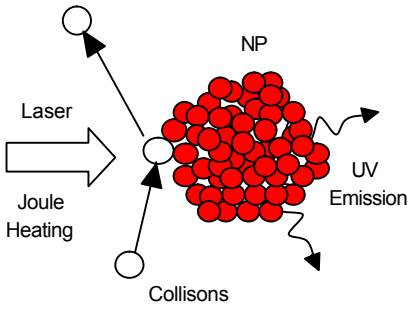

Figure 1. NP emitting QED induced EM radiation

In these and many other applications, QED induced EM radiation finds basis in simple physics – that photons of wavelength λ are created if EM energy is supplied to a quantum mechanical box having sides separated by λ/2. However, the QED induced photons only have significant EM energy if created in submicron structures. Conversely, macroscopic structures create far infrared (FIR) photons that by classical heat transfer are conserved by increase in the temperature of the structure.

IV. THEORY

The DNA in a biological cell may be damaged by NP in the extra or intra-cellular water. A NP that has entered a cell is depicted in Fig. 2. However, NPs in the extra cellular water may also damage the DNA by emitting UV radiation that penetrates the membrane. Regardless, the water molecules continuosly collide with and transfer their thermal kT energy to the NP. Since the water molecules are small compared to the NP, the collisions are inelastic and the transfer of kT energy to the NP is very efficient. Conservation of absorbed kT energy proceeds by the emission of EM radiation at the EM confinement frequency of the NP, usually beyond the UV that is sufficient to induce DNA damage

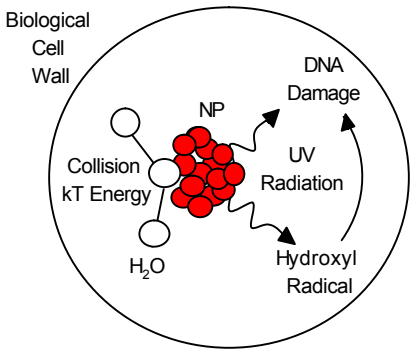

Figure 2 NP emitting UV Radiation inside Biological Cell

By photolysis, EM radiation beyond the UV may directly damage the DNA, or indirectly by forming hydroxyl radicals that chemically damage the DNA. The chemical path is more likely as only 5.2 eV is required [5] to form the hydroxyl radical compared to 7-10 eV necessary [4] for SS and DS breaks in dry DNA.

A. EM Confinement Frequencies

The EM resonant wavelength λ and Planck energy E_p in the NP upon the absorption [2] of the kT energy of the colliding molecules,

$$\lambda = 2n_r D \text{ and } E_P = \frac{hc}{2n_r D} \quad (1)$$

where, n_r is the refractive index and D is the NP diameter. The index $n_r > 1$ corrects for the retardation of the speed of light c in the solid NP.

B. QM Restrictions

The Einstein-Hopf relation for the harmonic oscillator [17] showing the dispersion of average Planck energy E_{avg} with wavelength λ at T ~ 300 K is given in Fig. 3.

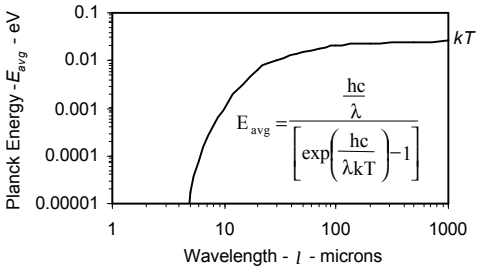

Figure 3 Harmonic Oscillator at T ~ 300K
In the inset, h and k are Planck and Boltzmann constants, and c is the speed of light in vacuum

NPs with D < 100 nm have EM wavelengths $\lambda < 0.4$ microns for an upper bound $n_r < 2$. Fig. 3 shows that for an atom confined in a NP, the average Planck energy << $1x10^{-5}$ eV. In contrast, a free atom absent EM confinement has full kT energy ~ 0.0258 eV. Hence, NPs under EM confinement at UV wavelengths $\lambda < 0.050$ microns have vanishing small kT energy << $1x10^{-5}$ eV.

C. Vanishing Specific Heat

Classical heat transfer conserves absorbed EM energy by an increase in temperature, but is not applicable to NPs because of QM restrictions on thermal kT energy. To show this, consider the specific heat $C = \partial U/\partial T$ from the Einstein-Hopf relation to give the dimensionless specific heat C*,

$$C^* = \frac{C}{3Nk} = \frac{\left(\frac{hc}{\lambda kT}\right)^2 \exp\left[\frac{hc}{\lambda kT}\right]}{\left[\exp\left(\frac{hc}{\lambda kT}\right) - 1\right]^2} \quad (2)$$

At 300 K, Fig. 4 shows C* vanishes for $\lambda = 2n_rD < 5$ microns. For n_r =1.2, the absorbed EM energy for D > 2 microns is conserved by a temperature increase while EM emission occurs for D < 2 microns.

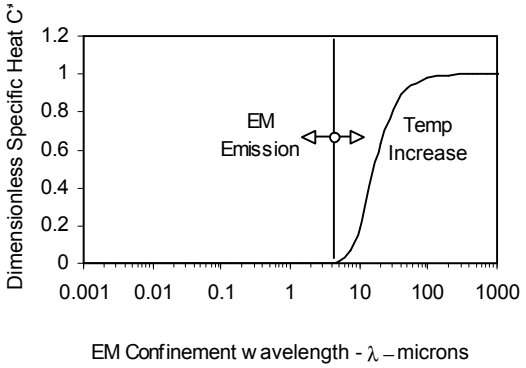

Figure 4 Dimensionless Specific Heat C* at T ~ 300 K

D. Collisonal Power and QED Induced Photons and Rate

The power Q_C transferred [18] in collisions of intracellular water molecules to the NPs,

$$Q_C = \frac{\pi}{2\sqrt{3}} pPD^2 \sqrt{\frac{kT}{m}} \quad (3)$$

where, p is the probability of full kT energy transfer, and P is the ambient pressure. For inelastic collisions, p is unity. The mass m of the water molecules is, MW/N_{avag} where MW = 18 is molecular weight and N_{avag} is Avagadro's number.

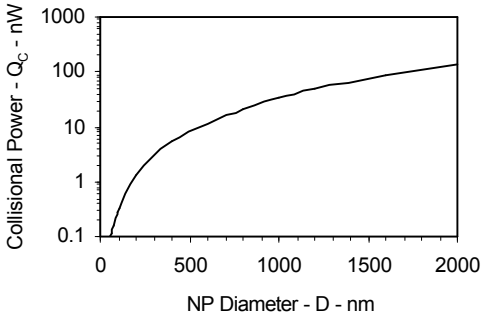

Figure 5 Collisional Power Q_C v. NP Diameter D

Absent an increase in NP temperature, the power Q_C is conserved by the emission of EM radiation,

$$E_P \frac{dN_P}{dt} = Q_C \quad (4)$$

where, dN_P/dt is the rate of QED induced photons produced in the NP having Planck energy E_P. For silver NPs having n = 1.35, the QED induced photon energy and rate is shown in Fig. 6.

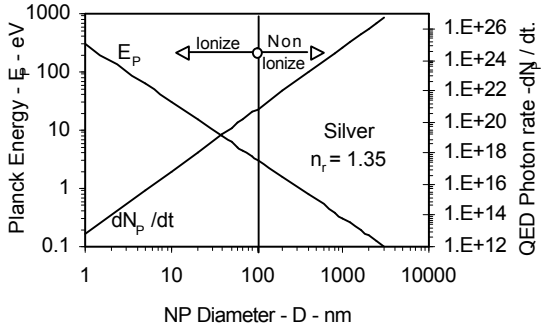

Figure 6 Planck Energy E_P and Photon Rate for Silver NPs

Silver NPs <100 nm emit ionizing radiation beyond the UV. DNA SS and DS breaks at 5.2 and 7 eV (238 and 123 nm) occur for d = 88 and 65 nm NPs, respectively. But NPs > 100 nm, emit non-ionizing radiation in the VIS and NIR.

V. ANALYSIS

In QED Induced EM radiation, the NP oxidative stress paradigm for fine <100 nm NPs need not be invalidated by the greater DNA damage found in coarse 300-1500 nm NPs. To show this, consider an arrangement of fine NPs of diameter d in relation to coarse NPs of diameter D shown in Fig. 7.

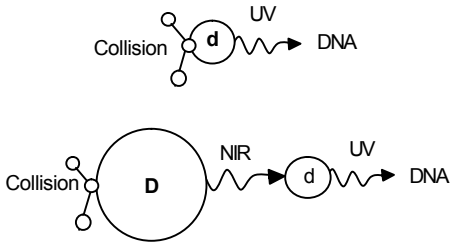

Figure 7 NIR enhanced UV Radiations

Collisions induce the fine NPs to emit UV and the coarse NPs to emit NIR power,

$$Q_{UV} = \frac{\pi}{2\sqrt{3}} pPd^2 \sqrt{\frac{kT}{m}} \text{ and } Q_{NIR} = \frac{\pi}{2\sqrt{3}} pPD^2 \sqrt{\frac{kT}{m}} \quad (5)$$

Mie theory [19] gives the efficiency Q_{abs} of the fine NPs absorbing the NIR radiation from the coarse NPs,

$$Q_{abs} = F\left(\frac{d}{\lambda_{NIR}}\right) \quad (6)$$

where, $$F = \frac{24\pi ab}{\left(a^2 + b^2 + 2\right)^2 + 4a^2b^2}$$

The NIR wavelength $\lambda_{NIR} = 2n_rD$, where n_r is the refractive index of the coarse NPs. The parameters a and b are the real and complex refractive index of the fine NPs.

The collisional power absorbed by the DNA is,

$$Q_{UV-NIR} = Q_{abs} Q_{NIR} + Q_{UV} \quad (7)$$

The ratio R of UV enhancement,

$$R = \frac{Q_{UV-NIR}}{Q_{UV}} = \left(\frac{D}{d}\right)\frac{F}{2n_r} + 1 \quad (8)$$

For fine silver NPs, the parameters a = 1.35 and b = 4 and silica coarse NPs having n_r = 1.45, the enhancement ratio R is shown in Fig. 8.

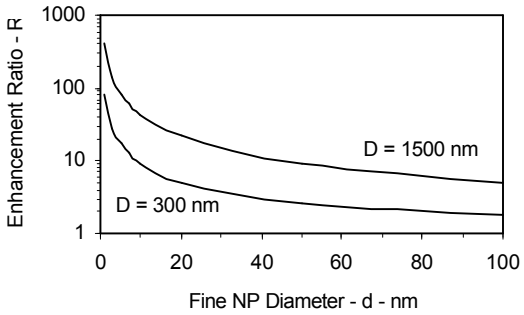

Figure 8 Enhancement Ratio R of Fine NPs by Coarse NPs

DNA damage by silver NP induced hydroxyl radical SS breaks at 5.2 eV and DS breaks at 7 eV occurs at d = 88 and 65 nm is shown enhanced for coarse 300 and 1500 nm NPs by ratios R of about 2 and more than 5, respectively.

VI. DISCUSSION

A. Modified NPInduced Oxidative Stress Mechansims

The NP oxidative stress paradigm that claims the ROS correlate with the area of fine <100 nm NPs is not modified because of the greater DNA damage found with the coarse 300-1500 nm NPs. The only modification necessary is that the coarse NPs should not be considered as damaging, but rather acting to enhance the DNA damage caused by the fine <100 nm NPs.

B. Consequences of QED Induced EM Radiations

1) Similarity of NP induced UV to Ionizing Radiations. Air pollution [8,9] studies give direct evidence of DNA damage by PM_{10} having < 50% by mass of combustion derived nanoparticles (CDNPs) in < 100 nm NPs. The CDNPs are carbon centered NPs from automobile exhausts, but NP induced DNA damage mechanisms are currently not known.

QED induced EM radiation claims <100 nm NPs produce at least UV radiation from which molecular mechanisms for DNA damage may be formulated. Indeed, NP induced respiratory DNA damage mimics [1] that by ionizing radiation, albeit at lower UV levels. This means DNA damage mechanisms under ionizing radiation are applicable to NP induced DNA damage.

2) NP Induced Oxidative Stress Paradigm. Recent pulmonary studies on rats [11] present evidence to contradict the NP induced oxidative stress paradigm that states DNA damage is caused by toxicity that correlates with the surface area of <100 nm NPs. Indeed, the toxicity of 500 nm mined α-quartz (Min-U-Sil) particles was found equivalent to that from synthetic 12 nm quartz NPs. The hemolytic potential of α-quartz in red blood cells was attributed to the surface activity [6] caused by defects, jagged edges, or the vague ease in producing ROS. Silica is known to generate hydroxyl ions from hydrogen peroxide, and indeed both have been detected aqueous suspensions α-quartz. However, the specific reactions leading to the formations of hydrogen peroxide from silica have never been identified.

In contrast, QED induced EM radiation from <100 nm NPs unequivocally provides the UV to directly form the hydroxyl radicals and hydrogen peroxide. In fact, the surface activity of α-quartz thought to produce the hemolytic potential in RBCs is most likely caused by the absorptions of QED induced UV radiations in the solution adjacent the NP surfaces. There is no need to invoke the unquantifiable notion of surface activity to explain ROS for α-quartz.

3) Anti-Microbial Silver Nanoparticles. Silver NPs having the greatest degree of commercialization are of interest in DNA damage because of the potential treatment of inflammations in the blood. Indeed, the antimicrobial activity in controlling infections [20] and limiting bacterial growth [21] in the food industry are only a few of the many applications of silver NPs.

However, silver NPs also damage [12] the DNA. The ROS including hydroxyl radicals and hydrogen peroxide are thought produced by surface chemistry. But surface chemistry cannot be the mechanism for bactericidal action of silver NPs because polysaccharide coated silver NPs produced greater DNA damage than for bare silver NPs. EM energy is required to produce ROS that cannot be produced by surface chemistry. But QED induced EM radiation is produced in NPs beyond the UV. Indeed, the 3-fold increase in the diameter of the coated to bare NPs corresponding to EM confinement wavelengths from 68 to 200 nm suggest the NPs exposed the DNA to UV beyond 6.2 eV. To avoid DNA damage, NPs larger than 100 nm are required, but this would negate the bactericidal action of the silver NPs.

4) Sun Screen. The interaction of sunlight with the human skin has led to a fragile equilibrium between the EM radiation necessary for life and UV levels that damage the DNA. Prompted by the nearly epidemic increase in skin cancers over the past few decades, the European Commission has lowered the acceptable ratio UVA/UVB. Here UVA (320-400 nm) and UVB (280-320 nm). However, only about 6 % of sunlight is in the UV with 52% in the VIS and 42% in the NIR suggesting the VIS and NIR may also be producing DNA damage.

Indeed, the ROS in the form of free radicals were found [14] in human skin under both UV and VIS/NIR radiation. UVB is ionizing radiation that is expected to produce free radicals, but the VIS/NIR is not. The free radicals measured were thought caused by heat from the VIS/NIR increasing the skin temperature. But there is no known mechanism by which simply raising the temperature produces free radicals.

QED induced EM radiation at UV levels produces ionizing radiation provided <100 nm NPs are present on the skin surface. Adherent subcutis and fascia [14] were removed, but the concentration of the remaining natural NPs was not given to assess the importance of QED induced EM radiation in producing free radicals directly from VIS/NIR radiation. Nevertheless, it is highly likely NPs were in fact present to explain the free radicals observed.

Sunscreens use white colored zinc oxide particles to deflect [22] damaging UV radiation, but the zinc oxide may be made transparent and more absorbent by shrinking the particles down to <100 nm NPs. By QED induced EM radiation, the zinc oxide NPs absorb fractions of the UV/VIS/NIR radiation only to produce higher energy UV radiation that damages the DNA. To avoid DNA damage, the <100 nm NPs should be replaced by NPs > 100 nm that would convert the UV content in sunlight to VIS/NIR levels. The claim [22] that NPs are absorbed in the skin and therefore cannot cause DNA damage to the brain or liver does not consider the capability of UV radiation to penetrate the skin an induce DNA damage in the RBC. With the wide use of NPs in sunscreens, it is no wonder that the increase in skin cancer has reached epidemic levels over the past 20 years.

5) Gold Nanoparticles The interaction between gold NPs and aniline give [13] the formation of free radicals in contrast to the hydroxyl radicals [12] formed between silver NPs in intracellular water solutions. Both gold and silver NPs are induced by QED to produce UV radiation and free radicals that depend on the solution. Surface activity is almost inconsequential to the ionizing UV radiation.

6) Cancer Therapy. In PDT, photosensitizers in the form of NPs that preferentially attach to cancer cells and activated by NIR radiation are claimed [23] to produce singlet oxygen, thereby destroying the cells by chemical reaction. But cancer cells are destroyed without photosensitizers, thereby begging the question of what actually induced cancer necrosis in PDT.

Prior to photosensitizers, high temperature was thought to induce cancer necrosis in PDT. But NPs lack the specific heat [15, 16] to allow a temperature increase to conserve the absorbed NIR radiation, and therefore QED induces the NP to emit EM radiation beyond the UV that causes cell necrosis, thereby obviating the need for photosensitizers in PDT to activate the oxygen singlet state.

Whether DNA is not damaged by a certain frequency range of ionizing radiation that is damaging to a specific cancer is an unlikely conjecture. But if research shows otherwise, the selection of a NP size tuned solely to the frequency causing necrosis of the cancer may be possible. Only then may NPs be justified in cancer therapy.

VII. Conclusions

Conclusions based on NP induced DNA damage and cancer risks rely on the theory of QED induced EM radiation to allow NPs to produce UV radiation that mimics that caused by conventional sources of ionizing radiation.

- NPs < 100 nm produce EM radiations beyond the UV that damages DNA and increases the risk of cancer.
- NIR lasers used to activate NPs of photosensitizers are not necessary to produce UV radiation. The EM energy required to produce the UV radiation is the thermal kT energy of surrounding extra and intracellular water molecules that collide with the NPs and upon absorption is induced by QED to be frequency up-converted to UV levels.
- QED only induces EM radiation beyond the UV at NP diameters <100 nm NPs.
- QED induces the large 300-1500 NPs to produce VIS/NIR radiation that enhance the UV emission from adjacent <100 nm NPs.
- The NP induced oxidative stress paradigm that DNA damage is caused by ROS produced proportional to the area of <100 nm NPs needs to be modified to exclude the larger 300-1500 nm NPs.
- Surface activity based on the area of <100 nm NPs. Is non-quantifiable.
- Sunscreens having NP < 100 nm NPs should be banned in favor of NPs > 100 nm that would absorb UV radiation that then is frequency down-converted to DNA non-damaging VIS and NIR radiation.
- The widespread use of silver NPs in limiting bacteria in food processing and anti-microbial action should cease immediately for risk of developing cancers.
- The DNA damage induced by NPs is a cancer risk if not properly repaired. Given that NPs produce ionizing radiation beyond UV levels from the QED induced kT energy of surrounding solution molecules, and that natural and man-made NPs are ubiquitous, the conjecture is made that NPs are the most likely cause of cancers in ALL mammals. Where possible, the US and European Union therefore should ban the use of <100 nm NPs in all man-made products.
- The sensitivity of DNA to ionizing radiation should be determined to see if cancers can be selectively targeted by NPs without causing DNA damage.

References

[1] R.M. Mroz, et al., "Nanoparticle-driven DNA damage mimics irradiation-related carcinogenesis pathways," Euro. Respir. J, vol. 31, pp. 241–251, 2008.

[2] T. Prevenslik, "QED induced EM radiation," See www.nanoqed.org, 2004-2009

[3] B. Boudaiffa, P. Clotier, D. Hunting, M.A. Huels, and L. Sanche, "Resonant Formation of DNA Strand Breaks by Low-Energy (3-20 eV) Electrons," Science, vol. 287, pp. 1658-1660, 2000.

[4] K. Hieda, "DNA damage induced by vacuum and soft X-ray photons from Synchrotron radiation," J. Radiat. Biol., vol. 66, pp. 561, 1994.

[5] M. Kuwarara, A. Minegishi, K. Takakura, K. Hieda, and T. Ito, "Photolysis of water VUV radiation and reactions with DNA and related compounds in aqueous systems," In Photobiology, Edited by E. Riglis, New York, Plenum, pp. 355-363., 1991.

[6] B.L. Razzaboni and P. Bolsaitis, "Evidence of an Oxidative Mechanism for the Hemolytic Activity of Silica Particles," Environ. Health Persp, vol. 87, pp.337-341, 1990.

[7] X. Shi, N.S. Dalal, and V. Vallyathan, "ESR evidence for the hydroxyl radical formation in aqueous suspension for quartz particle and its possible significance to lipid peroxidation in silicosis." J. Toxicol Environ Health, vol. 25, pp. 237-245, 1988.

[8] K. Donaldson, "The biological effect of coarse and fine particulate matter," Occup Environ Med, vol. 60, pp. 313-314, 2003.

[9] J.T. Shi, et al., "Temporal variation of hydroxyl radical generation and 8-hydroxyl radical generation and 8-hydroxy-2'-deoxyguanosine formation by coarse and fine particulate matter," Occup. Environ Med, vol. 60, pp. 315-321, 2003.

[10] T. Xia, et al., "Comparison of the Abilities of Ambient and Manufactured Nanoparticles to Induce Cellular Toxicity According to the Oxidative Stress Paradigm," Nano Lett., vol. 6, pp. 1794-1807, 2008.

[11] D.B. Warheit, T.R. Webb, V.L. Colvin, R.L. Reed, and C.M. Sayes, "Pulmonary Bioassay Studies with Nanoscale and Fine-Quartz Particle in Rats: Toxicitry is not Dependent upon Particle Size but on Surface Characteristics," Toxicological Sciences, vol. 95, pp. 270-280, 2007.

[12] M. Ahmed, et al., "DNA damage .response to different surface chemistry of silver nanoparticles in mammalian cells," Toxico Appl. Pharmacol, vol. 233, pp. 404-410, 2008.

[13] P. Ionita, F. Spafiu, and C. Ghica, "Dual behavior of gold nanoparticles, as generators and scavengers for free radicals," J. Mater. Sci, vol. 43, pp. 6571-6574, 2008.

[14] L. Zastrow, et al., "The Missing Link – Light-induced (280-1600nm) Free Radical Formation in Human Skin," Skin Pharmacology and Physiology," vol. 22, pp. 31-44, 2008.

[15] T. V. Prevenslik, "Nanoparticles in Cancer Therapy," presented at GEM Conference on Cancer in conjunction with Inter. Conf. Mat. App. Tech. 2007, Singapore, July 1-4, 2007.

[16] T. Prevenslik, "Cancer Therapy by QED induced EM radiation," See www.nanoqed.org , 2007.

[17] R.W. Christy and A. Pytte. The Structure of Matter: Introduction to Modern Physics. New York: Benjamin, 1965.

[18] K.K. Das, Y.V. Rostovtsev, K. Lehmann, M.O. Scully, Optics Communications, vol. 246, pp. 551, 2005.

[19] C. F. Bohren and D. R. Huffman, Absorption and Scattering of Light by Small Particles, J. Wiley & Sons, 1983.

[20] J.S. Kim, E. Kuk, J.H. Kim, S.J. Park, and H.J. Lee, "Antimicrobial effect of silver nanoparticles," Nanomedicine, vol. 3, pp. 95-101, 2007.

[21] C.F. Chau, S.H. Wu, and G.C. Yen, "The development of regulations for food nanotechnology," Trends Food Sci. Technol., vol. 16, pp.269-280, 2007.

[22] D. Biello, "Do Nanoparticles and Sunscreen Mix?," 2007 www.sciam.com/article.cfm?id=do-nanoparticles-and-sunscreen-mix

[23] X. Huang, I.H. El-Sayed, W. Qian,, and M.A. El-Sayed, "Cancer Cell Imaging and Photothermal Therapy in the Near-Infrared Region by Using Gold Nanorods," J. Am. Chem. Soc., pp. 2115-20., 2006.

3A1-5

Rapid Identification of *Candida albicans* Based on Raman Spectral Biosensing Technology

Yong-Li Pan[1], Tzyy-Schiuan Yang[2], Tsung-Chain Chang[3], and Hsien-Chang Chang[1,4*]

[1]*Institute of Biomedical Engineering, National Cheng Kung University, Taiwan*
[2]*Department of Chemistry and Biochemistry, National Chung Cheng University, Taiwan*
[3]*Department of Medical Laboratory Science and Biotechnology, National Cheng Kung University, Taiwan*
[4]*Institute of Nanotechnology and Microsystems Engineering, National Cheng Kung University, Taiwan*

***Abstract* — Traditional identification methods of pathogenic *Candida albicans* are time-consuming due to the long-term incubation. The purpose of this study is to develop a noninvasive biomolecular sensing technology for rapid identification of *Candida albicans*. Surface enhanced Raman scattering (SERS) based on colloidal sliver was used to rapidly detect specific molecules on the surface of cells cultured on SDA plate. A home-made fluidic chamber was fabricated to enlarge the random sampling area, increase the path length and avoid sampling error caused by disturbance or evaporation. SERS signal was detected by a 514 nm laser with a 10x objective lens. The exposure time of CCD was 10 s. Normalization, second derivative, principal component analysis (PCA) and hierarchical cluster analysis (HCA) were also integrated for discrimination of *Candida albicans* by spectral patterns precisely. The results show that SERS can be used to detect high-concentration suspended cells of *Candida albicans*. *Candida albicans* can be discriminated to genus and species level by principal component analysis and hierarchical cluster analysis of high frequency features of SERS spectral patterns.**

Keywords — Candida albicans, colloidal silver, pattern recognition, spectral analysis, surface-enhanced Raman spectroscopy (SERS).

I. INTRODUCTION

Candida albicans is an obligatory commensal of warm-blood animals. It also ever occasionally appeared in some plants, water or soil. Some strains are normal flora on the skin or the gut of human beings. *Candida albicans* can induce opportunistic infection in patients with suppressed immunity [1]. It is the most common species in candidiasis. It is also a common pathogen of nosocomial infection in hospitals (primarily on intensive care units) [2]. Recently, *Candida albicans* is also used as an indicator microorganism of beach water [3].

Candida albicans is a kind of fungus. When it infects host tissue, the yeast form can transform into an invasive hyphae form. It also can generate pseudo hyphae and true hyphae when cultured in medium with serum. When a clinical or environmental specimen is suspected to contain *Candida albicans* or other pathogenic yeasts, it can be further identified according to the germ tube test or carbohydrate assimilation test [4]. However, these methods are usually time-consuming due to the long-term incubation. They also easily cause false negative due to failed incubation.

DNA is the most common used biomolecule for rapid identification of different microorganisms and diagnosis of infectious diseases due to the specific DNA sequence of different kinds of microorganisms [5]. However, the invasive sample pretreatment procedure is complicated and time-consuming.

Raman spectra can be used as the specific fingerprint of a molecule. The polarization of covalent binding is induced by the electric field of incident light [6]. It also can be accounted by a quantum mechanical model [7]. There is only one photon in every 10^6-10^8 scattered photon is Raman scattering. Therefore, the intensity of normal Raman scattering is very weak. Normal Raman spectroscopy (Stokes Raman scattering) has been used to detect single colony or dried cells of *Candida albicans* on Si or Au coated substrate. However, it was easily interfered by the fluorescence background and time-consuming.

Surface-enhanced Raman scattering (SERS) can be used to increase the signal-to-noise ratio of weak normal Raman scattering. According to the mechanism of electric field enhancement, the electric field (E) of the incident light and Raman scattering light can induce the localized surface plasma resonance (LSPR) of the electron cloud on metal nanoparticles [8]. Therefore, the localized electric field on the surface of metal nanoparticles can be enhanced enormously. The signal enhancement factor is correlated to the fourth power of the electric field of the incident light (E^4).

The purpose of this study is to develop a noninvasive biomolecular sensing technology by SERS for rapid identification of *Candida albicans* without complicated sample pretreatment procedures. SERS based on colloidal silver was used to detect specific molecules on the surface of cells cultured on SDA plate. The cell wall of *Candida albicans* is composed of several layers [9]. Mannoprotein is the outermost molecule [10]. A fluidic chamber was fabricated to detect suspended cells in liquid phase by Raman microspectroscopy. In addition, normalization, second derivative, principal component analysis (PCA) and hierarchical cluster analysis (HCA) were also integrated to help discriminate *Candia albicans* objectively and precisely.

*Contact author: please contact **hcchang@mail.ncku.edu.tw.***

II. Materials and Methods

A. Colloidal silver

The nano-Ag colloid was synthesized using the citrate-reduction method [11]. TEM images show these Ag nanoparticles have a variety of sizes and shapes. The UV-visible absorption spectra of this colloidal silver show the peak of localized surface plasma resonance (LSPR) is located at 452 nm. The 50 μl high-concentration solution of Ag nanoparticles (20×) was prepared by centrifugation of 1 ml newly synthesized Ag nanoparticles (1×). After removing 950 μl supernatant, Ag nanoparticles was suspended in the residual solution.

B. Microorganisms

Samples of microorganisms for discrimination to the genus level include three kinds of *Candida* species (3 strains of *C. albicans*, *C. parapsilosis* and *C. tropicalis*), one kind of *Saccharomyces* species (1 strain of *Saccharomyces cerevisiae*) and one kind of *Shewanella* species (1 strain of *Shewanella decolorationis*). Samples of microorganisms for discrimination to the species level include six kinds of *Candida* species (26 strains of *C. albicans*, *C. parapsilosis*, *C. tropicalis*, *C. glabrata*, *C. krusei*, and *C. lusitaniae*). All strains of *Candida* species were obtained from the Bioresource Collection and Research Center (BCRC, Hsinchu, Taiwan (R.O.C.)), and Centraalbureau voor Schimmelcultures (CBS, Utrecht, The Netherlands). One strain of *Saccharomyces cerevisiae* for bread baking was purchased from Sunlight Food Corporation, Taipei, Taiwan (R.O.C.). *Shewanella decolorationis* (NTOU1) was provided by Mr. Shiue-Lin Li in the department of environmental engineering in National Cheng Kung University and Professor Shiu-Mei Liu in National Ocean University, Taiwan (R.O.C.).

Before SERS detection, *Candida* species and *Saccharomyces* species were subcultured on Sabouraud dextrose agar (SDA) at 35 °C in the incubator for 2 day. *Shewanella decolorationis* was subcultured in liquid lactate medium for 1 day aerobically.

C. Raman spectral detection and data analysis

Several colonies on agar plate were suspended in 50 μl deionized water. The final volume is about 60 μl. The cell concentration was measured by a turbidimeter. 1 MacFarland of yeast cells is about equal to 10^6 CFU/ml and 1 MacFarland of bacterial cells is about equal to 10^7 CFU/ml. The cell concentration of yeast was adjusted to larger than 10^8 CFU/ml. The MacFarland value was about 1 after 100-fold dilution. Cells of *Shewanella decolorationis* subcultured in liquid lactate medium were washed three times and then suspended in fresh deionized water. The cell concentration of bacteria was adjusted to larger than 10^9 CFU/ml. The MacFarland value was about 1 after 100-fold dilution. 50 μl suspended cells of microorganisms were then mixed sufficiently with 50 μl highly concentrated citrate-reduced Ag nanoparticles for 5 min. The mixture was finally filled inside a fluidic chamber (9 mm wideness and 1 mm thickness). The Polydimethylsiloxane (PDMS) spacer of the chamber and the glass slide were tightly bound together after treated with O_2 plasma. The chamber was sealed with a cover glass (0.17 mm thickness) after filled with the sample to avoid the sampling error caused by disturbance or evaporation.

SERS signal was detected by a 514 nm laser with a 10x objective lens of Raman microspectroscope (Renishaw, United Kingdom) through a cover glass (0.17 mm thickness) as shown in Fig. 1(a). The z-axis position of the focused laser spot was optimized by a prominent SERS signal. Then, six different sampling sites at the same optimal xy-plane of the pretreated sample were randomly selected as shown in Fig. 1(b). The exposure time of CCD was 10 s. The width of confocal slit was tuned to 50 μm and a grating of 1800 lines/mm was selected. Raman shift of the instrument was calibrated by a silicon wafer at 520 cm^{-1}.

The optimal range of Raman shift (400 cm^{-1}~2000 cm^{-1}) with significant peaks was chosen and truncated for further analysis by principal component analysis (PCA) [12] and hierarchical cluster analysis (HCA) [13]. SERS spectral data were preprocess by baseline correction, normalization, second derivative and smoothing (high-pass filtered by Savitzky-Golay algorithm). Baselines of all tilted spectra were corrected to be flat by WiRE 3.1 (Renishaw, United Kingdom). Then, the intensity range of all spectra was normalized between 0 and 1000. Spectral data points were aligned by GRAMS 8.0 (Thermo Fisher Scientific, USA). Finally, SERS spectra data were preprocessed and analyzed by Solo+MIA 5.2 (Eigenvector research, USA).

III. Results and Discussion

A. Detection of Candida albicans by SERS

Fig. 2(a) shows the comparison of SERS signal and normal Raman spectra of suspended cells of *Canida albicans* (BCRC 20512) with the same cellular concentration (10^8 CFU/ml) by using 514 nm laser. They were acquired by the same parameters of Raman microspectroscopy including 10x objective lens and 10 s of exposure time of CCD. SERS and normal Raman spectra were randomly sampled at 6 different sites. SERS Raman spectra have a lot of significant peaks in the range between 400 cm^{-1} and 2000 cm^{-1}. These SERS signals of *Candida albicans* may be from mannoprotein [14] or amino acid [15] which is the outermost molecules of *Candia albicans*. In addition, they may be from other secreted metabolites or from the component of Sabouraud dextrose agar. On the contrast, normal Raman spectra of suspended cells of *Candida albicans* are very weak. There are only broad peaks detected at 3200 cm^{-1} and 3400 cm^{-1}. These peaks are

originated from water by comparing with Raman spectral assignment in other literatures.

Fig. 2(b) shows the comparison of SERS signal and normal Raman spectra of suspended cells of *Shewanella decolorationis* (NTOU1) with the same cellular concentration (10^9 CFU/ml) by using 514 nm laser. They were also acquired by the same parameters of Raman microspectroscopy. SERS Raman spectra also have a lot of significant peaks in the range between 400 cm^{-1} and 2000 cm^{-1}. These SERS signals of *Shewanella decolorationis* may be from riboflavin or other molecules on the bacterial surface.

These results indicate that 514 nm laser is feasible for SERS detection of high-concentration suspended cells of *Candida albicans* (>10^8 CFU/ml) and other microorganisms based on citrate-reduced Ag nanoparticle. There is no significant G band and D band of carbon black induced by the thermo effect of laser and Ag nanoparticles in these SERS spectra. It may be due to the protection and cooling of water. It implies that 514 nm laser may induce the localized surface plasmon resonance (LSPR) of citrate-reduced Ag nanoparticles attached on yeast cells according to the field-enhanced mechanism. It also indicates that SERS has high spot-to-spot reproducibility at 6 different sites inside the large area of a fluidic chamber. In addition, the pretreatment procedure of samples for SERS detection is simple. It only needs to mix suspended cells of microorganisms and Ag nanoparticles for 5 min. These results also imply that SERS may be further applied for sensitive and rapid detection of yeast or bacteria inside other types of glass-based biochip.

B. Discrimination of Candida albicans by SERS patterns

Fig. 3 shows the preprocessed SERS of five different microorganisms at six sites of the fluidic chamber. The data was selected in the range of 400 cm^{-1} to 2000 cm^{-1}. Then, the data were baseline corrected and normalized between 0 to 1. The variance of SERS signals on six different sites can be diminished by baseline correction and normalization. Therefore, SERS spectra are very similar at six different sites and almost overlapped each other. SERS of *Candida albicans* is shown in Figure 3 (d) inside a red solid circle. It is similar to SERS patterns of other *Candida* or *Saccharomyces* species (Figure 3 (a)~(c)). The differences among these processed SERS signals of different microorganisms are subtle. On the contrast, it is significantly different from the SERS pattern of bacteria (Figure 3(e)).

Fig. 4 shows the principal component analysis of high-frequency feature of SERS of *Candida albicans* and other microorganisms preprocessed by Savitzky-Golay algorithm (second derivative and smoothing). SERS signals of *Candida albicans* at six sites are shown inside a red solid circle. SERS of *Candida albicans* on 6 different sites were clustered together. *Candida albicans* and the other two *Candida* species were also clustered together. Four yeast species can be discriminated from *Shewanella decolorationis* by principal component 1 (x-axis). In addition, *Candida* species can be discriminated from *Sacchromyces cerevisiae* by principal component 2 (y-axis). Therefore, *Candida* species can be discriminated from other genus of yeasts or bacteria by both principal component 1 and principal component 2. Therefore, *Candida albicans* can be precisely discriminated from other genera of fungus and bacterium by principal component transformation of high frequency features of SERS patterns.

Fig. 5 shows the hierarchical cluster analysis of the high-frequency feature of SERS of *Candida albicans* and other microorganisms preprocessed by Savitzky-Golay algorithm. The dissimilarity of different clusters is defined by a variance-weighted distance and calculated by Ward's method. SERS signals of *Candida albicans* at six sites are clustered together initially and marked by a red solid circle. The dendrogram shows that three *Candida* specieses were clustered together with high precision. However, *Candida albicans* is more similar to *Candida parapsilosis* than to *Candida tropicalis*. In addition, *Candida* species is more similar to the other yeast species (*Saccharomyces cerevisiae* for bread baking) than to bacterial species (*Shewanella decolorationis*). Therefore, *Candida albicans* can be precisely discriminated and classified to the genus level by this method. The discrimination results of *Candida albicans* by the hierarchical cluster analysis agree with the principal component analysis as shown in Fig. 4.

Fig. 6 shows the hierarchical cluster analysis of the high-frequency feature of SERS of 26 strains of 6 different *Candida* genera preprocessed by Savitzky-Golay algorithm. 12 strains of *Candida albicans* are marked by a red solid circle. There are 8 strains of *Candida albicans* clustered together precisely (66.7%). 4 strains obtained from CBS are clustered with other *Candida* species (33.3%). It indicates that *Candida albicans* could be further discriminated to the species level by this method with lower precision.

IV. CONCLUSION

Surface-enhanced Raman spectral biosensing technology based on 514 nm laser and citrate-reduced Ag nanoparticles is feasible for sensitive and rapid detection of high-concentration suspended cells of *Candida albicans* (>10^8 CFU/ml) and other microorganisms in liquid phase. The pretreatment procedure of samples for SERS detection is simple. It only needs to sufficiently mix suspended cells of microorganisms and Ag nanoparticles. The variance of SERS signals on six different sites can be diminished by baseline correction and normalization. Therefore, SERS has high spot-to-spot reproducibility at 6 different sites inside a fluidic chamber and do not need a lot of sampling points to represent the sample.

Candida albicans can be precisely discriminated to the genus level by principal component transformation or hierarchical cluster analysis of high frequency features of SERS patterns. The discrimination results of *Candida albicans* by the hierarchical cluster analysis agree with the principal

component analysis. Moreover, *Candida albicans* can be further discriminated to the species level by this method with lower precision.

ACKNOWLEDGMENT

We thank the Center for Micro/Nano Science and Technology at National Cheng Kung University for the instrumental support of Renishaw Raman Microspectrocope.

REFERENCES

[1] A. H. Rose and J. S. Harrison, *The Yeasts*, Oxford: Academic Press, 1987, pp. 223-236.
[2] M. Ruhnke, "Epidemiology of Candida albicans infections and role of non-Candida albicans yeasts," *Curr. Drug Targets*, vol. 7, pp. 495-504 ,2006.
[3] N. E. Brinkman, R. A. Haugland, L. J. Wymer, M. Byappanahalli, R. L. Whitman, and S. J. Vesper, "Evaluation of a rapid, quantitative real-time PCR method for enumeration of pathogenic Candida cells in water," *Appl. Environ. Microbiol.*, vol. 69, pp. 1775-1782, 2003.
[4] W. C. Tsai, *Practical Clinical Microbiology*. Taipei: Jeou Chou, 2000, pp. 100-200.
[5] S. M. Barns, D. J. Lane, M. L. Sogin, C. Bibeau, and W. G. Weisburg, "Evolutionary Relationships among Pathogenic Candida Species and Relatives," *J. Bacteriol.*, vol. 173, pp. 2250-2255, 1991.
[6] R. L. McCreery, *Raman spectroscopy for chemical analysis*, New York: Wiley-interscience, 2000.
[7] E. Smith and G. Dent, *Modern Raman spectroscopy-A Practical Approach*, Chechester: John Wiley &Sons, 2005, pp. 15-19.
[8] P. L. Stiles, J. A. Dieringer, N. C. Shah, and R. P. V. Duyne, "Surface-enhanced Raman spectroscopy," *Annu. Rev. Anal. Chem.*, vol. 1, pp. 601-626, 2008.
[9] R. Prasad, *Candida albicans-Cellular and Molecular Biology*, Berlin: Springer-Velag, 1991, pp. 7.
[10] R. D. Nelson, N. Shibata, R. P. Podzorski, and M. J. Herron, "Candida mannan: chemistry, suppression of cell-mediated immunity, and possible mechanisms of action," *Clin. Microbiol. Rev.*, vol. 4, pp. 1-19, 1991.
[11] P. C. Lee, and D. Meisel, "Adsorption and surface-enhanced Raman of dyes on silver and gold sols," *J. Phys. Chem.*, vol. 86, pp. 3391-3395, 1982.
[12] J. E. Jackson, *A User's Guide to Principal Components*. New York: John Wiley & Sons, 1991, pp. 4-25.
[13] L. Kaufman and P. J. Rousseeuw, *Finding Groups in Data*. New York: Wiley-Interscience, 1990, pp. 224-238.
[14] A. Sujith, T. Itoh, H. Abe, A. A. Anas, K. Yoshida, V. Biju, and M. Ishikawa, "Surface enhanced Raman scattering analyses of individual silver nanoaggregates on living single yeast cell wall," *Appl. Phys. Lett.*, vol. 92, pp. 103901, 2008.
[15] E. Podstawka, Y. Ozaki, and L. M. Proniewicz, Part I: "Surface-enhanced Raman spectroscopy investigation of amino acids and their homodipeptides adsorbed on colloidal silver," *Appl. Spectrosc.*, vol. 58, pp. 570-580, 2004.

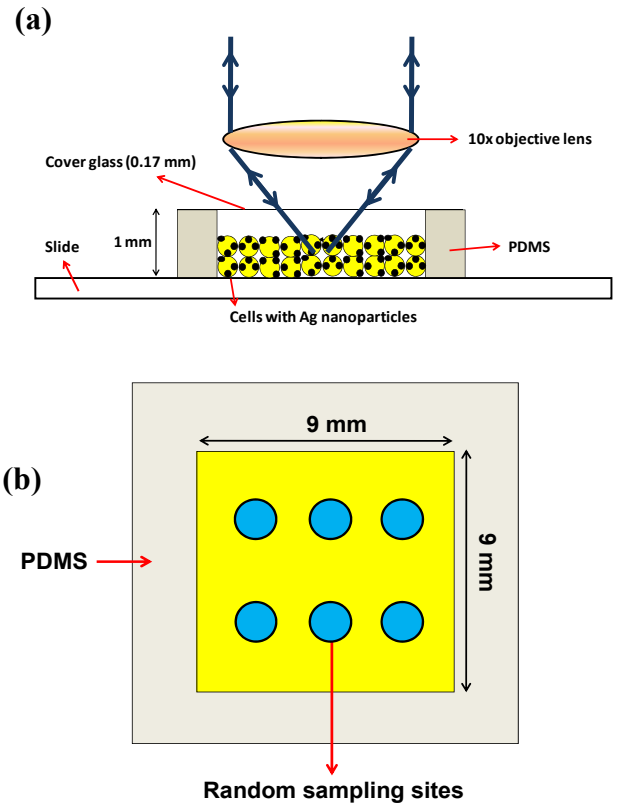

Fig. 1 Sampling methods of SERS inside a fluidic chamber. (a) Optimization of SERS signals by adjusting the z-axis position of laser spot. (b) Randomly selected six different sites at the same optimum xy-plane.

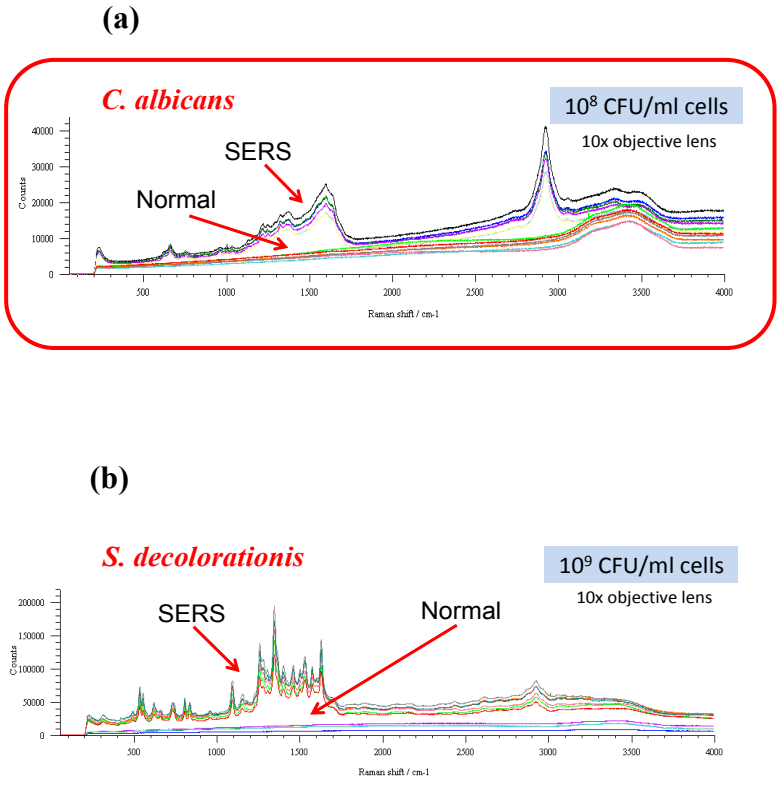

Fig. 2 Comparison of SERS and normal Raman spectra of suspended cells of (a) *Candida albicans* (>10^8 CFU/ml) and (b) *Shewanella decolorationis* (>10^9 CFU/ml).

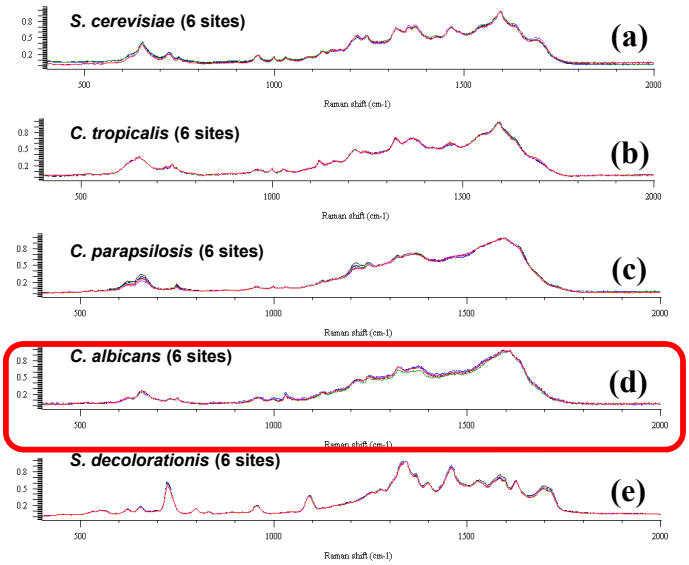

Fig. 3 Preprocessed 6 SERS data of 5 different microorganisms by baseline correction and normalization. (a) *S. cerevisae*. (b) *C. tropicalis*. (c) *C. parapsilosis*. (d) *C. albicans*. (e) *S. decolorationis*. The red solid-line circle is used to stand for *Candida albicans* in all figures.

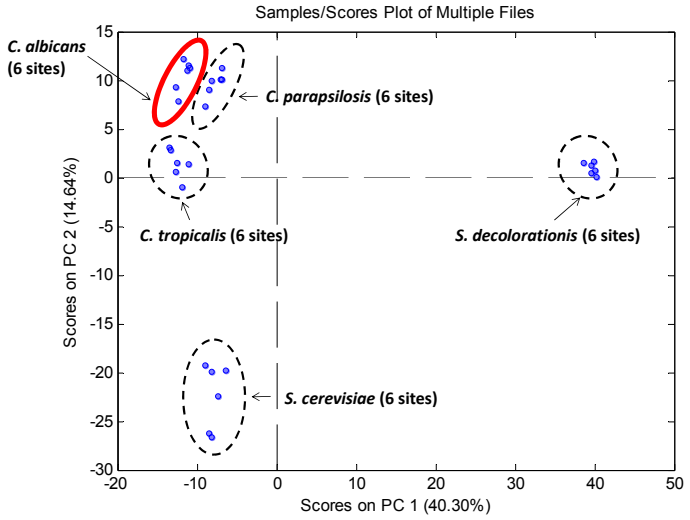

Fig. 4 Principal component transformation of high frequency features of three different genera of microorganisms processed by second derivative (high pass filter).

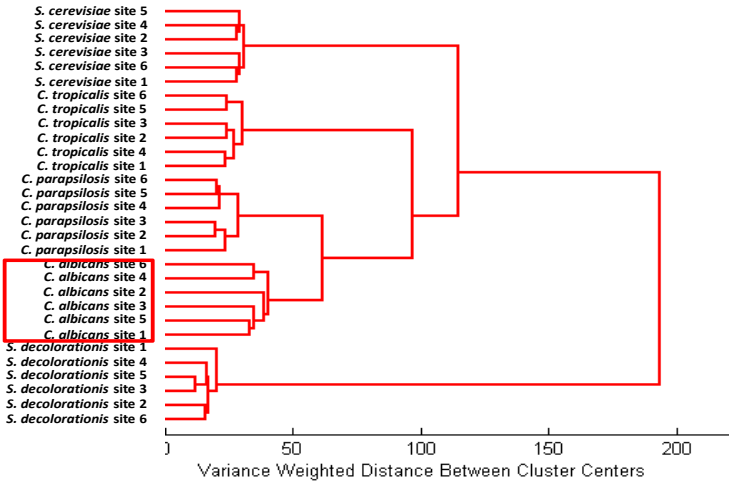

Fig. 5 Hierarchical cluster analysis (Ward's Method) of high frequency features of 5 strains of three different genera of microorganisms preprocessed by second derivative (high pass filter).

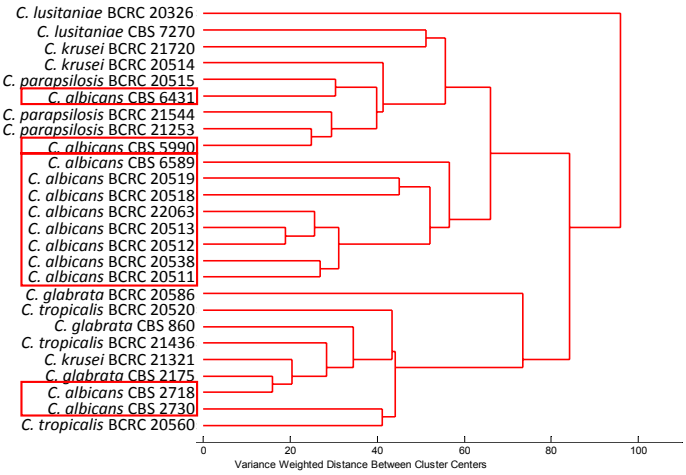

Fig. 6 Hierarchical cluster analysis (Ward's Method) of high frequency features of 26 strains of six different *Candida* species preprocessed by second derivative (high pass filter).

Using a New Method for Produce the Emulsions by Electrospraying Microfluidic Chip

Meng Hsuan Lee, Chia-Hsien Yeh, and Yu-Cheng Lin

Department of Engineering Science, National Cheng Kung University, Tainan, Taiwan

***Abstract* — In this paper, utilizing the microfluidic cross-junction and high electric field to generate uniform emulsions is reported. Our strategy was based on flow-focusing for the formation of a series emulsions by changing ratio of disperse phase and continuous phase flow rate and by adding the electric field to control the emulsion size decrease. We found the size of the emulsion decreased as the electric filed and the ratio of continuous phase disperse phase flow rate and increased. Experimental data showed that the emulsions were quite uniform with standard deviation less than 10%. When adding the electric field, the Taylor cone is formed and the smaller Na-alginate emulsions are generatee, the size of which is about 10 μm. Using the proposal electrospraying microfluidic chip, the alginate emulsion of smaller size could be obtained compare to the previous cross-junction shape researches.**

Keywords — ***Alginate, Emulsion, Taylor cone, Electrospraying***

I. INTRODUCTION

The technology of emulsion drop generation has a wide application in the food industry and in cosmetics, drug delivery, and in k-jet printing. Microfluidic technology provides a highly controllable means of emulsification. The flow focusing geometry [1, 2] is commonly used to generate droplets whose size is easily controlled by the flow rates. Lin and Lee used an air control system and create a moving-wall structures to generate tiny droplets which about 20 micrometers in diameter [3]. However, there are limits to the smallest droplet size that can be achieved by changing the geometry, the size of the channels, and the properties of the fluids. One potential means of overcoming these limitations is the use of electrospray which is caused by an electric force applied to a liquid surface, and many experiments have been carried out to make smaller droplets using electrospray. Bose reported electrohydrodynamic spraying from an electrified capillary [4].

Na-alginate is used as the dispersed phase which flows through the central channel. Na-alginate is currently gaining a lot of attention for medical applications as well as for the controlled release of drugs [5]. The success of Ca-alginate beads as carriers is due to the following features: (i) they can dissolve poorly soluble drugs and thus increase their bioavailability, (ii) they can stay in the body (in the blood) long enough to provide gradual accumulation in the required area, (iii) their sizes permits them to accumulate in body regions with leaky vasculature, (iv) they can be tailored to achieve targeting or other desired properties by attachment of a specific ligand to the outer surface, (v) they have low toxicity and high loading capacity, as well as minimize drug degradation and loss, and (vi) they can be easily produced in large quantities [6-8].

Applications using the flow behavior of immiscible liquids at the microscale level have been reported. For example, Song et al. [9] presented a microfluidic system that forms aqueous droplets in a continuous flow of a water-immiscible fluid. The droplets act as microreactors, which rapidly mix reagents and transport them with no dispersion. Zhao et al. [10] proposed a strategy to control the flow of immiscible liquids in microchannels by patterning surface free energies, which were applied in the fabrication of a semipermeable membrane. Hisamoto et al. [11] used an immiscible system to develop a new method of performing multi-ion sensing. The proposed immiscible system maintains stable multilayer interfaces for a long distance and completes the ion pair extraction reaction inside the microchannel.

II. MATERIALS & METHOD

Commercial sample of high viscosity Na-alginate was purchased from Sigma Chemical Co. (MO, USA), which was used as the dispersed phase (viscosity 27 cP in 0.5 % solution at 25 °C). The sunflower seed oil was used as the continuous phase (viscosity 42 cp) purchased from Uni-President Enterprises Corp. The emulsion is formed due to the hydrodynamic-focusing and electric field effect. Because the disperse phase and continuous phase are not mutually dissolved, the continuous phase has compressed the disperse phase to generate the hydrodynamic-focusing. The parallel electrodes have induced the electric field effect in the cross-junction position, as shown in Fig. 1, and the dimension of the chip was shown in Fig. 2. The backward of the cross-junction position was reduced to width of 50 μm and it would make the electric field effect bigger than the origin shape, for the observation zone is increased to 200 μm and 400 μm. The ANASY® 11 was used to simulate the electric field effect between the different designs. The proposed electrospraying

*Contacting Author: Yu-Cheng Lin, National Cheng Kung University, Department of Engineering Science; University Road, Tainan 701, Taiwan, R.O.C (phone: +886-6-276-2395; fax: +886-6-276-2329; e-mail: yuclin@mail.ncku.edu.tw).

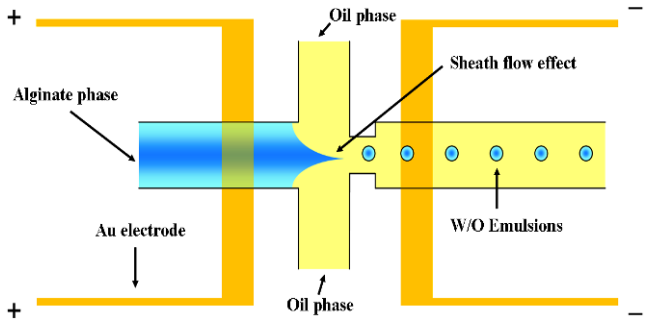

Figure 1. Schematic drawings of Na- alginate emulsions generation system. This method included the cross-junction part and the parallel electrodes.

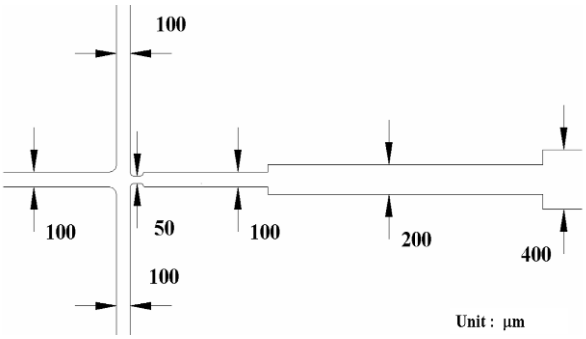

Figure 2. The design dimension of the microfluidic chip, the unit is μm.

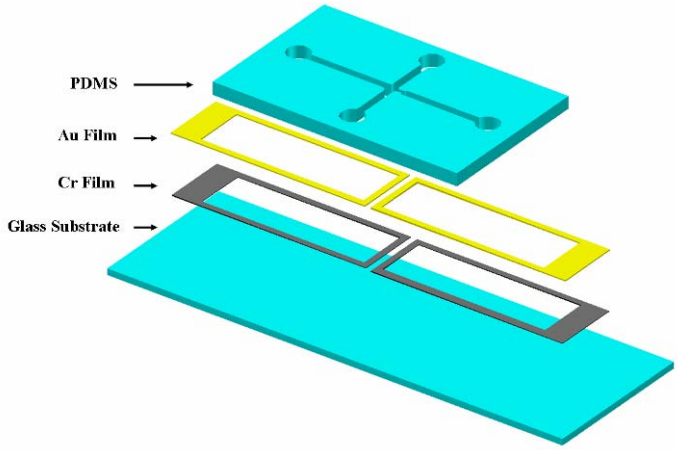

Figure 3. Illustration of microfluidic chip, including glass substrate, Cr film, Au firm and PDMS microstructure fabricated using the MEMS technology.

microfluidic chip consists of two components: the PDMS cross-junction chip and parallel electrodes, as shown in Fig. 3., the Au film and Cr film are made by e-beam evaporation. The thickness of Cr film is 20 nanometer and that of Au film is 200 nanometer, and the role of Cr film is an adhesion layer between Au film and glass substrate. The MEMS technology was used to fabricate the gold/chromium thin film electrodes and PDMS chip. The parallel electrode in the glass was bonded with the PDMS chip by the O_2 plasma machine. Channels were coated by Aquapel (YC C-805) to prevent water droplets from wetting the walls. The coating makes the surfaces more hydrophobic.

The liquid should be slightly conducting to form a Taylor cone. If the liquid has a high conductivity, it cannot form a Taylor cone because there would be no potential difference in the liquid.

The formation of a Taylor cone is necessary to generate very fine droplets. When an electric field is applied, the water-oil interface at the tip is charged and behaves as a capacitor. As the voltage increases, the charges on the interface increase resulting in a higher attraction downstream. The tip of the Taylor cone is stretched to a narrow filament and is broken into tiny droplets due to the Rayleigh instability.

III. RESULT AND DISCUSSION

In the simulation results, we set the scale bar both from 0 V/cm to 220 V/cm, the 50 μm width channel was found to have the bigger electric field (165 V/cm) effect than the 100 μm (105 V/cm) width channel under fixed 100V/cm electric field in the parallel electrode, and as shown in Fig. 4. So the Fig. 4(b) is the better design for electro-spraying microfluidic chip.

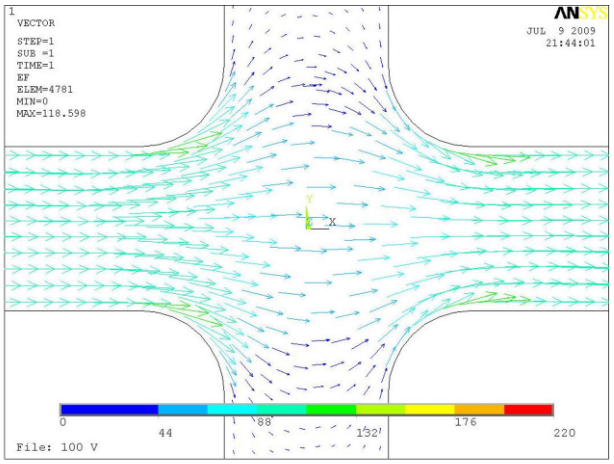

(a)

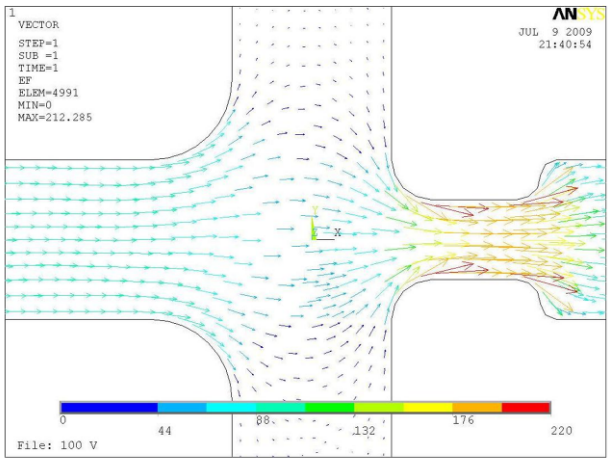

(b)

Figure 4. The electric field of parallel electrodes is simulated in the cross-junction position. (a) The width of channel is 100 μm; (b) the width of channel is 50μm.

The Taylor cone is appeared in cross-junction positions, the new design not only could make the higher electric field increase the electrospraying effect but also increase the sheath force to generate smaller emulsion size. When fixing disperse and continuous phase flow rate, the emulsion size could be decreased by increasing the electric field, as shown in Fig.5. When the electric field is increased to about 500 V/mm, because of the relationship between the mutually exclusive charge, the emulsions from top to bottom show in the channel as shown in Fig. 5 (c), (d).

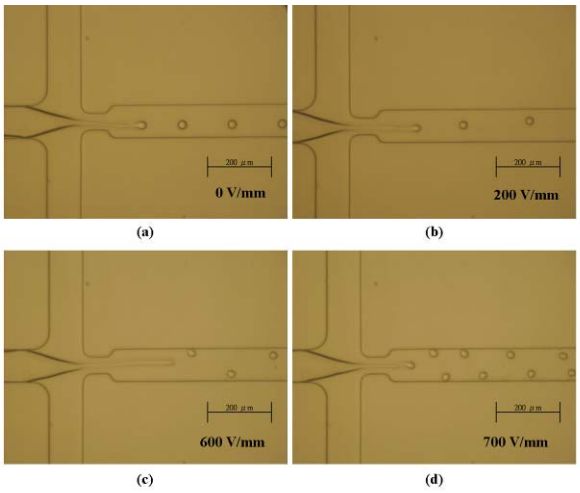

Figure 5. When fixing the flow rate of dispersed phase at 1 μL/min and flow rate of the continuous phase at 5 μL/min, the emulsion size is decreased by increasing the electric field. (a) 0 V/cm, (b) 200 V/cm, (c) 600 V/cm, and (d) 700 V/cm.

The relationship between emulsion size and electric field is shown in Fig.6. Smaller droplet sizes are produced at smaller ratios of flow rates of dispersed fluid to continuous fluid, at the same voltages, the emulsion size can be effectively reduced when increasing the electric field. And the smallest droplet size is less than 10 μm in diameter.

When the electric field is increased to 1000 V / mm or more, it will not be able to generate the uniform emulsion. With a random distribution in the channel, alginate even began to be dissociative, resulting in a number of bubbles, as shown in Fig. 7. The alginate started to solidify due to overheating, when the electric field is more than 1500 V / mm, finally channel will be obstructed by alginate, as shown in Fig. 8

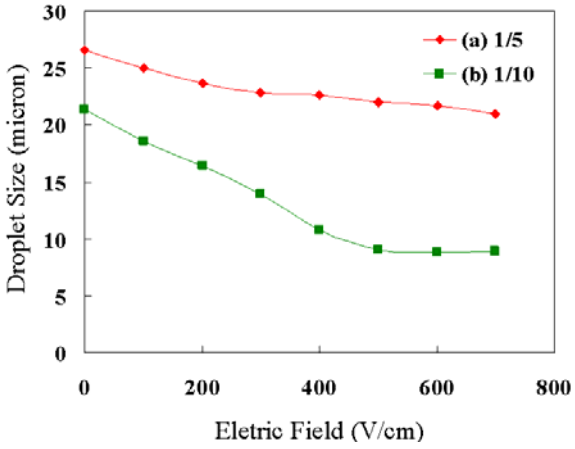

Figure 6. The relationship between droplet size and electric field and fixed the ratio of dispersed and continuous phase flow rate. (a) Dispersed phase at 1 μL/min, continuous phase at 5 μL/min; (b) dispersed phase at 1 μL/min, the continuous phase at 10 μL/min.

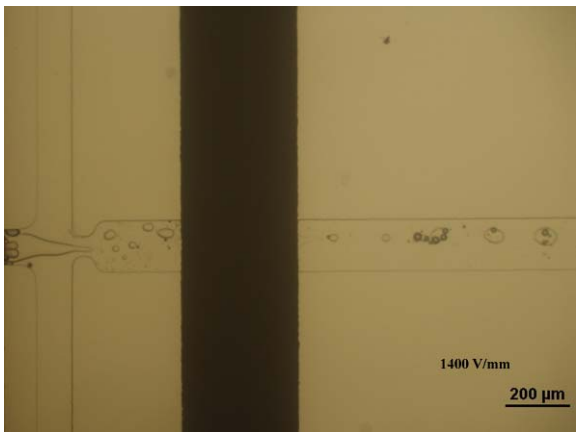

Figure 7. Bubbles generated when the electric field reaches 1400 V/mm

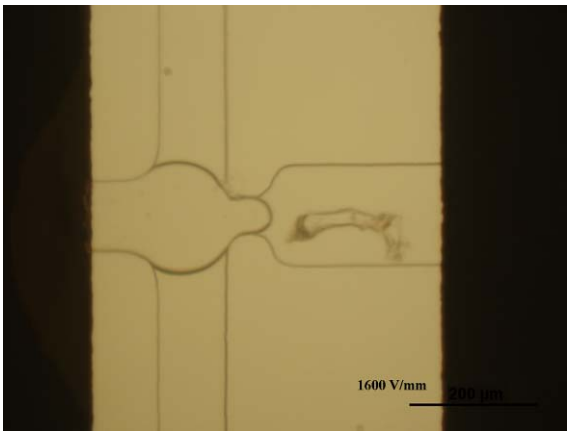

Figure 8. Alginate solidify due to overheating when electric field is 1600 V/mm

IV. CONCLUSIONS

We have successfully demonstrated the elecrospraying microfluidic chip to produce the alginate emulsions. In this

method, the electric field and sheath force influences were combined to generate smaller emulsion. The parallel electrode provided the stable electric field to obtain the Taylor cone, which could produce the about 10 μm alginate emulsions with a narrow size distribution (< 10%). When increasing the electric field and ratio of disperse and continuous flow rate, emulsions of smaller size could be generated. The approach in manipulation of Na-alginate will provide many potential usages for pharmaceutical applications.

REFERENCES

[1] M. Ganan-Calvo and J. M. Gordillo, "Perfectly Monodisperse microbubbling by capillary flow focusing," Phys. Rev. Lett, vol. 87, pp. 274501, 2001.

[2] S. L. Anna, N. Bontoux and H. A. Stone, "Formation of dispersions using 'flow-focusing' in microchannels", Applied Physics Letter, vol. 82, pp. 364-366, 2003.

[3] S. K. Hsuing, C. T. Chen and G. B. Lee, "Micro-droplet formation utilizingmicrofluidic flow focusing andcontrollable moving-wall chopping techniques," J. Micromech. Microeng, vol. 16, pp. 2403-2410, 2006.

[4] G. Bailey, Electrostatic Spraying of Liquids (Wiley, New York, 1988).

[5] I. W. Sutherland, "Alginates. In Biomaterials: Novel Materials from Biological Sources," Eds: Byrom D. Stockton, pp. 309-331, 1991.

[6] W. R. Gombotz & S. F. Wee, "Protein release from alginate matrices," Adv. Drug Deliv. Rev, vol. 31,pp. 267-285, 1998..

[7] R. M. Iskakov, A. Kikuchi & T. Okano, "Timeprogrammed pulsatile release of dextran from calciumalginate gel beads coated with carboxy-n-propylacrylamide copolymers," J. Control. Release, vol. 80, pp. 57-68, 2002.

[8] M. Leonard, A. R. De Boisseson, P. Hubert, F. Dalencon & E. Dellacherie, "Hydrophobically modified alginate hydrogels as protein carriers with specific controlled release properties," J. Control. Release, vol. 98, pp. 395-405, 2004.

[9] Song H, Tice JD, Ismagilov RF (2003) A microfluidic system for controlling reaction networks in time. Angew Chem Int Ed Engl 42:768–772

[10] Zhao B, Viernes NOL, Moore JS, Beebe DJ (2002) Control and applications of immiscible liquids in microchannels. J Am Chem Soc 124:5284–5285

[11] Hisamoto H, Horiuchi T, Uchiyama K, Tokeshi M, Hibara A, Kitamori T (2001) On-chip integration of sequential ion sensing system based on intermittent reagent pumping and formation of two-layer flow. Anal Chem 73:5551–5556

Bio-Sensing and Monitor System Design with Micro Array Probes and Amplifier on an Active RFID Tag

Jium-Ming Lin[1*], Po-Wei Lin[2], and Li-Chern Pan[3]

[1]*Dept. of Mechanical Engineering, Chung-Hua University, R. O. C.*
[2]*New Business Center, Taipei Medical Universityy, R. O. C.*
[3]*Dept. of General Education, Taipei Medical University, R. O. C.*

***Abstract* — This research provides a micro array bio-probe device, integrated with Thin-Film-Transistor (TFT) amplifier formed of bottom-gate MOS (Metal-Oxide Semiconductor) type thin film transistors, on an active RFID tag to improve the signal-to-noise ratio and impedance matching problems. The bio-probe device can be disposed to conform to the profile of a living body's portion so as to improve the electrical contact property.**

Keywords — ***bio-sensing probe, thin film transistor amplifier, signal-to-noise ratio, active RFID tag***

I. INTRODUCTION

Conventional micro array biological probes are produced on a hard silicon wafer substrate [1-8]. This kind of product is not only heavy but also frangible. Moreover, the conventional micro array biological probes fail to be designed and disposed relying on the profile of a living body's portion, and adversely affecting contact between the biological probes and living body. Besides, after a signal detected from the conventional micro array biological probes, additional devices for signal processing are required to improve the signal-to-noise ratio and impedance matching problems.

As shown in Fig. 1 this research provides a micro array bio-probe device integrated with TFT amplifier formed of bottom-gate thin film transistors, which utilizes a micro-electro-mechanical process and a semiconductor process to integrate micro array bio-probes and an amplifier, formed of top-gate MOS type TFTs on an active RFID tag. As such, the signal obtained by the probes can be amplified nearby to improve the signal-to-noise ratio and impedance matching.

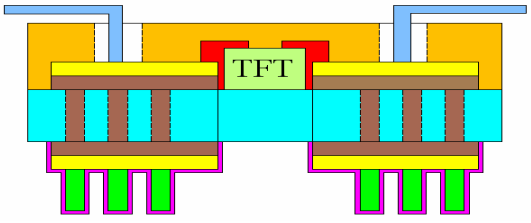

Figure 1. The side view of the proposed module for micro array bio-sensing probe device integrated with a semiconductor amplifier.

The micro array bio-probes are formed on the active RFID tag (915 MHz) as shown in Fig. 2 such that the present bio-probe device can be disposed to conform to the profile of a living body's portion and improve the electrical contact property.This research can vary the density, occupied area and sharpness of the tip ends of the probes to change the contact impedance so as to meet different needs.

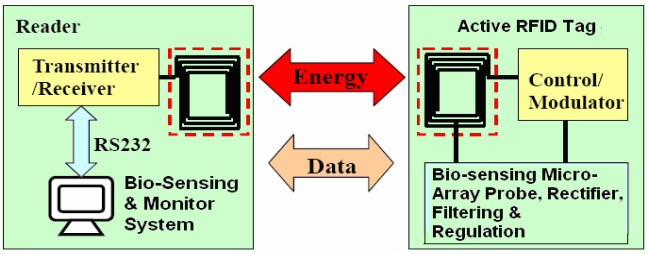

Figure 2. The bio-sensing and monitor system design with micro array probes and integrated amplifier on an active RFID tag.

The organization of this paper is as follows: the first section is introduction. The second one is the fabrication steps of semiconductor amplifier and bio-sensing probe device. The third one is system integration of probe and RFID tag. The next are microprobe integration test and discussions. The last part is the conclusion.

II. DEVICE FABRICATION

A. *Semiconductor Amplifier Design*

Step 1. By using laser to make through hole vias on the flexible substrate for electrical signal conduction between both surfaces. The result is in Fig. 3. The result is in Fig. 3.

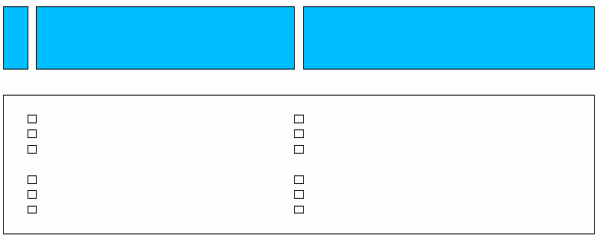

Figure 3. The result of design step 1.

Step 2. The next is by E-gun evaporator (a low temperature process) to deposit a layer of TiN (0.1 μm) on each side of substrate as seed for electroplating copper (100μm). The result is in Fig. 4.

This project was funded by National Science Council R. O. C. (Project code: NSC-95-2622-E-216-CC3 and NSC-96-2622-E-216-005-CC3).

Contact author: for fabrication aspects of this project please contact* ***jmlin@chu.edu.tw.*

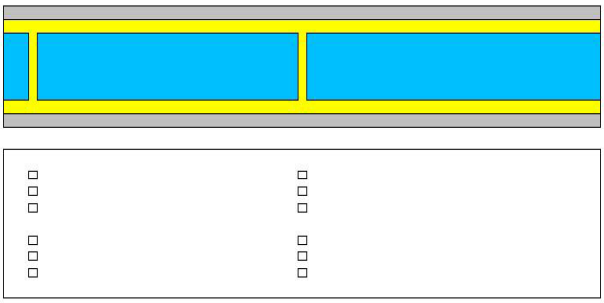

Figure 4. The result of design step 2.

Step 3. By E-gun evaporator deposit an insulating layer of SiO2 or Si3N4 (2μm) on the lower surface of substrate. By using mask #1 and Photolithography And Etching Process (PAEP) to make vias on those holes made in Step 1 through copper, TiN, and SiO_2 (or Si_3N_4) layers deposited in Step 2. Finally, remove Photo Resist (PR), and the result is in Fig. 5.

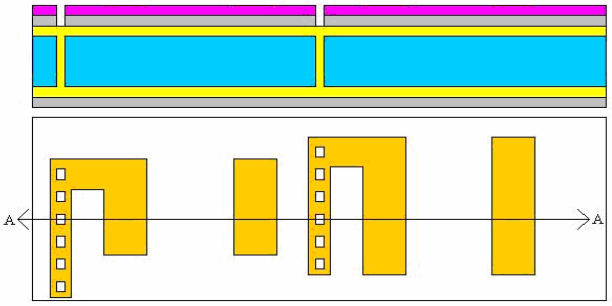

Figure 5. The result of design step 3.

Step 4. Evaporating a layer of chromium (Cr, 2μm) to be used for the gates of thin-film-transistors, and then using mask #2 with PAEP to left four gates of MOS transistors. Then evaporate a layer of SiO_2 (2μm) with mask #3 and PAEP to make the holes through SiO_2 for wirings connecting to the probes. Finally remove the PR, and the result is in Fig. 6.

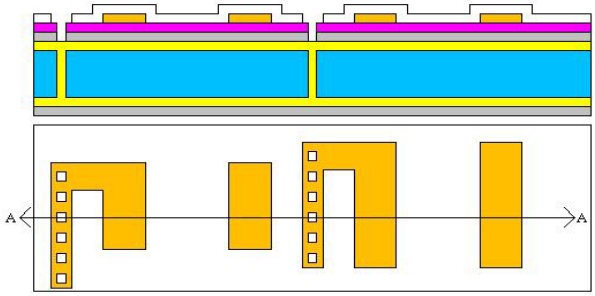

Figure 6. The result of design step 4.

Step 5. Evaporate a layer of amorphous silicon and applying mask #4 and PAEP to make the regions for making the channels of the transistors as well as the wiring connection through the holes obtained in Step 4. Finally remove the PR, and the result is in Fig. 7. Then applying an Nd:YAG laser to anneal the amorphous silicon into poly-Si to raise the carrier mobility performance of the TFTs.

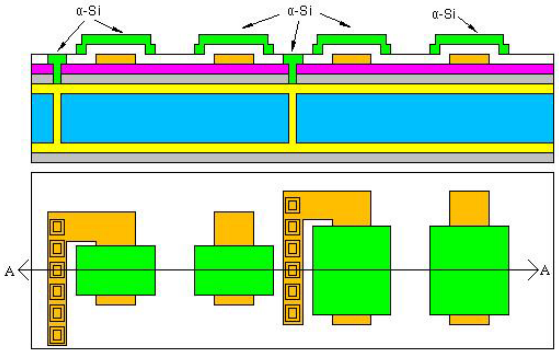

Figure 7. The result of design step 5.

Step 6. Evaporate a layer of SiO_2, and using mask #5 and the PAEP to etch SiO_2 away at the sources, drains and wiring holes on the left three N-MOS transistors for phosphorous (N+ donor type) ion implantation. Finally remove the PR, and the result is in Fig. 8.

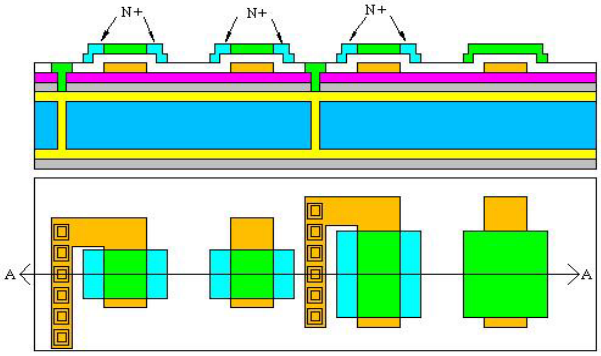

Figure 8. The result of design step 6.

Step 7. Evaporate a layer of SiO_2, By using mask #6 with the PAEP to etch some regions of SiO_2 away at the sources, drains and wirings on the right hand side P-MOS transistors for boron (P+ acceptor type) ion implantation. Finally remove the PR, and the result is in Fig. 9.

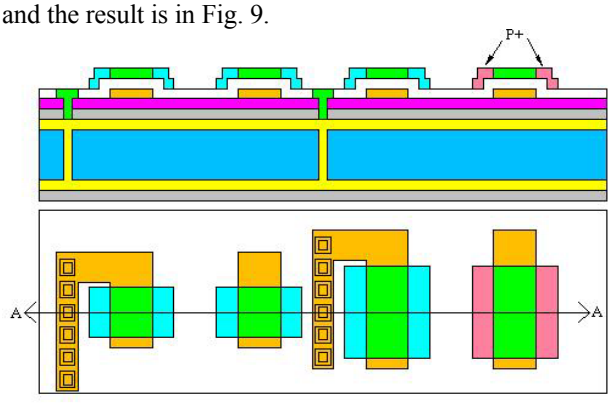

Figure 9. The result of design step 7.

Step 8. Evaporate a layer of Si_3N_4 or SiO_2 (2μm), and with mask #7 and PAEP to make the contact holes for all the

electrodes of MOS transistors and wirings. Finally remove the PR, and the result is in Fig.10.

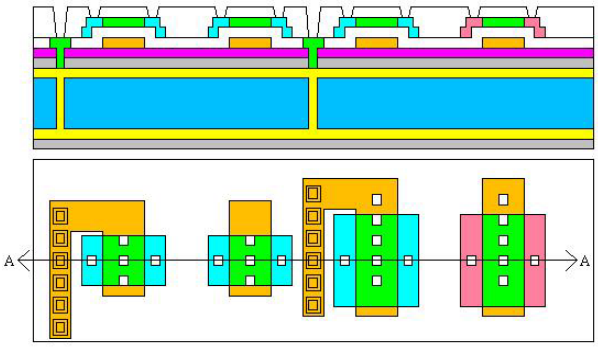

Figure 10. The result of design step 8.

Step 9. Evaporate a layer of aluminium (2μm) and with mask #8 and PAEP to make the contact metallization for all the electrodes of MOS transistors and wirings. Finally remove the PR, and the result is in Fig. 11.

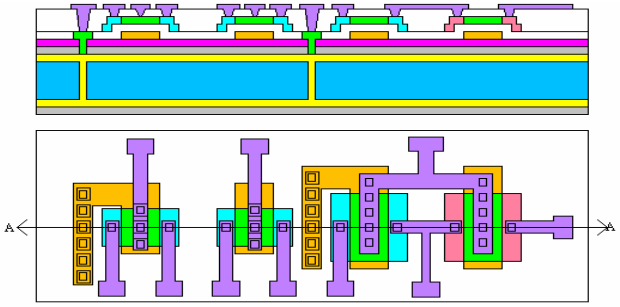

Figure 11. The result of design step 9.

Step 10. By E-gun evaporator deposit a layer of S_iO_2 or Si_3N_4 (2μm) for insulation and passivation, using mask #9 with PAEP to make the pad holes for wire bonds. Then electroless plating two layers of nickel and gold. Finally, remove PR, and the result is in Fig. 12.

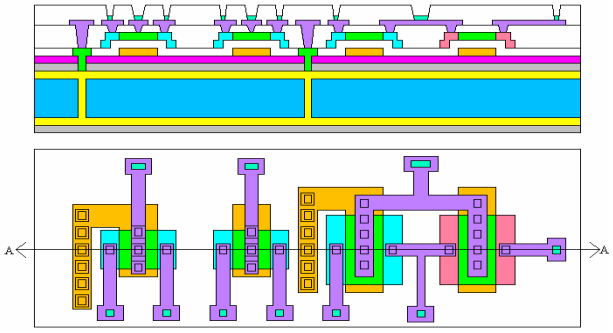

Figure 12. The result of design step 10.

Step 11. Making bumps to connect to the outer circuit by solder screening and the reflow processes. The result is in Fig.13. The four transistors are connected as two sets of amplifiers in Fig. 14; they can be used for impedance matching and increasing signal-to-noise ratio.

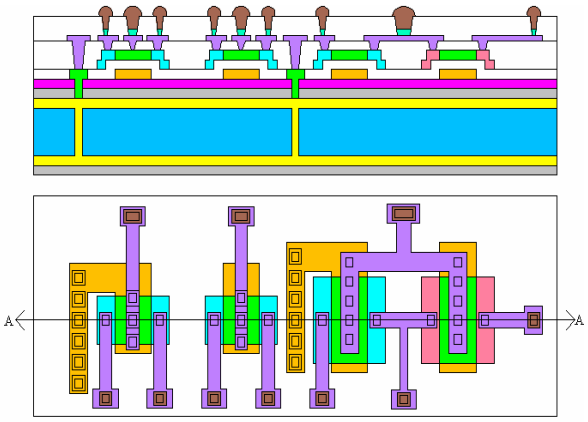

Figure 13. The result of design step 11.

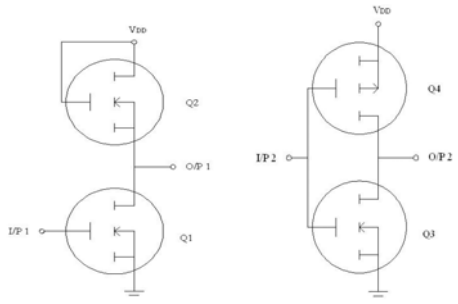

Figure 14. The four MOS transistors are connected as two pairs of amplifiers.

B. Micro Array Bio-Probe Design

The fabrication steps of the micro array bio-sensing probe device are as follows:

Step 1. The conducting vias of the micro array bio-sensing probe formed by using Nd:YAG laser ablation or some other method such as spray sands method. The result is in Fig. 15.

Figure 15. The result of design step1.

Step 2. SU-8 thick PR (500 μm) formed on each side by using mask #9. The result is in Fig. 16.

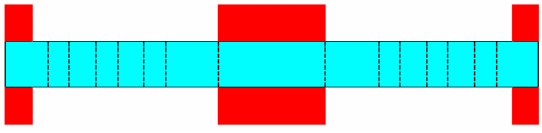

Figure 16. The result of design step 2.

Step 3. Evaporate copper and TiN on each side with thickness 100 μm. The result is in Fig. 17.

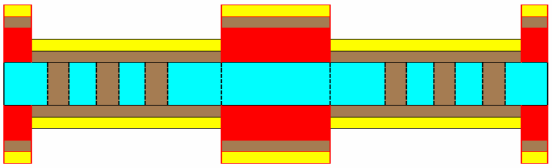

Figure 17. The result of design step 3.

Step 4. Stripe PR away. The result is in Fig. 18.

Figure 18. The result of design step 4.

Step 5. Forming a layer of Lift-Off-Resist (LOR) (500 μm) on the back side with mask #10. The result is in Fig. 19.

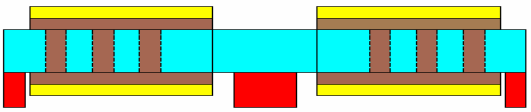

Figure 19. The result of design step 5.

Step 6. SU-8 thick PR (500 μm) formed on the back side with mask #3. The result is in Fig. 20.

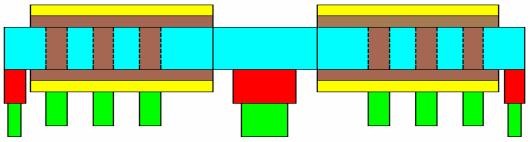

Figure 20. The result of design step 6.

Step 7. By E-gun evaporator deposits a layer of TiN (2 μm). The result is in Fig. 21.

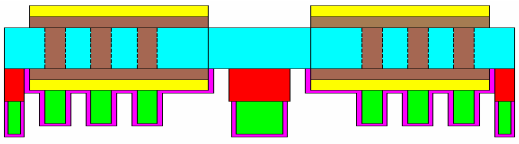

Figure 21. The result of design step 7.

Step 8. Stripe LOR PR away and the micro array bio-sensing probe formed. The result is in Fig. 22. Then one can adjoint these two parts and wire bond for signal connection. The result is in Fig.1.

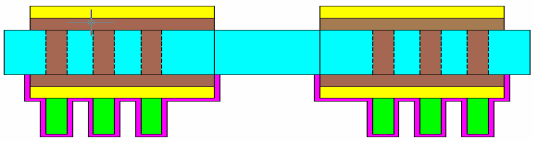

Figure 22. The result of design step 8.

III. System Integration of Probe and RFID Tag

The system integration of micro array probe module and active RFID Tag is shown in Fig. 23, in which Q_1 is a switch enabled by a pulse type high voltage (V_{DD}) at point A, Q_2 is a current source by connecting gate to drain. The current output from point C is connected to micro array probe module on human body under test. Meanwhile, the voltage output at point C is connected to a CMOS amplifier previous mentioned for impedance matching as well as raising the signal-to-noise ratio of measurement. Finally, the amplified voltage at point D is converted to digital by an A/D converter in active RFID chip.

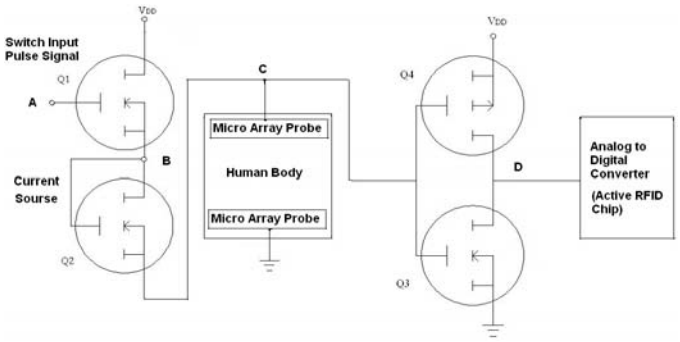

Figure 23. The system integration of probe module and active RFID Tag.

IV. Microprobe Integration Test and Discussions

This section is for impedance test [11] via RFID reader. The probe and bio-skin model are shown in Fig.24, in which Rp and Cp are respectively the resistance and capacitance of the probe model, and Rs is the resistance of the skin model.

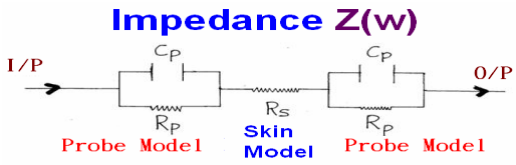

Figure 24. Equivalent circuit model of probe and skin.

The impedance **Z** (ω) can be obtained as:

$$Z(\omega) = Rs + 2(Rp // \frac{1}{jWCp}). \quad .1$$

$$= Rs + \frac{2Rp}{1+jwCpRp} = Rs + \frac{2Rp(1-jwCpRp)}{1+w^2Cp^2Rp^2}. \quad .2$$

$$= Rs + \frac{2Rp}{1+w^2Cp^2Rp^2} - j\frac{2wRp^2Cp}{1+w^2Cp^2Rp^2} \quad .3$$

$$R(\omega) = Rs + \frac{2Rp}{1+w^2Cp^2Rp^2}. \text{ (Real part of } \mathbf{Z}(\omega)) \quad .4$$

$$X(\omega) = \frac{-2wRp^2Cp}{1+w^2Cp^2Rp^2}. \text{ (Imaginary part of } \mathbf{Z}(\omega)). \quad .5$$

The frequency response of R (ω) is measured as in Fig. 25. By (4) and Fig. 8 for very low frequency, one has

$$R(0) = Rs + 2Rp = 5880\ \Omega. \quad .6$$

By (4) and Fig. 8 for very high frequency one has

$$R(\infty) \fallingdotseq Rs = 330\ \Omega. \quad .7$$

By (6) and (7) one has Rp＝2735 Ω. In addition, Cp can be obtained from (4) and Fig. 25. The average value of Cp is 60.665 pf.

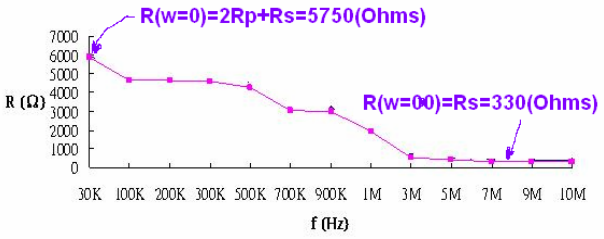

Figure 25. The frequency response of R (ω).

V. Conclusions

This research employs the MEMS process to integrate TFT amplifiers and micro array biological probes on an active RFID tag. It becomes possible to dispose the bio-sensing probe in conformity with the profile of the living body's portion by forming the bio-probe on an active RFID tag. As such, the contact effect between the biological probes and living body becomes better. On the other hand, the TFT amplifier is also produced on the RFID tag such that a signal detected from the biological probes can be amplified through a short path. In addition, since the input and output impedances of the MOS type TFT amplifier are respectively very high and low, the signal-to-noise ratio and impedance matching problems also are improved.

Acknowledgment

This research was supported by National Science Council R. O. C. with the contracts NSC-95-2622- E-216-CC3 and NSC-96-2622-E-216-005-CC3.

References

[1] G. Lin, and A. Pisano, "Silicon-processed microneedles," J. of Microelectro-Mechanical Systems, vol. 18, pp. 78–84, 1999.

[2] Y. Wu, Y. Qiu, and S. Zhang, "Microneedle-Based Drug Delivery: Studies on Delivery Parameters and Biocompatibility," Biomedical Microdevices, vol. 10, no.5, pp. 601–610, 2008.

[3] K. Nomura, H. Ohta, K. Ueda, T. Kamiya, M. Hirano, and H. Hosono, "Thin-film transistor fabricated in single-crystalline transparent oxide semiconductor," Science, vol.300, no.5623, pp.1269–1272, 2003.

[4] Y. Wu, Y,. Qiu, S. Zhang , G. Qin, and Y. Gao, "Microneedle-based drug delivery: studies on delivery parameters and biocompatibility," Biomedical Microdevices. vol. 10, no. 5, pp.601–610, 2008.

[5] B, Chen, J . Wei, F. Tay, Y. Wong, and C. Iliescu, "Silicon microneedle array with biodegradable tips for transdermal drug delivery," Microsystem Technologies, vol. 14, no. 7, pp 1015–1019, 2008.

[6] J. Zahn, N. Talbot, D. Liepmann, and A. Pisano, "Microfabricated polysilicon micro-needles for minimally invasive biomedical devices," Biomedical Microdevices, vol. 2, no.4, pp 295–303, 2008.

[7] S. Davis, M. Prausnitz, and M. Allen, "Fabrication and characterization of laser micromachined hollow microneedles," 12th International Conference on Transducers, Solid-State Sensors, Actuators and Microsystems, , pp1435–1438, 2003.

[8] D. McAllister, F. Cros, S. Davis, L. Matta, M. Prausnitz, and M. Allen, "Three-dimensional hollow microneedle and microtube arrays," J. of Micromechanics and Microengineering,vol. 14, pp.:597–602, 2004.

[9] Z. Meng, M. Wang, and M. Wong, "High performance low temperature metal-induced unilaterally crystallized polycrystalline silicon thin film transistors for system-on-panel applications," IEEE Trans. on Electron Devices, vol. 47, no. 2, pp.404–409, 2000.

[10] M. Wong, Z, Jin, G. Bhat, and P. Wong, "Characterization of the MIC/MILC interface and its effects on the performance of MILC thin-film transistors," IEEE Tran. on Electron Devices, vol. 47, no. 5, pp. 1061–1067, 2000..

[11] J. Rosell, J. Colominas, P.Riu, R.Pallas-Areny, and J. Webster, "Skin impedance from 1 Hz to 1 MHz," IEEE Trans. Bio-med Eng., vol. BME-35, no. 8, pp. 649–651, 1988.

3A2-2

Surface plasmon resonance biosensor based on compact discs

Sheng-Yu Chou[1], Wen-Yi Meng[2], Kuo-Chi Chiu[3], Chih-Ming Lin[4], Yung-Sung Lan[3], Nai-Jen Cheng[2], and Jenq-Nan Yih[1,*]

[1]*Electrical Department, Kaohsiung University of Applied Sciences, Taiwan*
[2]*Institute of Photonics and Communications, Kaohsiung University of Applied Sciences, Taiwan*
[3] *Electronics and Optoelectronics Research Laboratories, Industrial Technology Research Institute, Taiwan*
[4]*Department of Applied Science, National Taitung University, Taiwan*

***Abstract* — This paper presented a grating-coupled surface plasmon resonance (SPR) biosensor based on the structure of compact discs (CDs). The reflectance graph with incidence angle is simulated according to the modified CD. In order to verify how the angle shift of SPR depends on a bio-molecular layer, a protein of bovine serum albumin (BSA) is employed as a target to test the sensitivity of the CD biosensor. Although the SPR angle and the reflectivity from the simulation differed slightly with those from the measurement, the direction and the quantities of angle shift are quite consistent with its measured results and also proportional to the thickness of bio-layer. The preliminary results showed that SPR bio-sensors based on CDs promise to be a low-cost, rapid, high throughput screening sensor product for biological molecules detection.**

Keywords — surface plasmon resonance (SPR), biosensor, compact disc (CD), Bovine serum albumin (BSA)

I. INTRODUCTION

Surface plasmon resonance (SPR) biosensor with the advantages of label-free analyte and high sensitivity, kinetic analysis, can characterize and quantify the analysis of bio-molecular interactions. In addition, compact discs (CDs) of the metal reflective layer is suitable for the high-quality preparation of self-assembly monolayer (SAM) and the electrochemical analysis [1]; and SPR can be excited by CDs with the grating whose periodic geometry structure provides an additional wave vector when a surface light wave propagates at its interface (metal and dielectric) [2,3]. Because of the need of high throughput detection and cost reduction, this study combined with CDs fabrication processes and SPR techniques to develop the CD-type bio-sensors toward a new field of commercial application.

II. STUDY BACKGROUND

A. SPR biosensors

In general, the biosensor comprises two components: the element of specific recognition for molecules and the transducer for converting identified impulses into the signal. Signal conversion can be reached by many ways, including optical, weight, electrical, and thermal measurements. Label-free optical biosensing without tags is mainly comprised of the SPR, interferometer, waveguide, fiber Bragg grating, ellipsometry, resonant mirrors, and photonic crystals and so on [4]. SPR is a photoelectric phenomenon, when the photon energy transferred to surface plasmons on metal, the surface plasmons resonate in the metal at excited states rather than radiate. In this condition, the electromagnetic field at the interface will be much stronger than that of the incidence light wave; and the intensity of reflected light will be significantly weakened. Resonance conditions of SPR would be changed when molecules approached the metal surface. By measuring changes of resonance conditions (wavelength or angle), the quanty of molecular bonding layer can be estimated. In theory, the wave vector of high-order diffraction and the surface plasma wave on metal grating satisfy the following equation [3,5]:

$$\frac{2\pi}{\lambda} n \sin(\theta) + m\frac{2\pi}{\Lambda} = \frac{2\pi}{\lambda}\mathrm{Re}\left\{\sqrt{\frac{\varepsilon' n^2}{\varepsilon' + n^2}}\right\}$$

where λ is the wavelength of incidence light; θ is the incidence angle; Λ is the grating period; ε' is the dielectric constant of the metal; n is the refractive index of the dielectric medium; and m is the diffraction order.

B. Compact disc used for biosensing

E. M. Richter et al. and H.-Z. Yu et al. put forward to the CD in favor of the formation of SAM on gold-film and of the study as an electrochemical electrode, not only is low cost but also good effectiveness of gold electrode compared with commercial ones [6,7]. H.-Z. Yu et al. proposed such a combination of CDs and CD-ROM drive is expected to be a low-cost bio-medical diagnosis and genetic analysis tools [1,8]. D. D. Nolte and F. E. Regnier published a spinning-disk interferometry, called "BioCD" [9,10], and extended to two-dimensional molecular interference imaging [11,12]. J. Tominaga et al. proposed to utilize DVD disc as a biological sensor, known as "BioDVD" [13,14]. Two key points summarized: First, gold films with high chemical stability are help for quantitatively analyzing chemical molecules and also suitable for the electrochemical studies. Second, CDs have the potential of high throughput screening, low cost and the advantage of mature fabricating process. Although the metal grating of SPR theory and experiment has been much studied from the 1980s, the phenomenon of SPR on CDs is not disclosed until E. Fontana published the CDs research of both experimental measurements and theoretical analysis [15]. W. A. Challener first utilized the CDs as a molecular sensor, coated with a layer of silver for SPR excitation, to measure ammonia concentration [16]. Because of the advance of lithography and thin-film coating technology, this type of the nano-structural devices can detect nano-sized biomolecules with excellent reproducibility.

This project was funded by Industrial Technology Research Institute, Taiwan
* ***jnyih@cc.kuas.edu.tw***

III. EXPERIMENTS

A. Grating design and fabrication

The commercial software – GSOLVER –, based on the rigorous vector diffraction, is used to calculate the diffraction efficiency of reflected and transmitted electromagnetic waves. A gold grating layer of about 50 nm thickness, excited SPR to enhance the electromagnetic field at interface, will greatly enhance the sensitivity of biosensor. In order to simplify the geometrical structure and reduce the computation time, the rectangular profile grating structure is assumed for simulation. The modulation depth and thickness of metal grating for simulation are defined based on the atomic force microscopy topography, as shown in Figure 1. The grating structure of 0.5μm cycle for simulation is shown in Figure 2, which the duty cycle is 0.438 and the modulation depth is 15 nm. The refractive index of the bio-molecular layer is assumed as 1.46 and its thickness is changed from 0 nm; 5 nm; to 10 nm, whose corresponding resonance angles of simulation resulted in 12.1°, 10.7° and 9.7°, as shown in Figure 3.

B. Preparation of the CDs of immobilized protein

Self-assembled monolayer (SAM) is one of the methods often used to alter surface properties to immobilize the biomolecures like protein on the gold surface. Materials used to prepare SAM on gold contain two terminated groups. One is -SH, which forms Au-S covalent bond on gold [17]. The other terminated group with special property is exposed to the surface for protein adsorption due to the electrostatic interaction, hydrophobic interaction or formation of chemical bond between protein and the other terminated group. Utilizing the charged properties of the functional groups of SAM, such as COOH negatively charged or NH_2 positively charged attracts some complementary charged parts of protein, proteins can be immobilized effectively.

In this work, SAM is prepared with carboxylate-terminated 16-mercaptohexadecanoic acid (MHDA). The modification steps is shown in Figure 4 and described as follows:

a) A gold-coated CD was rinsed in deionized water, cleaned with ethyl alcohol, and then dried with pure nitrogen gas.
b) Following the step (a), the disc was immersed in 1 mM MHDA ($HS(CH_2)_{15}COOH$) for 24 hrs, gradually forming into a SAM. After then, the disc was cleaned with the same procedure of the step (a).
c) Following the step (b), the disc was immersed in 2 mM EDC ($C_8H_{17}N_3 \cdot HCL$); 5 mM NHS ($C_4H_5NO_3$) solution for 12 hrs of activation. After then, the disc was cleaned with the same procedure of the step (a).
d) Following the step (c), three parts of the disc were immersed in 10 mM phosphate-buffered saline (PH 7.4) containing 10 mg/ml BSA to interact with the SAM for 0 min., 30 min., and 60 min., respectively.
e) Following the step (d), the CD was copiously rinsed with deionized water and ethyl alcohol in order to remove weakly adsorbed BSA, and then dried with pure nitrogen gas.

C. Metrology

The system configuration is shown in Figure 5, which adopted a similar structure with the corner reflector, so that the system needs not to locate the two angles –the incidence angle and the reflection angle– at the same time by using two rotators. For our measurements, the apparatus consists of a He-Ne laser, a linear polarizer, a beamsplitter (BS), a rotation stage, a reflection mirror, two photodetectors, and a personal computer with Nation Instruments LabView software. When the incidence angle changed, the system can measure the angles of incident and reflected light at the same time just to rotate a shaft of CD on the rotation stage. The configuration described as follows: the laser light was transferred to a transverse magnetic (TM) wave through the linear polarizer, and then separated by BS, reflected light detected as reference intensity and the other part of the transmitted light to be as the incident light of the CD. After reflected by the CD and the 90° mirror, then the zero-order reflected light is conducted by the BS to the signal detector. The reflectivity at one incidence angle is obtained with the signal intensity divided by reference intensity. Finally, the graph of reflectivity depended on the incident angle can be obtained by rotating the electrically controlled rotation stage. The SPR angle is obtained by searching the angle of the minimum reflectivity with the curve fitting of eighth degree polynomial from the average data of ten times measurements.

IV. DISCUSSIONS AND CONCLUSION

Three testing conditions was employed to verify the sensitivity of the modified CD, which were no BSA; reacted BSA with 30 min.; and with 60 min.. The corresponding SPR angles obtained are 10.02°, 9.62°, and 9.21°, respectively; and the SPR angle shifts are -0.40° and -0.41°. Although the SPR angles and the curves of reflectivity obtained from the measurement, shown in Figure 6, varied slightly with those from the simulation, shown in Figure 3, but the direction and the quantities of SPR angle shift agree well with those, and the angle shift is proportional to the thickness of bio-layer. Besides, the configuration of the measurement system has the advantages of simplification, stabilization, and high repeatability. If the CD-ROM drive control technology can be modified for the measurement system of this type of bio-disc, a biological CD of low-cost, convenient, portable, yet high screening will be conducive to the development of biological technology.

ACKNOWLEDGMENT

The authors gratefully acknowledge the financial support provided to this study by the Industrial Technology Research Institute of Taiwan.

REFERENCES

[1] H.-Z. Yu, "New chemistry on old CDs," *Chem. Commun*., pp. 2633 – 2636, 2004.
[2] H. Raether, *Surface plasmons on smooth and rough surfaces and on gratings*, Springer-Verlag, Berlin, 1988.
[3] J. Homola, S. S. Yee, and G. Gauglitz, "Surface-plasmon resonance sensors - review," *Sensor. Actuat. B Chem.*, vol. 54, pp. 3-15, 1999.
[4] X. Fan, I. M. White, S. I. Shopova, H. Zhu, J. D. Suter and Y. Sun, "Sensitive optical biosensors for unlabeled targets: A review", *Anal. Chim. Acta*, vol. 620, no. 1-2, pp. 8-26, 2008.

[5] J. Dost´alek, J. Homola, M. Miler, “Rich information format surface plasmon resonance biosensor based on array of diffraction gratings,” Sensors and Actuators B, vol. 107, pp. 154–161, 2005.

[6] L . Angnes, E. M. Richter, M. A. Augelli, G. H. Kume, “Gold electrodes from recordable CDs”, *Anal. Chem.*, vol. 72, no. 21, pp. 5503-5506, 2000.

[7] H.-Z. Yu, “Self-Assembly on “Recordable CDs””, Anal. Chem., vol. 73, pp. 4743-4747, 2001.

[8] C. Ho, D. M. Soolaman, H.-Z. Yu, “Analytical – materials chemistry on old CDs — Beyond self-assembly”, Canadian Journal of Chemistry, v. 83, no. 5, pp. 403-12, 2005.

[9] D. D. Nolte and F. E. Regnier, "Spinning-Disk Interferometry: The BioCD," *Opt. Photonics News*, vol. 15, pp. 48-53, 2004.

[10] X. Wang, M. Zhao, and D. D. Nolte, "Common-path interferometric detection of protein monolayer on the BioCD," Appl. Opt., vol. 46, pp. 7836-7849, 2007.

[11] M. Zhao, X. Wang, G. M. Lawrence, P. Espinoza, and D. D. Nolte, “Molecular Interferometric Imaging for Biosensor Applications”, *IEEE J. Sel. Top. Quant.*, vol. 13, no. 6, pp. 1680 – 1690, 2007.

[12] M. Zhao, X. Wang, and D. D. Nolte, "Molecular interferometric imaging," Opt. Express, vol.16, pp. 7102-7118, 2008.

[13] T. Arai, S. C. B. Gopinath, H. Mizuno, P. K. R. Kumar, C. Rockstuhl, K. Awazu, and J. Tominaga, “Toward Biological Diagnosis System Based on Digital Versatile Disc Technology”, *Jpn. J. Appl. Phys.*, vol. 46, pp. 4003-4006, 2007.

[14] S. C. B. Gopinath, K. Awazu, J. Tominaga and P. K. R. Kumar, “Monitoring Biomolecular Interactions on a Digital Versatile Disk: A BioDVD Platform Technology”, ACS Nano, vol. 2, no. 9, pp. 1885–1895, 2008.

[15] E. Fontana, "Theoretical and Experimental Study of the Surface Plasmon Resonance Effect on a Recordable Compact Disk," *Appl. Opt.*, vol. 43, pp. 79-87, 2004.

[16] W. A. Challener, R. R. Ollmann, K. K. Kam, “A surface plasmon resonance gas sensor in a ‘compact disc' format”, *Sensor. Actuat. B Chem.*, vol. 56, no. 3, pp. 254-258, , 1999.

[17] R.G. Nuzzo, D.L. Allara, “Adsoption of biofunctional organic disulfides on gold surfaces”, J. Am. Chem. Soc., vol. 105, pp. 4481-4483, 1983.

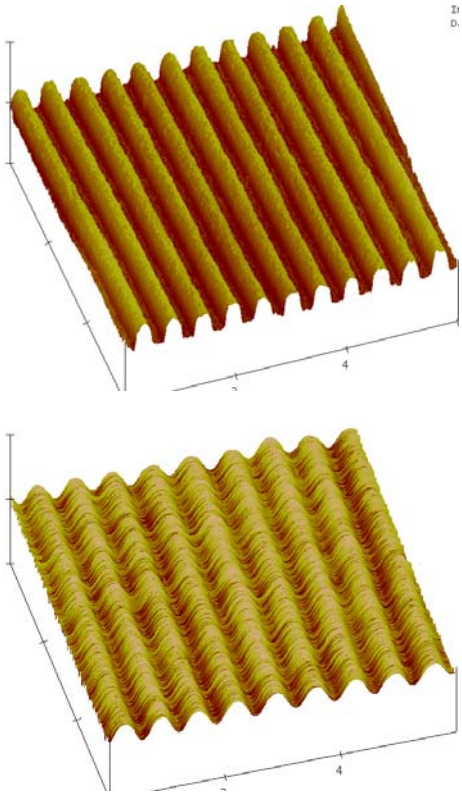

Figure 1. The AFM topographies: without gold grating, groove depth of 15 nm and groove width of 281 nm (top); with gold coated, groove depth of 10 nm and groove width of 258 nm (bottom).

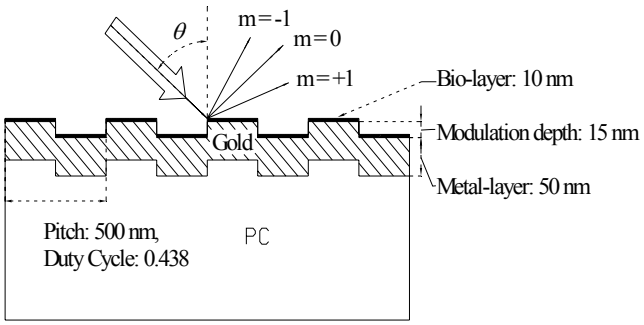

Figure 2. The geometrical profile of the CD of 0.5 μm grating cycle.

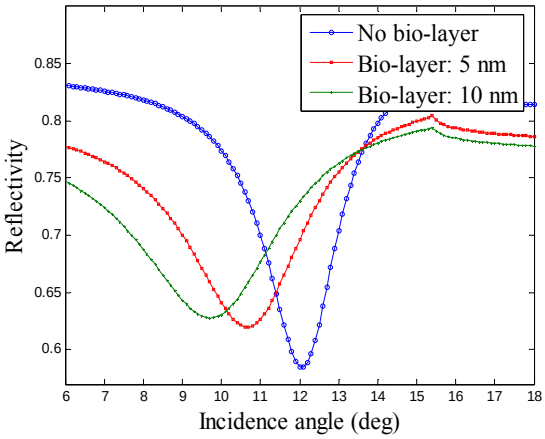

Figure 3. The simulated zero-order reflectivity of the modified CD without and with a biological molecular layer (5 nm and 10 nm), whose corresponding resonance angles of simulation are 12.1°, 10.7° and 9.7°, respectively.

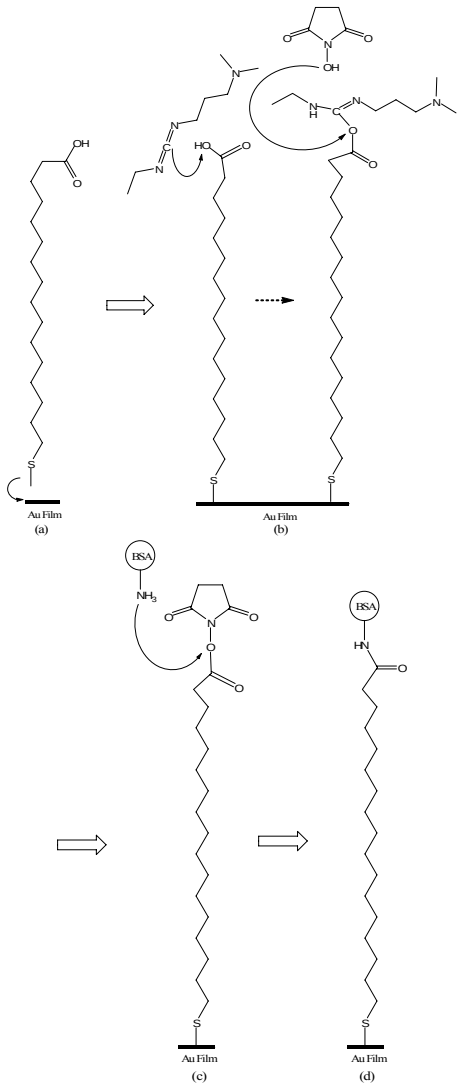

Figure 4. Immobilizing BSA on gold surface: (a) Immersing in 1 mM MHDA ethanol solution for 24 hours; (b) Immersing in 2 mM EDC and 5 mM NHS ethanol solution for 12 hours of activation; (c) Immersing in BSA solution; (d) BSA is immobilized on the gold surface.

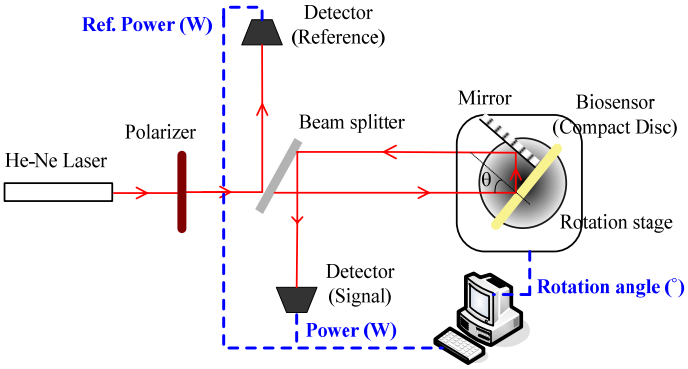

Figure 5. The configuration of optical metrology system.

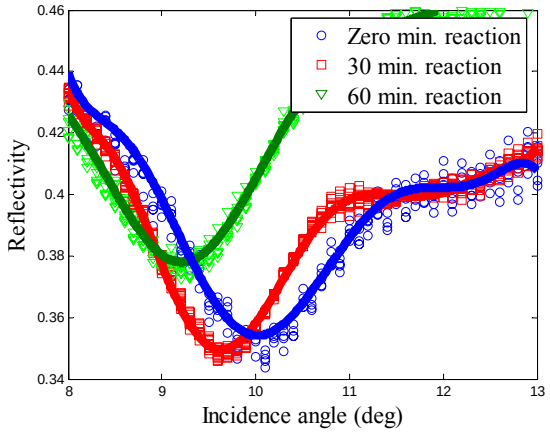

Figure 6. The zero-order reflectivity graph of the CDs without and with BSA reacted (30 min. and 60 min.), where the curve-fitted SPR angles correspond to 10.02°, 9.62° and 9.21°, respectively.

3A2-3

Formation, Transportation, and Evaporation of Encapsulated Droplets

Yao-Wen Hsu[1], Chiun-Hsun Chen [1], Shih-Kang Fan[2,*]

[1] *Department of Mechanical Engineering, National Chiao Tung University, Taiwan, R.O.C*
[2] *Institute of Nanotechnology, National Chiao Tung University, Hsinchu, Taiwan, R.O.C.*

***Abstract* —We successfully manipulate dielectric (silicone oil) and conductive (water) droplets by dielectrophoresis (DEP) and electrowetting on dielectric (EWOD) on a digital microfluidic chip. Encapsulated droplets with different volumes of oil shell and water core are formed by merging two quantitatively created oil and water droplets. Transportations of the encapsulated droplets of different core-shell ratios with silicone oil of various viscosities are examined. The driving voltages to transport the encapsulated droplets at different velocities are measured. Furthermore, the evaporation of the water in the encapsulated droplets is reduced. The relation of the evaporation rate to the core-shell ratio and the viscosity of the oil are discussed.**

Keywords — ***EWOD, DEP, Encapsultaed droplet***

I. INTRODUCTION

Digital microfluidics has emerged in recent years. Different from traditional microfluidics handling fluids continuously in microchennals, digital microfluidics manipulates one or multiple liquids in the format of droplet(s) on a single device at the same time. Each droplet can be considered as an individual reaction chambers for different tests. Electrowetting-on-dielectric (EWOD), one of the ways to drive liquid droplets in parallel-plate devices, is an electric method to change the surface wettability. The nature of high surface-to-volume ratio of droplets on the micro scale leads to severe evaporation in air [1]. For reducing droplet evaporation, some approaches have been proposed, including placing the droplet in an oil filler medium [2] and in a moisturized environment [3]. Although droplet in an oil filler medium almost prevents evaporation, packaging and sealing the device with oil is difficult.

Previously, we successfully manipulated the encapsulated droplet on a digital microfluidic chip [4]. Related research of water-oil core-shell droplet has been proposed [5]. Capsulation of a water droplet by an oil shell reduces water evaporation and keeps the device packaging simple. Evaporation of bare droplets and encapsulated droplets with an oil shell were investigated. The volume of the oil shell influences the rate of evaporation. A larger amount of oil shell avoids evaporation more effectively. Therefore, the evaporation rate of the water droplet would be controlled by a proper water-oil ratio. Although the volume ratio of water and oil can be approached by carefully pipetting, precise volume of different oil with different viscosity, surface tension, and density is difficult to be dispensed. Here in order to precisely dispense oil and water droplets, EWOD and dielectrophoresis (DEP) [6] are used to manipulate DI water and silicone oil, respectively. The two liquids are merged to form an encapsulated droplet spontaneously. Furthermore, the evaporation rates are investigated for encapsulated droplets with different water-oil ratios using different silicone oils with different viscosities.

* *Contacting Author: Prof. Shih-Kang Fan, Institute of Nanotechnology, National Chiao Tung University (NCTU), Address: 1001 Ta Hsueh Road, Hsinchu, Taiwan 300, ROC, (Tel: 886-3-571-2121 #55813, Fax: 886-3-5729912, mail: skfan@mail.nctu.edu.tw.).*

II. PRICIPLE

A. EWOD

Droplets are able to be pumped on a EWOD device as shown in Fig. 1. When applying an AC signal on a driving electrode, contact angle of the pumped droplet decreases due to EWOD. Because of the difference of contact angle between two sides of the droplet, it is moved toward the energized electrode. In this paper, driving electrodes were designed and fabricated on glass substrates by patterning Cu/Ti (2000 Å/ 200 Å). The electrodes were covered with a 1μm-thick SU-8 insulator as a dielectric layer and then coated with a 55-nm-thick Teflon layer.

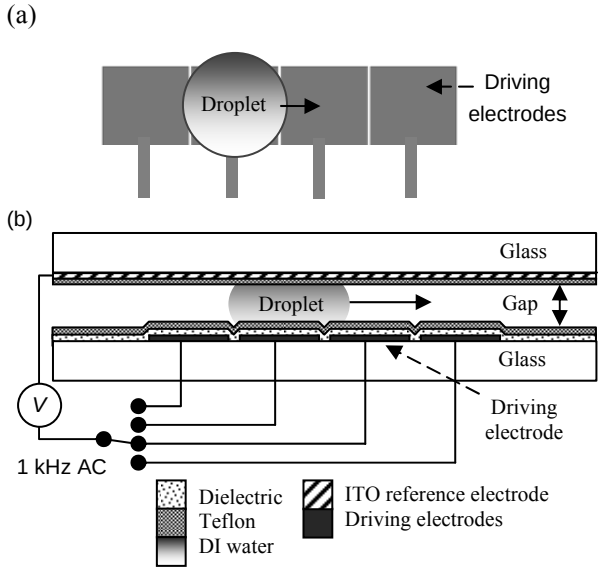

Figure 1. Illustration of EWOD: droplet between two parallel plates is pumped with applied AC voltage. (a) Top view. (b) Cross section.

B. DEP

Previously, we successfully utilized DEP force to manipulate dielectric droplets between two parallel plates [2], because DEP force would draw a dielectric droplet (silicone oil in this case) of high permittivity into the region of low permittivity (air in this case). Figure 2 shows the dielectric droplet pumped between two parallel electrodes due to the electric field.

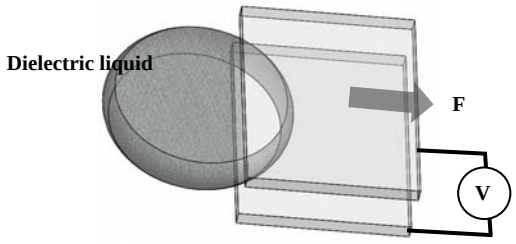

Figure 2. Illustration of using DEP force to contol dielectric liquid by applying an electric field bewteen two parallel electrodes.

C. EWOD and DEP

Figure 3 illustrated the concept of oil and water pumping by EWOD and DEP forces. Figure 3(a) shows that the water droplet is pumped by EWOD with an AC signal, and the oil droplet is transported by DEP with a DC voltage applied between the parallel plates. After merging the two droplets, an encapsulated droplet is formed and driven by EWOD (Fig. 3(b)).

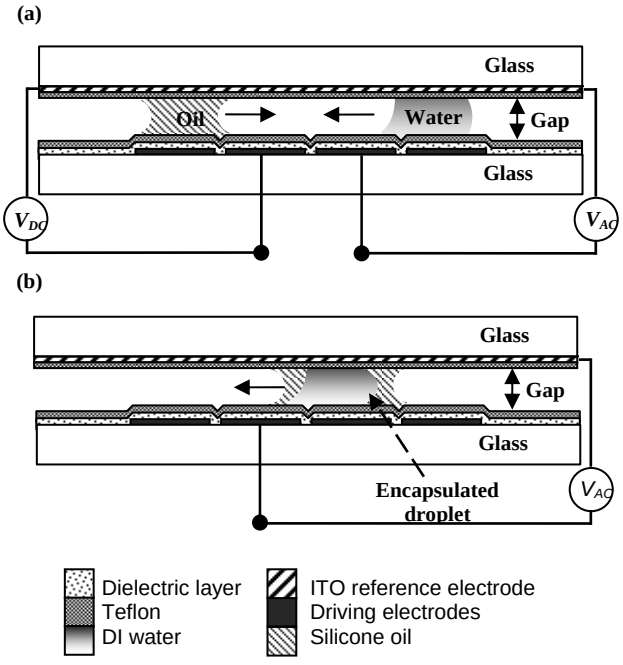

Figure 3. Configuration of the device to manipulate water and oil droplets. (a) EWOD-pumped water droplet was achieved by applying an AC signal, while the oil droplet was transported by DEP when a DC voltage was applied between the parallel plates. (b) An encapsulated droplet was obtained by merging the water and oil droplets.

III. Results and Discussion

A. Design of driving electrodes

Figure 4 shows the device design with the electrode layout. The water and oil are created from their own reservoirs. The size of the driving electrodes for water and oil are different to create the desirable volume ratio between the water core and the oil shell. The driving electrodes are 316 μm x 316 μm for the oil droplets and 1 mm x 1 mm for the water droplets. The volumes of the created droplets are determined by the size of the driving electrodes and the gap between plates. The created droplets are then merged together to form an encapsulated droplet as shown in Fig. 4(b). The volume ratio of water to oil is 10: 1 in the case shown in Fig. 4(b). Multiple oil or water droplets can be created to achieve an appropriate water/oil ratio by the designed device.

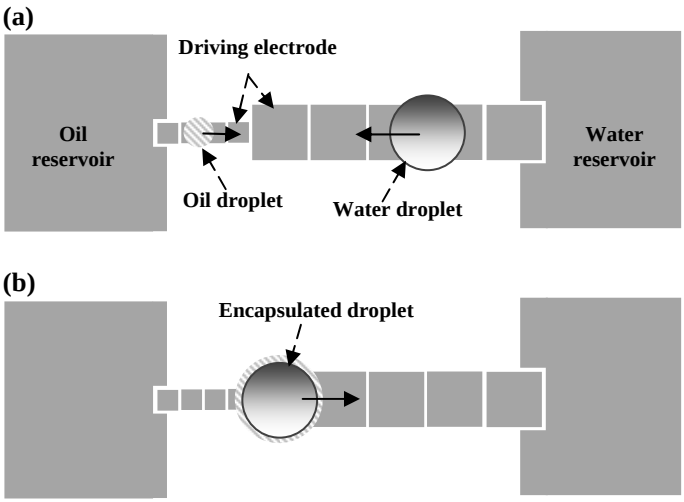

Figure 4. Electrode design of device. (a) Water and oil droplets were created from their own resvervoirs. (b) Encapsulated droplet was formed by merging two immiscible droplets.

B. Creation of quantitative encapsulated droplet

Figure 5 shows the manipulation of the water and oil droplets by EWOD and DEP, respectively. Water and oil were first placed above the own reservoir electrode as shown in Fig. 5(a). By applying an AC signal on the larger square driving electrodes (1 mm x 1 mm), water was drawn from the reservoir (Fig. 5(b) and (c)). A 25 nl water droplet was created on the second driving electrode from the right as shown in Fig. 5(d). After pumping the created water droplet to the left driving electrode, an oil droplet was created through the similar procedure by applying DC voltage on the smaller driving electrodes (316 μm x 316 μm) as shown in Fig. 5(e)-(h). After creating water and oil droplets, the two immiscible droplets were merged to form an encapsulated droplet which was pumped by the EWOD force as shown in Fig. 5(i) and (j).

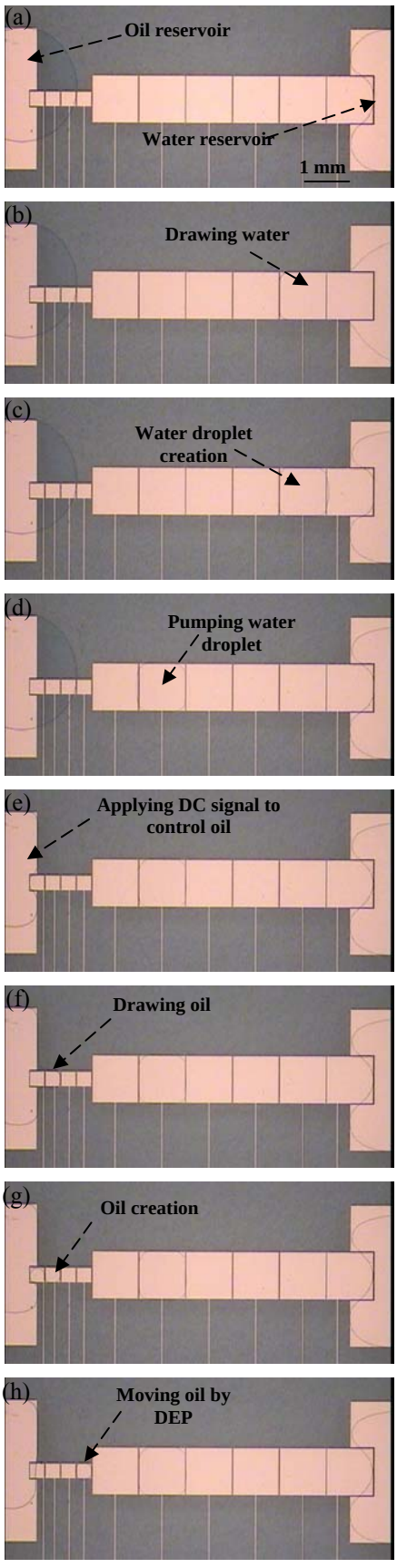

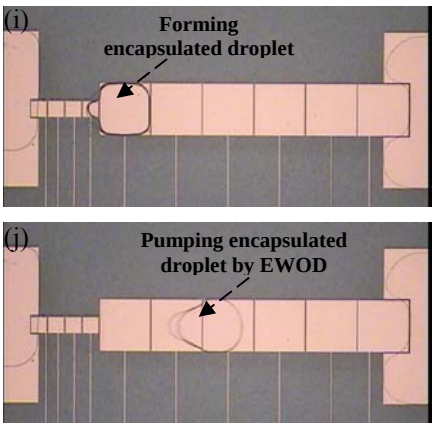

Figure 5. Sequencial experimetal photographs of droplet encapsulation. (a) Applying an AC signal on the water reservoir. (b) Drawing water on the driving electrodes. (c) Creating a water droplet. (d) Pumping water droplet to the designated electrode. (e) Applying a DC voltage on the oil reservoir to fix the silicone oil. (f) Drawing oil on the driving electrodes. (g) Creating a quantitative oil droplet. (h) Moving oil droplet to the designated electrode. (i) Merging two immesicle droplets to form an encapsulated droplet. (j) Manipulating the encapsulated droplet by EWOD.

C. Driving voltage of encapsulated drople

The required AC voltage to transport the encapsulated droplets with silicone oil shells of various viscosities was measured and plotted in Fig 6. The driving voltage of the encapsulated droplets was influenced by the viscosity of the oil shells. Three kinds of silicone oil were tested, including 10 cSt, 100 cSt, and 1000 cSt. As can be seen from Fig. 6, a larger driving voltage was required for the encapsulated droplet with a higher viscosity oil shell. The droplets with 10 cSt silicone oil needed the lowest driving voltage. The curve of a bare droplet was also plotted in Fig. 6.

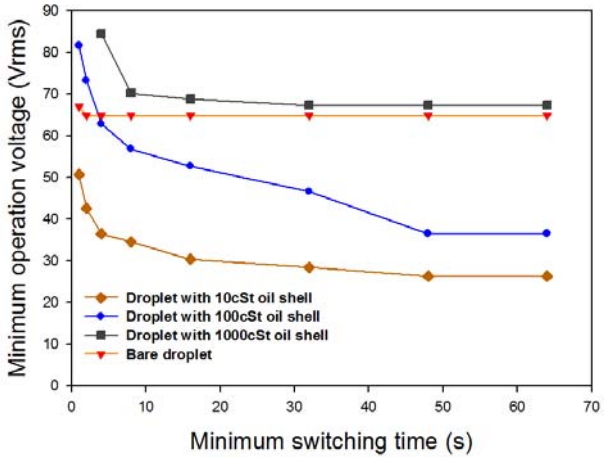

Figure 6. The chart for relation between encapsulated droplets with different viscosities oil shell and the minimum switching time.

D. Static evaporation of encapsulted droplet

Figure 7 shows droplet evaporation in different conditions. All experiments were conducted in controlled environment at the temperature of 20±1 °C and the relative humidity of 45±5 %. The bare droplet was fully evaporated in the air after 60 min (Fig. 7(b) and (e)). No volume loss was observed for the droplet in an oil filler medium during 150 min (Fig. 7(d) and (g)). In 150 min, there was a little water in encapsulated droplet as showed in Fig. 7(f). The ratio of oil to water for the studied encapsulated droplet was 1:10. The water droplet capsulated by 100 cSt silicone evaporated least as can be seen in Fig. 7(a). Different water-oil ratio would affect the evaporation, which calls for further studies in the future by the developed techniques to create quantitative encapsulated droplets.

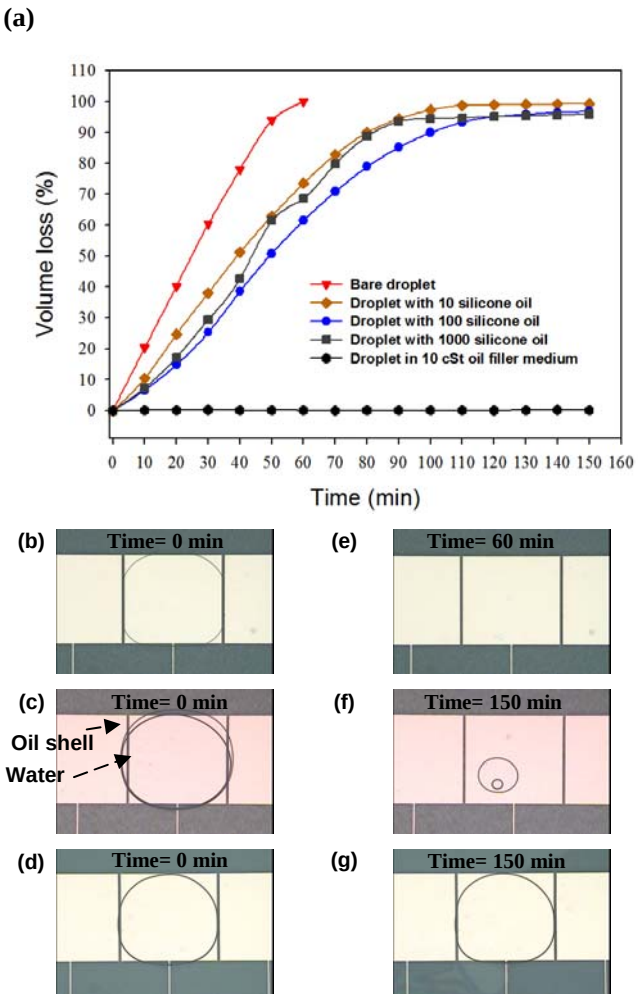

Figure 7. Chart and photographs for evaporation studies of droplet in different conditions. (a) Evaporation of the bare droplet, the encapsulated droplet, and the droplet in oil filler medium. (b) and (e) Bare droplet evaporation in the air. (c) and (f) Droplet with an oil shell. (d) and (g) Droplet in the oil filler medium.

IV. CONCLUSION

We successfully manipulated dielectric (oil) and conductive (water) liquids by DEP and EWOD forces on the same device. By the design of the driving electrodes, the volume of water and oil droplets could be controlled. The encapsulated droplets were subsequently formed by merging two immiscible droplets. For encapsulated droplet studies, we discussed the effect of the viscosity of the oil shell to the driving voltage. The encapsulated droplet with a higher viscosity needed a larger driving voltage. The driving voltage of the encapsulated droplet with a 10 cSt oil shell was the smallest. We also discussed the evaporation of the droplets in the air environment, in an oil filler medium, and with an oil shell. Bare droplet was fully evaporated in the air in 60 min. Droplet in the oil medium has almost no evaporation after 150 min. For the ratio of oil to water of 1:10, there was a little of water remained in the oil shell in 150 min. By droplet encapsulation, the evaporation was decreased, while the driving voltage was reduced, which largely enhances the performance of the droplet manipulation and simplifies the device packaging. EWOD and DEP were implemented on a device capable of quantitative dielectric and conductive droplet creations for the study of encapsulation droplet studies.

REFERENCES

[1] S. K. Cho, H. Moon, C.-J. Kim, " Creating, Transporting, Cutting, and Merging Liquid Droplets by Electrowetting-Based Actuation for Digital Microfluidic Circuits," *J. Microelectromech. Syst*, Vol. 12, pp. 70-80, 2003.

[2] M. G. Pollack, A. D. Shenderov, and R. B. Fair, "Electrowetting-based Actuation of Droplets for Integrated Microfluidics," *Lab chip*, vol. 2, pp. 96–101, 2002.

[3] V. Babin and R. Holyst, " Evaporation of a Sub-Micrometer Droplet," *J. Phys. Chem. B*, pp. 11367-11372, 2005.

[4] C.-W. Chen, Y.-W. Hsu, Y.-C. Chang, C.-H. Chen, and S.-K. Fan, "Digital microfluidic packing by droplet-level encapsulation", *APCOT'08 Conference*, Tainan, Taiwan, 2008.

[5] D. Brassard, L. Malic, F. Normandin, M. Tabrizian, and T. Veres, "Water-oil core-shell droplets for electrowetting-based digital microfluidic devices", *Lab Chip*, vol. 9, pp. 1342-1349, 2008.

[6] S.-K. Fan T.-H. Hsieh and Di-Yu Lin, "General Digital Microfluidic Platform Manipulating Dielectric and Conductive Droplets by Dielectrophoresis and Electrowetting," *Lab Chip*, vol. 9, pp. 1236-1242, 2009

3A2-5

Cell Optimizing Glucose Concentration by Using Gradient Microfluidic Chips and Microimprinting Technology

Ching-Wei Hsu, Chien-Hsien Chen, Chia-Hsien Yeh, Kuei-Ling Su, Yu-Chen Lin*

Department of Engineering Science, National Cheng Kung University, Tainan, Taiwan

***Abstract* — This study proposed a Polydimethylsilcoxane (PDMS) concentration gradient microfluidic chip fabricated using MEMS, casting molding, and microimprinting technology. The chip is used to research on optimizing concentration of endothelial cells on glucose concentration gradient is extracted using this chip. In the experiment a concentration gradient in solution was generated by a microfluidic network, and the effect of concentration gradient in different flow rates were observed. Besides, it conjugates micropatterns that cell adhesion space width with 300 μm and gap with 200 μm to discuss the optimizing glucose concentration (0~10%, 0~20%, and 5~15%) of endothelial cells. From the experimental data, we can prove that the concentration gradients are all stable under different flow rates (20, 30, 40, 50 μL/min). However, when flow rates reach over 20 μL/min, the cell would not remain on the substrate surface. The result shows that the glucose concentration gradient in the 8.66~15% is the optimizing concentration of endothelial cells, and too high or low concentration will lead the cell to leave the substrate surface or to die. This study can solve the problems of the different drug concentrations during drug preparation and test. It will be used to drug concentration test and hypersensitive test in the future.**

Keywords — ***MEMS, Microfluidic Chip, Microimprinting Technology, Endothelial Cells, Glucose***

I. INTRODUCTION

Concentration gradients of diffusible substances applying to cell of chemotaxis or adaptability play an important role in biological pattern formation and angiogenesis. Despite the importance of concentration gradients in biology, there are only a few capable techniques of generating and maintaining gradients easily in low fluid flow rates. Jiang et al. constructed the microfluidic chips and integrated the micromixer to generate concentration gradient [1]. Dertinger et al. fabricated three concentration gradient microfluidic chips to generate the complex effect of concentration gradients [2].

Micrometer scale patterning of cells on surfaces has been used in tissue engineering, biosensors, formation of neuronal networks, and in the investigation of fundamental cell biology questions. The general approach to cell patterning is based on modifying surface properties followed by selective cell attachment and spread. In related developments, microfluidic approaches are being increasingly used in performing cell based assays and other applications [3]. The photolithographic technique is highly developed and has been widely used for patterning cells. However, this technique has some disadvantages for certain biological applications, especially biocompatibility. Recently, several micropatterning techniques including microcontact printing (μCP), microfluidic patterning using microchannels, and laminar flow patterning, largely based on soft lithography, have been developed for biological applications. Those techniques have been employed extensively to explore and understand important processes and questions in fundamental cell biology such as adhesion, growth, migration, secretion and gene expression with various materials by engineering the neighbor environment in micron level [4, 5]. Patterning of adhesion molecules in arranged arrays may confine the number of cells on the fabricated surfaces in spots that are easily tracked.

Microfabrication techniques are used to generate patterns of cells on surfaces. The soft lithographic techniques mostly use polydimethylsiloxane (PDMS), which is biocompatible, optically transparent, permeable to gases, elastomeric, and durable. Cells can be cultivated on the surface of PDMS, and the surface properties can also be readily modified. The microfabrication and microfluidics technologies have following advantages as small size, multiple assays on one array, and multiple processes integrated on one chip. The small size allows researchers to use only a small amount of sample and reagent. Copies of a single device can be made at low cost using microfabrication technique [5].

The main causes of morbidity and mortality for the diabetic patients are vascular diseases. Vascular disease caused by diabetes mellitus which is directly related to high glucose levels represents a significant medical problem that has been firmly established in large clinical trials. At a cellular level, some researches have previously shown that high glucose exposure to human endothelial cells could induce anti-proliferation, predominantly due to pro-apoptotic effects, cellular hypertrophy [6, 7].

In this paper, our work is intended to demonstrate the generation of concentration gradient model and enable patterned cell culture inside microfluidic devices. The elastomeric PDMS stamp is embossed with surface features, with which we can define the cell adhesive/non-adhesive areas and a separate microfluidic PDMS piece with microchannels. Then on the microfluidic device, we are able to perform cell culture, observation and optimizing concentration analysis. This study included two steps: (i) maintaining the stable concentration gradient of glucose with micromixer fluidic systems and (ii) patterning the adherent ECs by utilizing μCP technique based on soft lithography and photolithography.

II. MATERIALS AND METHODS

A. Fabrication of Gradient Microfluidic Chip

The fabrication process of concentration gradient microfluidic chip is introduced as follows. First a photomask is designed using the AutoCAD®. Second, by employing MEMS technology, the SU-8 microstructure punch with the depth of 100 μm was fabricated on the silicon wafer which serves as the substrate. The schematic diagram of fabrication process is shown in Fig. 1. The negative photoresist (SU-8) is chosen in our experiment since it is available in a wide range of formulations to cover a film thickness range from 200 to 300 μm in a single coating process or to 3 mm by multi-coating processes. SU-8 100 (Microchem) has been spun onto silicon wafers using the standard Microchem protocol for 100 μm depth.

The microfluidic structure on the substrates was made up of SU-

*Contacting Author: Yu-Cheng Lin, Department of Engineering Science, National Cheng Kung University, Taiwan, 1 University Road, Tainan, Taiwan (Tel: +886-6-276-2395, Fax: +886-6-276-2329, Email: yuclin@mail.ncku.edu.tw).

8 thick photoresist. Moreover, the wafers are placed in a self-design device and a mixture of PDMS-prepolymer and catalyst (10:1 ratio) is poured over the substrate. The device is placed in an oven for 24 h at 60°C and then PDMS is replicated from the SU-8 mold.

In gradient microfluidic experiments, the phosphate buffer solution (PBS) and trypan blue solution have been injected into two inlets, respectively. The two solutions are marked with two different colors. Furthermore, the concentration gradient distribution is formed in the micromixer chip and the end area of the microfluidic chip is observed when varying fluid flow rates. The experiment steps are as follows: (1) using silicone tubes and connectors to connect injection holes with the concentration gradient microfluidic chip, (2) using syringes and micropump to inject two liquids into the microchannel, (3) removing air bubbles, and (4) taking photographs at observation area of microfluidic device.

B. Micropatterning Surface

PDMS is used to produce the micropattern stamp by employing MEMS technology. A detailed schematic outline of the μCP procedure is shown in Fig. 2. The region of non-adhesive cell is defined with PDMS stamps. The PDMS stamps, which have embossed desired surface patterns, are inked in BSA solution for 1 h at room temperature. Then, the stamps are taken out from the BSA solution dried in a N_2 stream. Finally the stamps are made to have close contact with the glass substrate for 1 min.

C. Cell Culturing Experiment

Mouse endothelial cell line MS1 (EC) is obtained from Department of Institute of Molecular Medicine, National Cheng Kung University. These cells are cultured in Dulbecco's Modified Eagle's Medium (DMEM) supplemented with 10% fetal bovine serum (FBS), 1% penicillin-streptomycin, 1% sodium pyruvate and 1% l-glutamine. The ECs are sub-cultured every 2-3 days. The processes are as follows (1) rinsing the cells with PBS solution, (2) pipetting trypsin-EDTA into the culture dish and placing dish into the incubator for 2-3 min at 37°C, (3) rinsing the culture vessel with medium to collect remaining cells and adding them into fresh medium in a new dish, and (4) cell culturing in a 5% CO_2 incubator at 37°C.

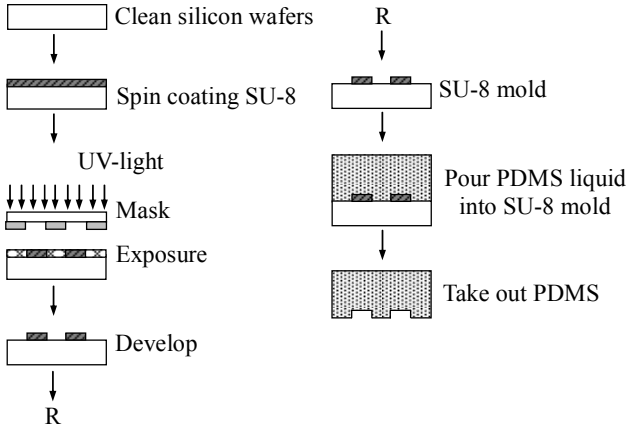

Figure 1. Schematic of manufacturing processes for SU-8 mold and PDMS chip. Process steps: cleaning the substrates, spin coating photoresist, exposure, developing. The PDMS is replicated from the SU-8 mold after the completion of the microstructure.

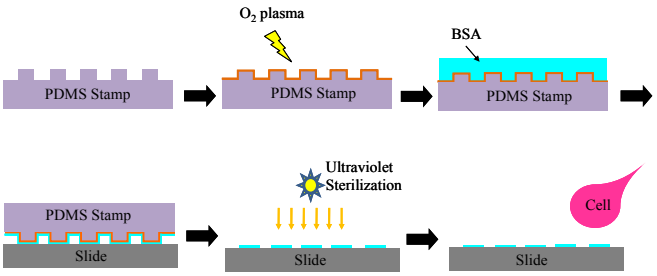

Figure 2. Schematic outline of the μCP procedure for micropatterning cells. With embossed surface patterns, the PDMS stamps are able to define the cell adhesive/non-adhesive areas.

D. Microfluidic Cell Culture Device Bonding

Bonding the microfluidc cell culture included two methods. The first method was to cover a layer of PMMA plate corresponding to the stamped strips patterns on the substrate. Then, the PDMS microfluidic chip and micropattern substrate were treated with O_2 plasma at the same time. Another method was to place the glass substrate into O_2 plasma equipment for 1 min, and then BSA micropatterns was transferred to glass substrate. The surface of PMDS microchannel were being treated with O_2 plasma, while at the same time micropatterns were transferred. Finally the surface of the PDMS replica and the glass substrate were activated with reactive O_2 plasma and integrated into one microfluidic cell culture device by visual alignment.

E. Optimizing Glucose Concentration of ECs

Fabricated using MEMS, casting molding, and microimprinting technology, the concentration gradient microfluidic chips were utilized to find optimizing glucose concentration of ECs. After ECs were cultured for 12 h in the microfluidc device, glucose and PBS solution were injected into the chip, which could mix the two different solutions uniformly by syringe pump, as shown in Fig. 3. Moreover, different flow rates (20, 30, 40, and 50 μL/min) were applied to observe the linearity of concentration gradients. The optimizing glucose concentration for ECs, including 0~10%, 0~20% and 5~15%, were tested in this experiment.

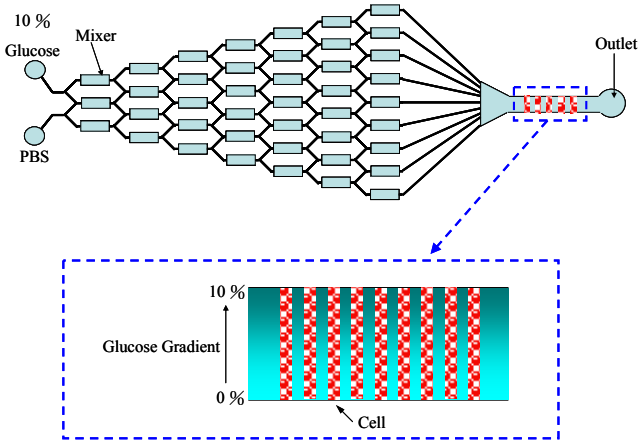

Figure 3. A schematic diagram of microfluidic cell culture device investigating cell adaptability in different glucose concentrations.

F. Microscope and Measurement

An inverted fluorescent microscope is used to observe the experimental results. The image and detection system consist of an optical microscope (BX60, Olympus, Japan) and a digital camera (DP70, Olympus, Japan). The gray level of trypan blue concentration gradient in the observation area of microfluidic chip is measured by Photoshop® and ImageJ software.

III. RESULTS AND DISCUSSION

Fig. 4 and Fig. 5 showed the concentration gradients of trypan blue solution and gray level distributions, respectively. We successfully fabricated the concentration gradient microfluidic chip which has a good mixing efficiency. The linear glucose concentration gradient was generated in the observation zone of the microfluidic chip, even when the flow rates were as slow as 20, 30, 40, and50 μL/min. Moreover, when increasing the flow rates, the experimental data showed that the concentration gradient distribution was linear.

Cell-adhesive and non-adhesive areas could be observed in Fig. 6, and the stamped strips had two different designs. In one of our design, the cell-adhesive width was 300 μm and the gap was 500 μm, while in the other design, both were 500 μm. It is found that the step of blowing off excess solution with N_2 stream has a significant impact on transferring micropatterns to glass substrate. Too long or too less blowing time could cause incomplete micropatterns on the substrate.

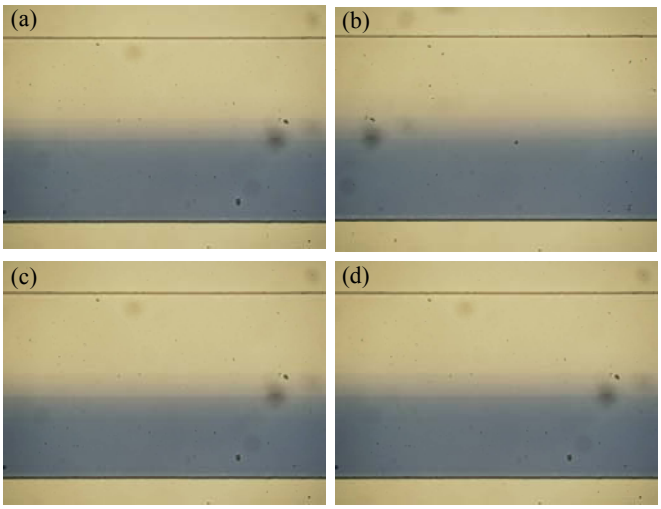

Figure 4. The concentration gradients of trypan blue solution were formed under four flow rates, including (a) 20 μL/min, (b) 30 μL/min, (c) 40 μL/min, and (d) 50 μL/min.

Two different processes of bonding microfluidic chip were used in this study. From the experimental data, the results showed that the first method caused the stamped strips corroded by O_2 plasma, while the second method could obtain good cell-adhesive regions. In order to avoid micropatterns destroying on the glass substrate, we adopted the second method to proceed in the subsequent experiments.

To illustrate the function and effectiveness of the cell culture microfluidic device, ECs were injected into the device and the biochip was placed in the incubator to culture for 12 h. The adaptive experiments of cells indicated that ECs would be washed away from glass substrate easily or a large number of cells died in a short time when the flow rate was over 20 μL/min. And then 20 μL/min flow rate was adopted in the following experiments, in order to avoid the inaccuracy of cell experiment caused by faster flow rates.

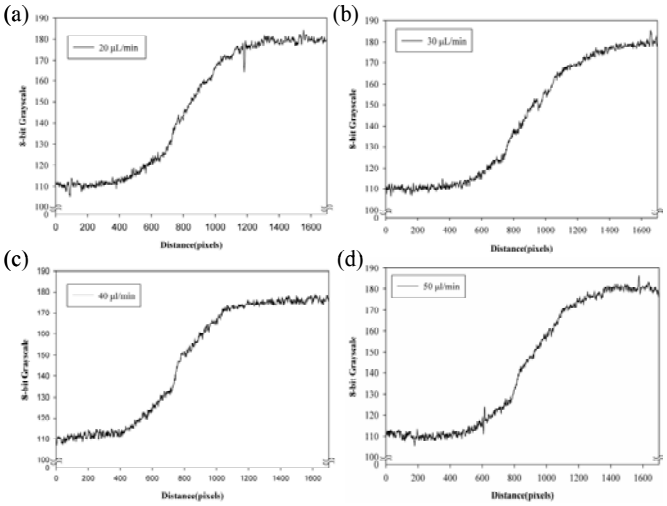

Figure 5. Plot of gray level distribution with four flow rates, including (a) 20 μL/min, (b) 30 μL/min, (c) 40 μL/min, and (d) 50 μL/min. The gray level of trypan blue concentration gradients were measured using Photoshop® and ImageJ software. While increasing the flow rate, it is found that the tendency of gray level will obtain better linear distribution.

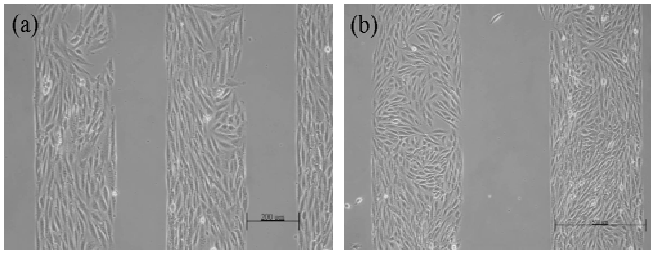

Figure 6. Micropatterns of endothelial cells (MS-1) were, by utilizing μCP technique with BSA solution to transfer protein to glass substrate, (a) cell-adhesive width with 300 μm, and gap with 200 μm, and (b) both cell-adhesive width and gap with 500 μm.

Figure 7 showed that the distribution of adhesive ECs in different interval concentrations,including (a) 0~10%, (b) 0~20%, and (c) 5~15%. In the process of concentration gradient experiment, it is found that the cells in the non-adhesive region were washed away from glass substrate quickly. With the increase of experimental times, cells in-adhesive regions were decreased gradually, because ECs could not survive in too high or too low glucose concentration. From the statistics of experimental data, the results of Fig. 7a showed that adhesive ECs had no significant alteration when the glucose concentration gradient within 7.92~10%. Besides, Fig. 7b illustrated that concentration ranges of cell-adhesive region were 7.14~15%. To confirm the optimal interval of glucose concentration in cell-adhesive experiment, concentration ranges of 5~15% were used. The distribution of cell-adhesive regions is shown in Fig. 7c. The results indicated these phenomena: (1) ECs are atrophied in glucose concentration less than 8.66% after 60 min. When (2) the apoptosis of ECs takes place when the glucose concentration is greater than 15% and the experiment time is 360-510 min.

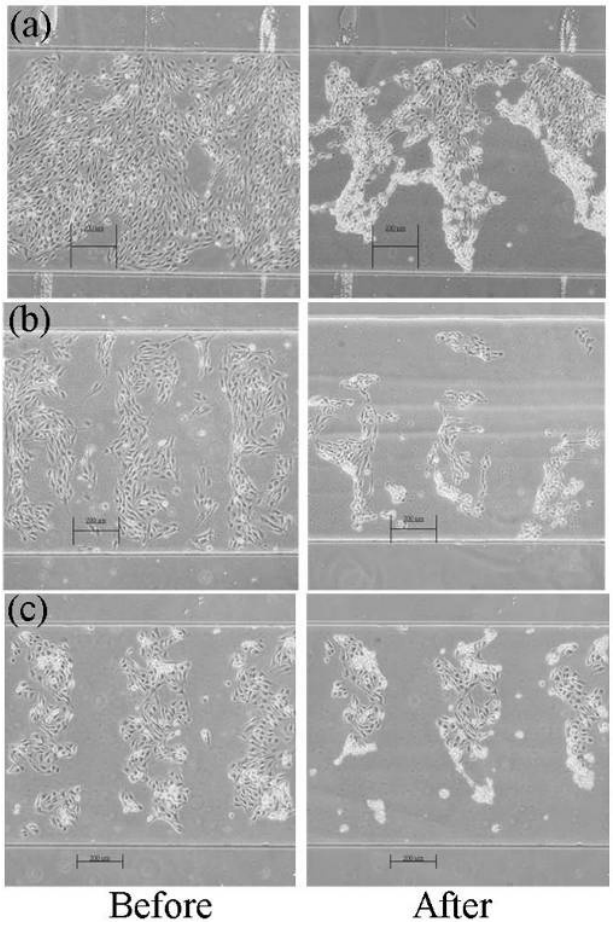

Figure 7. Micrographs of adhesive ECs distribution in different glucose concentration gradients. The intervals of glucose concentration are (a) 0～10%, (b) 0～20%, and (c) 5～15%.

IV. CONCLUSION

We successfully fabricated the biochip which included a small elastomeric PDMS stamp piece with embossed surface patterns to define cell adhesive/non-adhesive areas and a separate microfluidic PDMS piece with mixing zone generating the concentration gradient. According to the results of this study, we concluded that: (1) Since the microfluidic chip and microstamp were fabricated using casting molding, the advantages included small feature size, high precision, mass production and low cost. (2) We successfully established uniform distribution effect of concentration gradient through biochips. (3) The processes which were treated by the O_2 plasma equipment with power 150 W for 10 min could modify the stamp surface well, and enhance adhesive effect of BSA solution. (4) We have successfully imprinted that cell-adhesive region with the width of 300 μm and the gap of 200 μm. And (5) we confirmed that the interval within 8.66~15% is optimized glucose concentration of ECs from the results of gradient experiments. In all, this study successfully realized the cell culture of concentration gradient microfluidic chip systems. This study not only improves the drug concentration test methods but also contributes to the development and applications of drug concentration and allergy testing in the future.

REFERENCES

[1] X. Jiang, Q. Xu, S. K. W. Dertinger, A. D. Stroock, T. Fu, and G. M. Whitesides, “A general method for patterning gradients of biomolecules on surfaces using microfluidic networks,” *Analytical Chemistry*, 77, pp. 2338-2347, 2005.

[2] S. K. W. Dertinger, D. T. Chiu, N. L. Jeon, and G. M. Whitesides, “Generation of gradients having complex shapes using microfluidic networks,” *Analytical Chemistry*, 73, pp. 1240-1246, 2001.

[3] S. W. Rhee, A. M. Taylor, C. H. Tu, D. H. Cribbs, C. W. Cotman, and N. L. Jeon, “Patterned cell culture inside microfluidic devices,” *Lab on a Chip*, 5 , pp. 102-107, 2005.

[4] T. Das, S. K. Mallick, D. Paul, and T. K. Maiti, “Microcontact printing of concanavalin a and its effect on mammalian cell morphology,” *Journal of Colloid and Interface Science*, 314, pp. 71-79, 2007.

[5] T. H. Park, and M. L. Shuler, “Integration of Cell Culture and Microfabrication Technology,” Biotechnol. Prog., 19, pp. 243-253, 2003.

[6] S. McGinn, P. Poronnik, M. King, E. D. M. Gallery, and C. A. Pollock, “High glucose and endothelial cell growth: novel effects independent of autocrine TGF-beta 1 and hyperosmolarity,” *Am J Physiol Cell Physiol*, 284, 1374–1386, 2003.

[7] S. M. Baumgartner-Parzer, L. Wagner, M. Pettermann, J. Grillari, A. Gessl, W. Waldhausl, “High-glucose-triggered apoptosis in cultured endothelial cells,” *Diabetes*, 44, 1323-1327, 1995.

Using an Ultrasonic Vibration Microfluidic Chip to Generate Alginate Microcapsule

Shian-Chin Lai, Chia-Hsien Yeh, Ying-Chieh Chen and Yu-Cheng Lin *

Department of Engineering Science, National Cheng Kung University, Taiwan

***Abstract* —This study managed to generate UV-crosslinking microparticles and wraped in the microcapsules by using an ultrasonic vibration microfluidic chip, and we had demonstrated that the UV-crosslinking microparticles is real wraped in the microcapsule and the microcapsules size was able to be controlled by altering the flow rate of the wraped and sheath phase. Through control this experiment conditions we had successfully generated microcapsules and its size distribution is from 89 μm to 248 μm. The proposed ultrasonic vibration microfluidic chip was easy to fabricate and capable of high throughput and low cost.**

Keywords — ultrasonic vibration, UV-crosslinking microparticles, microcapsule

I. INTRODUCTION

Control of the microparticle sizes and the size distribution is crucial for drug control release system due to their influence on the clearance rate from the body which ultimately determines the drug dosage. Thus it is of great importance to fabricate the uniform and small particle size microspheres [1]. The Albertini group generated the theophyline-loaded microparticles by using the ultrasonic spray-congealing method [2], and the Passerini group used the same way to fabricate the praziquantel (PZQ)-loaded microparticles [3]. The Serra group used an ultrasonic atomizer and the ultrasound spray drying technique to generate the dextrin microparticles [4]. Nowadays, the Chen group used the ultrasonic disintegrator to prepare BA/ST/AM nano particles [5]. These scholars obtained the ultrasonic vibration frequency by using the large-scale ultrasonic generator to fabricate the nano or microparticles. Then, some scholar bring up the microcapsule idea, that wraped a smaller particle into a big one. It provides a new direction for pharmaceutical applications. The Nisisako, Kumacheva and Weitz group used the multiple-phase microfluidic system and controlled the flow rate to generate microcapsules and wraped emulsions or microparticles in it [6-8]. In this study, we combine the microfluidic chip with ultrasonic vibration control loop circuit and transducer to generate the uniform microparticles and wrapped them into alginate microcapsule.

II. MATERIAL AND METHOD

The ultrasonic vibration microfluidic chip is made up of poly-methyl-methacrylate (PMMA) carved by CO_2 laser machine and through screw and nut to proceed soft binding and fabricate this device. In this experiment, the mineral oil (OSAKA, Japan) was used as continuous phase, while the dispersed phase was polymerizable solution consisted of 4-hydroxybuthyl acrylate (TOKYO KASDI KOGYO), ethyleneglycol dimethacrylate (SHOWA CHEMICAL CO, LTD), 2, 2-dimethoxy-2-phenyl-acetonphenone (ACROS ORGANIC) and acrylic acid (ACROS ORGANIC), the wraped phase was alginate (ACROS, USA), and sun flower oil (Uni-President Enterprises Corp., Taiwan) was sheath phase. An ultrasonic vibration frequency generate system, including ultrasonic vibration control loop circuit and transducer (WHIRL BELL TRADING Co, LTD) was also employed. The transducer is able to send out 2.4 mHz immovable vibration frequency, but we can change the transducer amplitude of vibration by altering the voltage provide to transducer from power supply, the working principle of proposed device is as follows. The power supply provides certain voltage to ultrasonic vibration control loop circuit, and the ultrasonic vibration control loop circuit exports a frequency signal for the transducer, then the transducer will generate an ultrasonic vibration frequency due to a resonance effect with the frequency signal. Thus we can generate the UV-crosslinking emulsions with many kinds of emulsion sizes by altering the voltage that power supply provides to transducer [9]. Then a 365nm UV light (365 nm, 1.2 mW/cm^2, Novacure, Photonic Solutions Inc.) used as a UV light source to solidify the UV-crosslinking emulsions into UV-crosslinking microparticles.

This experiment strategy as shown in Fig. 1, it is to inject mineral oil and UV-polymer solution into the microfluidic chip to form the laminar flow, and then the UV-crosslinking emulsions were generated by the ultrasonic vibration. The alginate is injected to wraped the UV-crosslinking emulsions, and the microcapsules was generated by sheath phase cut the mix fluid (UV-crosslinking emulsions and alginate layer). After 365 nm UV light was utilized to solidify the microparticles that wrapped in the alginate microcapsule.

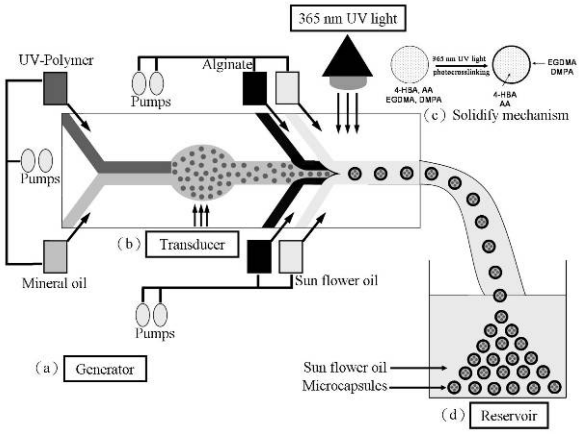

*Contact author: Y.C. Lin, National Cheng Kung University, Department of Engineering Science, 1 University Road, Tainan 701, Taiwan. Tel: +886-6-276-2395; Fax: +886-6-276-2329; E-mail: **yuclin@mail.ncku.edu.tw***

Figure 1. Illustration of the fabrication procedures of UV-photopolymerization microparticles.

The ultrasonic vibration microfluidic chip consisted of four layers, from top to bottom: the cover layer, the channel layer, the observation layer and the transducer layer, then through soft bonding to fabricate the ultrasonic vibration microfluidic chip, as shown in Fig. 2. We managed to generate the microcapsules and control the size distribution by altering the flow rate of the wrapped and sheath phase. The dispersed phase flow rate and the continuous phase flow rate were set to 0.05 mL/min and 0.5 mL/min, respectively. And consider the fluid stable, we decide the ultrasonic vibration distance was set to 3 mm, and the voltage was 10.0 V to generated UV-crosslinking microparticles to wrapped in the microcapsule.

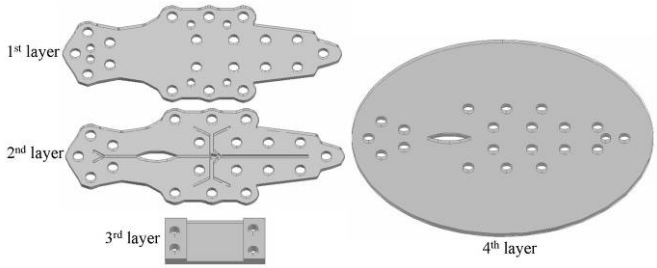

(a)

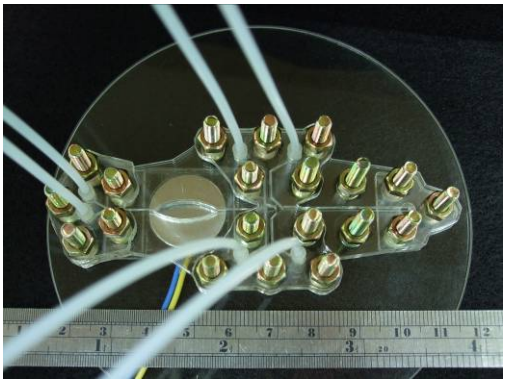

(b)

Figure 2. Schematic drawing and photo image of the proposed microfluidic chip: (a) the expanded view and (b) the chip actual photo.

III. RESULTS AND DISCUSSION

Fixing the wrapped phase flow rate at 0.01, 0.03 and 0.05 mL/min, and through adjust the sheath phase flow rate to collocate three kinds of wrapped phase flow rate, then we can generate microcapsules in different size distribution, as shown in Fig. 3 to Fig. 5.

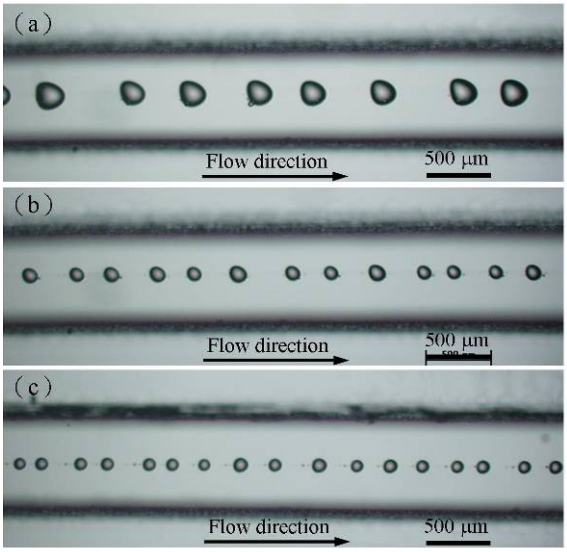

Figure 3. Fix the wraped phase flow rate on 0.01 mL/min and increased the sheath phase flow rate (a) 0.6 mL/min, (b) 0.8 mL/min, and (c) 1.0 mL/min.

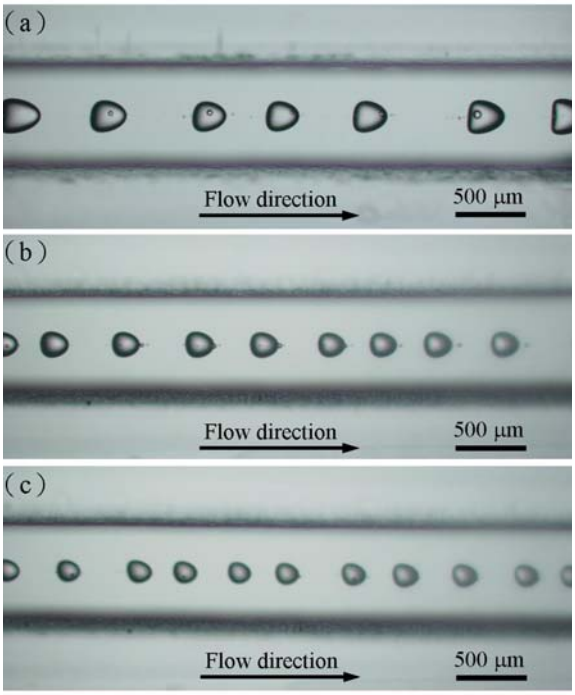

Figure 4. Fix the wrapped phase flow rate on 0.03 mL/min and increased the sheath phase flow rate (a) 1 mL/min, (b) 1.2 mL/min, and (c) 1.4 mL/min.

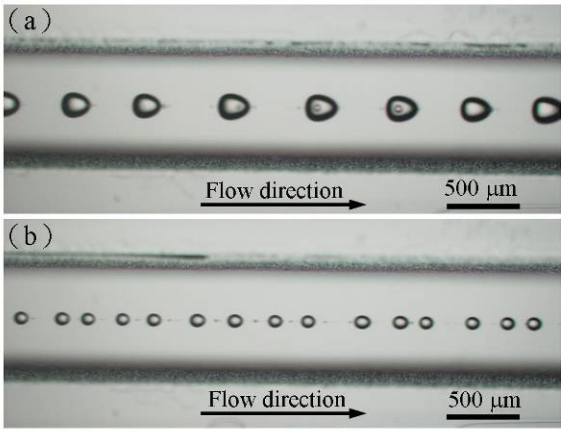

Figure 5. Fix the wrapped phase flow rate on 0.05mL/min and increased the sheath phase flow rate (a) 1.6 mL/min, and (b) 1.8 mL/min.

From the experiment, we can found that the laminar flow will generated if the wrapped phase flow rate was too fast for sheath phase flow rate, but the mixed phase (continuous phase, dispersed phase and wrapped phase) was push back when the sheath phase flow rate was too fast for mixed phase. Through this concept, we control the wrapped and sheath phase flow rate to generate the microcapsules. It was found that the microcapsule size was decreased when we fix the wrapped phase flow rate and increased the sheath phase flow rate, as shown in Fig. 6.

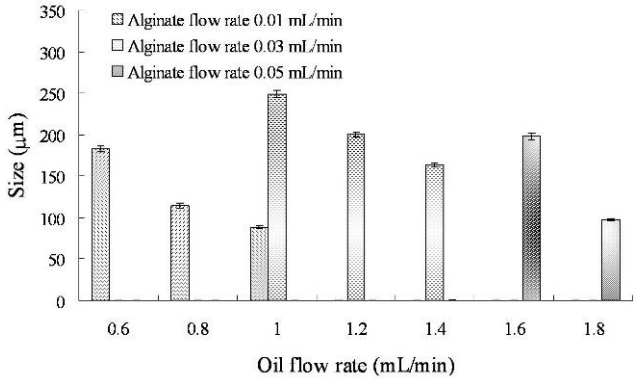

Figure 6. The relationship among microcapsule size and the flow rate of the wraped and sheath phase.

In order to proof the microcapsule included UV-crosslinking microparticles, through different microcapsule deep to take a photo, as show in Fig. 7(a), then we can find that the UV-crosslinking microparticles was indeed wraped in the alginate microcapsule, as shown in Fig. 7(b). Then, we can see in Fig. 8, the black layer of the microcapsule was alginate layer, and there are UV-crosslinking microparticles and mineral oil inner the black layer. Through Fig. 7 and Fig. 8, we can proof that we successfully wraped the UV-crosslinking microparticles into the alginate microcapsule.

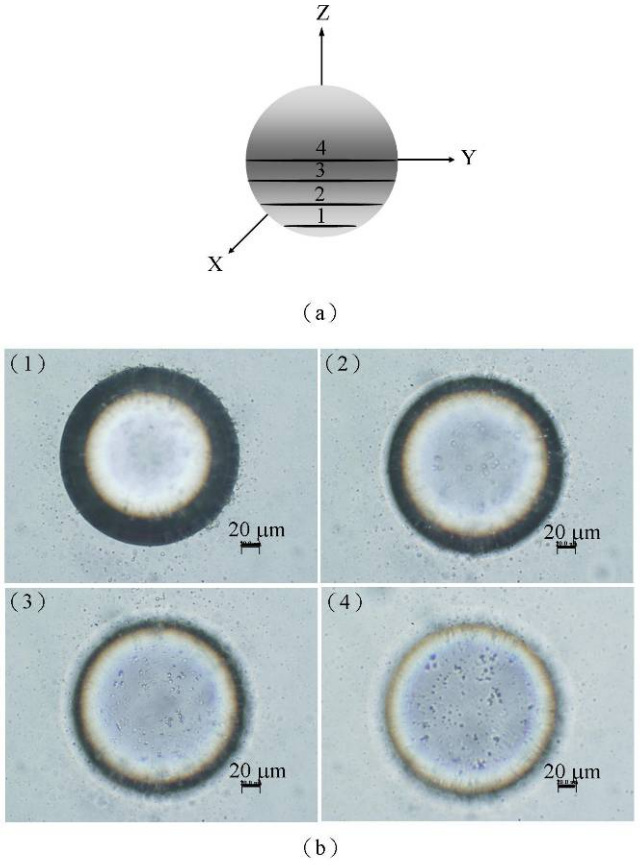

Figure 7. Photo image of the microcapsule: (a) 1-4 layers were respectively the position which was photographed by optical microscope was corresponding to image (b) 1-4.

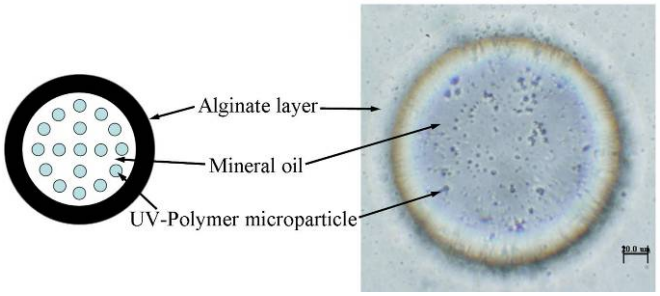

Figure 8. Photo image of the UV-crosslinking microparticles wraped in the alginate microcapsule clearly.

IV. CONCLUSION

In the study, UV-crosslinking microcapsules were successfully generated by using the proposed device. The measured diameter of microparticles ranged between 89 and 248 μm with a narrow size distribution (<10%). We managed to control the uniformity of the size of the alginate microcapsules by altering the wrapped phase flow rate and sheath phase flow rate. This study could provide many potential usages for pharmaceutical applications and effective to increase the quantity of microparticle that wrapped in the microcapsule.

REFERENCES

[1] C. H. Yang, K. S. Huang, P. W. Lin, Y. C. Lin, "Using a cross-flow microfluidic chip and external crosslinking reaction for monodisperse TPP-chitosan microparticles" *Sensors and Actuators B*, vol. **124**, pp. 510–516, 2007.

[2] B. Albertini, N. Passerini, M. L. Gonza´lez-Rodrı´guez, B. Perissutti and L. Rodriguez, "Effect of Aerosil® on the properties of lipid controlled release microparticles," *Journal of Controlled Release*, vol. **100**, pp. 233–246, 2004.

[3] N. Passerini, B. Albertini, B. Perissutti and L. Rodriguez, "Evaluation of melt granulation and ultrasonic spray congealing as techniques to enhance the dissolution of praziquantel," *International Journal of Pharmaceutics*, vol. **318**, pp. 92–102, 2006.

[4] P. P. Luz, A. M. Pires and O. A. Serra, "A low-cost ultrasonic spraydrryer to prodyce spherical miceoparticles fromipolymeric matrices," *Quim. Nova*, vol. **30**, pp. 1744-1746, 2007.

[5] N. Yin, K. Chen, W. Kang, "Preparation of BA/ST/AM nano particles by ultrasonic emulsifier-free emulsion polymerization" *Ultrasonics Sonochemistry*, vol. **13**, pp. 345–351, 2006.

[6] T. Nisisako, S. Okushima and T. Torii, "Controlled formulation of monodisperse double emulsions in a multiple-phase microfluidic system," *Soft Matter*, Vol. **1**, pp. 23–27, 2005.

[7] Z. Nie, S. Xu, M. Seo, P. C. Lewis, and E. Kumacheva, "Polymer Particles with Various Shapes and MorphologiesProduced in Continuous Microfluidic Reactors," *J. AM. CHEM. SOC.*, vol. **127**, pp. 8058-8063, 2005.

[8] A. S. Utada, E. Lorenceau, D. R. Link, P. D. Kaplan, H. A. Stone, D. A. Weitz, "Monodisperse Double Emulsions Generated from a Microcapillary Device," SCIENCE, vol. **308**, pp. 537-541, 2005.

[9] T. Lilliehorn, U. Simu, M. Nilsson, M. Almqvist, T. Stepinski, T. Laurell, J. Nilsson, S. Johansson, "Trapping of microparticles in the near field of an ultrasonic transducer" *Ultrasonics*, vol. **43**, pp. 293–303, 2005.

Indirect Activation of Porphyrin by Semiconductor Quantum Dot with Two-photon Excitation

Yanan Wen[1], Yanqiang Yang[1,*]

[1]*Department of Physics, Harbin Institute of Technology, China*

***Abstract* — Flourescence resonance energy transfer (FRET) between CdSe quantum dots (QDs) and *meso*-tetraphenylporphyrin (TPP) photosensitizers is studied by two-photon excitation fluorescent spectroscopy with 800nm femtosecond laser pulses. Evident transfer results are obtained in both the steady-state and time-resolved experiments. A slight peak shift to the red region in the emission of the CdSe QDs is observed after addition of TPP, which is speculated to be caused by energy transfer from QDs of small size to larger. An efficiency of about 0.3 accounts for the non-radiative energy transfer is estimated with the time-resolved method.**

Keywords — ***photodynamic therapy; quantum dots; fluorescence resonance energy transfer; two-photon excitation***

I. INTRODUCTION

Two-photon excitation photodynamic therapy (TPE-PDT) is known as a potential modality dealing with tumor by utilizing light-activated drugs under two-photon excitation [1-3]. Compared with traditional one-photon excitation PDT (OPE-PDT), it allows a deeper treatment of tumor and a selective activation of the photosensitizers, effectively enhances the spatial resolution and avoids unwanted damage to the normal tissue.

Porphyrins are typical photosensitizers with high singlet oxygen quantum yields and preferential accumulation in tumor. But small two-photon action cross section limits their application in TPE-PDT. Direct way to solve this problem include either design of new porphyrin sensitizers or chemical modification of existing ones to achieve efficient two-photon sensitization. But it's usually complicated and restricted. Using energy donors to indirectly activate the porphyrin sensitizers can effectively solve this problem. Semiconductor quantum dots possess not only large two-photon action cross section [3] but also high fluorescence quantum yields, superior photo- and chemical stability, broad excitation spectra and narrow luminescence spectra, making them perfect energy donors compared with traditional organic dyes for biomedical application [4-8].

II. METHOD AND MATERIALS

A. Experimental Design

In this work, energy transfer from CdSe QDs to *meso*-tetraphenylporphyrin (TPP) (solved in CH_2Cl_2) is investigated by steady-state and time-resolved fluorescent spectroscopy with two-photon excitation. A short overview of the experimental setup is given in Fig. 1. Femtosecond laser pulses at 800nm produced from a Ti: sapphire laser system (Spectra-Physics) are used as the two-photon excitation light source. Emission from the sample is collected by a spectrometer (Bruker Optics 250IS/SM) coupled with an intensified CCD detector (IStar740, CCI010, Andor). Attenuators are used to control the excitation power Time-resolved experiment is carried out by adjusting the delay time of the CCD shutter. Instrument response time is about 2ns when scattering light pulses are measured. UV-vis absorption spectra are recorded by a homemade UV-vis spectrophotometer.

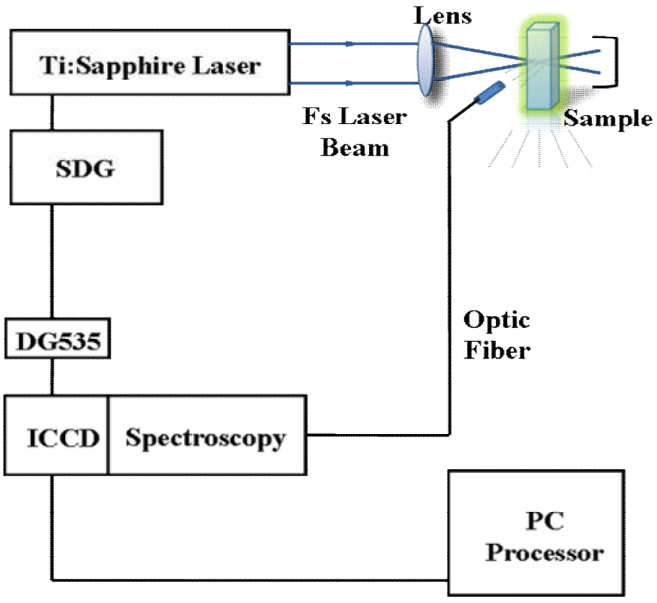

Figure 1. Experimental arrangement for two-photon excitation.

B. Materials

The CdSe QDs are prepared between Cd2+ and KHSe in the presence of 2-hydroxy-1-ethanethiol by electrostatic reaction. 4.2μL 2-hydroxy-1-ethanethiol is added to 30mL 4x10-4mol/L CdCl2 solution. PH value of the solution is adjusted to 11.0 by using of 1mol/L NaOH. Deaerate the solution by pure N2 for 30min. Meanwhile, take use of the strong reaction between selenium and KBH4, 4x10-4mol/L KHSe is prepared in 20mL 0.01mol/L NaOH solution. Then add freshly prepared KHSe solution with proper stir speed (the molar ratio of CH2OHCH2SH:$Cd2^{+}$:HSe^{-} is fixed at 5:1:0.7)

Center for Condensed Matter Science and Technology, Harbin Institute of Technology, Harbin, China

* Contacting author: Yanqiang Yang is with the Center for Condensed Matter Science and Technology, Harbin Institute of Technology, Harbin 150001, China (phone: +86-451-8641-8440: fax: +86-451-8641-8440; e-mail: yqyang@hit.edu.cn)

and reflux the reaction mixture for 1h to control the growth of the CdSe nanocrystals.

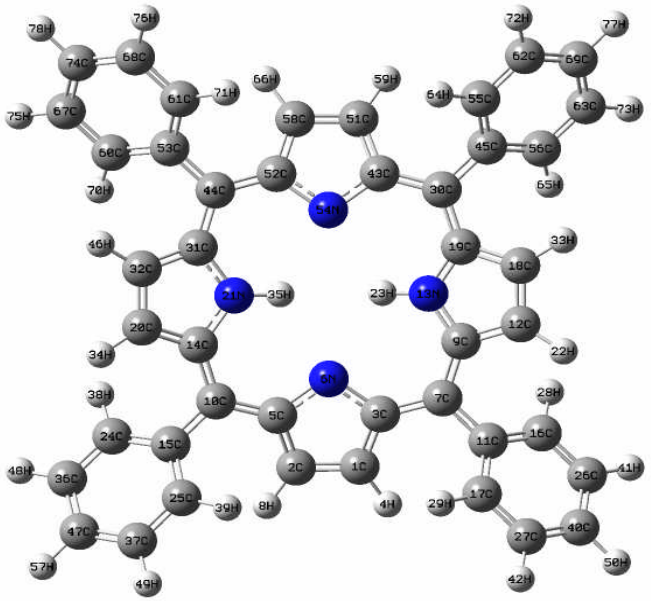

Figure 2. Molecular structure of TPP

Particles with a size-dependent luminescent maximum at about 556nm have been selected to match the Q band absorption of TPP. TPP powders are provided by our co-worker and used without further purification. The high symmetrical structure of TPP is shown in Fig. 2. The TPP molecular structure is made of a big porphine ring and four phenyls. In Fig.2 four blue balls stand for the atom "N", gray balls stand for "C" and white balls stand for "H"

III. Results And Discussion

A. Absorption Spectrum

Fig.3 shows the absorption spectrum of the CdSe donors (blue line) and TPP acceptors (black line), respectively. CdSe QDs have a broad light absorption range which allows a flexible light source selection in practical application. The extended π-conjugation system with 24-π electrons of TPP leading to a wide range of wave lengths for light absorption. In Fig.3 it can be seen that a strong absorption peak appears at 420nm ("Soret" band), corresponding to the transition of $1a_{1u}(\pi) \rightarrow 4e_g(\pi^*)$ $(S_0 \rightarrow S_2)$; and four weak peaks are observed at 514nm, 549nm, 591nm and 650nm (Q band), corresponding to the transition of $3a_{2u}(\pi) \rightarrow 4e_g(\pi^*)$ $(S_0 \rightarrow S_1)$. Two peaks of the Q band are enclosed in the emission area of the CdSe QDs, meeting the energy level matching condition of the energy transfer mechanism.

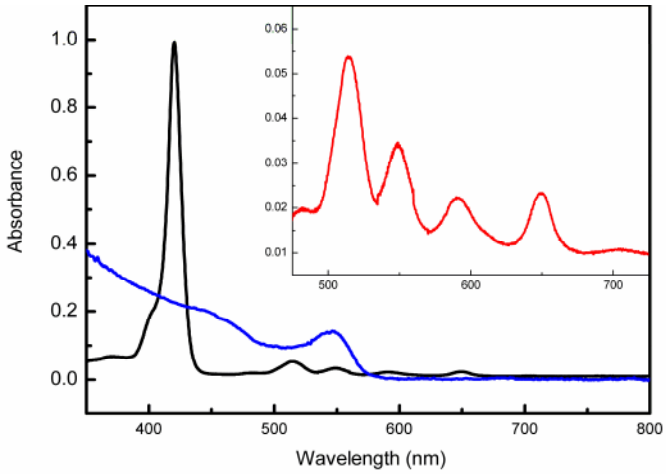

Figure 3. Absorption spectrum of TPP (black line) and CdSe QDs (blue line). Insert part: zoom in of the Q band of TPP (red line)

B. Steady-state Fluorescence Emission

After excitation, both of the steady-state and time-resolved fluorescence spectra are collected to investigate the spectral behavior of the donors before and after the energy transfer process. Fig.4. shows the normalized fluorescence luminescent intensity of Free QDs (blue line), Free TPP (black line) and the QD-TPP mixture (red line). It is seen evidently in Fig.4 that luminescent intensity of the CdSe QDs decreases strongly after addition of the porphyrins and meanwhile emission of TPP increases. No profile change in the emission spectrum is observed here, according to the characteristic of the non-radiative energy transfer. It is noticeable in this work that emission from the CH_2Cl_2 solution, which is treated as a background signal here, is well restricted due to the two-photon excitation mode. This should be valuable in the fluorescent imaging for the practical application.

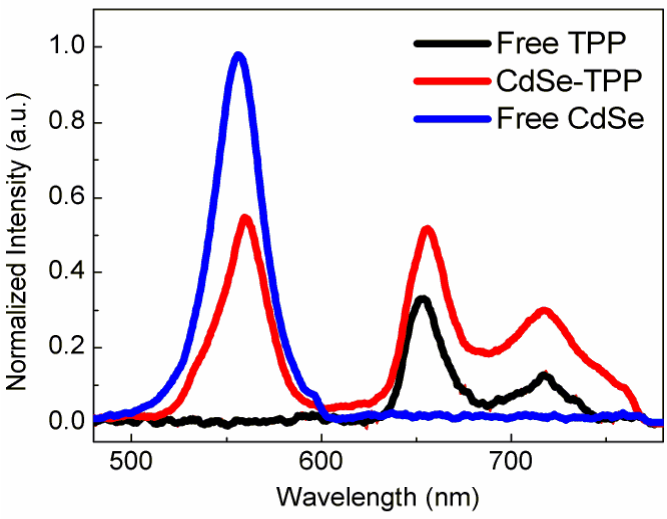

Figure 4. Steady-state two-photon fluorescence spectra of CdSe QDs, TPP and mixtures

It can also be found in Fig.4 that a red-shift of about 4nm in the emission spectrum of the CdSe QDs occurs after mixed with TPP. This may be explained by the energy transfer from QDs of small size to larger ones due to addition of the porphyrin sensitizers by reducing the distance of the particles. Moreover, the emission spectra of the donors and acceptors are separated so that can be easily distinguished, which is important in detecting and imaging of tumor.

C. *Time-resolved Experiments*

Decay kinetic curves of the CdSe QDs with and without TPP are displayed by Fig. 5. Fitting of the time-resolved experimental data are carried out after deconvolution using least square method follow the multi-exponential formula:

$$I(t) = \sum_{i=1}^{i} a_i \exp(-t/\tau_i) \tag{1}$$

In which τ_i is the decay lifetime of component i; a_i is the corresponding luminescent intensity at the time $t = 0$. When i is fixed to be 2, experimental data are well fitted by the bi-exponential decay curve. That means a combination of two components, excitonic and trapping emission, in the luminescent behavior of CdSe QDs, which has been discussed here and there.

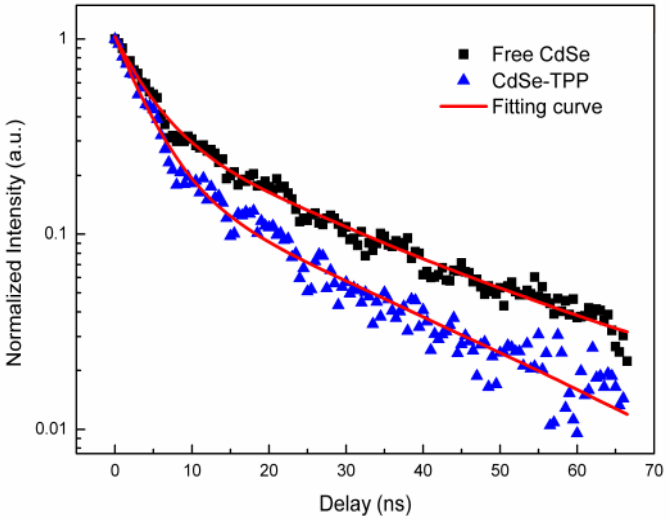

Figure 5. Luminescent decay kinetics of free CdSe QDs (filled black squares) and QDs in CdSe-TPP mixture (filled blue triangles) under 800nm laser excitation

It is obvious in Fig.5 that fluorescent decay kinetics course for CdSe QDs in mixture is faster than that in the free form, which confirms the existence of the fluorescence resonance energy transfer mechanism.

D. *Calculation of the Energy Ttransfer Efficiency*

For the non-radiative FRET, energy transfer efficiency can be estimated by not only the luminescent intensity of the donors measured with and without acceptors, but also the radiative lifetimes:

$$\Phi = 1 - \frac{\tau}{\tau_0} \tag{2}$$

In which τ and τ_0 are excited-state radiative lifetimes of donors measured in the presence and absence of acceptors, respectively.

For the multi-components condition, this formula should be modified by the average lifetime:

$$\Phi = 1 - \frac{\langle \tau \rangle}{\langle \tau_0 \rangle} \tag{3}$$

In this work, the average lifetime of the CdSe QDs in the presence and absence of acceptors is calculated to be 5.14ns and 7.48ns, respectively. Corresponding energy transfer efficiency is deduced to be 31.19%.

IV. Conclusion

The two-photon excitation spectral behavior of the quantum dot-organic dye system has been characterized to study the fluorescence resonance energy transfer from donors to acceptors in the present work. Both steady-state and time-resolved data of the CdSe QDs with and without the porphyrins have been recorded and compared. Evident transfer results are achieved. An energy transfer efficiency of about 31% is estimated taking use of the radiative lifetime of the donors. Background emission is effectively restricted by using of two-photon excitation geometry. This work confirms that combination of QDs and Porphyrins can provide an indirect way of activating the photosensitizers under two-photon excitation. It could be helpful to take advantage of the semiconductor QDs associated with two-photon excitation technique in the clinical application of PDT.

Acknowledgment

This work is supported by the National Natural Science Foundation of China (Grant Nos. 20573028 and 60478015). Our special thanks go to Doctor Limin An for providing the sample for the experiments and Doctor Wenzhi Wu for writing the lifetime calculation program.

References

[1] K. S. Samkoe, and D. T. Cramb, "Application of an ex ovo chicken chorioallantoic membrane model for two-photon excitation photodynamic therapy of age-related macular degeneration," *J. Biomed. Opt.* vol. 8, pp. 410-417, July 2003.

[2] S. Kim, T. Y. Ohulchanskyy, H. E. Pudavar, R. K. Pandey, and P. N. Prasad, "Organically modified silica nanoparticles co-encapsulating photosensitizing drug and aggregation-enhanced two-photon absorbing fluorescent dye aggregates for two-photon photodynamic therapy," *J. Am. Chem. Soc.* vol. 129, pp. 2669-2675, Feb. 2007.

[3] T. J. Beck, M. Burkanas, S. Bagdonas, Z. Krivickiene, W. Beyer, R. Sroka, R. Baumgartner, and R. Rotomskis, "Two-photon photodynamic therapy of C6 cells by means of 5-aminolevulinic acid induced protoporphyrin IX," *J. Photoch. Photobio. B: Biology* vol. 87, pp. 174-182, Apr. 2007.

[4] S. P. Wang, N. Mamedova, and N. A. Kotov, "Antigen/antibody immunocomplex from CdTe nanoparticle bioconjugates," *Nano Lett*. vol. 2, 817-822, July 2002.

[5] Y. Nagasaki, T. Ishii, and K. Kataoka, "Novel molecular recognition via fluorescent resonance energy transfer using a Biotin-PEG/Polyamine stabilized CdS quantum dot," *Langmuir* vol. 20, pp. 6396-6400, June 2004.

[6] A. R. Clapp, T. Pons, I. L. Medintz, J. B. Delehanty, J. S. Melinger, T. Tiefenbrunn, P. E. Dawson, B. R. Fisher, B. O'Rourke, and H. Mattoussi, "Two-photon excitation of quantum-dot-based fluorescence resonance energy transfer and its applications," *Adv. Mater*. vol. 19, pp. 1921-1926, 2007.

[7] A. C. Samia, X. Chen, and C. Burda, "Semiconductor quantum dots for photodynamic therapy," *J. Am. Chem. Soc*. vol. 125, pp. 15736-15737, Dec. 2003.

[8] L. X. Shi, B. Hernandez, and M. Selke, "Singlet oxygen generation from water-soluble quantum dot-organic dye nanocomposites," J. Am. Chem. Soc. vol. 128, pp. 6278-6279, Apr. 2006.

3B1-2

Development of Single Cell Biochip Platform based on Silicon for Multiple Patch Clamping Technology

Chih-Yuan Chen[1], Hao-Kai Ken[3], Shin-Hung Kuo[1], Jheng-Jhang Li[3], Ching-Hsing Luo[12], *IEEE member,* Jianmin Cui[4]

[1]Department of Electrical Engineering, National Cheng Kung University, Tainan, Taiwan,
[2]Micro/Nano Science and Technology, National Cheng Kung University, Tainan 701, TAIWAN
[3]Institute of nanotechnology and microsystems engineering, National Cheng Kung University, Tainan, Taiwan
[4]Department of Biomedical Engineering, Washington University, St. Louis, MO 63130, USA.

Abstract — The single cell study is crucial for tissue engineering, drug screening, and the opening of DNA code for life expressions. To study the single cell, it is involved in the second messengers or the ion channel activities concerned with the electrophysiological phenomena. However, it is so difficult to get the ion channel activity by whole cell clamp or even patch clamp. How to release the difficulty in patching clamp for the world wide use in any lab as easy as PCR becomes a hot issue now. Biochip fabricated by N/MEMS technique is one alternative to make it come true and this is the solution in this paper to present the possible idea and workout. Here we present the cell attachment technique to grab the cell successfully and the N/MEMS process to make a micrometer hole in one of an array of electrode for the cell clamp. The breakthrough is coming soon to push the opening of DNA code theory forward with a great step.

Keywords — ***drug screening, ion channel, patch clamp, PCR***

I. INTRODUCTION

Due to Human Genome Project (HGP), the human DNA code is opened. After that, some researches are beginning to focus on the interaction of DNA, protein and diseases. Drug discovery nowadays is needed to the screening large number of compounds achieved by using high-through put screening (HTS) technology [1]. Thus, how to accelerate the studied of ion channel will play an important role in this issue. Traditionally, patch-clamping is a powerful method for investigating the function and regulation of ion channel. However, it requires high precisely pulling pipettes placed in vicinity of the cell by a skillful operator using manipulator. Because of these, the patch-clamp technology has not been widely used in genomics, proteomics and drug screening [2].

In 2001, some researches try to design an automated patch-clamp planar chip for high-through put measurement. Next year, Lehnert *et al.* uses silicon wafer to manufacture a SiO_2 "micronozzle" for traditional patch-clamping pipette. The highest electrical seals they reported were on the order of 100–200 MΩ, and no ion channel activities were measured [3]. Because of the silicon wafer has free charge, it will result in capacitance effect for patch-clamp measurement. Therefore, how to get a gigaseal in planar patch-clamp chip is one of very important issues.

Recently, many researches manufacture the all kinds of planar patch clamp by Micro Electro Mechanical Systems (MEMS) technology and various substrates, such as silicon wafer, glass, quartz or PDMS and so on. For examples, Z. L. Zhang *et al.* manufactured the patch clamp ion-channel biosensor by silicon-on-insulator (SOI) substrate and focused ion beam (FIB) [4]. However, their fabrication process is too expensive to mass production. Anther one, Sigworth group in Yale University was the first to report successful recoding of cells using planar patch-clamp electrode. Their device was manufactured by PDMS. Although they can record the electrophysical signal of single cell, the gigaseal rate is so low. It is about 13% which may result from the surface geometry and roughness [5]. So, many researches tried to improve the gigaseal rate, successful recoding rate and reduce the cost.

Therefore, we manufactured the single cell biochip platform by MEMS technology and design the silicon nitride to be passivation layer to reduce the fabrication process in wet etching. Moreover, the single cell biochip platform was deposited silicon oxide film onto surface to decrease the capacitance effect. Additionally, we developed the cell attachment layer to crate a suitable environment for grasping single cell biochip onto the micro-aperture and getting gigaseal rate easily.

II. EXPERIMENTAL METHOD

A. Fabriction process

Four-inch silicon wafer was cleaned first by RCA clean process. Substrate was deposited silicon nitride on both sides by Low Pressure Chemical Vapor Deposition System (LPCVD). After depositing, AZ5214 (AZ5214, Clariant, Japan) was spin coating onto the bottom side to transfer our design pattern by photolithograph. The treated wafer was etched by TMAH. In the part of top side, we manufactured micro-apertures by photolithograph and ion coupled plasma (ICP). Additionally, the electrical isolation of the chip is necessary to reduce the capacitance and increase the signal to noise ratio (SNR) and effect for patch clamping. Thus, the silicon oxide was deposited on both sides (the thickness of top is 6μm and bottom is 3μm). Finally, the gold pattern was

This project was funded by landmark project (Project code: A0121) and the TW NSC (Project code: 96-2628-B-006-001-MY3).

**Contact author: Hao-Kai Ken, Institute of nanotechnology and microsystm engineering, National Cheng Kung University, No.1, University Road, Tainan City 701, Taiwan (R.O.C.) (Phone number: +886-6-2757575-62400#1975; e-mail: rustyzeon@gmail.com)*

#Contact author: Ching-Hsing Luo, Department of Electrical Engineering, National Cheng Kung University, No.1, University Road, Tainan City 701, Taiwan (R.O.C.)(Phone number: +886-6-275757-62375;E-mail:

transfer around the hole for modifying by photolithography. The chip was shown in Fig. 1.

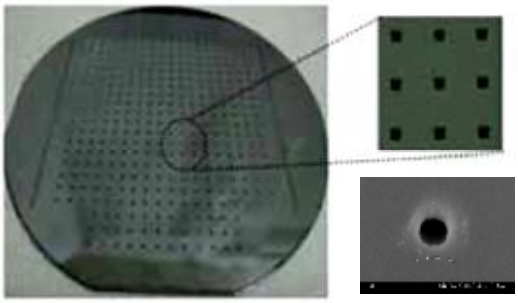

Figure 1. The microscopy images of single cell biochip

B. *Cell attachment layer*

Recently, the self-assembled monolayer was applied widely in many research fields. In this study, we integrate the self-assembled monolayer with micro contact imprinting technology to develop the cell attachment layer. The 11-MUA (674427, sigma-aldrich, USA) was used as cell attachment layer for grasping single cell. And, the RGD (A8052, sigma-aldrich, USA), tripeptide, was cross-linked onto the 11-MUA by EDC/NHS. Additionally, the PEOU was used as cell disfavor layer for preventing the cell absorption. After immobilizing the cell attachment layer, we test the cell capture efficiency by shake and suction. L929, HEK and CHO-K1 cell line were provided by Prof. Cui's lab in Washington University, St. Louis. (The coating process of cell attachment layer was shown in Fig. 2)

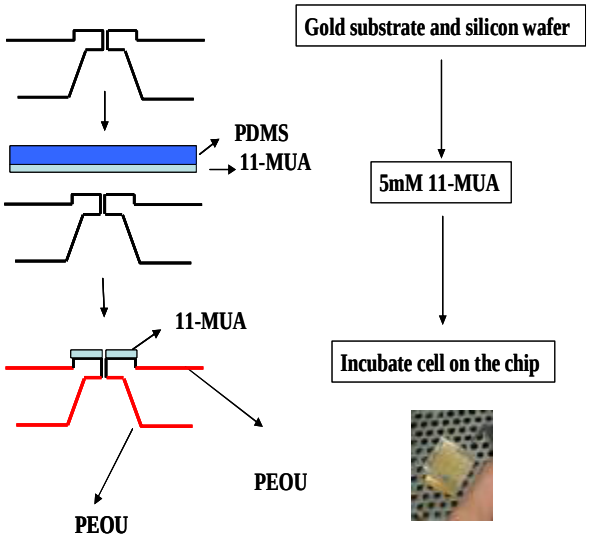

Figure 2. the coating process of cell attachment layer

C. *Prototype Package design*

In prototype package design, the single cell biochip platform was embedded into the poly-methylemethacrylate (PMMA) substrate by thermal bonding film (TBF-615, 3M, Taiwan). Then, the microcapillary pipettes (71900-100, Kimble, USA) were stuck onto the bottom side of prototype package. The Package process was shown in Fig. 3.

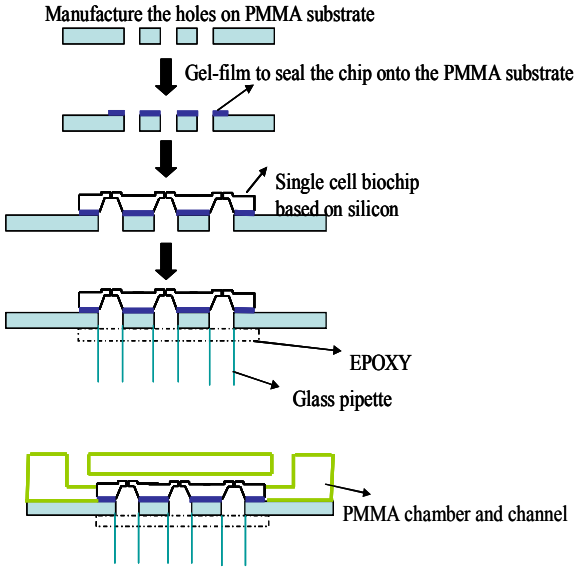

(a)

(b)

Figure 3. (a) The schematic of package process (b) the top view and bottom view of prototype package

III. RESULTS AND DISCUSSION

The single cell biochip platform was manufactured successfully by MEMS technology. The image of SEM was shown in Fig. 4. The diameter of aperture is about 3 μm after depositing the silicon oxide. However, the surface roughness around aperture is not very smooth. It may affect the formation of gigaseal.

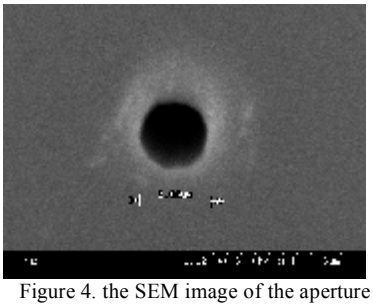

Figure 4. the SEM image of the aperture

In cell attachment test, the results of the cell attachment experiments (shown in Fig. 5), the performance of 11-MUA was better than 11-MUA/RGDS. Although the 11-MUA can grasp the single cell without shake and suction, the cell capture efficiency is low because of the cell was static onto single cell biochip after dropping. Moreover, the cell attachment layer of 11-MUA can sterilize by ethanol solution

and RGD is too expensive to use as the material of cell attachment layer and the capture efficiency is poor in this study. Therefore, the 11-MUA was used as the cell attachment of the single cell biochip platform. On the other hand, the PEOU was used as cell disfavor layer.

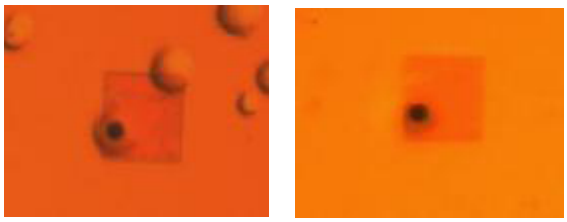

(a) (b)

Figure 5. (a) The CHO cell was capture onto the aperture with 11-MUA (b) no CHO cell was capture with 11-MUA/RGD

Due to the low capture efficiency of 11-MUA, we tested the cell attachment with shake in prototype package. The results show the cell capture efficiency can be improved by shake and the maximum efficiency of cell capture is about 30%~40%. The average cell capture efficiency is about 25% without suction (shown in Table 1). We tested the four different shake speeds and incubation methods (drop the cell onto the chip and shake for 30 mins and 1 hour and the others are incubated for 30 mins firstly and shake for 30 mins and 1 hour). Finally, we integrated the suction method with cell attachment layer to grasp the single cell onto apertures. The cell capture efficiency can achieve 100% with suction and cell will be grasped immediately.

Table 1: the efficiency of cell capture in prototype and new package chip

	Shake 30 mins	Shake 1 hour	Incubate 30 mins firstly and shake 30 mins	Incubate 30 mins firstly and shake 1 hour
100 rpm	x	x	x	x
50 rpm	x	x	x	x
25 rpm	**11.11%**	**11.11%**	**33.33%**	**22.22%**
Shake by hand	None	None	**44.44%**	None

X: failure, no cell on hole (all experiments times: n=5)

After coating cell attachment layer, we integrated the prototype chip and patch clamp equipment (Axon200B, USA) (shown in Fig. 6). The top side of prototype chip was put into bath chamber and the measure electrode inserted into glass pipette (in bottom side). Then, we measured the capacitance of the single cell biochip and compare with traditional patch clamping glass pipette.

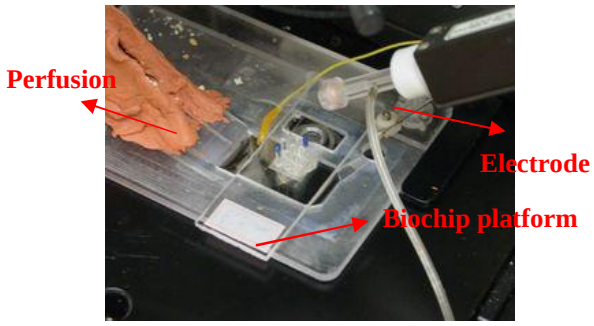

Figure 6. The single cell biochip platform integrated with patch clamp equipment

When the bath solution and glass pipette solution passed through the 3-4 μm micro apertures, the value of resistance was 2.89 MΩ (shown in Fig. 7 (b)). After incubating the CHO cell onto the chip, the resistance was increased to 5.87 MΩ. Compare to the traditional patch-clamping pipette (the resistance is 1.06 MΩ, shown in Fig. 7(a)), the resistance of single cell biochip was large than it. It will be easy to achieve the gigaseal. However, the suction force did not work on the cell membrane when achieving the gigaseal further. It may result from depositing the silicon dioxide reduced the capacitance effect in our fabrication process.

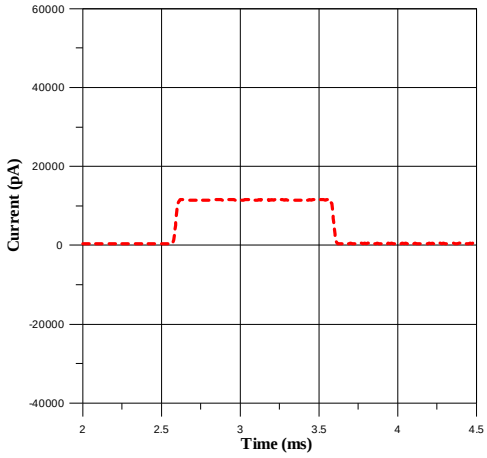

(a)

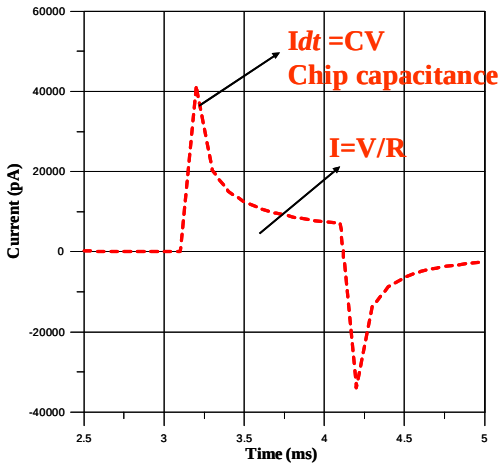

(b)

Figure 7. The measurement data of (a) traditional patch-clamping pipette, (b) the single cell bio chip platform passed through with solution and

To eliminate the block of aperture and reduce the surface roughness, BOE buffer was used. After washing BOE buffer, the value of resistance was 555 KΩ when the bath and pipette solution passed through the hole. After incubating the CHO cell, the resistance was increased to 1.6 MΩ. Although, we tried to get the gigaseal, the resistance did not increase when we use suction. It may result from the diameter of aperture (5-6 um) became bigger after washing BOE buffer or the hole blocks by debris of the cell after incubating (with suction). After washing the BOE solution, the capacitance effect became larger than without washing. In fabrication process, the silicon oxide was deposited to reduce the capacitance and condense the diameter of aperture.

Another hand, we use the LCR meter to measurement the capacitance after depositing various thicknesses of silicon dioxide. The schematic of whole set up was shown in Fig. 8.

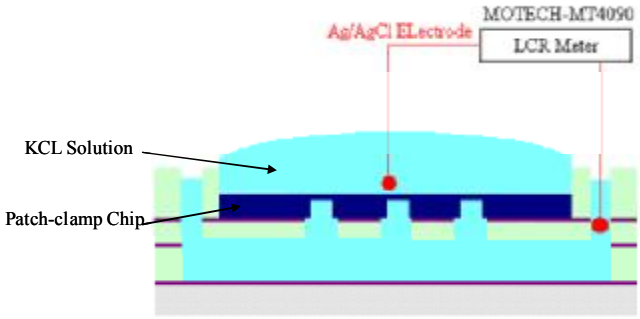

Figure.8 The schematic of the LCR meter measurement

According to the results, the capacitance will gradually reduce with increasing the thickness of silicon dioxide (Shown in Fig. 9). The silicon dioxide can not eliminate completely, and it may block the hole. Hence, how to deposit the reasonable thickness is another issue.

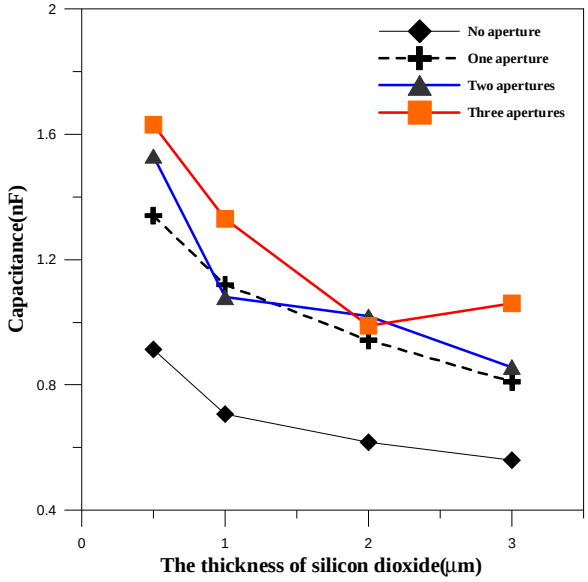

Figure 9. The capacitance with various thickness of silicon dioxide

IV. CONCLUSION

The single cell biochip was manufactured successfully by MEMS technology and packaged with PMMA. The chip was integrated with patch-clamping equipment completely and measured the capacitance and resistance. According to above results, the single cell biochip has higher resistance than traditional patch-clamping pipette. In theoretically, it can be easier to achieve the gigaseal than traditional patch-clamping pipette. However, the capacitance effect did not eliminate completely by depositing silicon oxide and the silicon oxide may result in the block of hole when achieving the gigaseal further. Although depositing silicon oxide can reduce the capacitance, the holes may block by it. Additionally, the surface roughness around the aperture is very important issue. It can affect the formation of gigaseal. Finally, we will manufacture the aperture by the excimer laser and try to eliminate the block hole and surface roughness by BOE solution.

V. REFERENCE

[1] A. Stett, V. Bucher, C, Burhardt, U. Weber, W. Nisch,"Patch-clamping of promary cardiac cells with micro-openings in polyimide films", Medical & Biological Engineering & Computing 2003, Vol. 41, pp.233-240.

[2] J. Seo, C. Ionescu-Zanetti, J. Diamond, R. Lal, L. P. Lee,"Integrated multiple patch-clamp array chip via lateral cell trapping junctions", APPLIED PHYSICS LETTERS, 2004, Vol 84, pp. 1973-1975.

[3] Lehnert, R. Netzer, U. Bischoff and M. A.M. Gijs, SiO nozzle array-based patch-clamp microsystem,*Proc. Micro Total Anal. Syst.* **1** (2002), pp. 28–30

[4] Z. L. Zhang, T. Asano, H. Uno, R. Tero, M. Suzui, S. Nakao, T. Kaito, K. Shibasaki, M. Tominaga, Y. Utsumi, Y. L. Gao, T. Urisu, "Fabrication of Si-based planar type patch clamp bio sensor using silicon on insulator substrate", Thin Solid Film, 2008, Vol. 516, pp. 2813-2815.

[5] T. Sordel, S. Garnier-Raveaud, F. Sauter, C. Pudda, F. Marcel, M. D. Waard, C. Arnoult, M. Vivaudou, "Hourglass SiO_2 coating increases the performance of planar patch-clamp", Journal of Biotechnology, 2006, Vol. 125, pp. 142-154.

[6] S. pandey, R. Mehrotra, S. Wykosky, M. H. White,"Characterization of a MEMS Biochip for planar patch-clamp recording", Solid-State Electronics, Vol. 48, pp. 2061-2066,2004.

[7] B. Matthews and J. W. Judy, " Design and Fabrication of a Micromachined Planar Patch-Clamp Substrate with Integrated Micro Fluidics for Single-Cell Measurements", JOURNAL OF MICROELECTROMECHANICAL SYSTEMS, Vol. 15, No.1, pp. 214-222,2006.

3B1-3

Building the Long, Periodic ssDNA Nanotemplate from Tumor Marker Recognition for Nanodevice

Ming-Yu Lin[1, 2]*, *Student Member*, *IEEE*, Fu Han Ho[1], Chung Yao Yang[1], Jiann-Shiun Kao[1], J. Andrew Yeh[3], and Yuh-Shyong Yang[1, 2]

[1]*Instrument Technology Research Center, National Applied Research Laboratories, Taiwan*
[2] *Institute of Biochemical Engineering, National Chiao Tung University, Taiwan*
[3] *Institute of Nanoengineering and Microsystems, National Tsing Hua University, Taiwan*

***Abstrac*—The programmable self-assembly of molecular nanostructures plays a crucial role in the development of nanodevices for molecule recognition. A self-assembly, periodic ssDNA nanotemplate based on aptameric recognition of tumor marker, PDGF was in situ constructed on the silicon-based substrate. The long, periodic ssDNA nanotemplate was further elongated up to 454 nm through rolling circle amplification at room temperature. The process of self-growing DNA nanotemplate based on aptameric recognition was directly visualized through nanoprobing technology.**

Keywords ***—nanodevice, nanotemplate, DNA, tumor marker***

I. INTRODUCTION

The field of DNA nanotechnology aims at the construction of complex nanostructures through self-assembly and self-organization strategies. DNA nowadays is more than just a carrier of genetic blueprint for life, but is also used as assembling materials to construct the DNA nanostructures. DNA is a remarkably perfect molecule for self-assembly with fine regulations, because of the extremely precise base-pairing rules, structure features, and serving as a high-promising template for organizing nanomaterials in a programmable way. The base-pairing strategy has been used to construct an artificial branched DNA tile[1], and build the tiles into a periodic complex two-dimensional (2D) lattice[2]. In recent years, there has been increasing interests in the utilization of nanostructures for nanodevices with strong potential for future medical applications. For example, complex sensors can be realized by integrating the sensors with artificial functionalized DNA nanostructure that recognized by targets and amplifying the molecular signals. In this study, we aim to construct the long, periodic DNA nanotemplate from the tumor marker, platelet derived growth factor (PDGF).

II. EXPERIMENTAL SECTIONS

Rolling circle amplification (RCA) performed at room temperature enables the construction of DNA nanostructure and self-assembled without tedious temperature control system for a wide range of applications, such in-field diagnosis. PDGF recognition by aptamers were followed by the previous reported article [4], except for denaturing the PDGF aptamer at 95 °C , cooled to room temperature slowly and scaling down to 10 μl as total reaction volume. Each cover glass was then incubated with 10 l of RCA mixture (40 mM Tris-HCl pH 7.5, 50 mM KCl, 10 Mm MgCl2, 5 mM (NH4)2SO4, 66.7ng/ l T4 gene-32 protein, 3 units of Phi 29 DNA polymerase, and 1 l of terminated circularized aptamers at room temperature for 2 hours).Fig. 1a showed that PDGF was recognized by PDGF aptamer on the artificial synthesized linear form of ssDNA. The binding of PDGF induced the conformation-switched of ssDNA, and formed the circular form of ssDNA by T4 ligase. ssDNA with PDGF-BB aptamer sequence formed the 2D structure was predicted through Mfold program [3] (Fig. 1b).

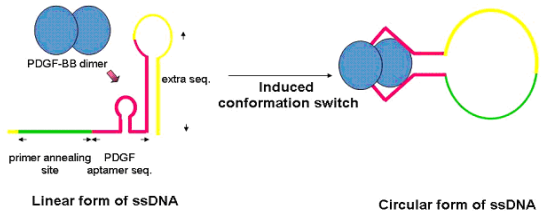

(b)

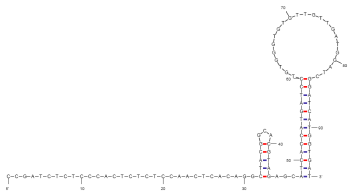

Fig. 1. Conformation-dependent aptamer-mediated RCA: (a) PDGF-BB and single-stranded DNA (ssDNA) sequence are used to recognize PDGF specifically. The red strand contains the PDGF-BB binding aptamer sequence, the green strand contains immobilized RCA primer binding site, and the yellow strand contains the extra sequence to form the circularized ssDNA. (b) Prediction the 2D structure of PDGF aptamer for the PDGF recognition by Mfold program.

III. CURRENT RESULTS

It was the first construction of long, self-growing ssDNA nanotemplate on the silicon-based substrate to recognize tumor marker at room temperature. The recognition event of tumor marker triggered the linear ssDNA refolding. Circularized ssDNA was recognized by immobilized RCA

primer and initiated the RCA reaction. Circularized ssDNA provides the code for the DNA nanostructure and serves as the template in the RCA reaction. Phi29 DNA polymerase served not only as the enzyme for the self-assembly of ssDNA nanostructure, but also as a gate keeper to proof-read the right sequence code on the DNA nanostructure. (Fig. 2a). In the study, we demonstrate the applicability of forming DNA nanotemplate on the glass through silanization (Fig. 2b).

Because of the rolling circle replication while DNA polymerization, the synthesized ssDNA nanotemplate inherent the features of concatamer, which provides the periodic structure in the ssDNA nanotemplate. The molecular ssDNA structure was predicted by Mfold programme (Fig.3). The length of each repeat was 106 n.t., separated with 10 n.t. and formed two loop structures. Precise orientation and controlled position are the crucial issue in the synthesized nanostructure and applied into the development of nanodevices with nanostructure. DNA with 5' to 3' orientation and sequence specificity enable the DNA-assembly nanostructure with precise orientation. Fig. 4 showed the three topographies of nanostructures on the glass. Figure 4a showed the SAM film formed by silanization of APTES at 1 × 1 μm2. Fig. 4b showed the immobilization of amine-labeled at the 5'-terminal of RCA primer around 23 nm in diameter at 1 × 1μm2 . Fig. 4c presented the self-assembly ssDNA nanotemplate synthesized by aptamer-based RCA reaction on the glass at 4 × 4 μm2. Some distinguished elongated DNA nanostructures with dumbbell-headed or comet-tail were observed.

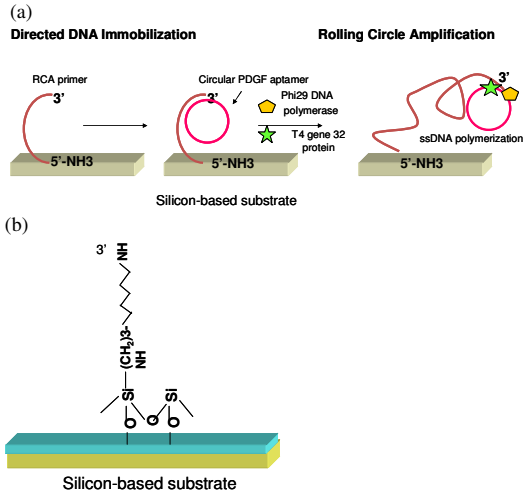

Fig. 2. Self-assembly DNA nanostructure through RCA. (a) A RCA primer labeled with –NH3 at its 5'-end was immobilized on a SiO2-based chip surface. Single-stranded DNA concatamer is synthesized by using circular PDGF aptamer as template. (b) Formation of ssDNA concatamer as 1D nanotemplate on the silicon-based substrate treated with silanization

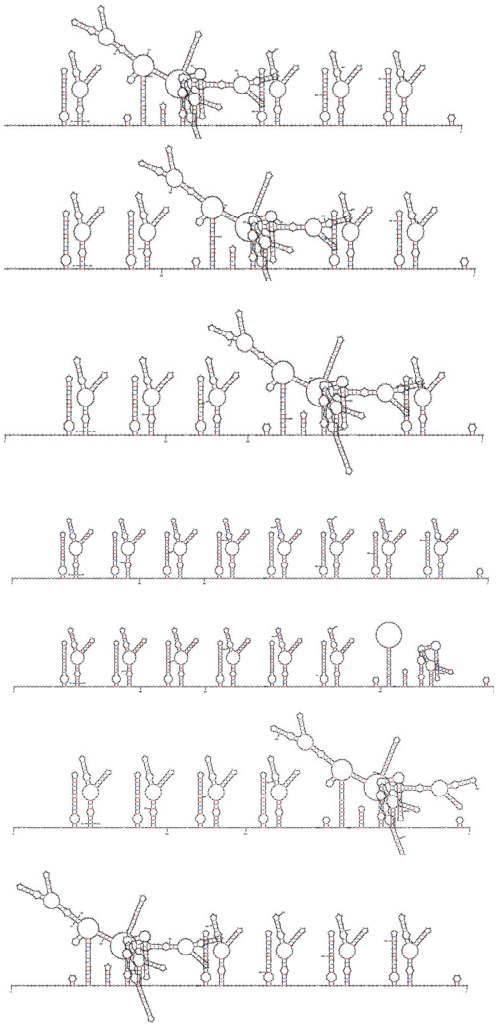

Fig. 3. Prediction the 2D ssDNA nanostructure after PDGF recognition by Mfold program(Zuker 2003; Markham and Zuker 2008). The prediction was based on the 9 repeated complementary sequence of PDGF aptamer on the DNA nanostructure with [Na+] = 50 mM, and [Mg2+] = 20 mM at 25 °C condition. The prediction showed that one of the periodic 2D ssDNA nanostructures was self-assembled by RCA reaction on the silicon-based substrate. The linear form on this structure can be another nanotemplate to form another expanded nanostructures.

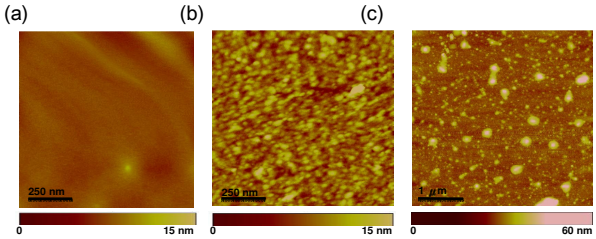

Fig. 4. AFM topography images of the time-dependent polymerization of the ssDNA concatamers by the RCA process (a) SAM film forming on the glass surface (b) RCA primer immobilized on the SAM surface (c) Self-assembly ssDNA nanostructure constructed after 2 hours RCA

IV. REFERENCES

[1] N. C. Seeman, "DNA in a material world," Nature, vol. 421, pp. 427-31, Jan 23 2003.
[2] C. Lin, Y. Liu, S. Rinker, and H. Yan, "DNA tile based self-assembly: building complex nanoarchitectures," Chemphyschem, vol. 7, pp. 1641-7, Aug 11 2006.
[3] N. R. Markham and M. Zuker, "UNAFold: software for nucleic acid folding and hybridization," Methods Mol Biol, vol. 453, pp. 3-31, 2008.
[4] L. Yang, C. W. Fung, E. J. Cho, A. D. Ellington, "Real-time rolling circle amplification for protein detection." Anal Chem *79*, pp.3320-3329. 2007

3B1-4

Integrated Microfluidic System for Electrochemical Sensing of Glycoslated Hemoglobin

Chao-June Huang[1], Hui-Ching Chien[2], Tse-Chuan Chou[3] and Gwo-Bin Lee[1*]

[1] *Department of Engineering Science, National Cheng Kung University, Tainan 701, Taiwan*
[2] *Department of Chemical Engineering, National Cheng Kung University, Tainan 701, Taiwan*
[3] *Department of Chemical Engineering, Tatung University, Taipei 104, Taiwan*

Abstract **- Accurate detection of glycosylated hemoglobin (HbA_{1C}) usually requires a time-consuming and labor-intensive process. Therefore, this paper reports an integrated microfluidic chip capable of detecting the concentration of HbA_{1C} in an automatic format. The integrated microfluidic system was fabricated by using microelectromechanical system (MEMS) techniques, which can perform several crucial process involved for detection of HbA_{1C} on a single chip, including separation of red blood cells (RBC), sample/reagent transportation, mixing, cell lysis, and an electrochemical sensing. Experimental data showed that the developed system can successfully detect the concentration of purified HbA_{1C} samples. The development of the integrated microfluidic system may be promising for monitoring of metabolic diseases.**

Keywords ***- cell separation, electrochemical, glycosylated hemoglobin, microfluidics***

I. INTRODUCTION

HbA_{1C} is one of the most prominent minor hemoglobin (Hb) components in normal human erythrocytes [1]. HbA_{1c} is formed by a non-enzymatic reaction of glucose with the amino-terminal valine of the β-chain [2]. The level of glycated Hb in the blood of diabetes patients can be clinically related to the average glucose level during the erythrocyte lifespan (100-120 days). With a normal turn-over of erythrocytes, the HbA_{1c} level therefore reflects the blood glucose concentration of the previous 3 months. Clinical methods for the determination of HbA_{1c} include a crucial separation step based on differences in either charges (ion-exchange chromatography [3] and electrophoresis [4]) or structures (immunoassay [5] and boronate affinity chromatography [6]) prior to colorimetric quantification of glycated hemoglobin. However, it is a labor-intensive and relatively costly process for clinical practice. Nowadays, blood glucose testing is a well established method by using electrochemical sensing [7]. Electrochemical methods for clinical diagnosis have advantages such as good selectivity, relatively low cost and the potential for miniaturization and automation [8, 9]. However, electrochemical determination of glycated hemoglobin is still under extensive investigation and a reliable platform for fast detection of HbA_{1C} is still of great need.

In this study, an electrochemical sensing system to detect the concentration of HbA_{1C} has been demonstrated. By using the cyclic voltammetry (CV) method, the amount of the HbA_{1C} can be precisely measured. Additionally, a microfluidic chip integrated with circular micropumps and normally-close microvalves was used to facilitate the transportation of the samples in an automatic mode with less human intervention. With this approach, automatic and precise measurement of HbA_{1C} can be performed with fewer samples (200 μL) within a shorter period of time (220 seconds).

II. MATERIALS AND METHODS

(a) Chip Design

The entire process for automatic detection of HbA_{1c} is schematically shown in Fig. 1. Briefly, human whole blood sample was first suspended in Dulvecco's modified eagle medium (DMEM) buffer and loaded into the red blood cells (RBC) separation/lysis chamber (Fig. 1(a)). The electrodes of the RBC separation module could generate a positive dielectrophoretic (DEP) force to trap the RBC on the electrode surface. The other substances such as white blood cells (WBC) and platelets were then washed away utilizing the micropumps (Fig. 1(b)). RBC lysis buffer was then transported into the RCB separation/lysis chamber, followed by gentle mixing of samples and reagents (Fig. 1(c)). The released HbA_{1C} was transported into the HbA1c detection chamber where sensing electrodes were used for electrochemical detection of HbA_{1c} (Fig 1. (d)).

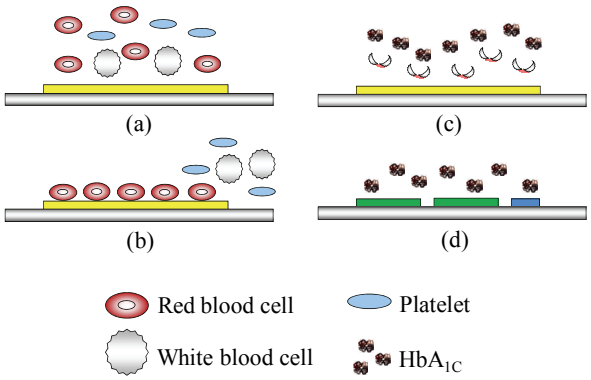

Figure 1. Schematic illustration of the experimental procedures for HbA_{1C} detection.

(b) Chip Fabrication

The chip was fabricated by using MEMS techniques. The layout of the microfluidic chip is schematically shown in Fig. 2. The chip consists of two PDMS layers and one glass plate patterned with electrodes for RBC separation and electrochemical sensing. Three major modules, including a microfluidic control module, a RBC separation module and an electrochemical detection module, are integrated on the chip to

This project was funded by National Science Council in Taiwan.
**Contact author: gwobin@mail.ncku.edu.tw*

perform the required functions. The microfluidic control module consists of micropumps, microchannels, microvalves, and microchambers. A set of microelectrodes are used to induce DEP forces for RBC separation. Another set of microelectrodes are used for electrochemical sensing.

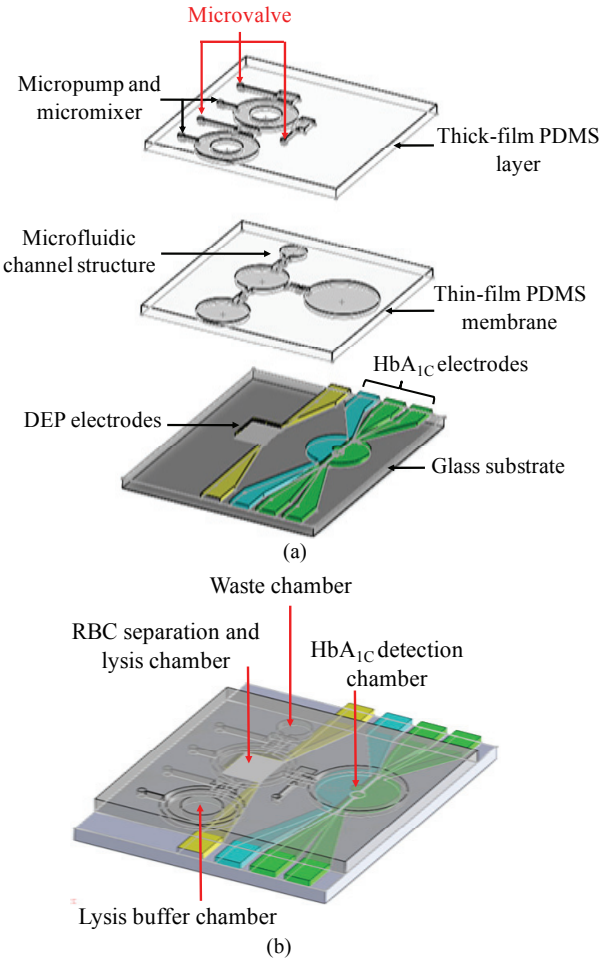

Figure 2 (a) An exploded view of the microfluidic chip. (b) A schematic illustration of the microfluidic chip, which is comprised of three major modules, including a microfluidic control module, a RBC separation module, and an electrochemical detection module.

The electrochemical HbA_{1C} detection module is composed of three electrodes on a glass substrate for sensing the concentration of the HbA_{1C} electrochemically. The three sensing electrodes, including a working (carbon paper), a counter (Pt) and a reference (silver, Ag) electrode, are designed and fabricated using the thin-film deposition process. Note that an Au DEP electrode is also fabricated on the glass substrate for purification of RBC from the whole blood.

Fig. 3(*a*) shows a simplified fabrication process of the sensing electrodes involving a standard lithography, thin-film deposition and lift-off processes. Note that the HbA_{1C} sensor was fabricated on a glass substrate. The glass substrate was first cleaned using a piranha solution (H_2SO_4:H_2O_2 = 3:1) at 190◦C for 3 min. A positive photoresist (AZ 4620, Clariant Inc., USA) was then spin-coated and patterned using the photolithography process. An electron-beam evaporation process was used to deposit a Pt layer onto the glass substrate that had previously been deposited with a thin titanium (Ti) layer to enhance Pt adhesion. The Pt layer was then patterned using a standard lift-off process to form the sensing electrodes of the HbA_{1C} sensors. Similarly, layers of Ag and Au were deposited and patterned to form the reference/DEP electrodes [10]. Finally, the carbon paper was fixed onto the working electrode utilizing colloidal silver. After the fabrication of the working (carbon paper), counter (Pt) and reference (Ag) electrodes, the reference electrode of the HbA_{1C} detection chip has an AgCl layer formed on top of the Ag electrode. This AgCl/Ag electrode was made by using a solution of FeCl3 (0.1 M) to form an AgCl layer. Finally, the fabrication process was completed by washing the reference electrode in distilled water [11].

The microfluidic control device is comprised of a double-layer PDMS structure. Fig. 3(b) is a schematic representation of the microfabrication process by using a computer-numerical control (CNC) machining process and a PDMS replication process. Master molds with microstructures on polymethylmethacrylate (PMMA) plates are first formed by using a CNC machine (EGX-400, Roland Inc., Japan) equipped with a 0.5 mm drill bit (Fig. 3(b-1)). The rotational speed and feed rate of the drill bit are 26000 rpm and 15 mm min^{-1}, respectively. This is then followed by a PDMS casting process to form inverse images of the air chamber molds and a PDMS spin-coating process to form inverse images of the fluidic channel (Fig. 3(b-2)). Finally, the PDMS structures and the glass substrate are bonded together utilizing an oxygen plasma treatment to form the complete HbA_{1C}-sensing chip (Fig. 3(b-3)) [12].

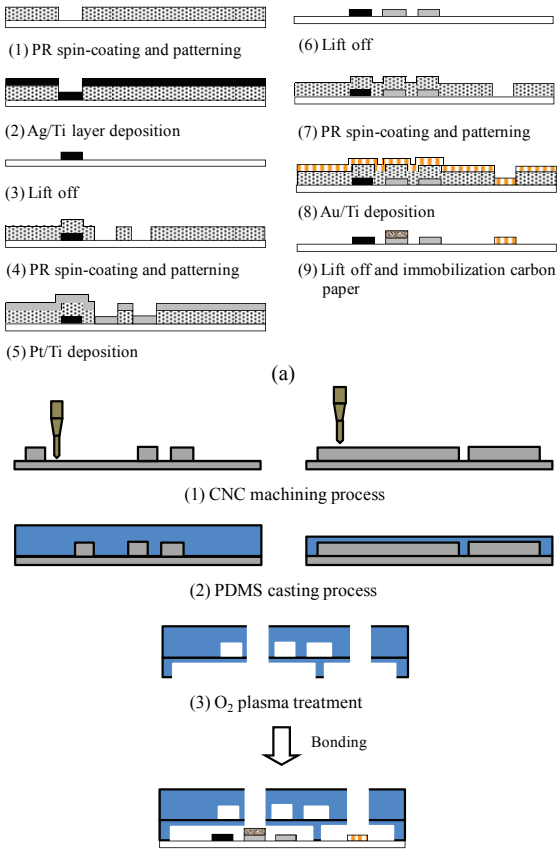

(b)

Figure 3. Simplified fabrication process for the microfluidic chip for HbA_{1C} detection. (a) Fabrication of HbA_{1C}-sensing and DEP electrodes. (b) Fabrication of the microfluidic control module with double-layer PDMS structures.

(c)Electrochemical Sensing principle

In this study, the HbA_{1C} detection was conducted by using the electrochemical sensing method, in which the HbA_{1C} was detected by measuring the difference of peak currents between a bare work electrode and an HbA_{1C}-adsorption electrode. The HbA_{1C} can be adsorbed on the carbon electrode. The HbA_{1C}-adsorbed surface of the carbon electrode cannot allow the electrochemical reaction. It then causes the drop of the response current which is related to the concentration of HbA_{1C} in the sample. Therefore, the concentration of HbA_{1C} can be measured from the drop of response current between a bare electrode and an HbA_{1C} electrode.

III. Results and Discussion

(a) Isolation and collection of RBC

RBC manipulation by using the DEP forces is successfully demonstrated as shown in Fig. 4. In order to generate the DEP forces, several crucial operation parameters need to be considered, including the applied voltage, the operation frequency, and conductivity and permittivity of the medium buffer. In the following experiments, cell samples are first suspended in DMEM buffer, and the operational voltage and frequency applied to the DEP microelectrode structure are 15 Vp-p and 16 MHz, respectively. During operation, the whole blood are first suspended in DMEM buffer with a conductivity of 72 μ S/cm [13]. The Cells are first randomly suspended around the microelectrode array region in the RBC separation and lysis chamber (Fig. 4(a)). When the positive DEP forces are generated, the RBC are captured and collected at the edge of microelectrodes, as shown in Fig. 4(b). The other substances such as WBC and platelets were then washed away utilizing the micropumps. The capture efficiency of the RBC was estimated to be approximately 81 %.

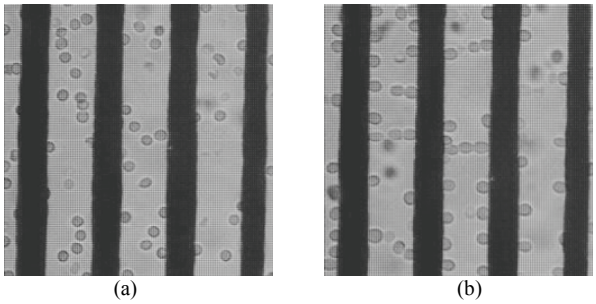

(a) (b)

Figure 4 (a) RBC are randomly distributed originally. (b) RBCs are attracted on the edges of the microelectrodes.

(b)Characterization of microfluidic control medule

The main functions of the circular micropump are for delivering liquid and liquid mixing. The performance of the micropump was characterized experimentally. The new pneumatic micropump integrated with a normally-closed microvalve [14] was adopted to rapidly transport the liquid. The PDMS-based membrane structure could be deflected downwards when compressed air is supplied. The sample flow was then transported forward inside the microchannel accordingly. Experimental results revealed that the flow rate can be regulated by adjusting the operational frequency of the EMV. The relationship between the liquid pumping rate and the driving frequency at 5 psi is shown in Fig. 5. When the driving frequency is higher than about 22 Hz, the pumping rate reaches a saturated value of about 25.4 µl/sec. This is caused by the lagging response of the PDMS membranes at high driving frequencies.

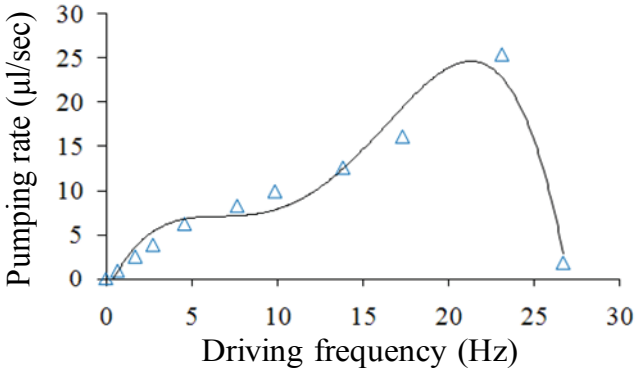

Figure 5. The relationship between the pumping rate and the driving frequency of EMV at an applied pressure of 5 psi.

In addition to the function of liquid delivery, observations also show that the circular micropump is able to successfully act as a micromixer when compressed air is supplied to the normally-close microvalve.

The liquid mixing function in the microfluidic system is also evaluated by mixing RBC and lysis buffer solution, as shown in Fig. 6. At first, RBC was loaded into the RBC separation/lysis chamber (Fig. 6 (a)). When the micromixer is driven at a frequency of 7 Hz and an air pressure of 5 psi, the RBC and lysis buffer are mixed to lyze the cells (Fig. 6 (b)). The released HbA_{1C} was then transported into the HbA1c detection chamber where sensing electrodes were used for electrochemical detection of HbA_{1c}. The entire process can be performed automatically by using the same microfluidic device.

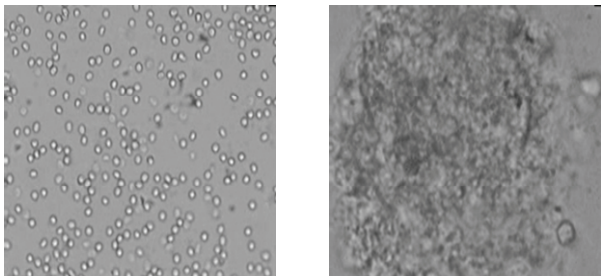

(a) (b)

Figure 6 (a) RBC before lysis. (b) RBC are mixed with lysis buffer and finally lyzed.

(c)Electrodechemical sensing of HbA_{1c}

For the measurement of the HbA_{1c} concentration, the phosphate buffer saline (pH value = 7.4) was injected into the HbA_{1C} detection chamber. Figure 7 shows the relationship between the output signal of the electrochemical sensor and the HbA_{1c} concentrations. The cyclic voltammetry was operated with a scan range from -0.1 to 1.0 V (versus Ag/AgCl) at a scan rate of 0.01 V/s by using a potentiostat equipped with a computerized electrochemical analyzer. The experimental results demonstrate the developed sensor can perform accurate measurement of the commercial HbA_{1C} concentrations ranging from 0 to 2 mg/ml. Measurement of HbA1c from clinical samples is undergoing. The developed system may provide a valuable tool to detect HbA_{1C} for routine monitoring of diabetic patients.

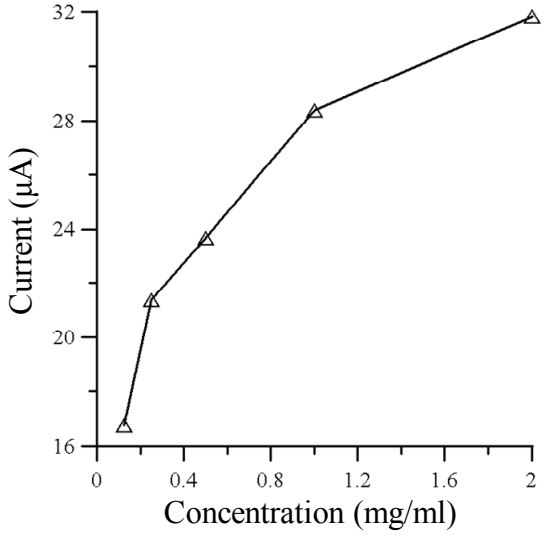

Figure 7. Output current of the HbA_{1c} sensor at various HbA_{1c} concentrations.

IV. CONCLUSION

This study presents an HbA_{1C} detection system using microfluidic and electrochemical sensing techniques. The experimental results showed that RBC can be successfully purified, collected and lysed in an automatic manner utilizing the DEP forces in a microfluidic system composed of a circular micropump and normally-close valves. The CV measurement can provide an approach to quantify the HbA_{1C} and may be useful as a simple method for the detection of HbA_{1C} concentration. The sample consumption of the proposed chip device is only 200 μL. When compared with the traditional HbA_{1C}-sensing method, smaller amounts of samples were required to perform faster detection by using the integrated microfluidic chip. Additionally, the microfluidic chip integrated with pneumatic micropumps and microvalves facilitates the transportation of the samples in an automatic mode with lesser human intervention. In this study, we only showed data using purified HbA_{1C} samples. In the future, clinic samples will be used for HbA_{1C} sensing. The developed system may provide a valuable tool to examine HbA_{1C} concentration for biomedical applications.

ACKNOWLEDGMENTS

The authors gratefully acknowledge the financial support provided to this study by the National Science Council in Taiwan (NSC 94-3112-B-006-002). The access provided to major fabrication equipment at the Center for Micro/Nano Technology Research, National Cheng Kung University is greatly appreciated.

REFERENCES

[1] R. Fluckiger and K. H. Winterhalter, “In vitro synthesis of HbA1,” FEBS Lett., vol. 71, pp. 356-360, 1976.

[2] H. F. Bunn, D. N. Haney, K. H. Gabbay and P. M. Gallop. “Further identification of the nature and linkage of the carbohydrate in hemoglobin A1c,” Biochem Biophys Res Commun., vol. **67**(1), pp. 103–109, 1975.

[3] D. E. Goldstein, R. R. Little, H. M. Wiedmeyer, J. D. England and E. M. McKenzie, “Glycated hemoglobin-methodologies and clinical applications,” Clin. Chem., vol. 32, pp. B64-B70, 1986.

[4] J. Hageman and G. Kuehn, “Assay of adenylate-cyclase by use of polyacrylamide-boronate gel columns,” Anal. Biochem., vol. 80, 547-554, 1977.

[5] A. P. F. Turner, B. Chen and S. A. Piletsky, “In vitro diagnostics in diabetes:meeting the challenge,” Clin. Chem., vol. 45, pp. 1596-1601, 1999.

[6] W. G. John, “Glycated haemoglobin analysis,” Ann. Clin. Biochem., vol. 34, 17-31, 1997.

[7] P. Connolly, “Clinical diagnostics opportunities for biosensors and bioelectronics,” Biosens. Bioelectron., vol. 10, pp. 1-6, 1995.

[8] G. Marko-varga, J. Emneus, L. Gorton and T. Ruzgas, “Development of enzyme-based amperometric sensors for the determination of phenolic-compounds,” TRAC-Trends Anal. Chem., vol. 14, pp. 319-328, 1995.

[9] J. Wang, “Amperometric biosensors for clinical and therapeutic drug monitoring: a review,” J. Pharm. Biomed. Anal., vol. 19, pp. 47-53, 1999.

[10] C. J. Huang, C. C. Lu, T. Y. Lin, T. C. Chou and G. B. Lee, “Electrochemical albumin-sensing system utilizing microfluidic technology,” J. Micromech. Microeng., vol. 17, pp. 835-842, 2007.

[11] C. J. Huang, Y. H. Chen, C. H. Wang, T. C. Chou and G. B. Lee, “Integrated Microfluidic Systems for Automatic Glucose Sensing and Insulin Injection,” Sens. Actuators, B, Chem., vol. 122, pp. 421-428, 2007.

[12] S. Y. Yang, J. L. Lin and G. B. Lee, “A vortex-type micromixer utilizing pneumatic-driven membranes,” J. Micromech. Microeng., vol. 19, Issue: 3, Article Number: 035020, 2009.

[13] C. H. Tai, S. K. Hsiung, C. Y. Chen, M. L. Tsai and G. B. Lee, “Automatic microfluidic platform for cell separation and nucleus collection,” Biomed. Microdevices, vol. 9 (4), pp. 533-543, 2007.

[14] K. Hosokawa, and R. Maeda, “A pneumatically-actuated three-way microvalve fabricated with polydimethylsiloxane using the membrane transfer technique,” J. Micromech. Microeng. vol. 10, pp. 415-420, 2000.

3B1-5

Detection of Staphylococcus Aureus Using Hydrothermally Roughened Substrates

Jung-Yen Yang[1], Yu Chen[2], Hui-Wen Cheng[3], *Student Member*, *IEEE*,
Chi-Hung Lin[1,2,4], and Yiming Li[1,3,5,*], *Member*, *IEEE*

[1] *National Nano Device Laboratories, Hsinchu, Taiwan*
[2] *Institute of Microbiology and Immunology, National Yang-Ming University, Taipei, Taiwan*
[3] *Institute of Communication Engineering, National Chiao Tung University, Hsinchu, Taiwan*
[4] *Graduate Institute of Biophotonics, National Yang-Ming University, Taipei, Taiwan*
[5] *Department of Electrical Engineering, National Chiao Tung University, Hsinchu, Taiwan*

***Abstract* — In this work, we fabricate a surface-enhanced Raman scattering (SERS)-active substrate with low background signals using bottom-up approach. Staphylococcus aureus has been used as Raman probe to evaluate its enhancement capability. The experimental results of this study show that Staphylococcus aureus was well resolved using gold-coated hydrothermally roughened TiO_2 substrates.**

Keywords—***Raman spectroscopy, hydrothermal treatment surface-enhanced Raman scattering (SERS), SERS-active substrate, confocal microscopic Raman spectrometer, scanning electron microscope (SEM), X-ray photoelectron spectroscopy (XPS), atomic force microscopy (AFM), Staphylococcus aureus, contact angle (CA), Maxwell's equations, FDTD, Local Field.***

I. Introduction

Raman spectroscopy has recently attracted a great deal of attention for rapid identification of bacterial samples in recent years owing to the capability for supply "whole-organism fingerprinting" information [1-12]. The degree of Raman enhancement is strongly dependent on the morphology of nanostructures. Several surface-enhanced Raman scattering (SERS)-active substrates were reported including metal-island films [13], metal nanocolloids films [14], spherical mask coating [15], roughened metallic substrates [16], and bio-templated substrate [17]. Recently, a top-down approach for the fabrication of plasmonics-active substrate was proposed [18]. However, expensive substrate, equipments and complicated process are needed. Therefore, development of a low-cost, environment friendly and ease fabrication for SERS-active substrate will be of great interest for basic and clinical researchers as well as for biotech industry. In this study, we propose a new method for the fabrication of SERS-active substrate for identification of Staphylococcus aureus.

This paper is organized as follows. In Sec. II, we brief the experimental procedure. In Sec. III, we state the instrumentation. In Sec. IV, we discuss the results of this study. Finally, we draw conclusions.

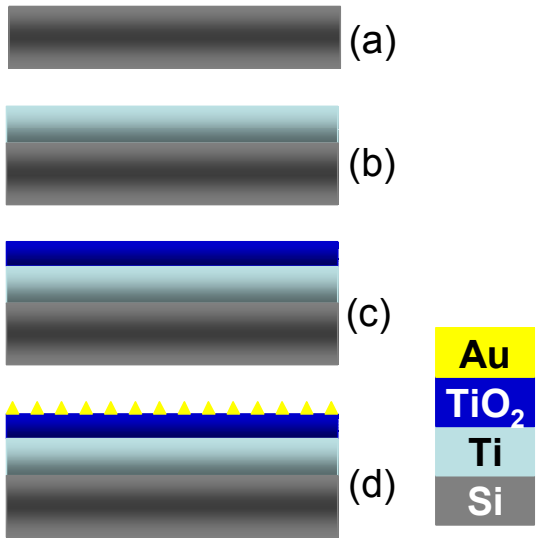

Figure 1. Schematic for the fabrication SERS-active substrate: (a) pre-cleaned Si substrate, (b) titanium deposition, (c) hydrothermal treatment, and (d) gold deposition.

II. Experiment

Figure 1 shows a schematic for the preparation of SERS-active substrate in this work. P-type silicon (100) wafers were first dipped into buffered oxide etchant (BOE) to remove the natural oxide on the surface. Subsequently, standard RCA cleaning was carried out to remove metal and organic species. Then, 100-nm-thick titanium films were deposited on the silicon wafers using reactive DC magnetron sputtering system. The as-deposited sample was cleaved into 0.5 cm x 1 cm

This work was supported in part by Taiwan National Science Council under NSC-97-2221-E-009-154-MY2. *Corresponding author: Professor Yiming Li, Department of Electrical Engineering, National Chiao Tung University, Hsinchu 300, Taiwan. Phone: +886-3-5712121 ext. 52974; Fax: +886-3-5726639; E-mail: ymli@faculty.nctu.edu.tw).

squares and rinsed with ethanol, and de-ionized water. Subsequently, the sample was put into a 23 mL Teflon-lined stainless steel autoclave filled with 20 mL distilled water, which was sealed, and heated at 200°C for 12 h. Then the treated sample was cooled to room temperature, washed with distilled water for several times, and dried with a stream of cylinder air. For SERS experiments, 3 ~ 5 L of bacteria suspension was placed on the TiO_2 substrate, dried in a laminar-flow cabinet for 5 min, then mounted with 0.5% agarose gel to immobilize the bacterial samples relative to the substrate.

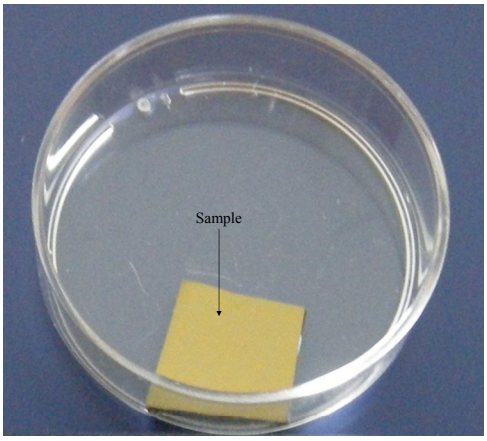

Figure 2. Optical microscopic image of the hydrothermally roughened titania substrate treated for 6 h.

III. INSTRUMENTATION

The structural and chemical properties of treated samples were studied using scanning electron microscopy (JOEL JSM 6500-F), scanning probe microscopy (Veeco Dimension 5000), X-ray photoelectron spectroscopy (VG Scientific Microlab 310F). SERS measurements were performed using a confocal microscopic Raman spectrometer (Jobin Yvon, LabRAM HR). 10 mW of 632.8 nm radiation from a He–Ne laser was used for excitation. The scattering light was collected by a 50× objective lens (NA= 0.75) to a charge-coupled device (CCD) detector. The Raman shift was calibrated using the signal of 520 cm^{-1} from a silicon wafer. All spectra reported here were the results of a single 5 s accumulation in a range of 400–1800 cm^{-1}. Rayleigh scattering was blocked using a holographic notch filter.

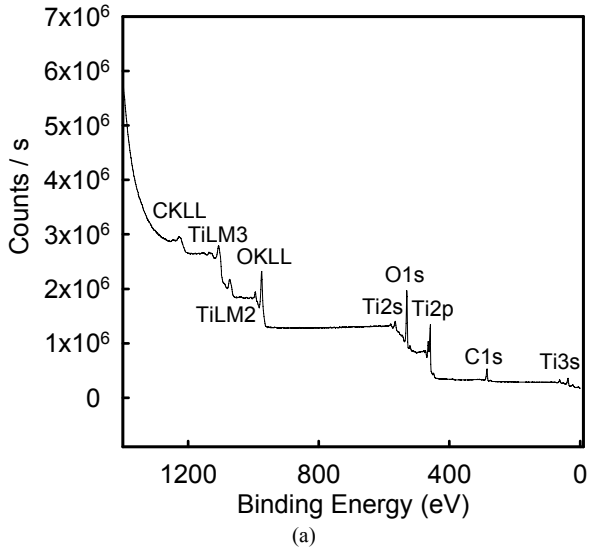

(a)

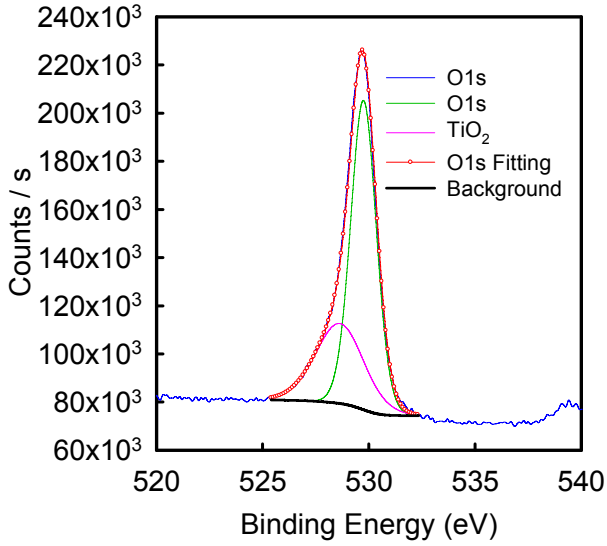

(b)

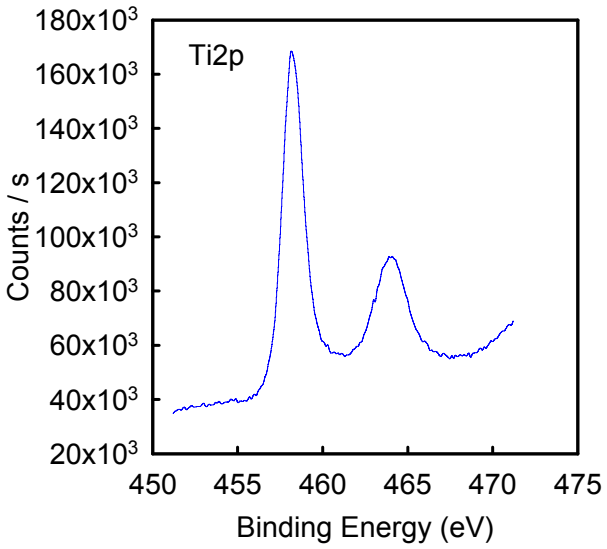

(c)

Figure 3. XPS spectra of (a) survey (b) O1s and (c) Ti2p. The XPS peaks of O1s correspond with Ti-O in TiO_2 and hydroxyl groups on TiO_2, respectively. The XPS peaks of Ti2p correspond with the characteristic peaks of TiO_2.

IV. RESULTS AND DISCUSSION

Fig. 2 is a photograph of the hydrothermally treated TiO_2 (titania) substrate treated for 6 h. The color of the titanium thin

film changes from silvery-white to golden at the first two hours. The color of the thin film darkened gradually with increasing treatment duration. Fig. 3(a) shows X-ray photoelectron spectroscopy (XPS) survey spectrum of the hydrothermally treated films. The results show that the compositions of the thin films contain not only Ti and O elements, but also carbon element. C1s Spectra is observed in survey spectrum due to the hydrocarbon from the instrument itself. Fig. 3(b) and 3(c) show narrow spectra of O and Ti element. O1s Spectra are best fitted with two peaks at E_b = 530.3 eV and 531.9 eV by using a Shirley background and those peaks correspond with the characteristic peak of O as TiO_2 and non-TiO_2 oxygen, respectively. Ti2p Spectrum is observed two peaks at Ti2p3 = 458.2 eV and Ti2p1 = 464.0 eV, which correspond with the characteristic peaks of TiO_2 [19]. Noble metal nanoparticles with anisotropic shape can provide the most field enhancement by theory [8]. Therefore, the gold-coated roughened titania surface can contribute to the

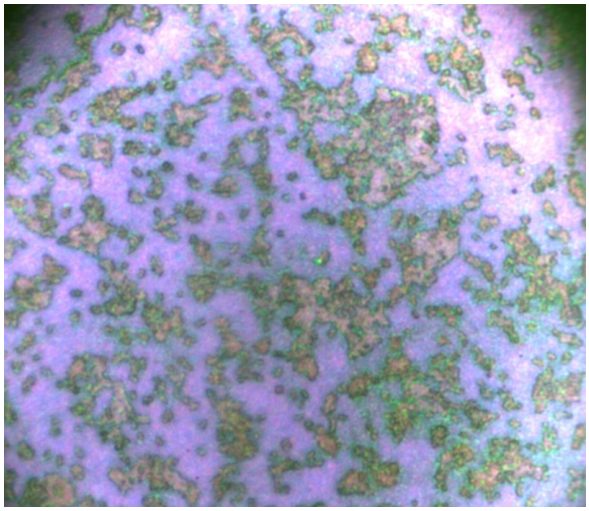

Figure 4. Optical microscopic image of Staphylococcus auaureus.

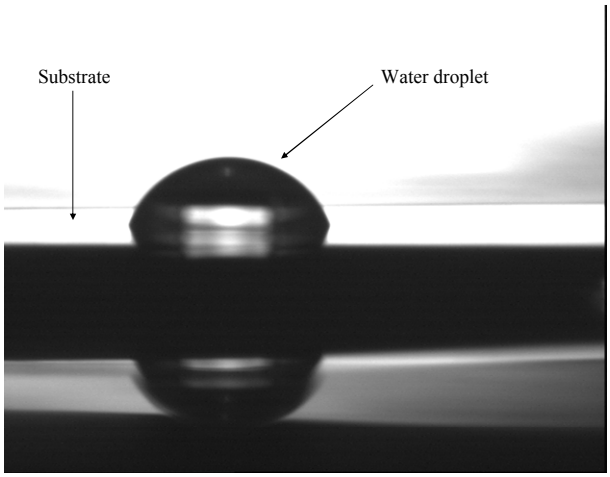

Figure 5. Optical image of water contact angle of the hydrothermally roughened TiO_2 substrate. The surface shows less hydrophilicity.

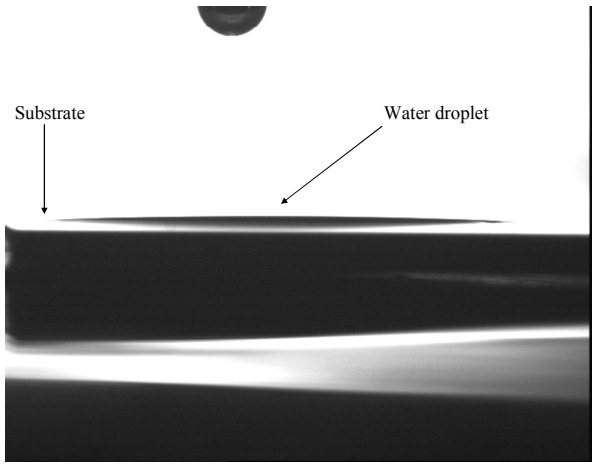

Figure 6. Optical image of water contact angle of the hydrothermally roughened TiO_2 substrate after UV irradiation. The contact angle is less than 5^o. The surface shows good hydrophilicity.

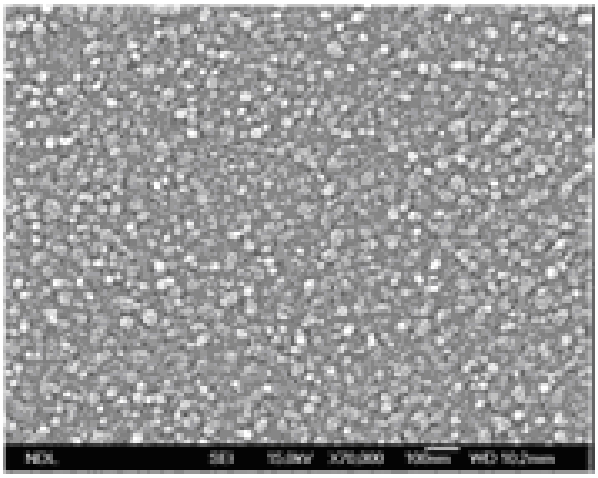

(a)

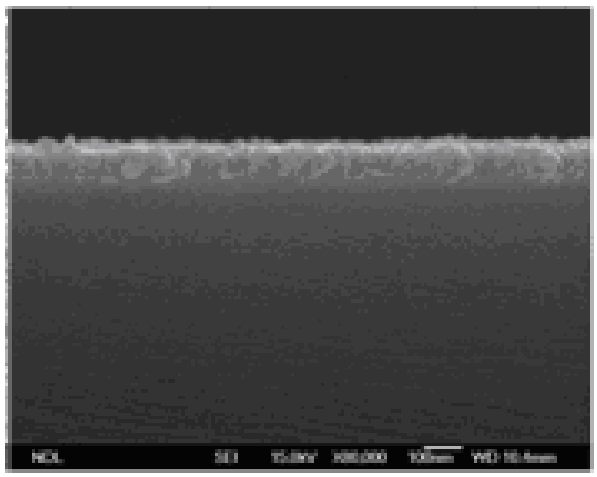

(b)

Figure 7. SEM (a) top-view and (b) cross-sectional image of titanium thin films treated under hydrothermal conditions for 12 h.

electromagnetic enhancement. Staphylococcus aureus is one of the fatal pathogens. It was used as a Raman probe in this work. The optical microscopic image of Staphylococcus aureus is shown in Fig. 4. The wettability of the titania substrates was characterized by the use of contact angle system. Static contact angles were measured with de-ionized water drops. The contact angle (CA) images of the hydrothermally treated substrates before and after treatment by UV illumination were shown in Figs. 5 and 6. The average CA is 67.8° and 2.4°, respectively.

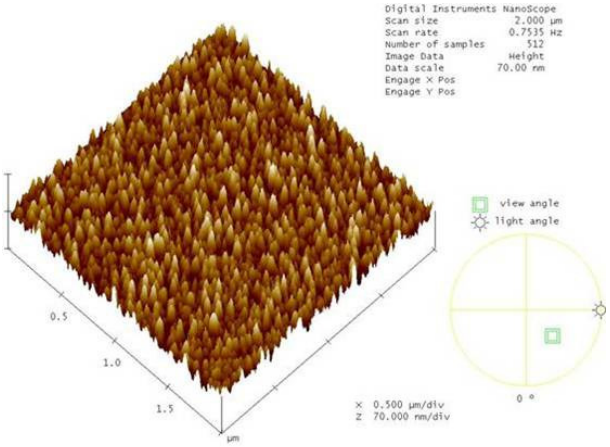

Figure 8. AFM image of titanium thin films treated under hydrothermal conditions for 12 h.

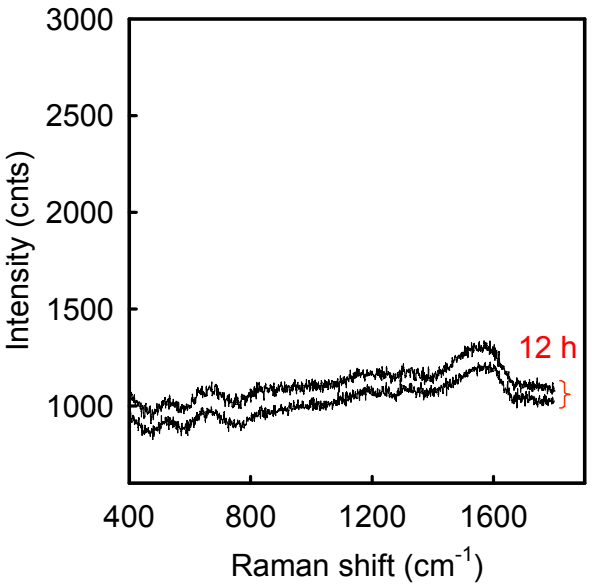

Figure 9. SERS spectrum of the TiO_2 substrate, the Raman spectrum was acquired twice and the acquisition time is 5 s

Fig. 7 are scanning electron microscope (SEM) (a) top-view and (b) cross-sectional images of the titanium thin films treated under hydrothermal conditions for 12 h. The surface of the treated films composes of nanoparticles with different.sizes. Smaller nanoparticles were located on the surface of the substrate and larger nanoparticles were randomly distributed over the substrate. The size of the nanoparticles increases with increasing treatment duration. Fig. 8 is three-dimensional atomic force microscopy (AFM) image of the titanium thin films treated under hydrothermal conditions for 12 h. The average roughness in a window of 2 x 2 m^2 is 8.38 nm. Noble metal nanoparticles with anisotropic shape can provide the most field enhancement by theory [20]. Therefore, the rough TiO_2 surfaces can provide an anisotropic morphology and subsequent coating with gold to contribute to the electromagnetic enhancement.

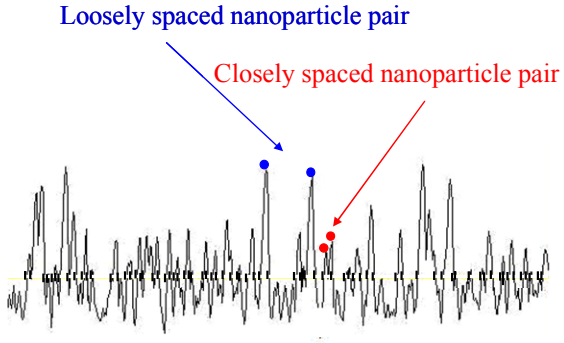

Figure 10. Schematic for the interparticle coupling effect. Nanopaticles deposited on the roughened surface. Closely spaced nanoparticles pair gives strong electromagnetic enhancement.

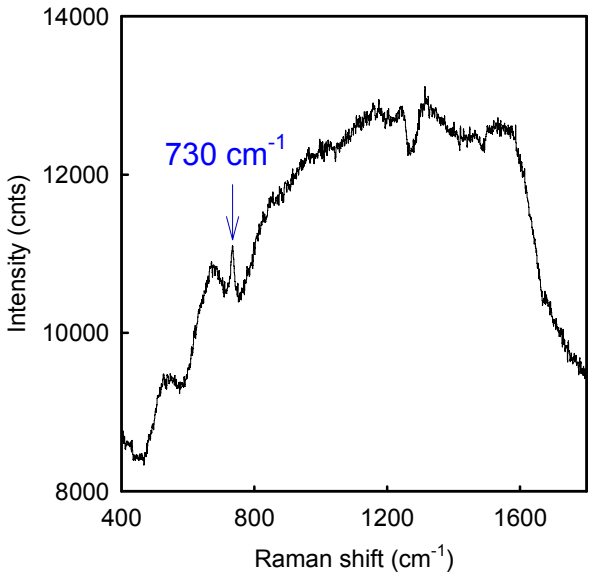

Figure 11. SERS spectrum of Staphylococcus aureus adsorbed on TiO_2 substrate, inset is an optical image of Staphylococcus auaureus. The characteristic peak of Staphylococcus auaureus is indicated by an arrow.

Staphylococcus aureus is one of the fatal pathogens. To test the sensing ability of the roughened TiO_2 substrates, it was used as a Raman probe in our work. Fig. 9 shows theRaman spectrum of the hydrothermally roughened TiO_2 substrate treated for 12 h. The Raman spectrum was acquired twice and the acquisition time is 5 s. The Raman spectrum of the substrate possesses relative weak Raman intensity. Such substrate with low background signals is advantageous to spectral analysis. The enhancement increases with decreasing surface roughness. That is, closely spaced gold nanoparticles pair gives strong electromagnetic enhancement. The roughness-dependent enhancement can be schematically illustrated, as shown in Fig. 10.

Fig. 11 shows the Raman spectrum of Staphylococcus aureus adsorbed on the gold-coated hydrothermally roughened TiO_2 substrate treated for 12 h. The characteristic Raman peak of Staphylococcus aureus at 730 cm^{-1} appears in the spectrum. The signal intensity of Staphylococcus aureus indicates that the substrate possess enhancement capability for the identification of bacteria. To analyze distributions of the local electric fields for the fabricated TiO_2 samples with Au particles, the Finite-Difference Time-Domain (FDTD) algorithms are conducted by solving differential form of coupled Maxwell's equations (Ampere's and Faraday's Laws). Therefore, FDTD could estimate electric fields at different position and time-step due to involving discretization of the Maxwell's equations in both the time and the space domains. The simulation results also show that the electromagnetic enhancement increases with decreasing surface roughness. In other words, the closely spaced gold nanoparticles pair gives strong electromagnetic enhancement.

V. Conclusions

We have successfully prepared new SERS-active substrates for the identification of Staphylococcus aureus. The surface enhancement effect by the substrates enables rapid identification of bacteria. The enhancement capability can be controlled by tuning the surface roughness of the substrates through varying treatment duration. More theoretical study of the fabricated samples is currently under investigation.

Acknowledgment

The samples were fabricated at National Nano Device Laboratories (NDL), Hsinchu, Taiwan, and characterized in Institute of Microbiology and Immunology, National Yang-Ming University (NYMU), Taipei, Taiwan. Technical supports from NDL and NYMU are gratefully acknowledged. This work was supported in part by Taiwan National Science Council under Contract NSC-97-2221-E-009-154-MY2.

References

[1] A. Campion and P. Kambhampati, "Surface-enhanced Raman scattering," *Chem. Soc. Rev*. vol. 27, pp. 241-250, 1998.

[2] A. Otto, I. Mrozek, H. Grabhorn and W. Akemann, "Surface-enhanced Raman scattering," *J. Phy.: Condens. Matter 4*, pp. 1143-1212, 1992.

[3] R. Goodacre, B. Shann, R. J. Gilbert, E. M. Timmins, A. C. McGovern, B. K. Alsberg, D. B. Kell, and N. A. Logan, "Detection of the dipicolinic acid biomarker in Bacillus spores using Curie-point pyrolysis mass spectrometry and Fourier transform infrared spectroscopy," *Anal. Chem*. vol. 72, pp. 119-127, 2000.

[4] L. Zeiri, B. V. Bronk, Y. Shabtai, J. Czege and S. Efrima, Colloid, "Silver metal induced surface enhanced Raman of bacteria" *Colloid Surf. A*., vol. 208, pp. 357-362, 2002.

[5] K. Kneipp, A. S. Haka, H. Kneipp, K. Badizadegan, N. Yoshizawa, C. Boone, K. E. Shafer-Peltier, J. T. Motz, R. R. Desari, and M. S. Feld, "Surface-enhanced Raman Spectroscopy in single living cells using gold nanoparticles," *Appl. Spectrosc.* vol. 56, pp. 150-154, 2002.

[6] R. M. Jarvis and R. Goodacre, "Rapid discrimination of bacteria using surface enhanced Raman spectroscopy," *Anal. Chem.* vol. 76, pp. 40-47, 2004.

[7] E. J. Bjerneld, Z. Foldes-Papp, M. Kall, R. Rigler, "Single-Molecule Surface-enhanced Raman and fluorescence correlation spectroscopy of horseradish peroxidase," *J. Phys. Chem. B*, vol. 106, pp. 1213-1218, 2002.

[8] B. J. Wiley, S. H. Im, Z.-Y. Li, J. McLellan, A. Siekkinen and Y. Xia, "Maneuvering the surface plasmon resonance of silver nanostructures through shape-controlled synthesis", *J Phys Chem B*, vol. 110, pp. 15666-15675, 2006.

[9] B. Nikoobakht and M.A. El-Sayed, "Surface-enhanced Raman scattering studies on aggregated gold nanorods," *J. Phys. Chem. A*, vol. 107, pp. 3372-3378, 2003.

[10] H. Y. Chu, Y.-J. Liu, Y.-W. Huang, and Y.-P. Zhao, "A high sensitive fiber SERS probe based on silver nanorod arrays," *Optics Express 15*, pp. 12230-12239, 2007

[11] S. Shanmukh, L. Jones, J. Driskell, Y.-P. Zhao, R. Dluhy, and R. A. Tripp, "Rapid and sensitive detection of respiratory virus molecular signatures using a silver nanorod array SERS substrate," *Nano Lett. 6*, pp. 2630-2636, 2006.

[12] S. Habuchi, M. Cotlet, R. Gronheid, G. Dirix, J. Michiels, J. Vanderleyden, F.C. De Schryver and J. Hofkens, "Single-Molecule surface enhanced resonance Raman spectroscopy of the enhanced green fluorescent protein," *J. Am. Chem. Soc.* vol. 125, pp. 8446-8447, 2002.

[13] B. D. Alexander and T. J. Dines, "Chemical interactions in the Surface-enhanced resonance Raman scattering of ruthenium polypyridyl complexes," *J. Phys. Chem. B*, vol. 109, pp. 3310-3318, 2005.

[14] C. Shi, H. Yan, C. Gu, D. Ghosh, L. Seballos, S. Chen, J. Z. Zhang and B. Chen, "A Double Substrate "Sandwich" Structure for fiber surface enhanced Raman scattering detection," *Appl. Phys. Lett.*, vol. 92, 103107, 2008.

[15] D. L. Stokes and T. Vo-Dinh, "Development of an integrated single-fiber SERS sensor," *Sens. Actuators B*, vol. 69, pp. 28-36, 2000.

[16] K. I. Mullen and K. T. Carron, "Surface-enhanced raman-spectroscopy with abrasively modified fiber optic probes," *Anal. Chem.*, vol. 63, pp. 2196-2199, 1991.

[17] G. Kostovski, D. J. White, A. Mitchell, M. W. Austin and P. R. Stoddart, "Nanoimprinted optical fibres: Biotemplated nanostructures for SERS sensing," *Biosens. Bioelectron*., vol. 24, pp. 1531-1535, 2009.

[18] A. Dhawan, Y. Du, H. Wang, D. Leonard, V. Misra, M. Ozturk, M. Gerhold and T Vo-Dinh, "Development of plasmonics-active SERS substrates on a wafer scale for chemical and biological sensing applications," *Int. Electron Devices Meeting Tech. Dig*., pp. 487-490, 2008.

[19] D. Rats, L. Vandenbulcke, R. Herbin, R. Benoit, R. Erre, V. Serin and J. Sevely, "Characterization of diamond films deposited on titanium and its alloys," Thin Solid Films, vol. 270, pp. 177-183, 1995.

[20] X.Hu, J. Aizpurua, M. Kall and P Apell, "Electromagnetic contributions to single-molecule sensitivity in surface-enhanced Raman scattering," *Phys. Rev. E*, vol. 62, pp. 4318-4324, 2000.

3B1-6

An Integrated MEMS Tactile Tri-axial Micro-force Probe Sensor for Minimally Invasive Surgery

Weizhong Wang, Yulong Zhao*, Qijing Lin

State Key Laboratory of Mechanical Manufacturing System, Xi'an Jiaotong University, P.R.China

***Abstract* — In this paper, we describes an integrated MEMS tactile tri-axial micro-force probe sensor based on piezoresistive for Minimally Invasive Surgery (MIS) as it's micro-structure, three-dimensional measurement and high resolution up to be micronewton (μN) scale. The sensor is 4×4×20.9mm^3. The sensing element of the sensor is fabricated on Silicon on Insulator (SOI) wafer by surface and bulk micromachining technology. It uses four cantilever beams supporting the suspended mass. Twelve relief pieoresisters formed by iron implant and Inductive Couple Plasmas (ICP) etching technology are placed on the beams to detect the applied force. The pyrex glass bonded on the bottom of the SOI wafer by anodic bonding technology is the overload protection element. The tactile element is the quartz fiber probe which is no-pollution, low cost, small size and easy to process. It is glued on suspended mass of the sensing element by epoxy resin. After fabrication, the sensor is packaged and tested by precision test bench and analytical balance. The experimental results illustrate that the sensor has excellent characteristics especially with resolution better than 3μN.**

Keywords* — *MEMS, Tri-axial, Micro-force, Probe sensor, Minimally Invasive Surgery

I. INTRODUCTION

Nowadays there is growing interest in Minimally Invasive Surgery (MIS) which led to a speedy return to daily. It is a new technology in the Surgery that has lots of advantages as small incision of about 1cm size, lower risk and pain, shorter postoperative stay and thus an overall reduction of health-care costs. However, lack of force feedback and direct land-eye coordination are the major limitations in the progress of MIS, it is difficult to control the force when manipulates the soft tissue via laparoscopic instruments that inserted in the skin through small incisions and may do some damages to the softest tissue or other parts of the body[1][2].3]. So, various force sensors have been designed and fabricated to solve the force feedback problem[4-7]. Some sensors are able to detect three-axis micro-force with resolution only newton scale that can't be used in MIS[5][6]. While others with resolution up to be uN scale usually can only sense one-axis or two-axis micro force[7][8]. So they can't help the surgeon locate precisely and operate fast enough.

In this paper, we will discuss the fabrication and testing results of a novel integrated MEMS tactile tri-axial micro-force probe sensor based on piezoresistive effect. It can monitor both the magnitude and dimensions of the force to improve the accuracy location, dexterity and security of a surgeon greatly for MIS. The sensor's enhanced sensitivity makes it possible to discriminate between tissues of different stiffness and to minimize trauma to the patient.

This project was funded by National Natural Foundation of China (Project code: 60776048) and the Chinese National 863 Plan (Project code: 2007AA04Z325).

Contact author: Please contact **zhaoyulong@mail.xjtu.edu.cn*

II. LAYOUT OF MICRO-FORCE SENSOR

A. Structure of sensor

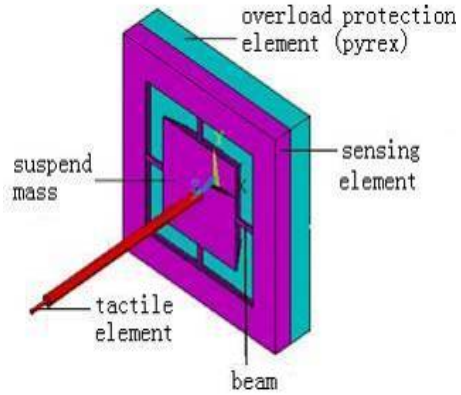

Figure.1 The structure of the sensor

The tactile tri-axial micro-force probe sensor is composed of three elements: the sensing element, the tactile element and the overload protection element shown in Fig.1. A cross-bream with a platform suspended within a frame forms the flexible structure of the sensing element. It is 4×4×0.4mm^3 which fabricated on the SOI (Silicon on Insulator) wafer by micromachining technology. Twelve relief sensing pieoresisters formed by iron implant and Inductive Couple Plasmas (ICP) etching technology are placed on the beams to detect the applied force. A quartz fiber probe with a probing sphere at its distal end is glued on the platform of the sensing element by epoxy resins to be the tactile element. A cubic pyrex glass which is 4×4×0.5mm^3 is bonded to the bottom of the SOI wafer as the overload protection element by anodic bonding technology to protect the sensing element. 5μm narrow air gap is left between the suspended mass and pyrex glass for the suspended mass fluctuating.

The force applied on the probe is transmitted to the flexible cross structure causing deformation of the beams. Then it is detected by the pieoresisters integrated on the beams through stress distribution result from the deformation.

B. Principle of sensor and resistors design

The micro-force sensor is based on piezoresistive effect which has the advantages of large measurement range, good linearity and simple measuring circuit. Piezoresistive effect describes the changing electrical resistance of the diffused resistors on the silicon chip due to applied mechanical stress on them resulting from a force. It can be expressed as:

$$\frac{\Delta R}{R} = \pi_l \sigma_l + \pi_t \sigma_t \quad (1)$$

where σ_l is the longitudinal stress (the stress, electric field and current of this piezoresistor are all in the same direction) and σ_t is the transversal stress (the stress is in perpendicular to the direction of electric field and current) induced in the resistor R, π_l is the longitudinal piezoresistance coefficient and where π_t is the transverse piezoresistance coefficient. So the sensitivity of the force sensor is determined by stress and piezoresistance coefficient of the piezoresistors.

In order to get high sensitivity, we make twelve resistors along the [110] and [1$\bar{1}$0] on the (100) SOI wafer as their higher piezoresistance coefficient in the two orientation shown in Fig.2 and Fig.3. As illustrated in Fig.4, four resistors are combined to a wheatstone bridge to detect the applied force from X, Y or Z and output the voltage signals. The relief piezoresistors are made like the island to solve the problem of temperature shift shown in Fig.5.

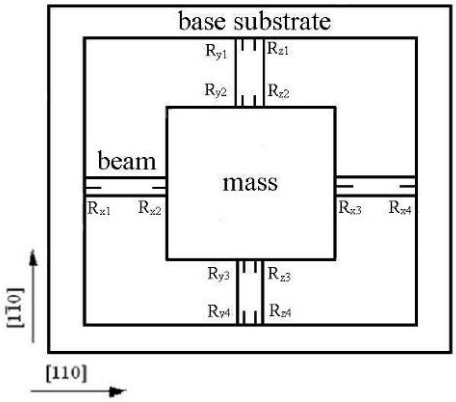

Figure.2 The distribution of the resistors

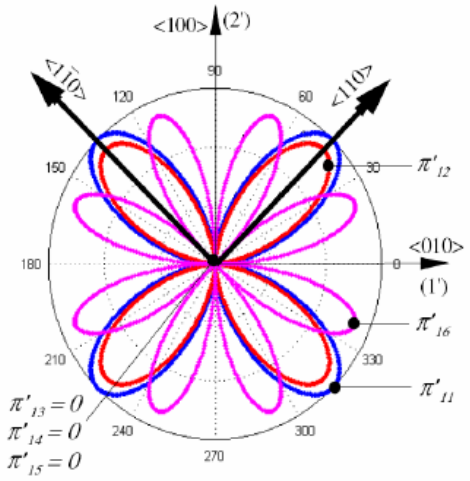

Figure.3 The distribution of piezoresistance coefficient on the (100) SOI wafer

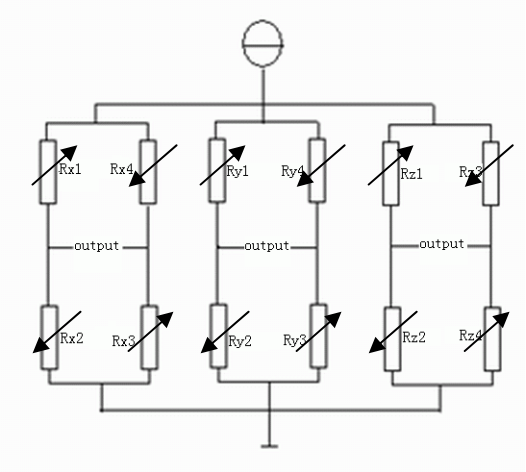

Figure.4 The wheatstone bridges used for detecting the tri-axial force

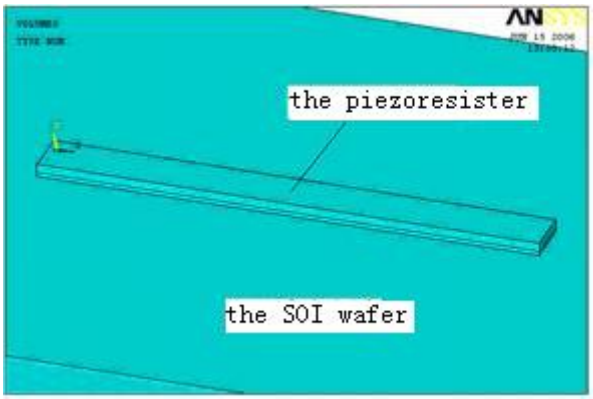

Figure.5 The relief piezoresistor

III. SENSOR FABRICATION

The process of sensor fabrication includes: fabrication of the sensing element, overload protection element and tactile element, and then assembling them together.

A. Sensor chip fabrication

This part includes the fabrication of the sensing and overload protection element.

The sensing elements are fabricated on a double-side-polished four-inch N-type (100)-oriented SOI wafer by surface and bulk micromachining technology. The wafer is composed of three layers: the 1.6μm active-silicon with resistivity of 10Ω/cm as the device layer, 0.3μm SiO_2 and about 400μm silicon substrate illustrated in Fig.6.

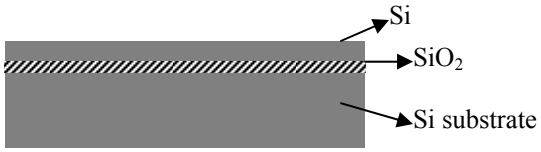

Figure.6 The structure of the SOI

One of the most important steps of the fabrication progress is the design of photolithographic masks. Fig.7 shows the

eight masks that integrated together for the fabrication of the sensor. They are designed via the Tanner L-Edit9.0: the ohm contact mask, the resistor mask, the contact hole mask, the wires mask, the beam forming mask, the metal electrode mask and two mask for producing the suspended mass and the supporting membrane.

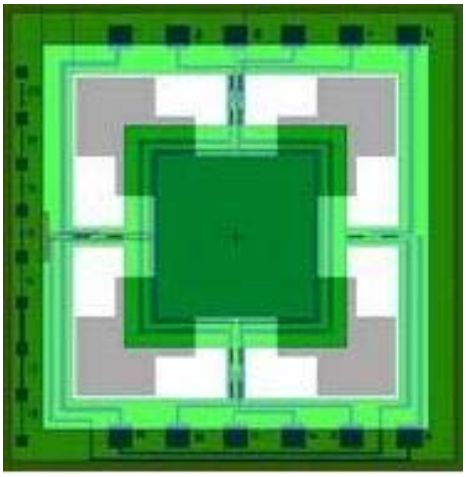

Figure.7 All the eight masks

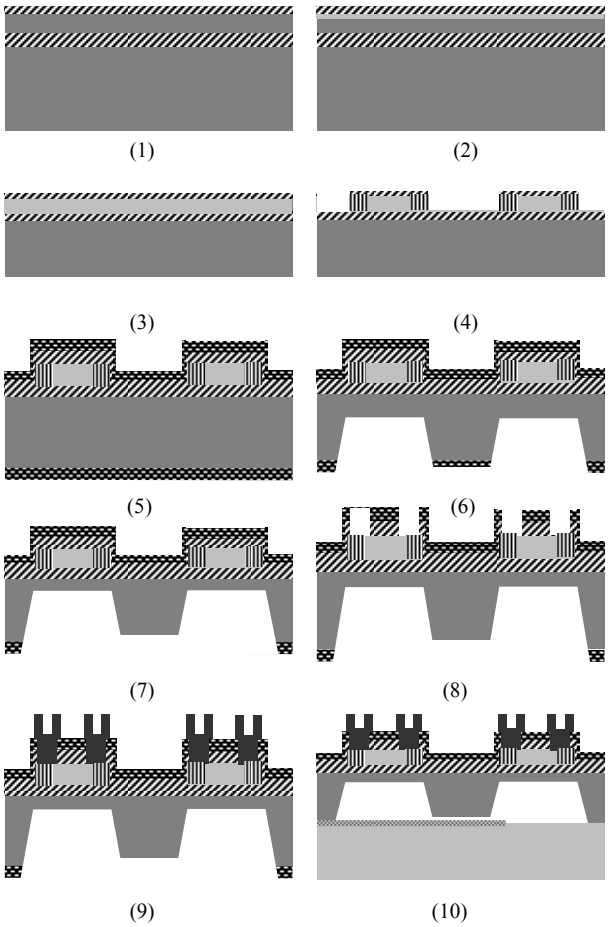

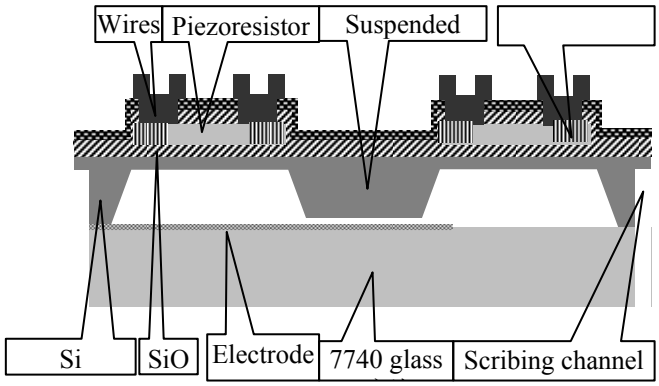

(11)

Figure.8 Schematic view of the fabrication progress of the sensing and overload protection element

The fabrication process for the sensing and overload protection element is shown in Fig.8.

1) First we washed the SOI wafer by hydrofluoric acid (HF) solution and formed a silicon oxide layer of 500 Å thick on the surface by thermal oxidization at 1100℃ for 5minutes. The silicon oxide layer is intended to minimize the damage to crystal lattice of the silicon surface by ion implantation and minimize channeling effect to make the ion distribute well.

2) After thermal oxidization, the p-dope piezoresistors are made by boron ion implantation on the device layer. The dose of the ion-implantation is $3\times10^{14}/cm^{-2}$ at the energy of 80 keV for 40 minutes. The ion concentration is $5.4\times10^{18}/cm^3$.

3) In order to obtain ion well-distributed, reduce crystal lattice of the silicon and active the ion, the wafer is annealed in the atmosphere of nitrogen at 1100℃ for 1.5 hours.

4) The boron-ion-implantation is done again with dose of $1.5\times10^{16}/cm^2$, energy of 80keV for 40 minutes via the ohm contact mask to form the contact area with little resistance. The ion concentration of the ohm contact mask is $2.2\times10^{20}/cm^3$. And then the relief piezoresistors and ohm contact area are formed by etching technique of inductive couple plasmas (ICP) via the resistors mask. The silicon as device layer is etched except the piezoresistors area and contact area at atmospheric pressure of 13.3Pa and the CF_4 flux of the 90ml/min. The etching rate of SiO_2 and Si separate are 30nm/min and 400nm/min. Fig.9 shows the photograph of the piezoresistors and the contact area. The resistor is 100μm×10μm×1.65μm with 200Ω per square, the contact area is 15Ω per square.

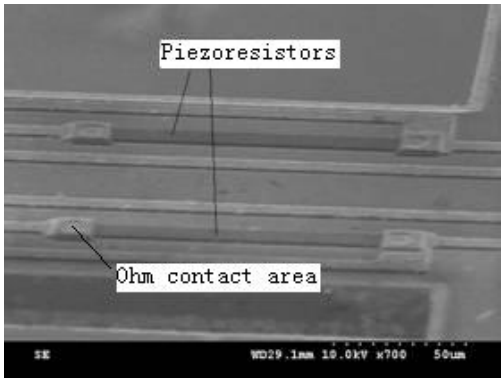

Figure.9 The photograph of the piezoresistors and the ohm contact area.

5) A 4000 Å thickness SiO_2 is formed by thermal oxidization at 1000℃ for one hour. The progress can make the ion distribute better. And then three layers of $Si_3N_4/SiO_2/Si_3N_4$ (1100 Å/2500 Å/ 1100Å) as the mask for the KOH etching are deposited by low pressure chemical vapor deposition (LPCVD) at 780℃. The SiO_2 layer can also reduce the effect of the Si_3N_4 film stress when it is fabricated.

6) To form the suspended mass, the support membrane and the narrow air gap between the Pyrex glass and the seismic mass, two-step wet anisotropic etching process on the backside of wafer are done using the 35% KOH solution with the $SiO_2/Si_3N_4/SiO_2/Si_3N_4$ as masks .

The two layers of Si_3N_4/ SiO_2 on the backside are etched away expect the region of the frame, suspended mass and corner compensation via the photolithographic masks. The frame area is covered by two layers of Si_3N_4/ SiO_2 while the suspended mass and corner compensation area are covered by only layer. The reactive ion etching (RIE) is used to etch the layer of Si_3N_4 with the rate 700Å/min. The SiO_2 layer is etched away by wet etching of BHF solution.

Then the wafer is put into the 35% KOH solution to get the suspended mass and the supported membrane at 80℃.The accurate thickness of etching is 365μm within 1%.

7) After the layer mask Si_3N_4/ SiO_2 on the suspended mass being removed by RIE and BHF etching, wet anisotropic etching is done again by KOH solution. The suspended mass is etched of 5μm to form narrow air gap between the Pyrex glass and the suspended mass.

8) The contact hole between the ohm contact area of resistors and metal tire are formed by RIE on the front side of the wafer via the contact hole photolithographic masks.

9) The wafer is dipped into the RCA solution which includes H_2SO_4, H_2O_2, HF, NH_4HOH and HCL to clean the surface of silicon. Then a 1000 Å thick Ti and a 15000 Å thick Al are separately deposed on the front side of wafer by PVD at the atmosphere of Ar with low pressure of 0.13~1.3Pa. The metal layer is etched to pattern the wires using ICP technology with the rate 50nm/min of Al and 20 nm/min of Ti at the atmosphere of $CHCl_3$ and N_2, then metallization pattern of the metal wire at 500 ℃.At last, the RIE etching is used to release the cantilevers which are 35μm thick, 450μm long and 150μm wide from the front side of the wafer. The finished wires, piezoresistors and beam are shown in Fig.10.

10) The 7740# Pyrex glass is selected as the overload protection element as its thermal coefficient is similar to that of silicon. The glass is 500μm thick and as big as the SOI wafer. The Cr/Au （500Å/2000Å）layer is deposed on the glass by PVD. And then the electrode via the electrode photolithographic masks is formed by lift-off technology to prevent suspended mass from sticking to the glass. Then the SOI wafer and the glass is bond together by the anodic bonding technology at 350℃ and 1000V direct current voltage for 10-30 minutes, illustrated in Fig.11.

11) The whole wafer is dice into individual chips along the scribing channel. The last step is to leave all single chips at 180℃ for 48 hours to wipe off the stress in the chip. Fig.12 shows the finished chip.

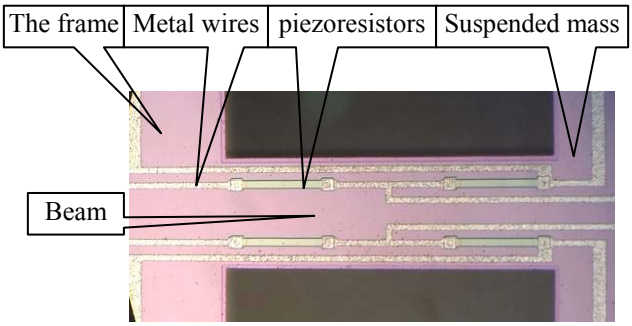

Figure.10 The photograph of the finished beam

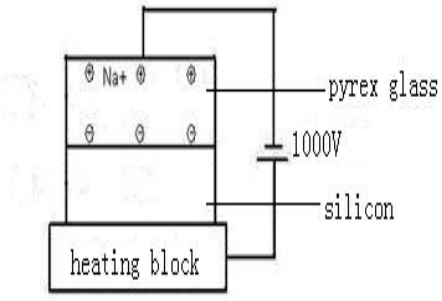

Figure.11 Schematic of anodic bonding technology

Figure.12 The finished sensor chip

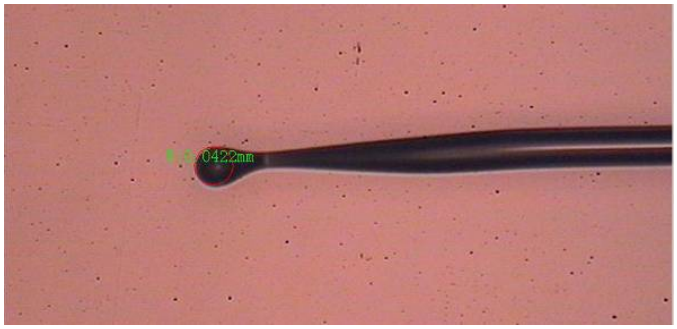

Figure.13 The photograph of the probe tip

B. *Probe fabrication*

The probe as the tactile element is the most important part of the sensor, as it contacts the tissue and organ directly in the progress of MIS. Due to the convenience in use, no-pollution, low cost, small size and good mechanical character, the quartz fiber is selected as the probe. It is more security then the metal probe[9] for the people when it acts in the body of the patient. In order to minimize the incision, we chose uncladded fiber as the fiber with the diameter only 125μm. The length is defined as 2cm to make the fiber more sensitive, dexterity and have ability to detect deeply and widely. The sphere as the tip of probe is drawn at high temperature to reduce the damage to the people. The diameter of the sphere is lesson than 100μm, it is small enough to apply in the MIS and more security than the sharp tip[10]. The tip of the sensor is shown in Fig.13.

C. *Sensor assembly and package*

Once the fabrication process of the three elements is completed, they are assembled. The final sensor dimensions are 4mm×4mm×20.9mm.

The sensor is assembled and packaged like Fig.14. It is comprised of the sensor, adhesive layer and printed circuit board (PCB). At first, the sensing and overload protection elements are attached to the PCB by a resin adhesive which has good electric, thermal and mechanical performance. The gold wires used for circuit contact are welded to the solder pads of the sensing element and the PCB by ultrasonic wire bonding machine. The next step is to glue the probe and the sensor chip together by the epoxy resin. The finished packaged sensor is shown in Fig.15.

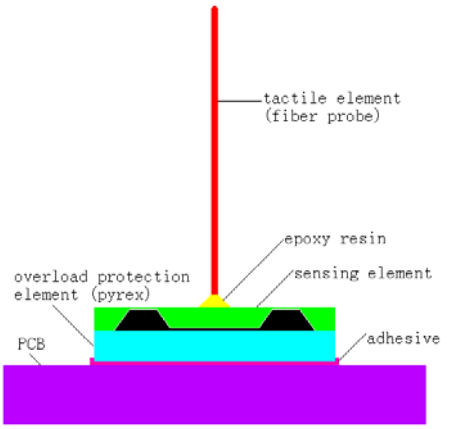

Figure.14 The schematic diagram of the packaged sensor

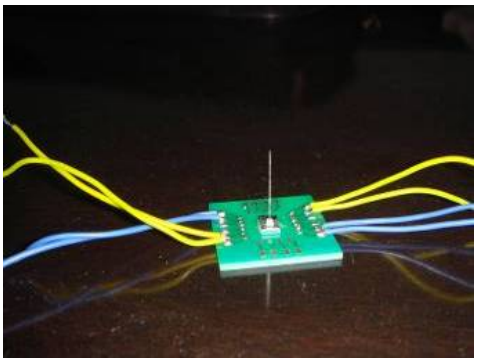

Figure.15 The photograph of the packaged sensor

IV. EXPERIMENTS RESULTS

To detect the characteristics of the sensor, a precision positioning stage with three degrees of freedom and nm scale resolution, analytical balance which can measure something with only 0.01mg and precision multimeter are employed. The gravitational acceleration in Xi'an is 9.79440m/s^2. Wheatstone bridge circuit is powered by 5V DC. Then the realised prototype is tested by applying a variable loads (0~1000μN) on the probe from X,Y and Z orientations, the experimental results show that this integrated probe sensor has good output characters. The resolution of the sensor is better than 3μN. The sensitivity is up to 0.1682mv/uN and non-linearity of the output voltage is 0.19%/FS in x-axis and y-axis, up to 0.0106mv/uN and non-linearity is 0.94%/FS in z-axis before amplification shown in Fig.16.

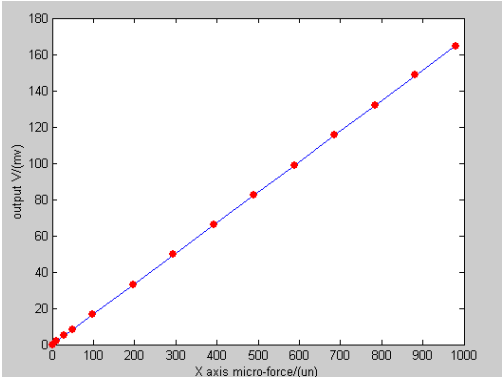

(a)The relationship between the loads and the output voltage in X(Y) orientation

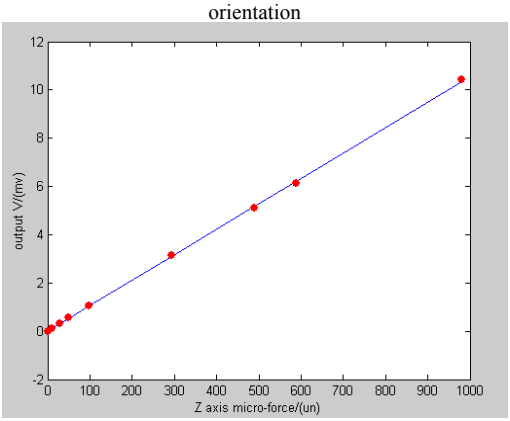

(b)The relationship between the loads and the output voltage in Z orientation

Figure16. The results of the experiment

V. CONCLUSION:

A kind of three-axis micro silicon probe force sensor based on MEMS technology, which is capable of monitoring three-axis micro force is reported. The fabrication, package, and measurement process of the micro force sensor are presented in the paper. The measured results show that the micro force sensor has good output characters about three-axis micro force and its resolution for sensing micro force can be up to the uN scale. As its characters of no-pollution, high sensitivity, high reliability, little volume and low cost, the three-axis micro force sensor will be widely used in MIS.. Future work will be required to optimize the response and the fabrication process and improve the measurement accuracy of the three-axis micro probe force sensor.

ACKNOWLEDGEMENT

This study is supported by the National Natural Science Foundation of China (Project code:.60776048) and Chinese National 863 plane (Project code:.2007AA04Z325). Authors are thankful to Dr Libo Zhao for giving us some useful advice on author's test experiment.

REFERENCES

[1] Jan Peirs , Joeri Clijnen , Dominiek Reynaerts, Hendrik Van Brussel, Paul Herijgers, Brecht Corteville, Sarah Boone, "A micro optical force sensor for force feedback during minimally invasive robotic surgery", Sensors and Actuators A, vol..115, pp. 447–455, 2004.

[2] George B. Hanna , Tim Drew, Graham Arnold, Morkos Fakhry, Alfred Cuschieri, "Development of force measurement system for clinical use in minimal access surgery", Surg Endosc, vol.. 22, pp.467–471, 2008.

[3] Pinyo Puangmali, Hongbin Liu, Kaspar Althoefer, Lakmal D. Seneviratne, 2008 IEEE International Conference on Robotics and Automation Pasadena, CA, USA, May 19-23, 2008

[4] M.E.H. Eltaib, J.R. Hewit, "Tactile sensing technology for minimal access surgery—a review," Mechatronics, vol. 13, pp. 1163–1177, 2003.

[5] Chang-Sin Park , Jongsung Park, Dong-Weon Lee, "A piezoresistive tactile sensor based on carbon fibers and polymer substrates", Microelectronic Engineering, Microelectronic Engineering, pp.1-4, 2009

[6] Kunnyun Kim, Kang Ryeol Lee, Dae Sung Lee, Nam-Kyu Cho, Won Hyo Kim, Kwang-Bum Park, "A silicon-based flexible tactile sensor for ubiquitous robot companion applications", Journal of Physics: Conference Series 34,pp. 399–403,2006.

[7] E. Peiner, A. Tibrewala , R. Bandorf, S. Biehl,H.L¨ uthje, L. Doering, "Micro force sensor with piezoresistive amorphous carbon strain gauge" Sensors and Actuators A,vol. 130–131, pp.75–82, 2006.

[8] T. Chu Duc, "Piezoresistive Cantilever Beam for Force Sensing in Two Dimensions", IEEE SENSORS JOURNAL, VOL. 7, NO. 1, pp.96-104, JANUARY 2007.

[9] P. Ruther, J. Bartholomeyczik, A. Trautmann, M. Wandt, O. Paul, W. Dominicus, "Novel 3D Piezoresistive Silicon Force Sensor for Dimensional Metrology of Micro Components", 2005 IEEE Sensors, Vols.1and 2, pp.1006-1009,2005.

[10] Zhe Lu, Hong Luo, Peter C Y Chen and Wei Lin, "An integrated probe sensor for micro-force measurement", Measurement Science and Technology, Vol.17, pp869–875, 2006.

3B2-1

A Cell Culture System with Better Spatial and Time Resolution

Yu-Cheng Ou[1], Chih-Wen Hsu[1], Lung-Jieh Yang[1,*], Hsieh-Cheng Han[1,2], and Chien-Yuan Chen[2]

[1]*Department of Mechanical & Electro-Mechanical Engineering, Tamkang University, Tamsui, Taiwan*
[2]*Institute of Microbiology and Biochemistry, National Taiwan University, Taiwan*

***Abstract* — A new cell culture system is demonstrated in this paper. This system includes a culture incubator with a compact optical monitoring module and an electro-chemical impedance sensor (ECIS) chip with gelatin micro patterns attracting living cells selectively. We provided a platform with a shorter observation interval of 4 hours and a finer line width of electrodes of sensor chips than the prior art in this work. The in-situ impedance measurement on HeLa cells was performed and shown the better spatial and time resolution.**

Keywords — ***glutaraldehyde, gelatin, cell culture, impedance sensing, in-situ monitoring***

I. INTRODUCTION

Techniques of cell culture were developed at the turn of the 20th century [1] and are still today an important tool for studies of basic biology [2], tissue engineering [3], bioelectronics [4] and biosensor fabricating [5]. During the cell culture process, cell adhesion and cell spreading are fundamental processes of adherent cells. Furthermore, cell adhesion and cell spreading are also crucial to signal transduction pathways of a cell [6], the formation of tissues [7] and the body's defense system [8]. Uncovering the cell adhesion and cell spreading processes of living cells is, therefore, important from view of biological science.

At the individual cell level, some properties of a living cell are associated with cell adhesion and cell spreading processes. Traditionally, the changes of individual cell morphology are measured using the optical methods [9-10] or mechanical method [11]. In addition to the optical methods used to monitor the cell morphology of living cells, biosensors provide another means to monitor the changes of cell morphology. Electric cell-substrate impedance sensing (ECIS) offer a simpler technique than the above techniques to measure cell adhesion and cell spread of many individual cells at the same time.

ECIS methods have long been regarded as a valid approach to monitor the morphology, viability, and environmental change of the adherent cells [12-13]. ECIS technique is a noninvasive and sensitive detecting technique for cell adhesion. Moreover, it can be used to record the time courses of overall impedance during the cell adhesion and cell spread. For this reason, various cell behaviors can be monitored by the sensing impedance. In recent twenty years, ECIS has been also practically employed to monitor many kinds of adherent cells [14-18]. Although the ECIS technique has many advantages for monitoring the cell morphology, there are still some technical defects needed to be solved in real-time measurement. In the ECIS chips, most sensing electrodes are fabricated by metal, like gold [19-20] or platinum [21]. Generally, all the mediums on optical path of microscopy employed to observing living cells must be transparent. If the sensing electrodes of the ECIS chip are not transparent, it will be difficult to observe the cell morphology of living cell on the electrodes in real-time. In the meantime, the ECIS data attributed to various cell behaviors are hard to confirm without real-time image.

This present study combines ECIS and optical methods to monitor the individual cell morphology. In order to monitor the growing situation of the living cells, a new cell culture system for the study of real-time cell morphology shown in Fig. 1 is demonstrated in this paper. This system includes a culture incubator with a compact optical observing module and an ECIS chip with gelatin micro patterns attracting living cells selectively [22]. The optical observing module is used for observing different targets of living cells in the incubator. More importantly, we could observe the real time morphology of living cells in the incubator, not like the traditional way of taking out the cell samples from the incubator. Moreover, an ECIS chip with smaller size and finer linewidth of electrodes was designed and developed. For observing the cell morphology of the living cells on the ECIS working electrodes, the transparent material, ITO (Indium Tin Oxid), fitting the optical requirement was here used to fabricate ECIS electrodes other than gold electrodes or platinum. In the meantime, the gelatin micro patterns fabricated firmly on the ECIS working electrodes have a small size which is purposely comparable to cells, and they are supposed to produce a selective attraction effect during the stages of falling and attachment of cell culture. By this way, the living cells can be controlled onto the given working electrode surface. It provides another means in place of contact-printed laminin [23], robotic protein printing onto amino-silane-modified glass slides [24], or the fibronectin-self-assembled monolayer on a patterned metal surface [25]. Therefore, the dynamic changes of the cell morphology can be recoded by the ECIS chip and the data attributed to various cell behaviors also can be confirmed by the real-time image of the optical module. We believe the novel cell culture system will be beneficial to the cell-based drug screening technology dealing with human diseases.

II. EXPERIMENT METHODS

A. *Fabrication of glutaraldehyde (GA)-crosslinked gelatin micropatterns*

In this work, we have combined the concepts of GA crosslinking and conventional photolithography to fabricate gelatin micropatterns with a biopatterning resolution as fine as 2 μm, and applied this technique to the cell culture [26]. The fabricated gelatin patterns observed by the Scanning Electron Microscope (SEM) are shown in Fig. 2. After the fabrication of gelatin micropatterns, the different GA-crosslinked gelatin

* Contact Author: Lung-Jieh Yang is with the Department of Mechanical and Electro-Mechanical Engineering, Tamkang University; 151, Ying-Chuan Rd., Tamsui, 25137, Taiwan. (phone: +886-932-159193; fax: +886-2-26209745; e-mail: Ljyang@mail.tku.edu.tw)

micropatterns are employed to observe cell extension. When the spatial resolution is close to the bio-patterning resolution, like the size of the cells, the single tumor cell can be controlled to attach on the gelatin micro pattern. The SEM photographs of single HeLa cell attaching on the micro gelatin patterns are shown in Fig. 3. Furthermore, the gelatin micropatterns are also fabricated on the ECIS working electrodes to attract living cells on to the given surface for recording the cell behavior. Such a small gelatin pattern cannot only be assigned as the biocompatible platform for cell culture but also has a size comparable to that of cells so as to possibly attract a very confined number of cells or even a single cell on the gelatin micropatterns both individually and in a parallel.

B. Optical system compatible with conventional incubators

This work proposes a novel optical subsystem compatible with conventional incubators for real-time monitoring living cells behavior on the ECIS chip. The conceptual cartoon of the compact machine is shown in Fig. 1(a). The subsystem is equipped with an optical path of differential interference contrast (DIC) for observing different targets of living cells on a three-axis electrically motorized stage specifically and continuously. By setting the x-y coordinate displayed on the control box of the motorized stage, multiple targets can be traced simultaneously; the z-coordinate is responsible for the right focus of cells.

In general, the cell morphology of living cells during incubation is observed by taking out the samples from the incubator and checked by a phase contrast microscope or a DIC (Differential Interference Contrast) microscope. Once the observation period is too long or the take-out times from the incubator is beyond some extent, the bio-contamination may occur. Moreover, the life cycle and vitality of the cells will be strongly affected. Therefore, a monitoring of living cells beyond 72 hours is not easy and not necessary to do from a practical aspect. For this reason, an incubator-on-a-chip has been developed [27], and the cells in the micro-environment can be directly observed from the microscope. However, the culture conditions compared with the traditional incubator are hard to control. In 2008, an ECIS was used to record the adhesion profile of cells [28], but there is still no real-time image to confirm the ECIS data. Herein, we implemented an optical monitoring subsystem for monitor of cell behavior during incubation.

The completed optical monitoring subsystem is shown in Fig. 4. Contrary to the concept of incubator-on-a-chip, we insert a microscope into a commercial cell incubator. The amplification factor of captured image is 450× and is proper for observing the cells with several tens of microns in size. The module of the optical monitoring subsystem is packaged by a gastight box from humility damage. As an example showing the elegance of our system, a chip with gelatin micropatterns was used to observe the adhesive and the migration behavior of HepG2 cells. The fabricated chips with gelatin micropatterns is 1.5×1.5 cm^2 in size and seeded with HepG2 tumor cells. The seeding density is 8.5×10^3 cells/cm^2. During the incubation, the same cells could be seen repetitively therefore the interesting target could be set in detailed investigation for a great amount of moment. Some real-time captured images of two cell targets are shown sequentially in Fig. 5.

C. Electric cell-substrate impedance sensor with gelatin micropattern

In the fabrication of the sensor, the chip is designed with smaller size of working electrodes to monitor the cell morphology of the very small amount of cells. To control the living cells on the working electrode, the GA-crosslinked gelatin micropatterns are also fabricated on each working electrode. For the requirement of the optical monitoring subsystem described above, the transparent material, indium tin oxide, ITO, is used to fabricate the sensing electrodes. The whole chip size is 2cm×2cm shown in Fig. 1(c). There are one counter electrode with 500 μm diameter and 11 working electrodes with 40 μm tips around the counter electrode shown in Fig. 1(d). A parylene C layer is deposited with PDS-2010 coating system to form a 1μm thick insulating layer. The ITO electrodes then are exposed in reactive ion etching process.

The fabrication process of the ITO electrodes is depicted in Fig. 6. Step 1, an ITO layer (1200Å) is pr-deposited on the glass. Step 2, a chromium layer (200 Å) was first deposited by E-beam evaporation, followed by the deposition of a gold layer (500 Å) to form the alignment key. Step 3, the shape of the electrodes on the chip is patterned with the photoresist (AZP-4620) as protection layer on the ITO layer in photolithography for ITO etching process. Then, the chip is dipped into the etching solution (H_2O ： 37% HCl=1:1 at 55 ^oC) to form ITO electrodes. Step 4, a parylene C insulating layer (1μm) is deposited. Step 5, the parylene C insulating layer is etching with O_2 plasma by RIE-1C for exposing the counter and working electrodes.

The fabricated chip is shown in Fig. 7. The fabricated gelatin micropatterns on each exposed area of the working electrodes are 60μm×60μm shown in Fig. 8. Additionally, a PDMS well with a volume of only 600 μL around the sensing electrode is fabricated on the chip shown in. The PDMS well can separate the signal I/O pads and the sensing area of ITO electrodes for cell cultivation. Such a miniaturization approaching is also beneficial to minimizing the dosage amount of incubating media and cells. Finally, the chip with the PDMS well is immobilized on a PCB and the signal I/O pads are connected with the PCB by wire bonding. The complete compact ECIS chip for monitoring the individual cell morphology is shown in Fig. 9.

III. RESULTS

Due to the smaller space limitation of the fore-mentioned compact incubator, we designed and developed an ECIS chip with smaller size and finer linewidth of electrodes than the prior art [21]. The smaller electrode areas are comparable to the cells attached to it. It takes the advantage of better sensing sensitivity if the very small amount of cells attached on the electrode has been confirmed. This confirmation is done by using the gelatin micro patterns to attract the cells selectively.

In this work, HeLa cells are applied to recording the impedance corresponding to different growth time. An *in-situ*

captured image shown in Fig. 10 or Fig. 11(a) is used to ensure the initial start of measurement. The impedance spectra are shown in Fig. 11(b). The measured parameters in previous work [21] and this work are compared and listed in Table 1. The sensing resolution of time in this work can be actually reduced to 1 hour) shorter than 1 day in previous work. In Fig. 11, cell growth for 24 hours (the time for cells lying down on the gelatin micropatterns) causes the maximal increase of impedance compared to none cell growth at 20 Hz, which is somewhat smaller than but close to 30 Hz in previous work. More interestingly, the impedance turns to reduce to or even lower than the initial impedance value of the culture beginning. Furthermore, the impedance is two-order larger than previous work. It means that the sensing current in the chip is two-order smaller and the cells are not damaged in the impedance measurement.

IV. CONDLUSION

In summary, the cell culture system developed in this work has a performance of providing better spatial resolution (40 μm) and time resolution (far less than 1 day). The impedance history measurement of a single HeLa cell proves the reasonable result compared to the prior art in the frequency domain. But it has two-order increasing in impedance value; the corresponding deceasing of sensing current preventing the damage on the living cells under monitoring. We believe it will be beneficial to the cell-based drug screening technology dealing with human diseases.

ACKNOWLEDGMENT

The authors would like to thank the financial support from the National Science Council of Taiwan with the research project numbers NSC-96-2221-E-032-013, -014, -52-MY2.

REFERENCES

[1] R. G. Harrison, "Observations on the living developing nerve fiber" Proc. Soc. Exp. Biol. Med., Vol. 4, pp. 140-143, 1907.

[2] C. S. Chen, M. Mrksich, S. Huang, G. M. Whitesides and D. E. Ingber, "Geometric control of cell life and death," Science, Vol. 276, Issue 5317, pp. 1425-1428, 1997.

[3] R. Langer and J. P. Vacanti, "Tissue engineering," Science, Vol. 260, No. 5110, pp. 920-926, 1993.

[4] P. Fromherz, A. Offenhauser, T. Wetter and J. Weis, "A neuron-silicon junction: A retzius cell of the leech on an insulated-gate field-effect transistor," Science, Vol. 252, No. 5010, pp. 1290-1290, 1991.

[5] G. W. Gross, B. K. Rhoades, H. M. E. Azzazy and M. C. Wu, "The use of neuronal networks on multielectrode arrays as biosensors," Biosensors and Bioelectronics, Vol. 10, Issue 6-7, pp. 553-567, 1995.

[6] B. Geiger, A. Bershadsky, R. Pankov, K. M. Yamada, "Transmembrane extracellular matrix-cytoskeleton crosstalk," Nat. Rev. Mol. Cell Biol., Vol. 2, Issue 11, pp.793-805, 2001.

[7] B. M. Gumbiner, "Cell adhesion: The molecular basis of tissue architecture and morphogenesis," Cell, Vol. 84, Issue 3, pp. 345-357, 1996.

[8] S. J. Fleire, J. P. Goldman, Y. R. Carrasco, M. Weber, D. Bray, F. D Batista, "B cell ligand discrimination through a spreading and contraction response," Science, Vol. 312, Issue 5774, pp. 738–741, 2006.

[9] D. Braun, P. Fromherz, "Fluorescence interferometry of neuronal cell adhesion on microstructured silicon," Physical Review Letters, Vol. 81, Issue 23, pp. 5241-5244, 1998.

[10] K. F. Giebel, C. Bechinger, S. Herminghaus, M. Riedel, P. Leiderer, U. Weiland, M. Bastmeyer, "Imaging of cell/substrate contacts of living cells with surface plasmon resonance microscopy," Biophysical Journal, Vol. 76, Issue 1, pp.509-516, 1999.

[11] S. Yang and T. Saif, "Micromachined force sensors for the study of cell mechanics," Review of Scientific Instruments, Vol. 76, Issue 4, pp. 1-8, 2005.

[12] I. Giaever and C. R. Keese, "Monitoring fibroblast behavior in tissue culture with an applied electric field," Proc. Natl. Acad. Sci. U.S.A., Vol. 81, Issue 12, pp. 3761-3764, 1984.

[13] I. Giaever and C. R. Keese, "A morphological biosensor for mammalian cells," Nature, Vol. 366, Issue 6455, pp. 591-592, 1993.

[14] C. D. Xiao, B. Lachance, G. Sunahara and J. H. T, Luong, "Assessment of cytotoxicity using electric cell–substrate impedance sensing: concentration and time response function approach," Anal. Chem., Vol. 72, Issue 22, pp. 5748-5735, 2002.

[15] J. H. T. Luong, M. Habibi-Rezaei, J. Meghrous, C. Xiao, K. B. Male and A. Kamen, "Monitoring motility, spreading, and mortality of adherent insect cells using an impedance sensor," Anal. Chem., Vol. 73, Issue 8, pp. 1844-1848, 2001.

[16] C. Xiao, B. Lachance, G. Sunahara and J. H. T. Luong, "An in-depth analysis of electric cell-substrate impedance sensing to study the attachment and spreading of mammalian cells." Anal. Chem., Vol. 74, Issue 6, pp. 1333-1339, 2002.

[17] M. Kowolenko, C. R. Keese, D. A. Lawrence and I. Giaever, "Measurement of macrophage adherence and spreading with weak electric fields," J. Immunol. Methods, Vol. 127, Issue 1, pp. 71-77, 1990.

[18] P. Mitra, C. R. Keese and I.Giaever, "Electric measurements can be used to monitor the attachment and spreading of cells in tissue culture," Biotechniques, Vol. 11, Issue 4, pp. 504-510, 1991.

[19] A. Rothermel, R. Kurz, M. Rüffer, , W. Weigel, , H. G. Jahnke, A. K. Sedello, H. Stepan, , R. Faber , K. Schulze-Forster, A. A. Robitzki, "Cells on a chip - The use of electric properties for highly sensitive monitoring of blood-derived factors involved in angiotensin II type 1 receptor signalling," Cellular Physiology and Biochemistry, Vol. 16, Issue 1-3, pp. 51-58, 2005.

[20] P. Seriburi, S. McGuire, A. Shastry, K. F. Bohringer and D. R. Meldrum, "Measurement of the cell-substrate separation and the projected area of an individual adherent cell using electric cell-substrate impedance sensing," *Anal. Chem.*, Vol. 80, Issue 10, pp. 3677-3683, 2008.

[21] M. Brischwein, S. Herrmann, W. Vonau, F. Berthold, H. Grothe, E. R. Motrescu, "Electric cell-substrate impedance sensing with screen printed electrode structures," Lab on a Chip, Vol. 6, Issue 6, pp. 819-822, 2006.

[22] L. J. Yang and Y. C. Ou, "The micro patterning of glutaraldehyde(GA)-crosslinked gelatin and its application to cell-culture," Lab on a Chip, Vol. 5, Issue 9, pp. 979-984, 2005.

[23] M. N. De Silva, R. Desai and D. J. Odde, "Micro-patterning of animal cells on PDMS substrates in the presence of serum without use of adhesion inhibitors," *Biomed. Microdev.*, Vol. 6, pp. 219-222, 2004.

[24] A. Revzin, P. Rajagopalan, A. W. Tilles, F. Berthiaume, M. L. Yarmush and M. Toner, "Designing a Hepatocellular Microenvironment with Protein Microarraying and Poly(ethylene glycol) Photolithography," Langmuir, Vol. 20, pp. 2999-3005, 2004.

[25] M. Veiseh, B. T. Wickes, D. G. Castner and M. Zhang, "Guided cell patterning on gold-silicon dioxide substrates by surface molecular engineering," *Biomaterials*, Vol. 25, pp. 3315-3324, 2004.

[26] Y. C. Ou, C. W. Hsu, L. J. Yang, H. C. Han, Y. W. Liu, C. Y. Chen, "Attachment of tumor cells to the micropatterns of glutaraldehyde (GA)-crosslinked gelatin," *Sensors and Materials*, Vol. 20, No. 8, pp. 435-446, 2008.

[27] J. B. Christen and A. G. Andreou, "Design, fabrication, and testing of a hybrid CMOS/PDMS microsystem for cell culture and incubation," IEEE Transactions on Biomedical Circuits and Systems, Vol. 1, Issue 1, pp. 3-18, 2007.

[28] Y. Qiu, R. Liao and X. Zhang, "Real-time monitoring primary cardiomyocyte adhesion based on electrochemical impedance spectroscopy and electrical cell-substrate impedance sensing," Analytical Chemistry, Vol. 80, Issue 4, pp. 990-996, 2008

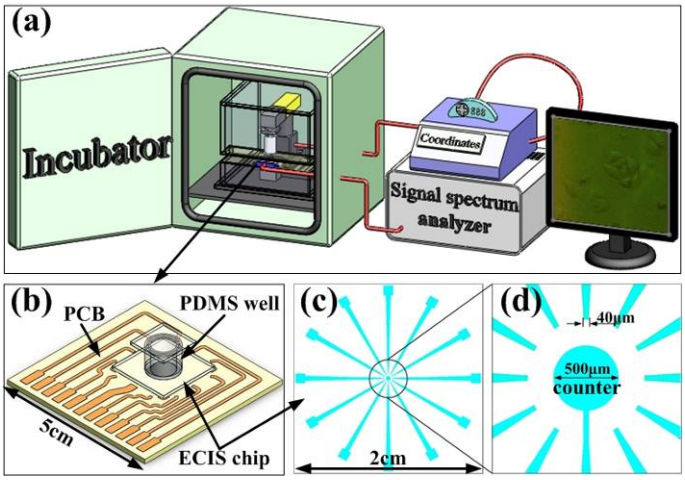

Figure 1 Diagram of whole system for real-time monitoring living cells.

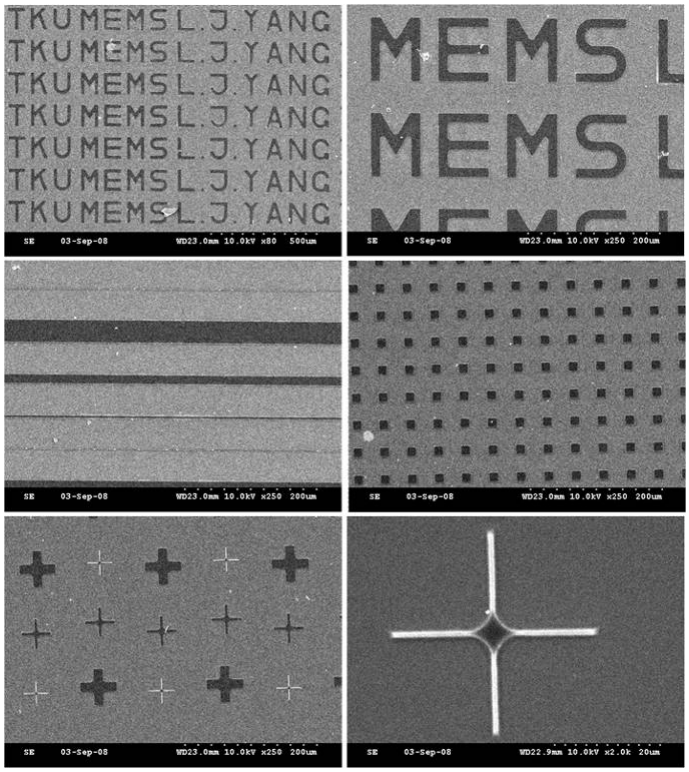

Figure 2 Photographs of fabricated gelatin micropatterns captured by SEM.

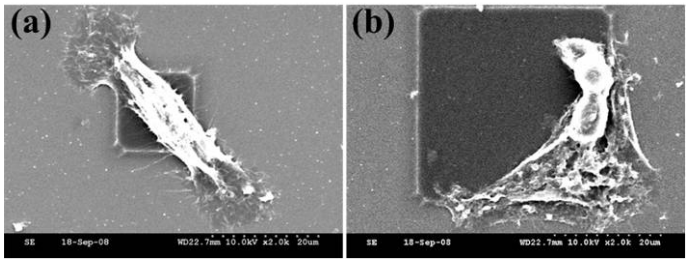

Figure 3 The SEM photographs of single HeLa cells attaching on gelatin micropatterns: (a) single HeLa cells attaching on 17 μm gelatin square; (b) single HeLa cells attaching on 37 μm gelatin square.

Figure 4 The completed setup of the novel optical monitoring system (middle pictures) into a commercial incubator (top-left picture); the bottom pictures show the compact module for microscopic observation with precise position control (top-right picture).

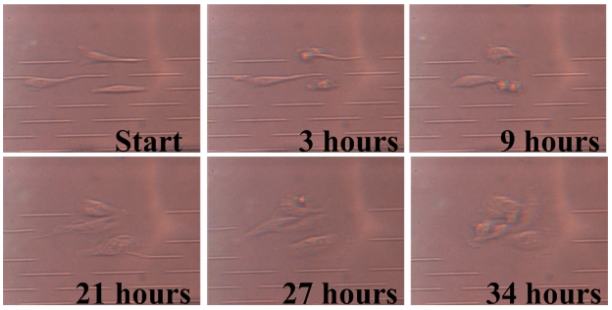

Figure 5 A demonstrated example of the optical monitor: the gelatin micropatterns are used to observe the adhesive behavior and the migration of the cells.

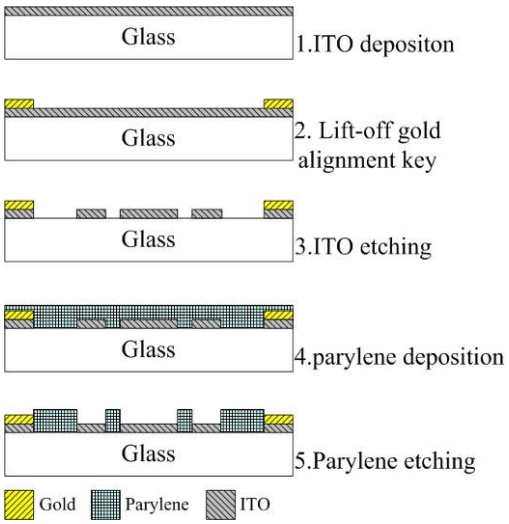

Figure 6 The flowchart of the ITO electrodes fabrication.

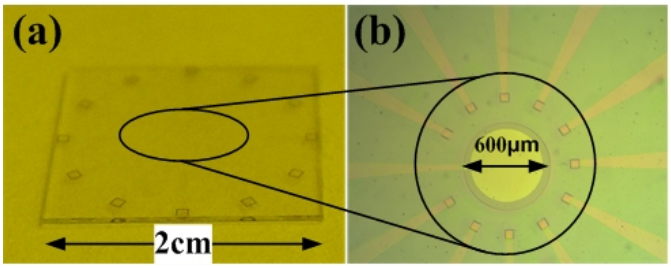

Figure 7 The fabricated sensor: (a) the fabricated ECIS chip with 2cm×2cm size; (b) the fabricated counter and working electrode.

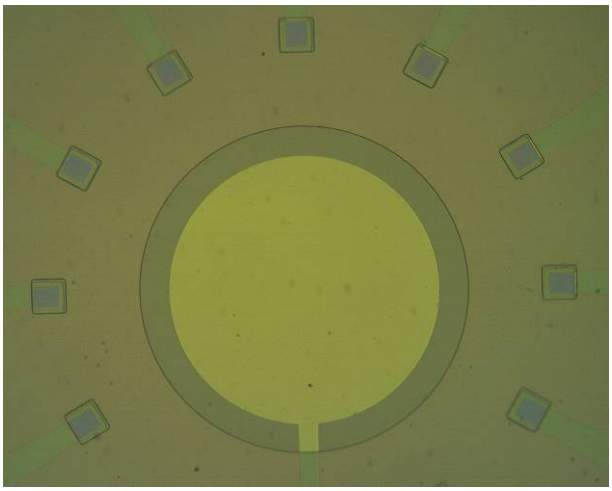

Figure 8 The working electrodes with 60μm×60μm square gelatin micropatterns.

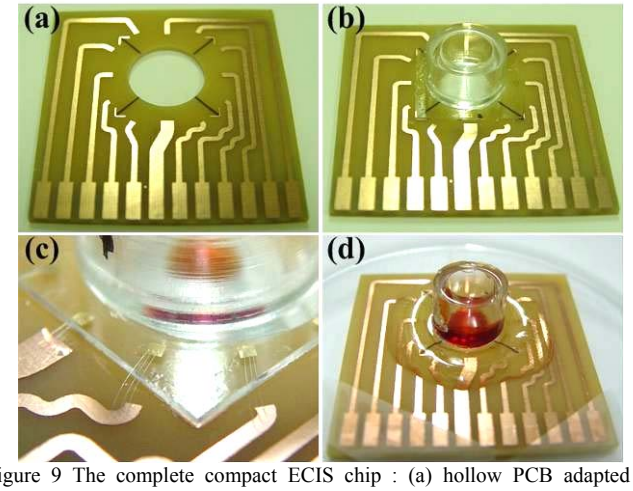

Figure 9 The complete compact ECIS chip : (a) hollow PCB adapted to requirement of the optical subsystem; (b) combination of PCB and ECIS chip with PDMS well; (c) signal I/O pads connected with the PCB by wire bonding; (d) packaged compact ECIS chip.

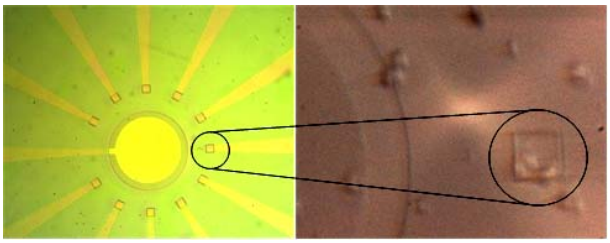

Figure 10 60μm×60μm square gelatin micropattern on the sensing electrodes (left picture) and HeLa tumor cells induced to attach on the 60μm×60μm square gelatin micropattern (right picture).

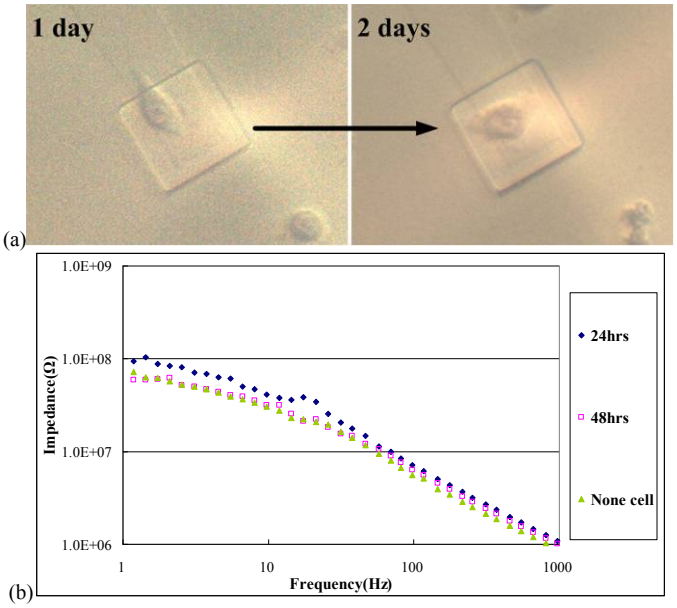

Figure 11 (a)Living cell images corresponding to different culture time (the starting "none cell" case denoting the suspension of the dosing cells; 24 hours denoting the round cells lying down on the gelatin micropatterns;48 hours denoting the spreading activity of cells); (b)The impedance spectra corresponding to different culture times of Hela cells on the gelatin micropattern.

Table 1: The comparison of impedance measurements.

Item	Frequency of maximal increase of impedance	Impedance range
Previous work [21]	30 Hz	10^5 Ω
This work	20 Hz	10^7 Ω

3B2-2

Study of the Annealing Effect of Low-Temperature Oxide on the Etch Rate in TMAH Solutions for Micro-Heater Applications

Wen-Chie Huang[1], Chung-Nan Chen[2], Shang-Hung Shen[2] and Cheng-Chia Chen[2]

[1]*Department of Electronic Engineering, National Kaohsiung University of Applied Sciences, Taiwan*

[2]*Institute of Photonics and Communications, National Kaohsiung University of Applied Sciences, Taiwan*

***Abstract* — Suspended structures are frequently used in some micro-electro-mechanical system (MEMS) devices. They are usually protected and supported by silicon oxide. Because the suspended structures are released from the silicon substrate in various etchants, the etch resistivity of the oxide layer is very important for suspended structure fabrication. In this paper, we improve the etch resistivity of low temperature chemical vapor deposition (CVD) silicon oxide layers by using annealing process to substitute thermal oxide grown in a high-temperature and high-cleanness furnace. We prepared thermal oxide and CVD oxide samples and then measured the etch rates after tetramethyl ammonium hydroxide (TMAH) anisotropic etching process and dry etch process. According to the experiment data, we found that the etch rates of CVD oxide were slightly decreased in dry etch and obviously decreased in TMAH solution. The etch rates of 600 ℃ annealed TEOS based oxide and 600 ℃ annealed SiH4 based oxide in 25 wt.% TMAH at 80 ℃ are 1.1 and 0.7 Å/min respectively. The etch resistivity of CVD oxide can compete the etch resistivity of thermal oxide when annealing temperature is up to 600 ℃. The stress characteristics of annealed oxide layer were also measured in this paper. The stress has a minimum value at 600 ℃ annealing temperature.**

In our work, a single crystalline silicon heater was successfully completed by using annealed CVD oxide as passivation layer. The heater with a resistance of 200 ohms glowed as bias current is up to 38 mA. We also simulated and characterized the temperature distribution of the microheater. The ANSYS simulation shows the central temperature of the microheater is 1135 ℃ as the bias power is 0.59 W.

Keywords —***Annealing process, CVD silicon oxide, MEMS, Microheater, TMAH***

I. INTRODUCTION

Micro-electro-mechanical systems (MEMS) technology [1] encompasses an enormous variety of medical and biological applications, including pulse measurement, body temperature sensing [2], DNA cloning [3], gas monitor [4], biological analysis, fluid pumping and delivery [5], temperature control and heating [6]. The DNA lab-on-a-chip is a device that integrates microheater, microsensor, reaction chamber and one or several laboratory functions on a single chip of only millimeters to a few square centimeters in size. It is high-speed and low reagent volume for real-time genotyping and diagnosis. Polymerase chain reaction (PCR) chips, consists of a microheater, a temperature sensor and a bulk-micromachined silicon reaction chamber, can be used for DNA amplifying and integrated into a fully automated DNA assay chip [7].

There are many materials, such as platinum (Pt), polycrystalline silicon (poly-Si) and single crystalline silicon (Si), are used in microheaters. The Pt thin film was usually used in microheater applications due to its high melting temperature and low oxidation rate at elevated temperatures [8]. However, it has poor long-term stability at high temperature operation [9]. The single crystalline silicon has high melting point, excellent mechanical property and superior CMOS process compatibility, it is suitable to serve as a microheater material layer. Backside etching of silicon-on-insulator (SOI) wafers and the etch stop of heavily boron-doped silicon were commonly used for forming Si suspended structures [10]. The main advantage of using SOI wafers is the simplicity of the device processing. However, SOI wafer is expensive, moreover, it needs to spend a lot of time in backside etching process. The etch stop technique of heavily boron-doped silicon can increase the etch resistivity of Si in some anisotropic etching process. The diffusion furnace process was used to form the heavily boron-doped silicon layer, but the heavy boron diffusion is not a standard CMOS process. In our design, the Si structure on <111>-oriented silicon wafer was doped by ion implantation and protected by CVD oxide layer during TMAH etching process. The floating silicon structure was completed due to the high etch selectivity of <100> silicon to <111> silicon in TMAH etchant. The suspended structure of our design have shorter etching time than backside etching process. Furthermore, the process is compatible to standard CMOS process.

Suspended structures were frequently used in BioMEMS devices, such as temperature sensors, flowmeters, pressure sensors and heaters, due to their excellent thermal and electrical isolation [11]. Since the etch resistivity of thermal silicon oxide is better than CVD oxide, thermal oxide layers were constantly

This project was funded by the National Science Council Plan (Project code NSC 97-2221-E-151-006).

Contact author: please contact **cn_chen@cc.kuas.edu.tw*

employed as the structure layers of the suspended structures. In semiconductor process, thermal oxide is grown at high temperatures from 800 ℃ to 1200 ℃. For the reason of process compatibility, we utilize an annealed low-temperature PECVD oxide films to protect the suspended structures during anisotropic etching. We found the annealed CVD oxide can get a lower etch rate in TMAH [12], dual doped TMAH etchant [13, 14], ICP, and RIE process.

II. Characterization of Annealed PECVD oxide

In this work, we prepared silicon oxide thin film samples, include thermal oxide, TEOS based and SiH_4 based PECVD oxide, and measured the etch rates of annealed samples after dry etch process and TMAH process. From the results, we found the etch rate of annealed CVD oxide obviously decreased in TMAH solution.

Initially, oxide layers were grown and deposited on different wafer respectively. They include thermal oxide 10000Å, SiH_4 based oxide 7000 Å and TEOS based oxide 5000Å. After silicon oxide thin film samples were prepared, the samples were annealed under the annealing temperature of 400 ℃, 600 ℃, 800 ℃and 1000 ℃ respectively.

Oxide thin films samples were etched in TMAH, ICP and RIE process respectively. We use 25% THAH and 5% dual-doped TMAH solution in TMAH process. The 5% dual-doped TMAH solution consists of 3.8wt% silicic acid and 0.7wt% AP in order to decrease the etch rate of aluminum in anisotropic etching process.

Fig. 1 and Fig. 2 show the etch rates of oxide films with different annealing condition after ICP process and RIE process respectively. After annealing process, the etch rates of CVD oxide films are decreased with increasing annealing temperature. The etch resistivity was improved obviously by annealing process before annealing temperature larger than 800 ℃.

As shown in Fig. 3, the etch rates of TEOS based and SiH_4 based CVD oxide are 2.1 and 2.2 A/min respectively in 25wt.% TMAH at 80℃ before annealing process. After annealing, CVD oxide etch rate are obviously decreased with increasing annealing temperature. Before annealing, the etch rate of TEOS based and SiH_4 based CVD oxide are 1.3 and 2.0 A/min, respectively in 5wt%TMAH +3.8wt% silicic acid +0.7wt%AP at 80℃(Fig. 4). When annealing temperature larger than 600℃, CVD oxide etch rate was lower than thermal oxide.

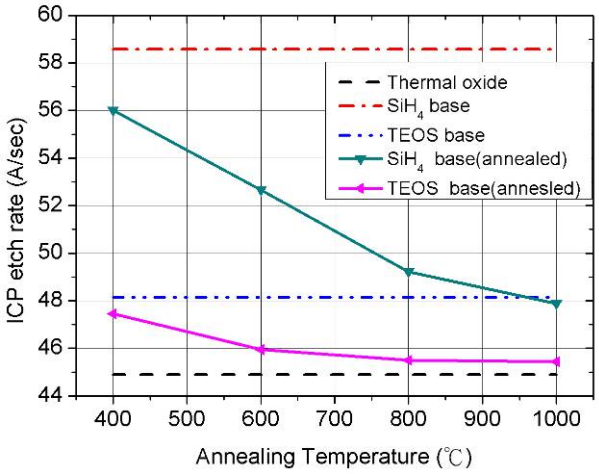

Fig. 1 Etch rate of oxide with different annealing temperature after ICP process

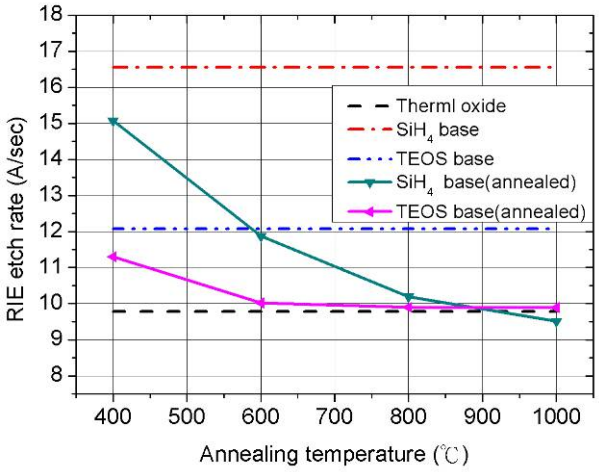

Fig. 2 Etch rate of oxide with different annealing temperature after RIE process

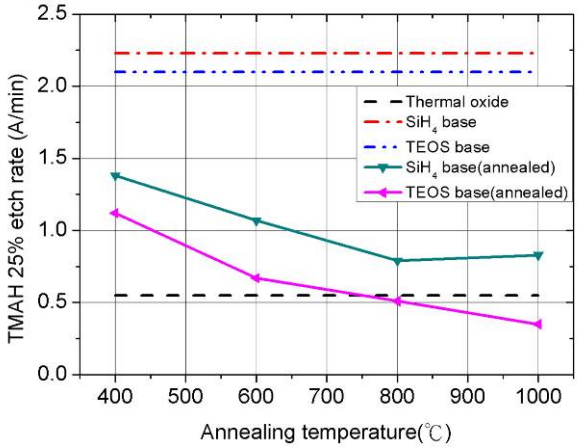

Fig. 3 Etch rate of oxide with different annealing temperature in TMAH solution

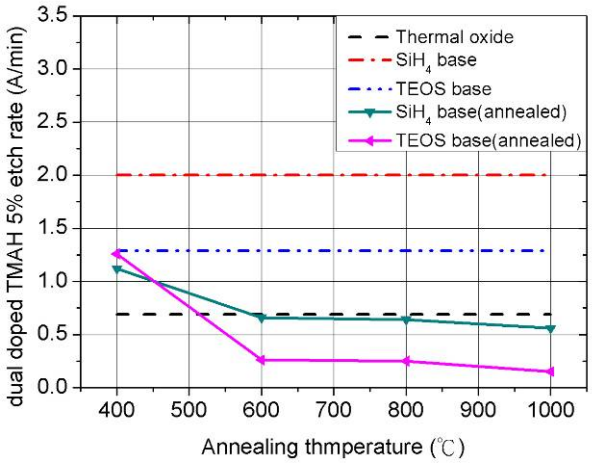

Fig. 4 Etch rate of oxide with different annealing temperature in dual doped TMAH solution

As shown in Fig. 5, TEOS based and SiH_4 based oxide are tensile stress before annealing process. After annealing, the stresses of SiH_4 based oxide films tend to change from tensile stress to compressive stress. The stresses of 600℃ annealed TEOS based and SiH_4 based oxide have minimum values of 2.56×10^8 and -1.7×10^7 respectively.

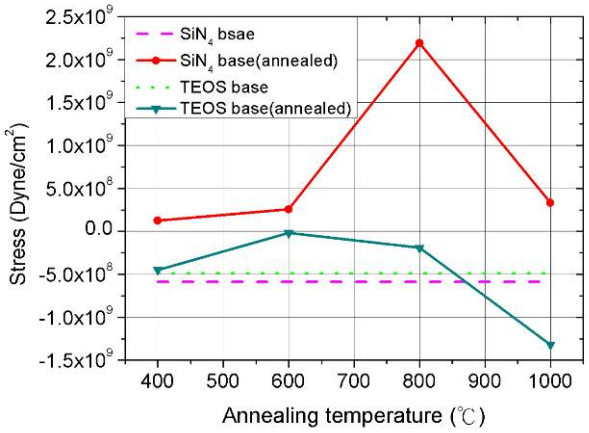

Fig. 5 The Stress of TEOS based and SiH_4 based oxide with different annealing temperature

III. FABRICATION AND MEASUREMENT

For the fabrication of the microheater, a five-layer mask set was used. Initially, the wafer was cleaned by RCA clean process (Fig. 6a). The thickness of microheater was defined by ICP etch process (Fig. 6b). The region of microheater was doped by ion implantation to reduce the resistivity of Si (Fig. 6c). A 200 nm PECVD oxide passivation layer was deposited by plasma-enhanced chemical vapor deposition (PECVD) (Fig. 6d) and then was patterned to define the metal contact holes by Reactive Ion Etching (RIE) (Fig. 6e). Afterward aluminum bonding pads with the thickness of 2um were deposited by using sputtering. It was patterned by aluminum etchant (Fig. 6f). Thus, the silicon substrate was contacted with bonding pads through by contact holes. Etching window were etched by RIE to expose silicon substrate. Then, the etch depth was etched by ICP process (Fig. 6g). Finally, suspended structure was released from the silicon substrate by anisotropic etching through the etching windows (Fig. 6h).

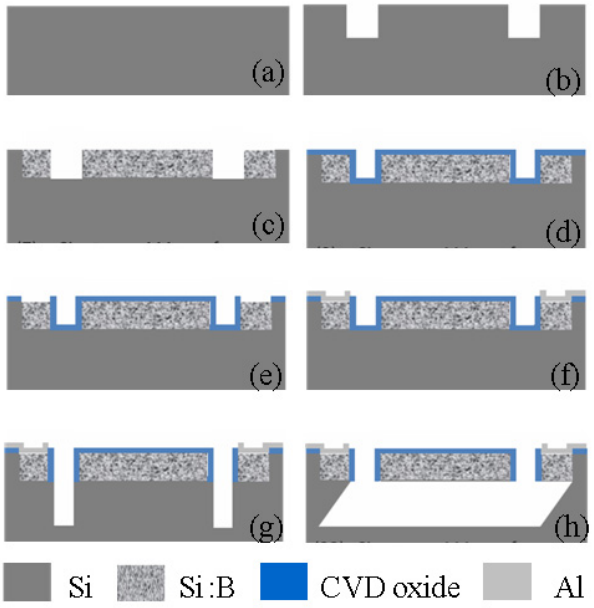

Fig. 6 Flowing chart of the microheater fabrication.

Finally, we successfully fabricated a bridge-type micro heaters on a <111>-oriented silicon wafer (Fig. 7). The performance of the microheater was measured by Keithley 2400 Source Meter on a probe station. Fig. 8 shows the microscope photographs of the heater biased in the current range of 38 mA to 42 mA. As the bias current was up to 38mA, we can find the device glowed. The power consumption of the heater was calculated as 0.4 W to 0.59 W. The frequency response was measured by pulse voltage. Voltage and frequency of pulse voltage were controlled through NI ELVIS workstation by LabVIEW program. The microheater was operated with a pulse voltage of 14 V in the frequency range of 1 to 5000Hz. As shown in Fig. 9, we can find the brightness of the microheater decreased with increased frequency. The microheater stopped to glow when the operating frequency was larger than 5000Hz. It implies that the thermal time constant of the microheater should be larger than 0.2 ms.

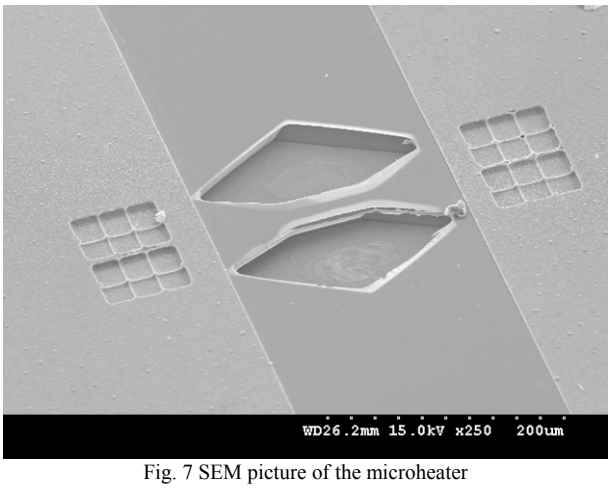

Fig. 7 SEM picture of the microheater

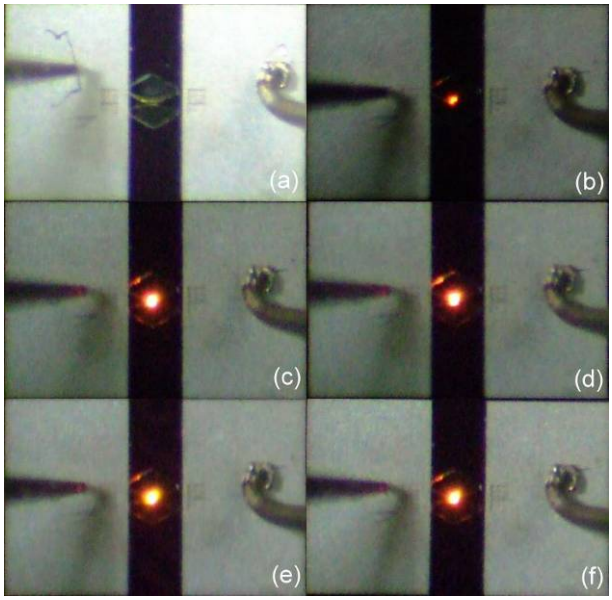

Fig. 8 The picture of a micro heater: (a) before biasing (b)38mA (c)39mA (d)40mA (e)41mA (f)42mA

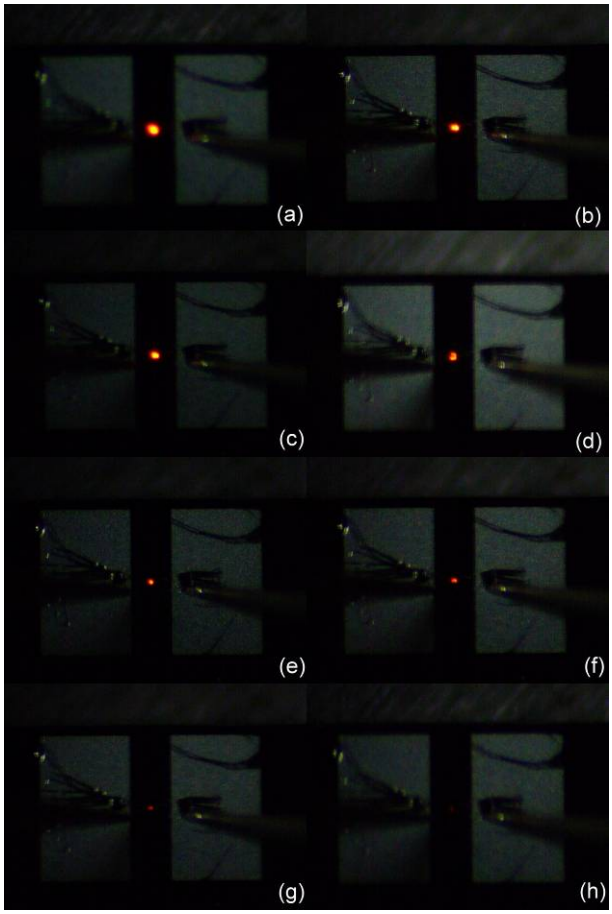

Fig. 9 The frequency response of a microheater: (a) 1Hz (b)10Hz (c)100Hz (d)1000Hz (e)2000Hz (f) 3000Hz (g) 4000Hz (h)5000Hz.

The performance of the microheater was also simulated and characterized by ANSYS. Fig. 10 shows the temperature distribution of the microheater at 0.59 W operating power. The central temperature of the microheater was 1135 ℃. Fig. 11 shows the silicon thickness effect on the central temperature of the heater. When operating at constant power, the central temperature was increased with lowering thickness due to the decreasing of solid thermal conductance.

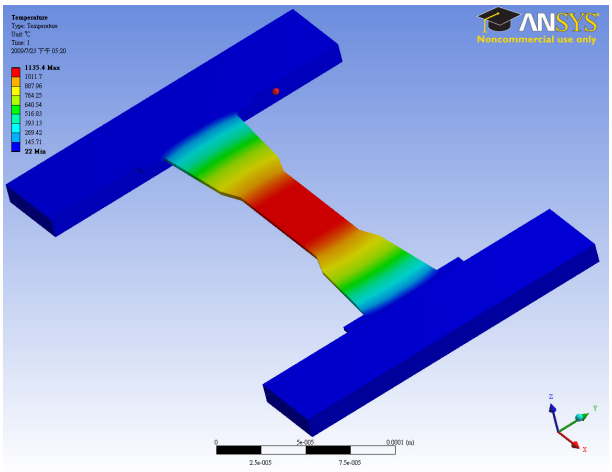

Fig. 10 The temperature distribution of microheater at 0.59W

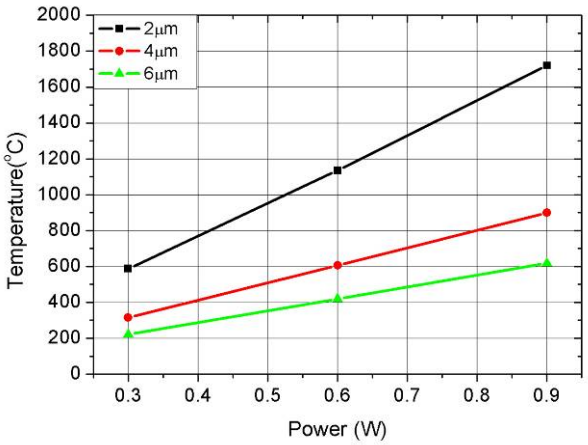

Fig. 11 The temperature of microheater at different thickness and operate power

IV. CONCLUSIONS

In this work, we improve the etch resistivity and the stress of CVD silicon oxide by using annealing process. In the dry etch process, the etch resistivity of CVD oxide was increased with increasing annealing temperature. When annealing temperature at 1000 ℃, the etch resistivity of CVD oxide was near the thermal oxide. Similarly, the etch resistivity of CVD oxide was increased with increased annealing temperature both 25% TMAH solution and dual doped TMAH solution. The etch resistivity of CVD oxide even lower than thermal with dual doped TMAH solution when annealing temperature larger than 600 ℃. Finally, we find a becoming annealing process parameter at 600 ℃ that have lower stress and highly etch resistivity. The stresses of 600 ℃ annealed SiH_4 based oxide and 600 ℃ annealed TEOS based oxide have minimum values

of 2.56×10^{8} and -1.7×10^{7} respectively.

Besides, the microheater was fabricated by using annealed CVD oxide as a passivation layer. As the bias current was up to 38mA, we can find the device glowed. When the heater biased in the current range of 38 mA to 42 mA, the power consumption was calculated as 0.4 W to 0.59 W. The pulse voltage was used for measured frequency response that was controlled through NI ELVIS workstation by LabVIEW program. We can find the brightness of the microheater decreased with increasing frequency. The microheater stopped to glow when frequency was larger than 5000Hz. We also simulate and characterize the performance of microheater by ANSYS. The centra temperature of microheater was 1135 ℃ at 0.59 W operating power.

REFERENCES

[1] Gary K. Fedder, "MEMS Fabrication", Department of Electrical and Computer Engineering, and The Robotics Institute Carnegie Mellon University, Pittsburgh, PA 15213-3890, 2003, pp.691-698

[2] A. Faes, F. Giacomozzi, B. Margesin, A. Nucciotti,"Fabrication of Silicon Bolometers with Bulk Micromachining Technology", Nuclear Instruments and Methods in Physics Research A 520, 2004, pp. 493-495

[3] Dae-Sik Lee, Se Ho Park, Kwang Hyo Chung, and Hyeon-Bong Pyo, "A Disposable Plastic-Silicon Micro PCR Chip Using Flexible Printed Circuit Board Protocols and Its Application to Genomic DNA Amplification," IEEE SENSORS JOURNAL, VOL. 8, NO. 5, MAY 2008, pp. 558-564

[4] Bhaskar R. Sathe, Mandar S. Risbud, Sanjay Patil, K.S. Ajayakumar , "Highly Sensitive Nanostructured Platinum Electrocatalysts for CO Oxidation: Implications for CO Sensing and Fuel Cell Performance", R.C. Naik, Imtiaz S. Mulla, Vijayamohanan K. Pillai, Sensors and Actuators A 138, 2007, pp. 376–383

[5] Bin Ma, Sheng Liu,Zhiyin Gan,Guojun Liu, Xinxia Cai, Honghai Zhang, Zhigang Yang "A PZT Insulin Pump Integrated with a Silicon Micro Needle Array for Transdermal Drug Delivery", Electronic Components and Technology Conference, 2006, pp.677-681

[6] P.K. Guha, S.Z. Ali, C.C.C. Lee, F. Udrea, W.I. Milne,T. Iwaki, J.A.Covington, J.W. Gardner, "Novel design and characterisation of SOICMOS micro-hotplates for high temperature gas sensors", Sensors andActuators B 127, 2007, pp. 260–266.

[7] C. Ke, A.M. Kelleher, A. Mathewson and M. M. Sheehan NMRC, Lee Maltings, Prospect Row, Cork, Ireland "Design and fabrication of a silicon microreactor for DNA Amplification" Proceedings of the 26th Annual International Conference of the IEEE EMBS San Francisco, CA, USA • September, 2004, pp. 1-5

[8] WILSON A. CLAYTON,"Thin-Film Platinum for Appliance Temperature Control",WILSON A. CLAYTON ,IEEE TRANSACTIONS ON INDUSTRY APPLICA71ONS. VOL. 24, NO. 2, MARCHIAPRIL 1988, pp.332-336

[9] Jan Spannhake, "High-temperature MEMS Heater Platforms: Long-term Performance of Metal and Semiconductor Heater Materials", Sensors 2006, 6, pp. 405-419.

[10] R. Edwin Oosterbroek," Etching Methodologies in<111>-Oriented Silicon Wafers". JOURNAL OF MICROELECTROMECHANICAL SYSTEMS, VOL. 9, NO. 3, SEPTEMBER 2000.

[11] Jan Spannhake,*, Olaf Schulz, Andreas Helwig, Angelika Krenkow, Gerhard Müller and Theodor Dol,l"High-temperature MEMS Heater Platforms: Long-term Performance of Metal and Semiconductor Heater Materials", Sensors 2006, 6, pp. 405-419

[12] Microelectronics Laboratory," Etch characteristics of KOH, TMAH and dual doped TMAH for bulk micromachining of silicon". Microelectronics Journal 37 , 2006, pp.519–525.

[13] K. E. Bean, "Anisotropic etching of silicon," IEEE Transactions of Electronic Devices,25, 1978, pp 1185-1193

[14] Mitsuhiro Shikida, "Differences in anisotropic etching properties of KOH and TMAH solutions," M. Shikida et al./Sensors and Actuators 80, 2000, pp.179–188.

3B2-3

Reusable CNTs-Based Chemical Sensors

Mengxing Ouyang and Wen J. Li*

Centre for Micro and Nano Systems, The Chinese University of Hong Kong, Hong Kong SAR, P.R. China

***Abstract* — Recovery time, which is one of the key metrics in gauging sensor performance, is crucial for CNTs sensors since it directly affects the reusability, reliability and accuracy of the sensors during detection. Using the resistive f-CNTs based ethanol vapor sensor as an example, we proved that the annealing method of heating up the sensor with a sufficient high current for a certain time period can effectively facilitate the sensor return to its original status. During experiments, chemical sensors, batch fabricated by forming bundles of chemically functionalized multi-walled carbon nanotubes along the Au electrodes on SiO2/Si substrates using dielectrophoresis technique, were developed for ethanol vapor detection. In addition, experiments were carried out to determine the relationship between recovery time and other parameters during ethanol vapor detection, such as annealing current, exposure time, and ethanol vapor concentration.**

Keywords — ***Carbon nanotubes, functionalized CNTs Sensors, ethanol vapor detection, sensor recovery.***

I. INTRODUCTION

For the last decade, carbon nanotubes have been receiving considerable attention as the sensing element for MEMS sensors due to their extraordinary properties such as minute size of the sensing element and the correspondingly small amount of material required for a response [1]. However, CNT sensors suffer from several drawbacks, one of which is their slow recovery time after exposure to stimuli. Some researchers have reported that without any processing on the sensor, it takes about 12 hours for CNTs to return to the original base resistance [2]. In order to overcome this limitation, a variety of methods have been used, such as heating up the sensor for desorption of the chemical molecules [3, 4], ultraviolet (UV) light illumination [5], Pd modification of carbon nanotube [6], and exposing the sensor towards humid air instead of dry air [7]. However, most of those methods require extra components (e.g., UV source and microheater) or complex procedure (e.g., CNT modification and humidity control) to achieve the purpose of accelerating the recovery process, which not only complicates the fabrication process of the sensor, but also raises the cost of the sensor, and even might make the sensors implausible for applications that require ultra-small sensing systems. In our lab, without the requirement of further implementing any component, we use carbon nanotube itself as the heating element to anneal the sensor back to its original reference resistance and the recovery time is controlled by the annealing current we applied to the sensor.

In our previous research, we have investigated the sensing performance of f-CNTs based ethanol vapor sensors, which not only proved good responsivity upon exposure to ethanol vapors by exhibiting an immediate sharp resistance increase, but also demonstrated fast response time [8]. During experiments, we found that the natural recovery process of the f-CNTs sensor towards its initial status is time consuming and sometimes unreliable. In order to further enhance the sensor reusability as well as to improve sensing accuracy, we used an annealing method to treat the sensor after each measurement by applying a relatively high current to heat up the sensor for a few minutes to accelerate its recovery. In this paper, we will demonstrate that this method is effective during measurements. Besides, three parameters that relate to the recovery time will be discussed in detail.

II. SENSOR FABRICATION

A. Sensor Fabrication and Experimental Setup

In our research, DEP manipulation was used to form carbon nanotube linkage between microelectrodes, which were fabricated on Si substrate by photolithography procedure. Chemical oxidation method was used to graft COOH group along the sidewall and the tube ends of the MWNTs. During the DEP formation, a droplet of f-CNTs solution was transferred to the gap between a pair of Au microelectrodes, which were excited by AC bias voltage. After a while, solvent will evaporate, and leave the f-CNTs connection between the two tips. This fabrication process has the advantages of simple fabrication procedure, low cost, and makes batch fabrication plausible.

After the successful fabrication of f-CNTs linkage, the sensor chip was then fixed and wire-bonded to a printed circuit board (PCB) board, where several small holes were drilled for the outlet of alcohol vapor, for the purpose of electrically connection with the measuring unit. And then, a plastic cover was put on top of the sensor chip. During the experiments, the ethanol vapor as generated by directing a well-controlled flow of compressed air into the mixed ethanol solution. A commercial source meter (Keithley 2400 Source Meter) was employed to measure and collect the electrical signals of f-CNTs sensors under constant-current configuration. The experimental setup is illustrated in Fig. 1.

This project is jointly funded by the Hong Kong Research Grants Council (project code: 413906) and the Chinese National 863 Plan Project (Ref. no.: 2007AA04Z317).

**Contact author: Prof. Wen J. Li: wen@mae.cuhk.edu.hk.*

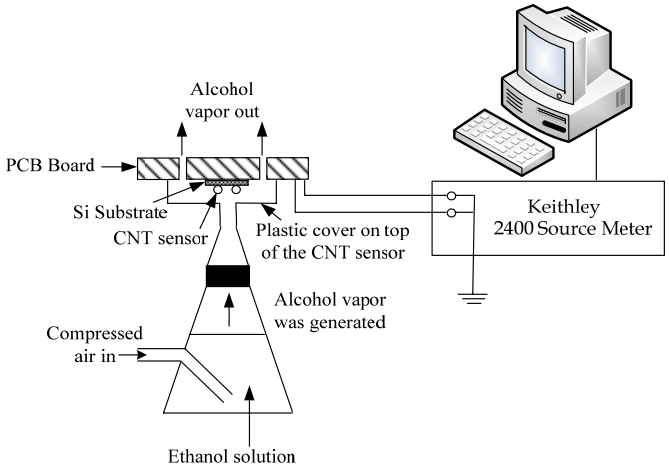

Fig. 1 Experimental setup of a constant-current f-CNTs ethanol vapor sensor.

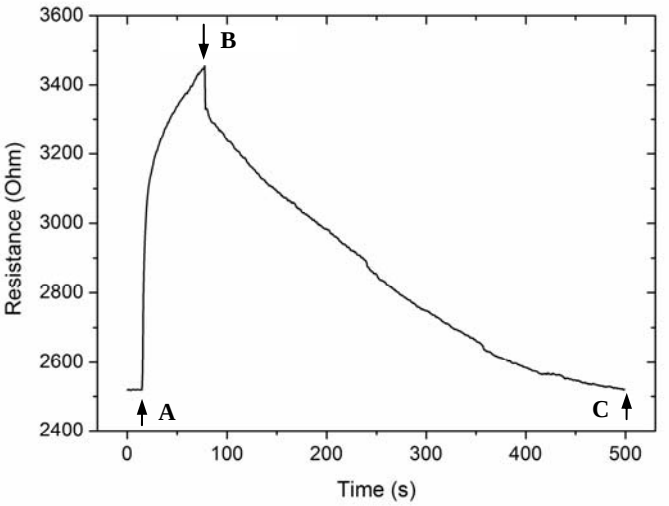

Fig. 3 Typical resistance change during ethanol vapor detection and recovery.

B. Sensing Mechanism

Fig. 2 shows a schematic diagram of how the ethanol molecules interact with the COOH groups through hydrogen bonds. We believe that with polar COOH groups attached onto the nanotube surface, the sensors will give stronger response towards the ethanol vapor as their absorption efficiency with these volatile organic molecules will be increased due to the fact that there are dipole-dipole interactions (mainly hydrogen bonding) between the COOH groups on the MWNTs and the polar organic molecules like ethanol. As illustrated in Fig. 2, the proposed mechanism of f-MWNTs sensor is described here: Once encountering the OH group of ethanol molecules in the ambient environment, the -COOH group attached to the carbon nanotubes would interact with the OH group through hydrogen bonds, which further leads to the resistance change of the ethanol vapor sensors. The main chemical reaction is given below:

$$-COOH+OH^- \rightarrow -COO^- + H_2O$$

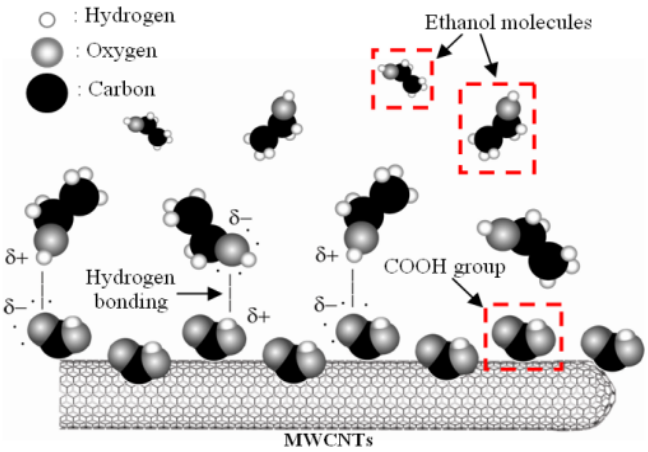

Fig. 2 Proposed Mechanism of f-MWNTs based Ethanol Vapor Sensing.

It has been noticed that the whole process is reversible if the ethanol molecules attached to the sensor surface are eliminated. During the experiments, we anneal the sensor by blowing the compressed air onto the sensor surface and apply relatively high current to heat up the sensor and clear up the residual molecules, where the previous method targets eliminates those molecules attached to the sensor surface physically while the latter approach untie the chemical bond between ethanol molecules and –COOH group.

III. Investigation of Sensor Recovery Process

During recovery of f-CNTs sensors, several factors would affect the recovery time: annealing current, exposure time and ethanol vapor concentration. In order to investigate how those parameters contribute to the recovery process, series of experiments were carried out.

For all the results presented in this section, we define the recovery time as the time interval that the sensor takes from the beginning of the annealing to the moment that it returns to the same resistance as the moment before it was exposed to ethanol vapor, i.e., the time interval between point B and point C as illustrated in Fig. 3. The reason that we use the above definition of recovery time is for the consistence of measurement and for the convenience during results comparison. However, we do realize that the comparison between resistance at point A and point C was conducted under different current (activating current at point A and annealing current at point C); it also has been noticed that at moment C, if we switch the current that applied to the sensor back to the activating current used at point A, the sensor resistance would increase for a certain value. This phenomenon could be expected from the negative Temperature Coefficient of Resistance (TCR) of the f-CNTs employed in our experiments. Moreover, based on this increased resistance only, we still lack evidence to prove whether the sensor has returned to its original status yet. Because after being heated-up during annealing process for several minutes, the temperature of the f-CNTs sensor is higher than ambient environment, i.e., room

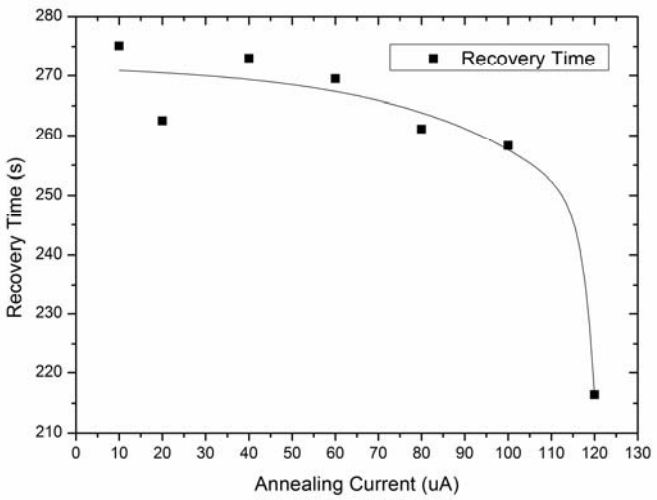

Fig. 4 Recovery time under different annealing current.

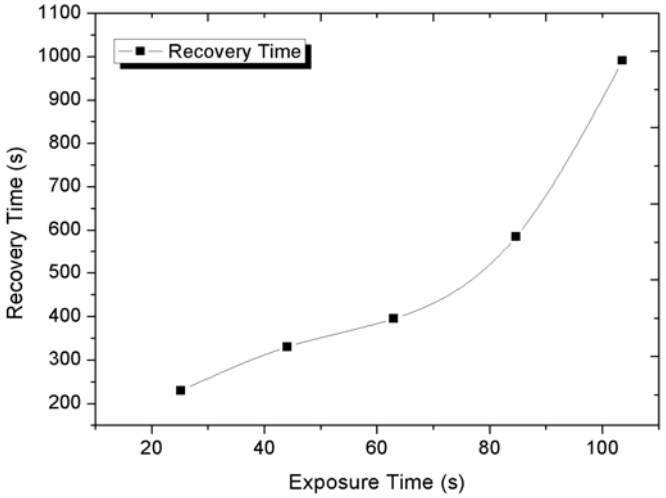

Fig. 5 Recovery time under different exposure time.

temperature in our case. Not to mention that under this circumstance, the instability of the sensor would jeopardize the sensor performance during the next cycle of measurement. However, according to our observation, after each recovery process, withdrawing the activating current and cool down the sensor for a while (~1-2 min) would stable the sensor and prepare it for a steady performance during further detection.

A. Typical Recovery Curve

As we mentioned previously, upon exposure to ethanol vapor, an instant sharp increase of resistance was observed. The process of ethanol vapor detection as well as the recovery of a typical f-CNTs sensor is illustrated in Fig. 3. At moment A, the sensor began exposure to ethanol vapor and exhibited a sharp resistance increase. After an exposure period of ~40 seconds, the ethanol vapor was withdrawn at moment B and the sensor was immediately activated with a relatively high current (e.g. 60μA in Fig. 3). Then, after ~420 seconds, the sensor gradually returned to its initial resistance. There are two main reasons that accelerate the decreasing of resistance once the sensor was heated up: The withdrawn of ethanol vapor that led the sensor to return to its original resistance, as well as the negative TCR of this kind of CNTs, i.e., the sensor resistance decreases in the non-linear I-V region due to heated temperature. Besides, higher energy stored on the sensor surface can also burn out the residue ethanol molecules attached onto the sensor surface which speed up the annealing process. In the response curve shown in Fig. 3, an immediate shift of the sensor resistance at moment B was observed, which is due to the fact that at the very moment, the activating current, which was within the linear region, was changed to the annealing current, which was in the non-linear region. Therefore, the negative TCR of the sensor determined that the sensor resistance exhibited a sudden drop.

B. Recovery under Different Annealing Current

Fig. 4 illustrates the recovery time versus annealing current. During the experiment, the annealing current applied to the sensor ranged from 10μA to 120 μA, and as shown the corresponding recovery time under the annealing current of 120 μA could reduce the recovery time from ~275s to ~216s. The decreasing trend in the figure showed that the larger the current we applied to the sensor, the shorter the recovery time. Also, we presume that the dramatic decrease of recovery time between 100 μA and 120 μA was due to the over-heat effect of our f-CNTs sensors annealing within non-linear region, i.e., under the high annealing current. Previously, we have demonstrated in our work [8] that overheating the CNTs is not desirable for the operation of f-CNTs ethanol vapor sensors, as the sensors exhibited larger responsivity and shorter response time when operated in the linear I-V curve region. However, for recovery process, the overheating of the sensing element was utilized to further accelerate the sensor annealing.

We note here that, although larger annealing current results in a shorter recovery time, which is desirable for actual applications, an excessively high current also increase the risk of burning out part or the whole CNTs network, further leading to the fluctuation of sensor resistance and jeopardizing the detecting precision, or even cost the sensor. Therefore, it is essential to find the optimal annealing current during experiments in order not only to reset the sensor within shortest time period, but also to maintain the stability of the sensor.

C. Recovery under Different Exposure Time

Another factor that affect the recovery time of the f-CNTs sensor is the exposure time of the sensor towards ethanol vapor. To investigate the relationship between them, a f-CNTs sensor was exposed towards the same ethanol concentration (i.e., 100ppth) for different time intervals and the recovery time during each cycle of measurement were compared. In Fig. 5, while the exposure time was elongated from 25 s to 105s gradually with a step of 20 s, the recovery time increased from ~230s to ~991s. The activating current and the annealing

(a)

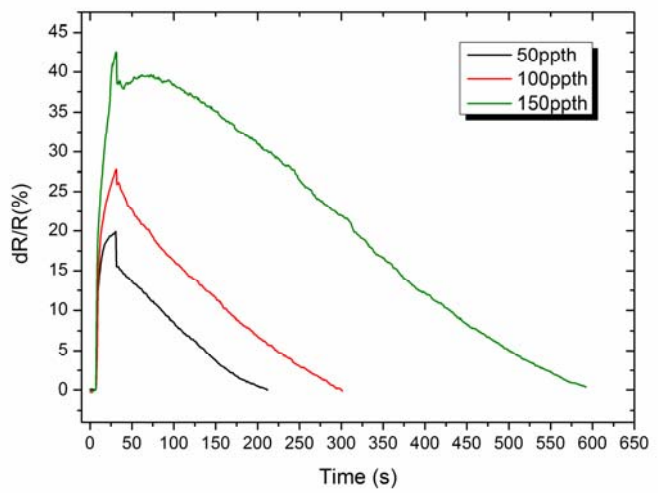

(b)

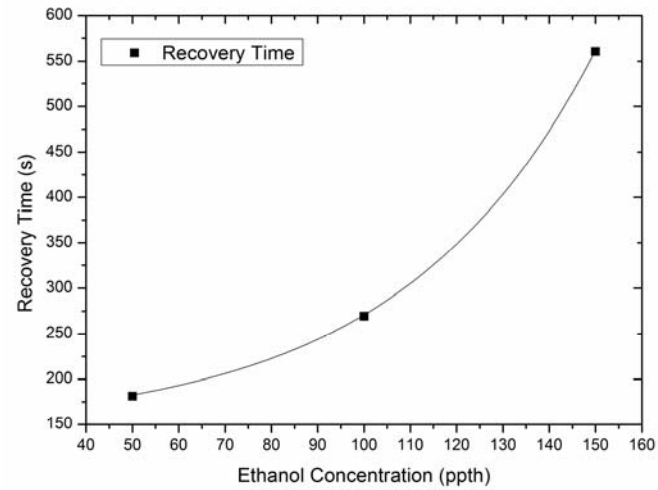

Fig. 6 (a) Response and recovery curve under different ethanol vapor concentrations; (b) Recovery Time versus ethanol vapor concentrations.

current used during the experiments were 1 μA and 30 μA, respectively. This result proves that longer exposure time towards chemical requires longer recovery time.

D. Recovery under Different Ethanol Vapor Concentration

In addition, experiments were carried out to determine the relationship between recovery time and ethanol vapor concentration. Other parameters such as exposure time and annealing current were kept constant during measurement. The sensor was exposed to ethanol vapor for ~20s under an activating current of 1 μA and then applied with an annealing current of 60 μA. The response curve using three ethanol vapor concentration (50ppth, 100ppth and 150ppth) were plotted in Fig. 6 (a) and the recovery time of each curve was calculated and compared in Fig. 6 (b). In the response curve under 150ppth, the resistance did not immediately decrease once the recovery process started as the other two curves. Instead, the resistance kept increasing for ~20s before it eventually began to drop. The explanation is that the high concentration

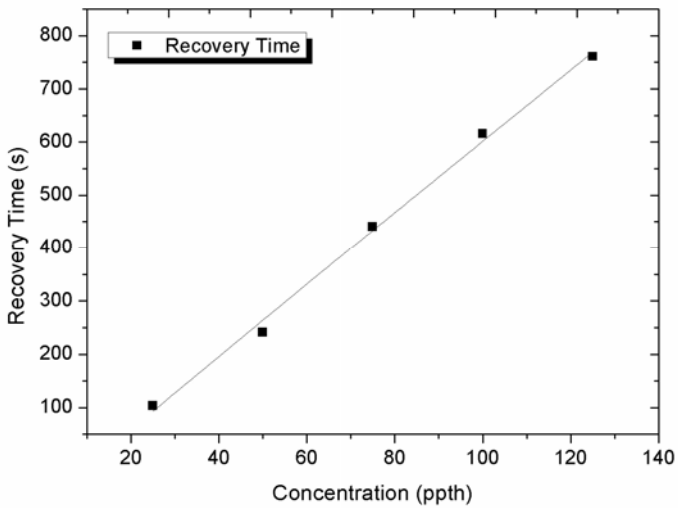

Fig. 7 Recovery time under different ethanol vapor concentrations.

(150ppth) still managed to have a strong influence on the sensor resistance for several seconds at the beginning of the annealing process, even if the sensor was already operated under a high current and was over-heated. Fig. 7 shows the detailed results of recovery time versus ethanol vapor concentration for another f-CNTs sensor. While the sensor was exposed to five different ethanol concentrations from 25ppth to 125ppth with a step of 25ppth, the recovery time using an annealing current of 30 μA increased from 104s to 761s. Results from both sensors reveal that longer recovery time is needed when sensor is exposed to higher ethanol vapor concentration.

IV. CONCLUSION

In order to overcome the limitation of long recovery time of the f-CNTs sensors, a successful attempt by means of using f-CNT itself as heating element to heat up the sensor after detection was investigated. Experimental results have proved that provided with sufficient annealing current, this method could effectively shorten the recovery time to the order of minutes (e.g. 5 min for our application) without fabricating or implementing additional heating component to the sensing system. Experiments proved that the larger annealing current, the shorter the recovery time. Moreover, longer exposure time and higher chemical concentration both require longer recovery time. For realistic applications, we should take into consideration all these factors and choose a well controlled and optimized annealing current that enable the sensor to recover within shortest time without causing instability or the burnt out of the CNTs sensing elements. In addition, the recovery process would be even more efficient if other annealing method were also employed, such as using dry air to blow on the sensor surface and cool down the sensor after each cycle of measurement, to guarantee the reset and the stability of the sensor status.

REFERENCES

[1] Ray H. Baughman, Anvar A. Zakhidov, Walt A. de Heer, "Carbon Nanotubes—The Route Toward Applications", *Science*, vol. 297, pp. 787-792, 2002.

[2] Cho, Taeg S., "An Energy Efficient CMOS Interface to Carbon Nanotube Sensor Arrays," *MS Thesis*, Massachusetts Institute of Technology, June 2007.

[3] W. Cho, S. Moon, Y. Lee, Y. Lee, J. Park, and B. Ju, "Multiwall Carbon Nanotube Gas Sensor Fabricated Using Thermomechanical Structure". *IEEE Electron Device Lett*., vol. 26, pp. 498-500, 2005.

[4] I. Sayago, H. Santos, M. C. Horrillo, M. Aleixandre, M.J. Fernandez, and E. Terrado et al, "Carbon Nanotube Networks as Gas Sensors for NO2 Detection", *Talanta*, vol. 77, pp. 758-764, 2008.

[5] J. Li, Y. Lu, Q. Ye, M. Cinke, J. Han, and M. Meyyappan, "Carbon Nanotube Sensors for Gas and Organic Vapor Detection", *Nano Lett*., vol. 3, pp. 929-933, 2003.

[6] J. Kong, M. G. Chapline, and H. Dai, "Functionalized Carbon Nanotubes for Molecular Hydrogen Sensors", *Adv. Mater*., vol. 13, pp. 1384-1386, 2001.

[7] S. Mubeen, T. Zhang, B. Yoo, M. A. Deshusses, and N. V. Myung, "Palladium Nanoparticles Decorated Single-Walled Carbon Nanotube Hydrogen Sensor", *J. Phys. Chem*., vol. 111, pp. 6321-6327, 2007.

[8] M. X. Ouyang, L.Y. Sin, K.H. Tsoi, C.T. Chow, M. K. Wong, and Wen J. Li *et al*, "Constant-Power Operation of Functionalized Carbon Nanotube Sensors for Alcohol Vapor Detection", *IEEE Int. Conf. on Nano/Micro Engineered and Molecular Systems*, pp. 747-752, January 6-9, Sanya, China, 2008.

3B2-5

Transparent Microelectrode Array in Diamond Technology

Z. Gao[1]*, V. Carabelli[2], E. Carbone[2], E. Colombo[1, 2], M. Dipalo[1], Ch. Manfredotti[3], A. Pasquarelli[2], M. Feneberg[4], K. Thonke[4], E. Vittone[3] and E. Kohn[1]

[1]*Institute for Electronic Devices and Circuits, Ulm University, Germany*
[2]*Department of Neurosciences and NIS Center, CNISM Unit, University of Torino, Italy*
[3] *Experimental Physics Department and NIS Center, University of Torino, Italy*
[4]*Institute of Semiconductor Physics, Ulm University, Germany*

***Abstract* — We report on the development of a diamond-on-sapphire microelectrode quadrupole array, substituting the commonly used inert metal electrode material by nanocrystalline diamond (NCD). This allows to combine the transparency (desired for fluorescence analysis) with the properties of an inert quasi-metallically doped diamond electrode. The NCD film was nucleated by BEN (Bias Enhanced Nucleation) on double side polished sapphire substrates and outgrown by hot filament CVD. Early quadrupole results on isolated adrenal chromaffin cells show the detection of amperometric signals corresponding to the quantal release of catecholamines contained in a single nanometric secretory vesicle.**

Keywords* — *MEA, nanodiamond, cell secretion analysis

I. INTRODUCTION

Planar microelectrode arrays are commonly used to detect amperometric and voltammetric signals in electroanalysis and biomedical sensing like in the in-vivo characterization of cell membrane channel activities. They are mostly based on a patterned array of inert metal electrodes (like Au or Pt) deposited onto Si, glass or plastic substrates. Metal electrodes allow the analysis of redox activities within the water dissociation window (~ 1.5 V), not easily allowing the detection of organic molecules with higher oxidation potential (like phenols). In the case of Boron Doped Diamond (BDD), water dissociation is suppressed across a wider potential window (~ 3 V), where the detection of substances like dopamine, histamine and even phenols has already been reported [1]. In addition, metal electrodes are non-transparent and do not allow high resolution fluorescence imaging from the backside of the sample. Even the surrounding silicon on which they are located is only transparent in the IR range, while bio-glass may display a cut-off wavelength in the mid-UV, depending on its composition [2]. Diamond on the contrary, possessing a semiconductor bandgap of 5.47 eV, is transparent between 225 nm and 12 μm [3]. NCD has been deposited onto transparent substrates like sapphire, glass and even high temperature stable plastic [4][5][6]. However, up to now the properties of the deposited nanocrystalline films have not been discussed in conjunction with biochemical and electrochemical applications, which require high corrosion resistance. In addition, the diamond surface can be functionalized in many ways to tailor its electrochemical sensitivity or further improve its already high biocompatibility [1][7]. An oxygen termination is mostly used, like in this investigation, resulting in a highly corrosion resistive surface.

We report here on the realization of a first simple quadrupole array with quasi-metallically doped diamond electrodes deposited onto a double side polished sapphire substrates. First amperometric tests have been performed on mouse adrenal chromaffin cells. The measurements show that diamond MEAs are able to detect quantal releases of catecholamines in terms of amperometric current spikes related to the oxidation of the secreted molecules.

II. EXPERIMEMTAL

A. Diamond Growth and Materials Characterization

The NCD electrode material stack has been deposited by hot filament CVD (HFCVD). It contained a nucleation layer on the double polished sapphire substrate, an undoped NCD layer and a highly boron doped top electrode layer. The nucleation layer was Si-based and nuclei generated by a bias enhanced nucleation (BEN) process at 800 °C. This layer may be mostly consumed in the gas phase (0.75 % CH_4/H_2) reactions leading to the generation of diamond nuclei and other carbon or Si containing clusters [8]. In spite of its inhomogeneity, this layer has a final thickness in the order of 10 nm, therefore affecting the transparency of the entire stack only to a small extent. The nucleation density has been ~ 3×10^{10} cm^{-2}. The further outgrowths were performed at 750 °C in a mixture of 0.3 % CH_4 in H_2 for both the undoped NCD layer (200 nm) and the highly boron doped top electrode layer (350 nm), resulting in a total thickness of ~ 550 nm.

To combine high electrochemical activity with high corrosion resistance, the outgrown NCD film has to contain a low grain boundary density as mentioned before, which is difficult to obtain with ultra-NCD. Furthermore, the grain boundary network should possess high energetic strength (leading to high chemical inertness) and contain therefore a large fraction of low angle grain boundaries. Such a condition has been obtained by α-parameter engineering [9] and an outgrowth to an average grain size of 70 nm (see Fig. 1), usually evaluated by SEM and AFM. The electrochemical "quality" has been assessed by comparison of the cyclic voltammograms with those of a Pt electrode. The optical properties in the wavelength range of 300 nm to 900 nm have been determined with a Varian CARY 300 UV-Vis spectrometer.

**Contact author: zi-yao.gao@uni-ulm.de, Institute of Electron Devices and Circuits, University of Ulm, Albert-Einstein-Allee 45, Ulm, 89081, Germany. Phone: (+49)(731)5026181, Fax: (+49)(731)5026155*

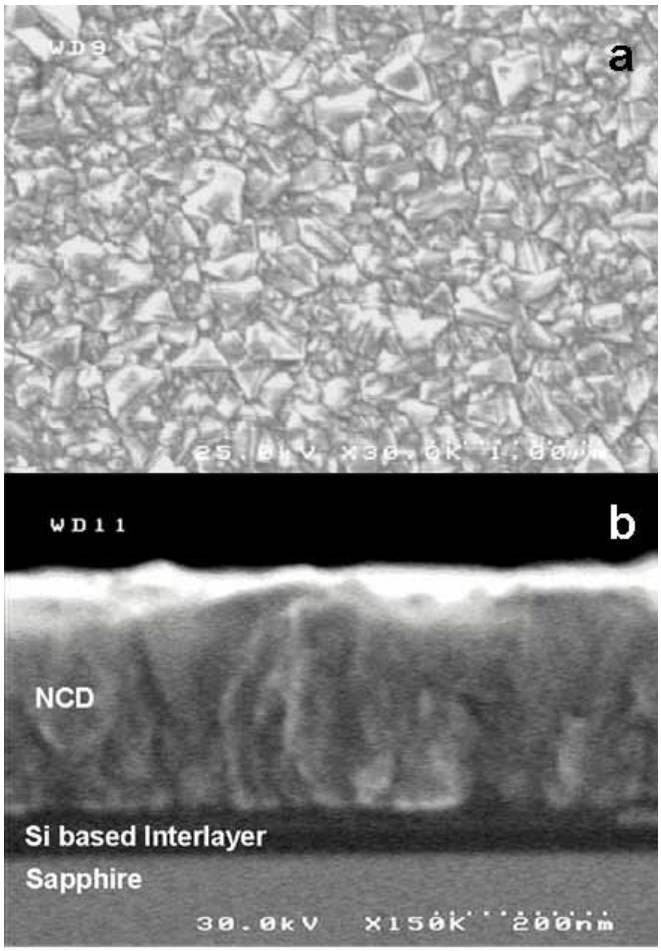

Figure 1. (a) shows a SEM micrograph of a BDD sample surface, (b) an SEM cross section also showing the Si-based nucleation layer.

B. Micro Array Fabrication

A micrograph of the micro array is show in Fig. 2. It shows the diamond/sapphire structure passivated with SU-8. The circular area is the active quadrupole opening of around 16 µm in diameter exposed to the liquid and cell. The areas A, B, C and D are the four electrodes, reaching into the centre as small triangular structures. The electrodes are separated by 5 µm gaps dry etched (by Ar/O_2) down to the insulating substrate. Ohmic contacts were obtained by Ti/Au metallization at the outside (not shown).

C. Cell Preparation and Handling

We isolated chromaffin cells obtained from mouse adrenal glands following a similar procedure used to isolate rat adrenal chromaffin cells [10]. Immediately after excision, the glands were placed in Ca^{2+} and Mg^{2+} free Locke's buffer containing (in mM): 154 NaCl, 3.6 KCl, 5.6 $NaHCO_3$, 5.6 glucose, and 10 HEPES, pH 7.2, at room temperature. Soon after, the glands were decapsulated and the medulla was precisely separated from the cortex. To obtain the chromaffin cells, the medulla was digested in the Locke's buffer, containing 20 U/ml of papain (Worthington Biochemical Corp., Lakewood, NJ) for 60

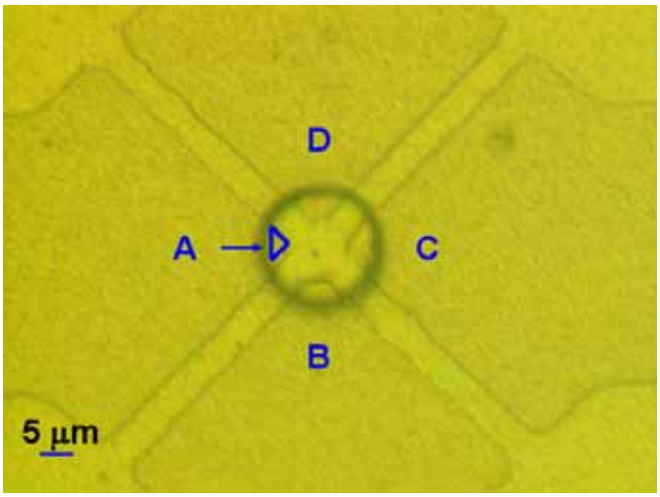

Figure 2. MEA micrograph as described in the text.

min at 37 °C. The cell suspension was then centrifuged for 5 min at 900 rpm, washed two times and resuspended in 2 ml DMEM supplemented with 15 % foetal calf serum (FCS). The typical experiment to detect amperometric signals consisted in placing an isolated chromaffin cell on top of the MEA and setting the diamond electrode potential between + 650 and + 800 mV. The cell was then chemically depolarized by applying an external solution containing 135 mM TEACl and 10 mM $CaCl_2$ delivered through a perfusion glass pipette pointing the cell. This depolarization causes the opening of voltage-gated Ca^{2+} channels, increases Ca^{2+} influxes through the open channels and vesicle exocytosis, with consequent release of catecholamines.

Cells signals were sampled with the set-up described in [11].

III. Results and Discussion

A. Electrode Characterization

The average grain size has been evaluated with around 70 nm as mentioned before and shown in Fig. 1, while the surface roughness was around 12 nm (rms) according to AFM images.

Before immersing the electrode into the physiological solution, the surface had to be stabilized, in essence by removing all residual sp^2-bonded carbon clusters by anodic treatment in 0.1M KOH at + 1.8 V vs. SCE, in the range of the oxygen evolution reaction. Fig. 3 shows the cyclic voltammograms measured after 3 priming cycles in 0.1 M KCl: the diamond electrode shows the typical potential window of 3.5 V (- 2.0 V ÷ 1.5 V vs. SCE), while the Pt-black electrode shows only 1.9 V. Also, the background current level of the diamond electrode differs as expected from Pt one by around 2 orders of magnitude (scan rate 50 mV/sec). The doping concentration extracted from a Mott-Schottky plot shows an average doping concentration of around 3×10^{20} cm^{-3}. When comparing these films with NCD grown on silicon under identical outgrowth conditions [12], we can conclude that no degradation of the electrochemical properties, e.g. potential window width and background current level, could be seen.

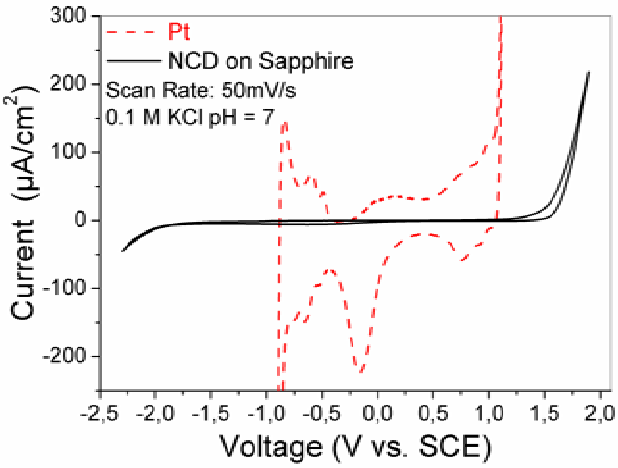

Figure 3 Cyclic voltammograms of a NCD-on-sapphire electrode compared to a platinum electrode in KCl solution (pH = 7).

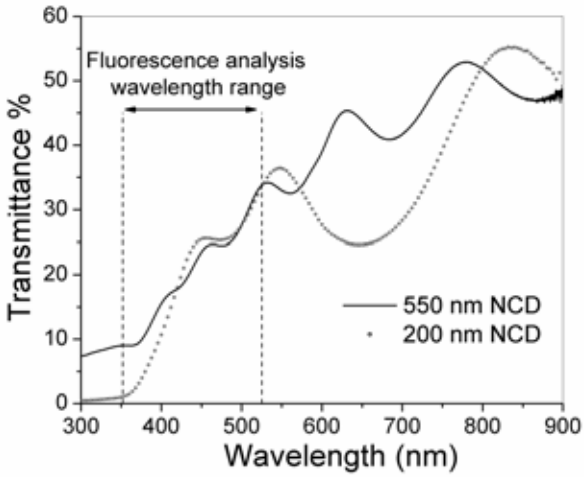

Figure 4. Transmittance spectra of two NCD samples: a 200 nm intrinsic layer (A) and a 550 nm one obtained by overgrowing a 200nm undoped layer with a 350nm B-doped layer (B).

B. Transparency Characterization

Fig. 4 shows the transmittance spectra of two NCD samples: (A) a 200 nm intrinsic (nominally undoped) layer and a 550 nm layer stack containing a 200 nm undoped layer and (B) a 350 nm boron-doped top electrode layer, the second one being similar to the stack used for the MEA fabrication discussed here. The spectra show different periodicity of the interference patterns due to the two different thicknesses and to the nucleation layer, the latter being more evident for sample (B) in the low wavelength range due to the smaller thickness. A decrease of transparency with shorter wavelength is observed for both samples. In fact, it is well known that surface roughness, graphitic phases embedded in the bulk, scattering at grain boundaries and thus also the average grain size influence the transmittance of diamond films [4][13][14]. In general it is found that ultra-NCD films show higher transparency due to their extremely small grain size [5]. However, the transmittance of diamond films on transparent substrates degrades generally towards lower wavelengths, probably also influenced by properties of the nucleation layer and the nucleation process itself. Usually outgrowth on transparent and electrically insulating films is performed on nanoseeds deposited from a solution. Here BEN is used and little information is available on the optical properties of this nucleation layer.

Both films with a 70 nm average grain size and a surface suitable for electrochemical applications reveal a maximum transmittance of ~ 55 % at 800 nm. Furthermore, Fig. 4 depicts the wavelength range usually used for fluorescence analysis, showing a suitable transmittance of the two samples until the blue region of the visible spectrum and confirming the suitability of NCD on sapphire for bio-chips applications.

C. Functional Measurement of Cell Secretion

Amperometric measurements have been performed on chromaffin cells from mouse adrenal glands. After standard preparation [15], the cells were dispersed in a hyperpolarizing KCl-free solution and placed into the ~ 0.5 ml perfusion chamber of the MEA. Electronically-controlled micro-manipulators were employed to precisely place one single cell at the time on top of the four electrodes recording area. The NCD electrodes were biased between +650 and +800 mV as described before, corresponding to the optimal potentials for catecholamines oxidation. Subsequently, a 10 mM $CaCl_2$ /135 mM TEACl solution was applied in order to depolarize the cell and open the voltage-gated Ca^{2+} channels. Ca^{2+} ions were then able to flow through the open channels causing the Ca^{2+}-dependent release of catecholamines, which chemically oxidize at the diamond surface. Fig. 5 shows a group of redox spikes generated and acquired simultaneously a few seconds after the chemical stimulation at the four electrodes A, B, C and D facing the cell. Persistent activity was detected as long as two minutes after cell depolarization. As shown in Fig. 5, simultaneous signals have distinct peak amplitudes and durations, due to the release of differently sized vesicles containing catecholamines and/or to a diverse vesicle

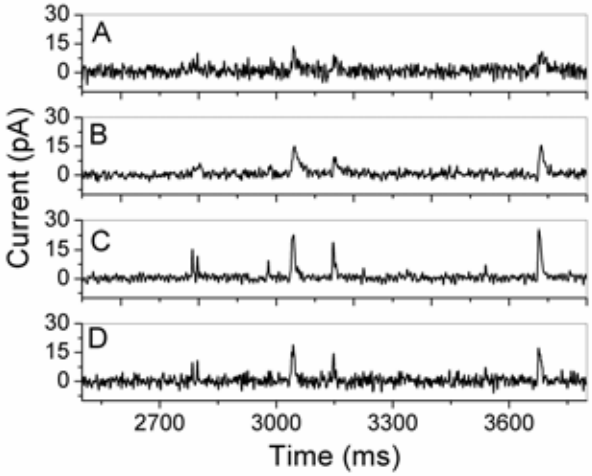

Figure 5. Simultaneous acquisitions of amperometric "spikes" from the MEA few seconds after a TEACl-induced depolarization of the cell. Each spike corresponds to the oxidation current of the catecholamine molecules contained in a single vesicle which firstly fuses to the cell membrane and then releases its content to the bath. Each recordings last approximately 1.2 s and shows the sequential fusion and release of five vesicles simultaneously detected from the four NCD microelectrodes.

orientation with respect to the diamond electrodes. We revealed spike signals with amplitudes ranging from 5 to 80 pA and durations between few milliseconds and several tens of milliseconds that were comparable in size and shape with the amperometric spikes detected using standard carbon microelectrodes with 5 μm tip diameter [10].

IV. CONCLUSION

A quadrupole microelectrode array based on quasi-metallic CVD diamond electrodes (BDD) patterned on a sapphire substrate has been fabricated and tested in the amperometric mode of operation with chromaffin cells from mouse adrenal glands. Amperometric spikes could be clearly detected by the four recording diamond electrodes, corresponding to the oxidation current of the catecholamine molecules. The simultaneous responses of single exocytotic events were detected with a high signal to noise ratio.

The electrodes consisted of a materials stack, containing a nucleation layer, an undoped NCD layer and a highly boron doped electrode layer. Thus, this stack is highly inhomogeneous, generating light scattering and also absorption due to graphitic phases, remaining Si in the nucleation layer and the high boron doping level of the electrode layer. However, each of these films has been scaled down as much as possible in thickness, still maintaining an average grain size of 70 nm at the surface. The stack becomes opaque at short wavelength, the reason not being entirely clear at present, since this tendency is also seen for NCD films deposited with different techniques and on various other transparent substrates. Nevertheless in the visible range, fluorescence can be detected and experiments to combine amperometric measurements and fluorescence labeling seem possible.

These first experiments indicate therefore the possibility to combine cell analysis based and highly localized fluorescence detection with amperometric MEA measurements identifying the dynamic behavior of single cell membrane activities. Thus, diamond based MEAs can indeed combine the features of fluorescence and electrical redox analysis. Moreover, being sapphire a common substrate to GaN-electronics, this materials configuration may eventually enable the combination of high density BDD electrode arrays with GaN electronic on-chip readout [16].

ACKNOWLEDGMENTS

This work was supported by the "Landesstiftung Baden-Württemberg", the Vigoni program and the Regione Piemonte. The authors want to thank C. Pietzka and Dr.-Ing. F. Demaria for their scientific contribution to this work.

REFERENCES

[1] Y. Zhou, J. Zhi, Talanta, 79 (2009) 1189.
[2] R.D. Gardner, A. Zhou, N.A. Zufelt, Sensors and Actuators B, 136 (2009) 177.
[3] M.E. Thomas, W.J. Tropf, A. Szpak, Diamond Films and Technology, 5 (1995) 159.
[4] M. You, F. Chau-Nan Hong, Y. Jeng, S.M. HuangM., Diamond and Related Materials, 18 (2009) 155.
[5] P.T. Joseph, N. Tai, Y. Chen, H. Cheng, I. Lin., Diamond and Relatated Materials, 17 (2008) 476.
[6] M. Daenen, O.A. Williams, J.D'Haen1, K. Haenen1, M. Nesládek1, Physica Status Solidi (a) 203 (2006) 3005.
[7] P. Ariano, P. Baldelli, E. Carbone, A. Gilardino, A. Lo Giudice, D .Lovisolo, C. Manfredotti, M. Novara, H. Sternchulte, E. Vittone., Diamond and Related Materials 14 (2005) 669.
[8] R. Stöckel, M. Stammler, K. Janischowsky, L. Ley, Journal of Applied Physics 83 (1998) 531.
[9] C. Wild, P. Koidl, W. Müller-Sebert, H. Walcher, R. Kohl, N. Herres, R. Locher, R. Samlenski, R. Brenn, Diamond and Related Materials, 2 (1993) 158.
[10] V. Carabelli, A. Marcantoni, V. Comunanza, A. de Luca, J. Diaz, R. Borges, E. Carbone, Journal of Physiology, 584 (2007) 149.
[11] A. Pasquarelli, V. Carabelli, Y. Xu, Z. Gao, A. Marcantoni, E. Kohn, E. Carbone, contribution to the 11th World Congress on Medical Physics and Biomedical Engineering, September 2009, Munich, "unpublished".
[12] A. Denisenko, G. Jamornmarn, H. El-Hajj, E. Kohn, Diamond and Related Materials, 16 (2007) 905.
[13] D. Franta, L. Zajíčková, M. Karásková, O. Jašek, D. Nečas, P. Klapetek, M. Valtr, Diamond and Related Materials 17 (2008)1278.
[14] L.C. Chen, T.Y. Wang, J.R. Yang, K.H. Chen, D.M. Bhusari, Y.K. Chang, H.H. Hsieh, W.F. Pong, Diamond and Related Materials, 9 (2000) 877.
[15] A. Marcantoni, V. Carabelli, D.H. Vandael, V. Comunanza, E. Carbone, European Journal of Physiology 457 (2009) 1093.
[16] M. Dipalo, Z. Gao, J. Scharpf, C. Pietzka, M. Alomari, F. Medjdoub, J.-F. Carlin, N. Grandjean, S. Delage, E. Kohn, Diamond and Related Materials 18 (2009) 88.

3B2-6

Nanofabrication of reactive structure for low temperature bonding

Yu-Ching Lin[1], Jörg Bräuer[2], Lutz Hofmann[3], Mario Baum[2], Jörg Frömel[2], Maik Wiemer[2], Masayoshi Esashi[1], Thomas Gessner[1,2,3]

[1]*WPI Advanced Institute for Materials Research, Tohoku University, JAPAN*
[2]*Fraunhofer ENAS, GERMANY*
[3]*Center for Microtechnologies, Chemnitz University of Technology, GERMANY*

***Abstract* — Microsystems that are used for medical application mostly consist of temperature sensible components. Therefore the temperatures during the fabrication process must be limited. This paper deals with the fabrication of reactive nanostructures that have the capability to be used as local heat source and thus can be used for processes during the fabrication of temperature sensible systems. Hereby, heat is produced during a self propagating exothermal reaction of two different materials that are present in a multilayered system of horizontal or vertical arranged material films in nanoscale dimensions. In this paper the principle of the self propagating reaction of those reactive systems as well as their fabrication is shown.**

Keywords — **nanofabrication, self-propagating exothermic reactions, reactive multilayer, silicon bonding**

I. Introduction

The system integration and packaging of microelectronics, micromechanical and microanalysis systems are increasingly affected by three dimensional chip stacking [1]. Major roles therein play the fabrication of bonding on wafer or chip scale [2-4]. Microsystems that are used for medical application mostly consist of temperature sensible components. Therefore the temperatures during the fabrication process must be limited. Therefore new low temperature processes are under investigation in the recent years. Another promising method is local heating of the joint interface (e.g. by the use of lasers).

Here we would like to introduce a new method of local heating for wafer bonding processes that is based on reactive nanoscale multilayer systems [5-10]. Especially, technologies using local and controllable heat sources have been developed recently. With these internal heat sources the required thermal bonding energy acts directly on the join, so that temperature sensitive components would not be damaged, see also Figure 1.

Such multilayer consist of several (up to thousand) alternating layers of two different thin metallic films each with thicknesses in the range of tens of nanometers. With the application of an initial energy pulse (ignition) the system starts to form intermetallic phases by interdiffusion of adjacent material layers. By choosing material combinations with negative enthalpy of formation this reaction runs exothermic. Moreover, the materials for reactive multilayer systems have to be a combination of a reactive component and a low melting component. The reaction is additionally promoted by the low thickness of the single layers due to a reduced diffusion path length. If the rate of thermal energy production is higher than the rate of thermal energy loss, the reaction is self propagating in lateral direction through the whole layer system [3].

This paper deals with the fabrication of reactive nanostructures that have the capability to be used as local heat source and thus can be used for processes during the fabrication of temperature sensible systems. Hereby, heat is produced during a self propagating exothermal reaction of two different materials that are present in a multilayered system of horizontal or vertical arranged material films in nanoscale dimensions.

II. Self-propagating reaction with NanoFoils

One typical example for the internal heat sources is the use of nanostructured reactive multilayers. These systems consist of numerous nanometer thick layers alternating between two elements that react exothermically during intermixing (c.f. Figure 2). Once the reaction is initiated by a pulse of energy the reaction can be self-propagating (velocities up to 30 m/s). This heat of reaction can be used as an internal heat source to melt intermediate layers.

As shown in Figure 2, nanoscale reactive multilayer systems typically consist of two alternating elements, for example A and B. In general, such systems are generated by layer-by-layer magnetron sputtering. The driving force in such a system to self-propagate is the reduction in chemical bond energy. In A-B multilayer systems compounds A_xB_y are formed when the constituents, A and B, intermix due to thermally induced atomic diffusion. This local intermixing produces a large amount of heat which is transmitted down to the neighboured constituents and so continues further intermixing. The heat faster generated due the exothermic

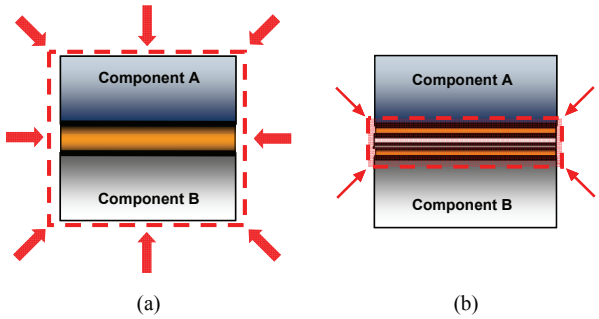

Figure 1. Heat flow during bonding: (a) external and (b) internal.

Contact author: Yu-Ching Lin, ***yclin@mems.mech.tohoku.ac.jp***
WPI Advanced Institute for Materials Research, Tohoku University, 6-6-01, Aramaki-Aza-Aoba, Aoba-ku, Sendai 980-8579, JAPAN
phone: +81-22-795-6256; fax: +81-22-795-6259

reaction than is removed by heat losses, like conduction or radiation, the reaction can be self-propagating. For the above mentioned reactive multilayer structures, the so called NanoBond© process, is used to join two silicon chips. Such systems are actually used as freestanding Ni/Al foils, so called NanoFoils© (product of Reactive Nano Technologies, USA) consisted of hundreds of Ni and Al layers, for joining (soldering) macroscopic parts of different materials as schematically shown in Figure 3. This process eliminates the need for further external heat sources, and with the very localized and fast heating rate even temperature sensitive materials or components could be joined at room temperature.

Herein, the 40 µm to 140 µm thick NanoFoils© are embedded in two sheets (several µm thick) of solder preforms and placed between the joining parts. Afterwards the components are pressed together and finally the reaction is initiated by a small pulse of energy, such as an electric spark [6]. Figure 4 shows two Silicon chips that were joined using two pieces of SnAg solder (25 µm thick) and a Ni/Al foil (60 µm thick). The NanoFoil© cracked during the joining process due to the applied pressure and the high heating and cooling rates. Furthermore it can be seen that the molten solder flowed into these cracks.

However, for bonding techniques in microsystems with bond frame dimensions of a few ten microns this method is not applicable similarly, because of handling issues and the limited ability of structuring such foils with smaller dimensions.

III. FABRICATION OF NEW TYPE NANO REACTIVE STRUCTURES

For developing substrate integratable process and fabrication simplification, new type nano reactive structures have been proposed as shown in Figure 5. Two different principles of reactive structures, conventional layer-by-layer (multilayer) and vertical arranged structures, will be produced by MEMS fabrication such as sputtering, electroplating, etching and so on. In comparison with the commercial freestanding Ni/Al nanofoils, new type reactive structures are fabricated directly onto substrates. The aim is to deposit such multilayer as integrated systems.

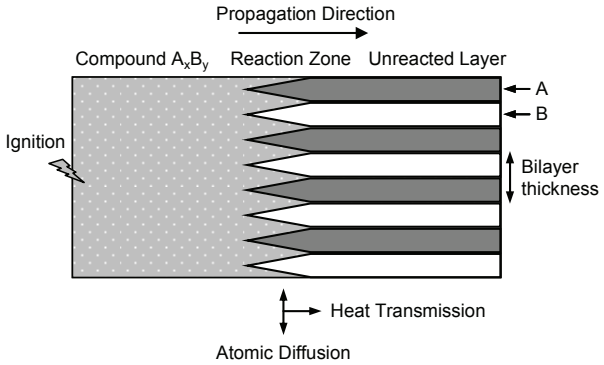

Figure 2. Schematic drawing of a self-propagating reaction in a multilayer system.

i. Multilayer fabrication - sputtering

Our approach is focused on the direct deposition of the reactive multilayer as well as the solder material onto the substrates. In the first instance we used sputter deposition to investigate the principle feasibility of the multilayered deposition as well as the principle of the reactive effect. As materials a combination of Al/Ti as well as Ti/Si were used.

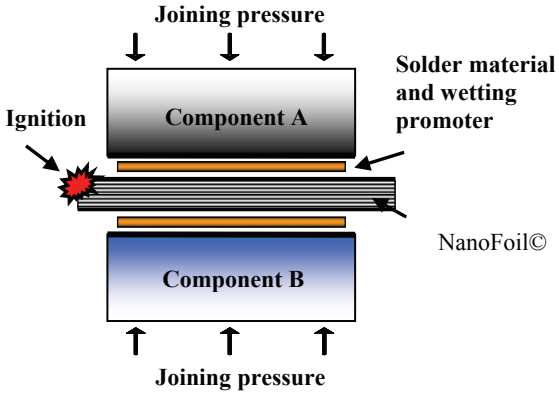

Figure 3. Schematic drawing of the reactive bonding process. Principle of joining process with reactive multilayer as thermal energy source.

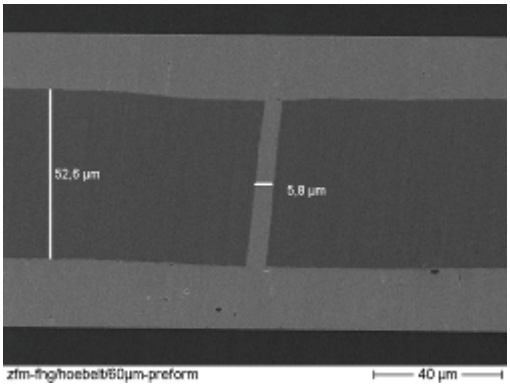

Figure 4. SEM of joined silicon substrates using NanoFoil© and SnAg solder.

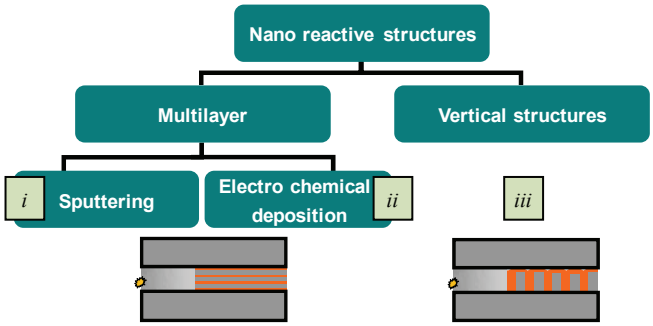

Figure 5. Schematic drawing of the nano reactive structures.

Reactive Al/Ti multilayer structures were fabricated by magnetron sputtering onto silicon substrates. The total thicknesses of the structures were up to 4 µm with 114 Al and Ti layers. TEM and NanoSpot-EDX analysis showed that no noticeable intermixing occurred during the deposition. Additionally, the structures were analyzed by DSC technique showing typical exothermic characteristics [9]. Though, self-propagating exothermic reactions could be detected. A typical microstructure of a non-reacted Al/Ti multilayer is shown in Figure 6. Herein the darker layers represents the Ti and the brighter the Al layer, respectively. In these structures no self-propagating reaction could be generated in structures directly onto substrates. By peeling-off the structures from the substrates self-propagating reactions could be generated, see also Figure 7.

By deposition of Ti/a-Si multilayer self-propagating reactions could be detected in relatively small (total stack layer thickness < 2 µm, see also Figure 8 for SEM cross section) structures directly onto substrates. To enhance the propagation of the reaction the substrates have to be heated up. With this additionally energy the reaction propagates over a four inch wafer area as shown in Figure 9.

ii. Multilayer fabrication - electro chemical deposition

The electro chemical deposition (ECD) or electroplating of these multilayers is an alternative technique to generate multilayer fast at low process temperatures. The motivation therefore is on the one hand the possibility of pattern plating what prevents the complex etching of structures after a blanket multilayer deposition. On the other hand the ECD process helps to reduce the process time and process complexity.

In principle there are two ways for ECD multilayer deposition. One is to use a two bath method, which means an alternating deposition in two different plating baths. The drawback is the process time and the limited minimal thickness of each single layer because of the permanent intermediate process steps (rinsing, pre treatment). Another way is a one bath method, whereupon our primary interest is laid on. Hereby, the plating chemistry of both film components is present in one bath. The deposition of each single material is controlled by a pulsed current/potential signal and by adjusting the concentration of the materials. The more noble metal is present only at low concentrations, whereas the less noble material is present at high concentrations. At low current densities the deposition of the noble metal is favoured; at higher current densities the less noble material is deposited and the deposition of the noble metal is suppressed due to the concentration based diffusion limitation. The number of materials that are suitable for ECD of reactive multilayer systems is limited.

For initial experiments we chose materials from the platinum group (Component A) in combination with the materials Sn, Zn or In (Component B). We investigated the deposition characteristic of electrolytes with different contents of each material in the electrolyte. The mass concentration ratio of Comp. A to Comp. B was derived from EDX measurements. For an electrolyte with very low concentration of Comp. A, this ratio is shown in Figure 10 in dependence on the used current density.

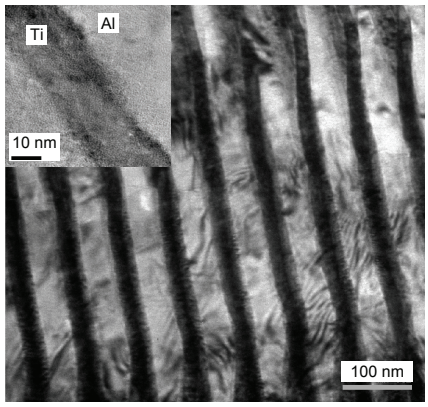

Figure 6. TEM images of a sputter-deposited Al-Ti multilayer.

Figure 7. Al/Ti multilayer after the reaction, note that some parts remain un-reacted.

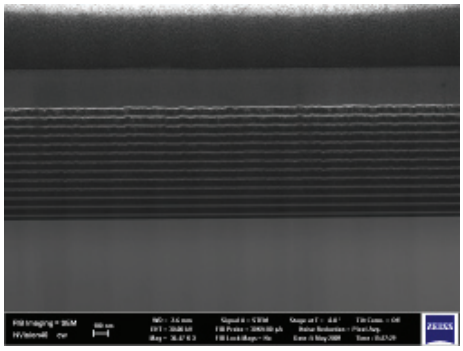

Figure 8. SEM micrograph of an Ti/a-Si multilayer.

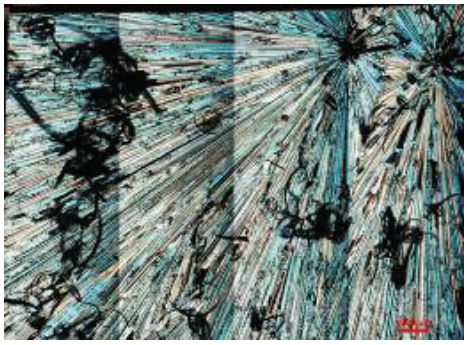

Figure 9. Ti/Si multilayer after the reaction.

Optimization of the purity of the materials in each single layer can be done by adapting the concentration of the corresponding component in the electrolyte. In primary experiments we deposited alternating layers from an electrolyte with low content of Comp. A. An example of two alternating layers is shown in Figure 11. The irregularities (roughness, unequal film thicknesses) are due to deviations in certain process parameters (purity of electrolyte, mass flow). By optimization of the process more homogenous multilayer can be deposited with thinner single layers (~10-30 nm) and higher numbers (10-50) of alternating layers.

iii. Vertical stuctures fabrication

Another approach regarding reactive bonding is the use of vertical nano structures instead of reactive multilayers. The principle is to rotate the multilayer system by 90°. Hereby the different materials are not stacked but they are arranged side by side. Those nano structures are created in a two step process. First of all needles in the silicon substrate are created by a Si dry etch process. Afterwards those needles are covered with second material by a sputter process and/or by electrodeposition. With the vertical alignment of the reactants the deposition of thousands of single layers is no longer required. This leads to large reduction in process time and to a minimization of process complexity. Fabricated nanostructures after dry etching and after coating are shown in Figure 12-14.

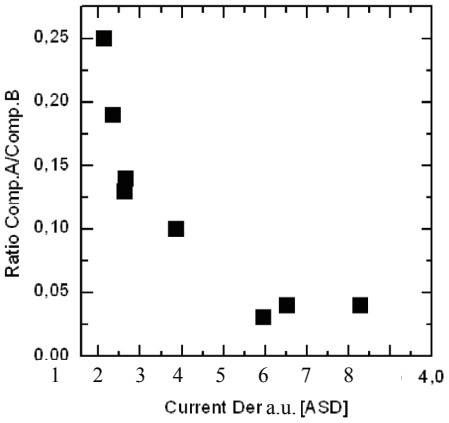

Figure 10. Mass concentration ratio of Component A to Component B in the deposited film in dependence on the current density with Comp. A being the noble metal at low electrolyte concentration.

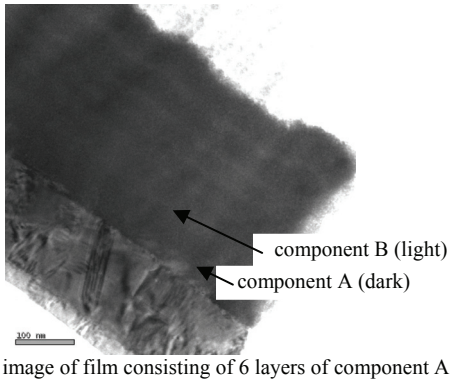

Figure 11. TEM image of film consisting of 6 layers of component A and 5 layers of component B

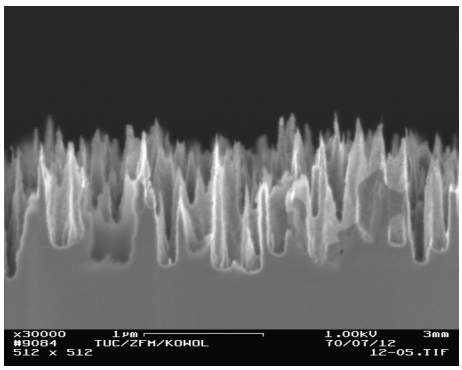

Figure 12. SEM micrograph of fabricated nanostructures.

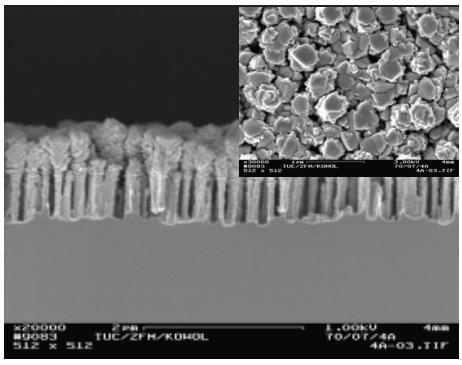

Figure 13. Nanostructures after coating by sputtering. Inset shows the top view of the structure.

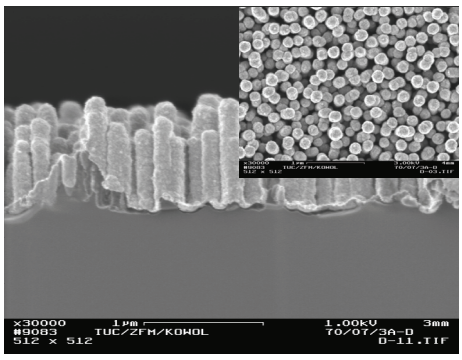

Figure 14. Nanostructures after coating by electrodeposition. Inset shows the top view of the structure.

The subsequent bonding process is done by aligning the substrate with the fabricated nanostructures to a second substrate. The aim is to use those nanostructures as reactive heat source for e.g. melting solder materials.

IV. CONCLUSIONS

With the nanofoils already applications were developed, where temperature sensitive components were joined onto substrates (Paper from RNT: Assembly of a polymer based microlense). The next step should be the adaption of this process to wafer level technologies and with structured reactive zones that could realize a selective bonding of semiconductor-like substrates. At least these processes could be performed for joining temperature sensitive biological activated substrates for

in-vitro diagnostics or even for medical polymer devices. Especially disposable micro fluidic devices (Lab-on-a-Chip) with sensing function and with already immobilised cells could be assembled to other substrates using this low temperature reactive bonding technology.

For these purposes, in this study, the multilayer and vertical arranged nano reactive structures are on-chip fabricated and analyzed. Reactive multilayer with Al/Ti and Ti/a-Si are fabricated by magnetron sputtering; moreover electro chemical deposition was investigated for the multilayer deposition. For the vertical nanostructure, black silicon fabrication process is used for patterning, and then the so generated holes are filled up by sputtering and electroplating deposition with Ni. Self-propagating exothermic reactions are also detected.

V. AKNOWLEDGMENTS

The authors thank the colleagues in the Center for Microtechnologies (ZfM) of Chemnitz University of Technology and Fraunhofer ENAS, for their valuable supports for experiments and characterization.

REFERENCES

[1] C. K. Tsang, P. S. Andry, et al., "CMOS-Compatible Through Silicon Vias for 3D Process Integration", Proceedings of Mater. Res. Soc. Symp., vol. 970, 2007.

[2] L. Hofmann, M. Kuechler, T. Gumprecht, R. Ecke, S.E. Schulz, T. Gessner, "Investigations on via geometry and wetting behavior for the filling of Through Silicon Vias by copper electro depostition", MRS Conf. Proc. AMC XXIV, pp. 623, 2008.

[3] Y. –C. Lin, M. Baum, M. Haubold, J. Frömel, M. Wiemer, T. Gessner, M. Esashi, "Characterization of eutectic wafer bonding using Gold and Silicon", Proceedings of international conference on smart system integration, 2009.

[4] Y. –C. Lin, M. Baum, M. Haubold, J. Frömel, M. Wiemer, T. Gessner, M. Esashi, "Development and evaluation of AuSi eutectic wafer bonding", Proceedings of international conference on solid-state sensors and actuators (Transducers '09), 244-247, 2009.

[5] A. J. Gavens, D. Van Heerden, A. B. Mann, M. E. Reiss, T. P. Weihs, "Effect of intermixing on self-propagating exo-thermic reactions in Al/Ni nanolaminate foils", Journal of Applied Physics, vol. 87, pp. 1255-1263, 2000.

[6] J. Wang, E. Besnoin, A. Duckham, S. J. Spey, M. E. Reiss, O. M. Knio, M. Powers, M. Whitener, T. P. Weihs, "Room-temperature soldering with nanostructured foils", Applied Physics Letters, vol. 83, pp. 3987-3989, 2003.

[7] J. Wang, E. Besnoin, O. M. Knio and T. P. Weihs, "Investigating the effect of applied pressure on reactive multilayer foil jointing", Acta Materialia, vol. 52, pp. 5265-5274, 2004.

[8] J. Wang, E Besnoin, A. Duckham, S. J. Spey, M. E. Reiss, O. M. Knio and T. P. Weihs, "Jointing of stainless-steel specimens with nanostructured Al/Ni foils", J. Appl. Phys., vol. 95, no. 1, pp. 248-256, 2004.

[9] J. Braeuer, M. Baum, M. Wiemer, T. Gessner, "Reactive micro joining by using nanoscale effects", Proceedings of Mikro-Nano-Integration, Seeheim, Mar 12-13, 2009.

[10] T. Namazu, H. Takemoto, H. Fujita, Y. Nagai, and S. Inoue, "Self-propagating explosive reactions in nanostructured Al/Ni multilayer films asalocalized heat process technique for MEMS", Proceedings of international conference on micro electro mechanical systems (MEMS '06), 2006.

P02

Application of a novel focused microlens to the LED packaging

Chi-Chang Hsieh[1], Pa-Yee Tsai[2*], Yan-Huei Li[3]

[1]*Department of the Mechanical and Automation Engineering, National Kaohsiung First University of Science and Technology, Kaohsiung, Taiwan*

[2]*Department of the Mechanical Engineering, National Cheng Kung University, Tainan, Taiwan*

[3]*Department of Mechanical and Electro-Mechanical Engineering, National Sun Yat-sen University, Kaohsiung, Taiwan*

***Abstract* — The light-emitting diode (LED) has been extensively applied to the lighting system. In this paper, a novel optical structure design of the focused microlens, it can achieve a specific light focusing effect through changing the structural design. We modified and redesigned the optical microlens structure from the basic specification of the present LED packaging, and the light pattern can be altered through adjusting the proportion of depth and width of the structure. The light focusing ability of this novel focused microlens has been greatly enhanced within the range ±15° of the lighting angle. The maximum illuminance has been enhanced 99.3% in comparison with the traditional LED packaging, and the average luminous flux rayed out through within the range ±15° from the normal of the LED has been enhanced 34% as well.**

Keywords — Diffractive Optical Element; LED packaging; Microlens; Optic Design

I. INTRODUCTION

The LED has become the primary development for solid lighting system in the future for the advantages of its small dimension, low energy consumption and strong reliability [1-3]. The LED lighting angle is basically wide and it is effective and applicable for short distance, indoor and indicator lighting systems. Nevertheless, the performance for outdoor and long distance lighting systems is not satisfying due to the scattering of wide angle lighting. The LED light is rayed out uniformly among the range of the lighting angle between ±60°~±90°, and will cause a total internal reflection in the semi-spherical packaging [4]. Therefore, partly of the light can not be used efficiently, and it has to increase the number of LED for the practical use of long distance lighting system. At present, it is common to enhance the illuminance by using more LEDs and modify the ray trace when the light passes through a lampshade. But it will cause an energy loss when the light passes through it and the more usage of LEDs will also increase the temperature. Most of the LED packaging materials are epoxy resin, which will shorten the life of the LED under high temperature circumstances [5-6].

In this research, the microlens was investigated by the 1st ray optics to improve the LED lighting angle and to achieve the focusing effect of the LED light energy. From this reason, the LED lighting system can use less amount of LEDs for the same illuminance to save more energy and also to reduce the system heat and the emissions of the carbon-oxide.

Therefore, a novel optical structure design of the focused microlens in this paper, which combines the properties of reflection and diffraction [7-8], is proposed in the application of the LED packaging. The surface structure of the microlens can be adjusted according to the various output lighting requirements, and the total internal reflection caused by the packaging surface can be mostly reduced.

II. METHODOLOGY

Due to the lighting property of the LED, the lighting ray can be focused by the assistance of the LED packaging, but the focusing ability is limited to the traditional semi-spherical lens structure. At present, most of the LED focusing ability is enhanced by the 2nd ray optics methodology through the law of reflection. Although this can achieve the focusing effect, the light cannot be used efficiently and will cause some energy lost through the reflection process.

In this research, a novel focused microlens applied to the LED packaging is proposed and investigated by the assistance of the optical simulation software to develop its structure. We utilized the property of diffraction (Fig. 1) to develop and design the LED packaging structure. Fig. 2 illustrates the novel focused microlens packaging structure which replaces the traditional LED packaging structure. This micro-structure design achieves not only the property of the traditional LED packaging structure, but also enhances the refraction of the light to become highly focused. Most researchers utilized the geometrical optics, scalar diffraction theory and vector diffraction theory in general when designing the diffraction optical elements.

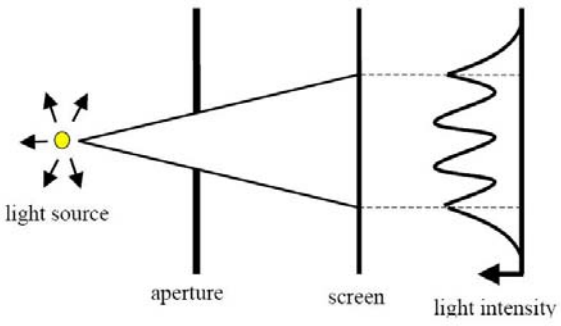

Figure 1. The phenomenon of the ray diffraction.

This project was funded by the National Science Council of Taiwan under contract NSC 96-2221-E-327-045-MY2 and the Metal Industries Research & Development Centre.

**Contact Author: Pa-Yee Tsai is with the Department of Mechanical Engineering, National Cheng Kung University, Tainan 70101, Taiwan. (Phone: +886-6-2757575 ext. 62245; E-mail: payee@ms56.url.com.tw)*

The geometrical optics is chosen in this research for the optical simulation software to predict the direction after the ray passes through the element by grating equation and ray tracing method. The most beginning purpose of this present design is to reduce the dimension of the traditional convex lens structure. The incidence ray produces phase delay to achieve the same optic effect in comparison with the original size through the micro-structure surface of the element. Therefore, the LED package structure with specific ray property can be developed by this present design.

Fig. 3 illustrates a standard simulation LED model with 8.75 mm in length and 5 mm in diameter, and two receiver planes are set in the distance at 5 mm and 15 mm from the tip of the LED respectively. The packaging material is PMMA and the refractive index is 1.49. The subject of this research is to find out the effect of the ray which projected out of the focused microlens LED. Therefore, the material of the die and ray parameters are selected and decided from the simulation software. The total illumination is 0.3 lm and the simulation condition remains unchanged.

The two-order, four-order, and eight-order focused microlens structures were designed with the assistance of the simulation software, and the results were compared with the traditional semi-spherical LED. The LED light was designed to produce the optimal focused effect by the 1st ray optics, and the light was projected directly out from the microlens surface without a reflection device to save energy lost. It is effective for the application to any kinds of specific lighting systems. Fig. 4 illustrates the ways of the LED focusing by the 1st and 2nd ray optics.

III. RESULTS AND DISCUSSIONS

In this research, a novel focused microlens structure has been designed by the optical simulation software in the application to the LED packaging surface. The focused microlens structure has a fixed order in this design, and the focus ability is in direct proportion to the number of orders.

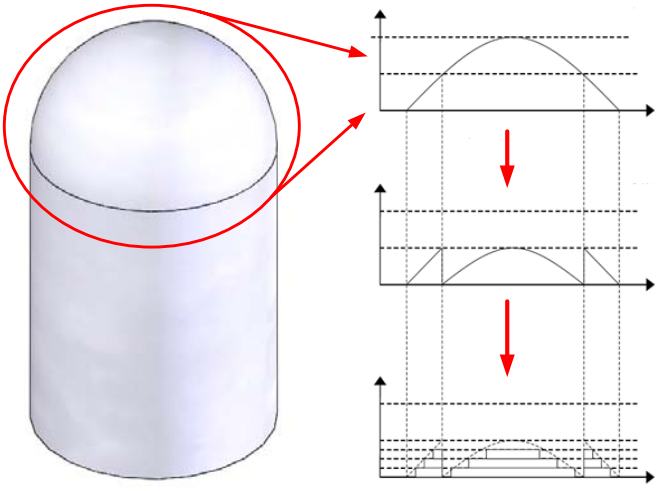

Figure 2. The replacement of the traditional LED packaging structure with a novel focused microlens packaging structure.

Fig. 5 illustrates the simulation results of the receiver plane in the distance at 15 mm for the traditional LED packaging and the novel focused microlens LED packaging. Fig. 5-a and 5-b illustrates the illuminance of the traditional LED and eight-order focused microlens LED by simulation. From the results, Fig. 5-b shows an obvious ring of light due to the novel focused microlens in this research. The design of the novel microlens structure follows the traditional semi-spherical curvature and the micro-structure is established based on the 1st ray optics. Fig. 5 also illustrates the differences of the focusing abilities from the two structures.

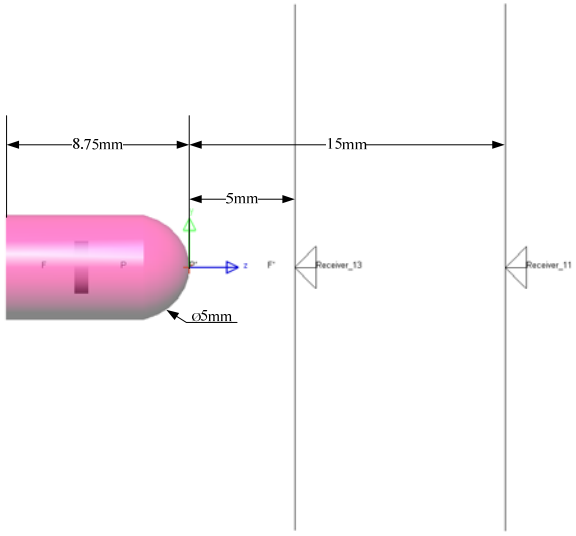

Figure 3. The simulation of standard LED model.

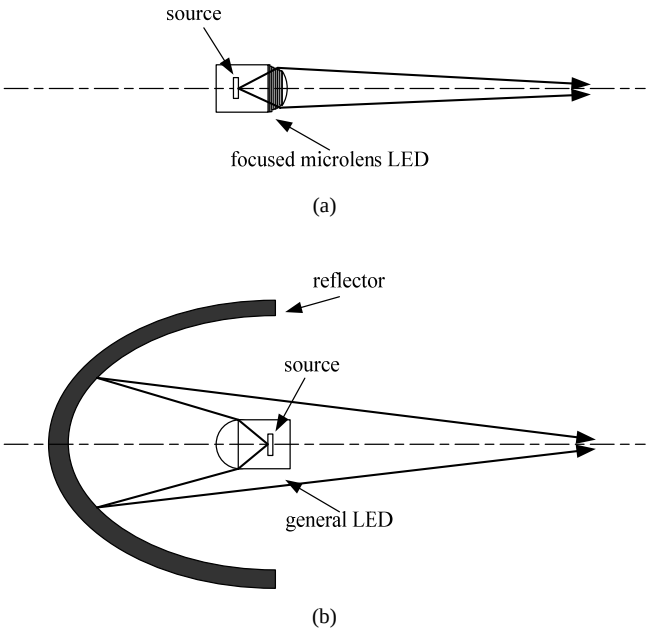

Figure 4. The ways of the LED focusing; (a) 1st ray optics (b) 2nd ray optics

Table I. The maximum illuminance simulation of the different order focused microlens in comparison with the traditional LED for the receiver plane in the distance at 5mm

	Traditional	2-order	4-order	8-order
Maximum illuminance(Lux)	1578.45	1578.45	2251.09	2720.95
Relative enhancement (in comparison with traditional LED)	–	0%	42.6%	72.3%

Table II. The maximum illuminance simulation of the different order focused microlens in comparison with the traditional LED for the receiver plane in the distance at 15mm

	Traditional	2-order	4-order	8-order
Maximum illuminance(Lux)	392.66	392.66	550.58	782.95
Relative enhancement (in comparison with traditional LED)	–	0%	40.7%	99.3%

Table I and II illustrate the maximum illuminance of the traditional LED and different order focused microlens LEDs with the receiver planes in the distance at 5 mm and 15mm respectively.

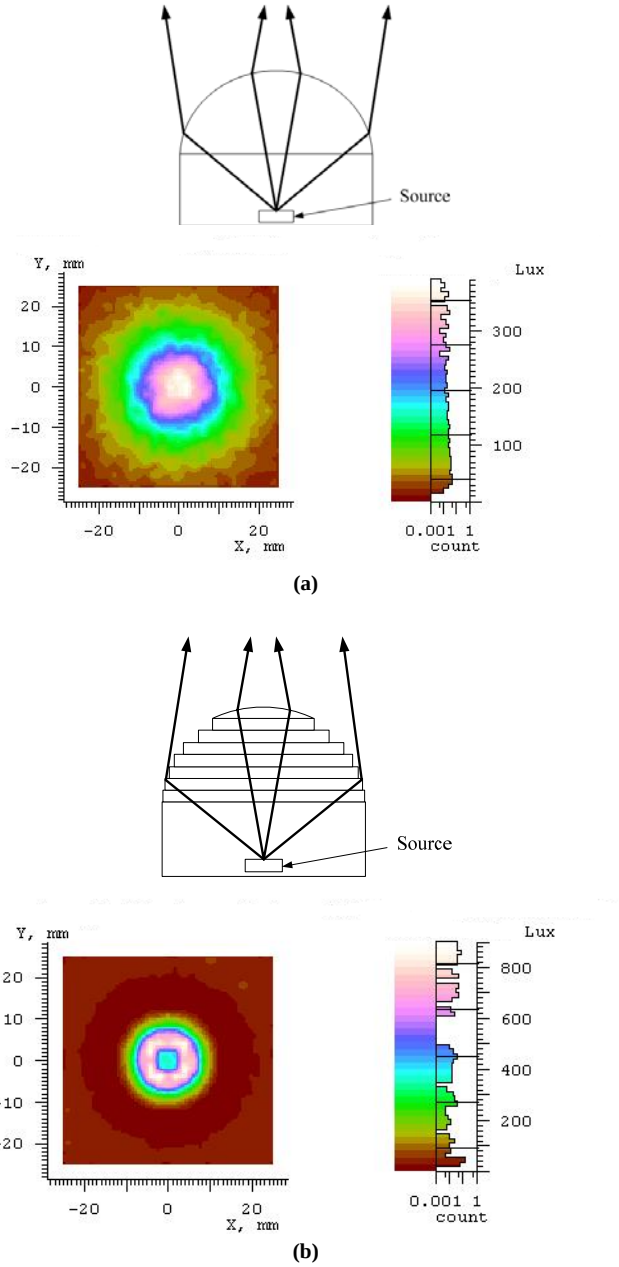

Figure 5. The illuminance of different LED packagings; (a) traditional LED and (b) eight-order focused microlens LED.

It shows that the maximum illuminance from simulations between the two-order focused microlens LED and the traditional LED are almost the same. This is because the traditional semi-spherical LED has a certain focusing ability, and partly the curvature of the two-order focused microlens LED are the same as the traditional one. The less orders of the focused microlens structure leads to a worse focusing ability, where illuminance is in direct proportion to the increasing of the designing orders.The maximum illuminance of the four-order focused microlens LED is 42.6% better than the traditional LED for the receiver plane in the distance at 5 mm, and 40.7% better for the receiver plane in the distance at 15mm. When the order is increased up to eight, the maximum illuminance of the eight-order focused microlens LED is 72.3% better than the traditional LED for the receiver plane in the distance at 5 mm, and 99.3% better for the receiver plane in the distance at 15mm. The result shows that the novel design not only enhance the light focusing ability, but also maintain and keep the energy to enhance the ability of the light projecting distance.

Fig. 6 shows the ray trace simulation results of the traditional LED and the eight-order focused microlens LED. The light displays uniformly dispersed from the traditional LED, where it displays more concentrated instead from the eight-order focused microlens LED.

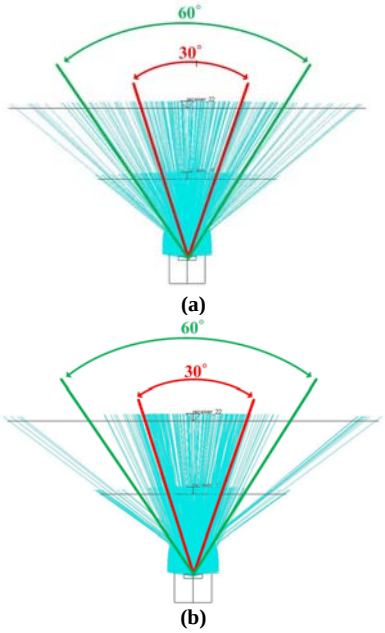

Figure 6. The ray trace simulation results; (a) traditional LED and (b) eight-order focused microlens LED.

Table III. Comparison for the luminous flux between the traditional LED and the focused microlens LED on the area of the receiver planes in the distance at 5 mm for the 30˚ LED lighting angle.

	Traditional	2-order	4-order	8-order
The total simulated luminous flux (lm)	0.23452	0.22109	0.21646	0.21257
Luminous flux on the area for the 30˚ lighting angle (lm)	0.05806	0.05806	0.07153	0.09921
Percentage of the luminous flux in the area for the 30˚ lighting angle out of the total luminous flux (lm)	24.7%	26.2%	43.4%	46.6%

Table IV. Comparison for the luminous flux between the traditional LED and the focused microlens LED on the area of the receiver planes in the distance at 15 mm for the 30˚ LED lighting angle.

	Traditional	2-order	4-order	8-order
The total simulated luminous flux (lm)	0.23366	0.21326	0.20830	0.20407
Luminous flux on the area for the 30˚ lighting angle (lm)	0.08203	0.08464	0.13524	0.14109
Percentage of the luminous flux in the area for the 30˚ lighting angle out of the total luminous flux (lm)	35.1%	39.6%	73.1%	69.1%

It is obvious to observe the phenomenon of the ring of light from Fig. 7 by the ray trace simulation. Fig. 8 illustrates the simulation results of the receiver plane in the distance at 5 mm for the traditional LED, the two-order, the four-order and the eight-order focused microlens LED. It shows that the maximum illuminance of the simulation is nearly 1580 Lux for both the traditional and the two-order focused microlens LEDs, where the four-order focused microlens LED is about 2250 Lux and the eight-order focused microlens LED is increased up to 2720 Lux. When the order is equal or more than four, the ray was greatly focused within ±15° and the lighting distance may be increased as well.

Table III and IV illustrate the luminous flux of the focused microlens LED in comparison with the traditional LED with the receiver planes in the distance at 5 mm and 15mm respectively.

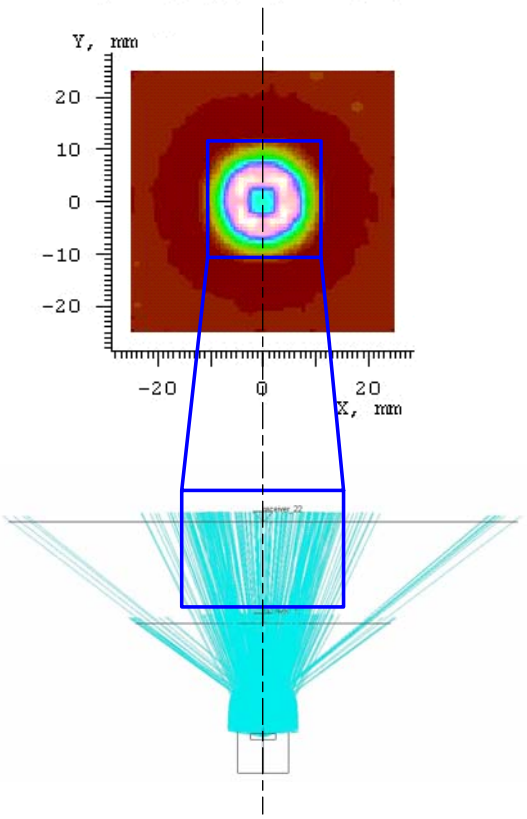

Figure 7. The simulation result of the ray trace in comparison with the ring of light for the focused microlens LED.

On the area of the receiver planes in the distance at 5 mm for the 30˚ LED lighting angle, table III shows that the luminous flux of the traditional LED is 24.7% out of the total luminuos flux, where the eight-order focused microlens LED is 46.6%. On the area of the receiver planes in the distance at 15 mm for the 30˚ LED lighting angle, table IV shows that the luminous flux of the traditional LED is 35.1% out of the total luminuos flux, where the eight-order focused microlens LED is 69.1%. All the models in this research have the same light source setting and total luminous flux. It demonstates that the proposed focused mirolens structure can effectively focus the light ray.

IV. CONCLUSIONS

In this paper, a novel focused microlens structural design, which based on the law of deflection and diffraction, has been proposed and applied to the LED packaging. This novel design not only has a superior focusing performance to the traditional LED packaging, but also a smaller size in dimension. Due to the property of the high focusing performance, the amount of LEDs can be reduced in a lighting system to achieve the same illuminance. Therefore, more energy can be saved and it also reduces the system heat and the emissions of the carbon-oxide to make a better environment for the earth. The novel focused microlens LED has been investigated and proposed to demonstrate the enhancement of illuminance and the farther lighting distance of a single LED. It can be efficiently and extensively applied to the vehicle LED headlamp systems, the LED streetlamps, and also to the LED outdoor long-distance lighting devices in the future.

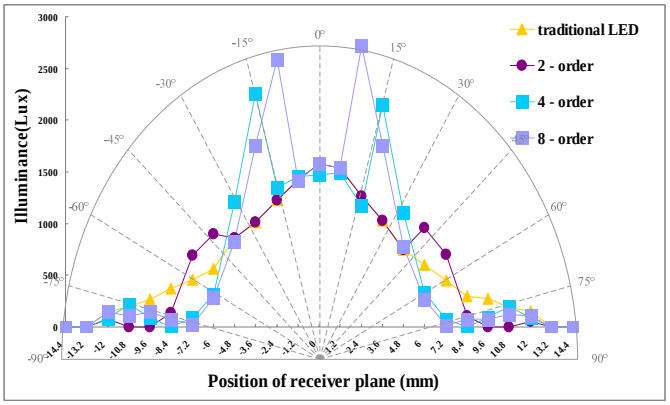

Figure 8. The illuminance of the traditoinal LED in comparison with different orders of focused microlens LED.

ACKNOWLEDGMENT

This research was partly sponsored by the National Science Council of Taiwan under contract NSC 96-2221-E-327-045-MY2 and the Metal Industries Research & Development Centre.

REFERENCES

[1] B.-J. Huang, P.-C. Hsu, M.-S. Wu and C.-W. Tang, "Study of system dynamics model and control of a high-power LED lighting luminaire," *Energy*, Vol.32, Issue 11, 2007, pp. 2187-2198.

[2] E. F. Schubert, *Light-emitting diodes*, Cambridge: Cambridge University Press, 2nd ed., 2006.

[3] *LED lighting technology: lessons from the USA*, Report of a DTI global watch mission, 2006.

[4] M. Alan, "Advances in LED packaging," *III-Vs Review*, Vol.17, Issue9, 2005, pp. 16.

[5] S. Sinzinger and J. Jahns, *Microoptics*, Wiley VCH, ISBN-13: 978-3527294282, pp.129-131, 1999.

[6] B. Kress and P. Meyrueis, *Digital diffractive optic*s, WileyBlackwell, ISBN-13: 978-0471984474, 2000.

[7] C. W. Wessner, *Partnership for solid-state lighting: Report of a workshop*, Washington, DC: National Academy Press, ISBN-13:978-0309083195, 2002 , pp. 58–61.

[8] F. M. Steranka, J. Bhat, D. Collins and L. Cook, ''High power LEDs – Technology status and market applications,'' *Physica Status Solidi (A)*, Vol.194, No.2, 2002 , pp. 380–388.

Magnetic Controlled Navigation System for Endoscopic Micro Robot

Mingyuan Gao, Chengzhi Hu, Zhenzhi Chen, Honghai Zhang, Sheng Liu*, *Member, IEEE*

***Abstract*—A novel magnetic controlled navigation system is proposed for controlling endoscopic micro robot's locomotion and location in the gastrointestinal tract. The proposed approach exploits permanent magnet and mechanical movement to generate quasi-static magnetic field instead of AC alternating magnetic field, and thus can be applied to the noninvasive exploration of gastrointestinal tract with minimum level of harm to human body. The proposed 5-axis system has a patient support, a magnet assembly with two permanent magnet positioned oppositely, and a magnet support. By driving the five coupling axes, the magnetic navigation system is capable of steering the endoscopic micro robot through the gastrointestinal tract in any direction in 2D space. Experiments in simulated intestinal tract are conducted to demonstrate controlled translation, rotation, and rototranslation of the micro robot. The proposed technique has great potential of enabling the application of controlled magnetic navigation in the field of gastrointestinal endoscopy.**

***Index Terms*—Biomedical equipment, Gastrointestinal endoscopy, Micro-robot, Magnetic navigation**

INTRODUCTION

With the development of micro-electro-mechanical systems (MEMS) technology, research and progress on self-propelled capsule endoscope have been the topic of interests for several years [1]-[7].

A wide variety of active and wireless control mechanism have been developed for gastrointestinal endoscopy which exploits a swallowable capsule endoscope including a digital camera, ASIC transmitters, an antenna, illuminating LEDs, and batteries [8]. Concept and prototype of next generations of capsule endoscope which contains location tracking, rotating camera, wireless power supply mechanism, drug delivery devices, and micro-mechanical arm to perform therapy have been proposed and patented recently[9]-[18]. In this paper, we propose a novel magnetic controlled navigation system used for steering capsule's location and locomotion in the gastrointestinal tract. In addition, a special design of endoscope's configuration and integration is proposed for improving the level of miniaturization and being compatible with external controlled magnetic apparatus.

PROPOSED CONCEPT

The system proposed here comprises a patient support, a magnet assembly with two groups of permanent magnets positioned oppositely, and a magnet support. By combining movements of these three moveable components, we can steer a magnet built-in endoscopic micro-robot and control its movement, location and orientation in the gastrointestinal tract.

Given the requirement of miniaturization, a special design for capsule endoscope's configuration and system integration is proposed as shown in Fig. 1. ASICs for image sensor and processing, RF transmission, pressure sensing, PH detecting, and drug delivery are mounted onto a hexagonal flexible substrate, leaving sufficient central area for implanting a permanent magnet. Cutting-edge technologies of 3D system integration such as TSV(Through-Silicon-vias), 3D-stacking, and SiP(System in Packing) can also be utilized for further miniaturizing capsule endoscope as well as improving its electrical interconnectivity, thermo-mechanical reliability, imaging quality, transmission rate, and multi-functionality[19].

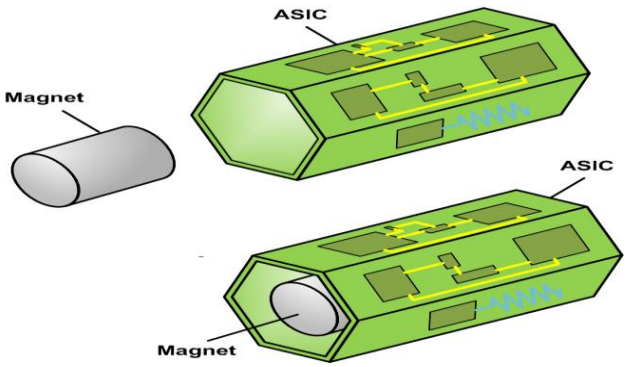

Fig. 1. Proposed Concept of Integration Approach for Capsule Endoscope

This work was supported by the National High Technology Research and Development Program of China under Ministry of Science and Technology (Program 863) under Grant 2008AA04Z313. The work of Mingyuan Gao and Chengzhi Hu was supported by the Graduate Innovation Foundation Program from the Huazhong University of Science & Technology under Grant No. HF0601108100.

*Contact author: Sheng Liu is with the School of Mechanical Science & Engineering and Wuhan National Laboratory for Optoelectronics, Huazhong University of Science & Technology, Wuhan, 430074, China(phone: 86-13871251668, fax: 86-27-87557074, e-mail: victor_liu63@126.com).

SYSTEM DESIGN AND LOCOMOTION ANALYSIS

Fig.2 illustrates the assembly drawing of magnetic navigation system. The patient support 1, which can be moved longitudinally forwardly and rearwardly and laterally inwardly and outwardly, is mounted on a pedestal, allowing the patient to be moved relative to the magnet assembly. The magnet assembly 2 comprises several Nd-Fe-B permanent magnets, ball screws, linear ball rails, and gripper device. The ball screws convert motor's rotary motion to ball nut's linear motion, exerting necessary force to move the permanent magnets along a longitudinal axis. Once the two groups of oppositely-positioned magnets are moved in the opposite direction parallel to the longitudinal axis, the magnet inside the capsule endoscope will be rotated about its lateral or vertical axis or any axis in the transverse plane according to the different positions of magnet support. The magnet support 3 contains a pair of worm/worm gear, a pivot, and aluminum framing. The magnet assembly is mounted onto the magnet support and can rotate about the longitudinal axis. The relative rotation between magnet assembly and patient support permits adjustment of the positions of magnet, allowing magnet built-in capsule endoscope to rotate about its longitudinal axis.

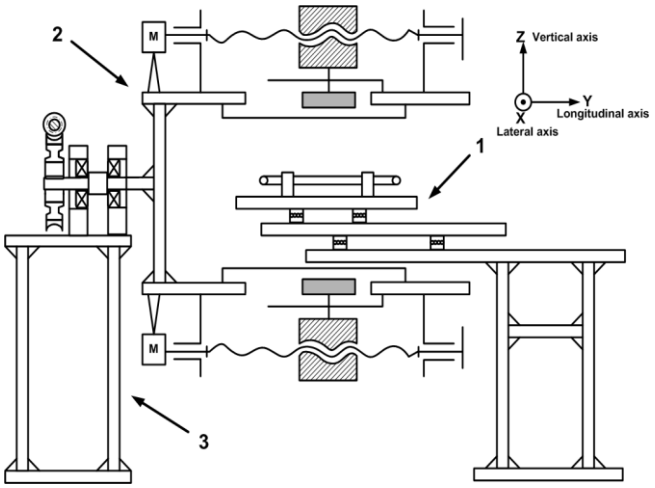

Fig. 2. Overall Assemble Drawing of Magnetic Navigation System

The right side view of the magnet assembly and magnet support is shown in Fig.3. The magnet assembly comprises ball screws 4, ball nuts 5, ball bearings 6, bearing supports 7, connectors 8, Nd-Fe-B magnets 9, linear rails 10, and sliding blocks 11. The magnet support contains a pivot 12, a worm 13, a worm gear 14, aluminum framing 15, and right-angle connectors 16. Under the synergistic effects of permanent magnets and mechanical movements, a controllable magnetic field will be generated in the operation area, within which the gastrointestinal tract of the patient is to be positioned.

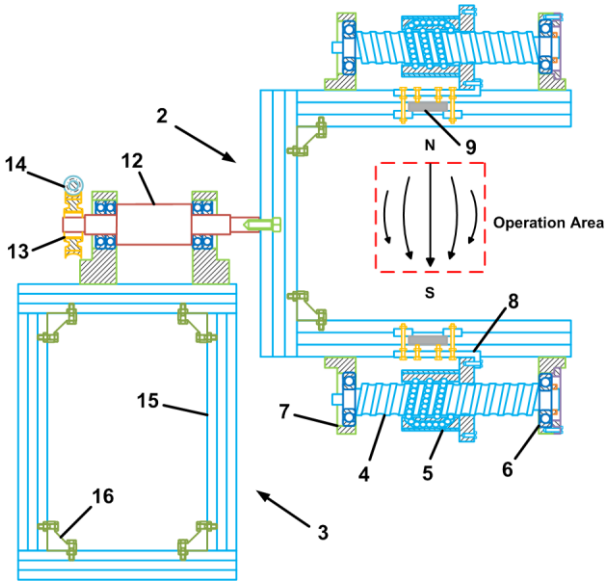

Fig. 3. Right Side View of the magnet assembly and support

The top plan view of the patient support is shown in Fig.5. The patient support comprises an elongate bed 17, a pedestal 18 including aluminum framing 19 and right-angle connectors 20, ball screws 21, ball nuts 22, linear rails 23, sliding blocks 24, connectors 25, ball bearings 26, bearing supports 27, shaft couplings 28, a simulated gastrointestinal tract 29, and GI supports 30. The ball screws convert motors' rotary motion to ball nuts' linear motion to realize elongate bed's translation in the longitudinal and lateral directions. Silicone rubber is used as the simulated gastrointestinal tract and experiments are conducted demonstrating the feasibility of proposed magnetic navigation system for controlling capsule endoscope's movements with desirable position and orientation.

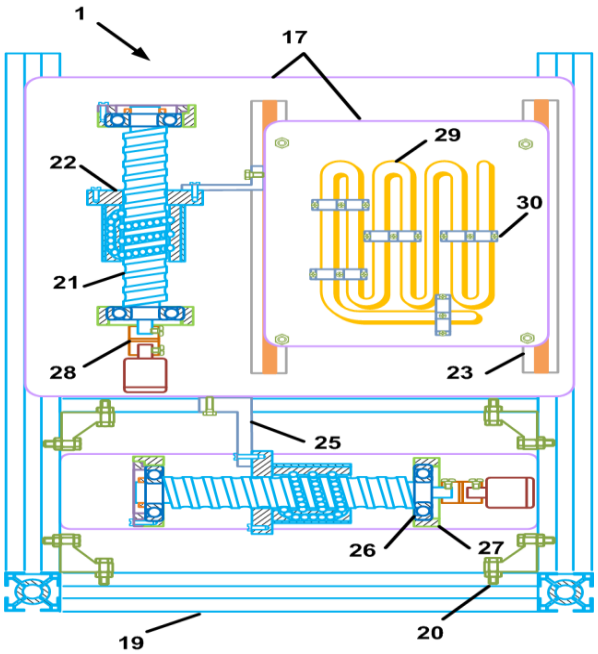

Fig. 5. Top Plan View of the Patient support

The proposed magnetic navigation system has five coupling axes which can realize capsule endoscope's multi-directional movement in the gastrointestinal tract. Fig. 5 demonstrates the principle of capsule endoscope's locomotion mechanism. The different movements of five axes are shown with numbers and corresponding arrowhead in (a), (b), and (c). Number 1 with red color indicates magnet assembly's rotation about its longitudinal axis, number 2 with green color shows two magnets' linear motion in opposite direction in the coronal plane, number 3 with blue color represents two magnets' linear motion in opposite direction in the sagittal plane, number 4 with purple color shows the patient support's linear movement in the lateral direction, and number 5 with orange color indicates the patient support's linear movement in the longitudinal direction. By combining movements of five axes in different permutation and sequence, we can navigate magnet built-in capsule endoscope's locomotion through the gastrointestinal tract in any direction in 2D space. Four main movements of capsule endoscope are shown in (d), the relative translation between patient support and magnet assembly will steer capsule moving in the lateral or longitudinal direction in term of patient support's motion path; the opposite motion of magnets in the coronal plane will drive capsule rotating about its vertical axis, this motion changes capsule's orientation, allowing to realize capsule's motion transition from the longitudinal path to the lateral path and vice versa. The capsule endoscope is also capable of rotating about its longitudinal axis by pivoting the magnet assembly in the magnet support, this movement is not only useful for adjusting capsule's orientation , but also necessary for enlarging viewing angle of the built-in micro camera to improve diagnosis effect of gastrointestinal endoscopy.

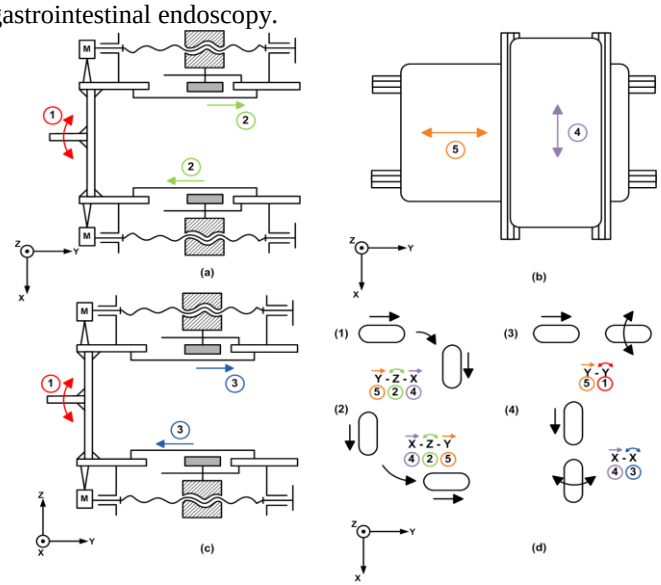

Fig. 5. Locomotion Analysis of Magnetic Navigation System

CURRENT RESULTS

Fig. 5 shows the relation between the magnetic flux density and the distance. The black line plots the simulation results, whereas the circle plots the experiment measurement values. The experimental data match well with the finite element analysis, demonstrating that our electromagnetic model is appropriate for analyzing the mechanical properties of the proposed propulsion system. As we can see, with the increase of the distance between magnetic sources and built-in magnets, the strength of the magnetic flux density drops rapidly. Thus, electromagnet is a better magnetic resource compared with permanent magnet because it can generate a stronger magnetic field.

Fig. 6 is a visualization of the solved magnetic field. The streamlines show the lines of magnetic force, and the background color shows the distribution of the magnetic field. The magnetic field is stronger when the magnetic force lines become denser. A maximum intensity of 0.34 T at the surface is obtained.

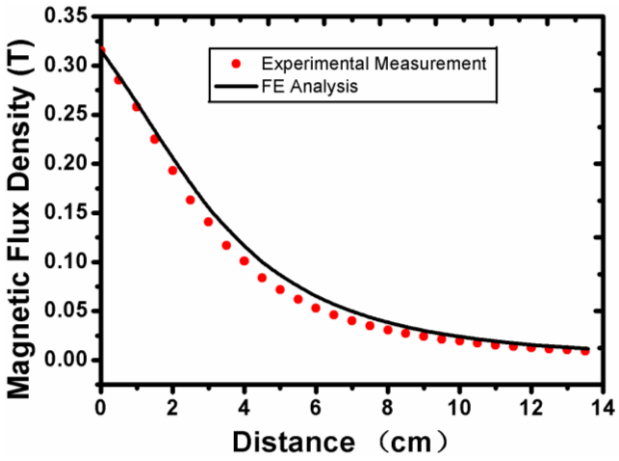

Fig. 6. Magnetic Flux Density as a function of distance

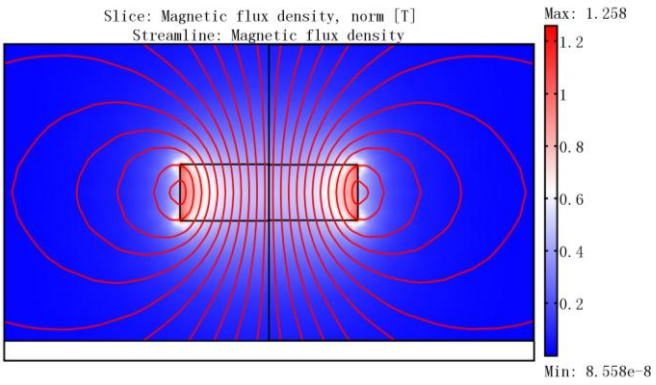

Fig. 7. Visualization of the solved magnetic field

Experiments of motion control are presented by the video frames reported in Fig. 8. Fig. 8 shows locomotion of the magnet built-in capsule inside a simulated gastrointestinal tract using silicone rubber tube. Due to the visible external manipulation of magnetic navigation system, NdFeB permanent magnets can move linearly in both longitudinal and lateral direction, rotate about its longitudinal and lateral axes, and pivot about its vertical axis. (a1) – (e1) shows the locations and movements of the built-in permanent magnet at different time in the simulated gastrointestinal tract. The position and orientation of the magnet

assembly and the patient support inducing these movements are reported in the related frames (a2) – (e2).

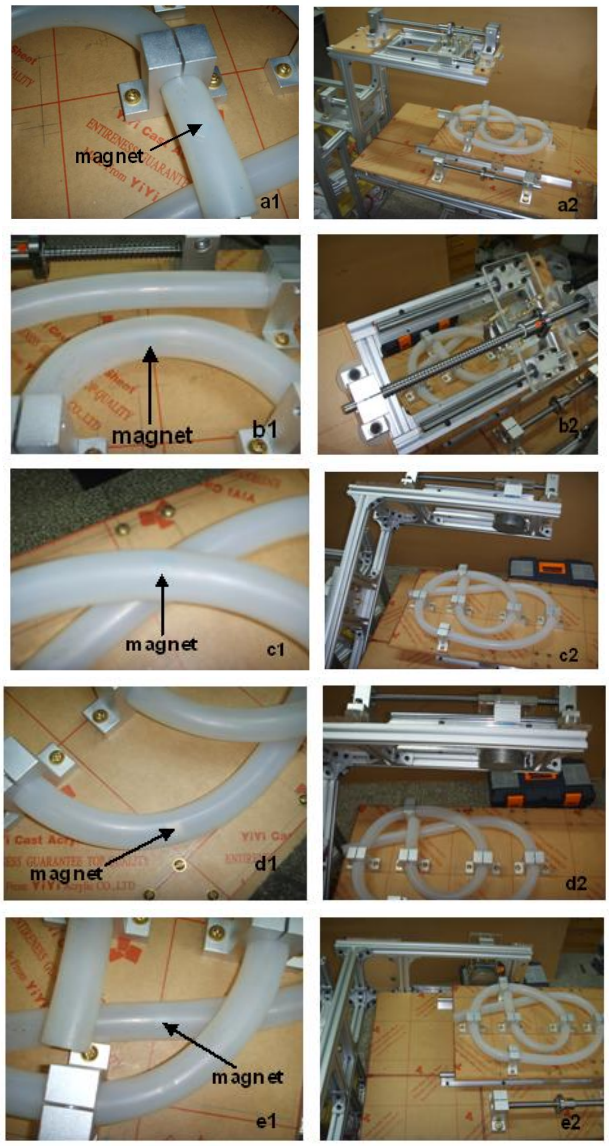

Fig. 6. Locomotion of the magnet in a simulated gastrointestinal tract.

CONCLUSION

A novel magnetic controlled navigation system was proposed and manufactured for controlling endoscopic micro-robot's movements in the gastrointestinal tract. Experiments were conducted, demonstrating this proposed multi-axis navigation system was capable of steering capsule's location and orientation in the simulated 2D gastrointestinal tract. Finite element methods were used to analyze the magnetic field distributions and mechanical properties of proposed navigation system. The proposed technique suggests a feasible approach in the field of gastrointestinal endoscopy. Further research is currently in progress for realizing endoscopic capsule's movements in 3D space and visualizing the locomotion control by ways of ultrasonic image.

REFERENCES

[1] J. Daveson and M. Appleyard, "Future Perspectives of Small Bowel Capsule Endoscopy," in *10th Endoscopy Forum Japan*, Otaru, JAPAN, 2008, pp. 262-270.

[2] M. Delvaux and G. Gay, "Capsule endoscopy: Technique and indications," *Best Practice & Research in Clinical Gastroenterology*, vol. 22, pp. 813-837, 2008.

[3] D. K. Iakovidis, S. Tsevas, D. Maroulis, A. Polydorou, and Ieee, "Unsupervised Summarisation of Capsule Endoscopy Video," in *4th International IEEE Conference Intelligent Systems*, Varna, BULGARIA, 2008, pp. 140-145.

[4] Z. Nagy, R. Oung, J. J. Abbott, and B. J. Nelson, "Experimental Investigation of Magnetic Self-Assembly for Swallowable Modular Robots," in *IEEE/RSJ International Conference on Intelligent Robots and Systems*, Nice, FRANCE, 2008, pp. 1915-1920.

[5] T. Nakamura and A. Teran, "Capsule endoscopy: past, present, and future," *Journal of Gastroenterology*, vol. 43, pp. 93-99, 2008.

[6] P. Valdastri, C. Quaglia, E. Susilo, A. Menciassi, P. Dario, C. N. Ho, G. Anhoeck, and M. O. Schurr, "Wireless therapeutic endoscopic capsule: in vivo experiment," *Endoscopy*, vol. 40, pp. 979-982, Dec 2008.

[7] K. Twomey and J. R. Marchesi, "Swallowable capsule technology: current perspectives and future directions," *Endoscopy*, vol. 41, pp. 357-362, Apr 2009.

[8] G. Iddan, G. Meron, A. Glukhovsky, and P. Swain, "Wireless capsule endoscopy," *Nature*, vol. 405, p. 417, May 2000.

[9] M. A. Imran, et al., "Capsule and method for treating or diagnosing the intestinal tract," U.S. Patent 7 160 258, Jan. 9, 2007.

[10] Available: http://www.rfamerica.com

[11] C.M. Caffrey, O. Chevalerias, C. O'Mathuna, K. Twomey, "Swallowable-capsule technogloy," *IEEE Pervasive Computing*, vol.1, pp.23-29, Jan.-Mar.2008.

[12] A. Moglia, A. Menciassi, M.O. Schurr, P. Dario, "Wireless capsule endoscopy: from diagnostic devices to multipurpose robotic systems," *Biomedical Microdevices*, vol.9, pp. 235-243, Apr. 2007.

[13] B. Kim, S. Lee, J. H. Park, and J. O. Park, "Design and fabrication of a locomotive mechanism for capsule-type endoscopes using shape memory alloys (SMAs)," Ieee-Asme Transactions on Mechatronics, vol. 10, pp. 77-86, Feb 2005.

[14] K. Ishiyama, K. I. Arai, M. Sendoh, A. Yamazaki, and I. Ieee, "Spiral-type micro-machine for medical applications," in International Symposium on Micromechatronics and Human Science, Nagoya, Japan, 2000, pp. 65-69.

[15] I. Kassim, W. S. Ng, G. Feng, S. J. Phee, P. Dario, C. A. Mosse, and I. Ieee, "Review of locomotion techniques for robotic colonoscopy," in 20th IEEE International Conference on Robotics and Automation (ICRA), Taipei, Taiwan, 2003, pp. 1086-1091.

[16] M. Quirini, A. Menciassi, S. Scapellato, C. Stefanini, and P. Dario, "Design and fabrication of a motor legged capsule for the active exploration of the gastrointestinal tract," Ieee-Asme Transactions on Mechatronics, vol. 13, pp. 169-179, Apr 2008.

[17] J. Peirs, D. Reynaerts, and H. Van Brussel, "Design of miniature parallel manipulators for integration in a self-propelling endoscope," in Eurosensors XIII Meeting, The Hague, Netherlands, 1999, pp. 409-417.

[18] B. Chen, Y. D. Liu, S. Chen, S. R. Jiang, and H. T. Wu, "A Biomimetic Spermatozoa Propulsion Method for Interventional Micro Robot," in International Conference on Bionic Engineering (ICBE 2008), Changchun, PEOPLES R CHINA, 2008, pp. 106-112.

[19] R.Y. Lu, S. Liu, X.J. Chen, "Micro system manufacture of capsule dndoscope based on SiP Technology," *Electronics & Packaging*, vol.7, no.2, pp.6-9, Apr. 2007(in Chinese).

To determine the adhesion by using AFM and the adhesive material volume estimation

K. Y. Chen[1]*, Y. L. Yeh[2], C. C. Wang[1], M. J. Jang[2], C. W. Lee[1]

[1]*Department of Mechanical Engineering, Far East University, K. Y. Chen, Tainan, Taiwan.*

[2]*Department of Automation and Control Engineering, Far East University, Y. L. Yeh, Tainan, Taiwan.*

[1]*Department of Mechanical Engineering, Far East University, C. C. Wang, Tainan, Taiwan.*

[2]*Department of Automation and Control Engineering, Far East University, M. J. Jang, Tainan, Taiwan.*

[1]*Department of Mechanical Engineering, Far East University, C. W. Lee, Tainan, Taiwan.*

***Abstract* — The paper studies the effect of the adhesive mass in the cantilever beam dynamic. In this paper, this determines the adhesive mass by using the adhesive material volume. The adhesive volume estimation is the semi-sphere volume. The adhesive volume in the cantilever beam can be determined by using the SEM (Scanning Electron Microscopy, SEM). From the analysis result, this can be found that the effect of the moisture in the cantilever beam resonance is very clear. These determined materials are four material included Mg, Cu, Fe and Ti. These analyzed result show that the determined adhesive mass error between the semi-sphere volume method and the resonance method is smaller 15.99% in these four materials. The adhesive mass big error shows in the handling material. This can know that the result by using the semi-sphere volume method is very closed the theoretical value by using the cantilever beam resonance.**

Keywords — ***AFM, adhesive***

I. INTRODUCTION

In 1986, Binning [1] is devised the Atomic Force Microscopy (AFM). The atomic microscopy determines the contour of the testing material surface by using the Van der Waals force between the cantilever beam tip and the surface of the testing material. The cantilever beam can be bended by the van der vaals force. When the leaser beam reaches to the cantilever beam, the leaser beam reflects into the position sensor. This can determine the deformation of the cantilever beam. The AFM can determine the surface of the metal and non-metal. Therefore, the AFM can be applied in any field, example as the material science, the bio-chemical, nano science, etc.

In the cantilever beam property, the Cleveland [2] and Lin [3], they determine the strange of the cantilever beam by using the reason of the cantilever beam. Bashir [4] measures the reason of the cantilever beam with the adhesive virus. Boisen [5] design the detecting system with the cantilever beam of the SU-8 material. The SU-8 material surface coats with the Au. When the coating time becomes long, the mass of the cantilever beam becomes bigger, and the resonance frequency of the cantilever beam becomes smaller. Mutharasan [6] determine the resonance of the cantilever beam by using the finite element method.

From this above literature, this can be known the adhesive mass can be determined by using the resonance of the cantilever beam. The object of the paper explores the effect of the moisture on the resonance frequency of the cantilever beam. This paper determines the adhesive mass of the cantilever beam tip by using the resonance method and the semi-sphere volume method.

II. THE RESONANCE THEORY

Form the above literature, this can be known that the resonance of the cantilever beam can be determined. Butt [7] explore the stiffness and resonance frequency of the cantilever beam. The relative function between the stiffness and resonance shown as:

$$\omega = 1.03\frac{d}{L^2}\sqrt{\frac{E}{\rho_c}} = 2.06\sqrt{\frac{k}{m_b}} \tag{1}$$

$$k = \frac{Ed^3w}{4L^3} \tag{2}$$

Where E is the elastic module, the d is the high of the cantilever beam, the ω is the weight of the cantilever beam, the L is the length of the cantilever beam, the ρ_c is the density of the cantilever beam and the m_b is the total mass of the cantilever beam (ρ_c x d x w x L). Cleveland [2] determine the stiffness of the cantilever beam by using the variable adhesive mass on the beam surface. The resonance frequency show as :

$$\omega_0 = \sqrt{\frac{k_c}{m^{**}}} \tag{3}$$

$$\omega_1 = \sqrt{\frac{k_c}{m+m^{**}}} \tag{4}$$

Where ω_0 is the first resonance frequency of the cantilever beam without the adhesive mass, ω_1 is the first

Identify applicable sponsor/s here. *This project was funded by the National Science Council of Taiwan under Grant Nos. NSC 98-2221-E-269 - 016.*

Contact author: for fabrication aspects of this project please contact* ***kuoying@cc.feu.edu.tw.*

resonance frequency of the cantilever beam with the adhesive mass. The is the total mass include the cantilever beam mass ($m^{**} = \frac{m_b}{2.06^2} \cong 0.24 m_b$), m is the adhesive mass. From the eq. (3) and (4), the stiffness of the cantilever beam can be got:

$$k_c = \omega_0^{\,2} \times m^* \tag{5}$$

$$k_c = \omega_1^{\,2} \left(m + m^{**} \right) \tag{6}$$

In real, the stiffness of the cantilever beam is only once. The eq. (5) equal eq. (6). From the eq. (5) and (6), this can be get as:

$$\omega_0^{\,2} \times m^* = \omega_1^{\,2} \left(m + m^{**} \right) \tag{7}$$

$$\omega_0^{\,2} = \omega_1^{\,2} \frac{m}{m^{**}} + \omega_1^{\,2} \tag{8}$$

$$\frac{m}{m^{**}} = \frac{\omega_0^{\,2} - \omega_1^{\,2}}{\omega_1^{\,2}} = \frac{\omega_0^{\,2}}{\omega_1^{\,2}} - 1 \tag{9}$$

III. EXPERIMENTAL PROCESS

This paper uses the four test materials. The materials include the Mg, Cu, Fe and Ti. In order to remove the effect of the residual stress on the material structure, the test material be used anneal treatment. The parameter of the anneal treatment is shown in Table1. In order to reduce the variable property, the material is used the pure material. The experimental device is the AFM (CPR-II ; Veeco/DI). In order to understand that the adhesive status between the cantilever beam and testing material, the analysis model is force curve, as shown in Fig. 1. The type of the cantilever beam is the NSC15/AIBS tapping. The detail parameter of the cantilever beam is shown in Table 2. The local diagram of the cantilever beam shown in Fig. 2 [8]. The experimental parameter of the force curve is shown in Table3. The resonance of the cantilever beam can be determined from the frequency diagram, as shown in Fig. 3. The surface of the testing material can be determined by using the SEM device. The material type of the adhesive mass can be determined by using the EDS (Energy Dispersive System, EDS) device. Using these devices, this can be found that the adhesive testing material place on the position of the cantilever beam.

IV. THE RESULT AND DISCUSSION

IV-I The effect of the moisture on the resonance of the cantilever beam.

In order to understand effect of the moisture, this experimental moisture conditions include 70%, 60% and 50%. As the moisture 70% is applied, the resonance of the cantilever beam can be determined about 359.854KHz. As the moisture reduce to 60% and 50%, the resonance of the cantilever beam can be determined about 359.876KHz and 359.896KHz, respectively. This result is shown in Fig. 4. From the result, this can be known that the resonance of the cantilever beam is decrease as the moisture on the air increase. This is the equivalent mass of the cantilever beam increase as the moisture on air increases.

IV-II The estimation of the adhesive material mass and volume

From the effect of the moisture on the resonance of the cantilever beam, this can be known that the variable resonance of the cantilever beam can be determined as the variable moisture is applied. Therefore, this experimental condition can be the same condition. The temperature on the air is 20℃（±1℃）. The moisture on the air is 50%（±3%）. The testing experimental cantilever beam for the any testing material is new. This can reduce the unknown parameter number. The experimental parameter is shown in Table3. The testing materials include the Mg，Cu，Fe and Ti. The surface contour of the testing material measurement by using SEM is shown in Fig.5. The Figs. 5 (a-1)，(b-1)，(c-1) and (d-1) is shown the new cantilever beam contour. The Figs. 5 (a-2)，(b-2)，(c-2) and (d-2) is shown as the cantilever beam tip with the adhesive mass. Compared the new cantilever beam tip contour with the experimental cantilever beam tip contour, the few material adhere to the surface of the cantilever beam tip. In order to understand the material element, the adhesive material can be determined by using the EDS. This result is shown in the Fig. 6. from the adhesive material element measurement by using EDS, this can be known that the few adhesive material element is the same as the testing material element. From the literature, Chung [9] study that the testing material surface can be damaged as the cantilever beam tip contact the surface of the testing material. As the hardness of the cantilever beam material is bigger that the testing material hardness, the testing material can adhere to the cantilever beam tip surface. This experimental result is the same the literature result.

In general, the adhesive material mass measurement method of the cantilever beam is the resonance method of the cantilever beam. In order to understand the adhesive mass status, this can determine the resonance of the cantilever beam with the adhesive variable testing material. This result is shown in Table 4. From the result, this can be found that the resonance of the cantilever beam with the adhesive testing material mass decrease. This can not know the adhesive mass and the damaged mass of the cantilever beam.

In order to understand the adhesive mass and the damaged mass of the cantilever beam, this introduces the semi-sphere volume method. This assumes that the adhesive mass volume is the separated semi-sphere volume. This can reduce the estimation error. The adhesive mass volume scale can be determined by using the SEM. This can get the radius of the semi sphere by using the SEM. The semi sphere volume can be calculated as substitute the radius of semi sphere into the Eq.(10).

$$V = \frac{2\pi r^3}{3} \tag{10}$$

Where the r is the radius of the semi sphere. The adhesive material volume can be determined and shown in Table5. The local diagram of the adhesive material is shown in the Fig. 7. In order to understand the adhesive testing material mass, the testing material density is known. The Table6 shows the density of these testing materials. From the adhesive volume and density, the adhesive mass can be got, as shown in the Table7. Substitute resonance of the cantilever beam into the eq. (10), the rate of the adhesive testing mass and the pure cantilever beam can be got. The adhesive testing mass can be determined by using the rate of the adhesive testing mass and the pure cantilever beam. This result is shown in Table8. From the Table8, this can be known that the error between the adhesive mass by using the semi sphere volume method and the resonance method is smaller than 15.99%. As the testing material is soft, the error is small, about 2.95%. When the testing material is hard, the adhesive mass by using the semi sphere method is larger than by using the resonance method. From this can be known that as the testing material is hard, the error of the adhesive mass estimation is large. The adhesive mass estimation by using the resonance method can not known the damage of the cantilever beam. This can cause the error between adhesive mass estimation by using the resonance method.

V. CONCLUSION

This paper investigates the testing mass adhered the cantilever beam surface by using the resonance and the semi sphere volume method. The testing material includes the four materials. From the above analysis, this can be follows as :

1. When the moisture on the air increase, the resonance of the cantilever beam decrease. Therefore, the mass of the cantilever beam become large, as the moisture on the air become large.
2. When the adhesive mass on the cantilever beam become large , the resonance of the cantilever beam become small.
3. When the adhesive mass on the cantilever beam become large , the resonance of the cantilever beam become small.
4. The adhesive mass estimation by using the resonance of the cantilever bema is very closed the adhesive mass estimation by using the semi-sphere volume. The large error of the adhesive mass estimation on the four testing materials is 15.99%. The small error of the adhesive mass estimation on the four testing materials is 2.95%.
5. The adhesive mass estimation error by using the resonance method on the hard testing material is large than the soft testing material.
6. The resonance method and the semi sphere volume method in simultaneous is applied to determine the adhesive mass and damage mass.

REFERENCES

[1] G. Binnig, C. F. Quate and Ch. Gerber, “Atomic force microscopy”,Phys.Rev.Lett., Vol. 56, pp. 930-934, 1986.

[2] J. P. Cleveland, S. Manne, D. Bocek and P. K. Hansma, “A non-destructive method for determining the spring constant of cantilevers for scanning force microscopy”, Rev. Sci. Instrum.,Vol.64, pp. 403-405,1993.

[3] S. H. Chean and H. N. Lin, “Measurement of the tip modulus of elasticity by using SNOM”, Instruments Today, vol. 21, pp. 56-59, 2000. (in chinese)

[4] A. Gupta, D. Akin, and R. Bashir, “Single virus particle mass detection using microresonators with nanoscale thickness”, Appl. Phys. Lett., Vol.84, pp.1976-1978, 2004.

[5] A. Johansson, M. Calleja, P. A. Rasmussen, and A. Boisen, “SU-8 cantilever sensor system with integrated readout”, Sensors and actuators A, pp.111-115, 2005.

[6] D. Maraldo, and R. Mutharasan,“Mass-change sensitivity of piezoelectric-excited millimeter-sized cantilever (PEMC) sensors: Model and experiments”, Sensors and actuators B, pp. 140-148, 2008.

[7] H. J. Butt, P. Siedle, K. Seifert, K. Fendler, T. Seeger, E. Bamberg, A. L.Weisenhoern, K. Goldie and A. Engel, “Scan speed limit in atomic force microscopy”, J. Microscopy, Vol.169, pp. 75-84,1993.

[8] http://www.spmtips.com/

[9] K. H. Chung, and D.E Kim, “Wear characteristics of diamond-coated atomic force microscopy probe”,Ultramicroscopy, Vol.108,pp.1-10,2007.

[10] S. C. Erickson，“Properties of Pure Metals” in Metals Handbook，10th ed.，ASM，Vol. 2，pp. 1133，1990.

[11] A. W. Blackwood and J. E. Casteras，“Properties of Pure Metals” in Metals Handbook，10th ed.，ASM，Vol. 2，pp. 1111，1990.

[12] L. R. Smith and W. C. Leslie，“Properties of Pure Metals” in Metals Handbook，10th ed.，ASM，Vol. 2，pp. 1119，1990.

[13] W. S. Lyman，“Properties of Pure Metals” in Metals Handbook，10th ed.，ASM，Vol. 2，pp. 1169，1990.

Table 1 The parameter of the annealing treatment

	Mg	Cu	Fe	Ti
temperature	400℃	600℃	950℃	800℃
time	30min	1hr	30min	2hr

Table 2 The type of the cantilever beam

Cantilever length , l±5,μm	125
Cantilever width , w±3,μm	35
Cantilever thickness , μm	4.0
Resonant frequency , kHz	325
Force contant , N/m	40
Tip material	Silicon
Tip radius , nm	10
Tip height , μm	20

Table 3 The experimental parameter of the adhesive material

Indentation Rate	240 (nm/sec)
Retraction Rate	120 (nm/sec)
Maximum sample loading	20 (μN)
Hold Time @ Max. Sampl. Loading	10 (sec)
The number of impression	15 time

Table 4 The resonance of the cantilever beam before experiment and after experiment

material	Resonance frequency before experiment (kHz)	Resonance frequency after experiment (kHz)	Different (kHz)
Mg	347.075	347.035	0.040
Cu	316.737	316.633	0.104
Fe	339.235	339.187	0.048
Ti	362.588	362.484	0.104

Table 5 The adhesive material volume

material	adhesive volume (m^3)
Mg	1.259659×10^{-18}
Cu	0.652017×10^{-18}
Fe	0.4174883×10^{-18}
Ti	1.382796×10^{-18}

Table 6 The density of the material

material	density(kg/m^3)
Mg	1738
Cu	8920
Fe	7694
Ti	4507

Table 7 The adhesive mass by using the semi sphere volume method

material	adhesive mass (kg)
Mg	2.18929×10^{-15}
Cu	5.81599×10^{-15}
Fe	3.21215×10^{-15}
Ti	6.23226×10^{-15}

Table 8 The adhesive mass by using the semi sphere volume method and by using the cantilever beam resonance method.

material	Adhesive mass by semi sphere volume method (kg)	Adhesive mass by resonance (kg)	error
Mg	2.18929×10^{-15}	2.25604×10^{-15}	2.95%
Cu	5.81599×10^{-15}	6.39868×10^{-15}	9.11%
Fe	3.21215×10^{-15}	2.76914×10^{-15}	15.99%
Ti	6.23226×10^{-15}	5.61619×10^{-15}	10.96%

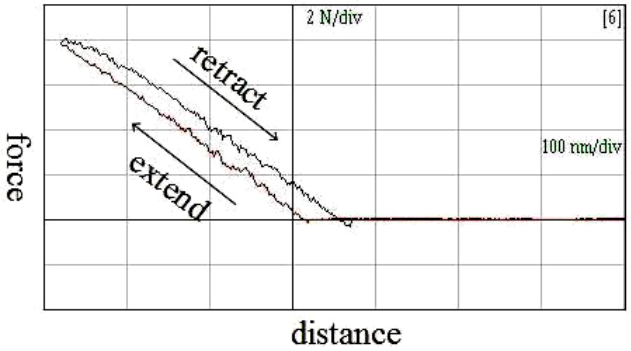

Figure1. force-curve

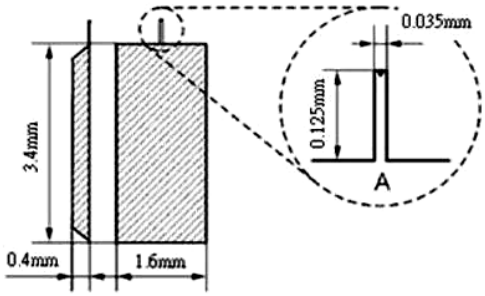

Figure 2. The local diagram of the cantilever beam [8].

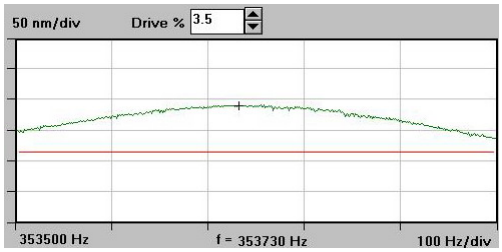

Figure 3. The resonance frequency of the cantilever beam

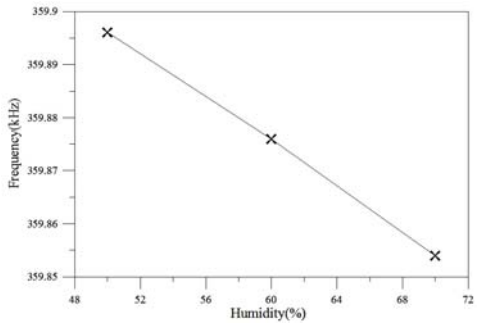

Figure 4. The resonance frequency and variable moisture

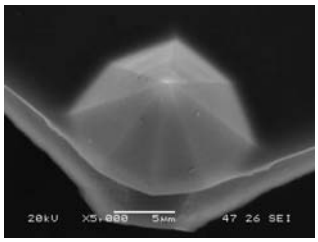
(a-1)Before experiment—Mg

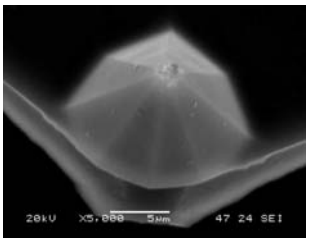
(a-2)after experiment—Mg

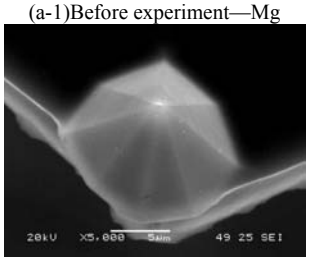
(b-1) Before experiment—Cu

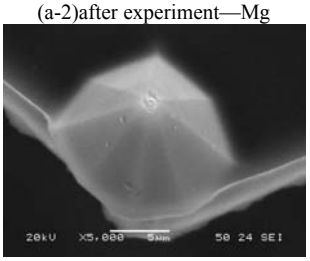
(b-2) after experiment—Cu

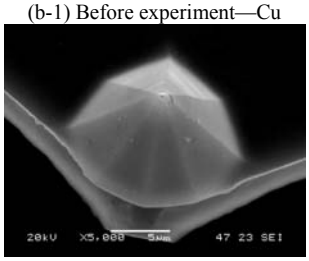
(c-1) Before experiment—Fe

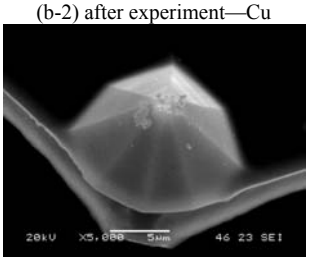
(c-2) after experiment—Fe

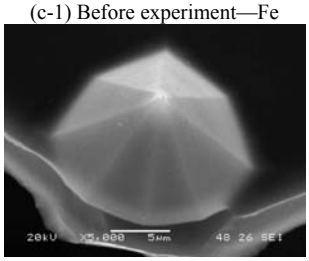
(d-1) Before experiment—Ti

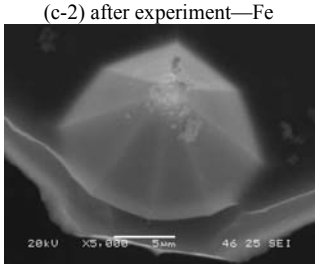
(d-2) after experiment—Ti

Figure 5. The surface contour of the cantilever bean by using SEM

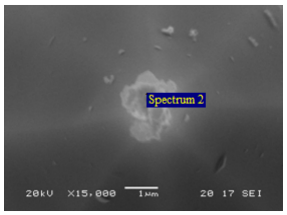

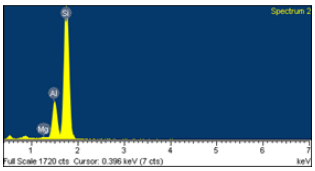

(a)Mg

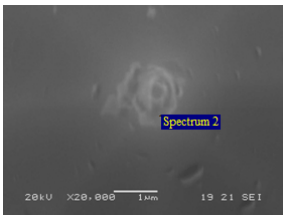

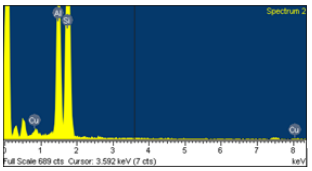

(b)Cu

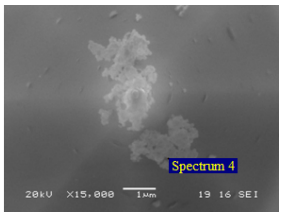

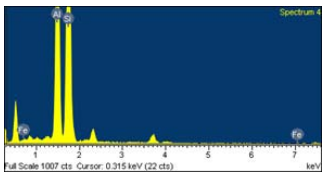

(c)Fe

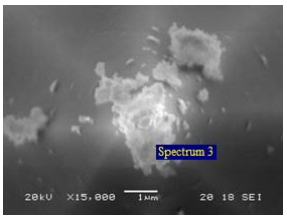

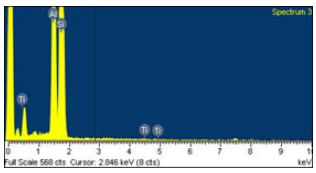

(d)Ti

Figure 6. The adhesive material element on the cantilever beam

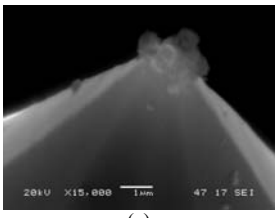
(a)

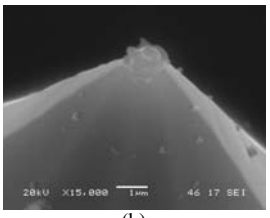
(b)

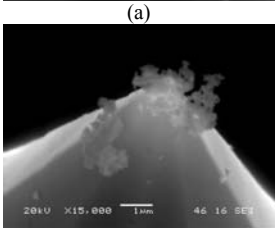
(c)

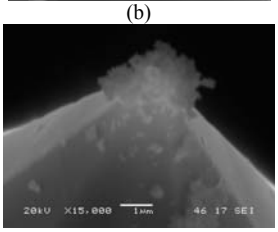
(d)

Figure 7. The local diagram of the cantilever beam tip; (a)Mg, (b)Cu, (c)Fe, (d)Ti.

P08

Fabrication of full glass chips with hybrid micro- and nanochannels and their application to protein concentration

Qiaohong He*, Hua Lu, Shuang Chen, and Hengwu Chen

Institute of Microanalytical Systems, Department of Chemistry, Zhejiang University, Hangzhou 310058, China

***Abstract* — In this paper, we proposed an alternative method that is simple and cost-effective to fabricate full glass chips with hybrid micro- and nanochannels. Double-lithography and double wet-etching technique was used for the fabrication of hybrid micro and nanostructures. The microchannels were firstly constructed on a glass substrate by standard UV photolithography and wet etching technique. After washing away the rest photoresist and spinning a new layer of photoresist on the microchannel-structured glass substrate, nanochannels with the depth less than 100 nm were produced on the same substrate by second lithography and wet etching. Then the channels-structured glass substrate was sealed to a cover glass plate by using previously developed room temperature bonding technique. Without using clean room facilities and expensive instruments, micro- and nanofluidic chips with delicate structures were well fabricated. The good nature of those nanofluidic chips was demonstrated by the successful concentration of FITC-labeled bovine serum albumin via electrokinetic ion trapping.**

Keywords — ***chip fabrication; double-etching technique; micro- and nanofluidic chips; protein concentration***

I. INTRODUCTION

When the cross-section of channels is down to nanometer scale (at least in one demention, most frequently in the dimension of depth), the channels exibit some special properties that make them attractive to the transportion, manipulation, concentration, separation and detection of biomolecules such as DNA [1-2] and protein [3-4]. However, the tiny size causes considerable fluid resistance and high-pressure loss inside nanochannels, consequently diminishing the feasibility of using nanochannels exclusively in biochemical analysis or other applications. Therefore, most nanofluidic analytical systems combine nanochannels with microfluidic networks which are usually used as bulk-fluid delivery paths for further reaction, separation and detection process that occurs in nanochannels. Recently, interests in fabrication of nanochips with hybrid micro- and nanochannels have been constantly increasing, because the hybrid micro- and nanofluidic chips have shown variaty of applications in the fields of chemical and biochemical analysis.

Hybrid micro- and nanofluidic chips were usually fabricated in two ways. One way is to prepare microchannels and nanochannels separately on two substrates and then bond them together after substrate-to-substrate alignment with the help of a microscope (short-termed as assembling of microchannels and nanochannels separately prepared on two substrates, AMNSP) [5]. However, fine substrate-to-substrate alignment is critical in this method. The alternative way is to fabricate micro- and nanochannels on one substrate by double lithography and various ecthing techniques [6-7]. This article presents our recent work on developing a low-cost and reliable double lithography and double wet ecthing (DLDWE) technique for fabricating micro and nanofluidic devices. This newly-developed DLDWE method was accurate enough to fabricate complicated hybrid channels. The most attractive merit of this method lies in the fact that glass nanofluidic chips can be fabricated by chemists themselves in their routine chemistry laboratories where may have no clean room facilities. With this technique, we fabricated a hybrid micro- and nanofluidic chip that was successfully applied to protein concentration.

II. FABRICATION

Two photomasks, one with the pattern of microchannels (Mask-I) and the other with the pattern of nanochannels (Mask-II), were prepared by respectively printing the channel designs onto polyethylene terephthalate (PET) films with a high-resolution (5080dpi) laser printer. The fabrication process for hybrid micro and nanofluidic chip using DLDWE method is as described in Fig.1.

1) The microchannel pattern on the Mask-I was transferred to the chromium and photoresist coated glass substrate with standard UV lithography. The glass substrate was then etched in an etchant of 1 M HF- 0.5 M NH_4F – 0.5 M HNO_3 at 40°C, leading to microchannels being patterned on the glass substrate. After the residual photoresist was removed by acetone (*note:* the residual chromim layer should not be removed at this point), the microchannel-structured glass substrate was cleaned with water and dried (Fig. 1(a) to (b)).

2) A thin layer of AZ4620 photoresist was spinned onto the chromium layer of the microchannel-etched glass substrate at the speed of 900 r/min for 40 s. After that, the substrate was baked in a oven at 90°C for 30 min to solidify the newly-coated photoresist (Fig. 1(c)).

3) The mask-II with the nanochannel pattern was aligned and tightly clamped to the glass substrate after making sure that the nanochannels and microchannels were correctly aligned to each other. Following UV exposure as mentioned above, the nanochannel pattern on the maks-II was then transferred to the glass substrate with newly-coated photoresist. The nanochannels were then etched in the etchant of 150 mM HF- 75 mM NH_4F – 75 mM HNO_3 at 40°C. Afterwards, the photoresist and chromium films were removed from the glass

This work was funded by the National Natural Science Foundation of China (project No. 20775068 and 20890020).

**Contact author: Qiaohong He is with the Institute of Microanalytical Systems, Department of Chemistry, Zhejiang University, Hangzhou 310058, China (Tel: +86-571-88206773; Fax:+86-571-88273572; Email: heqh@zju.edu.cn)*

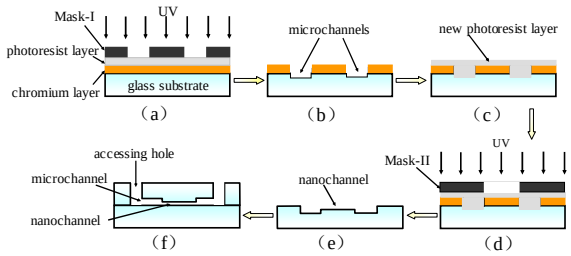

Figure 1. Schematic diagram of the fabrication process for micro- and nanofluidic chips by DLDWE method (not to scale).

substrate by acetone and chromium etchant solution, respectively (Fig. 1(d) to (e)).

4) After accessing holes being drilled on each of the microchannel terminals with emery drill-bit, the channel-structured glass substrate was finally bonded to a glass cover plate of the same material by using a room temperature bonding procedure (Fig. 1(f)) , as our previous work [8].

III. RESULTS AND DISCUSSION

A. Developing the techniques for fabrication of hybrid micro- and nanochannels

Nanofluidic analytical systems usually consisted of both micro and nanochannels. The microchannels are usually served as bulk-fluid delivery paths, while the nanochannel are used for ion concentration, fast chemical reaction, and species separation due to the specific behavoirs of nanochnnels. The present work aimed at developing a simple and facile technique for fabrication of hybrid micro and 1-D nanochannels on glass substrate in a routine chemistry laboratory. Thus, we checked three different fabrication methods including assembling microchannels and nanochannels separately prepared on two substrates (AMNSP), single UV-lithography followed by tape-shielded double wet ecthing (SLDWE), and double UV-lithography plus double wet ecthing (DLDWE) on the same substrate. The results can be seen in the Fig.2.

The fabrication of micro and nanochanels was relatively simple in the AMNSP method. However, it is challenging to precisely align the two channel-structured substrates, especially for those chips with long micro and nanochannels. Fig. 2(a) shows a CCD image of the part of a fabricated hybrid micro- and nanofluidic chip using AMNSP where the microchannel segments were laid on the top of the nanochannel. The microchannels can be clearly seen, but the nanochannel appears very dim. It should be noticed that the microchannels was not overlapped with the underneath nanochannel. This is because the nanochannel was so shallow that it could hardly be seen even with the help of a microscope during the alignment step. Minor shift of the two aligned substrates could lead to the fabrication failure and low yields. Thus, precise substrate-to-substrate alignment is critical in AMNSP method. Reference marks on the substrates were usually required in order to precisely align micro and nanochannels. Moreover, the aligning and assembly of the two substrates should be operated in a clean room to avoid contaminating from dust.

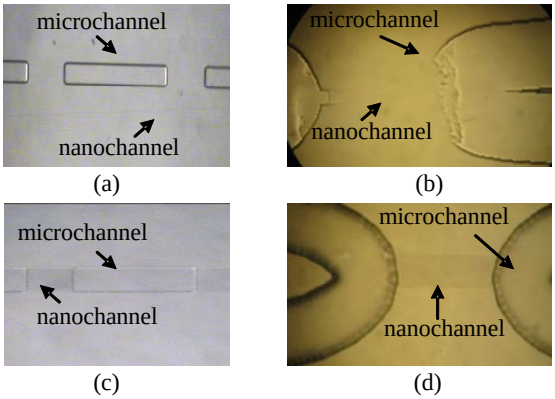

Figure 2. The CCD images of the hybrid micro- and naochannels (a) a part of the bonded hybrid micro- and nanochannels fabricated by AMNSP. (b) the central region of a hybrid micro- and nanochannels fabricated by SLDWE. (c) the similar structure as in (a) that was fabricated by DLDWE. (d) the central region of the similar hybrid structure as in (b) that was fabricated by DLDWE.

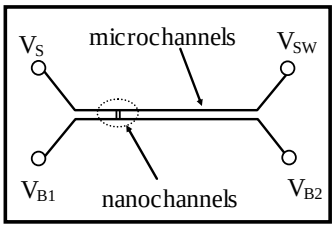

Figure 3. Schematic diagram of the chip with hybrid micro- and nanochannels (not to the scale) for protein concentration. V_B, V_S and V_{SW} represent buffer reservoir, sample reservoir and sample waste reservoir, respectively.

A single UV-lithography followed by tape-shielded double wet ecthing method (SLDWE) was also tested. After UV-lithography, the nanochannel region was gingerly shielded by a piece of adhering tape, and the microchanels were prepared on the substrate by wet etching for a given time at a specific etchant. Then, the shielding tape was peeled off and acetone was used to clean the ever-shielded region to remove the rest of the adhering tape. Afterwards, second wet chemical etching was carried out for a specified time to produce the nanochannel. Fig. 2(b) shows an image of the central part of a typical channel network prepared by SLDWE. The U-shape microchannel appeared obscure at the connection part. Obviously, this part of microchannels was deficiently etched due to being mis-shielded by the adhering tape. This mis-shielding was hardly avoided, because it was very difficult to have the narrow, adhering and flexible tape to be placed at the right position so as to shield only the nanochannle but microchannels.

The DLDWE process has been described in detail in Fabrication Section. After the microchannels had been etched

onto the glass substrate, a thin AZ4620 photoresist layer was coated afresh onto the microchannel-etched substrate. The pre-baking of the newly-coated photoresist was found to be the key step for the fabrication of nanochannels. One critical parameter for this step was the time duration. If the pre-baking time was too short, the photoresist might not be completely solidified. Consequently, the transferred pattern would have the risk to be distorted. If the time was too long, the photoresist might be too hard for properly developing the pattern after UV-lithography. Tests indicated that homogeneously baking at 90°C in an oven for 30 min was the optimum condition for pre-baking of secondly coated AZ4620 photoresist. Owing to the transparent lines (the pattern of nanochannels) on the printed mask can be clearly distinguished from the black background of the mask, it was easy to align the nanochannel pattern on the Mask-II to the etched microchannel line that was also transparent on the substrate with chromium and newly-coated photoresist layers. Compared to the alignment of the nanochannels and the microchannels on different substrates, this alignment was more convenient and easy. This guaranteed the accuracy of the second UV lithography, consequently, the quality of the fabricated channels. After second wet chemical etching for the nanochannels, the substrate with micro- and nanochannels was easily bonded to a glass cover plate without requirement of clean room facilities as described in our previous work [8]. Microchannels and nanochannels in Fig. 2(c) are very well aligned which was fabricated by DLDWE. And Fig. 2(d) also prensents us a great hybrid structure of microchannels and nanochannels fabricated by DLDWE on the same glass substrate.

Thus, we compared those three methods and found that DLDWE was the best one for fabrication of micro and nanofluidic chip in a routine chemistry laboratory.

B. Application of a nanofluidic filter for protein concentration

With the DLDWE technique, we fabricated a hybrid micro- and nanofluidic chip for FITC-BSA concentration. The chip (termed as nanofluidic filter) consists of two long U-shaped microchannels and two parallel, short nanochannels which were connected to the two microchannels as schematically illustrated in Fig. 3. The dimension of the microchannels was 20 μm wide, 1.5 μm deep and 15 mm in total length, and that of the nanochannels was 20 μm wide, 40 nm deep and 1 mm long.

During the test a solution of 1.2 μM FITC-BSA was first loaded into one of the U-shaped microchannels (that is the channel V_S-V_{SW}). A proper positive voltage was then applied to both V_S and V_{SW} reserviors while V_{B1} and V_{B2} were grounded. As soon as the electric voltage was applied across nanofluidic channels, more counterions (positive ions in this paper) than co-ions migrated across nanochannels. This resulted in the concentration polarization effect. An ion depletion region and enriched FITC-BSA molecule plugs were formed in the bulk solution within microchannel, near to the nanochannels. The changes of fluorescent intensity in the micro- and nanochannel interface region at the varied electric trapping time were observed with a fluorescence microscope and recorded with a CCD camera. Fig. 4 shows the performance of the nanofilter for protein concentration at varied applied electric voltages ranging from 30 V~100 V.

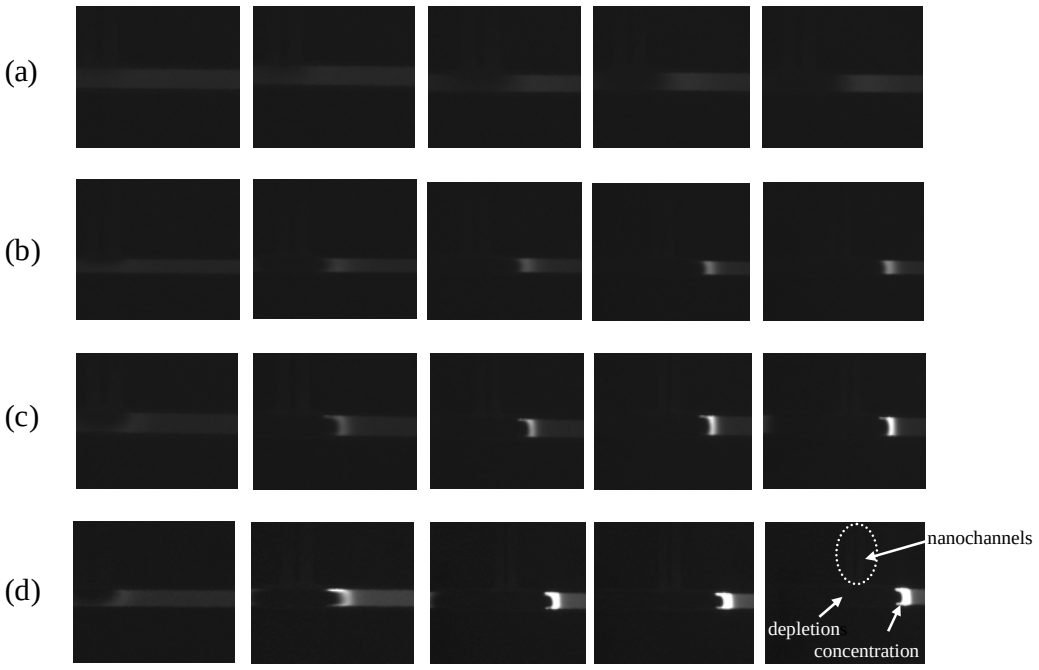

Figure 4. Images of FITC-BSA concentration taken respectively at 2 s, 8 s, 16 s, 24 s and 30 s after the specified electric votltage was applied to the hybrid channels. The voltage applied to the sample and sample waste reservoirs was 30, 50, 80 and 100 V for (a), (b), (c) and (d), respectively. A sample solution of FITC-BSA prepared in 10 mM phosphate buffer (pH9.1) containing 10 μM EDTA was loaded into the sample delivery microchannel (channel V_S-V_{SW}, as shown in Fig. 3). FITC-BSA concentration in the sample solution was 1.2 μM.

It can be seen in the figures that the higher the voltage was applied, the greater the concentration efficiency was obtained. Moreover, it was interesting that no matter how much the voltage was applied, the maximal concentration efficiency was achieved after trapping for around 30 s. When the trapping time was over 30 s, the concentrated sample plug significantly broadened (data not shown in Fig. 4). This was probably due to the strong vortical convective flows inside the depletion zone. Such vortices induced fast mixing, consequently destroying the concentration polarization effect.

CONCLUSION

We have doveloped a double lithography and double wet ecthing technique for the fabrication of hybrid micro- and nanofluidic chips on glass substrate without the requirement of expensive instruments and clean room facilities. The recommended technique features accuracy in the aligning of nanochannel to microchannel, high fabrication yields, and simple operation procedures. Successful protein concentration achieved with such fabricated hybrid micro- and nanofluidic devices demonstrated the promising potentials of this techinique in developing novel micro- and nanofluidic devices for various chemical, biological, and medical applications. By extending this technique to multi-lithograpy and multi-etching procedures, delicate channel structures with multi-depth might be fabricated.

REFERENCES

[1] K. Wang, S. Yue, L. Wang, A. Jin, C. Gu, P. Wang, H. Wang, X. Xu, Y. Wang, and H. Niu, “Nanofluidic channels fabrication and manipulation of DNA molecules,” *IEE Proc Nanobiotechnol*, vol. 153, pp. 11-15, 2006.

[2] J. Han, and H. G. Craighead, “Separation of long DNA molecules in a microfabricated entropic trap array,” *Science*, vol. 288, pp. 1026-1029, 2000.

[3] R. B. Schoch, A. Bertsch, and P. Renaud, “pH-controlled diffusion of protein with different pI values across a nanochannel on a chip,” *Nano Letter*, vol. 6, pp. 543-547, 2006.

[4] H. Yu, Y. Lu, Y. G. Zhou, F. B. Wang, F. Y. He, and X. H. Xia, “A simple, disposable microfluidic device for rapid protein concentration and purification via direct-printing,” *Lab on a Chip*, vol. 8, pp. 1496-1501, 2008.

[5] K.D. Huang, and R.J. Yang, “Formation of ionic depletion/enrichment zones in a hybrid micro-/nano-channel,” *Microfluid Nanofluid*, vol. 5, pp. 631–638, 2008.

[6] Y.C. Wang, A.L. Stevens, and J.Y. Han, “Million-fold preconcentration of proteins and peptides by nanofluidic filter,” *Anal. Chem.*, vol. 77, pp. 4293-4299, 2005.

[7] T. Tsukahara, K. Mawatari, A. Hibara, and T. Kitamori, “Development of a pressure-driven nanofluidic control system and its application to an enzymatic reaction,” *Anal. Bioanal. Chem.*, Vol. 391, pp. 2745-2752, 2008.

[8] Q. H. He, S. Chen, Y. Su, Q. Fang, and H. W. Chen, “Fabrication of 1D nanofluidic channels on glass substrate by wet etching and room-temperature bonding” *Anal Chim Acta*, vol. 628, pp. 1-8, 2008.

A 3-D Display System and Construction Method Based on MEMS Acceleration and Geomagnetic Sensor

En Wang[*], Xiangyu Zeng[2], Zuwang Liu[1,*], Jianzhe Li[3], Jinjing Zhang[3]

[1]Department of Electronic Engineering, Fudan University
[2]Department of Microelectronic, Fudan University
[3]Department of Computer Science, Fudan University

Abstract — **The paper constructed a 3-D display system which comprised of a ball-like controller, wireless transmitter/receiver, screen and software in host computer . The hard-core of ball-like controller consists of a tri-axial MEMS geomagnetic sensor MXR9500G [2] and a tri-axial MEMS acceleration sensor MMC3120MG [3] afforded by MEMSIC, Inc. in Wuxi, Jiangsu. With the system, when you rotate the ball-like controller, the same action will be reflected in Google Earth in the screen. What's more, if you pat the ball-like controller, the earth in the screen will zoom in, so that you can browse more details. And it'll zoom out when you shake the controller forcibly. With these functions, the system can display rich and colorful information on exhibition as well as geography teaching aids.**

Keywords ***—3-D display, MEMS sensor, virtual interaction***

I. INTRODUCTION

In this article, we presented a new method to monitor the status of the object. This method is different from all the traditional methods such as Gyro and RFID. According to our method, we can get the direction of x,y,z axis by using a tri-axial MEMS geomagnetic sensor and a tri-axial MEMS acceleration sensor.

Gravity Sensor has been applied in our daily use for a long time[4] [5] [6]. It has brought us some new kinds of user-interface. Games and application based on gravity sensor have been accepted by a lot of users. And people have fun with this kind of UI. But the traditional gravity sensor applications have a common disadvantage. They can only sense the state of an object at x and y axis. According to the technology in our paper, we can easily solve this problem.

As the MEMS technology has been developed a lot in these years, it becomes easy and cheap to build tri-axial MEMS geomagnetic sensor and a tri-axial MEMS acceleration sensor. It provides us with a chance to use this sensor in real applications at a large quantity. Unlike traditional two dimensional gravity sensor applications[10], the problems in three dimensional ones are more complicated. Using tri-axial gravity sensor alone will cause a severe problem called 'blind axes. The 'blind axis' happens under such a condition that when the object is rotated with any axis coinciding with the gravity's direction. The sensor will get same information when 'blind axis' happens. Thus the actual state of the object cannot be judged.

In order to solve this 'blind axis' problem, we focused on the gravity's brother----geomagnetism[8]. Geomagnetism is also one of the earth's inherent fields. Although the geomagnetism is changing, the changing speed is too low to affect our application. Thus it can be neglected. Geomagnetic has nearly the same characteristic as gravity, so it is easy to find the connection between them. In the system, an interactive globe is developed using our technology. Here we are going to introduce our demo system at first.

Assume that users' view point is fixed at the red marked point A on the ball-like controller. Fig.1 shows how users operate the system. The earth in the screen will rotate when users rotate the ball-like controller, and the displayed region in the screen is right the region around the view point A on the ball-like controller. When users pat the ball-like controller, the earth in the screen will zoom in and the information (e.g. music, pictures, video, etc) of the displayed area will appear, so that you can browse more details. And it'll zoom out when you shake the controller forcibly.

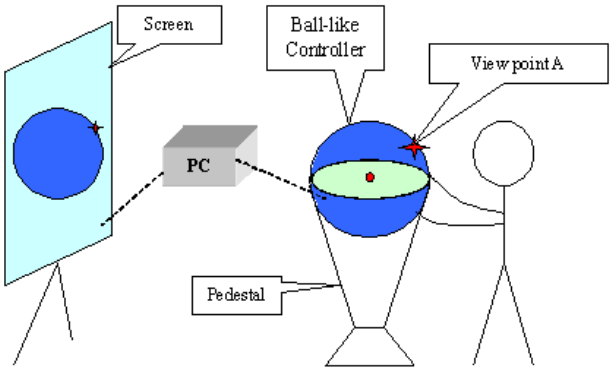

Fig. 1. Sketch map of operating the system

With these functions, the system can display rich and colorful information and may substitute traditional two-dimensional mouse or touch screen operation on exhibition as well as geography teaching aids, etc.

This paper is organized as follows. Section Ⅱ introduces system structure. In Section Ⅲ, system algorithm is presented as the core part of the paper. Host processing is mentioned in Section Ⅳ. Finally, two experiments are presented in Section Ⅴ.

The work was supported by National Key Technology R&D Program under Grand（ No.2009BAK43B22）

**En Wang: Master, Department of Electronic Engineering, Fudan University, 220 Handan Rd, Shanghai, 200433, China (phone: +86 21 65642756-6, email: wangenzk@gmail.com)*

**Zuwang Liu: Vice Professor, Department of Electronic Engineering, Fudan University, 220 Handan Rd, Shanghai, 200433, China (phone: +86 21 65643789)*

II. System Structure

Fig.2 shows the placement of each module in the ball-like controller. It includes Lithium Battery, Power Supply Module, MEMS Sensors, MCU Module and Wireless Transmitter, etc. Each module is fixed on the cylinder in the ball.

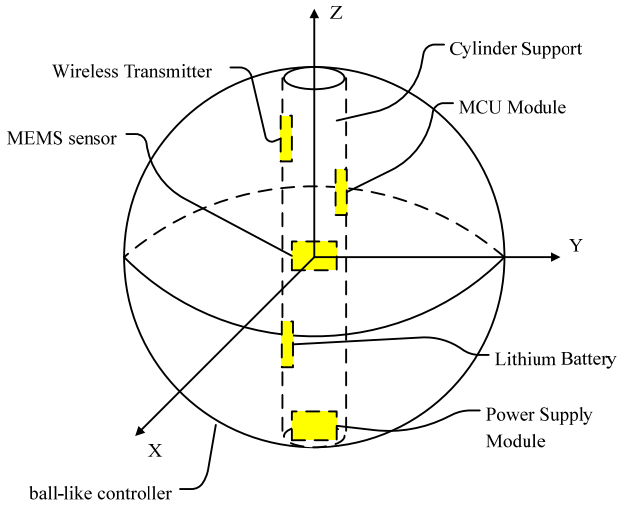

Fig. 2. Placement of each module

Fig.3 shows the functional block diagram. The power supply of the system is a lithium battery whose nominal voltage is about 3.7V. After voltage regulation by the power module, the voltage is changed to 3.3V which is available for other modules. MCU collects data from the two MEMS sensors through I^2C bus and on-chip ADC, respectively. After processing the collected data preliminarily, these data is sent to host computer through wireless transmitter. Then host computer will receive data through RS232 Serial Port, and make further processing of the received data by the algorithm referred in the following. Then the virtual earth controlled by the host computer in the screen will rotate, reflecting the rotation of the ball-like controller in real-time.

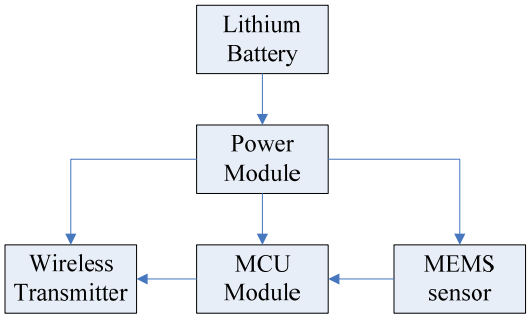

Fig. 3. Functional block diagram

Fig.4 shows the flow chart of software processing by MCU. After system initialization, MCU will collect data from MEMS sensors in turn. Then Wireless Transmitter will transmit data to host computer for further processing.

As a battery-powered equipment, it is important for power saving. In the system, Wireless Transmitter transmits data at normal rate which is about 20 times per second when the ball-like controller rotates. When the ball-like controller becomes static, Wireless Transmitter will transmit data at a low rate which is about 2 times per second. Further more, if the ball-like controller keeps static for more than 1 minute, then Wireless Transmitter will hibernate until the ball-like controller starts to rotate again.

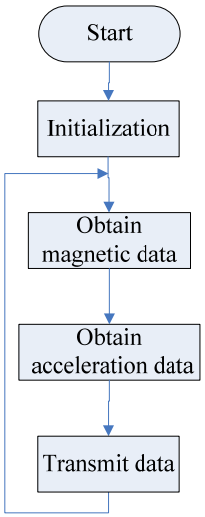

Fig. 4. Flow chart of MCU processing

III. System Algorithm

In this system, two coordinate systems are established. One is the coordinate system of the ball-like controller (Fig.5) and the other is the coordinate system of environment (Fig.6). The former one is determined by the three axes of the two MEMS sensors named X, Y, Z which follows the rotation of the ball-like controller. The latter one, which is assumed to be aptotic, is determined by the direction of gravity named -G and the direction of geomagnetic field named N. Through the coordinate transformation between the two coordinate systems whose origins are coincident, variables measured by the two MEMS sensors can be converted into the exact position of the users' view point in the coordinate system of the ball-like controller. Furthermore, through the Latitude and Longitude Conversion, we can obtain the latitude and longitude of the view point, that is to say, sphere surface location comes true.

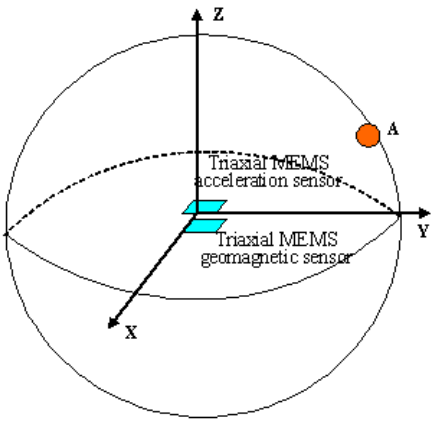

Fig. 5. Coordinate system of the ball-like controller

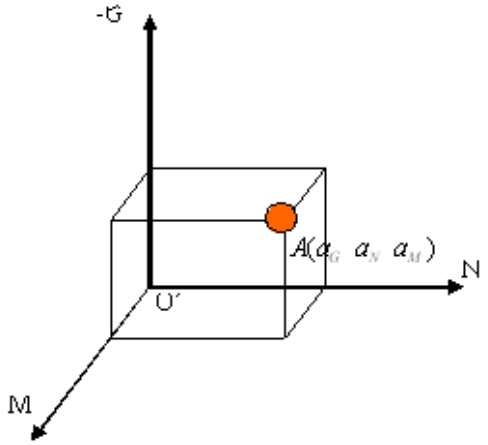

Fig.6. Coordinate system of environment

A. *Coordinate Transformation[1]*

The tri-axial MEMS acceleration sensor can decompose gravity on its three axes and the tri-axial MEMS geomagnetic sensor has a similar function, too. So, they can output three variables respectively, named $(g_X\ g_Y\ g_Z)$ and $(n_X\ n_Y\ n_Z)$. After normalization, we got the unit vector $G(g_X\ g_Y\ g_Z)$, $N(n_X\ n_Y\ n_Z)$ and they are normalized coordinates of –G and N in coordinate system of the ball-like controller. Through the right-hand rule, we got another unit vector named $M(m_X\ m_Y\ m_Z)$, and $M = G \times N$.

From (3.1), the coordinate of users' view point A in the coordinate system of environment which is assumed to be fixed will be transformed into A', which is the corresponding coordinate of the coordinate system of ball-like controller.

$$A' = A \times \begin{bmatrix} G \\ N \\ M \end{bmatrix} \tag{3.1}$$

B. *Latitude and Longitude Conversion*

We convert the coordinate obtained in the section above into Latitude and Longitude of the ball. We can calculate the Latitude and Longitude (φ, θ) from (3.2) and (3.3), which is like Polar Coordinate Transformation, shown in Fig.7.

$$\theta = \begin{cases} \arctan\left(\dfrac{a_Y}{a_X}\right), & a_X \geq 0; \\ \arctan\left(\dfrac{a_Y}{a_X}\right) + 180°, & a_X < 0,\ a_Y \geq 0; \\ \arctan\left(\dfrac{a_Y}{a_X}\right) - 180°, & a_X < 0,\ a_Y < 0; \end{cases} \tag{3.2}$$

$$\varphi = \arctan\left(\frac{a_Z}{\sqrt{a_X{}^2 + a_Y{}^2}}\right) \tag{3.3}$$

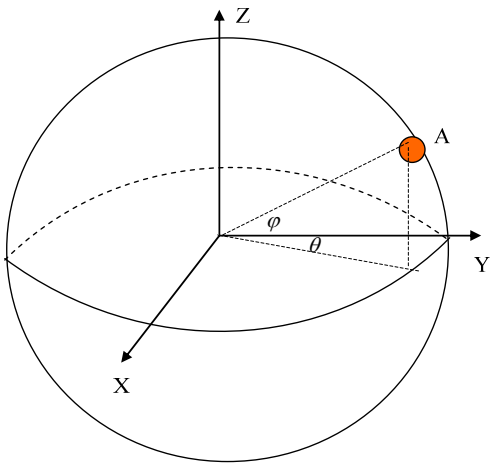

Fig.7. Sketch map of latitude and longitude conversion

C. *Calculation of Azimuth[9]*

Through calculating the deflection angle, the virtual earth can make correct actions when the ball-like controller rotates around the view point A.

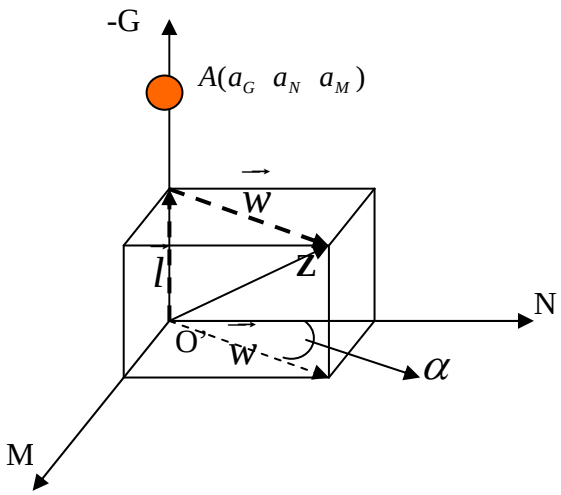

Fig.8. Sketch map of Deflection Angle

As shown in Fig.8, azimuth α is the angle between N axis and projection of the sensor's Z-axis on the horizontal plane. (Noting that the N axis is the calibrated direction of geomagnetic axis).

The coordinate of view point $A(a_G\ a_N\ a_M)$ is (1, 0, 0), and -G axis corresponds to unit vector $(-g_X\ -g_Y\ -g_Z)$ in the XYZ coordinates system. Thus, the projection vector of geomagnetic sensor's Z axis on the –G axis is $\vec{l}$, and the projection vector on the horizontal plane is $\vec{w}$,

Therefore, the angle between $\vec{w}$ and N-axis (which corresponds to unit vector $N(n_X\ n_Y\ n_Z)$) is the azimuth of the virtual earth when the view point $A(a_G\ a_N\ a_M)$ is （1，0，0）, as expressed in (3.4):

$$\alpha = \arccos\frac{\vec{w}\cdot N}{\left|\vec{w}\right|\cdot\left|N\right|} \tag{3.4}$$

D. *Compensation for the Geomagnetic Sensor*

Actually, there will be some magnetic interference in environment when the system works and we need to eliminate magnetic interference[7]. In our system, we put another two geomagnetic sensors near the ball-like controller. The two sensors and ball-like controller are placed on three vertices of an equilateral triangle. As the two sensors are fixed and the measured values do not change with the ball-like controller, they are able to respond to the external magnetic field interference accurately[11]. Through calculating the output of the two sensors, we can eliminate magnetic interference in environment.

E. *Recognition of Pat and Shake Actions*

When you pat or shake the ball-like controller, the output of the tri-axial MEMS acceleration sensor will be affected differently and we can recognize some pat actions through it. Detailed descriptions for recognition of pat and shake actions are in the Experiment Part (Part Ⅴ).

IV. HOST PROCESSING

Specific flow chart for software is showed in Fig 9.

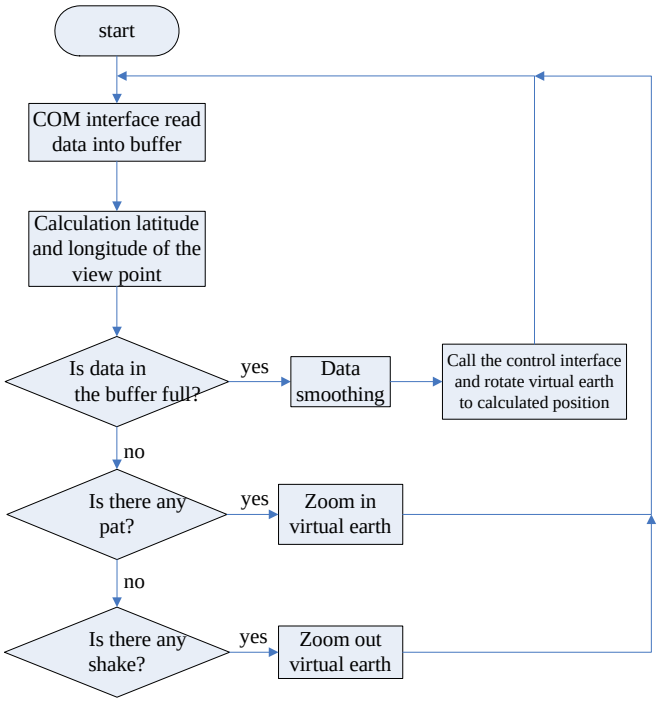

Fig.9. Flow chart of host processing

The host processing system is implemented by C#, which strengthens the efficiency of data transfers and improves the robustness for the display system.

In general, all operations on sensor data is a formation of message trigger (When data arrives, the host system will send a message to the processing module, and notify processing module to handle these data). Once a bundle of data arrives, it will record this bundle in the buffer in advance, and then fetch data from the buffer one by one. The processing module needs to calculate latitude, longitude, and azimuth and detects the pat and shake actions. Pat and shake actions are modeled by comparing the square-sum of the triple-data from tri-axial acceleration sensor with the average value when no shake actions occurred. Pat and shake actions are mapped to zooming in and zooming out in virtual earth respectively.

V. EXPERIMENTS

A. *Identification of Pat and shack*

As mentioned above, when you pat or shake the ball-like controller, the output of the tri-axial MEMS acceleration sensor will be affected differently.

Fig.10 shows quadratic sum of each axis' output data when patting the ball-like controller.

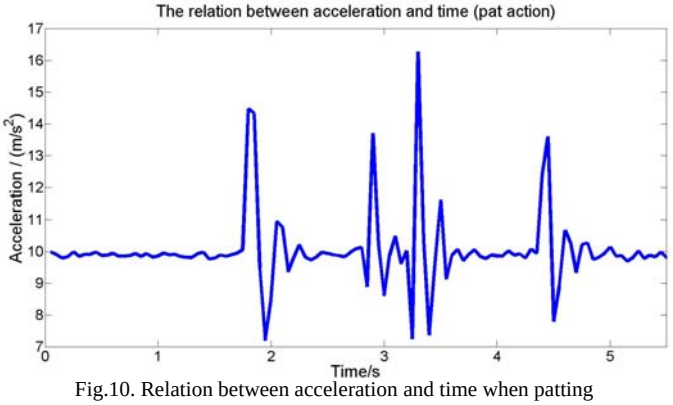

Fig.10. Relation between acceleration and time when patting

Table Ⅰ shows the results of pat actions identified by software algorithm. Corresponding to Fig.9, at the moment of 2.25 seconds, the action is identified to be Single tap in Table Ⅰ. And at the moment of 3.4 seconds, the action is identified to be Double taps homoplastically.

TABLE I. IDENTIFIED ACTIONS WHEN PATTING

Time(s)	2.25	3.40	4.85
Action	Single tap	Double taps	Single tap

Fig.11 shows quadratic sum of each axis' output data when shaking the ball-like controller.

Table Ⅱ shows the results of shake actions identified by software algorithm. During the interval between 4.20 seconds and 5.70 seconds, the action is identified to be shake.

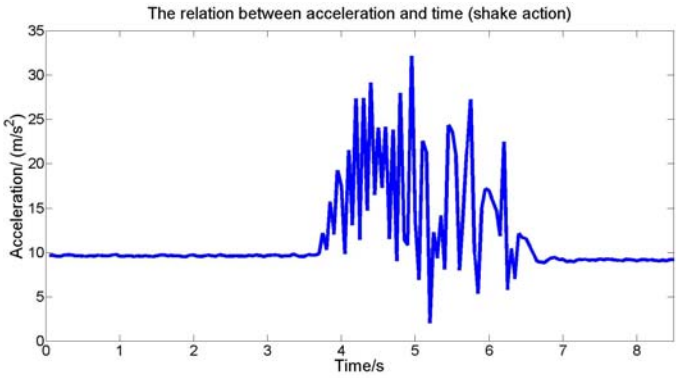

Fig.11. Relation between acceleration and time when shaking

TABLE II. IDENTIFIED ACTIONS WHEN SHAKING

Time(s)	4.20-5.70	5.90-6.75
Action	Shake	shake

B. Compensation for the Magnetic Sensor

The degree in Fig.12 describes the read of the geomagnetic sensor. Take the Y axis as an example, the read means the angle between the Y axis and magnetic north. The longitudinal coordinate means the normalized geomagnetic measurement. In Fig.12 the blue line describe the data of the normalized geomagnetic sensor's Y axis output. We can clearly identify that the mean of the output deviated the zero point. The red line describes the calibrated output. When the measured axis points to the north the geomagnetic sensor's max and min read has a great gap between them. At the point of extreme appearing is the angle of magnetic dip. Because of the existence of magnetic dip, the geomagnetic field is not always vertical to the gravity field. So when we make up the orthogonal coordinate system, we should calibrate the geomagnetic field's read at first. The green line describes the calibrated value. Our experiment result shows that after calibration we can get the idea geomagnetic field's direction and density.

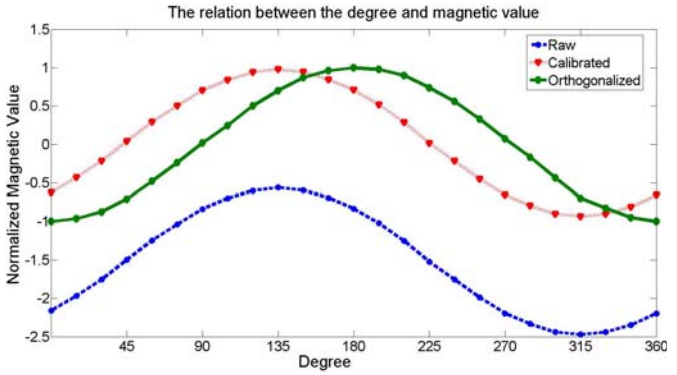

Fig.12. Relation between degree and magnetic value

VI. COMPARITION WITH TRANDITIONAL METHODS

In the paper, we presented a new method to monitor the status of the object. According to our method, we can get the x,y,z axis direction by using a tri-axial MEMS geomagnetic sensor and a tri-axial MEMS acceleration sensor.

In practical application, two representative methods of traditional state monitoring method are using Gyro or RFID. Gyro is a sensor which can measure the angular acceleration. When used for state monitoring, integral calculus is needed in order to get the current state of the whole system. The advantage of this method is that only one sensor is involved, so that the whole cost of the system is low. But as calculus exists, the inaccuracy is too high. RFID is the most popular method in recent years. It has high accuracy and can suffer poor working conditions. But the cost is so high since you have to set up a capture field and it needs several devices which cost a lot. Beside the expense problem, the measure range is limited by the capture field which has limited the use RFID in many situations.

The method in this paper not only has the high accuracy but also costs a little. The problem mentioned above can be solved with only two chip sensors by using the method in this paper. The cost of the method is far less than other methods but our performance is also far more better.

REFERENCES

[1] Yusun Tong, Chonghua Yu, Lu JIN and Wanguo Zhang, "Advanced Mathematics," HIGHER EDUCATION PRESS, 315-321, 2003

[2] Datasheet of MMC3120MG, Tri-axis Magnetic Sensor with I2C Interface, MEMSIC, Inc., 2008

[3] Datasheet of MXR9500G, Tri Axis Accelerometer with Ratiometric Outputs, MEMSIC, Inc., 2008

[4] Huaiyu Wu, ,Dong Sun, Zhaoying Zhou. Model Identification of a Small-Scale Air Vehicle for Loitering Control Design [A] .Proceedings of the 2004 IEEE International Conference on Robotics&Automatioa. New Orieans. 2004, .

[5] Gu mao, Tijing Cai, Yong Liu, Jun Song. Attitude Measurement System Based on MIMU. Ship Electronic Engineering.2008,03

[6] Verbree E , Maren G, Germs R , et al. Interaction in Virtual World Views-Linking 3D GISwith VR. Int J Geographical Information Science , 1999 ,13 (4) : 385～396

[7] YUAN Zhi-rong , All status error compensation about three axis magnetic heading sensor, Journal of Transducer Technology, 2003,09

[8] Caruso MJ. Applications of Magnetic Sensors for Low Cost Compass Systems[C] .IEEE2000.Position Location and Navigation Symposium(Cat.No.00CH37062). 2000, :177 .

[9] Cheng, P.L,Nicol, A.C.,Paul, J.P. Determination of axial rotation angles of limb segment—a new method .Journal of Biomechanics, 2000, 33 (7) :837～843

[10] Zhu R ,Zhou Z Y,Sun X F. MEMS navigation system for general vehicle[A] . IEEE International Conference on Mechatronics and Machine Vision in Practice[C] . 2001.

[11] LI Bingxi, ZHAO Zhong, SUN Zhaoxin Strapdown Magnetic Heading System and Error Compensation Based on Magnetoresistive Sensor, Journal of Transcluction Technology, 2003,02

P11

Microfluidic Device by Using Nano-magnetic Beads Conjugated Antibodies for Immunoassay

Chih-Hsiu Yin, Yu-Yin Tsai, Hui-Ju Cho, Chung-Hsien Tsai, Yuh-Jiuan Lin, and Hsiao-Chung Tsai*

Medical Electronics and Device Technology Center, Industrial Technology Research Institute, Taiwan

***Abstract* — We developed a fast and precision immunoassay-based microfluidic assay system that consisted of a microfluidic analytic cartridge and immunoassay reagents for point-of-care testing (POCT). The nano-magnetic beads conjugated antibodies, HRP-labeled analog, and color reagent were all pre-loaded and packaged in a microfluidic analytic cartridge. The whole assay process was completed within 30 min without any additional washing or loading of reagents once the sample was injected in the microfluidic analytic cartridge. The performance of the immunoassay-based microfluidic assay system had been examined by using mouse IgG model. The results indicated that the dynamic range of the measurement could be approached to two orders with low deviation. The present study demonstrated that the performance of our immunoassay-based microfluidic assay system was suitable for POCT for healthcare professionals or patients.**

Keywords — ***Immunoassay; microfluidic device; nano-magnetic beads; point-of-care testing.***

I. INTRODUCTION

POCT is a newly and fast-growing part of the market clinical of laboratory testing. Comparing with traditional center laboratories which test and report slowly, POCT is setup locally near the healthcare professionals or patients allowing for fast test and immediate report. POCT for biochemical test such as a portable glucose meter is more mature and achieves to patient self-testing in home. However, immunoassay-based POCT is still a challenge because of the complexity of the assay process. In general, an immunoassay consists of several steps of reactions and washing. This results in the difficulty of the development of instruments and reagents. Moreover, the imprecision of POCT is still a problem [1]. In the present study, we developed an immunoassay-based microfluidic analytic cartridge and reagents with broad detection range and fast testing ability which meet the requirement of POCT. The process of immunoassay was simplified so that the size of the microfluidic analytic cartridge could be decrease and the precision could be improved. An assay could be carried out on the microfluidic analytic cartridge within 30 min with two orders of dynamic range. The result indicated that our immunoassay-based microfluidic analytic cartridge was potential to accomplish the ability of immunoassay for POCT.

II. EXPERIMENTAL SETUP

A. Materials

N-hydroxysulfosuccinimide sodium salt (NHS) was a Fluka (Missouri, USA) product. 1-ethyl-3-(3-dimethylaminopropyl) carbodiimide (EDC) was a Thermo (Massachusetts, USA) product. Amplex UltraRed was provided from Invitrogen (California, USA). 3-Aminopropyltriethoxysilane (APTES), tetraethoxysilane (TEOS), 2-N-morpholinoethanesulfonic acid (MES), phosphate buffered saline (PBS), and bovine serum albumin (BSA) were purchased from Sigma (Missouri, USA). Mouse IgG-HRP and goat anti-mouse IgG were provided from Jackson ImmunoResearch (Pennsylvania, USA) and abcam (Massachusetts, USA), respectively. Human control serum was obtained from Bio-Rad (California, USA).

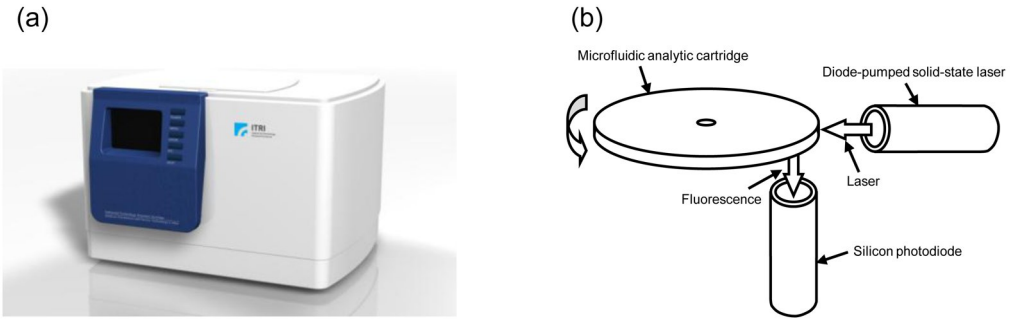

Figure 1. POCT microsample analyzer and analytic principle. (a) The portable analyzer is equiped with a user-friendly interface and analysis program. The dimensions of the analyzer are 30 cm length, 21 cm wide, and 20 cm high. (b) The microfluidic analytic cartridge is rotated in various speeds for blood cell separation, reaction, and liquid flow control. Color product is excited by 532 nm laser and emits 585 nm fluorescence that can be detected by a silicon photodiode.

*Contact author: for all aspects of this project, please contact ***tsaihsiaoc@itri.org.tw.***

B. POCT microsample analyzer

We developed a POCT microsample analyzer in previous project as shown in Fig. 1. A microfluidic analytic cartridge could be loaded in the portable analyzer. It performed analysis process and generated report automatically. The analyzer was equipped with a diode-pumped solid-state laser and a silicon photodiode to excite the color product in the cartridge and read the signal, respectively.

C. Design and manufacture of microfluidic analytic cartridge

The microfluidic analytic cartridge of the present study was manufactured by computer numerical control (CNC) machining for preliminary study to examine the design feasibility. For mass production, the cartridges were made with highly transparency polymethy methacrylate (PMMA) or polycarbonate (PC) by general injection plastic. The cartridges were sealed double sides with pressured sensitive high-transparent films.

The pattern of the cartridge is shown in Fig. 2 and arranged into three main compartments: sampling part, separation part, and analytic part. The sampling part consists of an injection port, a sample chamber connecting by a micro channel, and a capillary valve for stopping and quantifying sample volume at the upstream of flow path. The separation part consists of a separation chamber for separating and holding sample, and a capillary channel for drawing out the supernatant of the sample. The analytic part consists of a color chamber for optical analyzing, and a vent for flow path working.

D. Nano-magnetic beads production

Nano-magnetic beads used for immunoassay were synthesized by solvothermal reaction. Ferric chloride and sodium acetate were dissolved and stirred vigorously in ethylene glycol. The mixture was sealed in a pressure reactor and heated to 200°C for 8 hr. Black nano-magnetic beads were formed and then washed by ethanol once and distilled water three times. The nano-magnetic beads with average diameter 180 nm, were further functionalized with amine group by reacting with TEOS and APTES. The amine groups on the nano-magnetic beads were then replaced with carboxyl group for further antibody conjugation. Amine-terminated nano-magnetic beads were suspended in 1-methyl-2-pyrolidinone and sodium borate buffer consisted of 8 mg/ml sodium hydroxide and 47 mg/ml boronic acid, and then reacted with succinic anhydride for four hours. Finally, the nano-magnetic beads were washed by distilled water and stored in distilled water in room temperature.

E. Antibody conjugation

The nano-magnetic beads functionalized with carboxyl group were conjugated with antibodies for immunoassay. 30 mg nano-magnetic beads were washed twice with 1 ml MES buffer consisted of 25 mM MES, pH 5.0. The nano-magnetic beads were then activated by 1 ml NHS/EDC/MES solution on a rotary mixer by genial mixing at room temperature for 30 min. NHS/EDC/MES solution was MES buffer containing 50 mg/ml NHS and 50 mg/ml EDC. The nano-magnetic beads were washed by MES solution three times and subsequently removed the supernatant. The activated nano-magnetic beads were incubated in PBS with 100 μg/ml antibodies at 4°C overnight. To block the unreacted esters on nano-magnetic beads, a PBS contained 100 mM glycine was used and incubated at 4°C for 30 min. Finally, the nano-magnetic beads were stored in PBS with 1% BSA at 4°C.

F. Reagents loading in microfluidic analytic cartridge

The microfluidic analytic cartridge should be loaded three reagents for immunoassay: nano-magnetic bead-conjugated antibodies, antigen-conjugated HRP, and color reagent. The nano-magnetic bead-conjugated antibodies described previously were adjusted to the concentration of 60 mg/ml before loading. The antigen-conjugated HRP was consisted of 2.5 μg/ml mouse IgG-HRP and 1% BSA in PBS. The color reagent for final color reaction was consisted of 5 mM Amplex UltraRed and 0.15% hydrogen peroxide in PBS. Before all reagents were loaded, the back side of microfluidic analytic cartridge was sealed using a pressure sensitive film (ARseal™90697, Adhesives Research). Following 2 μl of the nano-magnetic beads conjugated antibody and 0.5 μl antigen-conjugated HRP were loaded at sample chamber, 0.5 μl color reagent was loaded at color chamber. Finally, the front side of the microfluidic analytic cartridge was sealed by another pressure sensitive film. In order to balance the pressure of the microfluidic channels of the microfluidic analytic cartridge and injecting sample, the pressure sensitive film that covered vents and injection port on the front side of cartridge should be opened.

G. Assay procedure

We used human control serum spiked with known amount of mouse IgG as sample to examine the performance of the microfluidic analytic cartridge. A sample of 50 μl was injected into a cartridge through the injection port. The cartridge with sample was loaded in the POCT microsample analyzer and ran the assay program for mixing, separation, color reaction, and measurement. The total assay procedure could be finished within 30 min.

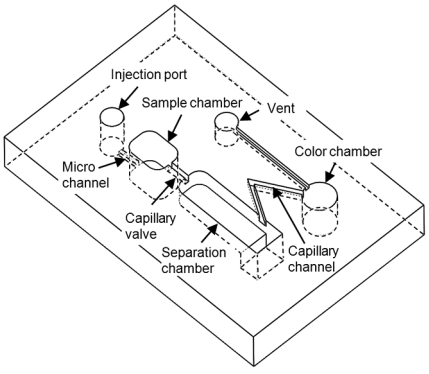

Figure 2. Pattern of microfluidic channels on microfluidic analytic cartridge.

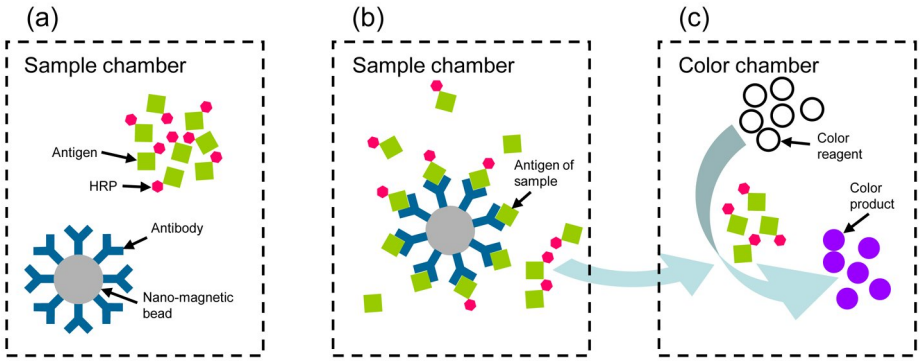

Figure 3. Principle of immunoassay in microfluidic analytic cartridge. (a) Nano-magnetic beads-conjugated antibodies and antigen-conjugated HRP are pre-loaded in sample chamber. (b) After sample injecting, antigens of sample compete with antigen conjugated HRP to the antigen-binding sites of the antibodies. (c) The residual of antigen-conjugated HRP flows into color chamber by centrifugal force and capillarity to react with color reagent.

III. Results and Discussion

This study aimed to construct an immunoassay-based system being included in a portable POCT microsample analyzer and the accompanied disposable cartridges meet the requirements of patient in-home self-testing. The performance of the developed reagents for each corresponding assay was also examined. The design of the whole system also took concerns regarding to wireless data transmission and the capability of internet connection to clinic's office or hospitals while these are sometimes important factors for medical professionals or in telehealth applications [2].

Fast assay is an important requirement for POCT. To reduce the reaction time, increase the reaction surface by use of glass beads [3], magnetic beads [4], or polystyrene beads [5] as supporter of antibody has been reported. Here, we used nano-magnetic beads functionalized with carboxyl group for further covalently conjugated to antibodies. Besides owing huge surface, nano-magnetic beads can further be applied under a variable magnetic field to improve mixing in solution.

In order to avoid contamination, analytic cartridge disposable design for POCT has been reported [6-8]. In our previous project, we have developed a disposable microfluidic analytic cartridge for serum biochemistry assay such as glucose, GOT, GPT, and BUN. Recently, we considered the possibility that immunoassay could be performed on the same microfluidic analytic cartridge.

To simplify the design, our microfluidic analytic cartridge did not provide washing function. Therefore, to adapt the design of the microfluidic analytic cartridge, an immunoassay method based on a competitive immunoreaction was used and shown in Fig. 3. Nano-magnetic beads-conjugated antibodies and antigen-conjugated HRP are pre-loaded in the sample chamber. When a sample is injected into the sample chamber, antigens in the sample compete with antigen-conjugated HRP to the antigen-binding sites of the antibodies that is conjugated on nano-magnetic beads. Simultaneously, the nano-magnetic beads-conjugated antibodies under a variable magnetic field can move in sample chamber to improve mixing and immunoreaction with the antigens and antigen-conjugated HRP. Following by applying a centrifugal force, the solution contains the residual of antigen-conjugated HRP flows into the separation chamber for further blood cell separation. The nano-magnetic beads-conjugated antibodies are remained in the sample chamber due to a strong constant magnetic field was applied. Subsequently, the supernatant containing the residual of antigen conjugated HRP in the separation chamber flows through a capillary channel into the color chamber by capillarity. Finally, HRP that conjugated with antigens reacts with the color reagent pre-loaded at the color chamber and the developing color can be measured. This competitive immunoreaction shows an advantage that washing is not required. Consequently, the microfluidic analytic cartridge does not require complex microfluidic design and additional chamber to store washing buffer and waste solution.

In order to examine the performance of our microfluidic analytic cartridge, we used mouse IgG as a model. A known amount of mouse IgG was spiked in human control serum since the effect of liquid property such as viscosity greatly affected the flow of liquid in the microfluidic channels. After injecting a sample, the cartridge was loaded in the POCT microsample analyzer and ran the assay program. Fig. 4 shows that samples contain 5, 0.5, and 0.05 μg/ml mouse IgG show different fluorescence intensity at 1770 ± 310, 365 ± 73.6, and 218 ± 37.1 RFU, respectively. The dynamic range of the microfluidic analytic cartridge in this study could reach to two orders.

The present study examined the possibility that the immunoassay could be performed on the disposable microfluidic analytic cartridge designed for a serum biochemistry assay in our early project. This work demonstrated that not only the immunoassay can be performed on the same disposable microfluidic analytic cartridge without washing, but also showd a broad dynamic range.

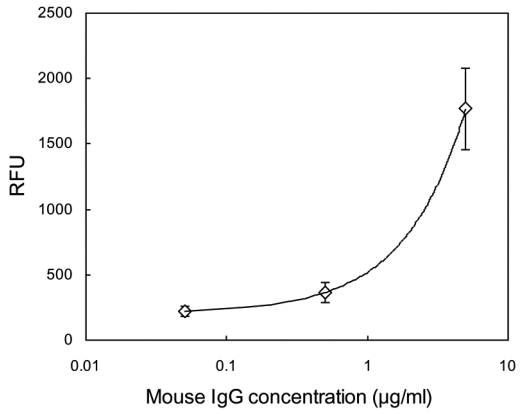

Figure 4. Mouse IgG assay in microfluidic analytic cartridge. Each point was tested four repeats indicates mean with standard derivation.

IV. CONCLUSION

In the present study, we developed an immunoassay-based microfluidic analytic cartridge and immunoassay reagents for our POCT microsample analyzer. The immunoassay was based on a competitive immunoreaction that washing was not required, hence the flow structure of the microfluidic analytic cartridge could be simplified capable of decreasing cartridge size and manufacturing cost. This competitive immunoreaction required few assay steps hence could reduce deviation accumulating during assay process thus capable of promoting the precision of assay. Moreover, the design of the cartridge demanded only 50 μl of blood sample, such the small volume of sample taken by a low invasive method "finger pricking" by patients themselves is adequate. The POCT microsample analyzer was also equipped with a user-friendly interface and performed the assay procedure and generated reports automatically. All of the assay process including blood sampling and instrument operating can be carried out by patients without assisting by physicians or nursing staffs. This property of the assay is very suitable for point-of-care and in-home environments. Besides easy of use, the immunoassay can be accomplished and generates report within 30 min. This fast assay can be satisfied for urgent examination including infectious disease screening or emergency room. In contrast, immunoassay in central laboratories may be finished in one hour, however, doctors or patients always receive reports after several days [9]. Although high precision in central laboratories is easy to be achieved, more and more studies have reported that the precision of POCT can comparative to the analyzers of central laboratories [10-13]. Consequently, POCT will play more and more important role in hospitals and in home. In the future, we will couple multiple biomarkers including immunoassays and serum biochemistry assays in the same microfluidic analytic cartridge for multiple assays. Lyophilized reagents are also under developing since regents in dry form allow maintain the shelf life. This study clearly shows a superior potential of developing a microfluidic analytic cartridge and regents for self-management of health in a fast and precise way using POCT analyzer.

REFERENCE

[1] M. Plebani, "Does POCT reduce the risk of error in laboratory testing?" Clin. Chim. Acta, 2009, vol. 404, pp. 59-64.

[2] L. Schlachta-Fairchild, "Telehealth: a new venue for health care delivery," Semin. Oncol. Nurs., 2001, vol. 17, pp. 34-40.

[3] N. Y. Lee, Y. Yang, Y. S. Kim, and S. Park, "Microfluidic immunoassay platform using antibody-immobilized glass beads and its application for detection of *Escherichia coli* O157: H7," Bull. Kor. Chem. Soc., 2006, vol. 27, pp. 479-483.

[4] J. Do and C. H. Ahn, "A polymer lab-on-a-chip for magnetic immunoassay with on-chip sampling and detection capabilities," Lab. Chip, 2008, vol. 8, pp. 542-549.

[5] K. Sato, M. Tokeshi, H. Kimura, and T. Kitamori, "Determination of carcinoembryonic antigen in human sera by integrated bead-bed immunoassay in a microchip for cancer diagnosis," Anal. Chem., 2001, vol. 73, pp. 1213-1218.

[6] J. S. Ahn, S. Choi, S. H. Jang, H. J. Chang, J. H. Kim, K. B. Nahm, et al., "Development of a point-of-care assay system for high-sensitivity C-reactive protein in whole blood," Clin. Chim. Acta, 2003, vol. 332, pp. 51-59.

[7] M. J. Pugia, G. Blankenstein, R. P. Peters, J. A. Profitt, K. Kadel, T. Willms, et al., "Microfluidic tool box as technology platform for hand-held diagnostics," Clin. Chem., 2005, vol. 51, pp. 1923-1932.

[8] M. Yamaguchi, S. Kambe, T. Eto, M. Yamakoshi, T. Kouzuma, and N. Suzuki, "Point of care testing system via enzymatic method for the rapid, efficient assay of glycated albumin," Biosens. Bioelectr., 2005, vol. 21, pp. 426-432.

[9] P. von Lode, "Point-of-care immunotesting: approaching the analytical performance of central laboratory methods," Clin. Biochem., 2005, vol. 38, pp. 591-606.

[10] R. F. Greaves, J. A. Northfield, and F. J. Cameron, "Haemoglobin A1c: evaluation of three point of care analysers for use in a paediatric diabetes clinic," Ann. Clin. Biochem., 2005, vol. 42, pp. 124-129.

[11] A. Haliassos, I. Drakopoulos, D. Katritsis, N. Chiotinis, S. Korovesis, and K. Makris, "Measurement of glycated hemoglobin (HbA(1c)) with an automated POCT instrument in comparison with HPLC and automated immunochemistry method: evaluation of the influence of hemoglobin variants," Clin. Chem. Lab. Med., 2006, vol. 44, pp. 223-227.

[12] H. Hallani, D. Y. Leung, E. Newland, and C. P. Juergens, "Use of a quantitative point-of-care test for the detection of serum cardiac troponin T in patients with suspected acute coronary syndromes," Intern. Med. J., 2005, vol. 35, pp. 560-562.

[13] S. W. Oh, J. D. Moon, S. Y. Park, H. J. Jang, J. H. Kim, K. B. Nahm, et al., "Evaluation of fluorescence hs-CRP immunoassay for point-of-care testing," Clin. Chim. Acta, 2005, vol. 356, pp. 172-177.

Biocompatibility Studies of Solution-Processable Organic Thin-Film Transistors for Sensing Applications

Giuseppe Scarpa[1,*], Anna-Lena Idzko[2], Stefan Götz[1], Teresa Neumaier[2], Stefan Thalhammer[2,#]

[1] *Institute for Nanoelectronics, Technische Universität München, Germany*

[2] *Institute of Radiation Protection, Helmholtz Zentrum München German Research Center for Environmental Health, Germany*

***Abstract* — We present for the first time biofunctionalization and biocompatibility studies of solution-processable organic semiconductors. Furthermore, low-operating voltage organic thin-film transistor devices have been fabricated, which can be used as sensors in electrolytes. The devices are based on regioregular poly(3-hexylthiophene), being both a reasonably conductive and optically active polymer. To overcome biocompatibility problems protein-based coatings and oxygen-plasma treatments have been adopted to enable growth of adherent living cells on those modified surfaces. With the demonstration of biocompatible semiconducting polymeric layers, we have overcome a substantial hurdle for the realizations of low-cost and mass-produced sensors in life science, opening new possibilities of biological sensing with organic electronic devices.**

Keywords — ***biocompatibility, biosensors, organic devices, organic transistors, polymers, surface treatments.***

I. Introduction

In recent years, scientific and technological advances have generated a remarkable number of approaches dealing with the problem of how diagnostic questions can be implemented. This was achieved by means of multifunctional and multi-parameter test-platforms. Among those, the most advanced is the development of chip-based technologies, where analyses are carried out more rapidly via small-scale systems and at lower cost than with current laboratory bench-scale methods. These so-called biochips are small sample-holders on which biological material is deposited for sample preparation, chemical/biological reactions and eventually analytical purposes. For these applications, there is a significant demand for small, portable, and inexpensive sensors, which can be used in clinical settings or basic medical research and in a wide range of sensing applications (e.g., food monitoring, detection of chemical, biological poisoning agents, environmental monitoring, etc.). Sensors based on organic semiconducting polymers, which are suitable for large-area, low-cost, flexible, and eventually single-use throwaway electronics, could satisfy this need in a very elegant way [1]. In the last few years, thanks to the advancements achieved by different research groups, organic biosensors based on electrical (or electronic) transduction mechanisms, have quickly evolved and a number of examples can be found in the literature. Among others, transistor-based devices (as gas, vapor and fluid sensors) [2-6], ion sensitive field effect transistors [7-10], sensors used in liquids [11-14] and organic electrode materials used in ampero-/voltammetry [15-19] have been reported. Unfortunately, the ensurance of biocompatibility and biofunctionalization of conducting and semiconducting polymers is still often lacking. In the present study, we concentrate on one of the most promising polymeric materials, rr-poly(3-hexylthiophene) (P3HT), being both a reasonably conducting and optically active polymer. By bio-functionalization and well-controlled plasma surface oxidation, we have successfully allowed adhesion, differentiation and proliferization of living cells on the polymeric layer. Organic thin-film transistors (OTFTs) with P3HT have been designed and fabricated aiming at the lowest possible working point for the use as sensor in electrolytes [20]. The electrical and conducting properties of the polymer are not affected by the treatments performed, hence allowing an easy adaptation to other organic semiconducting polymer layers.

II. Organic Thin-Film Transistors

Bottom-gate OTFTs based on solution processable polymers were fabricated on highly p-type doped Si wafers (purchased from Si-Mat, Landsberg), on which an 80nm or 45 nm thick SiO_2 layer was thermally grown in a dry oxidation process at 1000ºC. A multi-finger electrode structure consisting of a 2nm thick Ti layer (as adhesion promoter) followed by a 45nm Au layer was evaporated on top of the SiO_2 and patterned by lift-off in an optical lithographic step. The spacing between source and drain contacts of this interdigitated structure was chosen between 10 to 50 µm, determining the channel length. Regioregular P3HT (Sigma-Aldrich) was used as received as a semiconductor for the channel of our p-type OTFT and was deposited on top of the sample from a solution of 1wt% concentration in toluene or chloroform. Both spin-coating [20] as well as spray-coating [21] deposition techniques were applied. The polymer and the dielectric surface were not modified. A semiconductor characterization system (Keithley 4200-SCS) was used for all measurements. The analysis has been carried out at room temperature under ambient conditions. The channel has a large cross-section area (W/L) because of the interdigited electrode structure used for the contacts. Details on the performance of the OTFTs along with a theoretical analysis have recently been reported and can be found in [20]. A schematic cross-section of the transistor structure with optical images of the samples as well as output characteristics of a representative device with 20 µm channel length and a W/L= 13,350 are shown in Fig. 1.

This work was supported by the DFG within the German Excellence Initiative via the cluster of Excellence Nanosystems Initiative Munich (NIM).

Contact author: for fabrication and electronic aspects of this project please contact* ***scarpa@tum.de*

#Contact author: for biological aspects of this project please contact ***stefan.thalhammer@helmholtz-muenchen.de***

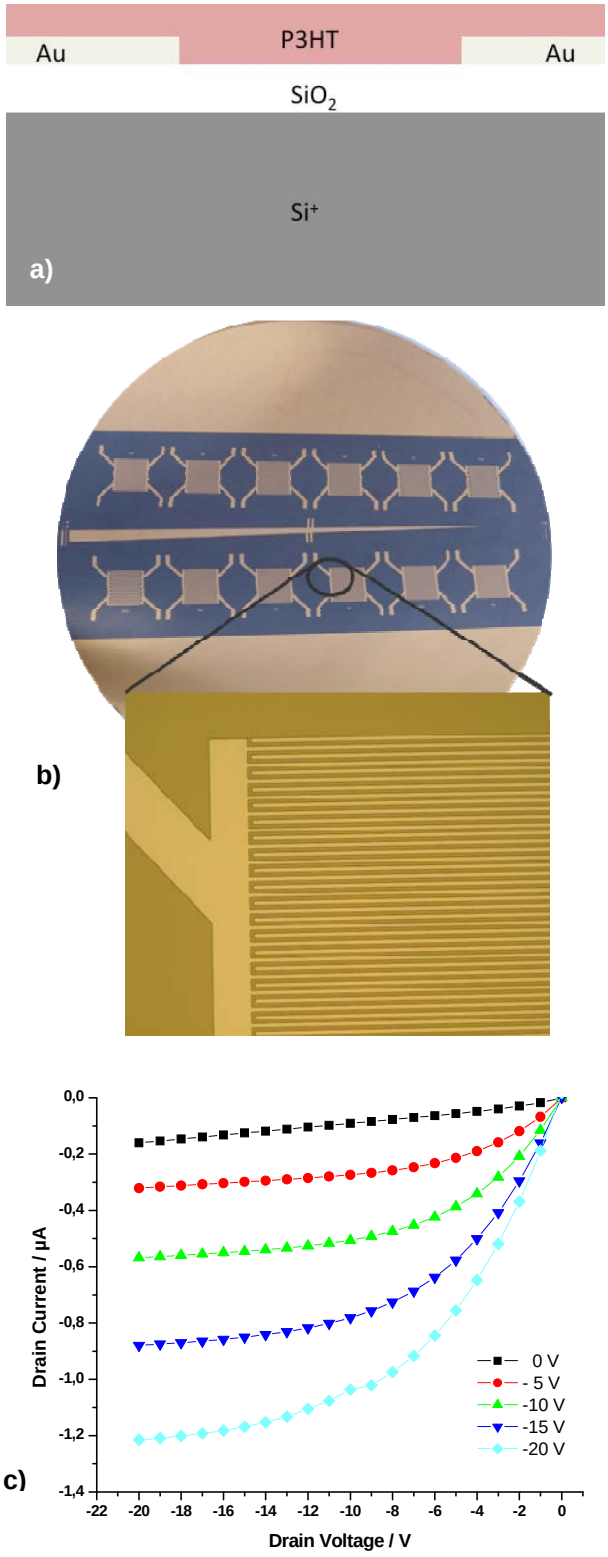

Figure 1. a) Cross section schematic structure of the organic thin-film transistor (OTFT), b) Optical image of the interdigitated source/drain layout used for the OTFT, c) Output characteristics of an OTFT with P3HT spun out of toluene with a channel length of 20 µm and W/L = 13350 on 80 nm silicondioxide. The OTFTs have been fabricated on two-inch boron-doped silicon wafers.

As the surface of the silicon dioxide was not treated separately, nearly all transistors showed a positive threshold voltage of about +5 V, thus displaying a clearly conducting channel already at a zero gate voltage, as can be seen from the picture. The field-effect mobility extracted from the transfer characteristics of the transistors was in the order of 10^{-4} cm^2/Vs, which was consistent with previous findings and experiments.

III. Functionalizytion And Biocompatibility

Thiophene-derivates such as P3HT represent promising organic materials. Therefore, its biocompatibility and biofunctionalization have been investigated. For these studies, glass substrates were coated with thin organic layers, by spinning and casting the polymer under nitrogen atmosphere. The latter method was applied in order to obtain films in the range of thickness between 100 nm to 10 µm. If not mentioned otherwise, these hydrophobic coatings have not been changed further electrochemically. Solutions of P3HT in toluene or chloroform were deposited and cured at temperature higher than the boiling point of the solvent used, yielding uniform layers, free of the toxic chemical solvents. With the purpose of evaluating the effect of surface-treatments and protein-based coatings on biocompatibility and cell adhesion, cell growth studies and adhesion experiments on the modified P3HT thin-film layers have been carried out with L929 mouse fibroblasts. L929 mouse fibroblasts derived from normal subcutaneous areolar and adipose tissue were grown routinely in RPMI media supplemented with 10% fetal calf serum. An optical micrograph of the L929 cell morphology can be seen in Fig. 2 (200x magnification). The spindle-shape states the adherent growth of the cells on the underlying surface. Thereby the surface characteristics have a significant impact on the adhesion, differentiation, and proliferation of surrounding cells.

The first step in testing the biocompatibility of the polymer was to plate cells on the samples without any further treatment beside the solvent removal under nitrogen atmosphere. Cell-growth experiments were carried out on P3HT-layers as follows. To sterilize the chips, they were rinsed with 70% ethanol and placed under UV-C radiation for 20 minutes. Subsequently, a well-defined concentration of cells was seeded onto the chips and left to grow. In these initial experiments, it could be shown that even after 24 h of incubation the cells did not adhere to the surface and were still in their non-adherent round shape. At this point, another important issue concerning simple biocompatibility was addressed, namely the adhesion of living cells to the molecular materials of interest. The formation of a healthy morphology/cytoskeleton and a stable sticking of cells represent an obligatory precondition for all further studies of chemo-physical interaction between organisms and electro-active polymers/materials. Thereby, surface characteristics such as charge density and hydrophobicity play a key role in protein adsorption and cell–substrate interactions. It has been shown that both cell–surface interactions and cellular functions (e.g., DNA synthesis) on thin films PPy can be controlled by either changing the oxidation state of the polymer or by changing the wettability

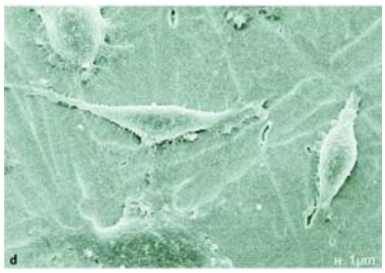

Figure 2. Morphology (200x magnification) of the L929 (mouse connective tissue fibroblasts) cells on sterilized glass substrates, established from the normal subcutaneous areolar and adipose tissue of a C3H/A mouse used as target in TNF detection assays.

(hydrophobicity) of the polymer film using appropriate dopants [22]. Since the cells poorly adhere to the hydrophobic surface of the chip, functionalizing-coating solutions based on different proteins (such as fibronectin, poly-l-lysine and collagen) were deposited onto the chips to improve the adhesion of the cells. Optical microscopic image analysis was used to quantify the effects of the treatments on cell proliferation. Fig. 3 summarize the results of cells grown on sterilized P3HT chip surfaces after different treatments using several combinations. The protein-based coatings were applied onto the chip surface and incubated for 30 min at T = 37°C in the incubator. After incubation, the chip was washed with PBS before the cells were seeded onto it again. In addition, a well-controlled plasma surface oxidation allowed for the adjustment of the surface properties of the film continuously on an unprecedented scale (Fig. 4). Unlike the untreated biosensor, the growth increased significantly. On the images it is possible to see cells adhering on all the pre-treated polymer chip surfaces (spindle-shaped form of the cells). It is apparent from the images that L929 cells attach and differentiate equally well on fibronectin (b) and on collagen (c) and more poorly on poly-l-lysine (a). The growth results on plasma-oxidized surfaces are shown in Fig. 3d). It is apparent from the micrograph how a well-controlled wettability of the surface allowed adherent growth of the cell. For comparison, we further functionalized the oxidized surfaces with collagen and fibronectin (images not shown). The L929 cells proliferated equally well on both surfaces.

To observe the effects of P3HT on the typical morphology of this cell type, confocal microscopy and atomic force microscopy (AFM) imaging studies were carried out on cultured L929 fibroblasts after 24 h. High-resolution AFM-images of cells fixed with gluteraldehyde on a collagen pre-treated P3HT chip are shown in Fig. 4. The image shows a micrograph of a well-defined cell culture (Fig. 4a) and a 3D magnified AFM image (Fig. 4b) of the same cell culture. From the magnified AFM picture it is apparent how the morphology of the cells is not influenced by the surface treatments. For future applications, AFM-based elasticity measurements should determine the quality of cell adhesion. The flexibility of engineering semiconducting polymer layers with varying surface properties offers many advantages. As can be seen in Fig. 5, by well-controlled plasma oxidation one can provide varied surface characteristics, on which liquid media

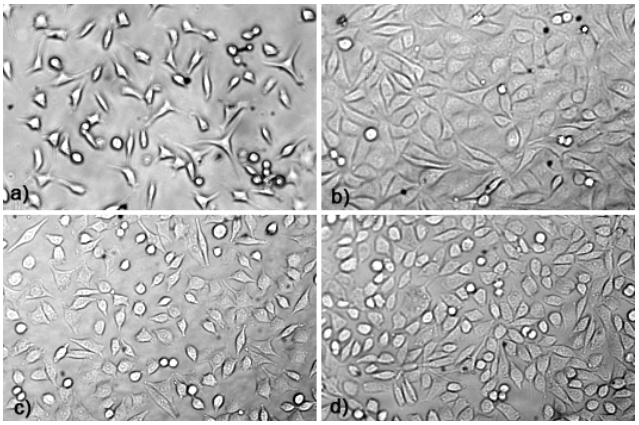

Figure 3. Optical microscopic images of plasma-oxidized and polymer-coated surfaces with the results of cellular growth for the diverse surface treatments. For biocompatibility studies, the polymer material was spun or casted onto glass substrates under an inert nitrogen atmosphere. The toxic solvents were removed by thermal treatment with subsequent application of the coating- or functionalizing materials. For all the experiments cells were seeded at a density of 54000 cells/cm^2. Cells were grown for 24 h on sterilized P3HT-coated glass pre-functionalized with a) poly-l-lysine b) fibronectin and c) collagen. In d) the sterilized P3HT-coated glass was plasma oxidized for 1 min prior cell deposition. The plasma oxidation strongly reduced the hydrofobicity of the polymer surfaces.

(water droplets) can be spotted, offering the possibility of patterning a surface with adhesive and non-adhesive areas.

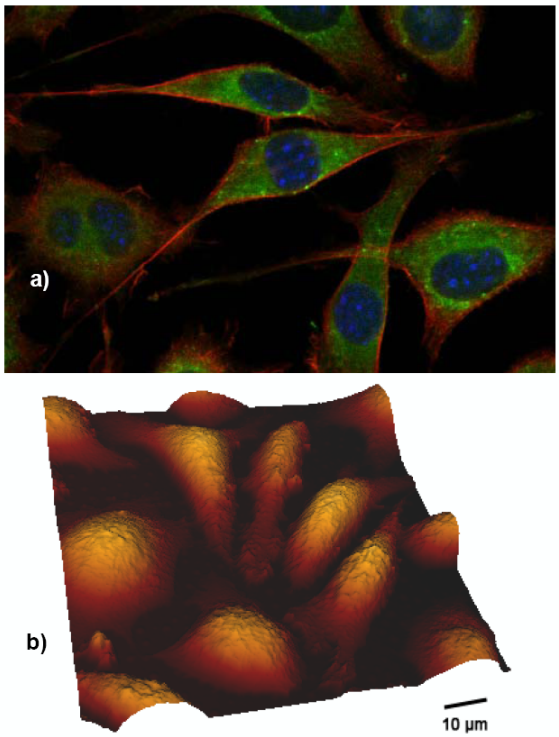

Figure 4. a) Confocal microscope image of fibroblasts grown and stained on the polymer surface. The cell membrane was labeled with DiO; after fixation and permeabilisation the F-Actin was stained with Rhodamine Phalloidin and the nuclei were counterstained with Hoechst 33342. b) High-resolution 3D atomic force microscopy (AFM) image of L929 cell fixed with gluteraldehyde on collagen-functionalized P3HT surfaces.

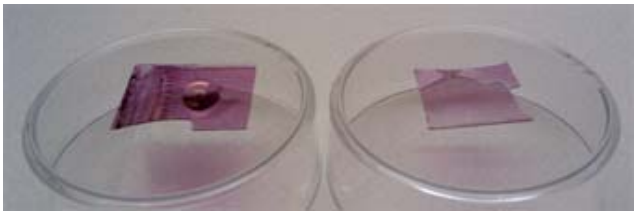

Figure 5. Optical images of P3HT-coated glass substrates with de-ionized water droplets on top before and after a controlled plasma oxidation. Left: due to the hydrophobicity of the surface the droplet flow is hampered (contact angle close to 90°). Right: the wettability of the surface has been changed by the oxidation process.

IV. CONCLUSIONS

For the first time we have successfully performed biofunctionalization and biocompatibibility studies of P3HT thin-films together with cell-growth studies, which can be easily adapted to other organic layers. Through screening a variety of protein-based coating layers and exploring the cumulative effects of plasma surface oxidation, we enabled adherent growth of L929 mouse fibroblasts. OTFTs with low driving voltages for biomedical applications using biocompatible P3HT polymeric layers have been also fabricated. The ability and flexibility at the level of controlling polymer surface properties provide a means to engineer materials that yield predictable and desirable cell–surface interactions. With the demonstration of biocompatible semiconducting polymeric layers, we have overcome a substantial hurdle for the realization of low-cost and mass-produced sensors in life science. Therefore P3HT is an interesting candidate for a range of medical applications, by virtue of its inherent semiconducting electrical properties, the ease with which one can control crucial surface properties such as wettability, and its compatibility with living cells. This work opens new possibilities of biological sensing using organic electronic devices.

ACKNOWLEDGMENT

Financial support by the Excellence Cluster “Nanosystems Initiative Munich (NIM)" is gratefully acknowledged. The authors would like to thank B. Fabel, R. Heilmann and M. Hofstetter for hands-on support in the lab.

REFERENCES

[1] J. T. Mabeck, G. G. Malliaras, “Chemical and biological sensors based on organic thin-film transistors,” Anal Bioanal Chem, vol. 384, pp. 343–353, 2006.

[2] L. Torsi, G. M. Farinola, F. Marinelli, M. C. Tanese, O. H. Omar, L. Valli, F. Babudri, F. Palmisano, P. G. Zambonin, F. Naso, “A sensitivity-enhanced field-effect chiral sensor,” Nature Mater 7, pp. 412–417, 2007.

[3] M. C. Tanese, D. Fine, A. Dodabalapur, L. Torsi, “Interface and gate bias dependence responses of sensing organic thin-film transistors,” Biosens Bioelectron 21, pp. 782–788, 2005.

[4] M. Kaempgen, A. Roth, “Transparent and flexible carbon nanotube/polyanilin pH sensors,” J Electroanal Chem 586, pp. 72–76, 2006.

[5] J. T. Mabeck, G. G. Malliaras, “Chemical and biological sensors based on organic thin-film transistors,” Anal Bioanal Chem 384, pp. 343–353, 2006.

[6] C. Bartic, B. Palan, A. Campitelli, G. Borghs, “Monitoring pH with organic-based field-effect transistors,” Sensor Actuat B-Chem 83, pp. 115–122, 2002.

[7] C. Bartic, A. Campitelli, G. Borghs, “Field-effect detection of chemical species with hybrid organic/inorganic transistors,” Appl Phys Lett vol. 82 (3), pp. 475–477, 2003.

[8] A. Loi, I. Manunza, A. Bonfiglio, “Flexible, organic, ion-sensitive field-effect transistor,” Appl Phys Lett vol. 86(10), pp. 103512, 2005.

[9] C. Bartic, G. Borghs, “Organic thin-film transistors as transducers for (bio)analytical applications,” Anal Bioanal Chem 384, pp. 354–365, 2006.

[10] A. Sargent, T. Loi, S. Gal, O. A. Sadik, “The electrochemistry of antibody-modified conducting polymer electrodes,” J Electroanal Chem 470, pp. 144–156, 1999.

[11] A. Sargent, O. A. Sadik, “Monitoring antibody-antigen reactions at conducting polymer-based immunosensors using impedance spectroscopy,” Electrochim Acta 44, pp. 4667–4675, 1999.

[12] M. G. H. Meijerink, D. J. Strike, N. F. de Rooij, M. Koudelka-Hep, “Reproducible fabrication of an array of gas-sensitive chemo-resistors with commercially available polyaniline,” Sens Actuator B-Chem 68, pp. 331–334, 2000.

[13] Y. Sakurai, H-S Jung, T. Shimanouchi, T. Inoguchi, S. Morita, R. Kuboi, K. Natsukawa, “Novel array-type gas sensors using conducting polymers, and their performance for gas identification,” Sens Actuator B-Chem 83, pp. 270–275, 2002.

[14] M. E. Roberts, S. C. B. Mannsfeld, N. Queralto, C. Reese, J. Locklin, W. Knoll, Z. Bao, “Water-stable organic transistors and their application in chemical and biological sensors,” Proc Natl Acad Sci USA vol. 105(34), pp. 12134–12139, 2008.

[15] B. Piro, L. A. Dang, M. C. Pham, S. Fabiano, C. Trans-Minh, “A glucose biosensor based on modifiedenzyme incorporated within electropolymerised poly(3,4-ethylenedioxythiophene) (PEDT),” J Electroanal Chem 512, pp. 101–109, 2001.

[16] S. K. Sharma, R. Singhal, B. D. Malhotra, N. Sehgal, A. Kumar, “Lactose biosensor based on Langmuir-Blodgett films of poly(3-hexyl thiophene),” Biosens Bioelectron 20, pp. 651–657, 2004.

[17] S. K. Sharma, R. Singhal, B. D.Malhotra, N. Sehgal, A. Kumar, “Langmuir-Blodgett film based biosensor for estimation of galactose in milk,” Electrochim Acta 49, pp. 2478–2485, 2004.

[18] L. Setti, A. Fraleoni-Morgera, B. Ballarin, A. Filippini, D. Frascaro, C. Piana, “An amperometric glucose biosensor fabricated by thermal inkjet printing,” Biosens Bioelectron 20, pp. 2019–2026, 2005.

[19] L. Setti, A. Fraleoni-Morgera, I. Mencarelli, A. Filippini, B. Ballarin, M. Di Biase, “An hrp-based amperometric biosensor fabricated by thermal inkjet printing,” Sens Actuator B-Chem 126(1), pp. 252–257, 2007.

[20] S.M. Goetz, C.M. Erlen, H. Grothe, B. Wolf, P. Lugli, G. Scarpa, “Organic field-effect transistors for biosensing applications,” Organic Electronics no. 10, pp. 573-580, 2009.

[21] A. Abdellah, D. Baierl, B. Fabel, P. Lugli, G. Scarpa, “Exploring Spray Technology for the Fabrication of organic devices based on Poly(3-hexylthiophene)”oral presentation and Proc. paper, 9th IEEE Conference on Nanotechnology IEEE-NANO-2009, Genoa, Italy, July 26-30, 2009.

[22] C. E. Schmidt, V. R. Shastri, J. P. Vacanti, R. Langer, “Stimulation of neurite outgrowth using an electrically conducting polymer,” Proc Natl Acad Sci USA 94, pp. 8948–8953, 1997.

The Affect of Bias Voltage to the DC Test of GMR Spin valve Biosensors

Fulong Zhao, Bingjun Qu*, Bo Lei, Tianling Ren, Litian Liu

Institute of Microelectronics, Tsinghua University, Beijing 100084, China

***Abstract* — This paper presents the fabrication process of a GMR spin-valve biosensor, and discusses the general design rules of the plane structure of the biosensor. The resistance variation of the sensor is studied versus the magnetic excitation field when 1ul solution of nanoparticles (150nm in diameter) with a concentration of 25mg/ml is directly dropped on the surface of the sensor. The experimental results show that the sensor's resistance had a non-zero change when the magnetic excitation field (H_f) equals zero, and it reaches the minimum when a particular negative magnetic excitation field (H_f) is applied. The detection accuracy of our biosensor is tested using a Wheatstone bridge circuit, and the results indicates that the fringe field of nanoparticles in 1μl solution with a concentration of 0.25μg/ml can be detected when the excitation field is -9Oe, but it is undetectable with a zero field.**

Keywords — ***Biosensor;Spin valve sensor;nanoparticle;DC test***

I. INTRODUCTION

In the past several years, giant magnetoresistance (GMR)-based magnetic biodetection technology, which involves labeling biomolecules with magnetic micro- or nanometer-sized particles and detecting the magnetic fringing fields of the particle labels by GMR sensors after capture by target-probe biomolecule recognition, has received increasing research and development efforts[1-4]. The basic idea of detecting magnetic nanotags is to excite the superparamagnetic nanoparticles with a magnetic field, and detect their magnetic responses (moments) or fields.

The magnetic excitation field, however, can be applied in different forms and directions. Generally, the detecting methods can be classified into DC test and AC test according to the form of the magnetic excitation field [5]. In comparison with the DC test, the AC test has the advantage of low noise, however, the AC test method which is utilized by the US Navel Research Laboratory [6] and Stanford research group [5] generally seems to be more complicated and costly because of the application of the lock-in Amplifier. Although the DC test method, which is utilized by the Portugal research group [2], is more easily interfered by various noises, our study is still focused on the DC test method because of its simple test system and more visual test results.

In this paper, we present the technological process of GMR spin-valve biosensor, and discuss the general design rules of the plane structure of the device. The response of the magnetoresistance to the magnetic excitation field is measured, and it is found that the detection accuracy reaches the highest point when a particular negative magnetic excitation field is applied.

This project was funded by the Chinese National 863 Plan (Project code: 2006AA03Z317)

**Contact author: Bingjun Qu is the vise professor of the Institute of Microelectronics of Tsinghua UniversityBeijing, China.(phone: 86-10-62789151-319; fax: 86-10-62771130; email:qubj@tsinghua.edu.cn)*

II. SENSOR DESIGN

A. Frabrication process

The spin valves were deposited onto a 4 inch Si wafer by magnetron sputtering and had the structure of Ta/NiFe/CoFe/Cu/CoFe/IrMn/Ta with a magnetoresistance of 9.1% and a sheet resistance of ~15Ω. Two Al leads (300nm) were then fabricated on the spin valve strips using liftoff technique. The spin-valve strips and leads were passivated with a 2000 Å thick sputtered SiO_2 layer for protection against various fluids used during experiments. Some of the spin valve strips were covered by a 2μm thick SU-8 layer, which was then heated for 10 minutes at 180 °C as a passivation. The passivated spin valve strips were effectively shielded from the magnetic particles and could serve as references to the unpassivated ones, so the unpassivated and passivated strips were called sensors and references. Finally, a layer of Ti20nm/Au50nm was deposited on the SU-8 holes for biologic functionalization. The cross section view of the biosensor was illustrated in figure 1.

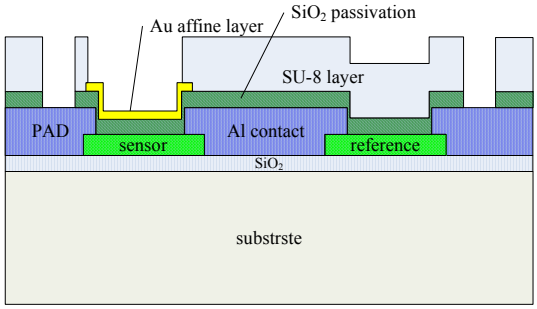

Figure.1. The cross-section diagram of the biosensor

B. Plane Structure

The quantity of the nanoparticles in the solution on the surface of sensors couldn't be the same even when the solution dropped on it had the same concentration. However, the larger the area of the sensor is, the more coherent the quantity between each two time drops is. Therefore, larger sensor would be a good choice for the biosensor design; however, the sensor couldn't be too large for that would be a waste to the wafer area. Because electrical noise, such as 1/f noise and John noise increase with the sensor resistance which is proportional to the length of the spin valve strips, shorter strips are preferred in design. According to the same reason, a wider strip will be preferred too, however, it is straightforward

to see that the narrower the strips, the more sensitive the sensor is to the magnetic fields of the nanoparticles. Therefore, the strips width should be a result of balancing the above two factors. In other word, the design principle of our biosensor is a trade-off of the dimension, length and width of the spin valve strips. In this study, the sensors and references were both constructed from ten stripes (4μm×200μm) in parallel, and the distance between every two stripes was 4μm. The plane paragraph of the biosensor was illustrated in figure 2. Its R-H curve was shown in figure 3, the coercivity (H_c) was 0.2Oe, coupled field (H_{cof}) was 0Oe，linear range (H_{range}) was about 50Oe.

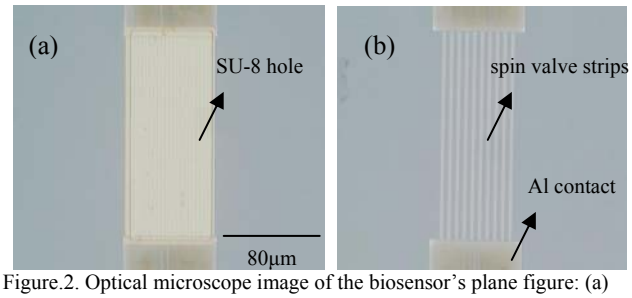

Figure.2. Optical microscope image of the biosensor's plane figure: (a) sensor; (b) reference

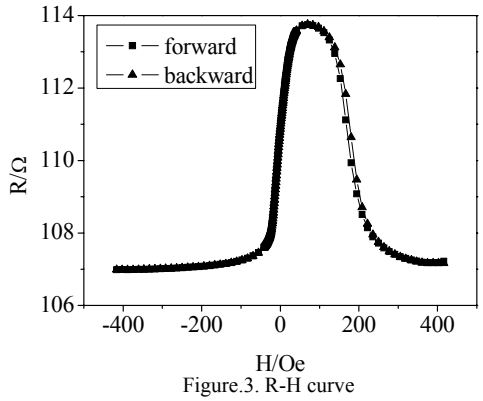

Figure.3. R-H curve

III. DETECTION RESULTS AND DISCUSSIONS

The real-time change of the sensor's resistance was collected by the computer via the KEITHLEY 2400 multimeter controlled by a Labview program. When the computer received the data collected by the multimeter, the real-time change of sensor's resistance was displayed on the front panel of the Labview program. The magnetic excitation field (H_f) was provided by a square Helmholtz coil, the magnitude and direction of the excitation field could be changed by altering the control voltage of the coil. In this study, H_f worked as both a bias field and an excitation field [7], and the magnitude of H_f was measured by a Guass-meter.

A. Evaluation

Before the test, an evaluation was made about whether the solvent of the solution of nanaparticles interfered the test result. The real-time transform law of the sensor's resistance was recorded when 1μl of liquid with and without nanoparticles was dropped onto the surface of the sensor separately, in this test the excitation field kept zero constantly. Figure 4(a and b) was the real-time transform curve of the sensor's resistance. From figure 3(a), we knew that the existence of the nanoparticles on the sensor made a 0.38Ω change to the sensor's resistance, and the resistance could recover to its original value when the nanoparticles were wiped away from the sensor surface, the little difference may due to the time deviation. From figure 3(b), we knew that the resistance of the sensor decreased rapidly as soon as the solution without nanoparticles was dropped on the sensor's surface at 1) and 3) because of the heat exchange between the solution and the sensor, and then the resistance slowly recovered to its original value, because of its temperature recovery as the solution evaporated. Based on the results, it could be concluded that the solvent had little influence on the test.

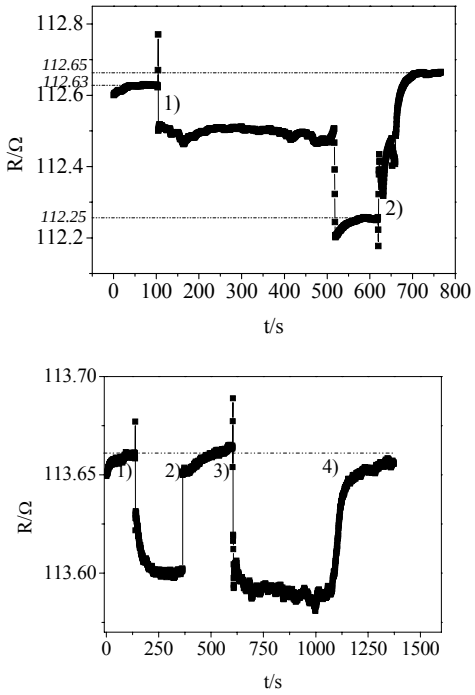

Figure.3. The real-time transform curve of the sensor's resistance:(a)the solution having nanoparticles dropped onto the surface of the sensor , the drop was added to the surface at 1) and wiped away at 2);(b)the solution having no nanoparticles dropped onto the surface of the sensor, the drop was added to the surface at 1) and 3) and the it evaporated totally at 2) and 4).

B. Test results versus different excitation fields

The test method was as follows, first, there were no nanoparticles on the sensor's surface, the magnetic excitation field H_f was changed according to the value listed in table 1 from negative to positive and from small to large, and the sensor's resistance under each field called R_{0i} was recorded at the same time; then, a 1μl solution of nanoparticles with a concentration of 19.3mg/ml absorbed by a micropipette of 5μl range was dropped on the surface of the sensor, after the solvent evaporated thoroughly, H_f was changed according to the value in table 1 from positive to negative and from large to small, the value of the sensor's resistance under each field

called R_{1i} was recorded at the same time; at last, the change of the sensor's resistance (ΔR_i) because of the effect of the nanoparticles' fringe field under various excitation fields could be obtained by subtracting R_{1i} by R_{0i}. The tests result was illustrated in figure 5.

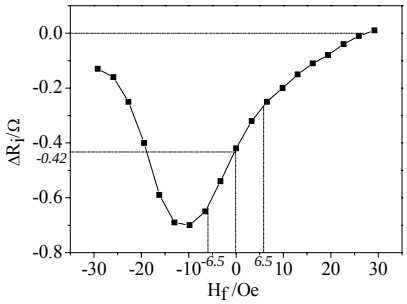

Figure.5. The resistance change of the sensor versus the magnetic excitation field

From figure 5, we can see that:

- When H_f=0Oe, the change of the sensor's resistance ΔR_i equaled 0.42Ω. The reason was that magnetostatic and sense current fields existed no matter whether H_f was zero or not, and the nanoparticls could always be excited by them.
- When H_f changed from the value close to -6.5Oe to the value close to +6.5Oe, the change of the sensor's resistance was proportional to H_f. The above phenomenon was easy to understand because the nanoparticles' fringe field was proportional to H_f, so was the sensor's resistance.
- When H_f changed from the value close to +6.5Oe to the value close to +29.2Oe, the sensor converted from its linear area to nonlinear area gradually since the sensor linear area ranged from -25Oe to +25Oe(figure 3), in addition, the nanoparticles' fringe field tended to be saturated under this H_f range. So the change of the sensor's resistance became smaller and smaller until it became close to zero.
- Because the fringe field of the nanoparticles was not zero when the H_f=0, the nanoparticles's fringe field became saturated earlier when H_f changed from 0 to -29.2Oe , comparing that when it changed from 0 to +29.2Oe. When H_f decreased close to -10Oe, the nanoparticles' fringe field became saturated and ΔR_i reached its maximum. Keeping on decreasing H_f, the sensor kept saturated and ΔR_i became smaller and smaller until it became close to zero
- In this test, the fringe field of nanoparticles made the sensor's resistance became larger when a positive H_f was applied, vice versa. The results just seemed to be opposite to other groups' research[8]. The effect of the nanoparticles beside the strips to the sensor was just opposite to those above them[7], and even much stronger. Our sensors were constructed by ten spin valves connected in parallel and the distance between every two stripes equaled to the strips width (Figure 2), so it could be suggested that the quantity of nanoparticles deposited upon the strips was the same as the ones beside them among the sensor area, the effect of nanoparticles to the sensor was the combined action of the above ones and beside ones, so the resulting effect was just opposite to that of nanoparticles on the sensor's surface.

C. *Detecting accuracy*

Finally, the detection accuracy of the biosensor was measured with the test system, as illustrated in figure 5. The wheatstone bridge was consisted of a sensor and a reference inside the biosensor, together with two separate resistors R_1 and R_2 outside the biosensor. The output of the bridge gone through an amplifier and a low-pass filter before it was measured in the multimeter. The biosensor in the test system included four GMR sensors, which could be enabled through the switch related to them, and only one reference was used.

The 1μl solution of nanoparticles with a concentration of 0.25mg/ml was dropped onto the sensor before test, the peak in the curve represented the moment when the solution was being dropped on the sensor's surface, since the pinpoint of the micropipette had a non-zero magnetic field and it was sure that the field made some change to the sensors' and references' resistance when approaching the sensor's surface, however their resistance nearly recovered to the original value when the micropipette was taken away from the biosensor's surface because of the very low covercivity of the spin valve stripes. When there was no excitation field applied, the output resistance of the test system nearly kept invariant (Figure 6(a)) so it indicated that the change of the resistance of sensor was so little that it submerged into the noise. In Figure 6(b), the output of the system kept invariant at the beginning of dropping the solution, however, the output became smaller and smaller because the nanoparticles in the solution became closer and closer to the surface of the sensor as the solvent evaporated slowly. When the solvent evaporated thoroughly, the nanoparticles became closest to the sensor surface and made a big change to the sensor's resistance, however, the reference's resistance had no change because of the thick SU-8 passivation layer. The test result was the output decreased 0.32Ω which was larger than the change when there was no excitation applied. The results kept consistent with the above real-time test results of the sensor's resistance.

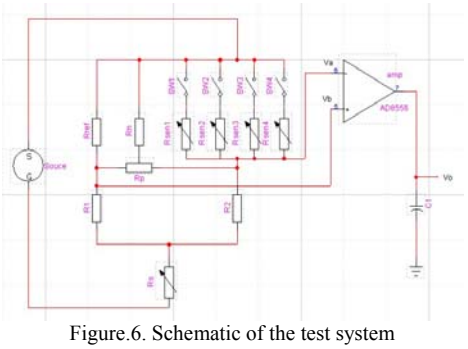

Figure.6. Schematic of the test system

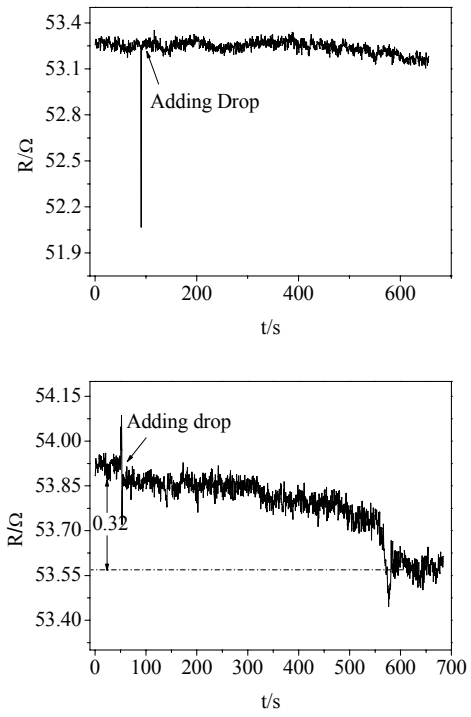

Figure.6. the real-time transform curve of the output of test system (a)the magnetic excitation field equaled zero;(b)the magnetic excitation field equaled -9Oe

IV. CONCLUSIONS

A series of highly sensitive spin valve sensors was fabricated. When dropping the solution of nanoparticles on the sensor's surface, it had a non-zero change even when the magnetic excitation field equaled zero, so the sensor could be applied in the cases of no excitation field, which may be preferred in portable applications. On the other hand, the change of the sensor's resistance reached the maximum when H_f equals to a particular negative value, so we could get a higher detecting accuracy, however, at the expense of the portability.

ACKNOWLEDGMENT

This research was supported by China's national 863 Program under grant 2006AA03Z317. Fulong Zhao would like to thank for the financial support during his master degree.

REFERENCES

[1] R.L. Edelstein, C.R. Tamanaha, P.E. Sheehan, M.M. Miller, D.R. Baselt, L.J. Whitman, R.J. Colton. The BARC biosensor applied to the detection of biological warfare agents. Biosensors & Bioelectronics ,2000, 14: 805－813.

[2] H. A. Ferreira , D. L. Graham , P. P. Freitas , J. M. S. Cabral.Biodetection using magnetically labeled biomolecules and arrays of spin valve sensors (invited). J. Appl. Phys., 2003, 93(10):7281－7286.

[3] Guanxiong Li, Vikram Joshi, Robert L. White, Shan X. Wang, Jennifer T. Kemp, Chris Webb, Ronald W. Davis, Shouheng Sun. Detection of single micron-sized magnetic bead and magnetic nanoparticles using spin valve sensors for biological applications. J.Appl.Phys., 2003, 93(10):7557－7559.

[4] C.R.Tamanaha, S.P.Mulvaney, J.C.Rife, L.J.Whitman. Magnetic labeling,detection, and system integration. Biosensors and Bioelectronics, 2008, 24:1－13.

[5] Guanxiong Li, Shouheng Sun, Robert J. Wilson, Robert L. White, Nader Pourmand, Shan X. Wang. Spin valve sensors for ultrasensitive detection of superparamagnetic nanoparticles for biological applications. Sensors and Actuators A , 2006, 126: 98-106.

[6] J.C.Rife, M.M.Miler, P.E.Sheehan, C.R.Tamanaha, M.Tondra, L.J.Whitman. Design and performance of GMR sensors for the detection of magnetic microbeads in biosensors. Sensors and Actuators A, 2003, 107:209-218.

[7] Shan X.Wang, Guangxiong Li. Advances in gaint magnetoresistance biosensors with magnetic nanoparticle tags: review and outlook. IEEE Transactions On Magnetics, 2008, 44(7):1687-1702.

[8] H.A.Ferreira, N.Feliciano and D.L.Graham, P.P.freitas. Effect of spin-valve sensor magnetostatic fields on nanobead detection for biochip applications,2005,97,10Q904.

Development of a Fiber Optic Biosensor with Core-Shell Nanoparticles

Yu-Zheng Su[1,*], Huihua Kenny Chiang[2], Min-Wei Hung[1], Wen-Hong Wu[1], and Kuo-Cheng Huang[1]

[1] *Instrument Technology Research Center, National Applied Research Laboratories, Hsinchu, Taiwan*
[2] *Institute of Biophotonic Engineering, National Yang-Ming University, Taipei, Taiwan*

***Abstract* — We report the development of core-shell nanoparticles with the silver core and SiO_2 shell for potential applications in fiber optic biosensor. The fluorescence intensity of the fluorescence probe (Fluorescein isothiocyanate, FITC) doped core-shell nanoparticles was approximately 50-fold higher than that without core-shell nanoparticles doping. In addition, four different kinds of organic solvents are used in this study and found to have influence on the fluorescence intensity from 1.3 to over 100 times. We conclude that core-shell nanoparticles have capability to enhance the fiber optic sensing through amplifying fluorescence intensity and expect that their potential applications are used in a variety of biological applications.**

Keywords — ***Biosensor, Metal-enhanced fluorescence, Nanoparticles, Fluorescence***

I. Introduction

Fiber-optic biosensors will play a significant role in the development of biosensors because they can be easily miniaturized and integrated for the determination of different target compounds in a wide variety of application fields, such as industrial process and environmental monitoring, food processing, and clinical applications [1].

For use in optical sensor, the end result must be a change in an optical property induced by interaction of the recognition element with the target. These changes may be due to the formation of a fluorescent, luminescent product, quench fluorescence, modification of refractive index or absorption spectrum [2]. Fluorescence sensing has become one of the dominant sensing technologies in medical diagnostics and biotechnology. The detection of a fluorophore is usually limited by its quantum yield, auto-fluorescence of the samples and the photo-stability of the fluorophores. Recently, there have been explosive developments in the Metal-Enhanced Fluorescence (MEF) technology to favorably modify the spectral properties and to alleviate photo-physical constraints [3].

The use of fluorophore–metal interactions has been termed radiative decay engineering, metal-enhanced fluorescence or surface-enhanced fluorescence. The presence of nearby metallic nanostructures can alter the free-space condition and can result in dramatic spectral spectral changes. Remarkably, metal surfaces can increase or decrease the radiative decay rates of fluorophores and can increase the extent of resonance energy transfer.

Following excitation a fluorophore in free space can either emit a photon with a radiative deactivation rate (Γ) or return to the ground state by a non-radiative rate (k_{nr}). For simplicity we are omitting the transitions to the triplet state and chemical processes leading to photodegradation. The quantum yield (Q_0) and lifetime (τ_0) of the fluorophore in the free-space condition are given by:

$$Q_0 = \Gamma/(\Gamma + k_{nr}) \qquad \tau_0 = 1/(\Gamma + k_{nr}) \tag{1}$$

The presence of a nearby metal surface increases the radiative rate by addition of a new rate Γ_m. In this case, the quantum yield (Q_m) and lifetime of the fluorophore (τ_m) near the metal surface are given by:

$$Q_m = (\Gamma + \Gamma_m)/(\Gamma + \Gamma_m + k_{nr}) \qquad \tau_m = 1/(\Gamma + \Gamma_m + k_{nr}) \tag{2}$$

These equations result in unusual predictions for a fluorophore near to a metallic surface. From Equations, we can see that as the value of Γ_m increases, the quantum yield Q_m increases, while the lifetime, τ_m, decreases, Fig. 1 [4].

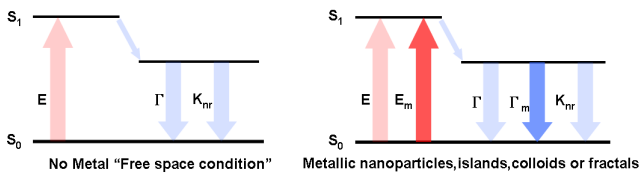

Figure 1. Fluorophore – metal interactions.

Metal nanoparticles, such as Au and Ag, are known to dramatically change the optical properties of nearby fluorophores. The fluorescence of fluorophores might be enhanced or quenched due to the presence of nearby metallic nanoparticles. The strength of the enhancement or quenching is influenced by many factors, such as size and shape of the metal nanoparticles, the orientation of the fluorophore dipole moments, the distance between a fluorophore and a nanoparticle, the organic solvents and quantum yield of the fluorophore [5]–[7].

Most studies on fluorescence enhancement are based on silver island films, which consist of silver nanoparticles with sub-nanometer sizes on the TIR (total internal reflection) measurement platform. Fluorescence enhancement of tens of folds was obtained using this method. However, metallic nanoparticles in colloid usually failed to yield fluorescence enhancement. This might be due to the relatively short

*Contact author: Yu-Zheng Su is with the Instrument Technology Research Center, National Applied Research Laboratories, Hsinchu, Taiwan (phone: 886-03-5779911; fax: 886-03-5773947; e-mail: yuzheng@itrc.org.tw).

fluorophore–metal distances or flexible spacers employed in these conditions [8], [9]. These results indicate that fluorophore–metal distance optimization is critical for fluorescence enhancement. If a nanoparticle is placed too close to a fluorophore, the nanoparticle extracts all electrons in the excited state from the fluorophore; if it is too far from a fluorophore, its strong surface plasmon polariton field (SPPF) may not reach the fluorophore and there will be no effect on the resulting fluorescence intensity; when placed at an appropriate distance from a fluorophore, can effectively enhance the fluorescence by transferring the free electrons of the fluorophore [5].

Evanescent wave fluorescent sensors have developed for 30 years. Nonetheless, the technology continues to evolve with new breakthroughs in optics, biochemistry, and chemical engineering. Therefore, our study focus in sensitivity, we develop evanescent wave fluorescence biosensor with core-shell nanoparticles.

II. METHODOLOGY

A. Measurement System

The measurement system has three major components: (1) the optics, including the waveguide (optical fiber, JTFLH6006301040, Polymicro Technologies), the light source (488 nm solid-state laser 10mw, Melles Griot), filter (530nm long-pass filter, CVI), objective lens (N.A. 0.4, Kyowa) and the spectrometer (SP-150, Princeton Instrument); (2) the fluidics for delivering sample and setting fiber optic probe; and (3) computer processor for analyzing the signal.

The optical setup for the measurement system involves the use of a 488 nm solid-state Laser. In order to achieve the best coupling efficiency of the laser beam to the optical fiber, an objective lens of NA＝0.4 was used. In addition, a multimode optical fiber was chosen in order to generate the evanescent wave on the fiber surface. Then, in order to separate the laser beam from the fluorescence signal, a long-pass filter was attached in front of the spectrometer in order to obtain a high SNR for the fluorescence signal. The set-up schematic diagram is shown in Fig. 2.

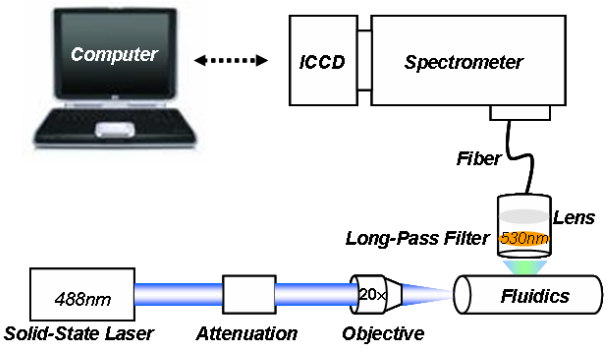

Figure 2. Measurement system.

After finishing the preparation of the silver core-silica shells, fluorophores (FITC, Sigma-Aldrich) were simply mixed with core-shell nanaparticles. In order to show the benefits of using core-shell nanaparticles, we prepared another controlled sample (pure FITC solution without sliver silica core shell) in the same fluorophore concentration (1μg/mL). The schematic diagrams are shown in Fig. 3.

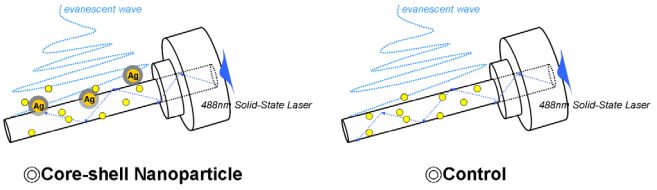

Figure 3. Fiber optic probe for compare.

B. Preparation of fiber optic probe

About 2.5 cm of the center part of a 600μm multimode fiber (JTFLH6006301040, Polymicro Technologies) was burned away the outside polymer jacket and cladding. The bare optical fiber probe was cleaned by the piranha solution (mixture solution of H_2SO_4 and H_2O_2, volume ratio 7:3) for 1 h. The cleaned fiber probe was rinsed with DI water before using.

C. Core-Shell Nanoparticles

The preparation of fluorescent core-shell nanoparticles was undertaken in three steps, shown in Fig. 4: (1) first, silver colloids are obtained from the reduction of silver nitrate by sodium citrate, (2) then a silica shell of various thickness was grown around the colloids by delicate controlling the concentration of TEOS (Tetraethyl orthosilicate), and (3) Each batch suspension of core-shell nanoparticles was washed and centrifuged, followed by re-suspension in water [6], [7].

Figure 4. Core-shell nanoparticles.

1) Preparation of silver colloids: Silver colloids were prepared by adding dropwise 2 mL of 38.8 mM sodium citrate (Sigma-Aldrich) aqueous solution to 98 mL of boiling aqueous solution containing 18 mg of silver nitrate (Sigma-Aldrich), under vigorous stirring. After boiling for 10 minutes the solution was cooled to room temperature. The as-prepared silver colloid solution was centrifuged at 500 rpm for 1 hour to remove larger colloids.

2) Preparation of core-shell nanoparticles: Under vigorous stirring, 0.4 mL of silver colloid solution was mixed with 100 mL of iso-propanol (Sigma-Aldrich) and 10 mL of deionized water. Immediately after the addition of 2 mL of 30% ammonium hydroxide (Fluka), different amounts of Tetraethyl orthosilicate (TEOS, Sigma-Aldrich) were added to the reaction mixture. To obtain different silica layer thicknesses, 40 μl of the same amount of TEOS solution with a

concentration between 50% and 100%, was added to the suspension. The reaction was stirred at room temperature for 30 minutes.

3) Purification of core-shell nanoparticles: Each suspension of core-shell nanoparticles was washed and centrifuged (at 3500 rpm for 30 min) three times with a water ethanol mixture (5:4) for 30 min, followed by resuspension in water. In addition, not only water but also four solvents were compared for solvent effect experiments.

III. Results and Discussion

A. Core-Shell Nanoparticles

Metallic nanoparticles, e.g. Au or Ag, have been previously studied for coupling the electrons involved in the self quenching to their strong surface plasmon polariton fields (SPPF), upon photoexcitation. For this electron transfer, it is very important that the fluorophore is placed at a particular distance from a nanoparticle. (Fig. 5) In this study, we employ the core-shell nanoparticles to control this condition.

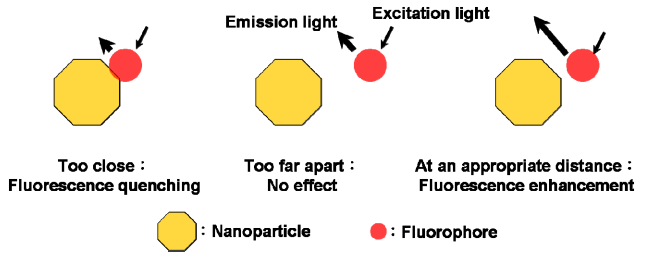

Figure 5. The effect of distance between a nanoparticle and a fluorophore.

Transmission Electron Microscope analysis shown in Fig 6 of the core shell nanoparticles has shown that the silver core was about 50 ±10 nm diameter, while the thickness of the shell could vary from 15 to 27 nm dependent on the controlled procedures. Figure 7 shows the absorption spectra of nanoparticles. The absorption of pure silver is located in first figure and that of the core shell structure is located in second.

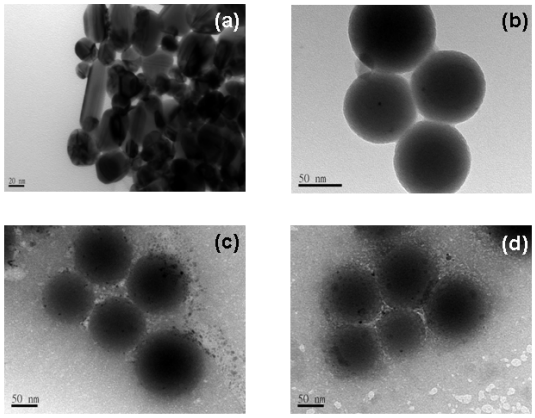

Figure 6. TEM images of (a)Ag nanoparticles, (b)、(c)、(d) show the samples with different tickness of the SiO_2 coating at 15, 25, and 27nm, respectively. The diameter of the Ag is 50 nm ± 10 nm for all the samples.

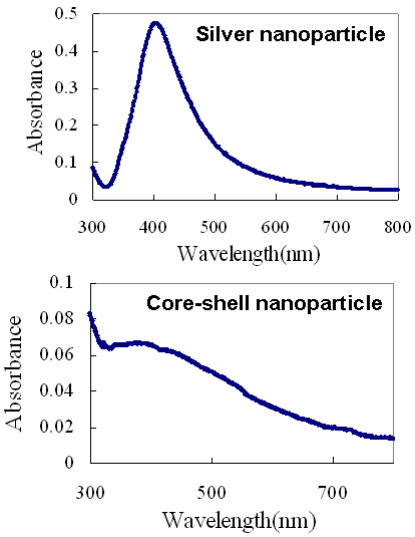

Figure 7. Absorption spectra of nanoparticles.

B. Fluorescence Enhancement – Distance Effect

The fluorescent emission intensity of the FITC-doped core-shell nanoparticles was approximately 50-fold higher than that of the solution without core-shell nanoparticles, shown in Fig. 8. In this sensing platform, the core-shell nanoparticles allows for the distance dependent MEF phenomenon, which we have determined the optimum shell thicknesses are about 25 nm.

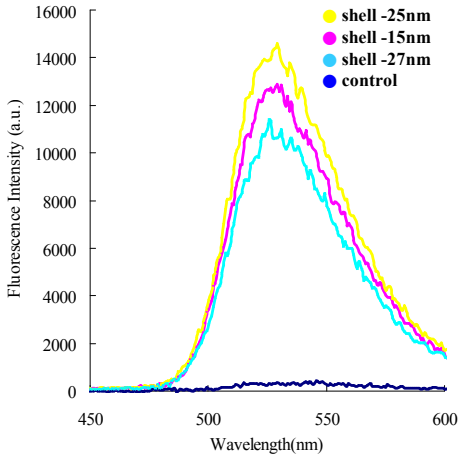

Figure 8. Fluorescence emission spectrum of FITC-doped core-shell nanoparticles and form the corresponding sample.

The relation between the fluorescence signals and the different FITC concentrations measured in the same nanoparticles shell diameter is shown in Fig. 9. The fluorescence intensity increases with increasing FITC-doped concentration. The increasing gradient also increases with FITC-doped concentration.

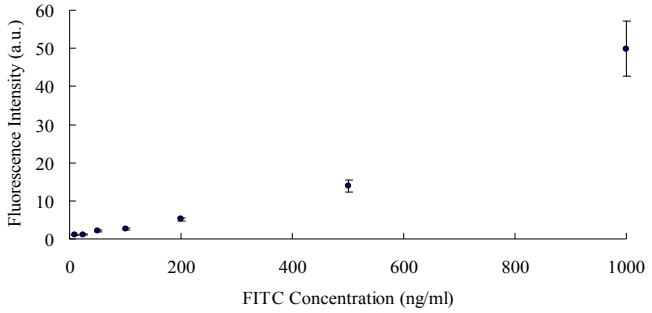

Figure 9. Fluorescence signal of FITC at different concentrations (shell-25nm).

C. *Fluorescence Enhancement – Solvent Effect*

Various physical/chemical properties of organic solvents, such as viscosity, polarity, etc., may also affect the fluorescence intensity [5]. Four solvents which are considered not too harsh to bio-molecules are used in this study. They are methanol (Fluka), ethanol (Shimakyu), 0.01M PBS (phosphate buffered saline, Sigma-Aldrich) and 0.05% tween 20 (Sigma-Aldrich). Figure 10 summarizes the experimental results measured from these four prepared solution to distinguish the solvent effect. We found that 1.3 times, 1.5 times, 13 times and over 100 times fluorescent intensity enhancements in respective organic solvents compared to that of the controlled sample. The 0.05% tween 20 is found to have the most significant effect among all.

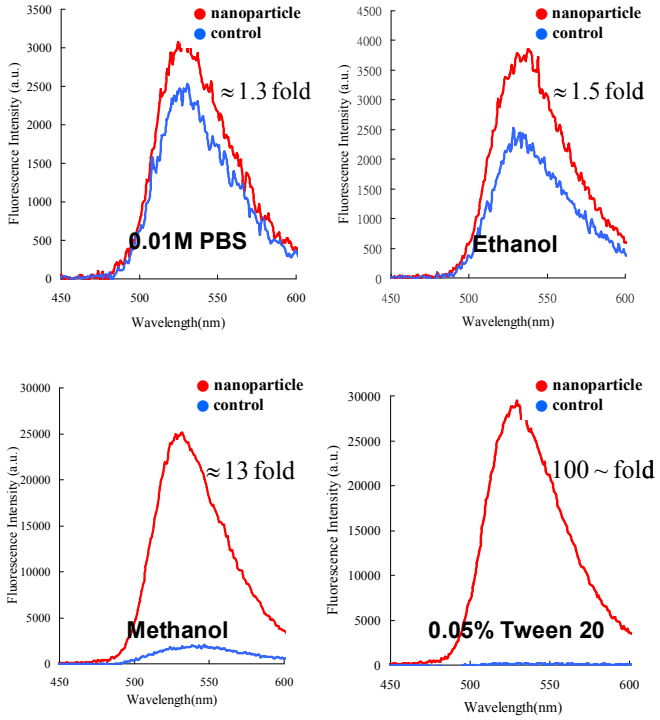

Figure 10. Fluorescence ehancement by various solvents.

Organic solvents affect the fluorescence intensity in biosensing, possibly by the shifting excitation/emission spectrums of the fluorophore, by the isomerization of the fluorophore, by shrinking fluorophore tagged proteins.

IV. CONCLUSIONS

Biosensors play a significant role in variety of application fields, e.g. medical, pharmaceutical, environmental, defense, bioprocessing, or food technology. Nonetheless, the technology continues to evolve with new breakthroughs in optics, biochemistry, and chemical engineering.

We report the development of core-shell nanoparticles with the silver core and SiO_2 shell for potential applications in fiber optic biosensor. The core-shell nanoparticles was able to increase the signal of sensing as much as 50 times. In addition, four different kinds of organic solvents can also affect the fluorescence intensity from 1.3 to over 100 times.

There has been an explosion in the use of core-shell nanoparticles to favorably modify the spectral properties of fluorophores and to alleviate some of these fluorophore photo-physical constraints. There is an optimal fluorescent molecule to metal distance for fluorescence enhancement provided by silica layers of core-shell nanoparticles. In addition, these layers also offer the versatility need for the conjugation of biomolecules and protect the silver core from ions present in biological media. We conclude that core-shell nanoparticles have capability to enhance the fiber optic sensing through amplifying fluorescence intensity and expect that their potential applications are used in a variety of biological applications.

REFERENCES

[1] M. E. Bosch, A. J. Sánchez, F. S. Rojas, and C. B. Ojeda, "Recent Development in Optical Fiber Biosensors," Sensors, vol. 7, no. 6, pp. 797–859, June 2007.

[2] C. R. Taitt, G. P. Anderson, F. S. Ligler, "Evanescent wave fluorescence biosensors," Biosensors and Bioelectronics, vol. 20, no. 12, pp. 2470–2487, June 2005.

[3] K. Aslan, I. Gryczynski, J. Malicka, E. Matveeva, J. R. Lakowicz and C. D. Geddes, "Metal-enhanced fluorescence: an emerging tool in biotechnology" Current Opinion in Biotechnology, vol. 16, no. 1, pp. 55–62, Jan. 2005.

[4] K. Aslan, J. R. Lakowicz, H. Szmacinski, and C. D. Geddes, "Metal-Enhanced Fluorescence Solution-Based Sensing Platform," Journal of Fluorescence, vol. 14, no. 6, pp. 677–679, Nov. 2004.

[5] B. Hong and K. A. Kang, "Biocompatible, nanogold-particle fluorescence enhancer for fluorophore mediated, optical immunosensor," Biosensors and Bioelectronics, vol. 21, no. 7, pp. 1333–1338, Jan. 2006.

[6] K. Aslan, M. Wu, J. R. Lakowicz and C. D. Geddes, "Metal Enhanced Fluorescence Solution-based Sensing Platform 2: Fluorescent Core-Shell Ag@SiO2 Nanoballs," Journal of Fluorescence, vol. 17, no. 2, pp.127–131, Mar. 2007.

[7] D. Cheng and Q. H. Xu, "Separation distance dependent fluorescence enhancement of fluorescein isothiocyanate by silver nanoparticles," Chem. Commun., no. 3, pp. 248–250 , Jan. 2007.

[8] E. Matveeva, Z. Gryczynski, J. Malicka, I. Gryczynski, and J. R. Lakowicz, "Metal-enhanced fluorescence immunoassays using total internal reflection and silver island-coated surfaces," Analytical Biochemistry, vol. 334, no. 2, pp.303–311, Nov. 2004.

[9] K. Aslana, P. Holleya and C. D. Geddes, "Microwave-Accelerated Metal-Enhanced Fluorescence (MAMEF) with silver colloids in 96-well plates: Application to ultra fast and sensitive immunoassays, High Throughput Screening and drug discovery," Journal of Immunological Methods, vol. 312, no. 1-2, pp. 137–147, May 2006.

P19

Novel Colored Pulse Laser Photography for High Speed Imaging

Chien-Sheng Liu[1,*], Cheng-Hsien Lin[2], Chia-Hsu Chen[1], Po-Heng Lin[1], Chung-I Huang[2], Cheung-Wen Chang[2], Chih-Hsun Lin[2], and Yung-Nien Sun[2,#]

[1]*Laser Application Technology Center, Industrial Technology Research Institute, Tainan 734, Taiwan*
[2]*Department of Computer Science and Information Engineering, National Cheng Kung University, Tainan 70101, Taiwan*

***Abstract* — In order to improve the imaging quality of conventional laser photography, this study proposes a new system for colored pulse laser photography to obtain high speed color microscopic imaging. Based on the RGB synthesis technique, three channels of red, green, and blue images are acquired from three cameras with three independent laser light sources. Then, a high quality color image can be obtained by assembling the monochromatic images with the image realignment and color calibration processes. The experimental results show that the proposed system can achieve a high quality colored pulse photography.**

Keywords — ***Biomedical imaging, image processing, image registration, laser measurement applications.***

I. INTRODUCTION

In high speed photography, a pulse laser is useful for providing high imaging quality [1], [2]. The short duration of the laser pulses can be used to illuminate and so "freeze" the motion of fast-moving objects in the camera image. The laser pulse duration required to freeze motion depends on the size of the object in question, and its velocity. If we assume a characteristic linear dimension, *d*, and a speed, *v*, then the laser pulse should have a duration, *t*, short enough for the object to move less than, 10% of its characteristic dimension during the pulse. The choice of 10% is arbitrary, but is sufficient blurring to degrade even qualitative measurements. In other words, we require that

$$t \le \frac{d}{10v}. \qquad (1)$$

Therefore, the laser photography which utilizes the short pulse to freeze the motion can obtain blur-free visualization of fast-moving objects [3].

However, to the best of our knowledge, due to adopt single frequency laser, images captured from the laser photography are monochrome images, which limit their color depth [4]–[10]. Accordingly, this study will develop a colored pulse laser photography to obtain color images.

II. IMAGE ACQUISITION

The structure of the proposed colored pulse laser photography is shown in Fig. 1. The colored laser photography comprises a laser control system, a novel splitting and combining system, and an image synthesis system. The laser control system mainly comprises a red (R), a green (G), and a blue (B) pulse lasers and a control electrical circuit.

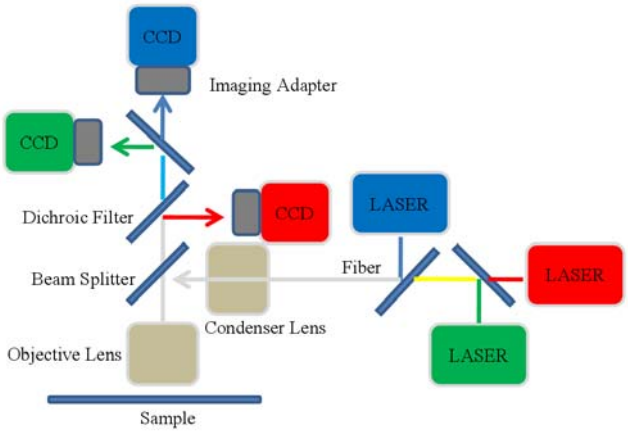

Figure 1. Structure of proposed colored pulse lasers photography.

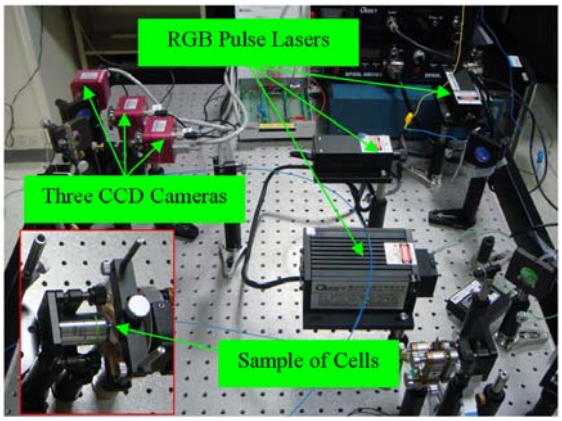

Figure 2. Photograph of experiment setup.

The novel splitting and combining system mainly comprises a light splitting part to split the RGB pulses and avoid laser interference and three CCD cameras to capture R, G, and B images, respectively. We use the three RGB pulse lasers to illuminate fast-moving objects and obtain three RGB monochromatic images from the novel splitting and combining system. Then the color images of fast-moving objects can be composed by using the image synthesis system.

This project was funded by the Ministry of Economic Affairs of Taiwan under 8301XS3E10.

Contact author: for laser aspects of this project please contact* ***chienshengliu@itri.org.tw.*

#Contact author: for image aspects of this project please contact ***ynsun@mail.ncku.edu.tw.***

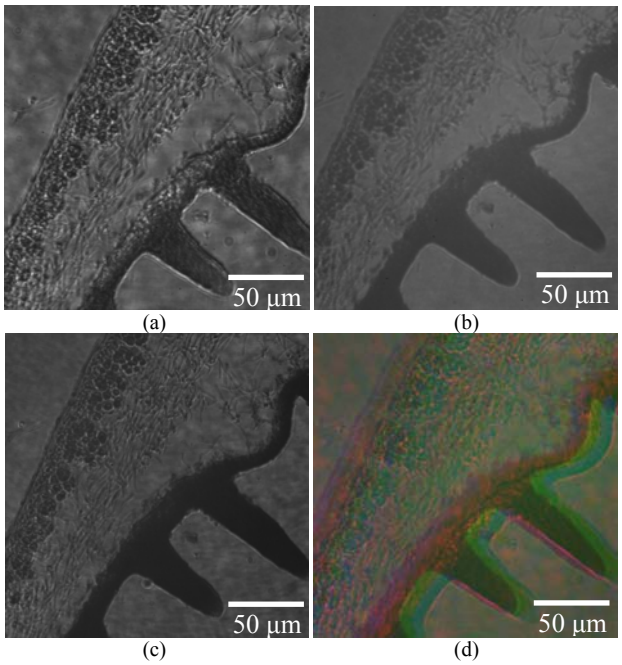

Figure 3. Images of cell with the pulse laser illumination: (a) R image, (b) G image ,and (c) B image. (d) Synthesis images from the R, G, and B images without using an image registration step.

Fig. 2 shows the photograph of the primary experiment setup. The duration of the laser pulses can be controlled to less than 10 μs and it is short enough to freeze the motion of fast-moving objects. The R, G, and B images captured from CCD cameras are shown in Figs. 3(a), 3(b), and 3(c), respectively.

III. Image Registration

As shown in Fig. 3(d), we observe that there is a misalignment problem among the RGB images during the synthesis process, Therefore, an RGB image registration is needed before assembling the three RGB monochromatic images in order to obtain a synthesis image with best imaging quality. In our applications, we adopt the mutual information (MI) as the registration criterion [11], [12]. By optimizing the translation, rotation and scaling parameters, the R and B images can be registered to the G image. Thus the monochromatic images acquired from the three independent cameras can be accurately registered for later assembling.

MI is a popular measure used in image registration in recent years. One intuitive advantage of this method is that it requires no prior model of the relationship between the images. Such a technique obtains the registration by maximizing the mutual information of the two images.

MI is based on the information theory [13]. Define two random variables, A and B, with marginal probability distribution, $p_A(a)$ and $p_B(b)$, and joint probability distribution, $p_{A,B}(a, b)$. MI, I(A, B), measures the degree of dependence of A and B by measuring the distance between the joint distribution $p_{A,B}(a, b)$ and the distribution associated with the case of complete independence $p_A(a) \cdot p_B(b)$, by means of the relative entropy or the Kullback-Leibler measure [14], i.e.,

$$I(A,B) = \sum_{a,b} p_{A,B}(a,b) \log \frac{p_{A,B}(a,b)}{p_A(a) \cdot p_B(b)} . \quad (2)$$

MI is related to the entropy by the equations

$$\begin{aligned} I(A,B) &= H(A) + H(B) - H(A,B) \\ &= H(A) - H(A \mid B) \\ &= H(B) - H(B \mid A) \end{aligned} , \quad (3)$$

with $H(A)$ and $H(B)$ being the entropy of A and B, respectively, $H(A, B)$ their joint entropy, and $H(A|B)$ and $H(B|A)$ the conditional entropy of A given B and of B given A, respectively. Their definitions are

$$H(A) = -\sum_{a} p_A(a) \log p_A(a) , \quad (4)$$

$$H(A,B) = -\sum_{a,b} p_{A,B}(a,b) \log p_{A,B}(a,b) , \quad (5)$$

$$H(A \mid B) = -\sum_{a,b} p_{A,B}(a,b) \log p_{A|B}(a \mid b) . \quad (6)$$

The entropy is a measure of the uncertainty of the random variable; it is a measure of the amount of information required to describe the random variable.

The 2D joint histogram, which is also known as feature space and intensity mapping plot (IMP) [15], was first introduced by Hill et al. [16] in 1993. Each point in one image will have a corresponding point in the other image and these two points each have an intensity value associated with them. Therefore, we can construct a scatter plot of these image intensity pairs point by point. The resulting plot is a type of two-dimensional (2D) histogram, which contains the number of a gray level value from one image against a specific gray level value in the other.

The underlying concept of MI is entropy, and the type of joint histogram has a decisive effect on these entropy values. In general, if a probability p is divided into a number of probabilities p_i's, the entropy of p will be smaller than the sum of the entropies of p_i's. The joint entropy $H(A, B)$ measures the dispersion of the joint probability distribution $p_{A,B}(a, b)$, which should have fewer and sharper peaks when the images are matched than for any case of misalignment. At misregistration, non-corresponding combinations of a and b will be aligned, causing dispersion in the distribution and hence a higher entropy value.

The joint histogram of an image pair can be defined as a function of two variables, A, the gray-level intensity in one image, and B, the gray-level intensity in the other. Each value h at the entry (A, B) is the number of corresponding pairs having gray-level A in the first image and gray-level B in the second. Estimation for the joint probability distribution $p_{A,B}(a, b)$ is

obtained by normalizing the joint histogram of the image pair as

$$p_{A,B}(a,b) = \frac{h(a,b)}{\sum_{a,b} h(a,b)}, \quad (7)$$

Thus the two marginal probability distributions can also be obtained directly from the joint probability distribution as

$$p_A(a) = \sum_b p_{A,B}(a,b), \quad (8)$$

$$p_B(b) = \sum_a p_{A,B}(a,b). \quad (9)$$

The MI registration criterion I(α) is then evaluated from (10) with transformation parameter α, and the optimal registration parameter α^* is found when I(α) is maximal as

$$\alpha^* = \arg\max_{\alpha} I(\alpha). \quad (10)$$

IV. Color Calibration

After registering the monochromatic images, a color calibration method is adopted to construct a more realistic color image. For this purpose, color images acquired from a color CCD with white LED light source (i.e., near the CIE standard D65) is taken as the standard image (see Fig. 4). By comparing to the standard images, three independent cameras are adjusted for white balancing by using a gray test procedure. Then, a prime color calibration method is adopted to construct the color transformation matrix.

Figs. 5(a) and (b) show the six gray and six prime color patches we used for color calibration. In Figs. 5(a) and (b), the first column shows the standard images acquired from a color CCD with white LED light source; columns two to four are the acquired monochromatic B, R, and G images; column five shows the corresponding synthetic images. The images acquired from the color CCD are taken as the standard references, and the goal is to reconstruct a color transformation such that the colors in the synthetic image from the three monochromatic sources can be close to the corresponding one of the standard color image.

A. Gray Test Procedure

For correcting the white balance of each monochromatic camera, a sRGB gamut correction model is adopted [19]:

$$F_r(mR) = 255 \times S_r \times \left(\left(\frac{mR - mR_0}{mR_{\max} - mR_0} \right)^{gamma\_r} + O_r \right), \quad (11)$$

where *mR* is the pixel value of the monochromatic R images and F_r is the corresponding calibration function. The maximum values of *mR* are calibrated according to the standard white patches that their values are ideally one which corresponds to (255, 255, 255) in pixel value. Note that only the red channel will be formulated as the example in the following descriptions, the functions of green and blue channels are defined in the same way.

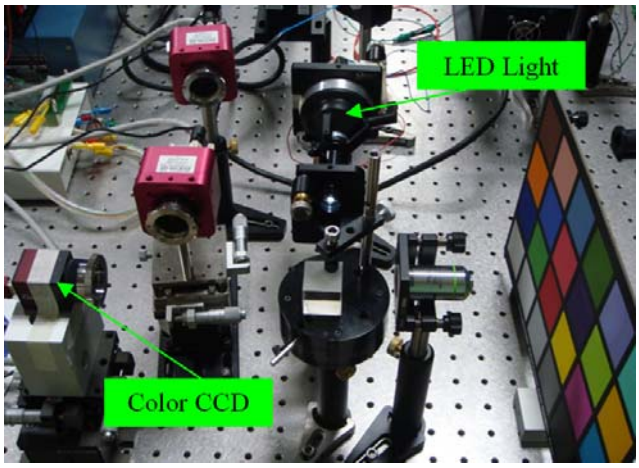

Figure 4. Experiment setup of color calibration.

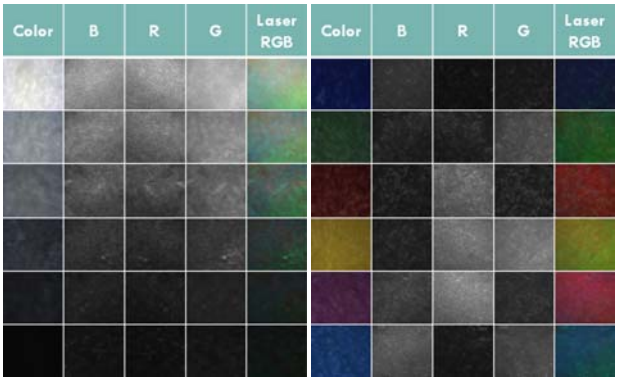

(a) (b)

Figure 5. (a) Six gray patches for gray test procedure. (b) Six color patches for prime color calibration.

As shown in Fig. 5(a), one white patch, one black patch, and four gray patches are used in the white balancing process. To estimate the calibration parameters (S_r, S_g, S_b, O_r, O_g, O_b, *gamma_r*, *gamma_g*, and *gamme_b*), three steps are used and calculated iteratively. In step 1, a dark patch test is adopted and Eq. (11) can be reformulated for estimating O_r, O_g, and O_b:

$$O_r = \frac{F_r(mR)}{255 \times S_r} - \left(\frac{mR - mR_0}{mR_{\max} - mR_0} \right)^{gamma\_r}. \quad (12)$$

In step 2, a white patch test is adopted for white balancing and Eq. (11) can be reformulated for estimating S_r, S_g, and S_b:

$$S_r = \frac{F_r(mR)}{255 \times \left(\left(\frac{mR - mR_0}{mR_{\max} - mR_0} \right)^{gamma\_r} + O_r \right)}. \quad (13)$$

In step 3, the four gray patches are used for estimating *gamma_r*, *gamma_g*, and *gamme_b*:

$$gamma\_r = \frac{1}{n} \sum_{i=1}^{n} \frac{\log\left(\frac{1}{255 \times S_r} \left(F_r(mR_i) - O_r \right) \right)}{\log\left(\frac{mR_i - mR_0}{mR_{\max} - mR_0} \right)}. \quad (14)$$

To obtain an optimal transformation, the three steps are iteratively calculated for estimating the optimal solution of parameters.

B. Prime Color Calibration

As shown in Fig. 5(b), six colors (blue, green, red, yellow, magenta, and cyan) are used as prime color for reconstructing the color transformation [20]. To reconstruct the color transformation, the color needs to be firstly mapped to a device independent color space. In this study, the CIE XYZ color space is adopted, and this color transformation is defined as $\mathbf{T_{RGB \rightarrow XYZ}}$. Thus the acquired RGB values after white balancing are firstly transformed into CIE XYZ values:

$$mC_i = \begin{bmatrix} mX_i \\ mY_i \\ mZ_i \end{bmatrix} = \mathrm{T}_{RGB \rightarrow XYZ} \times \begin{bmatrix} Fr(mR_i) \\ Fg(mG_i) \\ Fb(mB_i) \end{bmatrix}, \quad i = 1,\ldots,m, \quad (15)$$

where m is the number of prime colors.

To map the color appearance of the acquired monochromatic RGB image into the standard color image, the color transformation M can be formulated as:

$$C = M \times mC, \quad (16)$$

where C is the standard color, and the size of C and mC are both m×3. The color transformation M is with size 3×3, and can be calculated as

$$M = C \times mC^t \times (mC \times mC^t)^{-1}. \quad (17)$$

V. Experiment Results

Fig. 6(a) shows the synthesis image from the R, G, and B images of Fig. 3. Comparing to Fig. 3(d), it was observed that the monochromatic images can be realigned very well. By using the color calibration method, the synthetic image is then transformed to construct a more realistic color image, as shown in Fig. 6(b). According to the experimental results, the color appearance of the reconstructed color image is similar to the reference color image.

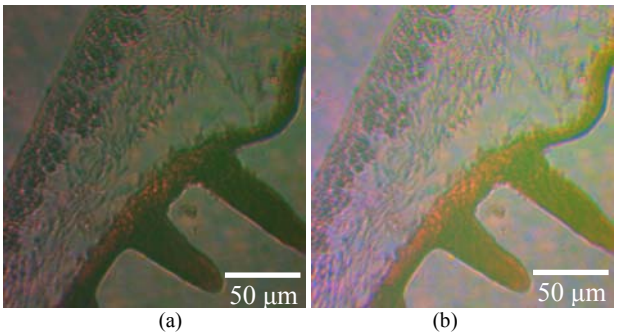

(a) (b)

Figure 6. (a) Synthesis images from the R, G, and B images of Fig. 3 by using the proposed image registration step. (b) Synthesis image after color calibration.

VI. Conclusion

In this research, a novel colored pulse lasers photography is designed for high speed imaging. Before assembling the RGB images, a MI-based image registration is adopted for the realignment of three monochromatic images. Then, a color calibration method is used to construct the more realistic colors for the acquired scene. The experiments show that the proposed laser photography can obtain high speed color microscopic imaging while the conventional laser photography can provide only high speed monochrome imaging.

We anticipate that the color depth of the high speed 2D/3D images can be improved by the proposed colored pulse laser photography and high speed imaging has further applications in biomedical research, such as high speed retinal imaging, etc., in the future.

References

[1] http://www.oxfordlasers.com/en

[2] I. Duwel, M. C. Drake, and T. D. Fansler, "High-speed, High-resolution Laser Imaging of Multihole Fuel Sprays in a Firing Spray-guided Direct-injection Gasoline Engine," ILASS-Europe 19th Annual Conference, 2004.

[3] A. Whybrew, "High Speed Imaging," Oxford Lasers T.M., 2001.

[4] T. Erdogan, "New Optical Filters Improve High-speed Multicolor Fluorescence Imaging," Biophotonics International, March, 2006.

[5] J. S. Baskin and A. H. Zewail, "Freezing Atoms in Motion: Principles of Femtochemistry and Demonstration by Laser Stroboscopy," J. Chem. Educ., vol. 78, no. 6, pp. 737–751, 2001.

[6] H. R. Petty, "Applications of High Speed Microscopy in Biomedical Research," Optics & Photonics News, pp. 40–45, 2004.

[7] T. Hirata and Z. Miyazaki, "High-speed Camera Imaging for Laser Ablation Process: for Further Reliable Elemental Analysis Using

Inductively Coupled Plasma-mass Spectrometry," J. Chem. Educ., vol. 79, no. 1, pp. 147–152, 2007.

[8] P. Immonen and A. Mäkynen, "Diode Laser Stroboscopy in High Speed Imaging," International Workshop on Imaging Systems and Techniques, pp. 190–192, 2006.

[9] V. Garbin, D. Cojoc, E. Ferrari, and E. D. Fabrizio, "Changes in Microbubble Dynamics Near a Boundary Revealed by Combined Optical Micromanipulation and High-speed Imaging," Appl. Phys. Lett., vol. 90, pp. 114103-1–114103-3, 2007.

[10] S. T. Thoroddsen, T. G. Etoh, and K. Takehara, "High-speed Imaging of Drops and Bubbles," Annu. Rev. Fluid Mech., vol. 40, pp. 257–285, 2008.

[11] F. Maes, A. Collignon, D. Vandermeulen, G. Marchal, and P. Suetens, "Multimodality Image Registration by Maximization of Mutual Information," IEEE Trans. Med. Imag., vol. 16, no. 2, pp. 187–198, 1997.

[12] S. Klein, M. Staring, and J. P. W. Pluim, "Evaluation of Optimization Methods for Nonrigid Medical Image Registration Using Mutual Information and B-Splines," IEEE Trans. Image Process., vol. 16, no. 12, pp. 2879–2890, 2007.

[13] T. M. Cover and J. A. Thomas, Elements of Information Theory, John Wiley & Sons, New York, 1991

[14] I. Vajda, Theory of Statistical Inference and Information, Kluwer Academic, Dordrecht, The Netherlands, 1989.

[15] J. Tsao and P. Lauterbur, "Generalized clustering-based registration for multi-modality images", in Proc. of the 20th Annual International Conference of the IEEE Engineering in Medicine and Biology Society, vol. 20, no. 2, pp. 667–670, 1998.

[16] D. L. G. Hill, D. J. Hawkes, N. A. Harrison, and C. F. Ruff, "A strategy for automated multimodality image registration incorporating anatomical knowledge and imager characteristics," in Information Processing in Medical Imaging, H.H. Barrett and A.F. Gmitro, Eds., vol. 687 of Lecture Notes in Computer Science, pp. 182–196, 1993.

[17] R. P. Woods, J. C. Mazziotta, and S. R. Cherry, "Rapid automated algorithm for aligning and reslicing PET images", J. Comput. Assist. Tomogr., vol. 16, iss. 4, pp. 620–633, 1992.

[18] R. P. Woods, J. C. Mazziotta, and S. R. Cherry, "MRI-PET registration with automated algorithm", J. Comput. Assist. Tomogr., vol. 17, iss. 4, pp. 536–546, 1993.

[19] M. D. Fairchild, Color Appearance Models, Addison-Wesley, Reading, MA, 1998.

[20] M. J. Vrhel and H. J. Trussell, "Color Device Calbration: A Mathematical Formulation," IEEE Trans. Image Process., vol. 8, no. 12, pp. 1796–1806, 1999.

A technique to enhance electrochemical signals and shorten response time by manipulating yeast near the sensing electrode

Tsung-Che Chou[1], Ching-Yu Chang[2], Kuei-Yui Lai[2], Chi-Han Chiou[1],
Chun-Hsun Chu[1], Tomokazu Matsue[3], Hsien-Chang Chang [2*]
[1]*Industrial Technology Research Institute South, Microsystems Technology center, Tainan, Taiwan, ROC*
[2]*Institute of Biomedical Engineering, National Cheng Kung University, Tainan, Taiwan, ROC*
[3]*Graduate School of Environmental Studies, Tohoku University, Sendai, Japan*

Abstract - In this work, we manipulated recombinant yeast cells onto a sensing electrode by using hydraulic and electrophoretic force; and thus the current response of trace enzyme activity was increased in p-aminophenyl- β -D-galactopyranoside (PAPG) solution. The recombinant yeast which can generate β-galactosidase (β-Gal) in response to steroidal hormone 17□-estradiol were employed as the sensing element of the developed cell-based biosensor. Cells was trapped and stabilized within a microwell structure when they flowed through the sensing electrode. A vertical trapping force was generated by applying +2.0 V across the sensing electrode and an Indium Tin Oxide (ITO). The geometrical electrode area (100 × 30 μm2) was defined by a photoresister layer. Since the treated cells were collected on the electrode surface, PAP concentration can be significantly changed around the sensing electrode. Consequently, the detection limit was extend to 0.5 ppb, and the response time was shorten as fast as 15 min by using this device.

Keywords — ***biochip, cell-based biosensor, cell manipulation***

I. INTRODUCTION

The progress of microfabrication technology provides a lot of advantages for the development of biosensor application. Unlike conventional analytical instruments, the sophisticated device integrated microfluidic and sensing units on a chip, and thus the analyzing operation can be simplified for a lay user. On the other hand, trace analyte in biomedical or environment sample could be detected by using electrochemical biosensor. Recently, there are several techniques developed to extend the detection sensitivity as low as micro molar level. The sensitivity of electrochemical detection can be improved either by a functionalized electrode or a concentrated analyte around the electrode surface.

Integration of passive manipulating techniques for cells around electrode may enhance electrochemical signals for rapid and high sensitive biosensor [2-3].Arrangement grouped cells as a matrix order takes many attractive advantages for biology research [4-6]. The patterned cells may be simultaneously treated and analyzed. In this study, recombinant yeast cells were injected into the fluidic channel. When they flowed through the sensing-well (100 × 30 × 25 μm), the cells were trapped and collected into the sensing-well by an electrophoretic force. β-Gal excreted by yeast cells which may dehydrate PAPG substrate to PAP redox compounds. The PAP oxidation current can be detected by the sensing-well electrode.Electrochemical electrodes in the bottom of the sensing-well may detect the oxidation current of PAP [7]. Yeast cells around the sensing electrode may improve the concentration gradient of PAP redox compounds to enhance the sensitivity and lower detection limitation, and speed up the detection of response time for enzymatic reaction. In this study, the comparison of the electrochemical current and response time between the results of yeast suspension and collection experiments were shown.

II. MATERIAL AND METHOD

A. Reagents and solutions

All solutions were prepared with Mili-Q water (Millipore). 17 β-Estradiol was purchased from Sigma. p-Aminophenyl-β-D-galactopyranoside (PAPG) was supplied by Tokyo Chemical Industry Co., Ltd., Japan. Triton X-100 was purchased from Polysciences, Inc. Dimethyl sulfoxide (DMSO), $Na_2HPO_4 \cdot 12H_2O$, $NaH_2PO_4 \cdot 2H_2O$, KCl, and p-aminophenol were purchased from Wako Pure Chemicals, Japan. $MgSO_4 \cdot 7H_2O$ was purchased from Kanto Chemical Co., Inc., Japan.[7]

B. Fabrication of the analyte collection well chip

The analyte collection well chip was sequentially integrated with an Au electrode arrays, SU-8, adhesive tape, and ITO cover (Fig. 1). To make an analyte collection sensing well, a SU-8 sheet (25 μm in thickness) was attached to the Au electrode array area of the glass slide. A flow channel (10×2 ×0.05 mm^3) was defined on a double-sided Adhesive (30 μm in thickness), and the well substrate was covered by an ITO glass [1]. The Sensing chip were a three-electrode configuration included the Ag/AgCl reference electrode, the counter electrode and the working electrode fabricated by gold

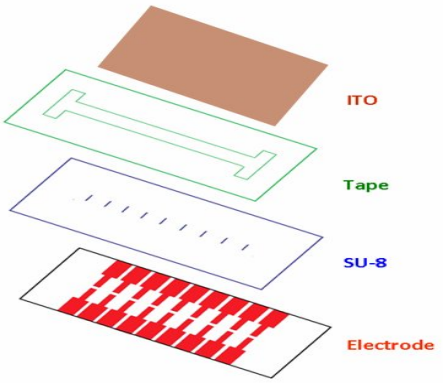

Fig. 1 Construction of the developed chip. The electrodes were defined by the SU-8 and patterned electrode, and then a tape with designed channel flow was integrated with ITO cover.

C. Recombinant yeast cells excreted β-Gal

Saccharomyces cerevisiae Y190 was purchased from Clontech. The expression plasmids for medaka estrogen receptor R (medERR: Oryzias latipes) which may bind with 17B-estradiol fused to the GAL4 DNA binding domain (GAL4 DBD) and coactivator TIF2 fused to the GAL4 activation domain (GAL4 AD) were tranferred into yeast cells carrying the β-galactosidase reporter gene (Fig. 2).[7, 8]

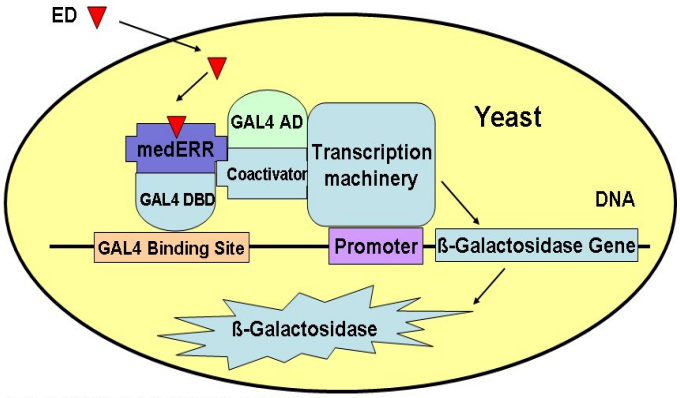

GAL4 AD: GAL4 Activation Domain
GAL4DBD: GAL4 DNA Binding Domain
HR LBD: Hormone Receptor Ligand Binding Domain

Fig. 2 Signal transduction of the recombinant yeast to 17 β-estradiol (ED) stimulation. β-galactosidase reporter gene will be expressed and β-galactosidase can be found in the cytoplasm.

The cells were incubated for 48 hr at 30 °C with shaking at 100 rpm in modified MSD medium. The yeast culture (700 μL) was then mixed with medium (700 μL) containing 0.5 ppb 17 β-estradiol and 2.0% (v/v) DMSO and incubated for 4 h at 30°C with shaking at 100 rpm to induce β-galactosidase expression. The 17 β-estradiol can dissolve into the DMSO. The toxicity treatment time was about 4 hr to induce enough enzymes, β-Gal in the yeast cells and the toxic treatment process must shake for protection the solution diffusion effect. An amount of 350 μL of Z buffer (60.0 mM $Na_2HPO_4 \cdot 12H_2O$, 39.7 mM $NaH_2PO_4 \cdot 2H_2O$, 10.0 mM KCl, 10.0 mM $MgSO_4 \cdot 7H_2O$, pH 7.0) including 1.5% (v/v) Triton X-100, a nonionic surfactant, was added to the culture and incubated for 1 hr at 30°C with shaking at 100 rpm in order to improve the permeability of the yeast cell membrane.[7] The yeast culture solution transferred into three tubes, 700, 700, 300 μL .The 300 μL tube of yeast cells were collected by centrifugation (6000 rpm for 5 min) and resuspended in 300 μL of 100 mM sugar solution for the yeast cells collection procedures.

In addition, the 700 μL tubes of yeast cells were collected by centrifugation (6000 rpm for 5 min) about 1.3×10^6 yeast cells and resuspended in 300, 200, 100 μL of PAPG solution for different reaction volumes and time, 0.5, 2, 3 hr in the yeast cells suspension procedures.

E. Yeast Trapping into the Sensing Well

The sensing well was covered with an ITO glass. The sensing well can be connected the 'positive' terminal to the electrode and the 'negative' terminal to the ITO cover. The suspended yeast cells can be trapped and collected by a perpendicular electrophoretic force (EOF) when a trapping voltage (+2.0 V vs. ITO) was applied to the sensing well (Fig. 3). The yeast cells can be accommodated into the sensing well by the vertical trapping force when it flows through the sensing well. The yeast cells can be captured and collected in the sensing well. After the trapping experiment, the channel solution was changed from deionized water with sugar 0.1 M to PAPG in Z-buffer for the yeast cells with β-Gal activity detection.

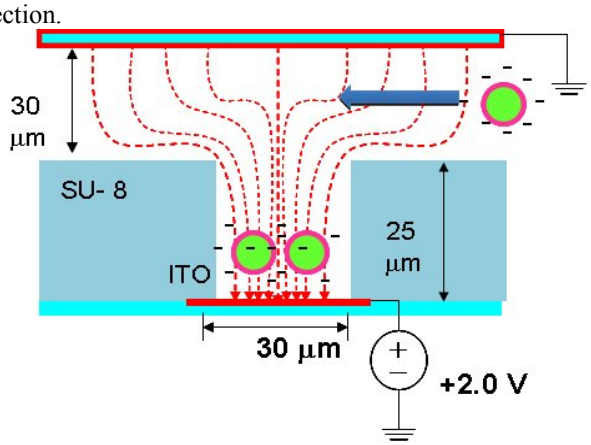

Fig. 3 Schematic drawing of the developed chip. The sensing electrode was embedded at the bottom of microwell. The dashed line indicates the electrophoretic force which was generated by applying a DC voltage across the sensing electrode and ITO cover.

D. Electrochemical Measurement of the Sensing Well

Initially, the Electrochemical measurement of the Sensing well were a three-electrode configuration included the Ag/AgCl reference electrode, the counter electrode and the working electrode fabricated by gold (Fig. 4-a). The potential control and current acquisition were carried out by an electrochemical measurement system. Cyclic voltammograms (CVs) of the Sensing well were tested. The PAPG 7.4 mM

solution, prepared with the Z-buffer solution, was used to detect voltage for the PAP products.

In this study, the comparison of the electrochemical current and response time between the yeast suspension and collection results were studied. In the process of the yeast cell suspension experiment, the substrate PAPG 7.4 mM solution 300 μL in Z-buffer was added into the tube with yeast cells excreted β-Gal for dehydrated reaction about 0.5, 2, 3 hr. Then centrifuge and transfer the suspension solution on the Au working electrode (100 × 30 μm) of the sensing chip. The currents with the different reaction time were collect by sensing electrode to study the reaction time effect. In addition, the substrate PAPG 7.4 mM solution 300, 200, 100 μL in Z-buffer was added into the three different tubes with yeast cells excreted β-Gal for de-hydried reaction for 2hr. Then centrifuge and transfer the suspension solution on the Au working electrode (100 × 30 μm) of the sensing chip. The currents in the different reaction volumes were collected by sensing electrode to study the reaction volume effect. In the process of the yeast cell collection experiment, the yeast cells excreted β-Gal were manipulated inside the sensing well according to the procedure described, the PAPG solution was introduced into the channel with ITO electrode as a top cover for electrochemical detection (Fig. 4-b).

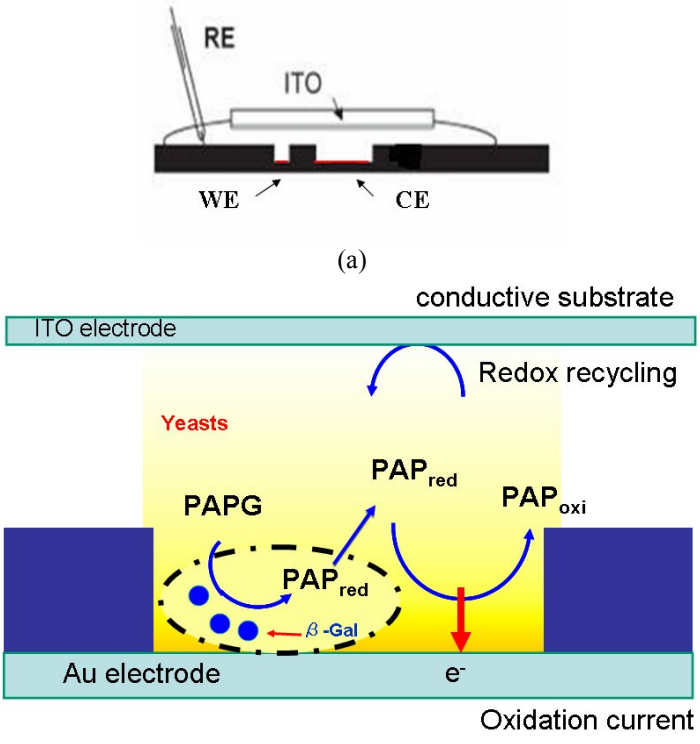

Fig. 4 (a) electrodes arrangement of the developed device. Ag/AgCl reference electrode was placed over the chip with a liquid junction to the chip electrode. (b) PAPG may diffuse into inter-yeast cell to react with β-gal, the production PAP could diffuse out of cell to contribute the oxidant current

III. Result and Disccusion

A. Generation of β-Gal after 17 β-estradiol treatment

In the process of the yeast cell suspension experiment, the substrate PAPG was added into the tube with yeast cells excreted β-Gal for dehydrated reaction. The dehydrated reaction of the PAPG and β-gal in yeast may be dependent on the reaction time. The oxidation currents of PAP on the dehydrated reaction time 0.5, 2, 3 hr were estimated in the 300 μL z-buffer solution containing 7.4 mM PAPG. The parameters of cyclic voltammograms were the scan rate 50 mv/s, san range from 0 to 0.55 V. The oxidation currents of PAP were appeared from 0.1 V [7].The time dependence of the cyclic voltammograms PAP from the B-GAL and PAPG dehydration reaction were observed to find out the significant signal. In the result, Comparing of the different reaction time can be indicated that the PAP oxidation currents of 2 hr reaction time reached a significant electrochemical current about 1 nA (Fig. 5). According to the results, the reaction time of volume effect experiment was collected the oxidant current of PAP on the 2 hr reaction time. This phenomena of the time dependence may be evaluated that the β-gal, large molecular weights may not release from yeast. Therefore PAPG may diffuse into inter-yeast cell to react with β-gal, the production PAP could diffuse out of cell to contribute the oxidant current.

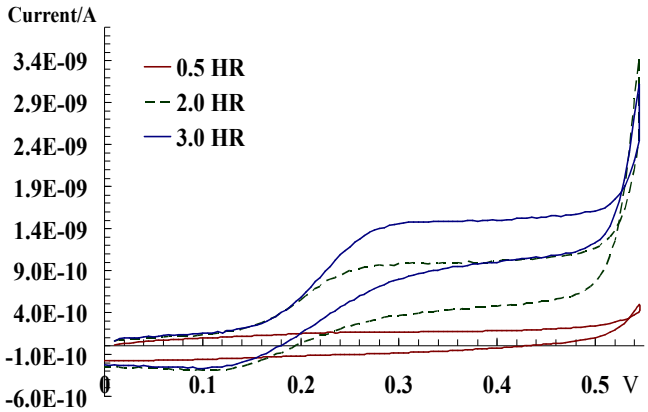

Fig. 5 The oxidation currents of PAP on the dehydrated reaction time 0.5, 2, 3 hr were estimated in the 300 μL z-buffer solution containing 7.4 mM PAPG

B. Volume effect for the trace β-Gal detection

The substrate PAPG was added into the tube with yeast cells excreted β-Gal for dehydrated reaction. Compare the different reaction volumes 300, 200, 100 μL z-buffer solution containing 7.4 mM PAPG to estimate the reaction volume effects on the same reaction time, 2 hr. The different reaction volumes of the cyclic voltammograms PAP from the B-GAL and PAPG dehydration reaction were observed to find out the volumes effects. The parameters of cyclic voltammograms were the scan rate 50 mV/s, san range from 0 to 0.55 V. The oxidation currents of PAP were appeared from 0.1 V. In the result, The oxidant currents may be corresponding to the concentration of PAP production. The comparing of the different reaction volumes may be showed that the Lower reaction volume have the higher oxidant current of PAP (Fig.

6). Therefore, the ultra low reaction volume of the analyte collection sensing well chip may have the higher oxidant current of PAP than the result of suspension experiment.

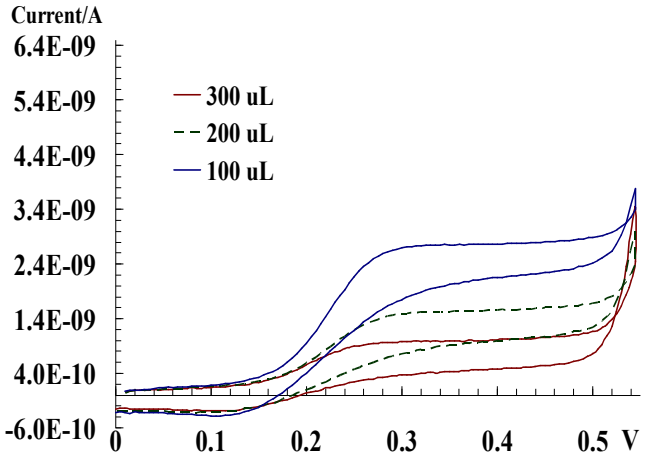

Fig. 6 Compare the different reaction volumes 300, 200, 100 μL z-buffer solution containing 7.4 mM PAPG on the same reaction time, 2 hr

C. Rapid response with the yeasts covered sensing electrode

Yeast cells were injected into the fluidic channel. Yeast cells may be trapped into the analyte collection sensing well by the electrophoretic forces. There are lots of yeast cells near or into the sensing well (Fig. 7).

(a) (b)

Fig. 7 (a) Before yeast were trapped into the sensing well, (b) The sensing well was full of yeast cells.

D. The cyclic voltammograms of the yeast trapped

After the yeast cells excreted β-Gal manipulated inside the sensing well according to the procedure described, the PAPG solution was introduced into the channel for electrochemical detection on the reaction time about 15 mins. The parameters of CVs were the scan rate 50 mV/s, san range from 0 to 0.55 V. In the result, the comparison of the electrochemical current and response time between the results of yeast suspension and collection experiments were shown the two times of the PAP oxidation current difference and the fast response time about 15 mins (Fig. 8). The suspension condition 300 μL for 2 hr induced the current about 1 nA (blue curve). The collection condition for 15 mins induced the current about 2 nA (red curve), so the ultra low volume of the analyte collection sensing well chip may have the higher oxidant current of PAP and fast response time than suspension experiment.

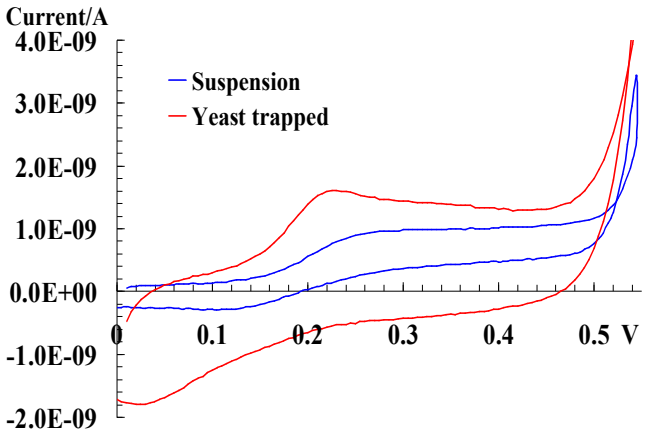

Fig. 8 The suspension condition 300 μL for 2 hr induced the current about 1 nA (blue curve). The Collection condition induced the current about 2 nA (red curve)

IV. Conclusion

In this study, yeast cells near the electrode surface of the sensing well by electrophoretic force may enhance the sensitivity and response time. The ultra low reaction volume of the analyte collection sensing well chip may have the higher oxidant current of PAP and fast response time than suspension experiment. In the future, it is possibility to lower detection limitation, and speed up the detection of response time. This analyte collection well biochip can provide for simple, portable and real time enzyme testing on health care, environment, safe control of food.

V. Reference

[1] C. Y. Chang, Y. Takahashi, T. Murata, H. Shiku, H. C. Chang, T. Matsue, "Entrapment and Measurement of a Biologically Functionalized Microbead with a Microwell Electrode", Lab Chip, 9 (2009), 1185–1192

[2] B. M. Taff and J. Voldman," A Scalable Addressable Positive-Dielectrophoretic Cell- Sorting Array", Analytical Chemistry, 77(2005), 7976-7983.

[3] A. Khademhosseini, R. Langer, J. Borenstein, and J. P. Vacanti, " Microscale technologies for tissue engineering and biology", Proc Natl Acad Sci U S A, 103(2006), 2480-2487.

[4] P. S. Dittrich, K. Tachikawa, and A. Manz," Micro Total Analysis Systems Latest Advancements and Trends", Analytical Chemistry, 78(2006), 3887-3907.

[5] M. Deutsch, A. Deutsch, O. Shirihai, I. Hurevich, E. Afrimzon, Y. Shafran, and N. Zurgil," A novel miniature cell retainer for correlative high-content analysis of individual untethered non-adherent cells", Lab Chip, 6(2006), 995-1000.

[6] J. R. Rettig and A. Folch," Large-scale single-cell trapping and imaging using microwell arrays," Analytical Chemistry, 77(2005), 5628-5634.

[7] T. Yasukawa, K. Nagamine, Y. Horiguchi, H. Shiku, M. Koide, T. Itayama, F. Shiraishi, T. Matsue," Electrophoretic cell manipulation and electrochemical gene-function analysis based on a yeast two-hybrid system in a microfluidic device", Anal. Chem., 80(2008), 3722-3727.

[8] T. Nishihara, J. I. Nishikawa, T. Kanayama," Estrogenic Activities of 517 Chemicals by Yeast Two-Hybrid Assay", Journal of Health Science, 46(2000), 282-298.

P21

A Novel CMOS-Compatible Polysilicon/Titanium Thermopile

Chung-Nan Chen[1], Wen-Chie Huang[2], Cheng-Chia Chen[1] and Shang-Hung Shen [1]

[1] *Institute of Photonics and Communications, National Kaohsiung University of Applied Sciences, Kaohsiung, Taiwan.*

[2] *Department of Electronic Engineering, National Kaohsiung University of Applied Sciences, Kaohsiung, Taiwan.*

***Abstract* — In this paper, we present a 0.8-µm 1P2M CMOS process compatible polysilicon/titanium thermopile with a gold black absorption layer. Instead of an aluminum layer of 0.6 µm thickness in the first metallization process, a titanium layer of 0.1 µm thickness was introduced to the fabrication of a CMOS compatible thermopile in order to enhance sensitivity by lowering the thermal conductance of the sensor. After the CMOS process, a 1.2-mm-square floating thermopile structure was formed by using a front-side anisotropic etching process in dual-doped tetra-methyl ammonium hydroxide (TMAH) solution, in which the etch rates of aluminum thin film are relatively low. The experimental data reveal that the etch rate of a thermally evaporated aluminum film could be smaller than 10 Å/min in 5 wt.% TMAH solution with the addition of 4 gm/l ammonium peroxodisulfate (AP) and 24 gm/l silicic acid. Eventually, a 0.8-mm-square porous gold black layer was thermally evaporated upon the sensor surface to serve as an infrared absorption layer. The FTIR spectrum shows that the absorber has near perfect absorptance in the wavelength range of 5 to 15 µm.**

The completed thermopile sensor consists of 96 poly-Si/Ti thermocouples pairs and has a resistance of 43.5 kilo-ohms. For reducing environment noises, the sensor chip was encapsulated in a TO5 metal-can with an 8-14 µm filter. The measurement result indicates the sensor has a thermal time constant of 103 ms in atmosphere and 173 ms in a pressure of 16 mTorr respectively. In addition to an increasing time constant, the output voltage also raises by a factor of 2.3 in vacuum environment.

Keywords — ***CMOS, infrared, MEMS, TMAH, thermopile***

I. INTRODUCTION

Thermopiles are currently used as the sensing elements of tympanic thermometers, NDIR gas monitors and low-resolution thermal imagers in medical applications. For the reasons of mass production, low cost and IC integration, CMOS compatible process was frequently employed to manufacture thermopile sensors. [1-4] In past years, poly-silicon layers and aluminum layers were the most popular materials for forming thermopile elements [5-8]. The thermal conductivity of bulk aluminum is about 237 W/m·K and bulk titanium is 21.9 W/m·K. The enormous thermal conductivity of aluminum results in sensitivity drop. In order to improve the sensitivity of thermopiles by reducing thermal conductivity, we utilized a low thermal-conductivity titanium thin film instead of an aluminum layer. The front end processes of sensors were carried out by using 0.8 µm CMOS process combined with additional Ti sputtering and patterning process. The post processes include a dual-doped TMAH anisotropic etching process for fabricating a suspended structure and a gold black thermal evaporation process for forming an infrared absorption layer. The dual-doped TMAH solution is a dilute TMAH solution in which added AP and silicic acid. This dual-doped solution was utilized to reduce the etch rate of aluminum pads and improve the surface roughness. [9] In the gold black process, gold granules were thermally evaporated onto the active regions of the sensors by metal mask patterning. The evaporation process is under a pressure of 0.8 torr to form a porous gold layer. The completed sensor was packaged inside a standard TO5-can attached with an 8-14 µm filter. The performance of the TO5 sensors, such as thermal time constant and relative output voltage, are measured and analyzed in atmosphere and vacuum.

II. PROCESS AND OF FABRICATION

A. *Structure and Process*

The thermally isolated structure of our thermopile sensor was designed as Fig. 1. A floating sensing element, including a structure layer, poly-silicon/titanium thermocouple pairs, ILD layers, a passivation layer and an absorber, is located at central region. Infrared energy emitted from a target is absorbed upon the gold black layer and then transferred to heat. The thermopile sensor generates an output voltage due to the temperature difference between hot junctions and cold junctions. Sensor signals are delivered through the aluminum pads to the pins of TO5 header.

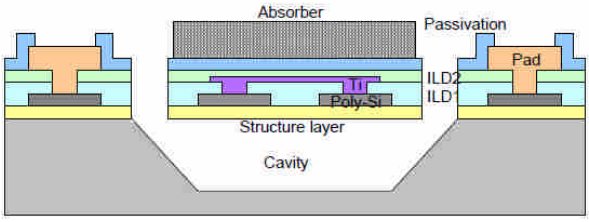

Figure 1. The structure of the thermopile sensor.

The process flow is shown as Fig. 2, dielectric structure layers were first formed on a <100>-oriented silicon wafer and then a phosphor-doped polysilicon layer was deposited and patterned on the top structure layer. After ILD1 layer deposition and contact window opening, a titanium thin film of 100 nm thickness was sputtered onto the ILD1 layer. As an ILD2 layer was deposited and contact via was etched, an aluminum film of 1µm thickness was next sputtered onto the ILD2 layer and patterned as wire bonding pads. A passivation layer covered the aluminum pads, the anisotropic etching

This project was funded by the National Science Council Plan (Project code: NSC 97-2221-E-151-006).

Contact author: please contact **cn_chen@cc.kuas.edu.tw*

windows and pad windows were subsequently opened. The suspended layer was completed in a dual-doped TMAH solution. The dual-doped TMAH solution consists of 5 wt.% TMAH solution, 4 gm/l ammonium peroxodisulfate (AP) and 24 gm/l silicic acid. Fig. 3 exhibits the etch rates of various aluminum films in the dual-doped TMAH solution, including thermally evaporated aluminum and sputtered aluminum under 300 W, 650W and 1000W bias power conditions. The etch results show the etch rates of a thermally evaporated aluminum film and low bias-power sputtered films are lower than 20 Å/min. Finally, a porous gold black was thermally evaporated onto the wafer and in-situ patterned as a square of 0.8 mm side length by using a metal mask. The gold black evaporation process was under a relative low vacuum of 0.8 torr to achieve the porous and black layer. The FTIR spectrum of the gold black layer shows the absorptance is almost 100% in the wavelength range of 5μm to 15μm as shown in Fig. 4.

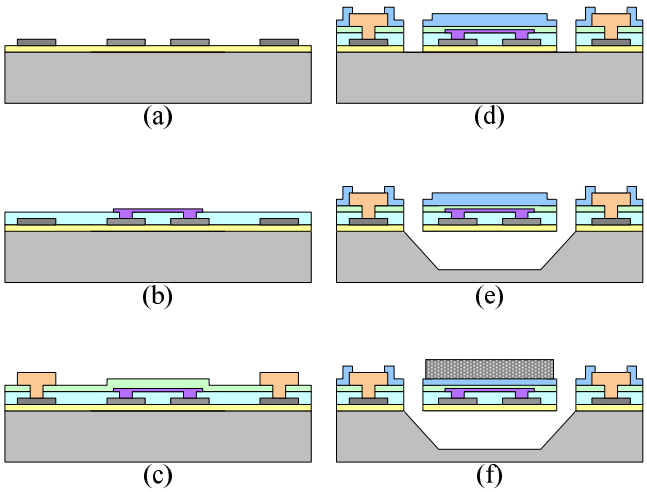

Figure 2. The process flow of the thermopile sensor. (a) polysilicon deposition and patterning; (b) titanium sputtering and patterning; (c) aluminum pads sputtering and patterning; (d) passivation deposition and window opening; (e) anisotropic etching; (f) gold black evaporation and patterning.

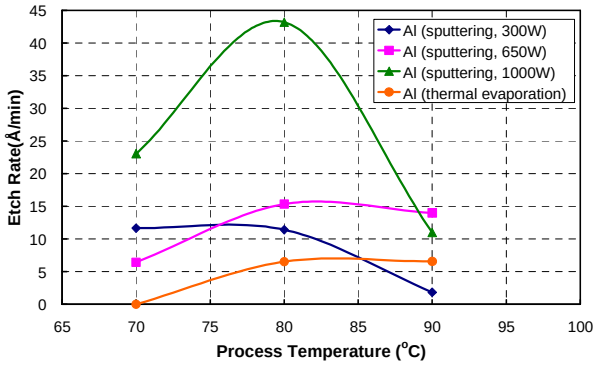

Figure 3. The etch rates of aluminum films in dual-doped TMAH solution at various process temperature.

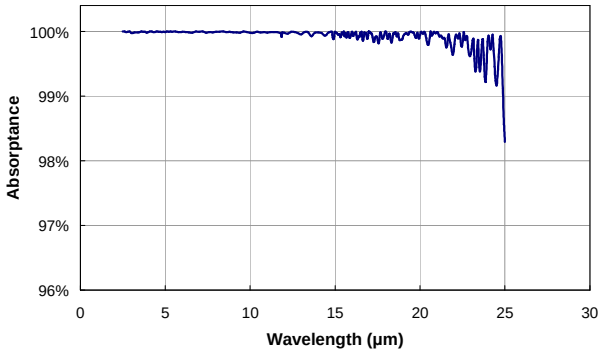

Figure 4.The FTIR spectrum of the gold black layer in the wavelength range of 2.5 μm to 25 μm.

B. Fabrication and Package

In order to reduce the thermal conductance and enhance the sensitivity of the thermopile, the sensor was manufactured by utilizing a 0.8 μm CMOS process with additional titanium processes. The suspended structure of the thermopile was formed by using a dual-doped THAH anisotropic etching process. Fig.5 is a picture of the completed thermopile with suspended membrane. The thermopile consists of 96 pairs of polysilicon/titanium thermocouples and has a floating area of 1.2 mm square. The cross shape (+) in the central region of the sensor is composed of 96 hot junctions and the small rectangles surrounding the floating layer are 96 cold junctions. In addition to the 4 triangular etch windows around the sensor, thin and long etch windows are designed to accomplish the fabrication process of the suspended membrane and improve the filled factor of the sensor.

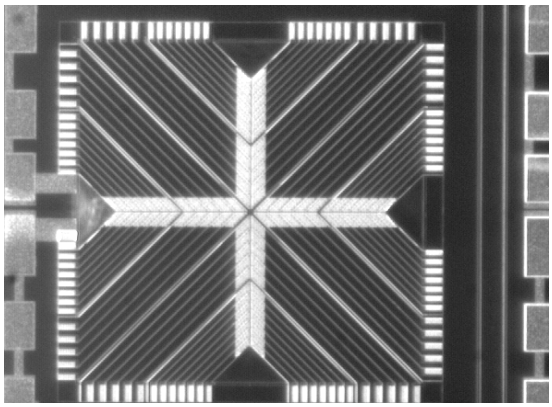

Figure 5. The photograph of the thermopile before black coating.

Fig.6 shows a photograph of the thermopile chip with gold black coating. A gold thermal evaporation process was carried out under a chamber pressure of 0.76 torr to form a gold black layer. The gold black area was patterned by using in-situ metal mask patterning. The color of gold black layer in the photograph is heavily black since the input light rays undergo multi-absorption inside the porous structure resulted

in totally absorption. Fig. 7 shows the SEM pictures of the completed thermopile, the floating sensor membrane is suspended above a silicon cavity by the dielectric structure layers and the polysilicon/titanium thermocouple pairs in Fig. 7(a). Fig. 7(a) also displays that the gold black film is a porous structure layer. Fig. 7(b) is a picture of the gold black absorber with magnification 2000 times, the rough and porous surface could effectively enhance the absorption of input infrared energy.

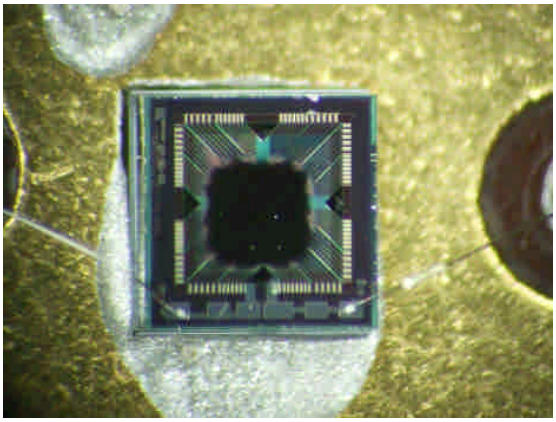

Figure 6.The photograph of the thermopile with gold black coating.

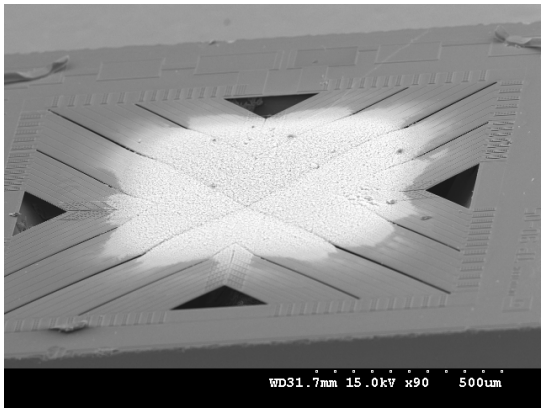

(a)

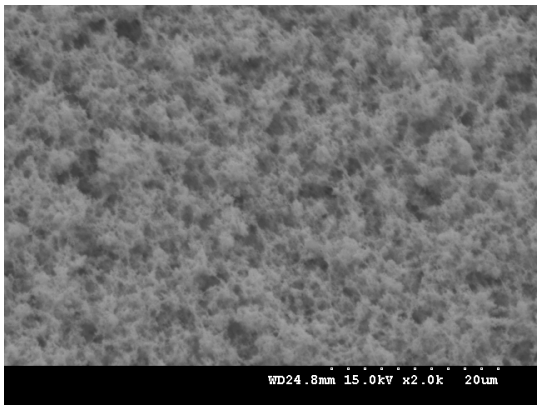

(b)

Figure 7.The SEM pictures of the thermopile sensor and the absorber.

The sensor was then fixed upon a TO5 header by using silver paste and electrically connected to the package by aluminum wire bonding. The completed TO5-packaged thermopile is shown as Fig. 8. In order to reduce environment noise, an 8-14μm bandpass filter is attached to the window of TO5 can. This 8-14μm infrared band is a transparent window in atmosphere without the absorption effect of water molecules. The 8-14μm filter is frequently applied in the application of non-contact infrared thermometers.

Figure 8. The photograph of the packaged thermopile with an 8-14μm bandpass filter.

III. MEASUREMENT AND ANALYSIS

The thermal time constant and the normalized output voltage of the packaged thermopile sensor were measured and characterized by using a lock-in amplifier and an optical chopper in atmosphere and in vacuum environment respectively. Fig. 9 and Fig. 10 present the frequency responses of the TO5-packaged sensor in atmosphere and in vacuum respectively. The normalized voltages are a function of the thermal time constants of the sensor. The function can be expressed as the following equation

$$V = V_0(1 - e^{-t/\tau}), \quad (1)$$

where V and V_0 are the normalized voltage at time t and flat band voltage respectively; τ is the thermal time constant of the sensor. The symbols in the figures indicate the measurement data and the curves show the fitting results. Fig. 9 shows the measured data and the fitting curves of the TO5-packaged sensor at the target temperature of 100 ^{o}C, 150 ^{o}C and 200 ^{o}C in atmosphere. In Fig. 9, all the normalized output voltages start to descend as the optical chopping frequency rises above 2 Hz and decline dramatically as the frequency is up to 5 Hz. The thermal time constant can be calculated as a value of 103 ms. Fig. 10 presents the frequency responses of the sensor at the target temperature of 100 ^{o}C and 150 ^{o}C in a vacuum of 16 mTorr. We found the thermal time constant is raised to a value of 173 ms and the output voltage is increased by a factor of 2.3 due to the decreasing of gas conductance.

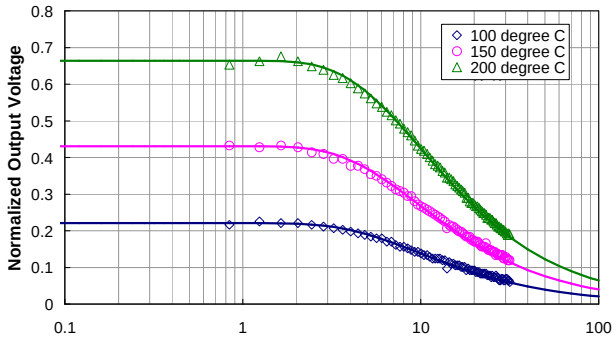

Figure 9.The frequency response of the packaged thermopile at various target temperatures in atmosphere.

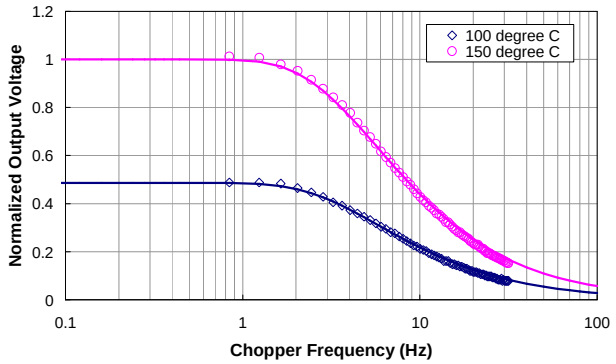

Figure 10. The frequency response of the packaged thermopile at various target temperatures in a vacuum of 16 mTorr.

The output voltage V of a thermopile is written as

$$V = n\alpha(T_h - T_c), \tag{2}$$

in which n is the pair number of thermocouples; α is the Seebeck coefficient; T_h is the temperature of hot junctions and T_c is the temperature of cold junctions which approaches ambient temperature T_a. In the steady state, the temperature difference can be given by

$$T_h - T_c = \frac{\varepsilon\Phi}{G}, \tag{3}$$

where ε is the emissivity of a infrared absorber; G is the total thermal conductance of a thermopile sensor. Φ is the input optical power given by

$$\Phi = \varepsilon_t \sigma A_s (T_t^4 - T_a^4), \tag{4}$$

in which ε_t is the emissivity of target; σ is the Stefan-Boltzmann' constant; A_s is the area of a thermal sensor; T_t and T_a are target temperature and ambient temperature respectively. The output voltage V of a thermopile can be rewritten by

$$V = \frac{n\alpha\varepsilon\Phi}{G}. \tag{5}$$

The output voltage V is inversely proportional to the total thermal conductance of a thermopile, which includes solid conductance G_s, gas conductance G_g and radiation conductance G_r. The total thermal conductance is given by

$$G = G_s + G_g + G_r, \tag{6}$$

where G_s is proportional to the solid thermal conductivity of floating materials; G_g is proportional to gas thermal conductivity and floating membrane area and G_g is also a function of pressure; the radiation conductance G_r is expressed by

$$G_r = 2\varepsilon\sigma A_s (T_h^2 + T_a^2)(T_h + T_a). \tag{7}$$

In general, the radiation conductance is negligible since the temperature of a thermopile sensor is only slightly higher than ambient temperature. From the measured data, we found that the gas conductance of the polysilicon/titanium thermopile is 1.3 times than the solid conductance. It implied that the sensitivity of the thermopile can be improved by sealing in a vacuum package.

The gold black effect on thermal characteristics is also estimated. Fig. 11 shows the thermal response of a thermopile without gold black coating as the target temperature is 150 °C. The thermal responses of the thermopile with a gold black layer under a target temperature of 150 °C are also displayed in Fig. 11. The thermal time constant of the uncoated thermopile is 43 ms and the normalized output voltage is only 0.293. The higher response speed results from the smaller heat capacity. The relation of a thermal time constant τ and heat capacity H of a thermal sensor is given by

$$\tau = \frac{H}{G}, \tag{8}$$

where

$$H = mc, \tag{9}$$

m is mass and c is specific heat. The gold black layer enhances the sensitivity of the sensor by a factor of 1.47 but lowers the response speed by a factor of 0.41. The emissivity of the evaporated gold black layer is almost equal to 1 in the wavelength range of 8-14μm. The emissivity of the uncoated thermopile can be evaluated as 0.68.

The measurement summary is listed in Table. 1. It is obvious that the black coating and vacuum environment could improve the output voltage due to the increasing absorptance of input optical power and reducing gas conductance of the thermopile sensor respectively. The total effect of the

absorption layer and the vacuum environment on the enhancement of the sensor responsivity could reach 3.4 times than the uncoated sensor in atmosphere. But the thermal time constant of the thermopile also increases since the heat capacity enlarges as an absorber is added on the sensor. In vacuum environment, the increasing thermal time constant is induced by reducing gas conductance of the sensor. The effects of the black coating and the vacuum environment on the increasing thermal time constant are by a factor of 2.4 and 1.7 respectively. The thermal time constant of the black coating sensor in vacuum is 4 times than the uncoated sensor in air. However, the response time of the thermopile sensor is qualified in the application of tympanic thermometers and non-contact infrared temperature thermometers.

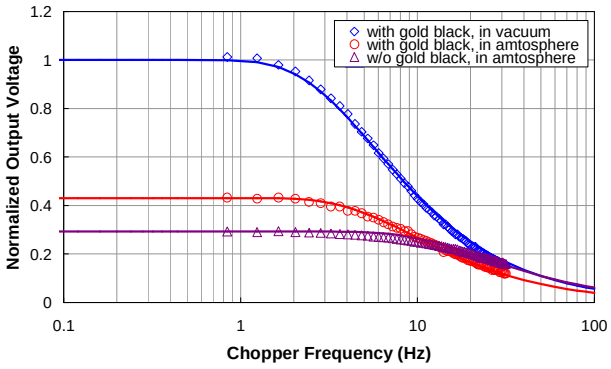

Figure 11. The frequency responses of the packaged thermopile with and without a gold black layer at the target temperature of 150 ^{o}C in vacuum and atmosphere.

TABLE I. MEASURMENT SUMMARY

Test Condition		Result	
Infrared Absorber	***Environment***	***Normalized Output***	***Time Constant***
None	In atmosphere	0.293	43 ms
Gold black	In atmosphere	0.431	103 ms
Gold black	In vacuum	1	173 ms

In this work, a non-contact temperature measurement system was established by using the polysilicon/titanium thermopile as the sensing element. As shown in Fig. 12, the thermopile sensor was placed behind the optical chopper in the right of the pictures. The output signal of the sensor was read out by a lock-in amplifier and then calculated by a LabVIEW program. The estimated temperature was next displayed on the screen of a notebook. Fig. 12(a) shows that the room temperature is 26.25 ^{o}C before the measurement of body temperature and Fig. 12(b) exhibits that the surface temperature of a body is 31.30 ^{o}C as a hand is placed in front of the sensor. The response

(a)

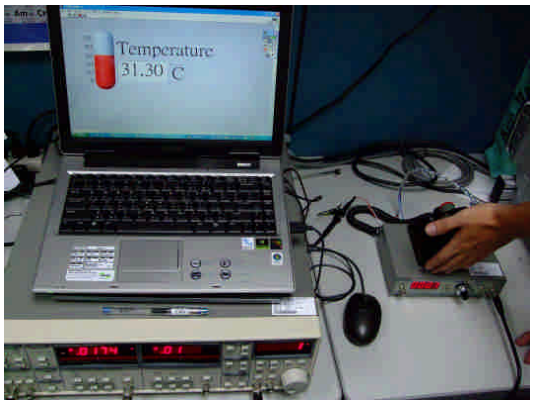

(b)

Figure 12. A non-contact temperature measurement system, (a) before measurement; (b) the surface temperature of a hand.

IV. CONCLUSION

We reveal a CMOS compatible polysilicon/titanium thermopile with low solid conductance in this study. The thermopile sensor was fabricated by a 0.8 μm CMOS process with additional titanium processes, a dual-doped TMAH etching process and a gold black evaporation process. The dual-doped TMAH solution contains 5 wt.% TMAH solution, 4 gm/l AP and 24 gm/l silicic acid. The experimental results show the etch rates of a thermally evaporated aluminum film and low bias-power sputtered films are lower than 20 Å/min. It is suitable to employ the dual-doped TMAH solution as the etchant in the fabrication process of a MEMS device with aluminum pads. A porous gold black was thermally evaporated onto the wafer and patterned as an infrared absorber. The FTIR spectrum of the gold black layer shows the absorptance is almost 100% in the wavelength range of 5μm to 15μm. The emissivity of the uncoated thermopile can be evaluated as 0.68.

The thermal characteristics of the completed thermopile are measured and analyzed by utilizing a lock-in amplifier and an optical chopper. The measured results show that the gold black layer could improve the sensitivity of the thermopile by a factor of 1.47 due to the increasing absorptance of infrared energy but reduces the response speed by a factor of 0.41 due

to the increasing thermal mass. The effect of gas conductance on the thermal characteristics of the infrared sensor is also estimated by using a vacuum chamber system. We found that the gas conductance of the sensor is 1.3 times than the solid conductance. It means that a vacuum package could enhance the output voltage by a factor of 2.3. The sensor has a relatively larger thermal time constant of 173 ms in vacuum due to the reducing thermal conductance. The response speed is qualified as a sensing element in tympanic thermometer and non-contact thermometer applications.

A simple non-contact temperature measurement system for detecting the body temperature was set in our laboratory by using a lock-in amplifier and an optical chopper. This system has high temperature resolution and fast response speed. The completed polysilicon/titanium thermopile is suitable to serve as a detecting device in non-contact temperature sensing applications.

REFERENCES

[1] A. Schaufelbuhl, N. Schneeberger, U. Munch, M. Waelti, O. Paul, O.Brand, H. Baltes, C. Menolfi, Q. Huang, E. Doering, M. Loepfe, "Uncooled low-cost thermal imager based on micromachined CMOS integrated sensor array," IEEE J. Microelectromechanical Systems, vol. 10, no. 40, 2001, pp. 503-510.J. Clerk Maxwell, A Treatise on Electricity and Magnetism, 3rd ed., vol. 2. Oxford: Clarendon, 1892, pp.68–73.

[2] H. Baltes, and O. Brand, "CMOS-based microsensors and packaging," Sensors and Actuators A, vol. 92, 2001, pp. 1-9.

[3] U. Munch, D. Jaeggi, K. Schneeberger, A. Schaufelbuhl, O. Paul, H. Baltes, and J. Jasper, "Inductrial fabrication technology for CMOS infrared sensor arrays," Transducers Conf., pp. 205-208, 1997.

[4] T. Akin, Z. Olgun, O. Akar, H. Kulah, " An integrated thermopile structure with high responsivity using any standard CMOS process," Sensors and Actuators A, vol. 66, 1998, pp.218-224.

[5] G. Kaltsas, A.G. Nassiopoulou, "Novel C-MOS compatible monolithic silicon gas flow sensor with porous silicon thermal isolation", Sensors and Actuators 76, 1999. pp.133–138.

[6] E. Socher, O. Degani, Y. Nemirovsky, "Optical design and noise considerations of CMOS compatible IR thermoelectric sensors", Sensors and Actuators vol. 71, 1998. pp.107–115.

[7] C. Escriba, E. Campo, D. Est`eve, J.Y. Fourniols, "Complete analytical modeling and analysis of micromachined thermoelectric uncooled IR sensors", Sensors and Actuators A vol. 120, 2005, pp267–276

[8] C. Calaza , N. Viarani, G. Pedretti, M. Gottardi, A. Simoni, V. Zanini, M. Zen, "An uncooled infrared focal plane array for low-cost applications fabricated with standard CMOS technology", Sensors and Actuators A vol. 132, 2006, pp129–138

[9] K. Biswas, S. Kal, "Etch characteristics of KOH, TMAH and dual doped TMAH for bulk micromachining of silicon", Microelectronics Journal vol. 37, 2006, pp.519–525

Heavily Boron-Doped Effect on the Etch Rates of <111> Single-Crystal Silicon in TMAH Solutions

Yong-Yi Chen[1], Chung-Nan Chen[1] and Wen-Chie Huang[2]

[1]Institute of Photonics and Communications, National Kaohsiung University of Applied Sciences, Kaohsiung, Taiwan.
[2]Department of Electronic Engineering, National Kaohsiung University of Applied Sciences, Kaohsiung, Taiwan

***Abstract* — The purpose of this paper is to study the heavily boron-doped effect on the etch rates of boron-doped <111> single-crystal silicon in different TMAH solutions. The boron atoms were heavily doped in <111> single-crystal silicon by using diffusion process.**

We change the pre-deposition time and annealing time of diffusion process to form different concentration distributions. The samples were pre-deposited at 1100°C and driven in at 1100°C to create relatively flat doping profiles with about 2 μm depth. In this study, we have investigated the etch-stop properties of heavily boron-doped silicon in 5% TMAH solution and 5% dual-doped TMAH solution at different process temperatures. In our work, the etch selectivity of undoped <111> silicon to boron-doped <111> silicon is 15:1 as the diffusion process is under the pre-deposition time of 90 minutes and the drive-in time of 60 minutes. The undoped <100>/ boron-doped <111> silicon etch selectivity can be achieved to about 260.

In this work, the suspended structures of <111> silicon layers were successfully manufactured by using <111> silicon substrate in a dual-doped TMAH solution. The suspended structures have high filled factor, large area and long legs. The large area of a device could increase the radiated power of a micro heater to enhance thermal radiation and raise infrared absorption of an infrared sensor to improve the output signal of the sensor. The long legs can reduce the thermal conductance of a thermal sensor to promote the sensitivity of the sensor. The applications of the suspended structures include gas sensors, flow meters, pressure sensors, micro heaters, infrared sensor, etc.

Keywords ***—diffusion, etch selectivity, etch stop, TMAH***

I. INTRODUCTION

In recent years, BioMEMS is an emerging field that has received increasing attention due to its high integration ability of IC devices, micro sensors and microstructures. The applications of BioMEMS include gas sensors, flow meters, pressure sensors, micro heaters, micro channels, micro valves and micro pumps. [1][2][3][4]

Etch stop and anisotropic wet etching techniques have been used to fabricate numerous suspended structures and micro structures for many years, such as bridges, membranes and cantilever, due to their low process cost, simple etch setup, higher etch rate and high degree of selectivity. TMAH (tetramethyl ammonium hydroxide) solutions have a higher etch selectivity between silicon and silicon dioxide than KOH and are compatible with CMOS process. These advantages result in the increasing popularity of TMAH solutions in MEMS process. In general, pure TMAH solutions form rougher etched silicon surfaces but when TMAH solution is doped with suitable amounts of silicic acid and AP(ammonium peroxodisulphate, $(NH_4)_2S_2O_8$), the mixture provides complete smooth etched surfaces and form a protective film on aluminum metal to prevent aluminum layers from being damaged. [5]

Many papers have studied the etch rates of heavily boron-doped single crystal silicon layers in KOH, EDP (ethylenediamine pyrocatechol) and TMAH in past years. The etch selectivity of undoped <100> silicon to 1E19 cm^{-3} boron-doped <100> silicon is 1.5:1 in 25 wt% TMAH solution. The etch selectivity of undoped <100> silicon to boron-doped <100> silicon of 3:1 can be achieved in 10%~57% KOH as the boron-concentration is 3E19 cm^{-3}. [6][7][8][9]

II. EXPREIMENTAL

A. Sample Preparation

The samples were prepared by utilized 4" <111>-oriented silicon wafers of 525 μm thickness. The silicon wafers were doped with boron in high temperature diffusion process at various pre-deposition and drive-in conditions. At first a boron glass layer was pre-deposited onto the wafer surface in oxygen environment and at a temperature of 1100°C by employing boron nitride as a boron source. The boron was then diffused from the boron oxide layer into the silicon wafers in a high temperature drive-in process. Finally, the glass layer was stripped by HF etching process. A PECVD oxide layer of 5000Å thickness was next deposited on the <111>-oriented silicon surface as an etching passivation layer in subsequent TMAH etching process.

Etching windows of about 5mm^2 on the oxide were opened by using standard photolithography and etching process. The wafers were cut into square samples with a side of 1cm. Before etching process, all samples were dipped in BOE for 15 seconds to remove a native oxide layer. All of samples with different boron concentrations were etched simultaneously in order to assure all samples were at the same etching conditions.

B. Etch Process Parameters

The roughness of etched silicon surface could be improved by replacing normal TMAH solution with dual-doped TMAH solution. The smooth surface is due to the suppression of hillock formation by the oxidizing agent AP. The dual-doped TMAH solution is that a dilute TMAH solution added with AP and silicic acid. The etch rate of the aluminum metal is also reduced in the dual-doped TMAH solution. The dual-doped TMAH is suitable to release a suspended structure from

This project was funded by the National Science Council Plan (Project code: NSC 97-2221-E-151-006).

**Contact author: please contact cn_chen@cc.kuas.edu.tw*

the silicon substrate without damaging the electronic connections [10][11][12]

In our study, the detail of etching conditions is listed as the Table 1. A dilute 5% TMAH and a 5% dual-doped TMAH solution doped with silicic acid and AP were used as silicon etchants at the process temperatures of 70, 80 and 90 ℃ respectively.

TABLE I. PROCESS PARAMETERS

TMAH concentration	5%	5%
25%TMAH (ml)	240	240
DI eater (ml)	960	960
Silicic acid (g)	0	54.72
AP (g)	0	8.4
Etch time	1 hr	1hr
Code/Etch (℃)	90°/80°/70°	90°/80°/70°

C. *Fabrication of suspended structures*

For the fabrication of the suspended structures of <111>-oriented silicon layers, a two-layer mask set was used. After RCA clean process, the thickness of the suspended structures was defined by RIE etch process (Fig. 1A). In order to improve the etch selectivity of the suspended structures to silicon substrate in TMAH solutions, the suspended structure was doped with boron by using BN (boron nitrite) diffusion process at 1100°C. A PECVD oxide layer of 5000Å thickness was next deposited on the silicon surface as a passivation layer (Fig. 1B) Etch windows were subsequently patterned and then the depth of the cavity beneath the floating membrane was etched by RIE process (Fig. 1C). Finally, the suspended structures of <111>-oriented were anisotropically etched by using 5% dual-doped TMAH etchant at 80℃ (Fig. 1D). The etchant contains 240ml 25wt.% of TMAH, 960ml DI water, 54.72 gm/l of silicic acid and 8.4gm/l of AP.

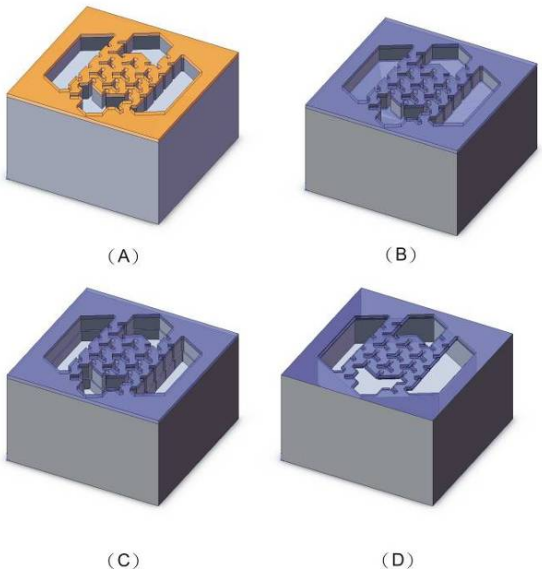

Figure 1. Fabrication process of a <111>-oriented silicon suspended layer. (A) Definition of the thickness of the suspended structures. (B) Deposition of a passivation layer.(C) Etch window patterning and opening. (D) Anisotropic etching.

III. RESULTS AND DSICUSSION

A. *SIMS*

In this study, Fig. 2-4 were the measurement results of the boron concentration profiles by using secondary ion mass spectrometry (SIMS). Fig. 2 shows the concentration distribution of different crystal orientation silicon wafers under the same diffusion process conditions. The crystal orientations do not impact the maximum concentration but only slightly impact the concentration distribution. Fig. 3 shows the concentration distribution of the <111> crystal orientation at different pre-deposition time. A maximum concentration of 3.55E19 atom/cm^3 is obtained as the pre-deposition time is 90 minutes in our work. Fig. 4 shows the concentration distribution of the <111> crystal orientation silicon at different annealing time. We found that the depth of concentration obviously depends on annealing time.

The process conditions and SIMS results of the samples were listed in table 2. The boron concentration profiles of all samples have a nearly flat depth of 1~3 μm.

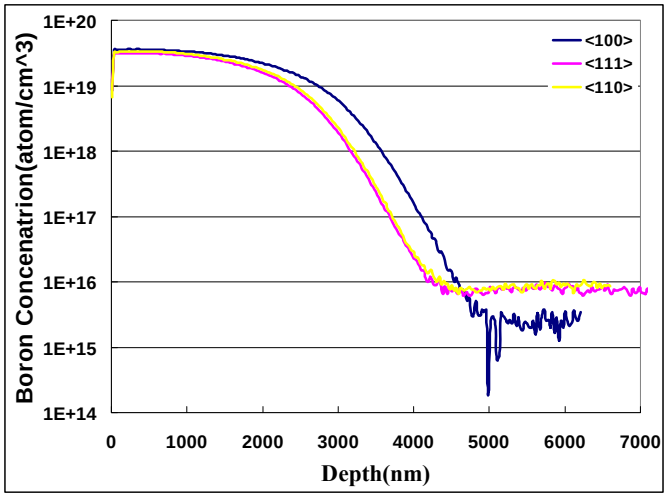

Figure 2. The concentration distribution of different crystal orientation silicon wafers under the same diffusion process conditions.

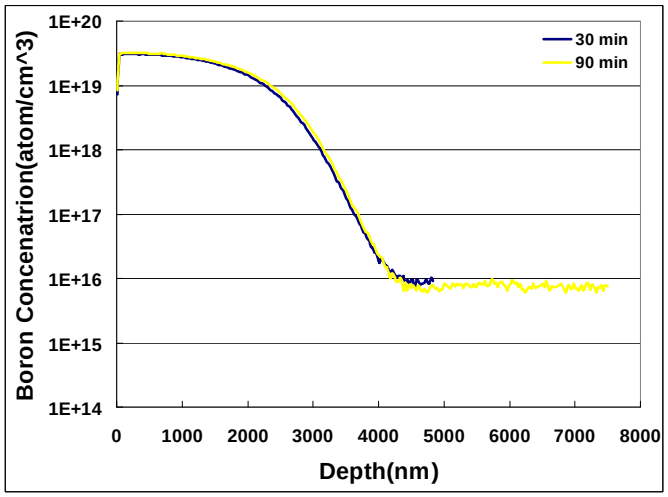

Figure 3. The concentration distribution of the <111>-oriented silicon at different pre-deposition time.

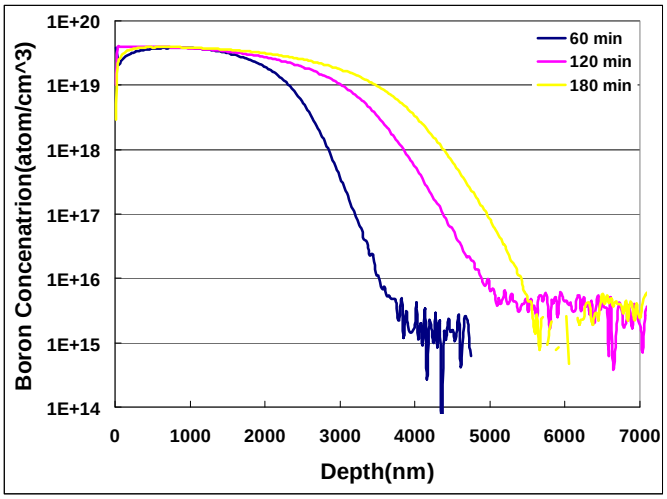

Figure 4. The concentration distribution of the <111>-oriented silicon at different annealing time.

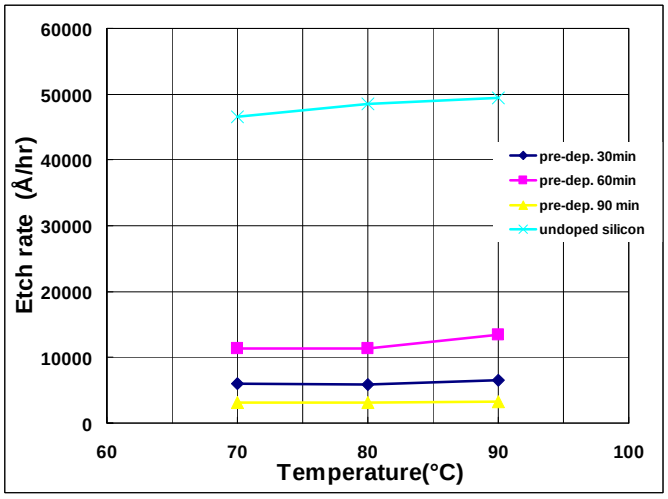

Figure 5. The etch rate of undoped <111> silicon to boron-doped <111> silicon in pure 5% TMAH at various etch temperature.

TABLE II. COMPARISON OF VARIOUS SIMS RESULT OF SAMPLES

Sample	Crystal type	Pre-dep.	Drive-in	Concentration	Depth
1	<100>	90 min	120 min	3.09E+19	1.9μm
2	<111>	90 min	120 min	2.65E+19	2.1μm
3	<110>	90 min	120 min	2.79E+19	2.5μm
4	<111>	60 min	180 min	3.55E+19	2.3μm
5	<111>	60 min	120 min	3.55E+19	1.5 μm
6	<111>	60 min	60 min	3.24E+19	1.9 μm
7	<111>	30 min	120 min	2.51E+19	2.35 μm

B. Etch Rate

Fig. 5 shows the etch rates of the boron-doped <111>-oriented silicon with the drive-in time of 60 minutes and undoped <111>-oriented silicon in the dilute 5% TMAH solution at different etch temperature. The etch rate of undoped <111>-oriented silicon is about 4.8 μm/hr in the 5% TMAH solution at deferent temperatures. The etch rate of the boron-doped <111> silicon is about 0.5 μm/hr in 5% TMAH at deferent temperature.

Fig. 6 shows the etch rates of the boron-doped <111>-oriented silicon with the drive-in time of 60 minutes and undoped <111>-oriented silicon in dual-doped 5% TMAH solution at different etch temperature. The minimum etch rate is about 2500 Å/hr as the diffusion condition is pre-deposition time of 90 minute and drive-in time of 60 minutes.

The etch rates of the undoped <111>-oriented silicon in the dilute TMAH solution is about twice than in the dual-doped TMAH solution. The etch rates of the boron-doped silicon have no much difference in the dilute TMAH and the dual-doped TMAH solution.

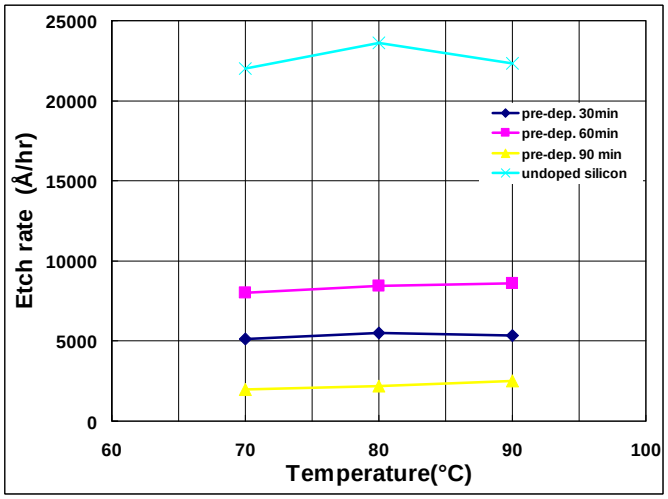

Figure 6. The etch rate of undoped <111> silicon to boron-doped <111> silicon in dual-doped 5% TMAH at various etch temperature.

C. Etch selectivity

Fig.7-8 show the etch selectivity of undoped <111>-oriented silicon to boron-doped <111>-oriented silicon in a dilute TMAH solution and a dual-doped TMAH solution at various etch temperatures. The maximum etch selectivity can be achieve to 15:1 under the diffusion condition of the pre-deposition of 90 minutes and the drive-in of 60 minutes in the dual-doped TMAH solution. The etch selectivity of undoped <100>-oriented silicon to undoped <111>-oriented silicon in dual-doped TMAH solution is about 34. [7] In our work, the etch selectivity of undoped <100>-oriented silicon to boron-doped <111>-oriented silicon in dual-doped TMAH solution is about 260. The etch selectivity of the <111>-oriented silicon substrate to the suspended structures of <111>-oriented silicon can be substantially improved in this study.

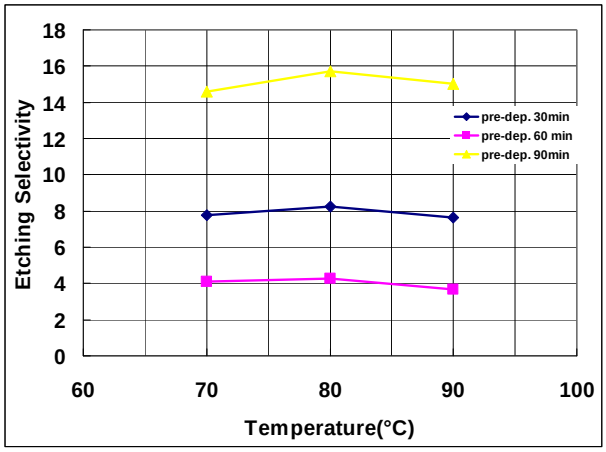

Figure 7. The etch selectivity of undoped <111> silicon to boron-doped <111> silicon at difference pre-deposition time in dual doped 5% TMAH.

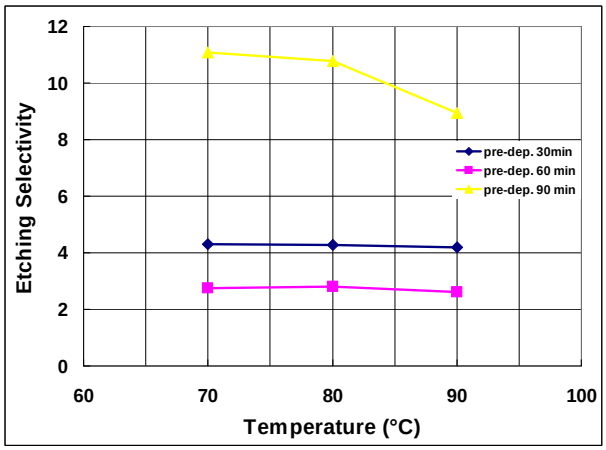

Figure 8. The etch selectivity of undoped <111> silicon to boron-doped <111> silicon at difference pre-deposition time in 5% TMAH.

D. Suspended structures

The Fig.9 shows the SEM pictures of the suspended structures of the <111>-oriented silicon. In order to reduce the etch time and raise filled factor, we design the Y-shaped etching window on the suspended structures of <111>-oriented silicon as shown in Fig.9 (A) (B) (C). The Fig.9 (B) and (D) show the SEM pictures of <111>-oriented silicon with long legs and large area for reducing the thermal conductance of a thermal sensor to promote the sensitivity of the sensor. These suspended structures of <111>-oriented have high filled factor and smooth surface in dual-doped TMAH solutions.

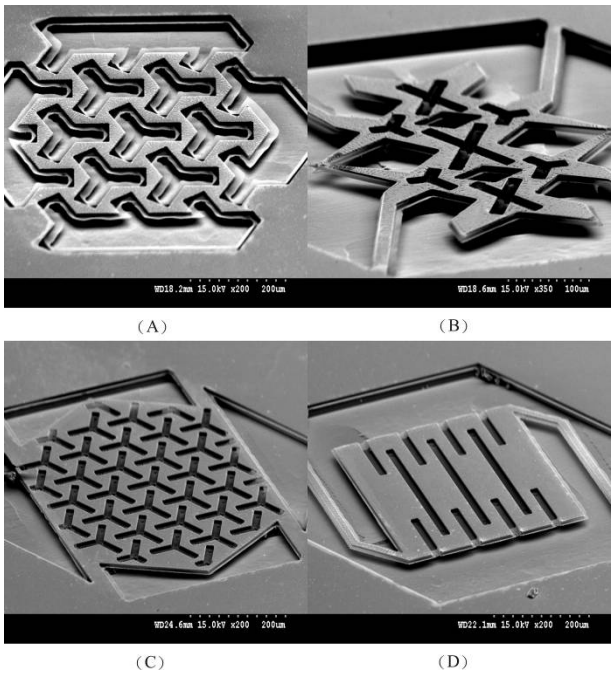

Figure 9. The suspended substrate of SEM.

IV. CONCLUSIONS

In this study, our samples were doped with boron by using BN diffusion process at 1100°C. The SIMS measurement result shows that the profiles of all samples have a nearly flat region of 1~3 μm.

The etch rates of undoped <111>-oriented silicon and boron-doped <111>-oriented silicon with pre-deposition 90 min in the dilute TMAH solution at different etch temperature is about 50000 Å/hr and 2500 Å/hr respectively. The etch rates of the undoped <111>-oriented silicon and the boron-doped <111>-oriented silicon with pre-deposition 90 min are about 25000 Å/hr and 2500 Å/hr in the dilute TMAH solution at different etch temperature respectively. The etch rates of the boron-doped silicon in the dilute TMAH and the dual-doped TMAH solution almost the same.

The etch selectivity of undoped <111>-oriented silicon to boron-doped is 15:1 as the diffusion process is under the pre-deposition time of 90 minutes and the drive-in time of 60 minutes. The etch selectivity of undoped <100> silicon to boron-doped <111> silicon can be achieved to 260. By using the 5% dual-doped TMAH solutions, the suspended structures of <111>-oriented silicon with long legs and large area were successfully manufactured.

REFERENCES

[1] K. Najafi, J. Ji, K. D. Wise, "Multichannel Intracortical Recording Microprobes: Scaling Limitations, Device Characteristisc, and Circuit Encapsulation", Transducers, 1987, June 1987, pp. 344-347.

[2] K. Suzuki, K. Najafi, K. D. Wise, "A 1024-Element High-Performance Silicon Tactile Imager", IEEE, 1988, pp. 674-677.

[3] C. L. Johnson, K. D. Wise, J. W. Schwank, "A Thin-film Gas Detector for Semiconductor Process Gases, IEEE, 1988, pp. 662-665.

[4] Ken Gilleo, Ph.D. "Rimems In Medicine", ET-Trends LLC Warwick.

[5] Schnakenberg, U; Benecke, W and Lange, L. "TMAH etchants for silicon micromachining", IEEE (1991) 815- 818.

[6] J. T. Borenstein, N. D. Gerrish, M. T. Currie, E. A. Fitzgerald, "Etch Selectivity of Novel Epitaxial Layers for Bulk Micromachining", MRS, 1998.,

[7] K. Biswas*, S. Kal , "Etch characteristics of KOH, TMAH and dual doped TMAH for bulk micromachining of silicon".

[8] Seidel, H Csepregi, L; Heuberger, A; BaumgZrtel, H. "Anisotropic Etching of Crystalline Silicon in Alkaline Solutions", J. Electrochem. Soc., Vol. 137, No. 11 (1990) 3626-3632.

[9] Elin Steinsland, Martin Nese, Anders Hanneborg, Ralph W. Bemstein, "Boron Etch-Stop In TMAH Solutions", Sensors and Actuators, Sweden, June 25-29, 1995.

[10] K. Biswas*, S. Das, D.K. Maurya, S. Kal, S.K. Lahiri , "*Bulk micromachining of silicon in TMAH-based etchants for aluminum passivation and smooth surface*".

[11] K. Lian, S. Smith, A.J. Walton, A.M. Gundlach, J.T.M Stevenson, "Characterisation of aluminium passivation for TMAH based anisotropic etching for MEMS applications".

[12] A. Faes, F. Giacomozzi, B. Margesin, A. Nucciotti, "Fabrication of silicon bolometers with bulk micromachining technology". Nuclear Instruments and Methods in Physics Research.

Study on the Acoustic Impedance Matching of Human Tissue for Power Transmitting/Charging System of Implanted Biochip

Yuh-Chung Hu[*1], Po-Lin. Liao[2], Wen-Pin Shih[3], Xuan-Yu Wang[2], and Pei-Zen Chang[2]

[1]*Department of Mechanical and Electro-Mechanical Engineering, National ILan University, ILan, Taiwan.*
[2]*Institute of Applied Mechanics, National Taiwan University, Taipei, Taiwan*
[3]*Department of Mechanical Engineering, National Taiwan University, Taipei, Taiwan.*

***Abstract* — This paper presents an acoustic impedance matching model for the power transmission in human tissue. Utilizing the piezoelectric effect, the acoustic wave provides a feasible way to wirelessly charge the battery of the implanted biochip. A modified matching method from Desilets microwave transmission theory is derived to match the acoustic impedance between the piezo-transmitter/receiver and the human tissue. The lead-zirconate-titanate (PZT, 39.71MRayl) is used to be the material of transmitter/receiver. Based on the results of the modified matching model, the double impedance matching layers are constructed by the aluminum alloy 6061T6 with impedance 17.1MRayl and polymethylmethacrylate (PMMA) with 3.33MRayl. The maximum power gain is 5.55 dB in simulation and 3.13 dB in experiment result**

Keywords —***Piezoelectric transducers, Acoustic impedance matching, Power transmission***

LIST OF SYMBOLS

Z	Characteristic acoustic impedance
$\underline{Z}$	Impedance which consist of equation
A	Area
h	Piezoelectric constant
ε^s	Permittivity of PZT
ρ	Density
v	Particle velocity
V	Phase velocity (Acoustic velocity)
σ	Stress
t	Thickness
U	Voltage
k	Wave number
λ	Wave length
ω	Angular frequency

I. INTRODUCTION

The long-term in-situ medical care and detection by implanted biochip is the trend of the future medical treatment on chronic disease peoples. However, at the present, the non-rechargeable battery is needed to be replaced when its power exhausts. Recently, several solutions were studied for recharging power system. The thermoelectric generator (TEG) utilizes the temperature difference to generate electric power, but limited by the height of device [1].Therefore, the volume reduction of implanted biochip would be a challenge to generate enough power for the micro electromechanical system (MEMS) actuators. The electromagnetic external recharge might be a feasible solution in the near future. However, its effective charging depth would be limited by the human tissue. The conductive human tissue causes the power dispersion which is proportional to the distance between transmission coil and implanted receiver coil [2].

For the purpose of long-distance (0.5-30mm) power transmission from external power transmitter to implanted chip, the acoustic wave is a feasible solution by mechanical impedance matching. Although the ultrasound detection is used for the medical ultrasonography more than 50 years, the acoustic energy absorption efficiency of the implanted receiver body still has not been studied clearly. Kobayashi et al. [3] presented a power and information transmission approach using piezoelectric transmitter and receiver without impedance matching. In Kobayashi's publication, water was used as the transmission path and the transmission efficiency up to 20%.

There have been many discussions over impedance matching of piezoelectric ultrasonic. Two of them belong to the microwave engineering, i.e. maximal flat function and Chebyshev's matching criteria [4]. Most of matching systems use maximal flat function to perform a simple matching (such like $Z_m = \sqrt{Z_{in} / Z_{laod}}$). In these matching models from microwave engineering, infinite thickness of source side is assumed instead of finite value. Desilets [5] and Souquet [6] considered piezoelectric layer as a finite layer and used KLM model [7] and Mason model [8] to modify matching criteria for piezoelectric system respectively. However, these four methods have a common disadvantage. If characteristic acoustic impedance of load and source is fixed, then characteristic acoustic impedance of each matching layers are decided by these matching methods. For PZT transducer to human tissue (the impedance of human tissue is almost the same as agar), it is hard to find exact matching materials for use.

In this paper, the authors establish a one dimensional acoustic power transmission model with matching layer of human tissue sandwiched in between a piezoelectric power transmitter and a piezoelectric power receiver. In order to select the impedance matching materials more easily, the maximum-flat condition of Desilets theory is ignored in this work to obtain more choices of matching material.

*Contact author: ***ychu@niu.edu.tw.***

II. METHODOLOGY

Fig. 1 shows the scheme of power transmission model (transmitter and receiver) with two matching layer. Z_{IN}, Z_{m1}, Z_{m2} *and* Z_t are characteristic acoustic impedance of input, first matching layer, second matching layer and body tissue, respectively. t_1 and t_2 are thickness of each matching material. Acoustic wave transmits from the outside transmitter into the receiver of implanted biochip in the human tissue. The following sections detail the derivation process.

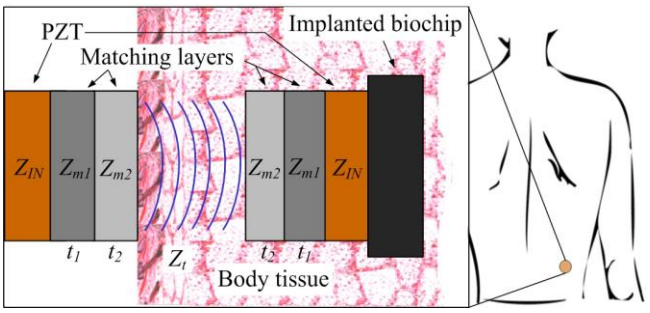

Figure 1. Scheme of piezoelectric transmitter and receiver both with double matching layers sandwich with the human tissue.

A. Power transmission model without matching

Piezoelectric material is an electro-mechanical coupling material. As shown in Fig. 2, if there is an AC voltage applied on a plate made of piezoelectric material, each side of the plate will induce period force (F_1 and F_2) and particle velocity (v_1 and v_2). By combining the theories of elasticity, electromagnetic, and piezoelectricity, the physical behavior of piezoelectricity can be expressed to an analytical equation (1).

$$\begin{bmatrix} F_1 \\ F_2 \\ U \end{bmatrix} = -i \begin{bmatrix} \frac{\bar{Z}}{\tan\theta} & \frac{\bar{Z}}{\sin\theta} & \frac{h}{\omega} \\ \frac{\bar{Z}}{\sin\theta} & \frac{\bar{Z}}{\tan\theta} & \frac{h}{\omega} \\ \frac{h}{\omega} & \frac{h}{\omega} & \frac{1}{\omega C_0} \end{bmatrix} \begin{bmatrix} v_1 \\ v_2 \\ I \end{bmatrix} \quad (1)$$

In equation (1), $\bar{Z} = Z_p A$, $\theta = kt$, $C_0 = \varepsilon^s A/t$, Z_p is characteristic acoustic impedance of piezoelectric material, h is piezoelectric constant, ε^s is permittivity of PZT in constant strain, A is area of cross-section. The relation between force and voltage can be observed in this equation. If there is an initial input voltage, then a reactive force can be induced, which is called direct piezoelectric effect. If there is an initial force applying on each side of the plate, it could induce a voltage out of piezoelectric material, called inverse piezoelectric effect. These two specific behaviors can be used to build an acoustic piezoelectric power transmission model. This power transmission model is built up by equivalent circuit of piezoelectric circuit which was derived by Mason [8], who used Kirchhoff's circuit laws to rearrange the matrix, as shown in (1), into an electro-mechanical circuit. The physical behavior of piezoelectric plate can be easily described and simulated by commercial electronic design software. The power transmission model consists of three parts, which are transmitter, propagation medium considering attenuation effect and receiver. Transmitter is made of piezoelectric material which receives electrical energy and then transforms the electrical energy into acoustic wave to human tissue. Propagation medium is a medium filled in between transmitter and receiver. Receiver is a piezoelectric transducer which receives acoustic wave from human tissue and then transfers the acoustic wave into electrical energy.

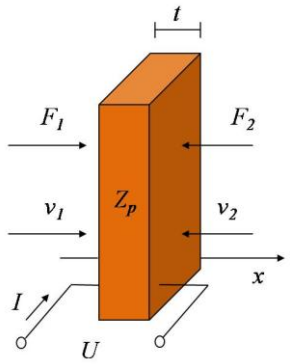

Figure 2. Physical sketch of piezoelectric plate

Fig. 3 shows the whole power transmission system which is a two port system with U_{in} as input and U_{out} as output. F_{out} is the output acoustic wave to human tissue. F_{in} is the input acoustic wave from human tissue to receiver. N represents transformation ratio ($N=hC_0$).

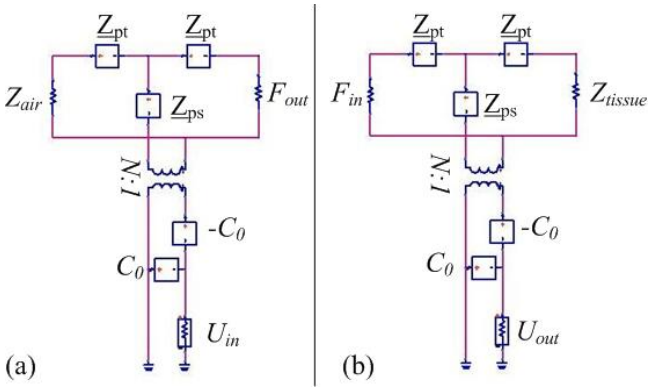

Figure 3. The equivalent circuits of power transmission model without matching layer (a) transmitter (b) receiver

B. Matching layer designing

One dimensional piezoelectric power transmission model has been derived in last section. However, that model has not been optimized yet. In general, adding matching layer in acoustic device can improve efficiency of power transmission. In acoustic matching, there has been a lot of discussion [5, 6] but the most important purpose of them is to obtain maximum bandwidth of transmission. This purpose could have some limitation on choosing matching material, while the bandwidth is not as important for the present transmission model. In this paper, the authors bring up a matching method which has less limitation on choosing matching material.

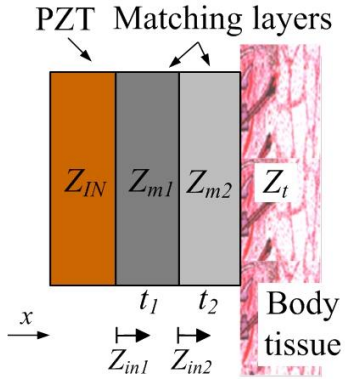

Figure 4. Sketch of transmitter in power transmission model

$$\begin{cases} \sigma(x) = Ae^{-kx} + Be^{kx} \\ v(x) = \dfrac{1}{\rho V}(Ae^{-kx} - Be^{kx}) \end{cases} \tag{2}$$

Equation (2) shows the stress and particle velocity in medium (at point x), As shown in Fig. 4, the acoustic impedance in medium is defined as the ratio of stress and particle velocity, that is

$$Z(x) = \frac{\sigma(x)}{v(x)} = Z\frac{(1-C^2) - i(2C)(\sin 2\theta)}{C^2 - 2C(\cos 2\theta) + 1} \tag{3}$$

where $C=A/B$ and A and B are constant, Z is characteristic acoustic impedance of medium. The acoustic impedance seeing into medium from each interface is shown in (4).

$$\begin{cases} Z_{in1}(x) = Z_{m1}\dfrac{(1-C_1^{\,2}) - i(2C_1)(\sin 2\theta_1)}{C_1^{\,2} - 2C_1(\cos 2\theta_1) + 1} \\ Z_{in2}(x) = Z_{m2}\dfrac{(1-C_2^{\,2}) - i(2C_2)(\sin 2\theta_2)}{C_2^{\,2} - 2C_2(\cos 2\theta_2) + 1} \end{cases} \tag{4}$$

There are 6 unknowns in (4). They can be solved by the imaginary and real part of three boundary conditions. The solutions of (4) are shown in (5).

$$\begin{cases} t_1 = \dfrac{\lambda_1}{4} \\ t_2 = \dfrac{\lambda_2}{4} \\ \dfrac{Z_{m1}}{Z_{m2}} = \left(\dfrac{Z_{IN}}{Z_t}\right)^{\frac{1}{2}} \end{cases} \tag{5}$$

The thicknesses of matching layers are both quarter wavelength, and the ratio of Z_{m1} to Z_{m2} is constant while Z_{IN} and Z_{m2} are fixed. However Z_{IN} is not equal to characteristic acoustic impedance of PZT (Z_p). Therefore, the characteristic acoustic impedance of input material needs to be modified. Further modifying (5) from Desilets [5] results in (6). Equation (6) would be used for designing matching layer in power transmission system.

$$\begin{cases} t_1 = \dfrac{\lambda_1}{4} \\ t_2 = \dfrac{\lambda_2}{4} \\ \dfrac{Z_{m1}}{Z_{m2}} = \left(\dfrac{Z_p}{Z_t}\right)^{\frac{3}{7}} \end{cases} \tag{6}$$

III. EXPERIMENT AND DISCUSSION

To verify the present model and matching method, we conduct an experiment to test impedance, reflection coefficient (S_{11}) and the power gain of power transmission model. We made two pairs of transmitters and receivers. One is consist of only two piezoelectric layers and propagation medium, another is consist of two piezoelectric layers with matching layers and propagation medium. Fig. 5 shows the framework of the experiment, both the transmitter and receiver are combined with matching layers. The propagation layer is agar and the thickness is 10mm. The piezoelectric layer is made of PZT (Eleceram, Inc., Taoyuan, Taiwan). The first matching layer is aluminum alloy (6061T6) while the second matching layer is PMMA (acrylic). Each layer is adhered by epoxy resin SA-58 (Silmore, Taipei, Taiwan). After spreading adhesive on each layer, C-shape fixture is used to hold the shape of device about 22 hour to let the adhesive layer dry. We use agar as the propagation layer to imitate human tissue, because the characteristic of these two materials are almost the same. The diameter of each layer is 16mm. The PZT layer is 2.1mm thick. Aluminum alloy and PMMA are 1.6mm and 0.68mm thick, both are quarter wavelength. The characteristic acoustic impedances of each material are shown in Table I. According to (6), the ratio of Z_{m1} to Z_{m2} should be 4.07. Aluminum alloy and PMMA, with ratio of 5.13, are used. The power transmission model with matching layers is shown in Fig. 6. Propagation medium is assumed as a half-infinite medium in the model. The electrical impedance of transducer is measured by Agilent 4395 precision impedance analyzer. The power gain and S_{11} are measured by Agilent 8714ES network analyzer.

TABLE I. MECHANICAL PROPERTIES OF MATERIALS USED FOR ACOUSTIC WAVE TRANSMISSION

	Density (kg/m^3)	***Acoustic Velocity (m/s)***	***Acoustic Impedance (MRayl)***
PZT	8000	4963	39.71
Al alloy 6061T6	2671	6400	17.1
PMMA	1184	2814	3.33
Agar	1069	1463	1.56
Human tissue	1490~1610	1060	1.58~1.70

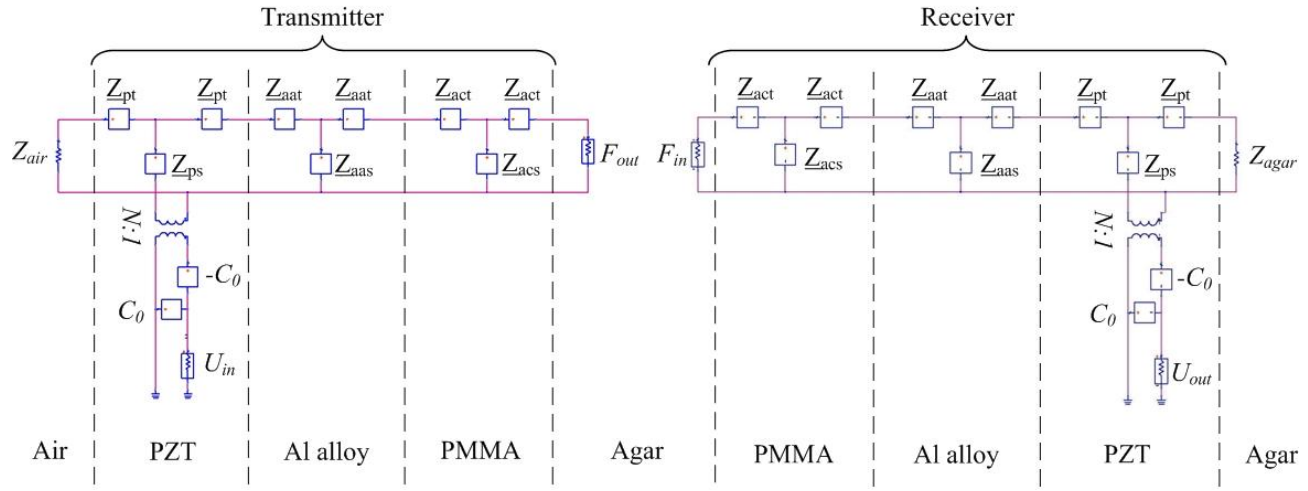

Figure 6. Power transmission model with matching layer

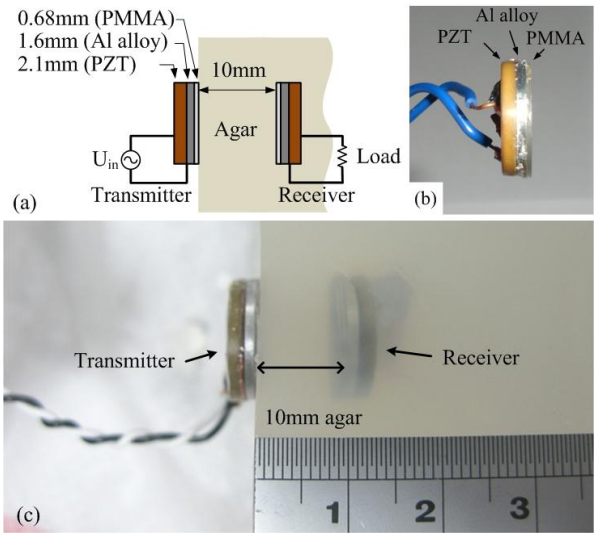

Figure 5. (a) The framework of power transmission which includes the piezo-transmitter, agar (imitating human tissue) and piezo-receiver, (b) the piezo-transmitter/receiver and (c) the picture of power transmission experiments

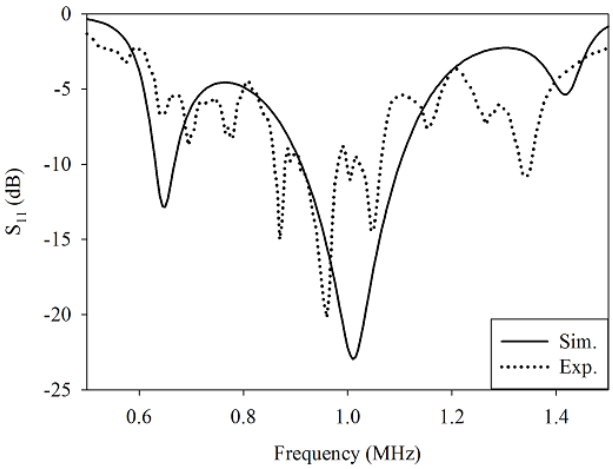

Figure 7. Reflection coefficient (S_{11}) of transmitter

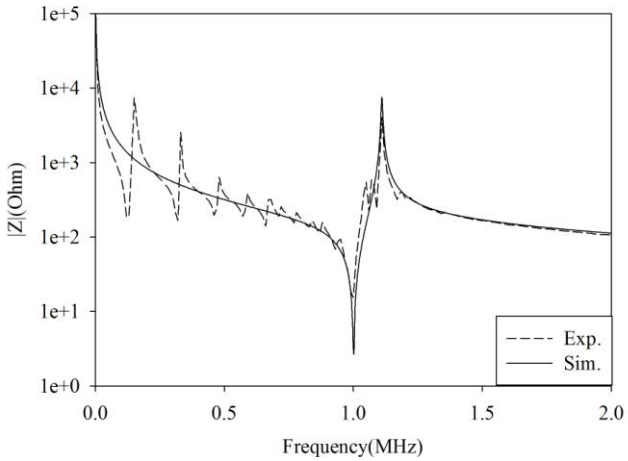

Figure 8. Electrical impedance of PZT layer

Fig. 7 shows the comparison between the simulated and measured impedance results of piezoelectric layer. The first resonance frequency of thickness mode is 1MHz. Peaks under 1MHz are radial mode resonance of piezoelectric layer, which are not concerned in this paper. The S_{11} of transmitter with matching layers is shown in Fig. 8. Simulation result shows that the reflection coefficient at 1 MHz is -23dB, which means about 99.5% power is transmitted into transmitter. Fig. 9 and 10 show the power gain of unmatched and matched system respectively. The central frequency of device has shifted lower about 0.03MHz. Simulations results in Fig. 9 and 10 are derived from the equivalent circuits shown in Fig. 3 and 6 respectively. We used $\alpha=0.79/cm$ as attenuation coefficient in simulation. The maximum power gains are remarkably increasing in simulation result (from -12.41dB to -6.86dB).

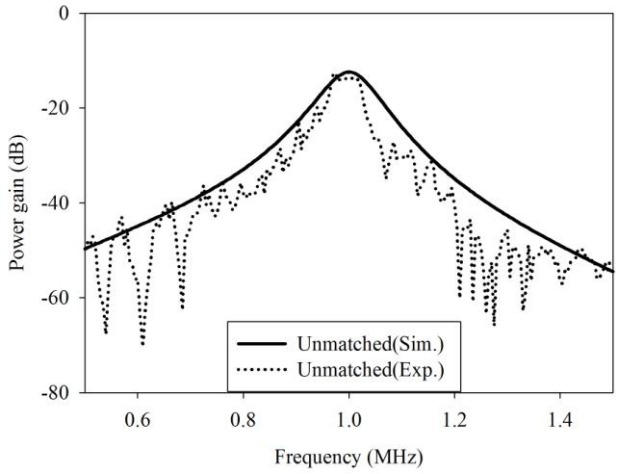

Figure 9. Simulation and measurement power gain of unmatched system

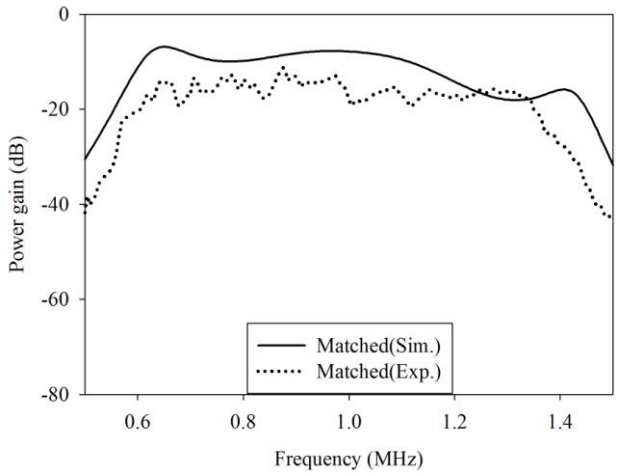

Figure 10. Simulation and measurement power gain of matched system

In experiments, the maximum power gains in unmatched and matched system are -12.41dB and -9.28 respectively. The maximum power gain has been increased 5.55dB in simulation result while 3.13dB in experiment result. The bandwidth has also been improved. In experiment, -20 dB bandwidth of unmatched and matched are 9% and 78% respectively. The attenuation coefficient is assumed to be proportional to frequency, but the relation between attenuation coefficient and frequency are not proportional in every material. Therefore, the error deviating from center frequency can be interpreted. There are some lower peaks in experiment results because of the agar is not a perfect half-infinite material in reality.

IV. Conclusion

This paper presents a one dimensional piezoelectric power transmission model and a matching method. By given geometric parameters, characteristic acoustic impedance, and piezoelectric constant, two results can be analyzed, which are reflection coefficient and power gain of the power transmission model. The present matching method can be used to increase the power gain of the power transmission system. It can also be predicted by the present model. In the future, the size of transmitter and receiver could be reduced, and could combine with implanted chip and biosensor.

Acknowledgment

The authors would like to thank C.W. Lin to correct this article.

References

[1] M. Strasser, R. Aigner, C. Lauterbach *et al.*, "Micromachined CMOS thermoelectric generators as on-chip power supply," *Sensors and Actuators A: Physical*, vol. 114, no. 2-3, pp. 362-370, 2004.

[2] H. Z. T. Chen, "A Study of RF Power Attenuation in Bio-tissues," *Journal of Medical and Biological Engineering*, vol. 24, no. 3, pp. 141, 2004.

[3] S.-n. Suzuki, S. Kimura, T. Katane *et al.*, "Power and Interactive Information Transmission to Implanted Medical Device Using Ultrasonic," *Japanese Journal of Applied Physics*, vol. 41, no. Part 1, No. 5B, pp. 3600, 2002.

[4] D. M. Pozar, *Microwave engineering*, Hoboken, NJ: J. Wiley, 2005.

[5] C. S. Desilets, J. D. Fraser, and G. S. Kino, "The Design of Efficient Broad-Band Piezoelectric Transducers," *IEEE Transactions on Sonics and Ultrasonics*, vol. 25, no. 3, pp. 115-125, 1978.

[6] J. Souquet, P. Defranould, and J. Desbois, "Design of Low-Loss Wide-Band Ultrasonic Transducers for Noninvasive Medical Application," *IEEE Transactions on Sonics and Ultrasonics*, vol. 26, no. 2, pp. 75-80, 1979.

[7] R. Krimholtz, D. A. Leedom, and G. L. Matthaei, "New equivalent circuits for elementary piezoelectric transducers," *Electronics Letters*, vol. 6, no. 13, pp. 398-399, 1970.

[8] W. P. Mason, *Electromechanical transducers and wave filters*, New York: D. Van Nostrand Co., 1948.

Numerical investigation of the effect of the transducer pulse on the drop ejection process

Jr-Ming Lai[1],and Jenn-Der Lin[1,*]

[1]*Department of Mechanical Engineering, National Chiao Tung University, 1001 Ta Hsueh Road, Hsinchu 30050, Taiwan*

***Abstract* — This study presents a detailed investigation on the effect of components of a single transducer pulse on the drop ejection process for a Picojet printhead, commercially available drop-on-demand (DOD) ink jet device. It is found in current results that the volume of the primary drop is closely related to the maximum displacement, Df of chamber wall induced by piezoelectric transducer in forward stage, while the velocity of the primary drop is dependent on the ratio of Df and $\Delta\tau$f, the time period of the forward stage. Moreover, the volume and the velocity of the primary drop are weakly dependent upon the conditions of the backward stage. It is also found that a decrease in time interval connecting forward stoke and backward stoke may suppress the formation of the satellite drops.**

Keywords — ***micro-fluidic, drop ejection, transducer-pulse, picojet printhead***

I. INTRODUCTION

Recently increased attention has been given to the inkjet printing in searching for new fabrication methods for oligo-nucleotide microarrays [1], color filter of liquid crystal display panels [2], multicolor polymer light-emitting diode displays [3], visualizing protein distribution [4] and transistors [5]. Microarrays consisting of a solid support with multiple probe sites bearing capture molecules that can specifically bind to a target molecule are currently used in the widespread range of genomic and medical diagnostics due to its rapid identification of disease states and gene expressions [6]. One of the key steps in the fabrication of microarrays is the deposition of capture molecules onto the substrate that requires the maximum number of probe sites increasing the amount of target species and small size of these sites decreasing the volume of capture molecules. The inkjet printing with piezoelectric actuator is particularly suitable for this deposition owing to its noncontact and precisely controlled manner, and the large extent of liquid compatibility. The basic mechanism of piezoelectric actuation is that when a voltage signal is applied to a piezoelectric transducer arranged to form one wall of the printhead chamber, it changes its dimensions and thus causes the contraction of chamber volume and dispensing drops out of the nozzle. With different fluids containing different capture molecules in the microarray fabrication, a suitable adjustment of the voltage signal applied to piezoelectric transducer is the key to precise micro-fluidic control. In most drop-on-demand (DOD) applications, the voltage waveform used to drive the piezoelectric actuator is a square-wave pulse or a succession of two square-wave pluses. The early experimental studies [7, 8] have focused mainly on the influence of the maximum amplitude and frequency of voltage signals on the drop ejection behaviors and on seeking optimal range of operating conditions in which the satellite drops fail to form based on trial-and-error method. While numerical calculations in the early researches [9, 10] have been focused on the fundamental understanding of the fluid mechanics of DOD inkjet printing that in generally involves the elucidation of the competition between the flow directed toward the nozzle outlet and that directed away from it, based on simplified printhead configuration and ideally imposed flow rate or pressure pulse function of time upstream of the nozzle outlet.

In this paper, we systematically divide a single transducer pulse with a so-called bipolar waveform composed of a succession of two square-wave pulses, the first is positive and the second negative, into components and completely investigate the effects of these components and their various combinations on the drop ejection in terms of volume, speed and breakup time of the primary drop and the formation of the satellite drops.

II. MATHEMATICAL MODELS AND COMPUTATIONAL METHODS

In the present study, we investigate the drop ejection behaviors of a Picojet printhead with the bend mode design of piezoelectric actuator [11]. We consider a system with isothermal, incompressible Newtonian fluid of constant density and constant viscosity. The origin of coordinate is based at the center of the nozzle exit plane and the axially unit vector is directed to the direction away from nozzle. Fig. 1 shows the schematic diagram of the Picojet printhead configuration considered and the numerical grids used in this study. The dimensions of pressure chamber are 1880 μm in length, 980 μm in width and 200 μm in height as well as those of ink supply channel are 1440 μm, 550 μm and 100 μm in length, width and height respectively. Moreover, the diameter of the nozzle outlet is 34.3 μm. It is well accepted that the dynamics of the drop formation phenomena are governed by the continuity and the Navier-Stokes equations subject to the appropriate boundary and initial conditions.

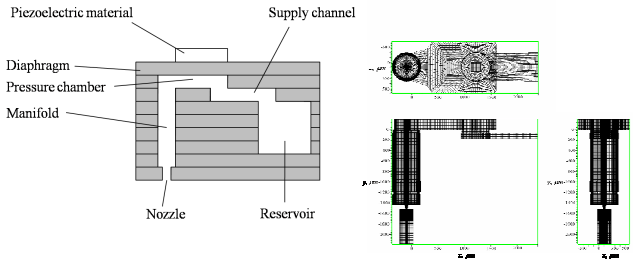

Figure 1. (a) Schematic diagram of Picojet printheadand and (b) numerical grids of Picojet printhead..

*Contacting author: Jenn-Der Lin is with the Department of Mechanical Engineering, National Chiao Tung University, 1001 Ta Hsueh Road, Hsinchu 30050, Taiwan (**Tel.: +886-35-712121. E-mail address: jdlin@cc.nctu.edu.tw) .***

In order to distinguish the dependent parameters and variables, nondimensionalization of governing equations, initial conditions and boundary conditions are conducted by using the radius of the orifice, R and capillary time, $t_c = \sqrt{\rho R^3/\sigma}$ where ρ and σ are the density and surface tension, as the characteristic length and time. Under the assumption that the fluid obeys the linear Newtonain friction law and neglect the compressibility effects, these equations can be written in the non-dimensional forms as what follows:

$$\nabla \cdot \underline{v} = 0 , \tag{1}$$

$$\frac{1}{Oh}[\frac{\partial \underline{v}}{\partial t} + \underline{v} \cdot \nabla \underline{v}] = \nabla \cdot [-p\underline{\underline{I}} + \nabla \underline{v} + (\nabla \underline{v})^T] + G\underline{k} \tag{2}$$

where t is time in units of t_c, $\underline{v}$ velocity vectors in units of $U = R/t_c$, p static pressure in units of $\mu U/R$ with μ denoting the viscosity of fluid, $\underline{\underline{I}}$ identity tensor, $\underline{k}$ gravitational unit vector, $Oh = \mu/\sqrt{\rho R\sigma}$ Ohnesorge number and $G = \rho R^2 g/\sigma$ Bond number. Except for the no-slip and no-penetration conditions at solid walls, the traction boundary condition at the free surface must be satisfied

$$\underline{n} \cdot [-p\underline{\underline{I}} + \nabla \underline{v} + (\nabla \underline{v})^T] = Oh\underline{n}\nabla \cdot \underline{n} . \tag{3}$$

where $\underline{n}$ is the local unit normal vector at free surface.

The physical phenomena of the drop formation involve the complex topological change of the liquid-air interfacial flow such as liquid break-up and coalescence. One of the thorniest problems researchers face in the numerical analysis is the mathematical description of the free surface. The probable solutions may arise either from Lagrangian methods or Eulerian methods. The former configure the mesh to adapt continuously to the time-dependent deformation of liquid-air interface, whereas the latter employ the fixed mesh through which the arbitrarily shaped interface moves. Although maintaining the discontinuity of the liquid-air interface with fidelity, Lagrangian methods have a difficulty dealing with the severe distortion of mesh allied to the complex topological change in the liquid-air interface. As an example, the Lagrangian finite element (FE) method can reasonably predict the development of the microthreads and overturning yet not the dynamics near the point of necking and pinch-off [10]. Here, we utilize an interface-capturing method, the variation of the volume-of-fluid (VOF) scheme and belonging to the Eulerian type, to resolve this transient behavior of free surface separating two incompressible and immiscible fluids in the drop formation process [12]. The most characterizing feature in this interface-capturing method is that the two fluids are considered as one effective fluid by a scalar variable, F, called volume fraction function. Suppose that the properties of the air and liquid are denoted by subscripts 1 and 2, respectively, and let V_2 and M_2 be the volume and mass of the liquid. V_2 and M_2 are then given as

$$V_2 = \int F dV , \tag{4}$$

$$M_2 = \int F\rho_2 dV \tag{5}$$

where F represents the volume fraction function and ρ_2 liquid density. The total volume V is then given by

$$V = \sum_{K=1}^{2} V_K . \tag{6}$$

Considering the mass conservation and constant fluid properties, we obtain the volume fraction evolution equation as follows:

$$\frac{\partial F}{\partial t} + \underline{v} \cdot \nabla F = 0 . \tag{7}$$

By definition, the volume fraction function is a ratio of volume occupied by liquid in a computational cell to total cell volume and takes the value 1 in the liquid side and the value 0 in the air side. The crossover region (0<F<1) depict the free surface, whose actual position generally defines at the value F=0.5. The critical issue in this free-surface capturing method is the discritization of convective term in (7). Here, we particularly use multidimensional upsplit advection algorithm along with piecewise linear interface construction (PLIC) scheme to discrete this convective term [12]. Moreover, surface tension at free surface is modeled in the numerical simulation with a localized volume force in the framework of the continuum surface force (CSF) model proposed by Brackbill et al. [13] and ideally suited for Eulerian interfaces of arbitrary topology. Notice that (7) must be coupled with (1) and (2). Velocity vectors are first updated by solving (1) and (2), then substituted into (7), so that the redistribution of the volume fraction function can be obtained. We suppose that the solid wall boundaries meet the no-slip and no penetration conditions. For the outlet boundaries surrounding the external flow field, the pressure conditions are set to be 1 atm.

In order to validate the present theoretical models, all computations were performed by the multipurpose commercial code, CFD-ACE+ based on the finite volume numerical method for solving three-dimensional Navier-Stokes equations and the iterative semi-implicit method for pressure-linked equations consistent (SIMPLEC) for velocity-pressure coupling. Diffusion fluxes are approximated by central differences. Here, the explicitly first-order backward Euler scheme is used for time discretization. The primary variables are the velocity, pressure and volume fraction, which cannot be determined until convergent criteria are satisfied for each time

step. The full theoretical model of the piezoelectric DOD inkjet printhead involves the coupling of structural, electric and interfacial flow fields. The direct coupled-field simulation of this printhead may require a considerable computing power and costs. In order to circumvent the inherent difficulties of this coupled-field simulation, we utilized a time-depended function of the wall displacement with a trapezoid shape and higher order vibration ripples ignored to model the variation in time of deformable diaphragm caused by the bending effect of the piezoelectric material, as shown in Fig. 2a. The piezoelectric material deflects outward in the time period of $\nabla\tau_s$, and stays unmoving in $\nabla\tau_{p1}$, enlarging the pressure chamber and causing liquid to fill it. In the time periods of $\nabla\tau_f$ and $\nabla\tau_{p2}$, the piezoelectric material in this so-called forward stage moves inward and keeps still to reduce the chamber volume and cause the liquid to be ejected from the nozzle outlet. In the time periods of $\nabla\tau_b$ and $\nabla\tau_{p3}$, the piezoelectric material resumes its equilibrium state, known as the backward stage. Fig. 2b shows the variation in time of basic voltage signal applied to Picojet printhead and wall displacement related to equilibrium state at the centroid of chamber wall adjacent to piezoelectric material. Considering the case of the microarrays that the capture molecules are commonly dissolved in aqueous solution with some additives, we here use the fluid whose density, viscosity and surface tension are 1000 kg/m^3, 3.5 cp and 0.0725 N/m, respectively.

III. RESULTS AND DISCUSSION

A. *Grid convergence study and model validation*

The numerical grids of the Picojet printhead used in this study for the drop ejection simulations are illustrated in Fig. 1b. The computational domain can be divided into five parts: the ink supply channel, the ink chamber, the manifold, the nozzle and the area outside the nozzle. In order to achieving a uniform distribution of the discretization errors, we utilize a non-uniform grids which adopt a small grid spacing in regions such as the neighborhood of the nozzle, the immediate solid walls and the trajectory of the flight drops where the derivatives of the variables are changed severely and large discretization errors may be expected. All numerical grids are three-dimensional hexagon with the smallest spacing of 1.5 μm, which corresponds to the criterion that with the VOF method, a minimum of 4-5 cells are required across the gap to provide adequate resolution of the free surface in that gap.

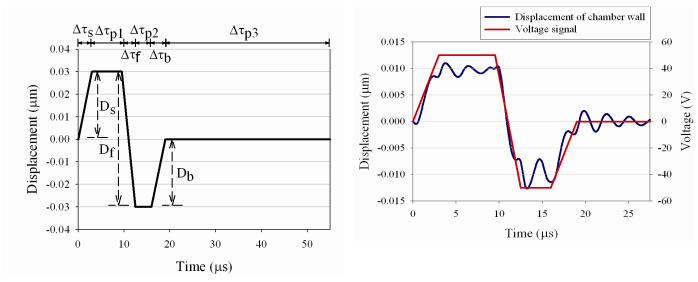

(a) (b)

Figure 2. (a) Time-depended function of the wall displacement and (b) profile in time of voltage signal and the displacement of the wall adjacent to piezoelectric transducer..

For the grid dependence tests, we devised the total number grids of 186898, 282408 and 411654 cells with adding 10 % of the total grid points in each dimension. Table Ⅰ-Ⅲ show the time of drop breakup, the volume of primary drop and drop head velocity defined as a measured velocity at tip of the drop using various mesh. It appears that the change in the computed quantity of interest is monotonic and difference in this quantity decreases with grid refinement. Therefore, satisfactory grid independence can be attained using a mesh setup of 282408 cells. Fig. 3 shows the comparison of the predictions with Yang et al.'s experimental observations of the time evolution of the drop tip position [11]. As can be seen, a reasonable agreement is obtained between the experiment and simulation.

TABLE I. DROP HEAD VELOCITY FROM VARIOUS MESHES

Time (μs)	186,898 (cells)	282,408 (cells)	411,654 (cells)
	Head velocity (m/s)		
15	5.81632	5.59234	5.66525
20	4.00525	4.15712	4.20037
25	2.97289	2.93412	2.83467
30	2.629	2.7965	2.65067
35	3.09152	3.19418	3.25551
40	2.84138	2.58049	2.46021
45	2.88741	2.40329	2.85257
50	2.75959	2.90791	2.75984
55	2.72461	2.37852	2.4972
60	2.66566	2.62038	2.75403

TABLE II. PRIMARY DROP VOLUME FROM VARIOUS MESHES

Time (μs)	186,898 (cells)	282,408 (cells)	411,654 (cells)
	Primary drop volume (pl)		
40	6.89494	7.34343	7.45479
42	6.87908	7.2838	7.44344
44	6.86204	7.25728	7.45349
46	6.8256	7.25934	7.43663
48	6.829	7.22777	7.41565
50	6.79859	7.19942	7.40755
55	6.74308	7.15191	7.38039

TABLE III. DROP BREAKUP TIME FROM VARIOUS MESHES

186,898 (cells)	282,408 (cells)	411,654 (cells)
Time to break-up (μs)		
30.512	30.512	30.515

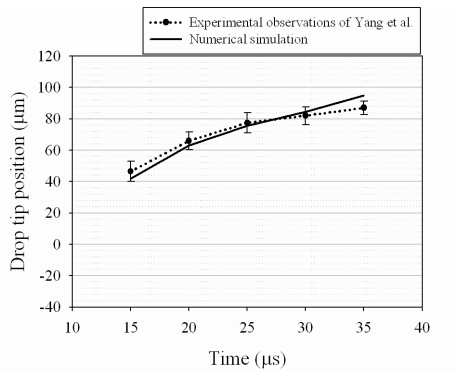

Figure 3. Comparison between the experiment and the numerical simulation.

B. *Forward stage*

In order to investigate the effect of $D_f, \Delta\tau_f$, and $D_f/\Delta\tau_f$ on the drop ejection process, a set of 6 numerical experiments were conducted, as shown in Table Ⅳ. The disruptions of fluid interface fail to happen in the experiment 2, while experiment 1with D_f increased to 0.06 μm and experiment 3 with $\Delta\tau_f$ decreased to 1.5 μs could lead to the drop breakup successfully. It would appear that an increase in the value of $D_f/\Delta\tau_f$, which represents the rate of chamber volume displacement and could be related to the Weber number (inertial/surface tension force), $We \equiv \rho Q^2/(\pi^2\sigma R^3)$ where ρ is fluid density, σ fluid surface tension, Q the rate of chamber volume displacement and R nozzle exit radius, is needed for successful drop ejection in experiment 2. Fig. 4 shows the volume variation of the primary drop in these different situations. The drop volume in experiment 1 equals that in experiment 5 and the drop volume in experiment 3 equals that in experiment 6, approximately. Moreover, the drop volume in experiment 4 is close to that in experiment 7. It illustrates that the drop volume fall into three zones which correspond to the three distinguishable values of D_f. Fig. 5 shows the velocity variation of the center-of-mass of the primary drop upon breakup in these cases. It is seen that the primary drop velocity increases substantially as $D_f/\Delta\tau_f$ is increased, therefore causing inertial force increased. Moreover, experiment 1, 3 and 4 show that the drop velocity is positively correlated with the primary drop volume. The similar relation could be seen in the experiment 5 and 6. It is certain that the large amount of ejected liquid could reduce restoring effect of surface tension by the less curvature of the fluid interface and is in agreement with the results of Feng [9]. Fig. 6 shows the variation with time of the volume flow rate at the nozzle entrance plane. It is appear that the total volume entering the nozzle during the forward stoke of the actuation in experiment 3 and representing the area underneath the line in Fig. 6a is 15.268 pl, whereas that in experiment 6 is 19.725 pl. Fig. 6b, moreover, shows that the total volume entering the nozzle during the forward actuation in experiment 7 is more than that in experiment 4. These results suggest that on account of mass conservation, the total volume ejected from the nozzle increases when the value of $D_f/\Delta\tau_f$ increases and that of D_f keeps constant. The variation of drop shapes at breakup with cases is shown in Fig. 7. The breakup time in experiment 3 is smaller than that in experiment1 and 4. It would seem that the breakup time increases as D_f increases and $D_f/\Delta\tau_f$ keeps constant. A possible explanation for this is that the large amount of ejected liquid corresponding to a large value of D_f could reduce the effect of driving breakup of surface tension by the small curvature of fluid interface. However, as mentioned above, the large ejected volume of liquid could weaken the restoring effect of surface tension and then has large forward momentum density, which facilitate drop breakup by fast elongation and necking, as shown in Fig. 5. Moreover, when $D_f/\Delta\tau_f$ is at large value, the increase in forward momentum density due to the increase in the ejected liquid volume is relatively larger, as shown in Fig 5. The breakup time in experiment 5 is smaller than that in experiment 6 since the driving breakup effect of increasing forward momentum density induced by increasing D_f is dominant, as shown in Fig. 7. Fig. 7 also shows that the breakup time of drop in experiment 5 is smaller than that experiment 1. It is possible

TABLE IV. LIST OF EXPERIMENTS TO FORWARD STAGES

Experiment	Supply stage			Forward stage			Backward stage	
	D_s (μm)	$\Delta\tau_s$ (μs)	$\Delta\tau_{p1}$ (μs)	D_f (μm)	$\Delta\tau_f$ (μs)	$\Delta\tau_{p2}$ (μs)	D_b (μm)	$\Delta\tau_b$ (μs)
Expt. 1	0.03	3	9	0.06	3	3.5	0.03	3
Expt. 2	0.03	3	9	0.03	3	3.5	0.03	3
Expt. 3	0.03	3	9	0.03	1.5	3.5	0.03	3
Expt. 4	0.03	3	9	0.12	6	3.5	0.03	3
Expt. 5	0.03	3	9	0.06	1.5	3.5	0.03	3
Expt. 6	0.03	3	9	0.03	0.75	3.5	0.03	3
Expt. 7	0.03	3	9	0.12	4.8	3.5	0.03	3

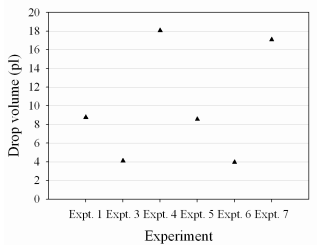

Figure 4. Volume variation of primary drop in experiments.

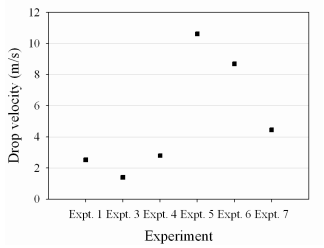

Figure 5. Velocity variation of primary drop in experiments.

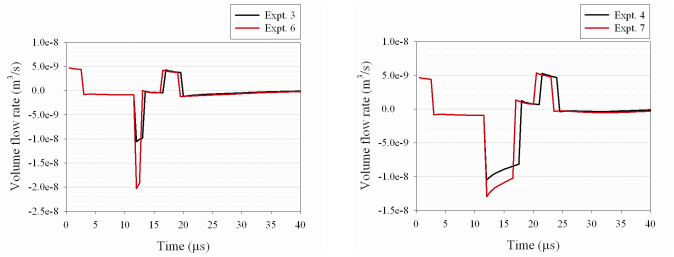

(a) (b)

Figure 6. Variation with time of the volume flow rate at the nozzle entrance plane.

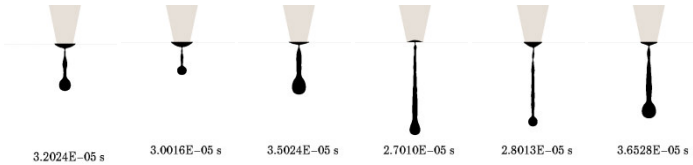

Expt. 1 Expt. 3 Expt. 4 Expt. 5 Expt. 6 Expt. 7

Figure 7. Variation of drop shapes at breakup with cases.

that when $D_f/\Delta\tau_f$ increases, the forward momentum density increases, which accelerates the drop breakup by fast elongation and necking and shown in Fig. 5. The similar relation can also be found between experiment 3 and 6. However, as shown in Fig. 6, when the value of $D_f/\Delta\tau_f$ increases, the ejected liquid volume increases, thus reducing the effect of driving breakup of surface tension and then decelerating the drop breakup. It is found in Fig. 7 that the breakup time in experiment 7 is greater than that in experiment 4 on account of the suppression of the driving breakup effect induced by the increase in ejected liquid volume when $D_f/\Delta\tau_f$ in experiment 7 is slightly larger than that in experiment 4.

C. Backward stage

Table Ⅴ shows the variation of the conditions of the backward stoke in five numerical experiments for the investigation of the effect of D_b, $\Delta\tau_b$ and $D_b/\Delta\tau_b$ on the drop ejection process. Fig. 8 shows the volume variation of the primary drop in these different experiments. It is noticed that the drop volumes are approximately the same in all cases. Fig. 9 shows the velocity variation of the center-of-mass of the primary drop upon breakup in these different situations. The measured values of the drop velocity in all experimental conditions fall into the same range. It is possible that the backward inertial force in all these cases is insufficient for drawing all ejected liquid back and the meniscus would invade the tube on account of mass conservation. Under the effect of the reversed flow caused by the backward actuation, liquid interface near the nozzle exit plane tends to be drawn back and the curvature of the interface becomes more and more negatively large. Therefore, after the period of the backward actuation ends up, the liquid in the nozzle would be pulled out again due to the effect of the imbalance of surface tension force and the inertia of the liquid in ink supply channel. The extent of tube invasion by the retracting meniscus as well as the acceleration of the thinning of fluid neck increase as $D_b/\nabla\tau_b$ increases. Experiment 8, the condition of the backward actuation of which has the same value of $D_b/\Delta\tau_b$ with experiment 9 but large working time interval, $\Delta\tau_b$, shows larger extent of tube invasion and the negatively large curvature of the liquid interface, thus causing the larger volume flow rate of the liquid toward the nozzle outlet. Fig. 10 shows the variation of the volume flow rate at the nozzle entrance plane with time. Upon the end of the backward stoke, the volume flow rate at the nozzle entrance plane is directed toward the nozzle outlet and turns gradually into the still state as time goes. As mentioned above, experiment 8 has the negatively larger volume flow rate compared to experiment 9 owing to large curvature of the retracting meniscus. In a similar fashion, experiment 11 may be expected to have negatively larger volume flow rate than the experiment 10, as shown in Fig. 10. Fig. 11 shows the variation with cases of the breakup shapes of drops. It would appear that drop breakup occurs in two different types in terms of the breaking point inside or outside the nozzle, as shown in Fig. 7 and 11. Experiment 11 seems to have the smallest breakup time. It is possible that the backward actuation of experiment 11 goes through a considerable period in which drop breakup occurs before the volume flow rate of liquid toward the nozzle outlet begins owing to the imbalance of surface tension.

TABLE V. LIST OF EXPERIMENTS TO BACKWARD STAGES

Experiment	Supply stage			Forward stage			Backward stage	
	D_s (μm)	$\Delta\tau_s$ (μs)	$\Delta\tau_{p1}$ (μs)	D_f (μm)	$\Delta\tau_f$ (μs)	$\Delta\tau_{p2}$ (μs)	D_b (μm)	$\Delta\tau_b$ (μs)
Expt. 1	0.03	3	9	0.06	3	3.5	0.03	3
Expt. 8	0.03	3	9	0.06	3	3.5	0.06	3
Expt. 9	0.03	3	9	0.06	3	3.5	0.03	1.5
Expt. 10	0.03	3	9	0.06	3	3.5	0.03	6
Expt. 11	0.03	3	9	0.06	3	3.5	0.06	12

Experiment 8 appears to have large breakup time since the large volume flow rate toward the nozzle outlet occurs behind the period of the backward stoke, as shown in Fig. 10, therefore decelerating the thinning of fluid neck and prolonging the breakup time. Though experiment 1, 9 and 10 have the distinguished value of $D_b/\Delta\tau_b$ and time interval $\Delta\tau_b$, causing different acceleration of the tinning of fluid neck, which facilitate the drop breakup and different extent of tube invasion, which obstruct the drop breakup by inducing the volume flow rate toward nozzle outlet, as shown in Fig. 10, out of time period of backward actuation, they turn out to have the same drop breakup time, as shown in Fig. 11.

D. Pause stage

In order to investigate the effect of $\Delta\tau_{p2}$ on the drop ejection process, Table Ⅵ summaries a set of 6 numerical experiments with varying vale of $\Delta\tau_{p2}$. Fig. 12 shows the evolution in time of the shape of the liquid drop near the point of the breakup for experiment 1 and 12. After the drop breakup occur, experiment 11 shows that the tail of the ejected liquid drop recoils toward the drop head while experiment 1 shows one satellite drop to be formed by end-pinching. In addition, both experiment 8 and 15 show one satellite drop to be formed but in the case of experiment 15, the satellite drop flies with a very larger velocity than the former primary drop does. Therefore, the satellite drop could catch up to and then merge with the primary drop. These results suggest that a decrease in $\Delta\tau_{p2}$

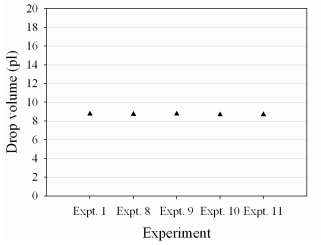

Figure 8. Volume variation of primary drop in experiments.

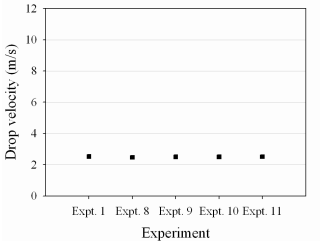

Figure 9. elocity variation of primary drop in experiments.

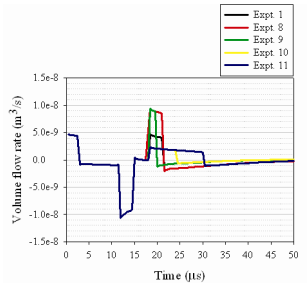

Figure 10. Variation with time of the volume flow rate.

Figure 11. Variation of drop shapes at breakup with cases.

could shorten the tail length of the ejected liquid drop and further damp the formation of the satellite drop. Fig. 13 shows the variation with cases of the stagnation point and drop tip position and drop length at breakup for these numerical experiments. Here, the drop length is a distance between the drop tip position and the stagnation point position separating the upward flow and downward movement of drop along the axis. Experiment 12, 13 and 16 show no satellite formation.

TABLE VI. LIST OF EXPERIMENTS TO PAUSE STAGES

Experiment	Supply stage			Forward stage			Backward stage	
	D_s (μm)	$\Delta\tau_s$ (μs)	$\Delta\tau_{p1}$ (μs)	D_f (μm)	$\Delta\tau_f$ (μs)	$\Delta\tau_{p2}$ (μs)	D_b (μm)	$\Delta\tau_b$ (μs)
Expt. 1	0.03	3	9	0.06	3	3.5	0.03	3
Expt. 12	0.03	3	9	0.06	3	1.75	0.03	3
Expt. 13	0.03	3	9	0.06	3	0.8	0.03	3
Expt. 8	0.03	3	9	0.06	3	3.5	0.06	3
Expt. 14	0.03	3	9	0.06	3	1.75	0.06	3
Expt. 15	0.03	3	9	0.06	3	0.8	0.06	3
Expt. 9	0.03	3	9	0.06	3	3.5	0.03	1.5
Expt. 16	0.03	3	9	0.06	3	1.75	0.03	1.5

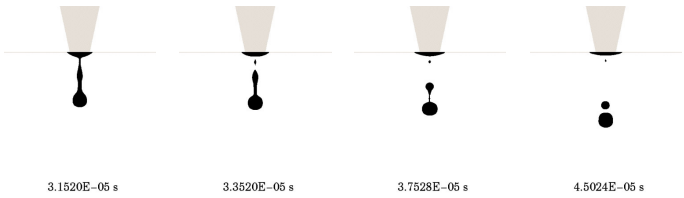

(a)

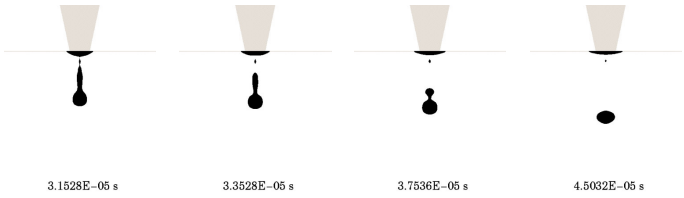

(b)

Figure 12. Evolution in time of the drop shape in (a) experiment 1 and (b) experiment 11.

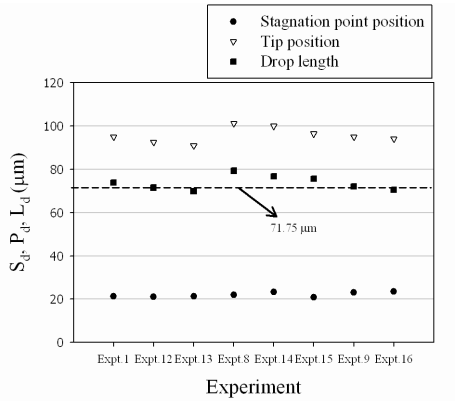

Figure 13. Variation with time of the stagnation point and drop tip position and drop length at breakup.

These results suggest that the formation of satellite drops is dependent on the drop length at breakup and in these cases considered, the tailed drops with the drop length less than 71.75 μm tend to have no occurrence of satellite drops behind the primary drop.

IV. CONCLUSION

The numerical simulations were carried out in this paper to investigate the effect of the actuation conditions on the drop ejection process of a Picojet printhead, commercially available drop-on-demand (DOD) ink jet device. For the investigation of the forward stage, the flow inertia i.e. We_f must be large enough if a DOD drop can be formed successfully in accord with intuition. The simulations also show that the volume of the primary drop increases as the product of We_f and $\nabla\tau_f$ increases. These results are consistent with the fact that the lager volume displacement of ink chamber, the larger the ejected volume of liquid from DOD nozzle. Moreover, an increase in We_f may lead to an increase in the velocity of the primary drop. It would also appear that the drop velocity slightly increases when the ejected drop volume increases. This result can be explained by assuming that an increase in the ejected drop volume may cause a decrease in the curvature of liquid interface, therefore accounting for the decrease in the restoring effect of surface tension. For the investigation of the backward stage, it is found from the results that the velocity and the volume of the primary drop seem to depend weakly on the varying conditions of the backward stoke. In addition, the extent of tube invasion by the retracting meniscus is closely related to We_b and $\nabla\tau_b$. For the investigation of the pause stage, the velocity and the volume of the primary drop remain constant but the formation of the satellite drops tends to be suppressed as $\nabla\tau_{p2}$ decreases. There is a strong possibility that a decrease in $\nabla\tau_{p2}$ could lead to a decrease in length of the ejected drop tail contracting into satellite drops.

ACKNOWLEDGMENT

The authors acknowledge the support of Aerothermal and Plasma Physics Laboratory of Department of Mechanical Engineering, National Chiao Tung University for the parallel computing machine.

REFERENCE

[1] J. F. Dijksman, and A. Pierik, "Fluid dynamical analysis of the distribution of ink jet printed biomolecules in microarray substrates for genotyping applications," *Biomicrofluidics,* vol. 2, no. 4, Oct-Dec, 2008.

[2] Y. Do Kim, J. P. Kim, O. S. Kwon *et al.*, "The synthesis and application of thermally stable dyes for ink-jet printed LCD color filters," *Dyes and Pigments,* vol. 81, no. 1, pp. 45-52, Apr, 2009.

[3] T. Shimoda, K. Morii, S. Seki *et al.*, "Inkjet printing of light-emitting polymer displays," *Mrs Bulletin,* vol. 28, no. 11, pp. 821-827, Nov, 2003.

[4] M. Komatsu, Y. Murayama, and H. Hashimoto, "Protein fragment imaging using ink jet printing digestion technique." pp. 1162-1164, 2008.

[5] B. A. Ridley, B. Nivi, and J. M. Jacobson, "All-inorganic field effect transistors fabricated by printing," *Science,* vol. 286, no. 5440, pp. 746-749, Oct, 1999.

[6] J. U. Park, J. H. Lee, U. Paik *et al.*, "Nanoscale patterns of oligonucleotides formed by electrohydrodynamic jet printing with applications in biosensing and nanomaterials assembly," *Nano Letters,* vol. 8, no. 12, pp. 4210-4216, Dec, 2008.

[7] R. Li, N. Ashgriz, and S. Chandra, "Droplet generation from pulsed micro-jets," *Experimental Thermal and Fluid Science,* vol. 32, no. 8, pp. 1679-1686, Sep, 2008.

[8] H. Y. Gan, X. C. Shan, T. Eriksson *et al.*, "Reduction of droplet volume by controlling actuating waveforms in inkjet printing for micro-pattern formation," *Journal of Micromechanics and Microengineering,* vol. 19, no. 5, pp. 8, May, 2009.

[9] J. Q. Feng, "A general fluid dynamic analysis of drop ejection in drop-on-demand ink jet devices," *Journal of Imaging Science and Technology,* vol. 46, no. 5, pp. 398-408, 2002.

[10] Q. Xu, and O. A. Basaran, "Computational analysis of drop-on-demand drop formation," *Physics of Fluids,* vol. 19, no. 10, pp. 12, Oct, 2007.

[11] A. S. Yang, J. C. Yang, and M. C. Hong, "Droplet ejection study of a Picojet printhead," *Journal of Micromechanics and Microengineering,* vol. 16, no. 1, pp. 180-188, Jan, 2006.

[12] W. J. Rider, and D. B. Kothe, "Reconstructing volume tracking," *Journal of Computational Physics,* vol. 141, no. 2, pp. 112-152, Apr, 1998.

[13] J. U. Brackbill, D. B. Kothe, and C. Zemach, "A CONTINUUM METHOD FOR MODELING SURFACE-TENSION," *Journal of Computational Physics,* vol. 100, no. 2, pp. 335-354, Jun, 1992.

A Study of Magnetic Domain Distribution in Ferrite by Magnetic Force Microscopy

Wei-Sheng Hsu[1], Min-Da Yang [1], Yi-Chen Wang [1], Li-Jiaun Lin [1]

[1]*Material and Chemical Research Laboratories, Industrial Technology Research Institute, Hsin Chu, Taiwan.*

Abstract — **In this study, vibration sample measurement (VSM) and magnetic force microscopy (MFM) have been used to observe the magnetic behavior and identify the magnetic domain distribution of NiZn ferrite, which was synthesized via chemical route and spray deposition method. Cases considered in the present study involve the types of NZF1 and NZF2 NiZn ferrite. VSM results show that the films with different deposition rate have the saturation magnetization from 200 to 900 emu/cm^3, and the resistance of the film is about 1 Mohm. The ferromagnetic resonance frequency is 1 GHz approximately. MFM results show that images were also discussed the domain wall motion between the particle of NiZn ferrite, which generated the different magnetic moment direction. Therefore, MFM could obtain the relationship results between the qualitative magnetic domain structure distribution and surface morphology of two types of NiZn ferrite.**

Keywords — ***NiZn Ferrite, Magnetic Force Microscopy, Magnetic Domain Distribution***

I. INTRODUCTION

Ferrites are a class of chemical compounds with the formula AB_2O_4, where A and B represent various metal cations, usually including iron. These ceramic materials are used in applications ranging from magnetic components to microelectronics. Ferrites are usually non-conductive ferrimagnetic ceramic compounds derived from iron oxides such as hematite (Fe_2O_3) or magnetite (Fe_3O_4) as well as oxides of other metals. Ferrites are like most other ceramics, hard and brittle. Ferrites are a class of spinels, materials that adopt a crystal motif consisting of cubic close-packed (FCC) oxides (O^{2-}) with A cations occupying one eighth of the tetrahedral holes and B cations occupying half of the octahedral holes.

The magnetic property of ferrites had been shown that magnetic behavior and magnetic wall motion in the recent experimental studies. Chun et al. [1] used MFM approach to determine the magnetic behavior and domain structure of Fe films. Georgescu et al. [2] discuss the interaction of magnetic force between cobalt-ferrite nanoparticle via MFM and Monte Carlo simulations. Rahman et al. [3] discuss a series of NiZnCu ferrite powders were prepared by chemical co-precipitation method with nominal compositions to observe the magnetic domain distribution in different calcinations temperature.

Since poly crystalline NiZn ferrites display the excellent performance that preferred over MnZn ferrites. Therefore, the magnetic properties of NiZn ferrite are the major stydy in our research. Because of the NiZn ferrite material have the advantage of high resistivity, high curie temperature, low temperature factor, low relative loss, good high permeability feature, which be widely used in home communication appliance, computer etc area. NiZn ferrites with their ease preparation and versatility for use in wide ranging application are very attractive materials from the commercial point of view. Microstructure and magnetic properties of NiZn ferrites are highly sensitive to the preparation methodology, sintering conditions and the amount of constituent metal oxides, impurities or doping levels. Efforts are being made to develop a low-power loss material operating in the MHz region in accordance with the miniaturisation of cores. The studies on microstructure and composition related magnetic properties have been reported for NiZn ferrites by several researchers in this field [4, 5, 6, 7].

In this study, we are specialized in exporting the magnetization performance involving two types of NiZn ferrite via the inspected instrument of VSM and MFM.

II. FABRICATION

In this study, the wet-chemical plating used to fabricate the different thin film morphology of NiZn ferrites. The substrate must have OH groups immersing a substrate surface by etching or surface plasma. The reaction solution containing Fe^{2+} and other metal ions M^{n+} are adsorbed on the surface mediated by the OH groups and releasing H^+. When we make use of the oxidizing reagent such as air or anodic current, some of the Fe^{2+} ions are oxidized to Fe^{3+}. The Fe^{2+} and M^{n+} ions are again adsorbed on the surface of the layer of the pre-adsorbed ions of Fe^{2+}, Fe^{3+} and M^{n+} ions. The ferrite layer thus formed has OH groups on the surface, the process is repeated and the ferrite film increases in thickness.

NiZn ferrite (NZF) films are grown on glass substrate by ultrasonic spray system. The thickness of NZF is controlled in a range between 200 nm to 2000 nm. The continuing NZF growth mechanism from equal-axed to columnar spinel with increasing temperature can be presented by SEM morphology as shown in Fig. 1. Adjusting the concentration of chemical droplet reaction, it would modulate the growth size of ferrite chain. Like the Fig. 2(a) and Fig. 2(b), the particle cluster of NiZn ferrite has the different grain size to form continue particle film, it called the NZF1 and NZF2 in this study respectively. It could have the weak inter-grain magnetic interaction. For ferromagnetic phases, a domain structure comprise of sub-grain domains was observed by MFM.

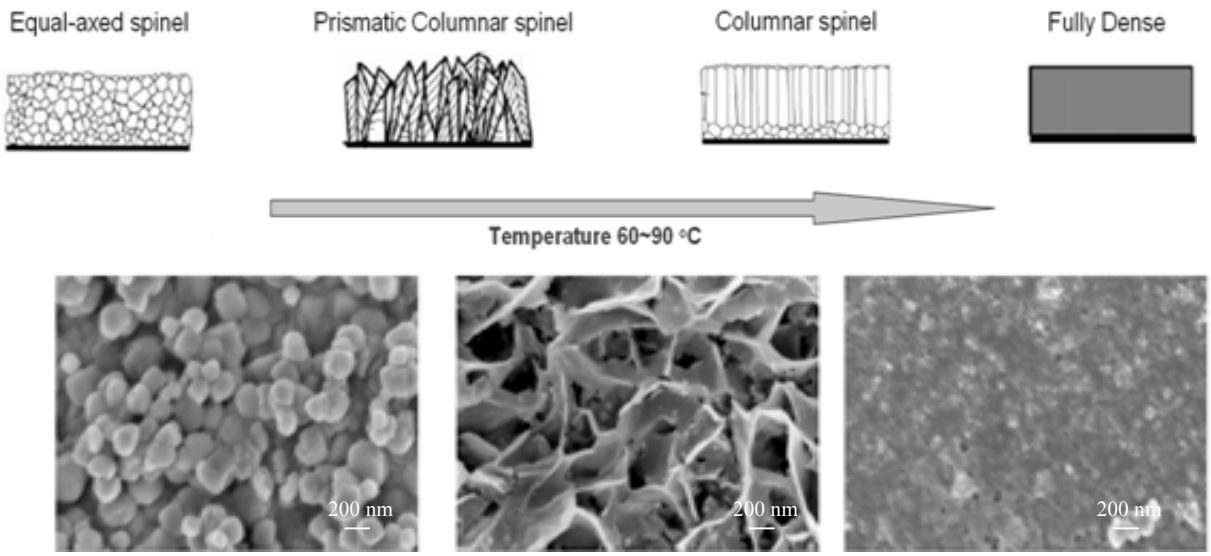

Fig. 1. The schematic view and related FE-SEM image of fabrication process of the NiZn ferrite in different temperature.

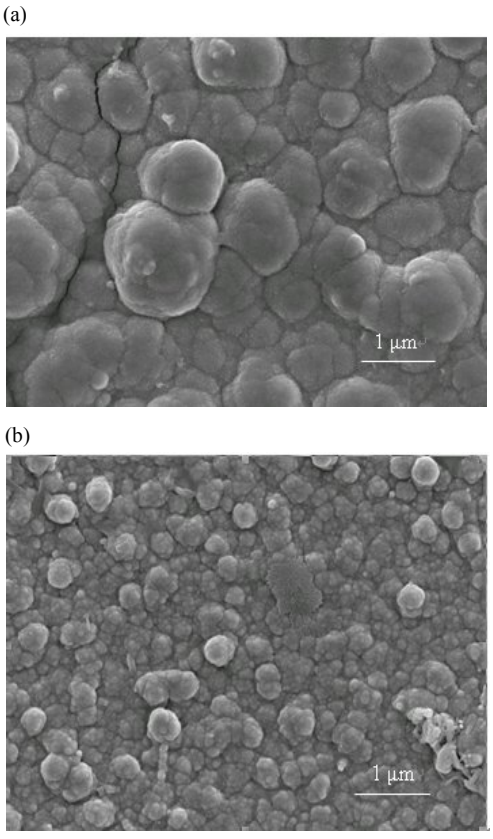

Fig. 2. A typical FE-SEM image of NZF1 (a) and NZF2 (b) are prepared via chemical route and spray deposition method.

III. MATERIAL CHARACTERIZATION

A. *Vibration Sample Measurement*

The effect range of moment measured is 10^{-4}~10^{3} (emu). The electric magnet can offer altering magnetic field between -1.2 ~ 1.2 Tesla. It can measure magnetization by Gaussmeter and Hall probe. When the magnetic materials are put on sample holder, we can get the variance voltage signal. The voltage induced in the coil will be calculated by equation (1)

$$V_s \propto \frac{d\Phi}{dt} = A\omega\cos(\omega t)\iint_{coil}\frac{dB_x(x_c, y, z(t))}{dz}dydz \qquad (1)$$

It can be realized that induced electromotive force and magnetization have the proportion relation to vibrate intensity and oscillation frequency. We can obtain the magnetization measurements showing that the spinel ferrite films present a hysteretic behavior at room temperature with a randomly oriented in-plane easy axis. The films with different deposition have saturation magnetization from 200 to 900 emu/cm^3, and the anisotropy coercive force ~ 200 Oe, and the resistance of the film is about 1 Mohm. The ferromagnetic resonance frequency is 1 GHz approximately. By the VSM measurement, it can show that the anisotropy structure influence saturation magnetization on in-plane and out-plane picture of NZF1 as shown in Fig. 3.

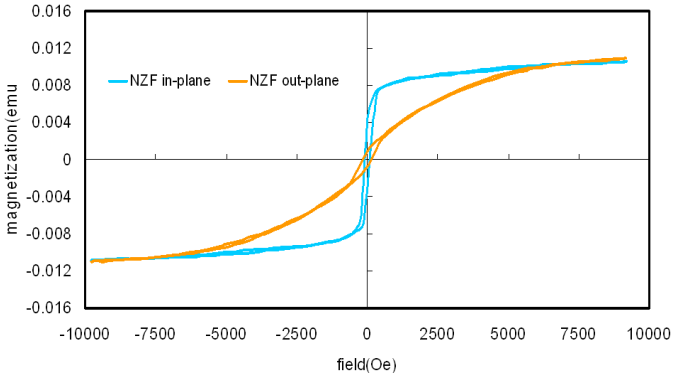

Fig. 3. Magnetization measured with the magnetic field applied along in-plane and out plane on NZF1.

B. Magnetic Force Microscopy

Magnetic force microscopy (MFM) is a well established experimental method used to investigate the magnetic surface microstructure of magnetic films or magnetic nanostructures. The MFM uses a small probe tip which is coated with ultra-thin ferromagnetic film that vibrating at resonance scans over an area of a sample surface [8]. MFM imaging can achieve spatial resolution of less than 10 nm. Therefore, many kinds of magnetic interactions of magnetic films or magnetic nanostructures are measured by MFM, including the magnetic dipolar interaction or the magnetic domain wall distribution [9]. MFM scanning often uses tapping mode atomic force microscopy (AFM) and a value of lift height to obtain the image of magnetic force distribution in spatial resolution. In MFM, the magnetic contrast is achieved through the magnetic interaction between a ferromagnetic tip and the micro-magnetic fields from the sample in particular at domain boundaries. The magnetic force between the tip and sample can be obtained using the equation (2)

$$F = (m \cdot \nabla)H \tag{2}$$

Where the m stand for magnetic dipole, and the H stand for the sample stray magnetic field. If the m would be magnetism only in z direction, the equation would be modify in equation (3)

$$F_z = (m \cdot \nabla)H \approx m_z \frac{\partial H}{\partial z} \tag{3}$$

During measurements, the tip of probe vibrates perpendicular to the sample surface, and the frequency and amplitude of the vibration change in the presence of gradients due to the magnetic fields. An image taken with a magnetic tip contains information about both the topography and the magnetic property of a surface, which effect dominates depends upon the distance of the tip from the surface, because the inter-atomic magnetic force persists for greater tip-to-sample separations than the van der Waals force. If the tip is close to the surface, in the region where standard tapping AFM is operated, the image will be predominantly topographic. As the separation between the tip and the sample increases, magnetic effects become apparent. Therefore, the MFM image of the same area taken in constant-height mode at a lift height of 30 nm and was done in high vacuum (10^{-5} Pa) to inspect the image of magnetic force distribution.

In this study, two types of NiZn ferrite are carried out using a commercial SPM instrument (Seiko SPA-300Hv). The topography and the magnetic domain structure of NZF1 are observed by MFM at the same position on sample as shown in Fig. 4(a) and Fig. 4(b) respectively. Usually, the light-coloured areas correspond to attractive interaction between the tip and sample, whereas darker areas correspond to repulsive interaction. The light-coloured areas always occur in particle boundary of NZF1, the light-coloured lines are the boundaries of the interaction domains which comprise many of the ~1000 nm grains, in other word, the direction of magnetic moment of the boundary is the same with tip, because of the magnetic domain wall motion [10], MFM was used to provide insight into the nature of magnetic inter-grain interactions in magnetic structure. The analysis results have been shown the weak inter-grain coupling in our ferrite of NZF1, the direction of magnetization would concentrate between the NiZn ferrite boundary of particle. The cross-section of MFM image (Fig. 4(c)) is marked with dotted line of Fig. 4(b), which have shown the cross-section of magnetic force. It corresponds to magnetic domain distribution and shown a phenomenon of non-uniform distribution.

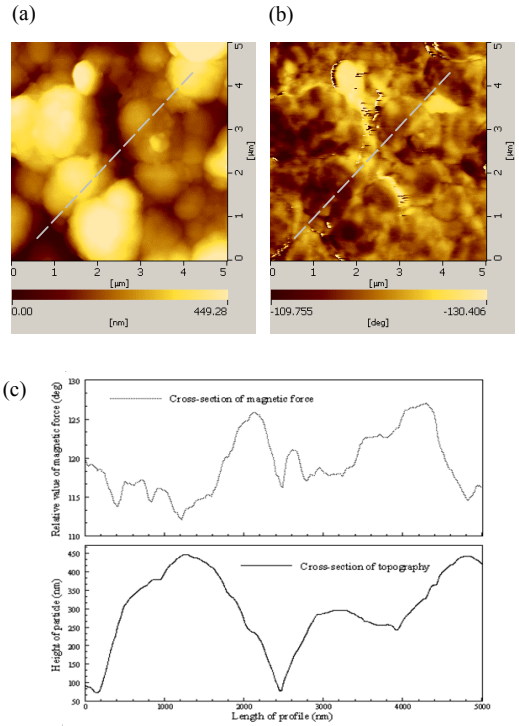

Fig. 4. Topography (a) and MFM (b) images (scan area: 5.0 μm × 5.0 μm, vertical scale (From dark to light): 450 nm and 20°, respectively.) and corresponding cross-section analysis of a sample of NZF1 (c). The cross-section layers were marked with dotted line (Length of dotted line: 5000 nm).

The topography and the magnetic domain structure of NZF2 are observed by MFM as shown in Fig. 5(a) and 5(b) respectively. The light-coloured areas of MFM image are the boundaries of interaction domains which comprise many of the ~500 nm grains. Cross-section of MFM image (Fig. 5(c)) is marked with dotted line of Fig. 5(b), which have shown the uniform magnetic force distribution. The analysis results have been shown the uniform inter-grain coupling in NZF2.

This phenomenon of variation of the amplitude and magnetic signal as the function of particle dimension, more or less particle dimension is well observed in Fig. 4(b) and Fig. 5(b). Zooming into any of those areas reveals two types of magnetic structure and contrast. The domain wall distribution of NZF2 is more uniform than NZF1 resulted from particle dimension. In other words, in larger particle region, the magnetic tip was inspected a stronger interaction, which cause a higher phase shift, and the particle magnetic moment stays out-plane due to dipolar interaction with their neighbors.

In addition, we also observed the surface roughness would affect the quality and precision of MFM image [11], such as Fig. 4(b), the inaccuracy can be observed due to more different height of surface roughness in grain boundary of NZF1, thus resulted in the magnetic contrast error extremely; comparison, Fig. 5(b), the particle dimension of NZF2 is smaller than NZF1, MFM recorded signal is uniform than NZF1. Therefore, in case of NZF1, the difference of particle dimension, when tip scanned over the sample, the tip would compress or increase the amplitude drastically, resulted in the error signal in particle boundary of MFM image. Consequently, for MFM image, the surface roughness and flatness requirements are still limited in our present study.

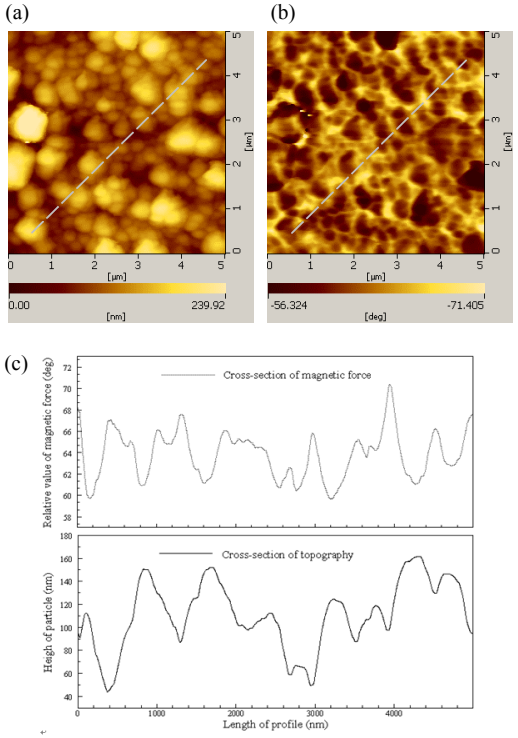

Fig. 5. Topography (a) and MFM (b) images (scan area: 5.0 µm × 5.0 µm, vertical scale (From dark to light): 240 nm and 15°, respectively.) and corresponding cross-section analysis of a sample of NZF2 (c). The cross-section layers were marked with dotted line (Length of dotted line: 5000 nm).

IV. CONCLUSION

In this study, the NiZn ferrite (NZF), which was synthesized via chemical route and spray deposition method. The wet-chemical plating used to fabricate the different thin film morphology of NiZn ferrites. NiZn ferrite films are grown on glass substrate by ultrasonic spray system. The thickness of NZF is controlled in a range between 200 nm to 2000 nm. The continuing NZF growth mechanism from equal-axed to columnar spinel with increasing temperature can be presented by FE-SEM.

The VSM and MFM technique had been applied to observe the saturation magnetization and magnetic domain distribution of NiZn ferrite. Cases considered in the present study involve the types of NZF1 and NZF2 NiZn ferrite. By the VSM measurement, it can show that the anisotropy structure influence saturation magnetization on in-plane and out-plane. VSM results show that the magnetization measured with the magnetic field applied along in-plane and out plane on NZF1, the films with different deposition rate have the saturation magnetization from 200 to 900 emu/cm^3. The anisotropy coercive force ~200 Oe, and the resistance of the film is about 1 Mohm. The ferromagnetic resonance frequency is 1 GHz approximately.

MFM image of the same area taken in constant-height mode at a lift height of 30 nm and was done in high vacuum (10^{-5} Pa) to inspect the image of magnetic force distribution. MFM was used to provide insight into the nature of magnetic inter-grain interactions in magnetic structure. The analysis results have been shown the weak inter-grain coupling in our NiZn ferrite. We observe that when the particle dimension of NiZn ferrite is smaller, the distribution of magnetic domain is more uniform. This phenomenon of variation of the amplitude and magnetic signal as the function of particle dimension, more or less particle dimension. The domain wall distribution of NZF2 is more uniform than NZF1 resulted from particle dimension. In other words, in larger particle region, the magnetic tip was inspected a stronger interaction, which cause a higher phase shift, and the particle magnetic moment stays out-plane due to dipolar interaction with their neighbors.

In addition, the surface roughness also discuss in our study. The inaccuracy of MFM image can be observed due to more different height of surface roughness in grain boundary of NZF1, thus resulted in the magnetic contrast error extremely; comparison, the particle dimension of NZF2 is smaller than NZF1, MFM recorded signal is uniform than NZF1. Therefore, in case of NZF1, the difference of particle dimension, when tip scanned over the sample, the tip would compress or increase the amplitude drastically, resulted in the error signal in particle boundary of MFM image. Consequently, for MFM image, the surface roughness and flatness requirements are still limited in our present study.

REFERENCES

[1] Y. S. Chun, K. M., Krishnan, “Interlayer perpendicular domain coupling between thin Fe films and garnet single-crystal underlayers,” Journal of Applied Physics, Vol. 95, pp. 6858-6860, 2004.

[2] M. Georgescu, J. L. Viota, M. Klokkenburg, B. H. Erné, D. Vanmaekelbergh, P. A. Zeijlmans, “Short-range magnetic order in two-dimensional cobalt-ferrite nanoparticle assemblies,” Physical Rewiew B, Vol. 77, pp. 024423-024426, 2008.

[3] I. Z. Rahman, T. T. Ahmed, “A report on structural and MFM analysis of Cu substituted Ni-Zn-Cu ferrite powders,” Physica Status Solidi (a), Vol. 12, pp. 3656-3659, 2004.

[4] P. S. Anil Kumar, J. J. Shrotri, C. E. Deshpande, S. K. Date, “Systematic study of magnetic parameters of Ni–Zn ferrite synthesized by soft chemical approaches,” Journal of Apply Physics, Vol. 81, pp. 4788-4790, 1997.

[5] P. S. Anil Kumar, S. R. Sainkar, J. J. Shrotri, S. D. Kulkarni, C. E. Deshpande, S. K. Date, “Particle size

dependence of rotational responses in Ni–Zn ferrite," Journal of Apply Physics, Vol. 83, pp. 6864-6866, 1998.
[6] B. Parvatheeswara Rao, K. H. Rao, "Effect of sintering conditions on resistivity and dielectric properties of Ni-Zn ferrites," Journal of Materials Science, Vol. 32, pp. 6049-6054, 1997.
[7] B. Parvatheeswara Rao, Chong-Oh Kim, CheolGi Kim, "Influence of V2O5 additions on the permeability and power loss characteristics of Ni–Zn ferrites," Materials Letter, Vol. 61, pp. 1601–1604, 2007.
[8] A. Carl, J. Lohau, S. Kirsch, E. F. Wassermann, "Magnetization reversal and coercivity of magnetic-force microscopy tips," Journal of Applied Physics, Vol. 89, pp. 6098-6104, 2001.
[9] M. R. Freeman, B. C. Choi, "Advances in Magnetic Microscopy," Magnetism and Materials, Vol. 294, pp. 1484-1488, 2001.
[10] J. Lyubina, K. Khlopkov, O. Gutfleisch, K. H. Müller, L. Schultz ,"Intergrain interactions in nanocomposite Fe–Pt powders," Journal of Applied Physics, Vol. 99, 930-1-903-4, 2006.
[11] W. Naoki, S. Kazuo, M. Nobuyasu, "Orientation control and domain structure of epitaxial (Ni,Zn) Fe2O4 thin film for ferromagnetic memory applications," Key Engineering Materials, Vol. 248, pp. 169-172, 2003.

Three-Dimensional Flexible Microprobe for Recording the Neural Signal

Chang-Hsiao Chen[1], Shih-Chang Chuang[1], Yu-Tao Lee[1], Shih-Rung Yeh[2,#], Yen-Chung Chang[2], and Da-Jeng Yao[1,*]

[1]*Institute of NanoEngineering and MicroSystems, National Tsing Hua University, Taiwan*
[2]*Department of Life Sciences, National Tsing Hua University, Taiwan*

***Abstract* — In this paper we have designed, fabricated and tested a novel three-dimensional (3D) flexible microprobe used for recording the neural signals of lateral giant (LG) on the escape system of America crayfish. We report an electrostatic actuation process to fold the planar probes to be the arbitrary orientations of 3D probes for neuroscience application. The batch assembly method based on electrostatic force techniques gave more simple fabrication compared with others. A flexible probe could reduce both the chronic inflammation response and material fracture when animal breathes or moves. Furthermore, the cortex corresponds to hypothetical cortical modules with mostly vertically organized layers of neurons. Therefore the 3D flexible probe suits to understand how the cooperative activity for different layers of neurons. Advisedly, we present a novel fabrication for 3D flexible probe by using parylene technology. The mechanical strength of the neural probe is strong enough to penetrate into a bio-gel. At the end, the flexible probe was used to record neural signals of LG cell from America crayfish.**

Keywords — ***Flexible, Microprobe, Neuron, Parylene, PEG, 3D***

I. INTRODUCTION

Although rigid types of microelectrode have been developed for recoding, but at in-vivo recording the mechanical mismatch between the stiffness probe and soft biological organization will aggravate inflammation in the implantation sites. While silicon has a Young's modulus of ~170 GPa, brain tissue has ~3 kPa. This large mechanical mismatch can contribute to shear induced inflammation at the implant site. This inflammation encourages the formation of a glial sheath. In response to brain injury, glial cells such as astrocytes and microglia proliferate to form a glial sheath [1, 2]. The biological sheath would encapsulate the probe, which would isolate the electrode from surrounding neurons with time [3]. The duration recording of chronically implanted probe of Michigan array about four months [4], of Utah array was about seven months [5]. A flexible probe could reduce both the chronic tissue inflammation response and material fracture when animal breathes or moves.

We present a batch assembly method based on electrostatic force techniques gave more simple fabrication compared with others. A schematic view of the 3D probe is shown in Figure 1. The first generation fabrication process for the planar flexible microelectrode array (MEA) was reported at APCOT '08 [6]. Our method differs from that of group Shaar [7]in the segments actuated by Lorentz force, and of group Takeuchi [8] actuated by the magnetic field method for the batch assembly. Moreover, we improve the limit that toxicity of magnetic materials for long-term and in-vivo recording application which would be very useful for further development.

Advisedly, we present a fabrication method for penetrating type of 3D flexible probe by using parylene technology. Parylene is an inert, vapor deposited polymer. The Parylene_C is selected as the main structure material of the flexible probe, which gives its excellent flexibility, large mechanical strength with Young's modulus about 3 GPa, and its United States Pharmacopoeia (USP) Class VI grade biocompatibility and the pinhole-free coating at the room temperature has low moisture permeability and has been used in the medical device industry as a biocompatible coating for implants. The flexible probe insert into cortex difficulty. In this paper, the polyethylene glycol (PEG) we used to stiffen and fix the flexible probe. Parylene probe were coated with the PEG, a biocompatible material that is solid state at room temperature, liquid state over 60 ℃ and which dissolves in water or body fluid.

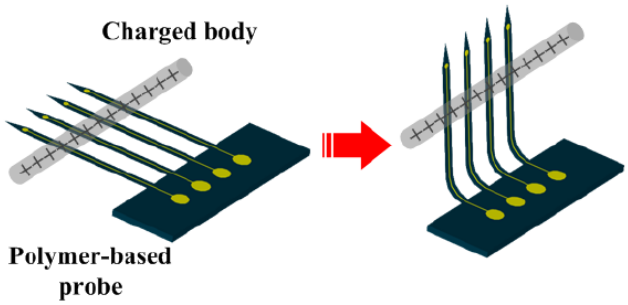

Figure 1. Schematic of the planar probe in the flat (left) and folded (right) configurations.

II. FABRICATION

MEMS technology was used to develop the fabrication of flexible probe, the fabrication starting from Parylene_C deposition and ending PEG coating. The probes are 3 mm long, 100 μm wide, and the thickness of the probe is 6 μm defined by the thickness of the first parylene layer. The fabrication process of flexible probe was outlined on figure 2. The fabrication process consisted of three steps, patterning the

*Contact author: for fabrication aspects of this research please contact ***djyao@mx.nthu.edu.tw***
#Contact author: for neuron aspects of this research please contact ***sryeh@life.nthu.edu.tw***

metal layer, the structure layer, and etching the structure to release the probe.

(a) RCA standard clean to remove particles and ion contamination before the approximately 5 μm Parylene_C is first deposited on silicon wafer by using specialty coating system.

(b) The process steps define patterning of electrodes by using lift-off method. Cr/ Au were evaporated by E-beam. The metal patterns are defined in an ultrasonic bath in acetone. The trace was defined with 5 μm wide and 100 nm thickness. In order to produce an embed electrode using oxygen plasma by reactive ion etching (RIE). The step added the adhesion the electrode with parylene.

(c) A second Parylene_c with 1 μm thickness layer was deposited on top of entire wafer as an intermediate dielectric layer.

(d) The 2,500 μm^2 via was patterned in the insulation layer, which over the ends of the Au electrodes, contact pads were opened to the Au-layer using O_2 plasma by RIE through a photoresist mask. The step at the same time defined the probe shape. The etch step went through the entire thickness of the parylene device layer on the wafer, which layer was etched 6 μm and stopping on the silicon.

(e) The flexible probe was peeled from the wafer by using tweezers and fixed on the glass substrate.

(f) The planar probes were folded by electrostatic force.

(g) The folded probes were fixed by a PEG drop with liquid state on 60 ℃ hotplate.

(h) Finally, dipped the probe with liquid state PEG on 60 ℃ hotplate. After cooling process, the PEG transfers to solid state which enhances the probe stiffness.

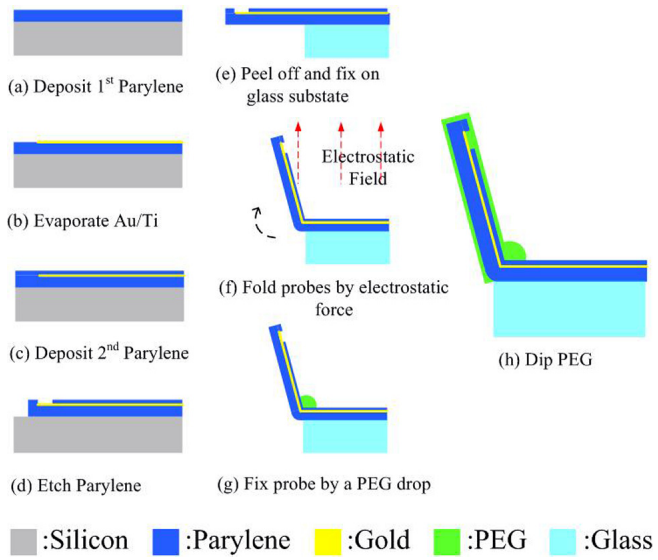

Figure 2. Fabrication process of the 3D flexible probe.

III. Results and Discussion

A. Scanning Electron Microscopy Images

The SEM images of completed MEA were shown in Figure 3. In the design, the flexible probe consisting of one electrode site on the each probe, shown on figure 3a. The width of probe is 100 μm at the outermost section. The thickness of probe is targeted to be 6 μm, but can be varied by depositing parylene with all kinds of thickness. The probe length is typically 3 mm. The size of recording electrode sites are 2,500 μm^2.

The forded probe was fixed a PEG drop by using the pipette. The flexible probe was coated with PEG by dipping process was shown in Figure 3b. The thickness of PEG was about 5 μm thickness. The dip coating process has a conformal surface on the implant site.

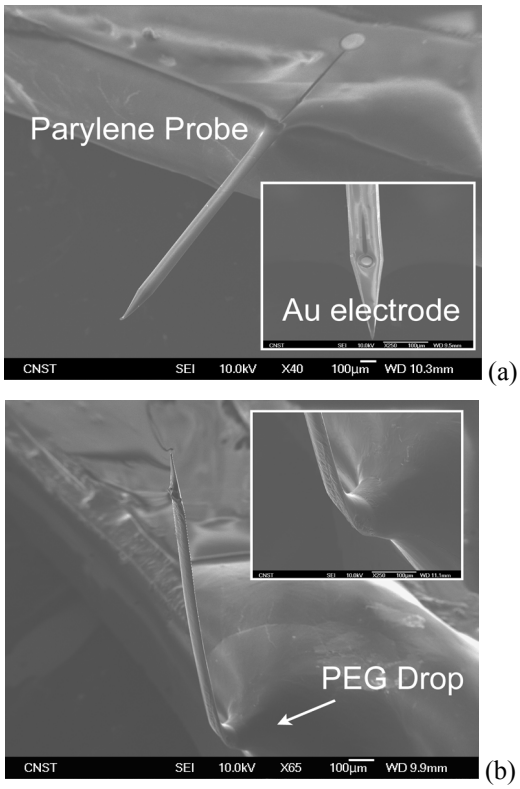

Figure 3. SEM images of 3D flexible probe. (a) The fabricated probe, (b) The folding probe after electrostatic actuation

B. Electrostatic Field Assembly

The electrostatic field was used to fold planar probe for the batch assembly which avoids the error of manual assembly. After fabrication, the planar probe was placed in a vertical electrostatic field which would stand up by varied electrostatic voltages. The voltage in the generator was gradually increased from 0 V to 8 KV, which folded the probe up from a horizontal position to about vertical. It was folded to near 90° when an external electrostatic field of 8 KV was applied, as shown in figure 4.

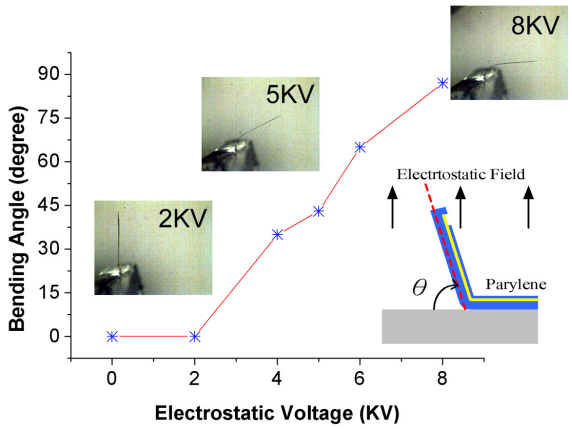

Figure 4. Electrostatic batches assembly of the probe.

C. *Mechanical Strength*

Because of the flexible probe would be used to in-vivo recording the neural signal of cortex in the future. The pure flexible probe was too difficult to be implanted into biological organization due to its soft property. The PEG material was as a supporting structure of the parylene probe. We have to verify that the overall neural probe structure is mechanically strong enough to penetrate test.

As shown on figure 5, the 3 mm parylene probe was coated with PEG, then inserted into and pulled back from the bio-gel smoothly to simulate the hardness of the cortex and without critical buckling failure or break off. After inserting the probe into bio-gel, the PEG was a biocompatible material. It would be dissolved in body fluid with the time and the probe would become the property of the flexibility again.

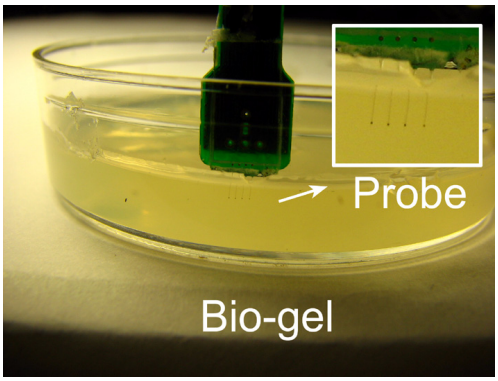

Figure 5. Photograph of parylene probe coated with PEG penetrated into bio-gel.

D. *A.C. Impedance*

The impedance of electrode influences the ability to record minute neural signals. In order to choose the cut-off frequency of neural signal recording system, the electrochemical impedance analysis was used to measure the impedance and phase between work electrode and reference electrode. The impedance of microelectrode was obtained by submerging only the recording in 0.9 % saline solution. The impedance measurement was built up with respect to a large reference electrode (Ag-AgCl wire).

The testing signal for impedance measurement was sinusoidal (AC voltage 20 mV, frequency 10 Hz ~ 10 kHz). For a typical electrode with 2,500 μm^2 opening area, the average measured impedance is around 566.5 KΩ at 1 kHz (nerve working frequency), as shown in Figure 6. At the higher frequency, the impedance of electrode decreased gradually because of capacitor effect.

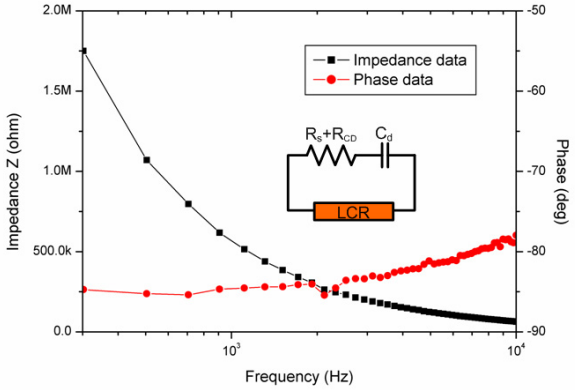

Figure 6. The impedance of gold electrodes on flexible probe submerged in 0.9 % saline.

E. *Neural Extracellular Recording*

In order to confirm the functionality of electrode on the flexible probe, the neural signals of the escape circuit from crayfish was measured by our developed microprobe. The schematic view of the electrophysiology system, shown in Figure 7, could be used to record the neuron signal from microprobe.

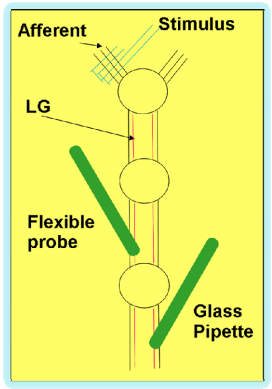

Figure 7. Schematic view of the electrophysiology system for recording the crayfish.

Juvenile crayfish are kept in water tank at room temperature. The 2~5 cm junior crayfish was selected in our experiments. The crayfish lost the ability of the moving

behavior upon the ice after ten minutes. The crayfish was pinned in the dish filled with van Harreveld's solution. The abdominal nerve cord of the escape circuits was exposed dorsally by removing the exoskeleton and separating phasic flexor musculature which's using isolated abdomens preparation. In the escape circuits of the crayfish, the mechanosensory primary afferents received the environmental excitation. Parts of the neural signal transmit directly to the lateral giant (LG) nerve fiber through the electrical synapses. Pairs of silver wires were placed on the mechanosensory primary afferent neurons for stimulation. The functions of the electrophysiology system were divided into two parts: one is electrical stimulation, and the other one is recording part. The electrical stimulation was produced by DAQ card and amplifier circuits. The amplitude and frequency of the input voltage was controlled by software in the personal computer.

In the extracellular recording experiment, the neural signal from dorsal side of lateral giant nerve fiber was recorded by shocking on the tailfin efferent. The once alternating square waveform of shock voltage was about ± 3.7 V with 0.1 ms period. The response amplitude of action potential of LG neuron was about ±75 μV with 1ms period, as shown in Figure 8.

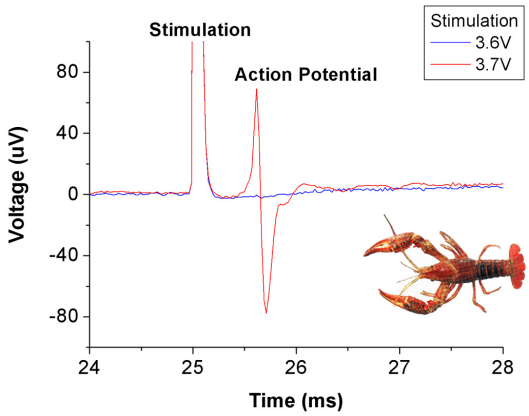

Figure 8. Neural signal was obtained from LG of crayfish by the flexible probe.

IV. Conclusion

In this paper, we designed and fabricated a 3D flexible microprobe for recording the neural signal, which would be used for the measurement system on bio-medical applications. The fabrication process of the implant flexible probe was accomplished by using MEMS technology. We report an electrostatic actuation process to fold the planar probes to be the arbitrary orientations of 3D probes. We present a fabrication method for penetrating type of flexible probe by using parylene technology. Moreover, to improve the mechanical stiffness of developed flexible probe, Polyethylene glycol (PEG) was used on the surface of probe. At the end, the 3D flexible probe was used to record neural signals of the escape circuit from America crayfish.

Future work would use current accomplished results for developing the completed measurement circuitry with fully-integrated analog and digital components realized in an industrial CMOS process. To improve signal-to-noise ratio of the neural signal is very important.

Acknowledgment

This research was partially supported by the National Science Council in Taiwan through Grant NSC 96-2627-E-007-002.

References

[1] V.S. Polikov, P.A. Tresco, and W.M. Reichert, "Response of brain tissue to chronically implanted neural electrodes," Journal of Neuroscience Methods, vol. 148, pp. 1-18, 2005.

[2] J.W. Fawcett and R.A. Asher, "The glial scar and central nervous system repair," Brain Research Bulletin, vol. 49, pp. 377-391, 1999.

[3] D.H. Szarowski, et al., "Brain responses to micro-machined silicon devices," Brain Research, vol. 983, pp. 23-35, 2003.

[4] R.J. Vetter, et al., "Chronic neural recording using silicon-substrate microelectrode arrays implanted in cerebral cortex," IEEE Transctions on Biomedical Engineering, vol. 51, pp. 896-904, 2004.

[5] A. Branner, et al., "Long-term stimulation and recording with a penetrating microelectrode array in cat sciatic nerve," IEEE Transctions on Biomedical Engineering, vol. 51, pp. 146-157, 2004.

[6] H.C. Su, et al., "Low temperature synthesis of multi-walled carbon nanotubes," Nanotube'08, Montpellier, pp. 142, 2008.

[7] N.S. Shaar, G. Barbastathis, and C. Livermore, "Cascaded mechanical alignment for assembling 3D MEMS," MEMS 2008, Tucson, pp. 1064-1068, 2008.

[8] S. Takeuchi, et al., "3D flexible multichannel neural probe array," Journal of Micromechanics and Microengineering, vol. 14, pp. 104-107, 2004.

Automatic Segmentation of Abnormal Cell Nuclei from Microscopic Image Analysis for Cervical Cancer Screening

Chin-Wen Chang[1], Ming-Yu Lin[1], Horng-Jyh Harn[2], Yen-Chern Harn[3], Chien-Hung Chen[1], Kun-His Tsai[2], and Chi-Hung Hwang[1]

[1]*Instrument Technology Research Center, National Applied Research Laboratories, Taiwan*
[2]*Department of Pathology, China Medical University Hospital, Taiwan*
[2]*Department of Computer Science and Information Engineering, National Taiwan University, Taiwan*

***Abstract* — In this paper, two methods of microscopic image analysis were presented to classify the abnormal cells in Papanicolaou(Pap) smear for cervical cancer screening. Our goal is to extract those cell nuclei which are abnormally large size, bizarre shape as well as hyper density and we hope to apply this method to the different kinds of abnormal cells. The global information of the image and the local image condition were meantime considered. The reported method searched whole picture by scanning on different axes and determined the locations of abnormal cell nuclei with high contrast This developed method is also able to find cell nuclei, those were almost as bright as the background. Using the reported cytological image analysis, we successfully recognized the abnormal cells such as squamous intraepithelial neoplasia (SIL) and differentiated them from the normal epithelial cells.**

Keywords — ***automatic segmentation, abnormal cell nuiclei, cervical cancer, line scanning, energy method***

I. INTRODUCTION

Cervical cancer is the second most common cancer in woman's cancer diseases and yield over 500,000 new striking cases worldwide each year [1]. Pap smear, the cytological gynecological investigation is the first-step routine method to diagnose the cervical cancer. In clinical diagnostics, cytotechnologists are responsible for examining Pap smear. It is time-consuming and the accuracy of diagnosis is dependent on training experience of cytotechnologists. Therefore there are increasing needs from cytotechnologists for the development of automated cytological classification system.

Different researchers have been studying on segmentation of cell tissues. Deformable model was presented to cell nuclei segmentation by M.E. Plissiti [2]. Fuzzy logic engine was applied by Grigory Begelman to handle the noise and uncertainty in cell nuclei data [3]. Gradient vector field was used for building 3D model [4]. Xiaowei Chen presented an automated segmentation, classification, and tracking of cancer cell nuclei in time-lapse microscopy [5].

Enlargement and deformation of cell nuclei are two major criteria to recognize the abnormal cells in Pap smear exam. Recently, automatic cell nuclei segmentation has been made much more attraction and also provided one of the most interesting topics in cytological image analysis. The inherent problems due to the video microscopy and the smear make this work a challenge. We attempt to identify and label those abnormal cells with enlarged and deformed nuclei in order to simplify the recognition process as screening purpose.

II. MATERIAL AND METHODS

A. Material

The smear images used in this work are provided by Pathology department, China Medical University Hospital, Taichung, Taiwan. All tumor cells are confirmed by two independent pathologists. These images are captured under 400× magnification lens and stored with 1280×960 pixels. The flowchart of reported automatic microscopic image analysis is shown in Fig 1.

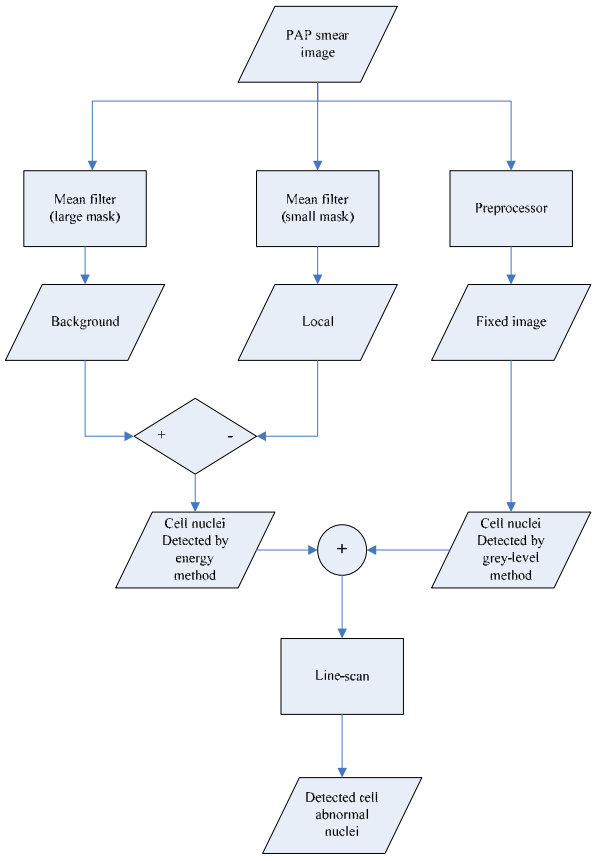

Figure 1. The flowchart.

*Contact author: Chin-Wen Chang is with the Instrument Technology Research Center. 20, R&D Rd. VI, Hsinchu Science Park, Hsinchu , 300, Taiwan.(phone:+886-3-5779911 #580; fax:+886-3-5773947; e-mail: fifer@itrc.org.tw)

B. Grey-Level Method

In an image, cell nuclei are generally darker than the other parts of the image. Thus, most of the time, we can tell where the cell nuclei are by grey level. However, in the PAP smear images we have, it's always lighter in the center and darker at the corner. This phenomenon makes it difficult to distinguish where the cell nuclei are by grey level. The promble comes from the light source and needs to be fixed.

Therefore, some preprocessing is necessary. First, we find the barycenter of this image which is weighted by grey level. Second, cluster the pixels according to the distance from the barycenter to each pixel, and then, rescale the grey level to each cluster.

Determining where the cell nuclei are, a threshold has to be given. If the grey level of a pixel is lower than the threshold, it would be taken as a part of cell nuclei. Otherwise, it would be ignored. The threshold is given by the mean value of the image multiplied by a factor. The factor is chosen by experience.

After determining the cell nuclei in the image, we apply line-scanning to the image. On a chosen axis, if there are sufficient number of pixels belongs to cell nuclei and continuously connected together, these pixels are marked as abnormal cell nuclei. If there are only several pixels, they would be taken as noise. By scanning on different axis, those large cell nuclei would be marked and smaller ones would be ignored. Line-scanning works as shown in Fig 2.

This method is applied Fig 3 and the fixed image is shown in Fig 4. The result is shown in Fig 5.

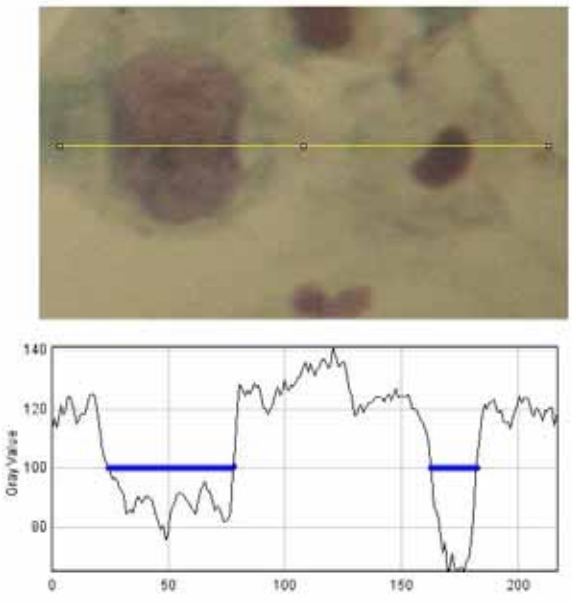

Figure 2. Line-scanning.

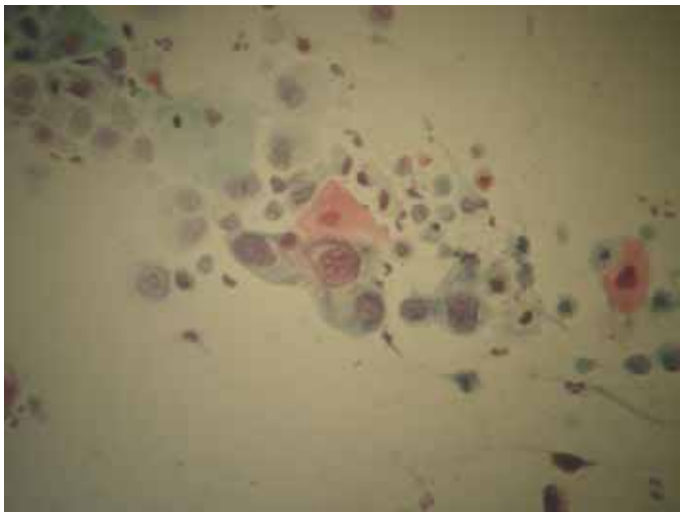

Figure 3. The original PAP smear image provided by China Media University Hospital.

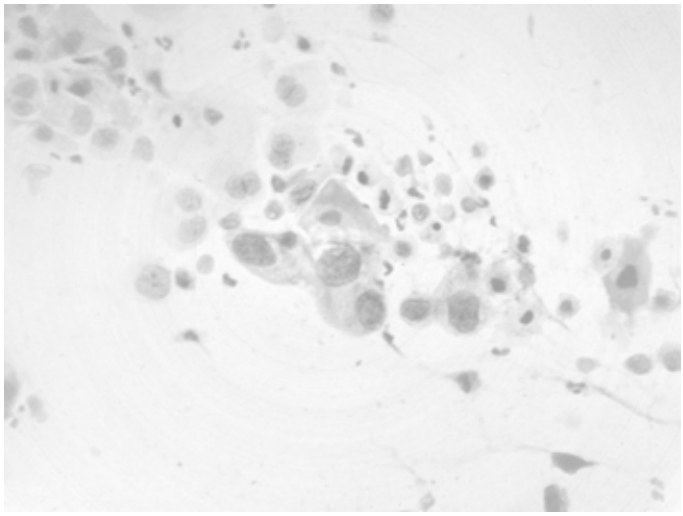

Figure 4. This image is rescaled by clusters.

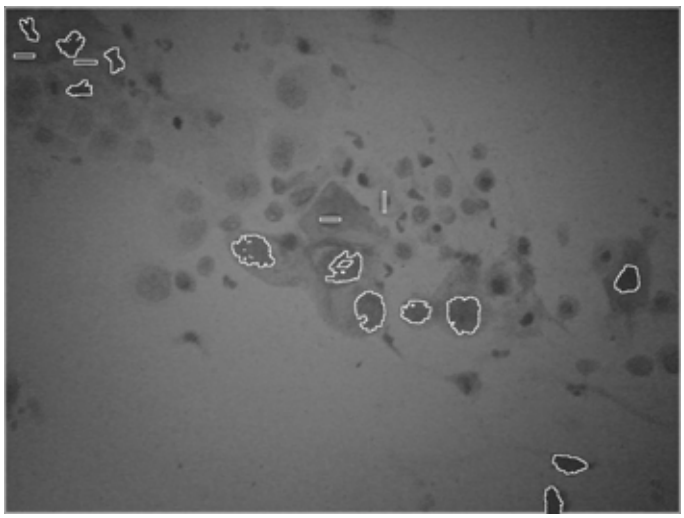

Figure 5. The cell nuclei detected by grey-level method.

C. *Energy Method*

Enlarged cell nuclei with lower grey level are a type of abnormal cell nuclei, but these abnormal cell nuclei cannot be captured by grey level method due to their low grey level. Therefore, energy method is provided. Energy method enhances these cell nuclei which have low grey level.

Energy method works with two mean filters. One of them has a larger mask and is taken as a background-energy operator. The other has a smaller mask and is taken as a local-energy operator. By subtracting local energy from background energy, cell nuclei in the image would be enhanced. And then, there should be a threshold to decide which pixel is part of cell nuclei and which is not.

The size of the filters and the threshold for the subtracting result are important factors. The size of the filters is chosen according to the size of normal cell nuclei. The threshold for the subtracting result is zero, since cell nuclei in the image are considered to be darker than the background.

Comparing the enhanced image to the original image, cell nuclei are clearer in the enhanced image. It's as shown in Fig 6. The image on left side is a original image and the other is the enhanced image. Obviously, the enhanced image has a higher contrast and is easier for setting threshold.

This method is also applied to Fig 3 and the enhanced image is as shown in Fig 7. The result of line-scanning is shown in Fig 8.

Some of the abnormal cell nuclei are not captured here, but are captured by the grey-level method. Combing these two methods, most of the abnormal cell nuclei are captured.

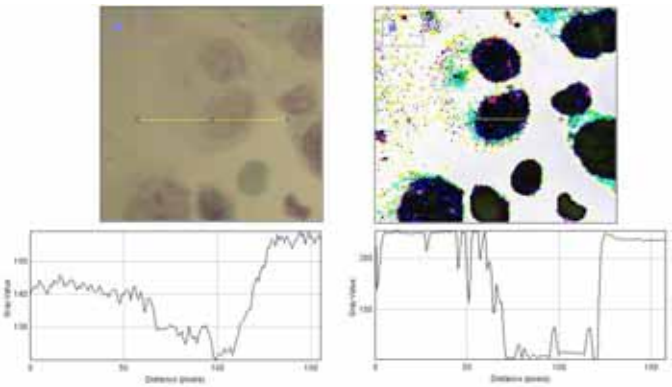

Figure 6. On the left side, it's a original image. On the right side, it's the enhanced image of the left one. In the plot of the left side image, it's obvious that choosing a threshold to determine whether a pixel is a part of cell nuclei is difficult. However, the enhanced image has high contrast and is easy for choosing threshold..

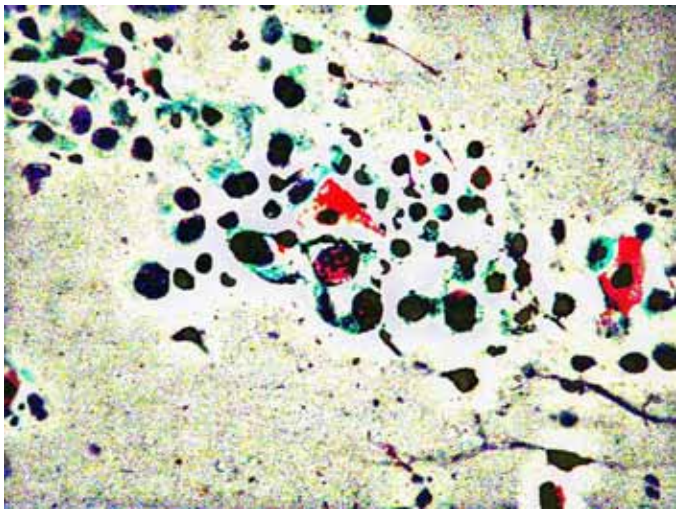

Figure 7. The enhanced image.

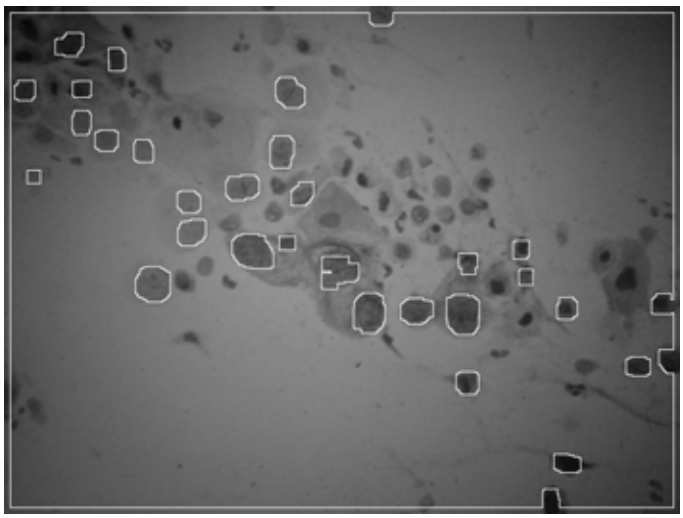

Figure 8. The cell nuclei detected by energy method.

III. CURRENT RESULT AND FUTURE WORK

We have come up with an efficient method capturing abnormal cell nuclei. All the suspicious cell nuclei in Fig 3 are found by combining Fig 5 and Fig 8. Even though the quality of the image is limited, we can still detect the abnormal cell nuclei. The reported automatic cytological specimen classification system is successful to recognize abnormal cells from normal cells with low complexity and high sensitivity from those low contrast images.

Applying our methods to different images, these methods still work as shown in Fig 9, but some special issues are disturbing us. Take Fig 10 as an example, the abnormal cell nucleus E is not captured. And the captured cell nucleus D is enlarged. The half on the right side shouldn't be involved. Figuring out the problem, we look into Fig 113, the enhanced image of Fig 10. It shows that the cell nucleus E can be seen in the enhanced image, but not as dark as other cell nuclei.

In the future, we will be working on recognizing the pattern of color in the enhanced images, or taking different imaging

technology into consideration.

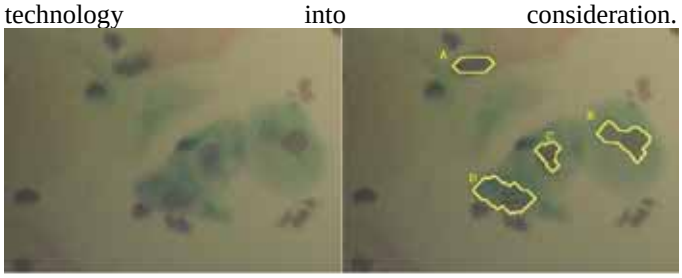

Figure 9. Four abnormal cell nuclei are captured.

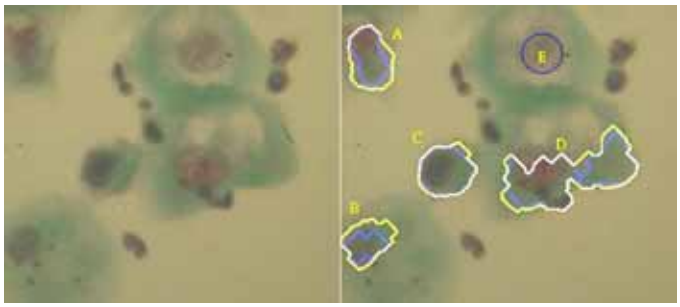

Figure 10. The image with several problems.

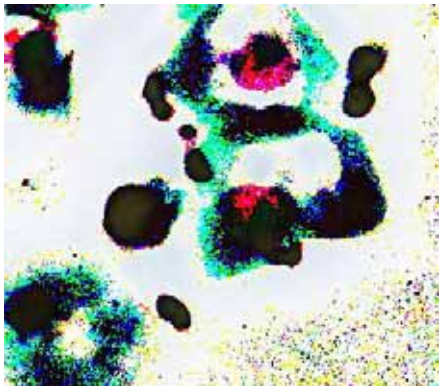

Figure 11. The enhanced image of Fig 9.

ACKNOWLEDGMENT

This work cannot be done without the help of the research team of Advanced Electronic System Division of Instrument Technology Research Center. Special thanks to T.S. Liao, C.F. Lin, R.C. Weng, S.J. Jou, and T.L. Huang. This project is also supported by the research team of Department of Pathology of China Medical University Hospital. Special thanks to Hung-Juan and Jia-Hui.

REFERENCES

[1] Paavonen J, "Human papilloma virus infection and the development of cervical cancer and related genital neoplasias", Int. I. Infect. Dis., 11, Supp 2:S3-9, Review, 2007.

[2] M.E. Plissiti, A. Charchanti, O. Krikoni and D.I. Fotiadis, "Automated segmentation of cell nuclei in PAP smear", Greece, in *proc.IEEE International Special Topic Conference of Information Technology in Biomedical, Oct. 26-28, 2006*

[3] Begelrnan G, Gur E, Rivlin E, RudzskyM and Zalevsky Z, "Cell nuclei segmentation using fuzzy logic engine", *Proceedings of International Conference on Image Processing, Volume 5, 2937 - 2940, 2004*.

[4] Gang Li, Tianming Liu, Jingxin Nie, Lei Guo andWong STC, "Segmentation of touching cells using gradient flow tracking", *Proceedings of International Symposium on Biomedical Imaging 2007, 77-80*

[5] Xiaowei Chen, Xiaobo Zhou, Stephen T.C. Wong, "Automated Segmentation, Classification, and Tracking of Cancer Cell Nuclei in Time-Lapse Microscopy", *IEEE Transactions on Biomedical Engineering, VOL. 53, No. 4, April 2006, 762-766*

Development of Wireless Batteryless Implantable Blood Pressure-EKG-Core Body Temperature Sensing Microsystem for Genetically Engineered Mice Real Time Monitoring

Darrin J. Young

Electrical and Computer Engineering, University of Utah, U.S.A.

Abstract — **Two wireless implantable microsystems; one for blood pressure sensing and one for EKG and core body temperature sensing; are developed for untethered genetically engineered mice real-time monitoring. A flat silicone blood pressure sensing cuff and a low power ASIC are employed to form a novel wireless less-invasive blood pressure monitoring microsystem, which demonstrates a packaged system weight of 130 mg representing at least ten times mass reduction compared to any commercially available implantable blood pressure sensing technology. The system is powered by an adaptively controlled external RF energy source at 4 MHz to ensure a stable on-chip 2V supply with 150 µA current load from the microsystem, and achieves a sensing resolution of 0.8 mmHg. A packaged EKG and core body temperature sensing microsystem exhibits a total size of 9 mm x 7 mm x 3 mm with a weight of 400 mg including a pair of stainless steel EKG electrodes and demonstrates wireless *in vivo* EKG and body temperature sensing capability under the same adaptive RF powering condition. On-going research effort is devoted to realize a standalone wireless implantable three-channel (blood pressure, EKG, and core body temperature) bio-sensing microsystem.**

Keywords — **Biomedical implant, Batteryless implant, *In vivo* blood pressure sensing, *In vivo* EKG sensing, RF powering, Wireless sensing.**

I. Introduction

DNA sequencing of small laboratory animals together with *in vivo* real-time biological information, such as blood pressure, core body temperature, and bio-potential signals, is ultimately crucial for biomedical and system biology research to identify genetic variation susceptibility to diseases, for example hypertension, obesity, epilepsy and cancers [1], and to potentially develop new treatment methods for similar human diseases. Due to the small size of laboratory animals, such as genetically engineered mice commonly known as knockout mice, a miniature, light-weight, wireless, batteryless, and implantable bio-sensing microsystem is highly desirable to capture accurate biological signals from an untethered animal in its natural habitat as shown in Figure 1, thus eliminating stress and post-implant trauma-induced information distortion. Remote RF powering based on inductive coupling has been widely used for biomedical implants [2]. However, the proposed microsystem is implanted in a freely roaming knockout mouse; hence, resulting in a drastically changing magnetic coupling as the mouse tilts and moves its position with respect to the external stationary RF powering coil. Therefore, an optimized system design with an adaptive RF power control capability is highly critical to ensure a sufficient and stable energy to power the implantable system in a varying magnetic coupling field. In addition, RF powering can eliminate the need of a battery, thus substantially reducing the overall implant size and weight. Furthermore, a miniature RF coil can be employed due to low-power consumption of the integrated electronics, thus resulting in a further system miniaturization.

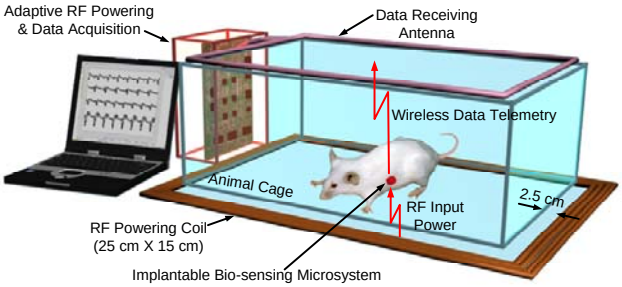

Figure 1. *In vivo* real-time wireless and batteryless bio-sensing microsystem.

In this paper, the design, implementation, and *in vivo* evaluation of two implantable microsystems; one for blood pressure sensing and one for EKG and core body temperature sensing; are presented with an adaptive RF power control capability for real-time untethered laboratory mice monitoring. On-going research effort to develop an adaptively RF-powered wireless implantable microsystem with blood pressure, EKG, and core body temperature sensing capability is also described.

II. Wireless Implantalbe Blood Pressure Sensing Microsystem

Among all the biological signals, blood pressure is one of the most important vital signals, and there is no adequate solution for its long-term *in vivo* monitoring to date. This section describes the development of a standalone, wireless, batteryless, implantable blood pressure sensing microsystem for small laboratory animals real-time long-term monitoring.

A. Less-Invasive Blood Pressure Monitoring

The most common technique for monitoring blood pressure in small laboratory animals relies on using an invasive catheter-tip transducer inserted into an artery or a tail cuff device. The implantable catheter-tip transducers require a

This work was supported by U.S. National Science Foundation under contract # EIA-0329811.

Contact author: **darrin.young@utah.edu*

complex surgical procedure and potentially suffer from hypertension, blood clotting, and reduced sensitivity with drift over time. Tail cuffs require animal restraint, thus resulting in a stress-induced signal distortion. Furthermore, tail cuffs can only obtain systolic and diastolic blood pressure levels instead of a continuous blood pressure waveform with detailed signatures, which are highly desirable for advanced biomedical research. Therefore, both approaches are inadequate for real-time long-term accurate monitoring. A miniature implantable pressure sensing cuff for tonometric blood pressure measurement was proposed [3]. This technique could solve the issues associated with the conventional methods listed above, but significantly deforms the blood vessel shape, which can cause adverse physiological effects to the vessel property and thus may not be suitable for long-term monitoring. It is, therefore, desirable to develop a long-term implantable blood pressure monitoring microsystem without the aforementioned concerns.

A novel, wireless, implantable, and less-invasive blood pressure monitoring system is presented in this section. The system employs an instrumented elastic cuff wrapped around a blood vessel to sense real-time blood pressure waveforms as illustrated in Figure 2.

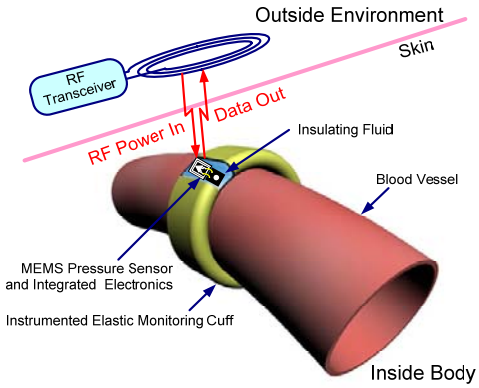

Figure 2. Wireless less-invasive blood pressure monitoring microsystem.

The elastic cuff is made of bio-compatible silicone and is filled with bio-compatible insulating fluid with an immersed MEMS pressure sensor and integrated electronic system. The MEMS sensor measures the pressure waveform coupled from the expansion and contraction of the vessel. The measured waveform represents a down-scaled version of the vessel blood pressure waveform and can be processed by nearby low-power integrated electronic system, consisting of MEMS sensor interface circuitry, analog-to-digital converter (ADC) and system configuration and control unit, for signal conditioning and coding followed by wireless data telemetry to an external receiver. A post-implant calibration can be performed to reconstruct the vessel blood pressure waveform from the measured data. The proposed design avoids vessel occlusion, bleeding, and blood clotting associated with the conventional catheter-tip-based technique. Furthermore, since the cuff is made of soft elastic material, the restrictive effect on the vessel is substantially minimized, thus suitable for long-term monitoring. The sensor, electronics, and RF powering coil are inside the cuff as depicted in Figure 2 for an illustration purpose. In the final system design, the coil will be located outside the cuff to minimize packaging complexity.

B. Implantable Blood Pressure Monitoring Cuff

Animal implant study has revealed that the proposed circular blood pressure sensing cuff can be successfully implanted in laboratory rats exhibiting an artery diameter around 1 mm [4]. However, genetically engineered mice have a much reduced artery size typically on the order of 200 μm. Therefore, it is difficult to apply the circular blood pressure sensing cuff in mice for *in vivo* real-time monitoring. A further miniaturized cuff with a reduced inner radius can be made but significantly increasing the complexity of fabrication and implant procedure. Therefore, a flat sensing cuff structure is proposed for mice implant with the cuff cross-sectional view depicted in Figure 3.

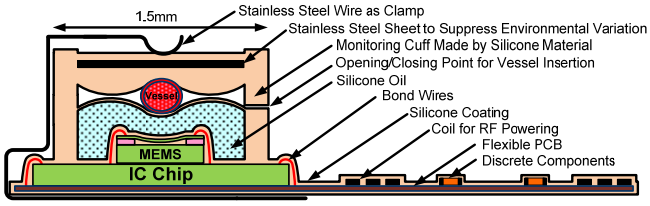

Figure 3. Cross-sectional view of flat blood pressure sensing cuff.

A blood vessel is sandwiched within the flat sensing cuff structure for blood pressure monitoring. A thin silicone sensing membrane and silicone side walls, together with a MEMS/IC base, constitute the bottom part of the sensing cuff. The top part of the sensing cuff is formed by a silicone layer with an embedded stainless steel sheet. The gap between the two parts, defined by a silicone spacer, is designed to be smaller than the blood vessel diameter to ensure a proper contact between the cuff and blood vessel. The cavity in the bottom part of the cuff is filled with silicone insulting oil with an immersed MEMS pressure sensor positioned over an IC base. The blood pressure waveform is coupled to the cavity caused by the vessel expansion and contraction and is then measured by the MEMS/IC pressure sensing module. Similar to the circular blood pressure sensing cuff, the measured waveform represents a down-scaled version of the blood pressure waveform in the vessel with a typical scaling factor of 10%. The flat silicone sensing cuff can be fabricated by a similar machining and molding process used for fabricating the circular cuff [4]. The operation principle is similar to the implantable tonometric blood pressure measurement device reported in [3]. However, flattening of blood vessel is not required for the measurement, thus avoiding significant vessel deformation. The stainless steel sheet embedded in the top silicone layer and the MEMS/IC base can effectively suppress environmental variations effect on the cuff performance. An opening/closing point is designed together with a stainless steel wire clamp for vessel insertion. During an implant, the clamp is first lifted up for a blood vessel insertion through the

opening/closing point and is then released to secure the cuff in position with respect to the vessel, thus substantially simplifying the implant procedure. A 300-μm thick flexible PCB containing discrete components and an RF powering coil is employed to hold the MEMS/IC base with bond wires used to form electrical connections between MEMS/IC and flexible PCB substrate.

C. Implantable Blood Pressure Sensing Electronic System

Figure 4 presents the overall implantable blood pressure sensing electronic system design architecture.

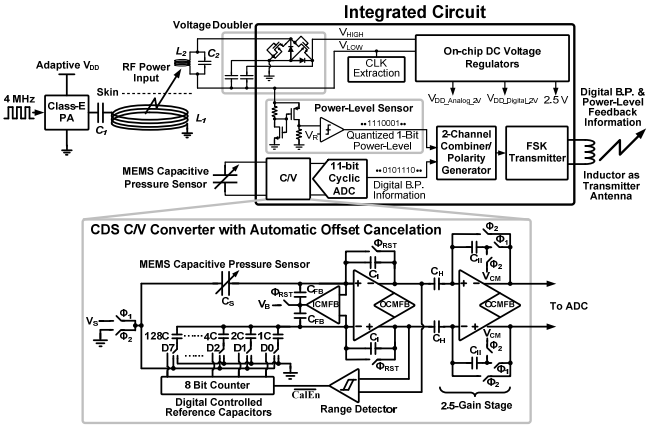

Figure 4. Implantable blood pressure sensing electronic system architecture.

A correlated-double-sampling (CDS) capacitance-to-voltage (C/V) converter is designed for a precision interface with a MEMS capacitive pressure sensor exhibiting a dimension of 0.4x0.5x0.4 mm^3 with a nominal capacitance of 2 pF and a sensitivity of 0.8 fF/mmHg [5]. An automatic capacitance offset cancellation scheme is incorporated at the input by employing an 8-bit digitally controlled reference capacitor array, C_R [6]. This technique allows a single-ended pressure sensor with a wide range of nominal capacitance value to be used, thus greatly simplifying MEMS fabrication process and tolerance requirements, and can also effectively suppress the output offset voltage. A fully differential architecture is chosen for the electronics to suppress common-mode disturbances. An input common-mode feedback (ICMFB) circuit is incorporated with the converter to minimize any residual offset due to mismatch of input parasitic capacitances and drift over time. A fully differential telescopic amplifier is chosen for the C/V converter for its low noise and low power dissipation. The amplifier is biased in weak inversion with a 6 μA bias current, achieving an input-referred noise of $13nV/\sqrt{Hz}$ which corresponds to a capacitance sensing resolution of approximately 75 aF or a pressure resolution of 0.1 mmHg over 1 kHz. With a typical cuff scaling factor of 10%, a vessel blood pressure sensing resolution of 1 mmHg is expected. A fully differential 11-bit cyclic ADC is designed to digitize the pressure information [7]. The digitized blood pressure signal is then Manchester-encoded and transmitted to an external receiver by a 433 MHz oscillator-based transmitter through FSK with a bias current of 120 μA.

D. Adaptive RF Powering Design

An external RF power is coupled into the microsystem via a tuned LC network followed by a CMOS voltage doubler and regulators to produce stable 2V supplies for the system and a 2.5V supply for controlling MOSFET switches as shown in Figure 4. An implantable coil is designed to be 5 mm in diameter as a trade-off between coil size and RF coupling coefficient. For a typical mouse cage floor size of 10 cm x 20 cm, an external RF powering coil is designed with a dimension of 15 cm and 25 cm as depicted in Figure 1, thus avoiding the powering peak zone and dead zone due to the magnetic flux direction with respect to the implantable coil orientation [8, 9]. Experimental characterizations reveal that an optimal power coupling efficiency can be obtained at 4 MHz with a 20-turn implantable coil and 4-turn external coil exhibiting an inductance value of 13 μH and 2.6 μH, respectively, for the designed microsystem power consumption requirement [9]. Further testing shows that the coupling coefficient, k, varies approximately from 0.001 to 0.004 in the operation region with a nominal gap size around 2 cm between the two coils and various implantable coil titling angles up to 60^o, which would result an 18 times variation in the received RF power from a constant power source. This level of power variation would cause a maximum V_{HIGH} over 70V from the CMOS doubler shown in Figure 4. This high voltage is well beyond the gate oxide breakdown voltage of the MOSFETs. Therefore, a power control function becomes highly critical to ensure the doubler output voltage below 10V for microsystem reliability. An integrated RF power level indicator is incorporated in the system design to sense the incoming RF power level and produce a one-bit control signal as illustrated in Figure 4. The circuit consists of a voltage level detector with a reference voltage, V_R, which can be designed for various power requirements. Using this configuration, a one-bit digital RF power-level signal can be produced. The RF power-level bit becomes "1" when there is more power than necessary being coupled to the implant and otherwise "0". The one-bit control signal is then wirelessly transmitted along with the blood pressure data to an external receiver to adaptively adjust the external RF power level by controlling the power supply voltage of the external power amplifier. An updating frequency of 10 Hz is chosen for the prototype design, which is adequate for tracking animal movement. The external power amplifier supply voltage is adjusted at a voltage step of 0.3V, which results in a negligible ripple at the voltage regulators output due to the regulators large supply rejection ratio at low frequency [8].

E. Packaged Implantable Blood Pressure Monitoring System

The electronic system is fabricated in AMI 1.5 μm CMOS process and occupies an area of 2.2 mm x 2.2 mm. Figure 5 presents the fabricated chip micrograph. The MEMS pressure sensor is directly attached over the IC by epoxy and wire bonded to form electrical connections for the prototype system. The module is then interfaced with an RF powering coil exhibiting 20 turns and 5 mm in diameter, and discrete

components over a thin flexible substrate with a thickness of 125 µm as shown in Figure 6.

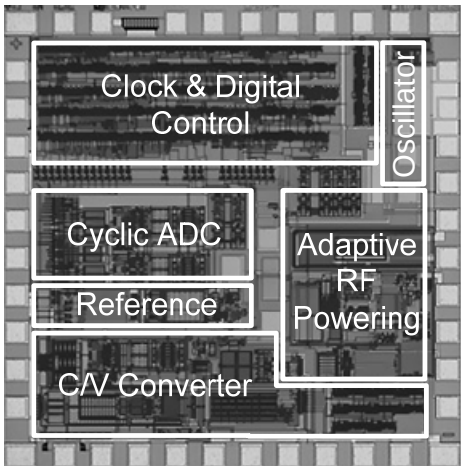

Figure 5. Micrograph of wireless blood pressure sensing ASIC.

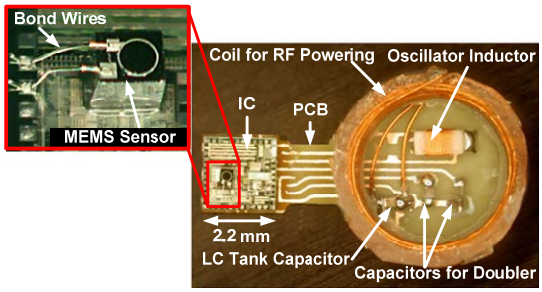

Figure 6. Electronic system packaging.

These components can be potentially integrated on chip at expense of silicon area and power dissipation. The overall microsystem is then coated with a thin silicone layer for system protection. Characterization shows that the MEMS capacitive pressure sensor performance is insensitive to the thin silicone coating. The overall electronic system is then interfaced with the flat blood pressure sensing cuff followed by silicone seal and silicone oil filling as shown in Figure 7.

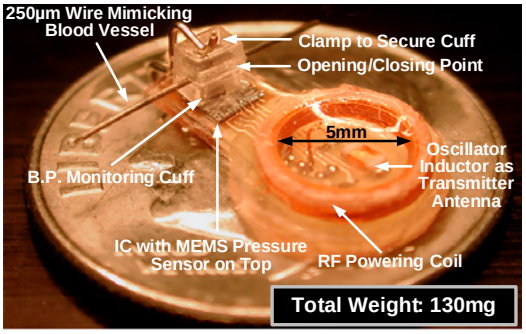

Figure 7. Packaged wireless blood pressure monitoring microsystem.

In the picture, a metal wire with a diameter of 0.25 mm is used to emulate a blood vessel for demonstration purpose. The microsystem achieves an overall weight of 130 mg, representing more than ten times mass reduction compared to any state-of-the-art commercial implantable blood pressure sensing technology.

III. Wireless Implantable EKG and Core Body Temperature Sensing Microsystem

EKG and core body temperature are two other important vital signals for system biology and genetic research. This section presents the development of a wireless batteryless implantable EKG and core body temperature sensing microsystem for laboratory animals real-time monitoring.

A. EKG and Core Body Temperature Sensor Configuration

Figure 8 illustrates a conceptual diagram of a such packaged wireless implantable sensing microsystem consisting of integrated electronics with external passive components, such as RF power receiving coil, data transmitting coil, filtering capacitors, and bio-potential sensing electrodes.

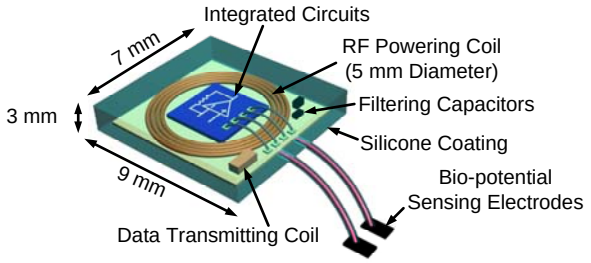

Figure 8. Wireless implantable EKG and core body temperature sensing microsystem package configuration.

The system occupying a volume of 9 mm x 7 mm x 3 mm with a total weight of 400 mg can be implanted inside an untethered mouse abdomen. The RF power receiving coil is constructed in a planar spiral configuration around the ASIC to reduce the overall system thickness for a compact design. The flat and thin configuration can provide a comfortable fit inside the mouse abdomen.

B. Electrical System Design Architecture

Figure 9 presents the overall electrical system design architecture. The integrated implant electronics are designed based on an on-chip 2V DC supply for minimizing system power consumption as well as power dissipated by the external adaptive RF energy source. The EKG signal with a typical amplitude from 20 µV – 5 mV within 100 Hz bandwidth, corresponding to an 8-bit dynamic range, is obtained by a pair of stainless steel EKG electrodes placed across a laboratory mouse chest. A CMOS PTAT temperature sensor is designed to detect core body temperature by sharing the same 8-bit ADC with 0.1 ºC sensing resolution. A charge-redistribution ADC architecture is chosen for its low power dissipation. The 8-bit EKG and core body temperature data are then appended with a 1-bit RF power-level sensing data. The digital information is processed by a parallel to serial converter and multiplexer to form a serial data bit-stream. In order to achieve system synchronization, the digital data is Manchester-encoded before wireless transmission by employing a similar FSK transmitter used for blood pressure data

transmission.

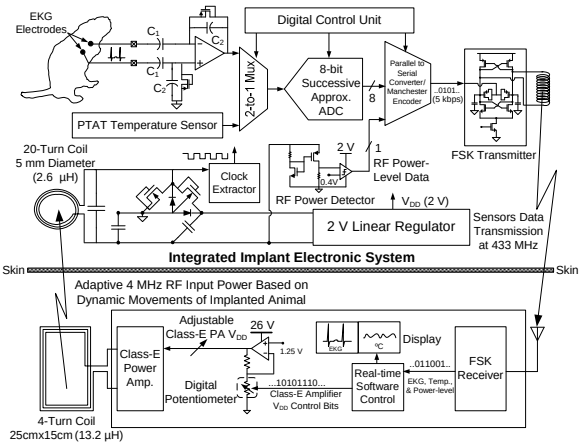

Figure 9. Overall system design architecture for wireless EKG and core body temperature sensing.

The received EKG and core body temperature can be displayed for real-time animal physiological monitoring. The received RF power-level data is used to adaptively control the Class-E power amplifier V_{DD} so that the transmitted RF power level is adjusted based on the untethered animal movement to ensure a stable on-chip power generation.

C. Assembley of Wireless Implantable EKG and Core Body Temperature Sensing Micorsystm

The prototype implantable microsystem consisting of a 2.2 mm x 2.2 mm 1.5 µm CMOS ASIC with an RF powering coil, two external filtering capacitors and one VCO tuning inductor/antenna is presented in Figure 10. To conduct an *in vivo* characterization, the implantable microsystem is packaged by using a sequential packaging process flow shown in Figure 11 [10]. The ASIC is mounted on a 0.6 mm-thick PCB with electrical connections formed by bondwires. A glob-top encapsulant is applied to protect the bondwires before three miniature discrete components, a pair of stainless-steel electrodes (100 mg), and a 5 mm diameter RF coil are attached. The final microsystem is coated with biocompatible silicone and exhibits a weight of 400 mg.

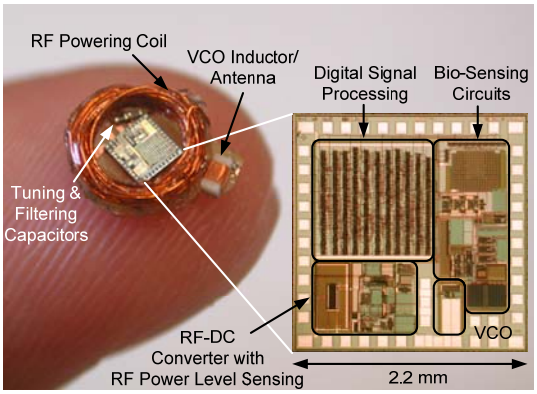

Figure 10. CMOS ASIC with RF powering coil and discrete components.

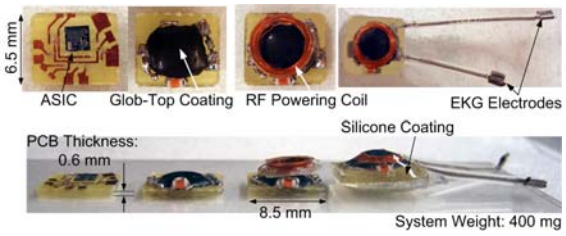

Figure 11. Packaging sequence of implant EKG and core body temperature sensing microsystem.

IV. Measurement Results

The blood pressure sensing cuff shown in Figure 8 was implanted in genetically engineered mice for *in vivo* characterization under a wireless and batteryless condition as shown in Figure 12.

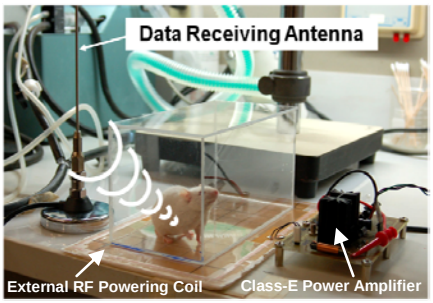

Figure 12. Wireless batteryless *in vivo* characterization in mouse.

Aorta artery was selected for the ease of implant procedure. The recorded blood pressure waveform after animal recovery is shown in Figure 13, indicating (1) the aorta artery blood pressure amplitude of 31 mmHg based on a scaling factor of 0.13 determined during the implant, and (2) the prototype microsystem can capture real-time high-fidelity blood pressure information [7].

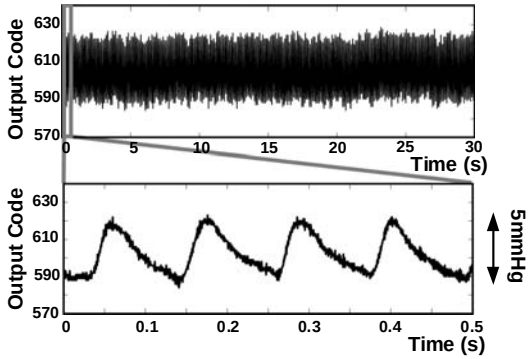

Figure 13. Wirelessly received blood pressure waveform.

The wireless EKG and core body temperature sensing microsystem was also implanted in an untethered laboratory mouse for *in vivo* evaluation. Figure 14 presents the wirelessly received real-time EKG and temperature data. The EKG signal exhibits a normal QRS complex waveform with a heart rate of 638 beats per minute. The amplitude variation is due to the mouse respiration with a fundamental frequency of approximately 1.5 Hz. The real-time temperature channel shows an average core body temperature of 35.4 ºC with a

peak-to-peak animal body temperature fluctuation of less than 0.35 ºC. The 1-bit RF power-level data together with real-time adaptively adjusted Class-E power amplifier V_{DD} for tracking the implanted mouse movement is also illustrated in Figure 14 [10].

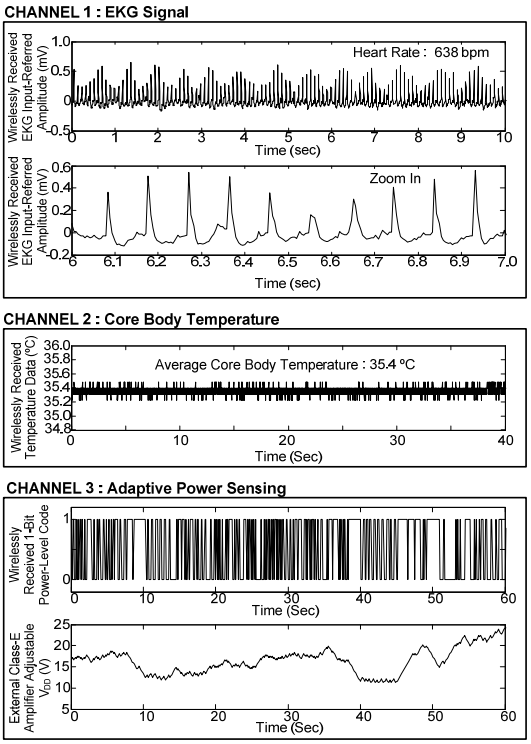

Figure 14. Wirelessly received EKG, core body temperature, and adaptive RF powering information.

V. Development of Implantable Blood Pressure-EKG-Core-Body Temperature Sensing Microsystem

The implantable EKG and core body temperature sensor can be incorporated into the blood pressure sensing module to realize a standalone wireless implantable three-channel (blood pressure, EKG, and core body temperature) sensing microsystem. Figure 15 presents the micrograph of a fabricated ASIC in AMI 1.5 µm CMOS process containing all required electronic circuitry for realizing a such system.

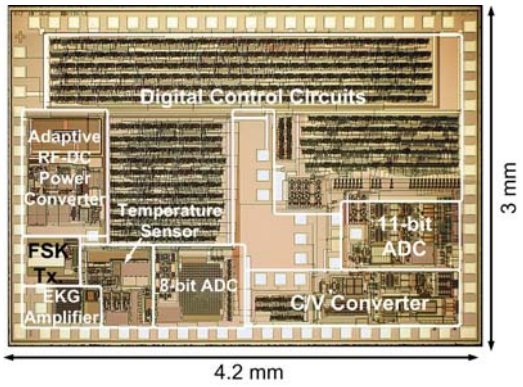

Figure 15. Micrograph of ASIC for blood pressure, EKG, core body temperature sensing microsystem.

Initial electrical testing reveals expected functionalities. On-going research effort is devoted to interface the ASIC with silicone blood pressure sensing cuff and EKG sensing electrodes to realize a three-channel bio-sensing microsystem.

VI. Conclusion

Two wireless implantable microsystems; one for blood pressure sensing and one for EKG and core body temperature sensing; are developed for untethered laboratory mice real-time monitoring. A silicone blood pressure sensing cuff made by conventional machining is critical for less-invasive blood pressure monitoring. Animal implant study reveals that a flat sensing cuff configuration is adequate for genetically engineered mice monitoring exhibiting an artery diameter around 0.2 mm. Low power ASICs are highly essential for accommodating small RF powering coils, thus enabling miniaturized microsystems. It has been demonstrated that adaptive RF powering is critical to ensure a sufficient and stable energy to power an implantable system in a varying magnetic coupling field. On-going research effort is devoted to develop a standalone adaptively RF-powered wireless microsystem with blood pressure, EKG, and core body temperature sensing capability.

References

[1] B. Hoit, S. Kiatchoosakun, J. Restivo, D. Kirkpatrick, K. Olszens, H. Shao, Y. Pao, and J. Nadeau, "Naturally Occurring Variation in Cardiovascular Traits among Inbred Mouse Strains," *Genomics*, vol. 79, no. 5, May 2002, pp. 679-685.

[2] W. H. Ko, S. P. Liang, and C. D. F. Fung, "Design of radio-frequencypowered coils for implant instruments," *Medical and Biological Engineering and Computing*, vol. 15, pp. 634-640, November 1977.

[3] B. Ziaie, T. Wu, N. Kocaman, K. Najafi, and D. J. Anderson, "An Implantable Pressure Sensor Cuff for Tonometric Blood Pressure Measurement," *IEEE Solid-State Sensor and Actuator Workshop*, pp. 216-219, 1998.

[4] P. Cong, D. J. Young, B. Hoit, and W. H. Ko, "Novel Long-Term Implantable Blood Pressure Monitoring System with Reduced Baseline Drift," *the 28th Annual International Conference of the IEEE Engineering in Medicine and Biology Society*, pp. 1854-1857, 2006.

[5] P. Cong, W. H. Ko, and D. J. Young, "Wireless Implantable Blood Pressure Sensing Microsystem Design for Small Laboratory Animals Monitoring," *Sensors and Materials*, vol. 20, Issue 7, pp. 327-340, 2008.

[6] P. Cong, W. H. Ko, and D. J. Young, "Low noise µWatt interface circuits for wireless implantable real-time digital blood pressure monitoring," *IEEE CICC* , pp. 523-526, 2008.

[7] P. Cong, N. Chaimanonart, W. H. Ko, and D. J. Young, "A Wireless and Batteryless 130 milligram 300 µW 10-bit Implantable Blood Pressure Sensing Microsystem for Real-time Genetically Engineered Mice Monitoring," *IEEE International Solid-State Circuits Conference (ISSCC)*, pp. 428-429, 2009.

[8] N. Chaimanonart, M. D. Zimmerman, and D. J. Young, "Adaptive RF power control for wireless implantable bio-sensing network to monitor untethered laboratory animal real-time biological signals," *the 7th IEEE Conference on Sensors*, pp. 1421-1424, 2008.

[9] M. Zimmerman, N. Chaimanonart, D. J. Young, "*In Vivo* RF Powering for Advanced Biological Research," *the 28th Annual International Conference of the IEEE Engineering in Medicine and Biology Society*, pp. 2506-2509, 2006.

[10] N. Chaimanonart and D. J. Young, "A Wireless Batteryless *In Vivo* EKG and Core Body Temperature Sensing Microsystem with Adaptive RF Powering for Untethered Genetically Engineered Mice Real-Time Monitoring," *the 15th International Conference on Solid-State Sensors, Actuators and Microsystems*, pp. 1473-1476, 2009.

P30

The Effect of Voltage and Diameter of Anodic Porous Alumina in Acid Solutions

[1]Guo-Dung Chen and [1]Cheng-Yang Liu

1 Center for Measurement Standards, Industrial Technology Research Institute, Hsinchu, Taiwan

Abstract — **Anodic aluminum oxide (AAO) is fabricated by electrochemical anodization of aluminum. This work is focused on the optimization on the diameter of the pores in anodic aluminum oxide (AAO) template. The Al sheet (20 x 20 x 0.15 mm) and Al (1 μm) deposited on silicon wafers (p-type) were used for anodic aluminum oxide (AAO) growth. The growing time, temperatures, kinds of electrolyte, working voltage were used to optimize the anodization of alumina. Besides, the effect of working voltage on the diameter of pores was also investigated. The porous array of alumina film has a uniform; closely packs honeycomb structure approximately 15 nm to 150 nm in diameter. Because of this, the structure is a good material for photonic crystal application in the future. This structure of alumina film is observed by scanning electrical microscope (SEM), and the density of porous channels was also obtained (10^{10} /cm^2).**

Keywords — anodic aluminum oxide, electrochemical process, and photonic crystal.

I. INTRODUCTION

The history of electrochemical process of aluminum anodic aluminum dates back to 20th century. Initially, the anodic treatment of aluminum was mostly used to protect and decorate its surface of film. As time goes by, the application of alumina which has a distribution of narrow pores has been developed [1, 2]. For example, several groups use this inorganic membranes (AAO) as a template for nanostructure-materials preparation, biological and chemical separations, solution flow regulation and biosensors [3-7], Nowadays, porous alumina became one of the most prominent template materials.

Anodic aluminum oxide, which is a simple and self-ordered structure, recently has tremendous attractions as a key material for developing devises for nanowires [8] or nanotubes growth and photonic crystal (PC) application. The geometrical structure of anodic aluminum oxide is schematically present as a hexagonally packed array of cylindrical cells (see the Fig. 1). Because of this, high aspect ratio; controllable diameter of nanowres or nanotubes can be obtained, and the periodic arrays of porous alumina also have advantages of fabricating the photonic crystal devices. However, the regular distribution and pore size of anodic alumina was concerned for these applications. Thus, the method about nanoimprint [9] which improved the regular arrangement of cells and pore size were developed. In addition, two steps process of anodization was also proposed. Improvement of well-distribution and pore size of anodic alumina is essential so that the performance of functional devices can be optimized. Here, we discuss the relation of working voltage and diameter of porous alumina and growth condition for anodic alumina template. The fabrication process and current results were described in this work.

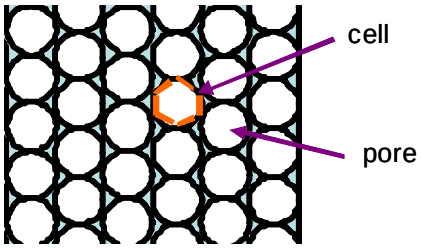

Fig. 1. The idealize structure of anodic alumina.

II. EXPERIMENTAL

Anodic aluminum oxide is fabricated as shown in Fig. 2. Briefly, an aluminum deposited on silicon substrate is cleaned with acetone (or $HF/HNO_3/HCl/H_2O$) and then annealed in N_2 at 500 °C for 3 h. Subsequently, it is electropolished under a constant voltage (or current) in a mixing solution of $HClO_4$ and C_2H_5OH at 10 °C for 4 min. After the pretreatment, First anodization is operated under a constant voltage in sulfuric acid, oxalic acid, and phosphoric acid at 10 °C for 2 or 5 min. However, the porous alumina film formed on surface is irregular in first anodization. Then, the first-anodized aluminum substrate is etched in the mixing solution of chromic acid and phosphoric acid for 8 or 20 min in order to obtain the hexagonally close-packed arrays at the interface of alumina layer and aluminum substrate. It is necessary to perform the second anodization after etching in the mixing acid. The second anodization is under the same condition as the first anodization except the growing time. Finally, to widen the size of pores, we can dip phosphoric acid on porous alumina film (all parameters are described on Table. 1.). After anodization, we investigated the morphology of porous alumina film by scanning electrical microscope as shown in following paragraph. In this work, we altered the working voltage in order to find the relation of voltage and diameter in

anodization. On the other hand, we also used three kinds of acids as electrolytes to fabricate the anodic alumina.

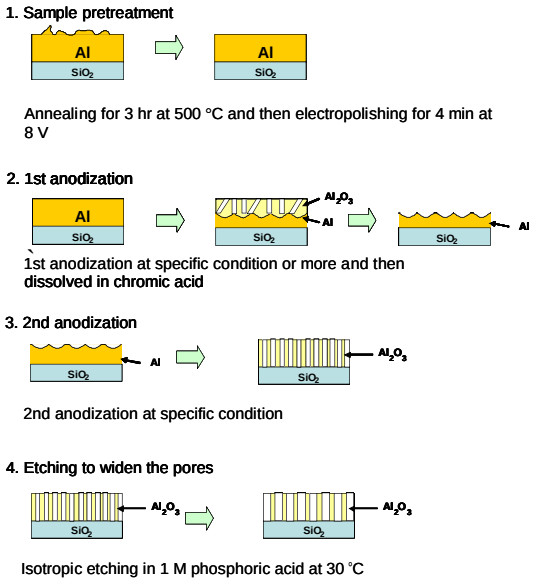

Fig. 2. The process for anodic alumina growth.

Everything we did is optimizing the diameter of pores for photonic crystal application and the results implied that the diameter of pores in aluminum oxide was influenced by the working voltage. we also found that the diameters of pores which grew in different electrolyte were changed even at the same voltage.

Table. 1. The parameters of anodization

Chemicals	**Oxalic acid, sulfuric acid, and phosphoric aicd**
Temperature	**10 °C**
Voltage	**5 V, 15 V, 20 V, 25 V, 40 V, and 135 V**
1st anodization time	**2 min,and 5 min**
Etching time	**8 min, and 20 min**
2nd anodization time	**10 min, 20 min, and 30 min**

III. RESULTS AND DISCUSSION

In this work, we used two kinds of substrates. One is the aluminum sheet (20 x 20 x 0.15 mm), and other is the aluminum deposited on silicon wafer. As shown in Fig. 3, there are two kinds of substrates grown in sulfuric acid. In Fig.3. (a) is aluminum sheet which grow at 20 V and 10 °C. Then, the Fig. 3 (b) is aluminum wafer which grown in the same conditions like Fig.3 (a). The morphology of two kinds of substrates is almost the same. This anodic alumina is periodic arrays and regular distribution. However, the anodic aluminum oxide on aluminum wafer is more regular than that on aluminum sheet. Besides, the diameter of pores in aluminum sheet and wafer are about 25 nm. Thus, the conditions of both substrates are successful to grow fine and regular anodic alumina so far. It is possible for photonic crystal application.

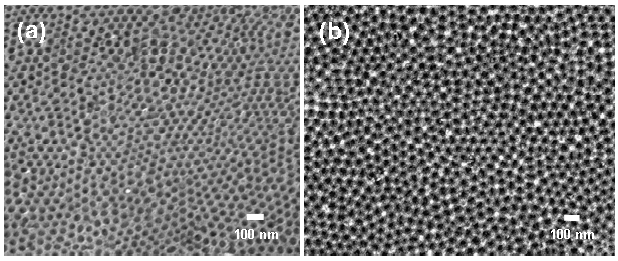

Fig. 3. The SEM micrographic of (a) aluminum sheet and (b) aluminum wafer anodized in sulfuric acid.

In addition to the successful alumina grown in sulfuric acid, we also used difference of electrolytes to anodize the aluminum sheet and wafer as shown in Fig. 4, and Fig. 5. It is quiet difference of anodic alumina grown in two electrolytes. In Fig. 4, both substrates were grown in oxalic acid. Besides, these growing conditions are also the same (10 °C, 35 V). Then, we can investigate the pores in aluminum wafer is more regular than that in aluminum sheet. The diameter of pores in aluminum wafer is more uniform than that in aluminum sheet. The diameter in aluminum wafer is about 55 nm and the other is 40 ~ 55 nm. In Fig. 5, both substrates are grown in phosphoric acid and the same conditions (10 °C, 130 V). the morphology of anodic alumina in Fig. 5. (b) is also more regular than that in Fig. 5 (a). In above results, we find that the different substrates influence uniformity of pores for anodization of alumina. Another phenomenon is different electrolytes result in diameter of pores. The diameter of anodic alumina grown in phosphoric acid is larger than the others acids. Because of this, we can control the diameter of pores for anodic alumina growth.

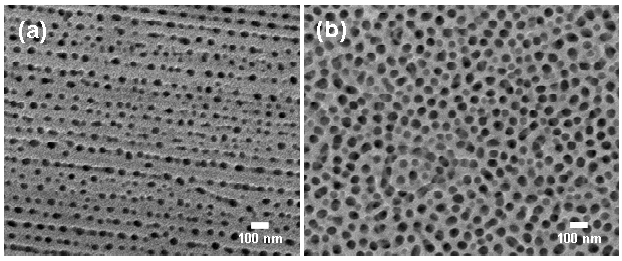

Fig. 4. The SEM micrographic of (a) aluminum sheet and (b) aluminum wafer anodized in oxalic acid.

In previous works, we find something interesting. Whether we use which electrolytes for anodization or not, we will investigate that the morphology of anodic alumina in aluminum wafer is more regular than that in aluminum sheet. We think the thickness is the key for anodic alumina growth. When we fabricate the anodic aluminum oxide (AAO), the growing time is equal. However the wafers are all thinner than sheets. The growing time for AAO growth in aluminum sheet

is not enough. It took much time for thick aluminum sheets anodization. Thus, the anodic aluminum oxide in aluminum wafer is more uniform.

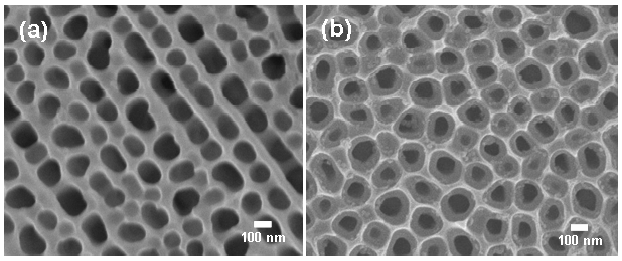

Fig. 5. The SEM micrographic of (a) aluminum sheet and (b) aluminum wafer anodized in phosphoric acid.

In Fig. 6, we alter the working voltage of anodization. In this work, the anodic aluminum oxide (AAO) is grown in oxalic acid and the substrate are all aluminum wafer. In Fig. 6. (a), the diameter of anodic aluminum oxide is smallest. Otherwise, the other condition of anodic aluminum oxide is large but the Fig. 6. (d) is much more irregular. The results implied that the higher working voltage we used, the wider pores of anodic aluminum oxide (AAO) were. Besides, we found the working voltage not only influence the diameter of pores but also the uniformity. Thus, the Fig.6. (b) is more regular and uniform arrays so far.

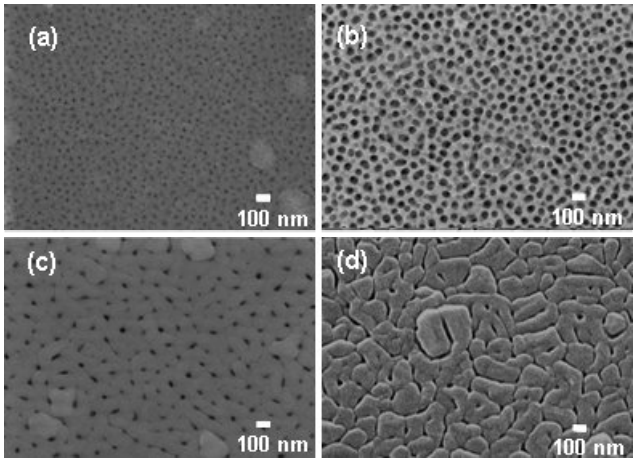

Fig. 6. SEM micrographics of the aluminum wafers substrate anodized in oxalic acid at (a) 25 V (b) 35 V (c) 70V and (d) 120 V respectively.

As shown in Fig. 7 (a) – (d), the morphology of anodic aluminum oxide (AAO) on aluminum sheets in sulfuric acid were at difference working voltage. We also observed the relations of diameter and working voltage. The highest working voltage of anodization results in largest pores and irregular distributions. The results are almost the same compared the former. Thus, no matter which substrate we used, the consequences were the same even in difference of electrolytes.

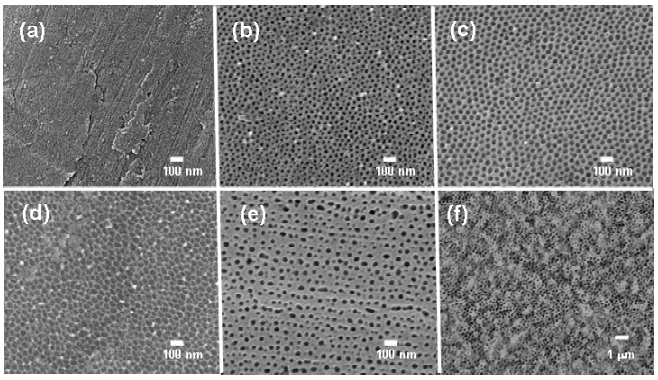

Fig. 7. SEM micrographics of the aluminum sheets anodized in sulfuric acid at (a) 5 V, (b) 15 V, (c) 20 V, and (d) 30 V. The aluminum wafers also anodized in (e) oxalic acid and (f) phosphoric acid respectively.

In Fig. 7. (d) - (f), these were anodized in equal voltage (30 V) but in difference of electrolytes. The diameter of these substrates was influenced by electrolytes. The results also the same with previous works even in equal voltages.

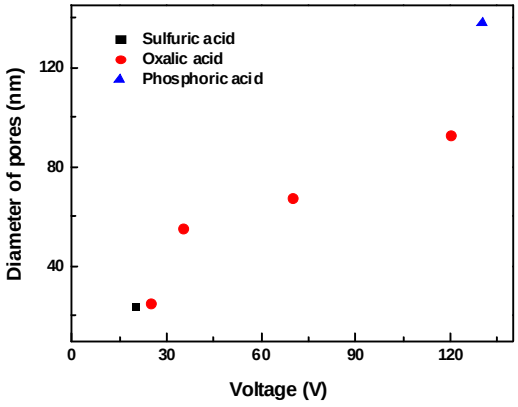

Fig. 8. Schematic diagram of the relation of working voltage and diameter for aluminum / silicon substrates anodization.

From integrating these results, these works can be described by plots. As shown in Fig. 8 and Fig. 9, it is clearly to present the relations between the working voltage and the diameter of pores. In Fig. 8, when the working voltage increases, the diameter of pores increases. No matter which electrolytes we used, the graph is presented linear even in different substrates (seeing in Fig. 9.). However, the regular arrays and working

voltage are not presented linear. In order to obtain fine and regular arrays, the condition for growing the anodic aluminum oxide (AAO) must be specific.

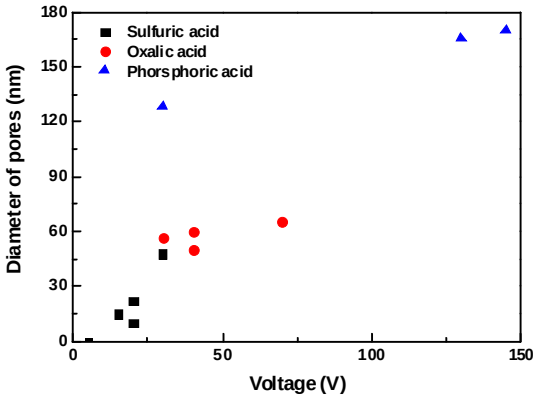

Fig. 9. Schematic diagram of the relation of working voltage and diameter for aluminum sheets anodization.

IV. CONCLUSION

In previous reports, we demonstrated the anodization process and observed the effects of working voltage and electrolytes on this procedure. We also have shown that the different thickness of substrates and the working voltage have a tremendous effect for the uniformity of pores in anodization. These results implied that the higher working voltage we use, the wider pores on alumina film are. Besides, we also found that the diameters of pores which grew in phosphoric acid was lager than that in sulfuric acid even in he same voltage. In this work, the ordered-anodic alumina is demonstrated and it will be a powerful material for many applications in the future.

ACKNOWLEDGMENT

The authors thank NCTU, NSC and CMS for technology supports. We also appreciate ITRI for financial support.

REFERENCES

[1] G. Eason, B. Noble, and I. N. Sneddon, “On certain integrals of Lipschitz-Hankel type involving products of Bessel functions,” Phil. Trans. Roy. Soc. London, vol. A247, pp. 529–551, April 1955. *(references)*

[2] J. Clerk Maxwell, A Treatise on Electricity and Magnetism, 3rd ed., vol. 2. Oxford: Clarendon, 1892, pp.68–73.

[3] I. S. Jacobs and C. P. Bean, “Fine particles, thin films and exchange anisotropy,” in Magnetism, vol. III, G. T. Rado and H. Suhl, Eds. New York: Academic, 1963, pp. 271–350.

[4] K. Elissa, “Title of paper if known,” unpublished.

[5] R. Nicole, “Title of paper with only first word capitalized,” J. Name Stand. Abbrev., in press.

[6] Y. Yorozu, M. Hirano, K. Oka, and Y. Tagawa, “Electron spectroscopy studies on magneto-optical media and plastic substrate interface,” IEEE Transl. J. Magn. Japan, vol. 2, pp. 740–741, August 1987 [Digests 9th Annual Conf. Magnetics Japan, p. 301, 1982].

[7] D. J. Odom, L. A. Baker, and C. R. Martin “Solvent-Extraction and Langmuir-Adsorption-Based Transport in Chemically Functionalized Nanopore Membranes,” in J. Phys. Chem. B, 109 (44), 2005.

[8] C. A. Huber , T. E. Huber , M. Sadoqi , J. A. Lubin , S. Manalis , and C. B. Prater, “Nanowire Array Composites,” in Science, Vol. 263. no. 5148, February 1994 pp. 800 – 802.

[9] H. Masuda, H. Yamada, M. Satoh, and H. Asoh,” Highly ordered nanochannel-array architecture in anodic alumina,” in Appl. Phys. Lett. 71 (19), 10 November 1997.

Nano-indentation patterns for surface enhanced Raman scattering

Ying-Yi Lin[1], Chia-Wei Chang[1], Li-Kai Lin[1], Jiunn-Der Liao[1, 2, 3 *]

[1]*Department of Materials Science and Engineering*

[2]*Institute of nanotechnology and Microsystems Engineering*

[3]*Center for Micro/Nano Science and Technology*

70101, National Cheng Kung Univerity, No.1, University Road, Tainan, Taiwan

***Abstract*: The technique of Surface Enhanced Raman Scattering (SERS) provides high informational content on the chemical structure of the probed substances, which makes this method a very promising tool in biomedical spectroscopy. In this study, we presented a novel method that utilizes nanoindentation to generate graphically indented patterns on Au surface. The modified Au surface was thereafter relevant to the applications of SERS. 5, 5'-Dithio-bis (2-nitrobenzoic acid) (DTNB) and Rhodamine 6G (R6G) were particularly grafted on the modified Au surface to verify an enhanced Raman Effect. DTNB was chemically adsorbed, while R6G was physically adsorbed on the modified Au surface. The particularly modified Au surfaces exhibited significant SERS enhancements and possibly applied for microorganism detection.**

***Keywords*: SERS, Nanoindentation, DTNB, R6G**

I. INTRODUCTION

Chemical structure of minor target species in the probed substance can be distinguished using Surface Enhanced Raman Scattering (SERS) technique, which makes this method a very promising tool in biomedical detections [1,2]. SERS technique provides greatly enhanced Raman signal from analytic molecules that is purposely adsorbed upon a specially prepared metal surface. Two primary theories to explain the mechanism of SERS: the electromagnetic (EM) theory[3-5], which involves in the excitation of localized surface plasmon and the chemical (CHEM) theory, which rationalizes the effect through the formation of charge-transfer complexes. The increased intensity of Raman signal has been regularly observed on the order of 10^4-10^6 [6], and is possibly enlarged as high as 10^8 and 10^{14} for some systems [7]. Means to control the size, shape, and material of the experimented surface has gradually reinvigorated in this field. In particular, the excitation of the localized surface plasmon resonance of a nanostructured surface or clustered nanoparticles is the major cause of SERS effect, so the ability to reliably control the surface characteristics has taken SERS-related studies from an interesting surface phenomenon to a rapidly developing analytical tool.

Most investigations on the surface for SERS utilize the lithographic technique as a micro-scale process that may provide a variety of patterns [8,9]. However, a deepened nano-scale pattern is still difficult to control in a quick way, which also leads to an additional cost of wastewater treatment. In this study, we present a method that utilize nanoindentation to generate graphic indented patterns on the gold surface and thereafter be relevant to the applications of SERS. By tuning pitch depth/width ratio, inter-distance of two pitches, and concentrations of molecular probes, this experiment aims to figure out which parameter dominates the enhanced mechanism. In addition, we expected this Raman-active substrate can be applied on the detection of membrane protein of microorganism, like bacteria and virus.

II. EXPERIMENT

In the study, the 100 nm Au/10 nm Ti/Si substrate (shorten as the *ap*Au) was prepared by thermal evaporation. The Au layer showed polycrystalline with a grain size of 20~50 nm, while the grains predominatly exhibited a (111) orientation. A nanoindenter with a Berkovich tip of 20 nm in diameter was chosen to produce pyramid-shape pitch on Au (shorten as the *n*Au). The *ap*Au and *n*Au were initially Raman-inactive and used as the reference substrates. To discuss the differences between chemical and physical adsorption, after indented Raman-active molecular probes, 5, 5'-Dithio-bis (2-nitrobenzoic acid) (DTNB) and Rhodamine 6G (R6G), are particularly grafted on the treated substrate to verify an enhanced Raman effect. DTNB belongs to chemical adsorption; R6G is physical adsorption.

In the test, molecular probes need stay close to the indented pattern on the SERS-active substrate. Additionally, to simulate the real text on the bio-chip, DTNB and R6G were solved in the phosphate buffer saline (PBS), then dipped into a specific designed holder, which is made of poly(dimethyl siloxane)

This project was funded by the Top 100 University Advancement of National Cheng Kung University (R017).

*Corresponding authors: Prof.Dr.Jinn-Der Liao

E-mail: jdliao@mail.ncku.edu.tw

Tel: 886-6-2757575 # 62971

(PDMS)to avoid solution evaporation during Raman scattering testing (as shown in Fig. 1).

III. Results and Discussion

The geometries of the *n*Au were firstly defined. To figure out the relationship of indented depth, tip-to-tip distance and the enhanced mechanism, six nAu samples #1~#6 were experimented with the variation of indentation depth measured by vertical displacement (D_v) and tip-to-tip displacement measured by instrument ($D_{t\text{-}t}$). These two expected values for the *n*Au samples were shown in Table 1. Fig.2 shows the SEM topographic images of the six samples. Based on the results, the creation of the *n*Au was partially resulted by plowing through the vertical displacement and an increase of mass accumulation surrounding the *n*Au. Concerning about the dimension of the measured area (≈1 μm^2) by Raman scattering, the sampling pattern on the *n*Au were 1 (#1~#3) and 4 (#4~#6).

Fig.3 is the AFM topographical results. As shown in the pictures, dissimilar patterns had totally different the mean roughness (Ra). The results responded to Fig. 2, which indicated #6 had the most disordered patterns on *n*Au.

Further we would like to comprehend the relationship between D_v and the SERS effect. Thus compared the Raman spectrum on the samples #4~#6 in fixed $D_{t\text{-}t}$ (Fig.4), #6 had the highest intensity due to the largest indented depth. On the other hand, the Raman intensity raised as indented depth increased. Lager D_v represented larger volume, which can contain more molecular probes, lead to higher enhanced Raman scattering. In addition, D_v also decided the surface roughness: surface plasmon dominated the enhanced mechanism in roughed samples[10,11]. In the next experiments sample #6 was chosen as the main SERS-active substrate.

Fig.5 shows the DTNB Raman spectrum of four concentrations on #6. The peak (1)1075, (2) 1340 and (3) 1570 cm^{-1} represents ν(C (arom.)-S), ν_s ((C-)NO_2) and ν(C=C) aromatics respectively[12]. According to the results, it is obvious that DTNB Raman intensity increased as the concentration raised. The detection limit is 2 x 10^{-8}M.

Similarly the R6G Raman spectrum of three concentrations on #6 was shown in Fig.6. The bands between 1300 and 1650 cm^{-1} are due to the aromatic stretch vibrations of the chromophore, the small peak at 1275 cm^{-1} which appears in ensemble spectra only as a shoulder because of the C–O–C stretch vibration, the bands at 776 and 1137 cm^{-1} are the C–H out of plane and in plane bending vibrations, and the line at 618 cm^{-1} is the C–C–C ring in plane vibration [13]. The detection limit is 2 x 10^{-6}M, which is less sensitive compared with DTNB. The main reason is DTNB would have chemisorp on gold surface, and Raman can detect even in the lower concentration.

As the discussion above, the nano-indented cavities with different sizes and dimensions were potential to apply in biological detection [14]. In Fig.7, SERS-active substrates #3 and #6 were taken as the examples. Adenoviruses, which belong to non-enveloped dsDNA viruses and can cause infections in mammals and birds, were chosen as the target micro-organism. In the experiment, the concentration of purified virus sample of 10^6 PFU/ml was employed. The result indicated #3 is more suitable for adenovirus detection than #6, because the diameter of adenovirus is about 80-90 nm. It means one adenovirus was possibly captured or entrapped into SERS-active substrate #3, while no adenovirus was competent to enter the sample #6 because of the overlapped nano-indented cavities on #6. Summarizing the discussion above, nano-indented cavites will be a powerful tool as SERS-active substrates by controlling their sizes and dimensions for variegated micro-organisms.

IV. Conclusions

The nano-indentation provides a new method to fabricate controlled surface characteristics. Based on the Raman scattering results on samples #4~#6, higher D_v had significant SERS enhancement due to larger volume and obvious surface plasmon. To aim at the difference of physical adsorption and chemisorptions, DTNB and R6G were chosen as the detected targets. In the experimental results, the detection limits are totally different in these two molecular probes. The former is 10^{-8} M and the later is 10^{-6} M. Finally, by controlling the sizes and dimensions, the SERS-active substrate made by nano-indenter can be used to detect microorganism, i.e. adenovirus.

Acknowledgment

The autors would like to thank Pro.Dr.Ai-Li Shiau and Pro. Dr. Chao-Liang Wu for their assistance on preparing adenovirus samples. This work was supported by Top 100 University Advancement and Center for Micro/Nano Science and Engineering of National Cheng Kung University (R017).

References

(1) Campion A.; Kambhampati, "Surface-enhanced Raman scattering", P. *Chem. Soc. Rev,* vol.27, 241,**1998**.
(2) Kneipp K.; Wang Y.; Kneipp H.; Parelman L. T.; Itzkan I.; Dasari R. R.; Feld M. S., "Single Molecule Detection Using Surface-Enhanced Raman Scattering (SERS)", *Phys. Rev. Lett.*, vol.78, 1667, **1997.**
(3) Bruzzone S., Malvaldi M., Arrighini G.P., Guidotti C., "Theoretical Study of Electromagnetic Scattering by Metal Nanoparticles", *J.Phys.Chem.B*, vol.109, 3807, **2005**.
(4) Lesuffleur A., Kumar L.K.S., Brolo A.G., Kavanagh K.L., Gordon R., "Apex-Enhanced Raman Spectroscopy Using Double-Hole Arrays in a Gold Film", *J.Phys.Chem.C*,

vol.111, 2347, **2007**.

(5) Shimada T., Imura K., Hossain M.K., Okamoto H., Kitajuma M.," Near-Field Study on Correlation of Localized Electric Field and Nanostructures in Monolayer Assembly of Gold Nanoparticles", *J.Phys.Chem.C*, vol.112, 4033, **2008**.

(6) Qiu T., Wu X.L., Shen J.C., Chu P.K., "Silver nanocrystal superlattice coating for molecular sensing by surface-enhanced Raman spectroscopy", *Appl. phys. Lett.*, vol. 89, 131914, **2006**.

(7) Mcfarland A.D., Young M.A., Dieringer J.A., Duyne R.P.V., "Wavelength-Scanned Surface-Enhanced Raman Excitation Spectroscopy", *J.Phys.Chem.B*, vol.109, 11279, **2005**.

(8) Lacus B.D., Kim J.S., Chin C., Guo L.J., "Nanoimprint Lithography Based Approach for the Fabrication of Large-Area, Uniformly-Oriented Plasmonic Arrays", *Adv. Mater.*, vol.20, 1129, **2008**.

(9) Li K., Clime L., Cui B., Veres T., "Surface enhanced Raman scattering on long-range ordered noble-metal nanocrescent arrays", *Nanotechnology*, vol.19, 145305, **2008**.

(10) S. Kruszewski, "Dependence of SERS Signal on surface roughness," *Surface and Interface Analysis*, vol. 21, 830-838, 1994.

(11) M. Baibarac, M. Cochet, M. Lapkowski, L. Mihut , S. Lefrant and I. Baltog, "SERS spectra of polyaniline thin films deposited on rough Ag, Au and Cu. Polymer film thickness and roughness parameter dependence of SERS spectra," *Synthetic Metals*, Vol. 96, 63-70, 1998.

(12) Sheela B., Yegnaraman V., Sandhyarani N., Murty K.V.G.K., Pradeep T., "Formation of a nickel hydroxide monolayer on Au through a self-assembled monolayer of 5,5%-dithiobis(2-nitrobenzoic acid): voltammetric, SERS and XPS investigations of the modified electrodes", *Journal of Electroanalytical Chemistry*, vol. 468,170,**1990**.

(13) Vosgröne T., Meixner A.J., "Surface and resonance enhanced micro-Raman spectroscopy of xanthene dyes at the single-molecule level", *Journal of Luminescence*, vol. 107, 13, **2004**.

(14) Wu E., Glen R.N., "Virus yoga: the role of flexibility in virus host cell recognition", *Trends Microbiol*., vol.12, 162, **2004**.

(15) Meier O., Greber U.F., "Adenovirus endocytosis", *J.Gene Med.*, vol.6, S152, **2004**.

Table 1 The size and dimension for six nAu samples #1~#6.

nAu sample	Dv (nm)	Dt-t (nm)
(#1)	50	1000
(#2)	70	1000
(#3)	90	1000
(#4)	50	500
(#5)	70	500
(#6)	90	500

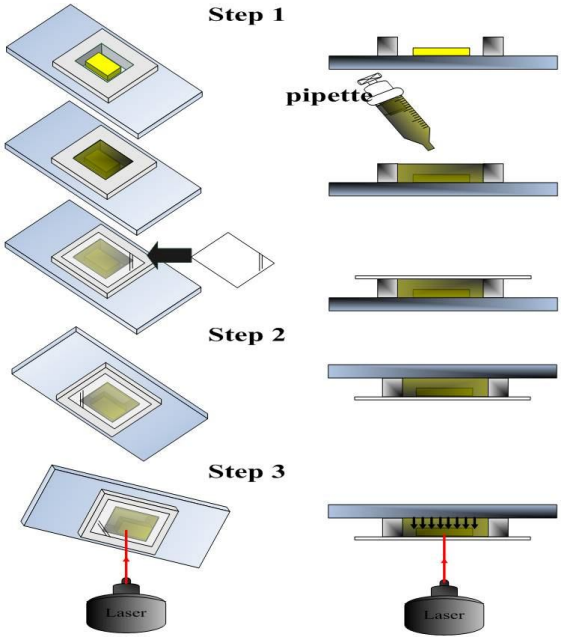

Fig.1 The chart of Raman scattering detection.

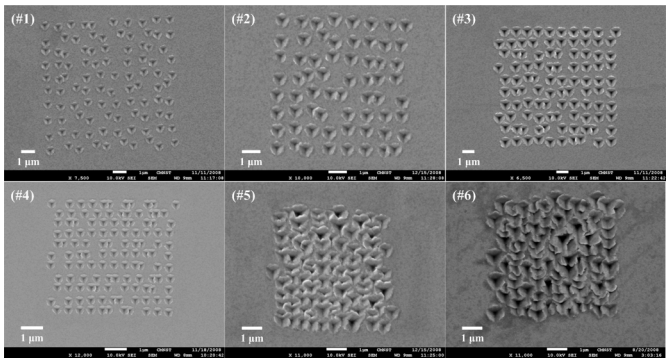

Fig.2 SEM topographic images of different indented substrates

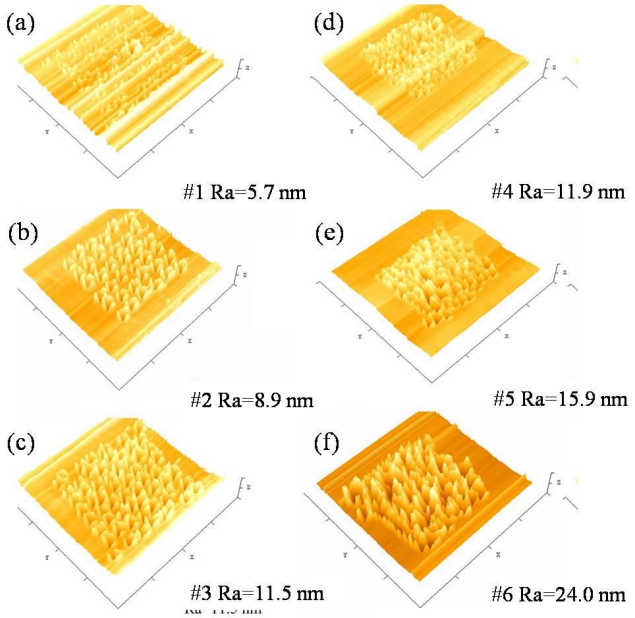

Fig. 3 The AFM morphology of the (a) Pattern 1, (b) Pattern 2, (c) Pattern 3, (d) Pattern 4, (e) Pattern 5, (f) Pattern 6.

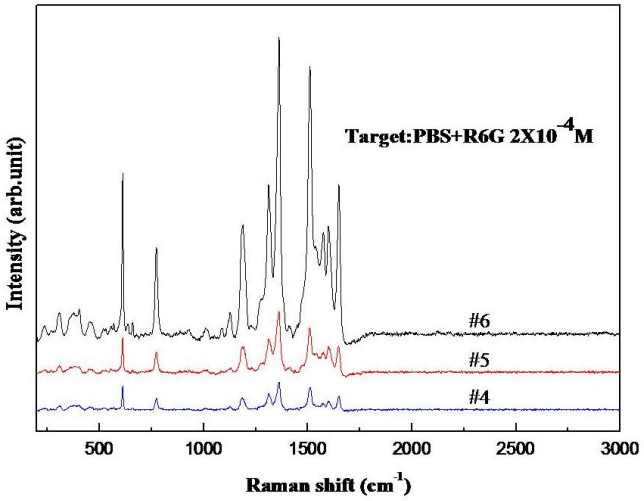

Fig.4 DTNB Raman spectrum on sample #4~#6: Raman intensity increased as indented depth raised.

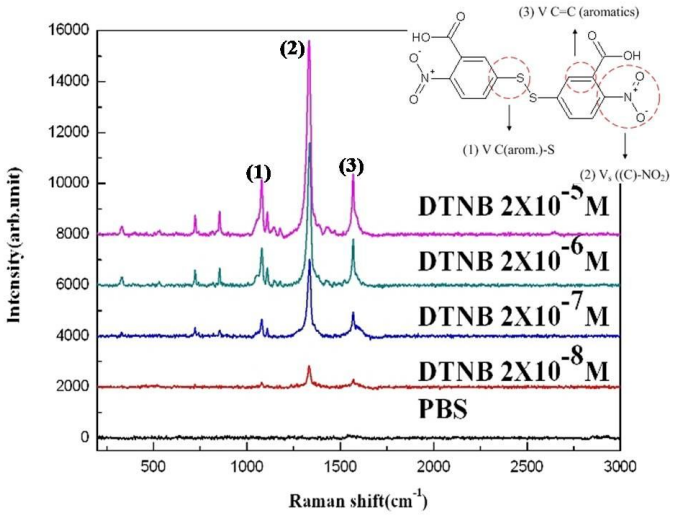

Fig.5 DTNB Raman spectrum: DTNB Raman intensity increased as the concentration raised.

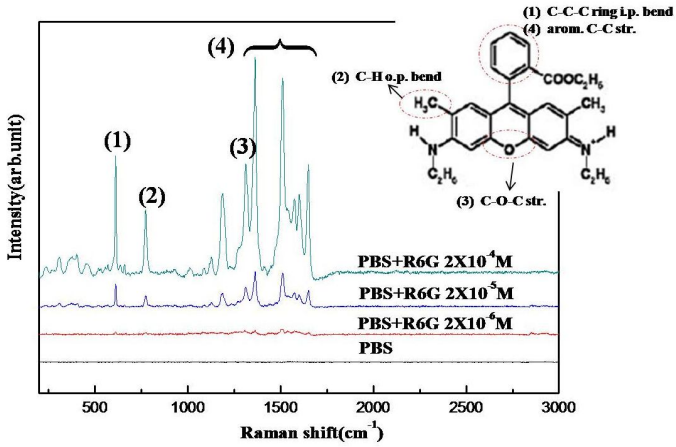

Fig.6 R6G Raman spectrum: R6G Raman intensity increased as the concentration raised.

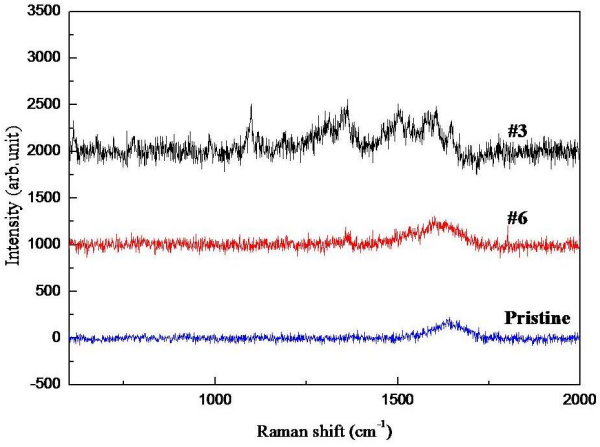

Fig.7 The detection of adenovirus on sample #3 and #6: The weak Raman intensity could be recognized as the characteristic Raman spectrum of adenovirus [15].

Model single ion channel for structure investigation

Fu-Chiang Young[1*], Ching-Hsing Luo[12#], *IEEE member*

[1]Department of Electrical Engineering, National Cheng Kung University, Tainan, Taiwan,
[2]Micro/Nano Science and Technology, National Cheng Kung University, Tainan 701, TAIWAN

***Abstract*-This project presents a method to model a single channel from protein sequences provided by common protein sequences databanks. Under single-cell level, concrete protein structures will provide a configuration to simulate structural mechanics. Here a potassium was modeled, voltage-gated channel (Kv channel), to investigate its corresponding mechanics of each subunit. In electrophysiology, the potassium channel is defined as slow delayed rectifier potassium current (I_{ks}) by LRd ventricular cell model which defined completely in 2005. It is constructed from the conformational shape of the Shaker Kv1.2 channel as a template to model single KCNQ1 channel (Kv7.1).**

Keywords — ***Voltage-gated Channel, Slow Delayed Rectifier Potassium Channel, LRd Model.***

INTRUDCTION

Potassium current plays a key role on repolarization phase to pull action potential back to resting potential. Potassium current (symbol as I_k) acts slow response as rectifier in electrical circuits separated into rapid and slow delayed rectifier potassium channels (symbol as I_{kr} and I_{ks}) which described in 2005 [1]. These two channels are homologous to voltage-gated potassium channels, symbolized K_V family channels [2]. So far, many studies were surveyed to discuss about the functions of corresponding residues, not to discuss about the mechanical theories on its structures. Under the voltage steps, Kv channel functions depend on the membrane potential to change its shape of the pore and translate voltage sensors subunits. Kinetic transitions of I_{ks} channel are consisted of closed and opened transition states simulated by Markov chain. A tetramer structure of Kv7.1 (KCNQ1) constructs an I_{ks} channel with KCNE1 (associated with KCNQ1) under mutation. This channel will prolong QT interval (Long QT Syndrome, LQTS) [3]. This study focuses on modeling Kv7.1 (KCNQ1) from its relationships, the Kv1.2 (KCNA2) channel. Because of that the conformational shape of the Kv1.2 channel is more homologous and adopted as a major template channel. However, the purpose of this project is to build a circumstance with embedded KCNQ1 channel to investigate its functions for future study its functions. The results of this model are a coordinative file to record its corresponding 3D structure positions. The coordinative file will be calculated by dynamic molecular on its structures and simulate its kinetics when membrane potential changing. For our future study, it will be much benefit to implement its functions.

MODELLER THE STRUCTURES

To package a tetramer structure of a single channel, the flow chart in Figure 1 is a good tool to merge the proteins into one PDB file [4]. It is also easy to define the positions of the residue mutations. This flow chart is to model a KCNQ1 channel from Kv1.2 (PDB code: 2R9R [4]). This work is mainly to show an easy way to model a tetramer from template protein in protein databank. However, the alignment tool is needed to align the protein sequences with its corresponding positions. There are two crucial works need to prepare: the first is template protein structure and the other is the target protein sequence. In this project, the template protein is Kv1.2 and the target protein is KCNQ1 protein sequence. The protein databank (**RCSB PDB**) provides many kinds of proteins to be the template protein but just on this case that RCSB databank provides two kinds of the most complete Kv1.2 structures, which pdb code are 2R9R and 2A79. The target protein sequences can be found in **Swissprot Database Website** which contains all kinds of protein sequences. Here may need KCNQ1 protein sequence. However, the purpose of this alignment work is to make sure the corresponding positions of the charged residues. Figure 2 the sequences of two proteins had been modified and regulated with positive and negative charges positions as the rhombus frame in Figure 1 (see manuscript in Figure 2) and cut other redundant residues until get the reasonable corresponding positions as expected.

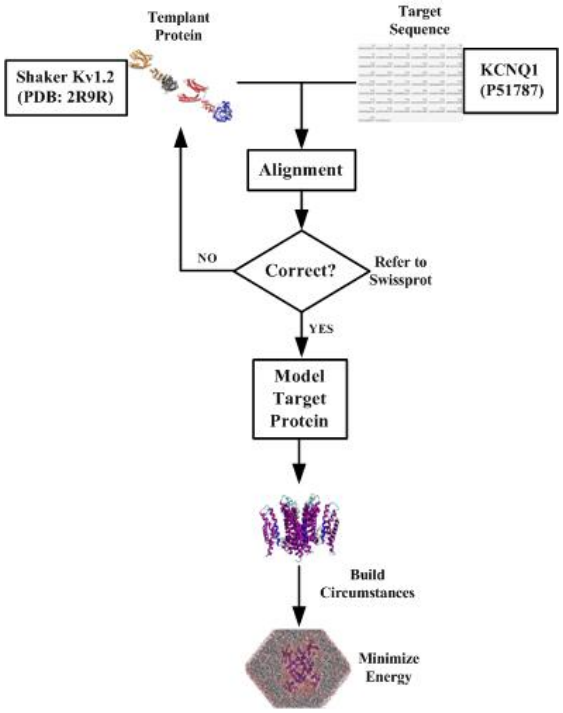

Figure 1. The flow chart to model a target protein (KCNQ1) from template protein (Kv1.2) [5].

The template protein, Kv1.2, was provided by RCSB Protein Data Bank and the target protein sequence was provided by Swissprot sequence database. The

This project was funded by landmark project (Project code: A0121) and the TW NSC (Project code: 96-2628-B-006-001-MY3)

**Contact author: n2896143@mail.ncku.edu.tw*
#Contact author: robin@ee.ncku.edu.tw

KCNQ1 tetramer structure needs lipid groups and water molecular to maintain its life and necessary energy. The all-atom environment is to combine the channel within pre-equilibrated phosphatidylcholine (POPC) membrane (dash line block diagram) in 0.8Å separated between lipid and protein. This membrane is constituent structure of a cardiac myocyte [6].

For the protein sequence alignment of KCNQ1 and Kv1.2, Figure 2 shows that the positive charges in S4 and the PVP motif in S6 subunit will be a little bit different in shapes with each other.

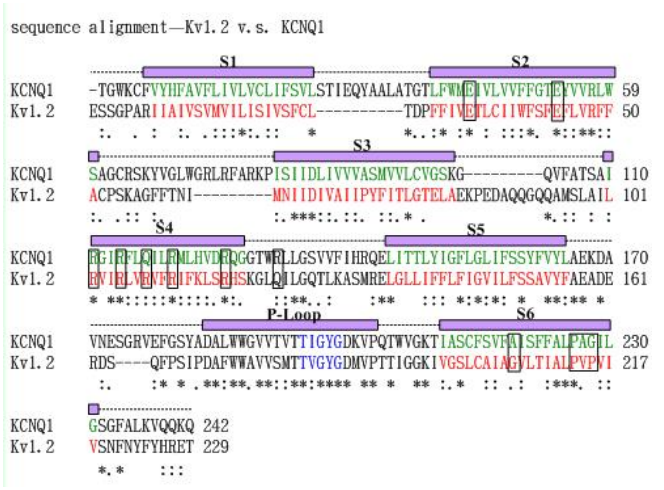

Figure 2. KCNQ1 protein sequence aligns with Kv1.2.
The corresponding positions of Kv1.2 channels compared with KvAP channel which S3 region was separated into two regions, S3a and S3b, formed a voltage paddle with S4 subunit was the most different with Kv1.2 [7][8][9]. KCNQ1 was modeled from one of the Kv family channel, PDB code: 2R9R. The square frames in sequences are positive (R1~R5 in S4) and negative charges (E1~E2 in S2) and the PVP motif in S6 subunit. KCNQ1 has an extra positive charge R6 in S4 different with Kv1.2. The PVP motif in S6 of KCNQ1 becomes PAG residues, not PVP motif in S6 as Kv1.2. From this aligned information, it can be guessed that the α-helix of KCNQ1 will be a little bit different with Kv1.2.

MINIMIZE EQUILIBRATED ENERGY

The target structure was built from template protein. But it was not considered its interactions and minimum energy. Minimize structure energy is a molecular dynamics simulation package based on the Charm^{++} parallel objects [10]. The package software can stabilize the structure by minimizing the energy. The tetramer structure modeled in this project was calculated by package software. Figure 3 was shown that the conditions of KCNQ1 channel before minimization and after minimization were overlapped together to show structures adjusted. The whole KCNQ1 channel with membrane are contained that 285 lipid groups and 36,424 water molecules. The total atom numbers of the channel are 162,966 atoms.


(a). top view, before minimization


(b). top view, after minimization

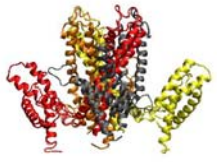
(c). side view, before minimization

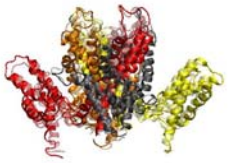
(d). side view, after minimization

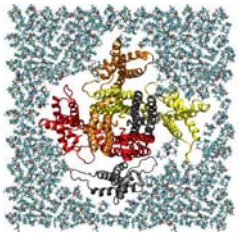
(e). top view with membrane, before minimization

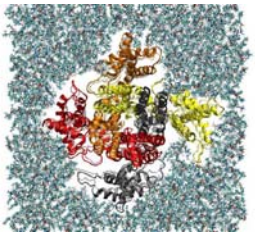
(f). top view with membrane, after minimization

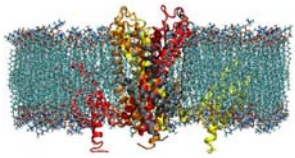
(g). side view with lipid layer, before minimization

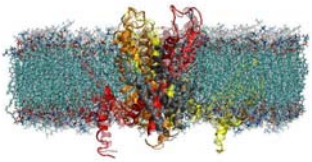
(h). side view with lipid layer, after minimization

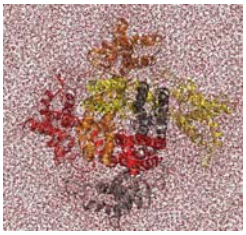
(i). top view with water layer, before minimization

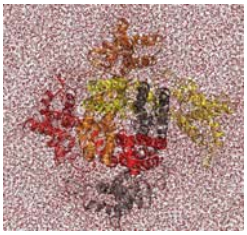
(j). top view with water layer, after minimization

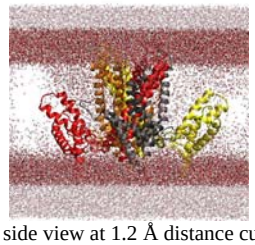
(k). side view at 1.2 Å distance cutoff resolution with water layer, before minimization

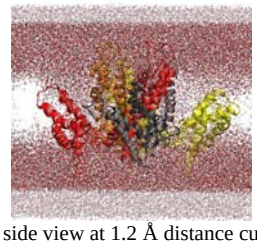
(l). side view at 1.2 Å distance cutoff resolution with water layer, after minimization

Figure 3. KCNQ1 channel was minimized structure energy
There are two tetramer structures overlapped together in each panel. The tetramer structure in transparent colors is original structure without any minimization. The opaque structure is adjusted by minimization. Panel (a)(b)(e)(f)(i)(j) are top views and panel (c)(d)(g)(h)(k)(l) are side views.

The minimized equation is similar to potential energy equation, shown as following empirical equation.

$$\Phi\left(\vec{d}^{\,N}\right)=\sum_{bonds}k_i\left(l_i-l_{i,0}\right)^2+\sum_{angles}\frac{k_i}{2}\left(\theta_i-\theta_{i,0}\right)^2+\sum_{torsions}\frac{V_n}{2}\left(1+\cos\left(n\omega-\gamma\right)\right)+\sum_{i=1}^{N}\sum_{j=i+1}^{N}\left(4\varepsilon_{ij}\left[\left(\frac{\sigma_{ij}}{r_{ij}}\right)^{12}-\left(\frac{\sigma_{ij}}{r_{ij}}\right)^{6}\right]+\frac{q_iq_j}{4\pi\varepsilon_0 r_{ij}}\right)$$

Where:

$\Phi\left(\vec{d}^{\,N}\right)$ is potential energy, $\vec{d}^{\,N}$ is the particle positions

$\sum_{bonds}k_i\left(l_i-l_{i,0}\right)^2$ is bonds potential interactions between l_i and $l_{i,0}$.

$\sum_{angles} \frac{k_i}{2}(\theta_i - \theta_{i,0})^2$ is valence angles potential of bonds potential interaction.

$\sum_{torsions} \frac{V_n}{2}(1+\cos(n\omega - \gamma))$ is torsion potential interaction.

$\sum_{i=1}^{N}\sum_{j=i+1}^{N}\left(4\varepsilon_{ij}\left[\left(\frac{\sigma_{ij}}{r_{ij}}\right)^{12} - \left(\frac{\sigma_{ij}}{r_{ij}}\right)^{6}\right] + \frac{q_i q_j}{4\pi\varepsilon_0 r_{ij}}\right)$ is Van Der Waals and two atoms electrostatic potential interactions.

The minimization calculates the structures with an empirical equation which accounts for bond length, angle bending, bond rotation (torsion), Van Der Waals and electrostatic non-bonded interactions [11].

RESULTS DISCUSSION

KCNQ1 channel is a mutated channel to cause LQTS. Because of that it will prolong the QT interval in electrocardiogram phase. In the action potential duration, the repolization phase will be prolonged as well as the potassium current activate more slowly than regular state [3]. This project does not discuss corresponding QT syndromes and the effects of the mutation caused at this phase but this project just discuss more about structure behaviors, because the main purpose here is to build the structure for future studying KCNQ1 channel behaviors, especially its behaviors are similar to Kv1.2 such as Shaker and Rat Kv1.2 and other Kv1.2 species. The membrane potential of its functions supplies protein energy and attracts the voltage sensors with the positive charge residues in S4 subunit to translate upward the membrane from downward with small angle rotations to cause pore gate open. In contrarily, when membrane potential reduced, the voltage sensors translated downward from upward will close the pore gate [12] [13]. This project will start to do these corresponding channel mechanics in the future study, but so far there are many bottleneck need to breakthrough.

Family Kv1.2 potassium channel is most used for a template to study potassium channel functions. KCNQ1 (Kv7.1) channel also was modeled from Kv 1.2 in this project When KCNQ1 channel activates or inactivates unusual, it will cause some disease [3]. This study devoted to build the structures with proper circumstances to investigate its functions. This method is not only able to model Kv family channel, but it can also model other proteins such as sodium channels and etc. In model software, it needs to exactly match the sequences of template protein structure. The target structure of this project was generated 100 models in units each adjustment per modeling and picked some favorite ones. The next step after modeled a tetramer structure is to shift the molecular to relative positions. The KCNQ1 channel finally was embedded into membrane and water. Minimization can adjust the structure with minimum energy to maintain its shape. So, this project also minimized the structure energy with whole circumstances included water molecular and lipid groups.

The whole system of the KCNQ1 channel in all-atom is a huge system which contains 285 lipid groups and 36,424 water molecules in total 162,966 atoms. The biggest problem to simulate minimize energy for the KCNQ1 channel with all-atoms, it may need mainframe to accelerate the calculations on structures. However, the KCNQ1 structure is shown in Figure 4. It is shown top view and side view with water molecular and lipid groups (see manuscript in Figure 4).

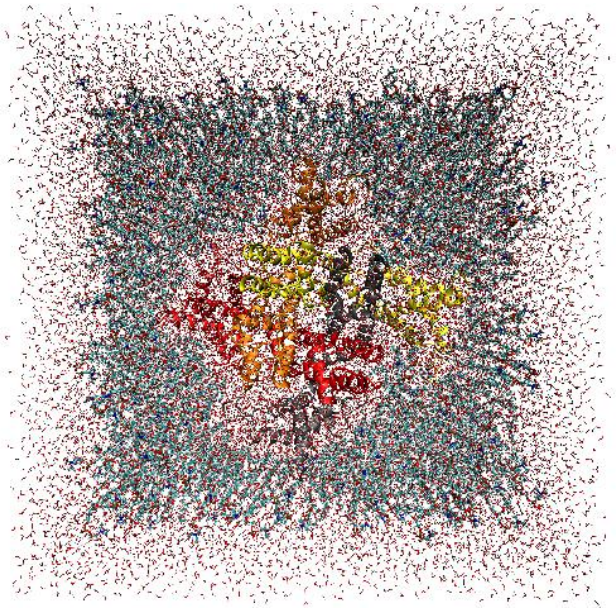

(a). Top view

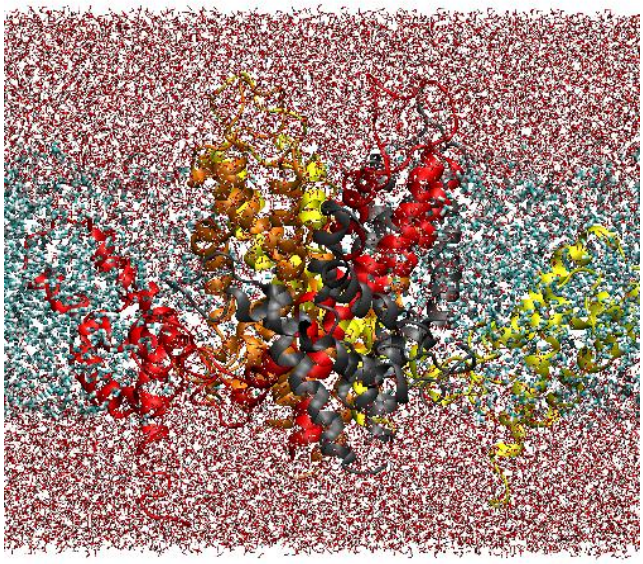

(b). Side view

Figure 4. Top view at panel (a) is equilibrated minimum energy force. Panel (b) is side view.

In panel (a) and (b), they are KCNQ1 channel modeled from Kv1.2 and minimize energy its structure with water molecular and lipid groups. The helices in red, yellow, black and brown colors are protein subunits, and the red point with white colors are water molecular, and the strips in blue color is lipid groups.

AKNOWLEDGE

Thanks for journal author **Dr. Jonathan R. Silva** who studied once in **CBAC** (the Cardiac Bioelectricity and Arrhythmia Center) laboratory in the department of Biomedical Engineering of Washington University in St. Louis, Mo., provided the precious and vital information to implement this project.

Thanks for the Fred Saigh Distinguished Professor of Engineering; Professor of Biomedical Engineering, Cell Biology & Physiology, Medicine, Radiology, and Pediatrics; Director of the Cardiac Bioelectricity and Arrhythmia Center

(**CBAC**) of Washington University in St. Louis, **Dr. Yoram Rudy** and Research Assistant Professor in Department of Biomedical Engineering of Washington University in St. Louis, **Dr. Ali Nekouzadeh** provided cooperated project.

Thanks for funded by **Landmark** project (Project code: A0121) of NCKU (National Cheng Kung University), Tainan, Taiwan, R.O.C. and **NSC** (National Science Council), Taiwan (Project code: 96-2628-B-006-001-MY3) to support this project the budget to cooperate with **CBAC** (the Cardiac Bioelectricity and Arrhythmia Center) laboratory in the department of Biomedical Engineering of Washington University in St. Louis, Mo, 63130.

REFERENCES

[1] J. Silva and Y. Rudy," Subunit Interaction Determines IKs Participation in Cardiac Repolarization and Repolarization Reserve," Circulation; Vol. 112, pp. 1384-1391, 2005.

[2] G.A. Gutman, K.G. Chandy, S. Grissmer, M. Lazdunski, D. McKinnon, L.A. Pardo, G.A. Robertson, B. Rudy, M.C. Sanguinetti, W. Stühmer, X. Wang, "International Union of Pharmacology. LIII. Nomenclature and molecular relationships of voltage-gated potassium channels," *Pharmacol Rev.*, Vol. 57(4), pp. 473-508, 2005

[3] J. A. Smith, C. G. Vanoye, A. L. George Jr., J. Meiler, and C. R. Sanders., "Stuctural Models for the KCNQ1 Voltage-Gated Postssium Channel", Biochemistry, Vol. 46, pp. 14141-14152, 2007.

[4] S. B. Long, X. Tao, E. B. Campbell & R. MacKinnon, "Atomic structure of a voltage-dependent K^+ channel in a lipid memebrane-like environment", Nature, Vol. 450, pp. 376-383, 2007.

[5] Manual Book: A Program for Protein Structure Modeling Release 9v4, r6262. http://salilab.org/modeller/

[6] E. Yechiel & Y. Barenholz, "Relationships between membrane lipid composition and biological properties of rat myocytes. Effects of aging and manupulation of lipid composition. J. Biol Chem, Vol. 260, pp. 9123-9131, 1985.

[7] Y. Jiang, A. Lee, J. Chen, V. Ruta, M. Cadene, B.T. Chait & R. MacKinnon, "X-Ray structure of a voltage-dependent K^+ channel", Nature, Vol 423, pp. 33-41, 2003.

[8] S.B. Long, W.B. Campbell, R. MacKinnon, "Crystal Structure of a Mannalian Voltage-Dependent Shaker Family K^+ Channel", Science, Vol. 309, pp. 897-903, 2005.

[9] S.B. Long, W.B. Campbell, R. MacKinnon, "Voltage Sensor of Kv1.2: Structural Basis of Electromechanical Coupling", Science, Vol. 309, pp. 903-908, 2005.

[10] J.C. Philips, R. Braun, W. Wang, J. Gumbart, E. Tajkhorshid, E. Villa, C. Chipot, R. D. Skeel, L. Kale & K. Schulten, "Scalable molecular dynamics with NAMD", J Comput Chem, Vol 26, pp. 1781-1802, 2005

[11] Manual Book: NAMD TUTORIAL-windows version. http://www.ks.uiuc.edu/Training/Tutorials/namd/namd-tutorial-win.pdf

[12] J. R. Silva, H. Pan, D. Wu, A. Nekouzadeh, K.F. Decker, J. Cui, N. A. Baker, D. Sept & Y. Rudy, " A multiscale model linking ion-channel molecular dynamics and electrostatics to the cardiac action potential", PNAS, vol. 106, no. 27, pp. 11102-11106, 2009.

[13] W. R. Silverman, B. Roux, & D. M. Papazian, " Structural basis of two-stage voltage-dependent activation in K+ channels", PNAS, Vol. 100, No. 5, pp. 2935-2940, 2003.

The Study of Polymer Pressure Sensor by Nanocomposites with MWNT and it's Characteristics Testing

H.T. Chen[1], H. S. Ko[1], and C. Gau[1]

[1]Institute of Aeronautics and Astronautics, National Cheng Kung University, Taiwan, ROC

Abstract —**Polyimide (PI)–carbon nanotube composites were fabricated by *in situ* polymerization using multi-wall carbon nanotubes (MWNT) as fillers. The composite film was characterized by some analytical instruments to ensure its structure and good dispersion of the MWNTs in the composites. The electrical resistivity of this composite was found to vary significantly with both the temperature and the stress in the material. The PI–MWNT composites possess a very linear piezoresistive nature which can be used as a good pressure sensor material, provided with proper temperature compensation. Fabrication of a micropolymer pressure sensor using this nanocomposite sensing material is demonstrated and sensor performance is evaluated. The sensor has a higher sensitivity than a polysilicon sensor, rapid response, and is thermally stable. The sensor is suitable for mass production, and can be widely applied or integrated in a microfluidic system or biochip where pressure information is required.**

Keywords —***PI–MWNT, nanocomposite, pressure sensor***

I. Introduction

Carbon nanotubes (CNTs) have been shown to have various potential applications in such areas as field emission display [1], gas sensor [2], resonator [3], CNT field effect transistor [4] and hydrogen storage [5]. A single CNT grown or placed between electrodes has been made into a gas sensor [6], temperature sensor [7] or biosensor [8]. Recent experiments [9, 10] have proven the single-wall carbon nanotubes' (SWNTs) potential for use as piezoresistors in a variety of applications. Most recently, Grow *et al* [9] studied the electromechanical response of semiconducting and small-gap semiconducting (SGS) SWNTs adhering to a silicon nitride surface. They found gauge factors of 400 and up to 850 for semiconducting and SGS SWNTs, respectively. Stampfer *et al* [11] fabricated a pressure sensor by connecting a single metallic SWNT with two electrodes made on a very thin layer of the Al_2O_3 membrane with a thickness of 100 nm. They found that this SWNT pressure sensor has a piezoresistive gauge factor of approximately 210. Despite the high gauge factor or high sensitivity of this sensor, however, fabrication of these kinds of sensors still requires expensive instruments such as focused ion beams for photolithography of the small neighboring electrodes and use of SEMs to locate the SWNT, and extensive effort. On the other hand, MWNTs are also demonstrated to disperse and interconnect together by using a careful AC dielectrophoretic manipulation on a PMMA diaphragm to make it into a pressure sensor [12]. However, all these sensors are not practical for real applications and mass production. The current paper proposes a new method of fabricating a pressure sensor which uses polyimide/CNT nanocomposites as sensor material. The characteristics and performance evaluation of this pressure sensor is also presented. Since CNTs possess a piezoresistive nature, by adding them to a polymer and producing a nanocomposite, similar or different piezoresistive characteristics may be expected in these nanocomposites. In this way, the polymer composite can be readily processed and made into a useful sensor by mass production. The piezoresistive property of a carbon nanotube/methylvinyl silicone rubber nanocomposite has been demonstrated in a recent work [13], which exhibits quite different piezoresistive properties from that of a single nanotube. Instead of linear, the resistance of the nanocomposite varies exponentially with the pressure force due to the soft nature of silicon rubber. One can expect, therefore, that the selection of different polymers may lead to different piezoresistive properties. The selection of polyimide as the host material is based on the advantages in that it can be handled readily and spin-coated above a polymer cavity to fabricate into a polymer pressure sensor for wide practical applications and mass production, especially in the area of microfluidics or lab-on-chip. In addition, polyimide has very good chemical, thermal and mechanical characteristics. This material has a much higher glass transition temperature and can endure under much higher temperatures than general polymers. It has been widely applied in the fabrication of aircraft structures, microelectronic devices and so on. However, the insulation nature of this polymer material has seriously limited its application. With proper addition and dispersion of nanomaterials in polyimide, such as CNTs, the electrical conductivity can be increased by more than 11 orders of magnitude to 10^{-4} S cm^{-1} at the percolation threshold [14]. Therefore, this material can be extended in application in the area of electronics and sensors, provided it possesses changes in resistivity when subjected to thermal or stress variation. This paper presents a test of the piezoresistive nature of this nanocomposite and fabrication together with SU- 8 material as a polymer pressure sensor. A theoretical model for the stress and deformation of the diaphragm is adopted for diaphragm and sensor cavity design consideration.

.

II. Preparation and characterization of the polyimide/carbon nanotube nanocomposites

A. Materials

The liquid *N*,*N*-dimethylacetamide (DMAc) required for blending with other materials to make into polyimide was

This research was sponsored by both the National Science Council of Taiwan under contract no. **NSC97-2212-E-006-057-MY2**.

[1]Institute of Aernnautics and Astronautics, National Cheng Kung University, Tainan, Taiwan 70101 ROC.

*Contact author: C. Gau (phone: +886-6-2757575 Ext.63684; e-mail: gauc@mail.ncku.edu.tw)

purchased from Tedia. It has a purity of 99%. In addition, powders of both pyromellitic dianhydride (PMDA) with a purity of 98% and 4,40-diaminodiphenyl ether (DADPE) with a purity of 99% were purchased from Chriskev. The multiwall carbon nanotubes required were supplied from Conyuan Biochemical Co., Ltd, Taiwan. The MWNTs have diameters of 20–40 nm, lengths of 5–15 μm and a degree of purity greater than 95–98%.

B. Preparation of the polyimide/carbon nanotube *nanocomposites*

The MWNTs were pre-treated in liquid DMAc under ultrasonics for 2.5 h to make them uniformly dispersed in the solution. The total amount of the DMAc is 15 ml. Since MWNTs are not soluble in DMAc, the treatment under sonication can made the MWNT networks become loose and uniformly dispersed. The viscosity of the solution containing MWNTs became very high after treatment. This indicates that the solvent has been percolated with large amounts of MWNT networks. Then the monomers, PMDA and equimolar amounts of DADPE were added to the DMAc solution containing MWNTs. The total amount of PMDA and DADPE is 15 ml. After stirring the solutions for 3 h in nitrogen gas at ambient temperature, a PMDA–DADPE polyamic acid (PAA)–MWNT solution was obtained. The concentration of the solution was 10 wt% oligomer against DMAc. The MWNT content against PAA was 0.1–5 wt%. The PAA solution with MWNTs was spin-coated on a glass substrate and dried in an oven at 60℃ for 3 h with nitrogen gas flow. Then the composite PAA films were cured at 220℃ in the same oven with nitrogen gas flow for 3 h to form PI–MWNT composite films. The films were subsequently removed from the glass substrate and characterized. The thickness of the films can be controlled by the speed of the spin coater and is approx. 10–30 μm.

C. Morphological structure and characterization

The surface morphology of the MWNT composite is studied with a field emission gun transmission electron microscope (model: Philips Tecnai G2 F20 FEG-TEM). Since the MWNTs may be covered by a thin film of polyimide, this makes observation of the MWNT network difficult in the SEM picture. Therefore, O_2 plasma is used to etch a thin layer of the polyimide on top so that the structure of the MWNTs in the film can be exposed and visualized in the SEM picture. The SEM picture for the O_2 plasma-etched surface of the MWNT composite is shown in figure 1, where the MWNT network can be clearly observed. The nanotubes are uniformly dispersed in the composite and no agglomeration of the nanotubes was found. In addition, a Fourier transform infrared (FT-IR) spectrometer (model: Thermo/Nicloet FT-IR, Integrated Scientific Services Group, Ltd) was adopted to study the structure of the nanocomposite. It is found that the FT-IR spectra of PI/MWNT nanocomposites do not change with increasing the MWNT content and are almost the same as that of pure PI, as shown in figure 2. These phenomena reveal that adding MWNTs into the PI matrix does not have a significant effect upon the chemical structure of the polyimide. To further study the structure of the polyimide/MWNT nanocomposites, an x-ray diffraction spectrometer (XRD, Bede D1 HR-XRD) was used. The results of the XRD characterizations of MWNTs, the pure PI and the PI/MWNT nanocomposites with 1, 2.5 and 5 wt% of MWNT content are shown in figure 3. In the case of MWNTs, the peak appearing at 18◦ corresponds to the interlayer spacing of the nanotube *(d_{002})* and the d_{100} reflection of the carbon atoms, respectively [15].

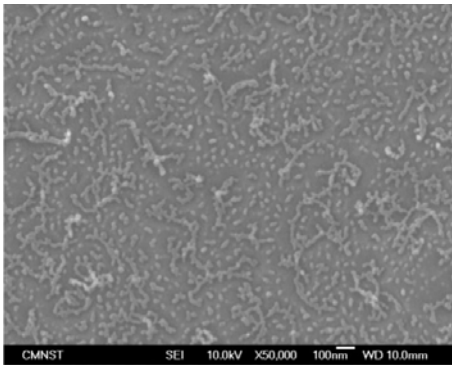

Fig 1. SEM picture for polyimide with MWNTs of 3 wt%.

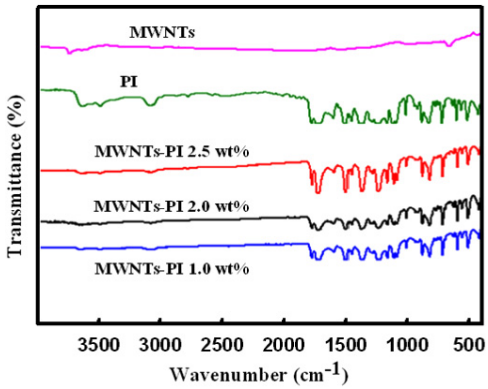

Fig 2. FT-IR spectra of MWNTs, pure polyimide, and the nanocomposite with different MWNT contents.

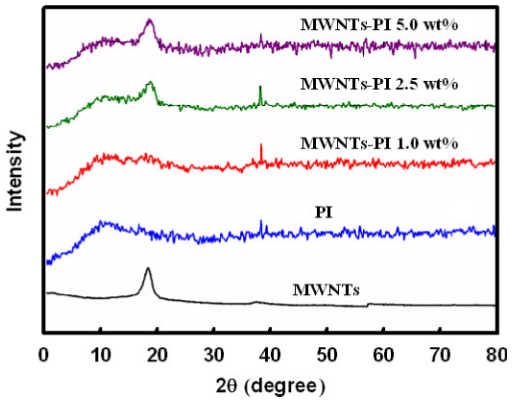

Fig 3. XRD patterns of MWNTs, pure PI, and the nanocomposites with different MWNT contents.

For the pure PI, a broad peak centered at 11.5◦ indicates that PMDA/ODA PI is amorphous. The XRD patterns of the PI/MWNT nanocomposites include both the characteristic peaks of the pure PI and MWNTs. Moreover, the intensity of the peaks assigned to the MWNTs in the composite increase with increasing content of MWNTs. However, the position of the peaks corresponding to the two constituents of the nanocomposite is the same as for the individual PI and MWNTs, which illustrates that either the orientation of the PI chains or the structure of MWNTs is not affected by each other during the process of preparation. The electrical resistance of the MWNT composites is measured by four-point probes (model CM-308 from ELCHEMA). Five different locations on the sample surface were selected for measurements. The averaged value was used for presentation. The thickness of the MWNT composite film is measured with a profilometer. From the thickness of the film, the resistivity of the composite can be calculated. The resistivity of the composite films with different MWNT contents is shown in figure 4. The resistivity of the composite film exhibits a drastic decrease at a certain percolation threshold of the MWNT content and decreases slowly thereafter. The slow decrease in the resistivity after a certain percolation threshold of the MWNT content further indicates uniform dispersion of the nanotubes in the composites.

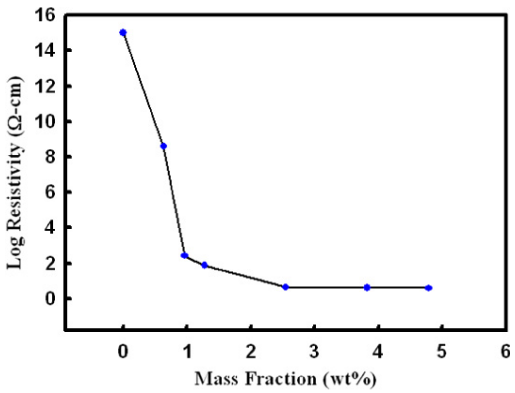

Fig 4. Resistivity variation of the nanocomposite with different MWNT contents.

D. Piezoresistive characteristics of the nanocomposite film

In order to test the piezoresistive characteristics of the composites with different MWNT contents, each of the nanocomposite films with different MWNT contents is made and is used to cover a PMMA plate with a cavity opened on the top,. The top of the nanocomposite film is covered with a PMMA cap with a metal tube for connection to the air flow supply system. Therefore, the nanocomposite film acts as a diaphragm. With the air supply at a given pressure, the diaphragm deforms, which leads to variations of the resistivity. The resistivity variation with air pressure for the nanocomposite at different MWNT contents is measured and presented, as shown in figure 5. The results indicate that the resistance of the film varies very linearly with the applied pressure force. In addition, at lower content of MWNTs, the resistivity of the composite has a greater variation with the pressure. The greater variation of the resistivity with the pressure for a pressure sensor means that the pressure sensor has a greater sensitivity of measurement. Therefore, to have a better sensitivity of the pressure sensor, the MWNT content in the composite should be lower.

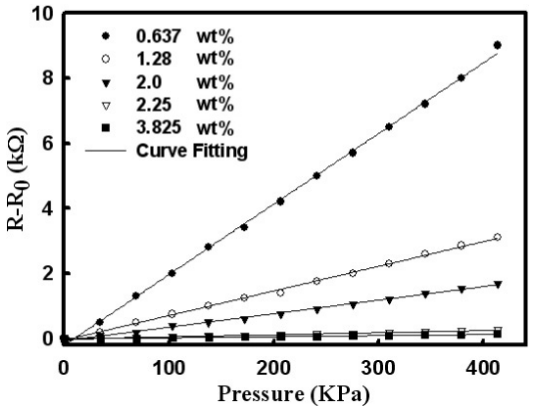

Fig 5. The resistivity variation with air pressure for nanocomposites at different MWNT contents.

III. Fabrication of micropressure sensor

A. Design and fabrication considerations

In general, the silicon pressure sensor made by a surfacemicromachining process is started by etching a cavity into the silicon substrate. Then, a polysilicon layer or a low stress nitride that acts as a diaphragm is deposited to enclose the cavity. Finally, piezoresistive material is deposited on top of the polysilicon layer to sense or measure the deformation of the layer or the pressure inside the cavity. However, before deposition of the polysilicon diaphragm a sacrificial layer, such as silicon oxide or PSG, is required which is deposited to fill up the cavity. Then, a planarization process, such as chemical mechanical polishing (CMP), is required to thicken the sacrificial layer. However, the sacrificial layer can also be created by thermal oxidation of the silicon in the cavity, due to expansion of silicon oxide, until the bottom of the oxide cavity rises up to the top surface of the substrate. In this way, the planarization process can be omitted. However, the cavity depth can be made only of the order of 1 μm, which significantly reduces the range for deflection of the diaphragm, and the range for pressure measurement. Even using deposition of a thick sacrificial layer, usually with low pressure (LP) or plasma-enhanced chemical vapor deposition (PECVD), the maximum cavity depth that can be made is less than 10 μm. This makes the deflection of the diaphragm or the range for the pressure measurement larger. However, in addition to the large residual stress there are a lot of other problems to be resolved before successfully depositing a thick sacrificial layer. In addition, during removal of the sacrificial oxide layer, the top diaphragm will be driven downward by the surface tension of drying water to touch the bottom wall of the cavity. Once the diaphragm touches the bottom, it can

never be separated and recovered from the wall, and eventually results in fatal and permanent damage [16–18].

However, a polymer pressure sensor does not have the problems of narrow depth of the cavity and stiction of the diaphragm. The most promising candidate for pressure sensor fabrication is the use of a photoresist, i.e. SU-8. The SU-8 can be readily spun-coated on the substrate from a few microns to a hundred microns thick. This can give us a much deeper cavity depth if a diaphragm layer can be properly deposited on top to enclose the cavity. The designed diaphragm uses the same material as the cavity sidewall in order to reduce any difference of the thermal expansion coefficient for the cavity wall and the diaphragm which may cause deflection of the diaphragm and significantly affect measurement accuracy. In this way, one would face another problem of selecting a suitable sacrificial material to fill into the cavity to create a flat surface in order to spin-coat the SU-8 diaphragm on it.

However, this difficulty can be readily overcome by reversing the fabrication process of the pressure sensor. That is, one can first spin-coat the SU-8 diaphragm layer and deposit the metal lines on the silicon substrate. Then we spin-coat and cure the nanocomposite layer on top, and then pattern the nanocomposite layer into a shape for sense the maximum stress occurring on the diaphragm. The nanocomposite layer with a content of 1.28 wt% MWNTs was made to determine how the resistivity of the film varies with stress or temperature in the film during the calibration process. The next step is to spincoat the SU-8 layer for the cavity wall at the desired thickness. Finally, a Pyrex glass can be bonded with the patterned SU-8 layer on top to enclose the cavities. Once the silicon substrate is completely removed by wet etching, a successful polymer pressure sensor can be readily achieved.

The design for the proper size of SU-8 diaphragm and the active cavity underneath can be made with the help of the following equations[19] for the maximum deflection, u_{max}, of the SU-8 diaphragm under a uniform pressure load, P:

$$u_{\max} = C(1-\nu^2)\frac{Pb^4}{Eh^3} \quad (1)$$

where C is $\frac{0.032}{1+\alpha^4}$ with the assumption that all edges of the plate are clamped, and α is the ratio of the width to the length of the plate. In addition, b and h are the width and the thickness of the diaphragm, respectively. E is the Young's modulus and ν is the Poisson ratio. The maximum strain, ε, of the SU-8 diaphragm is [20]

$$\varepsilon = 0.308(1-\nu^2)\frac{Pb^2}{Eh^2} \quad (2)$$

The maximum strain the SU-8 layer can sustain is found to be 0.77% [21]. With this constraint, to measure a pressure in the range from 0 to 400 kPa, the thickness of the SU-8 diaphragm is 60 μm for a cavity size of 900 μm × 900 μm underneath the diaphragm. The depth of the cavity should be greater than 30 μm.

B. Fabrication process

a) First, a 10 μm thick SU-8 layer is spun-coated on the substrate and patterned as part of the pressure sensing diaphragm.

b) Then, metalization was done by sputtering Al/Au layers of metal with a thickness of 0.9μm/0.04 μm, respectively, onto the substrate surface.

c) Then, a 40 μm thick SU-8 layer is spun again on the substrate and patterned into a mold to allow for a PAA–MWNT solution with the desired MWNT content to fill. The extra solution outside the mold is wiped up. Thus, the PI–MWNT sensors are made by the damascene process. After drying at 60℃ for 3 h and curing at 220℃ for 3 h in an oven with nitrogen gas flow, the PI–MWNT composite sensors are formed. Extra amounts of PAA–MWNT solution may be filled to compensate for the loss due to evaporation of the solvent.

d) After spin-coating a thin layer of SU-8 with a thickness of 10 μm to cover the PI–MWNT sensor, a 50 μm thick SU-8 layer is spun again on the substrate and patterned into the active cavity to allow for movement of the pressure diaphragm.

e) It is now ready to move the devices made on the silicon wafer onto a low thermal conductivity Pyrex glass. This is done first by bonding the silicon wafer with the Pyrex glass.

f) After the bonding process, the silicon substrate is ready for removal and cleaning off. This is done by wet etching the silicon with TMAH solution at 90 ◦C for 5–6 h. The cavities of the pressure sensors are successfully made, as shown in figure 6(a). No distortion was found. A top view of the sensor, which clearly shows the sensors and metal lines, are shown in figure 6(b).

g) A cap-shaped PMMA plate is then bonded, using epoxy resin, to enclose the test section, as shown in figure 7, to allow for pressurized gas.

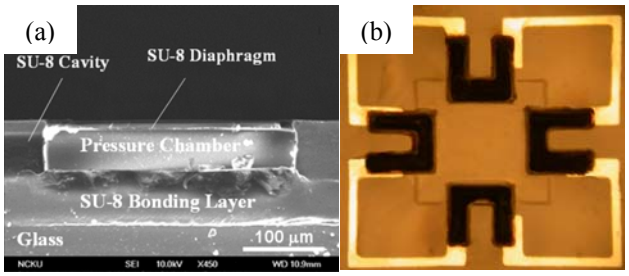

Fig 6. (a) Side view of SEM photographs for pressure sensor diaphragm and cavity made by SU-8 lithography and (b) top view

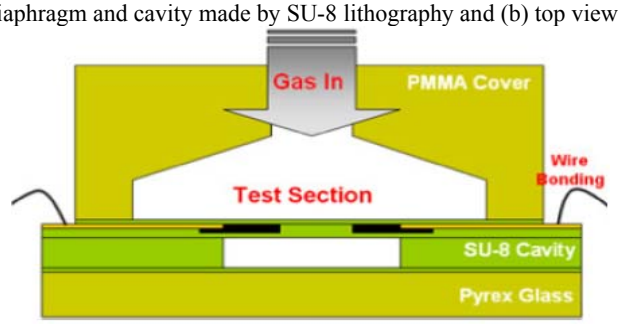

Fig 7. Fabrication process of micropolymer pressure sensor

IV. Calibration and performance evaluation for the polymer sensor

A. Characteristics of the nanocomposite sensors

A total of four sensors are designed on the four edges of the diaphragm to measure the strain or stress which is the maximum on the diaphragm. By connecting with a gas line at desired pressures, the sensor is ready for calibration and performance evaluation. The resistance of the designed sensors is very large and is about 213.7–215.8 kΩ. The pressure effect on the resistivity of the sensor is expected to be very large. Therefore, the sensors have a very high signal resolution. The characteristic curves for the sensors were obtained as shown in figure 8. The results show a very linear variation between the pressure and the resistance of the sensors. The calibration process for many different times showed no observable difference. Since the diaphragm is made of SU-8 material, which has a smaller Young's modulus than the polysilicon film, this leads to a higher strain in the SU-8 film. Therefore, the resolution for the present nanocomposite sensors is much higher than the polysilicon diaphragm sensors (20.88 Ω/psia or 3 Ω kPa^{-1}) [21] and is found to be 35 Ω/psig (5.08 Ω kPa^{-1}). Moreover, the gauge factor of the piezoresistive nanocomposite sensing element can be estimated by the following equation:

$$G = \left(\frac{\Delta R}{R_0}\right)\varepsilon^{-1} \qquad (3)$$

where R_o,_R, ε are the initial resistance of the sensor without applying pressure, the resistance change of the CNT under applied pressure and the strain of the sensor, respectively. With the applied pressure from 0 to 400 kPa (assuming that the initial strain is zero due to no deflection at 0 kPa), the maximum strain at the center of the diaphragm can be estimated from equation (2) and is calculated in the range from 0 to 7.7×10^{-3}. On the other hand, the resistance change due to the applied pressure can be experimentally obtained from three measurements, as shown in figure 8.

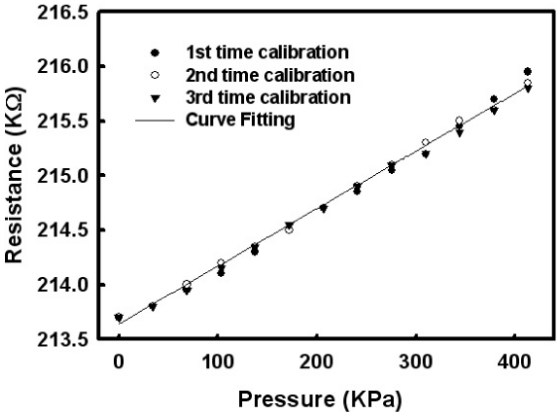

Fig 8. A very linear variation between the pressure and the resistance of the sensor.

Based on equation (3), the average estimated gauge factor of the piezoresistive CNT sensing element is ~1.27, which is less than that of a polysilicon sensing element in a similar configuration with a gauge factor of 2.68. In fact, these gauge factors can be much improved by using thinner diaphragms (or lower MWNT contents in the nanocomposite of the current work). Theoretical calculation indicates that the maximum gauge factor for a polysilicon pressure sensor can be 20 [22]. However, In comparison with a gauge factor of an SWNT pressure sensor as mentioned previously, the current nanocomposite apparently has a much lower value of gauge factor. This is attributed mainly to the size of the diaphragm we made being much thicker, which makes a smaller variation of composite resistance. In addition, the resistance of the nanocomposite is so large that variation of the nanotube resistance in the composites is relatively small, which causes a much smaller gauge factor. In order to test the reliability, i.e. the response, recovery and lifetime (fatigue) of the current pressure sensors, pressurized air is supplied to the sensor cavity for a period of 30 s and then released. The repeated sharp rise and reduction of pressure, as shown in figure 9, suggests that the present nanocomposite pressure sensor has very good reliability.

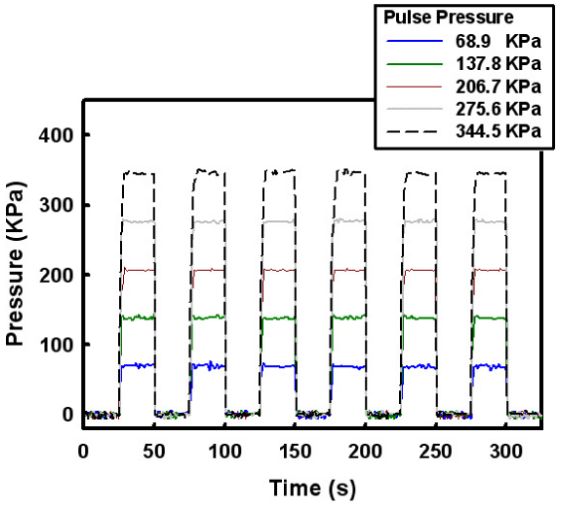

Fig 9. Response and recovery test for pressure sensor at different pulsed pressures.

V. Conclusions

Nanocomposites for MWNT-PI exhibit piezoresistive characteristics which make them ideal for fabrication of a polymer pressure sensor. As a sensor material, the linear variation of the film resistance with the pressure force of MWNTs–PI is much superior than the nonlinear behavior of MWNTs–silicon rubber. This suggests that the resistance of the composites is dominated by the nanotubes, not the resistance in the gap width between neighboring MWNTs. A polymer pressure sensor has the advantages of a large area, low temperature, solution process which means low cost. In addition, the cost for the nanocomposite material with PI–MWNTs is also very low in comparison with other conducting polymer materials. In addition, the polymer pressure sensor can be made flexible, which can be used for blood pressure

measurements or other medical applications. Fabrication of this kind of micropolymer pressure sensor has been presented. The fabrication process has been completely simplified and the absence of the stiction problem, like the one which occurred in the polysilicon pressure sensor, has been noted. In addition, this kind of sensor can be readily integrated with a complicated microfluidic system for detailed flow information measurements. However, care should be taken in the cavity formation in the SU-8 layer and the release of the residual stress in the diaphragm. Performance evaluation of this sensor has also been provided, which demonstrates that the sensor is highly reliable.

REFERENCES

[1] Wang Q H, Corrigan T D, Dai J Y and Chang R P H 1997 Field emission from nanotube bundle emitters at low field *Appl. Phys. Lett.* **70** 3308–10

[2] Kong J, Franklin N R, Zhou C, Chapline M G, Peng S, Cho K and Dai H 2000 Nanotube molecular wires as chemical sensors *Science* **287** 622–5

[3] Ghalkesar M, Barwich V, Lang H P, Braun T, Hegner M and Gerber C 2004 Real-time mass sensing by nano mechanical resonators in fluid *Proc. IEEE Sensor (Dec. 2004)*

[4] Tans S J, Verschueren A R M and Dekker C 1998 Room-temperature transistor based on a single carbon nanotube *Nature* **393** 49–52

[5] Dillon A C, Jones K M, Bekkedahl T A, Kiang C H, Bethune D S and Heben M J 1997 Storage of hydrogen in single-walled carbon nanotubes *Nature* **386** 377–9

[6] Zhang Y, Chang A, Cao J, Wang Q, Kim W, Li Y, Morris N, Yenilmez E, Kong J and Dai H 2001 Electric-field-directed growth of aligned single-walled carbon nanotubes *Appl. Phys. Lett.* **79** 3155–7

[7] Kuo C Y, Chan C L, Gau C, Liu C W, Hsiau S H and Ting S H 2007 Nano temperature sensor using selective lateral growth of carbon nanotube between electrodes *IEEE Trans. Nanotechnol.* **6** 63–9

[8] Im H, Huang X-J, Gu B and Choi Y-K 2007 A dielectric-modulated field-effect transistor for biosensing *Nat. Nanotechnol.* **2** 430–4

[9] Grow R J, Wang Q, Cao J, Wang D and Dai H 2005 Piezoresistance of carbon nanotubes on deformable thin-film membranes *Appl. Phys. Lett.* **86** 093104

[10] Cao J, Wang Q and Dai H 2003 Electromechanical properties of metallic, quasimetallic, and semiconducting carbon nanotubes under stretching *Phys. Rev. Lett.* **90** 157601–4

[11] Tombler T W, Zhou C, Alexseyev L, Kong J, Dai H, Liu L, Jayanthi C S, Tang M and Wu S 2000 Reversible electromechanical characteristics of carbon nanotubes under local-probe manipulation *Nature* **405** 769–72

[12] Fung C K M, Zhang M Q H, Chan R H M and Li W J 2005 A PMMA-based micro pressure sensor chip using carbon nanotubes as sensing element *MEMS 2005 (Miami): Technical Digest* pp 251–4

[13] Dang Z M, Jian M-J, Xie D, Yao S-H, Zhang L-Q and Bai J 2008 Supersensitive linear piezoresistive property in carbon nanotubes/silicone rubber nanocomposites *J. Appl. Phys.* **104** 024114

[14] Jiang X, Bin Y and Matsuo M 2005 Electrical and mechanical properties of polyimide–carbon nanotubes composites fabricated by *in situ* polymerization *Polymer* **46** 7418–24

[15] Vilkner T, Janasek D and Manz A 2004 Micro total analysis systems. Recent developments *Anal. Chem.* **76** 3373–86

[16] Core T A, TsangW K and Sherman S J 1993 Fabrication technology for an integrated surface micromachined sensor *Solid State Technol.* 39–47 Author: [28]: Please provide volume number.

[17] Kim C J, Kim J Y and Sridharan B 1998 Comparative evaluation of drying techniques for surface micromachining *Sensors Actuators* A **64** 17–26

[18] Madou M J 2002 *Fundamentals of Microfabrication* 2nd edn (Boca Raton, FL: CRC Press) pp 276–7

[19] Boresi A P *et al* 1993 *Advanced Mechanics of Materials* (New York: Wiley) pp 538–9

[20] Guckel H 1991 Surface micromachined pressure transducer *Sensors Actuators* A **28** 133–46

[21] Ko H S, Liu C W and Gau C 2007 A novel fabrication for pressure sensor with polymer material and evaluation of its performance *J. Micromech. Microeng.* **17** 1640–8

[22] French P J and Evans A G R 1984 Piezoresistance in polysilicon *Electron. Lett.* **20** 999–1000

CMOS Phototransistor Device : A total solution for Skin whitening Assays

Yen-Pei Lu[1*], Yu-Wei Chang[2], Ming-Yu Lin[1,3], Jiann-Shiun Kao[1], Yang-Tung Huang[2], Yuh-Shyong Yang[1,3]

[1]*Instrument Technology Research Center, National Applied Research Laboratories, Taiwan*
[2] *Institute of Electronics, National Chiao Tung University, Taiwan*
[3] *Institute of Biochemical Engineering, National Chiao Tung University, Taiwan*

Abstract — **Three skin whitening assays combining the semiconductor technology was demonstrated for screening the drug candidate and discussing the mechanisms of melanogenesis in medical cosmetics. We proposed a miniaturized photometric system using complementary metal oxide semiconductor (CMOS) phototransistor as a detector with high sensitivity. The CMOS phototransistor was a small, portable optoelectronic device with enlarged depletion region of the outer N_{well}/P_{well} ring-shaped photodiode, able to cause a sensitive shift of the threshold voltage and enhance photocurrent response. The device was further connected to IC system to show it ability for high-throughput screening needed in the pharmaceutical industry. Three methods for evaluating effects of skin whitening agent were applied, including 3-(4,5-dimethylthiazol-2-yl)-2,5-diphenyltetrazolium bromide (MTT) assay, melanin amount measurement, and tyrosinase assays. The change of light absorbance due to enzymeatic catalysis was easily measured with the proposed system. The skin whitening effects by kojic acid was determined and comparable to the commercial system.**

Keywords —CMOS phototransistor, melanogenesis, melanin, tyrosinase, kojic acid.

I. INTRODUCTION

There are increasing needs for the development of miniaturized colorimetric absorbance devices to screen the efficiency of skin whitening agents, because abundant candidates of whitening agents are developed. Melanogenesis has attracted attention in medical cosmetics for many decades. There are accumulating studies to support that the proliferation rate of melanocytes and tyrosinase activity are the key factors in the melanogenesis. Most of the targets that skin whitening agents take place are in the decreasing the proliferation rate of melanocytes, as well as the inhibition of tyrosinase activity. Melonocytes are key components of the skin's pigmentary system through their ability to produce melanin. Melanogenesis in melanocytic cells is regulated mainly by tyrosinase, a membrane-bound copper-containing glycoprotine, which is the critical rate-limiting enzyme. Tyrosinase is produced only by melanocytic cells and stores at special ovoid organelles, called melanosomes, wherein the melanin is synthesized and deposited [1]. Once melanins are produced the melanosomes are transferred form melanocytes to neighboring keratincytes distributed in skin and hair tissues, thus produced the visible color [2]. Biologists have been looking for the skin whitening agents by reducing the number of melanocytes, decreasing the amount of melanin through inhibiting tyrosinase activity or enhancing the antioxidant activity. Pharmaceutical companies normally apply robust automatic instruments for high-throghput screening because the pathway of melanogenesis and assays for evaluating the drug candidates are complicated. Recently, a number of melanin formation inhibitors for skin-care application on whitening have been reported. Kojic acid is well-known as one of the standard skin whitening inhibitors used to evaluate the potency of a new drug candidate [3, 4]. The cosmetic industry is rapidly growing and a miniaturized, portable platform to screen the efficiency of potential whitening agents is needed. In this report, we demonstrated that the CMOS optoelectronic platform can fulfill this requirement. The phototransistor in CMOS technology is widely using in the development of miniaturized optical detection system. The CMOS device is able to fabricate small geometry chip with a great deal of convenience and flexibility. The major assays: MTT assay for the evaluation of viability of melanoma cells; melanin assay, for the measurement of contents of melanin product; and tyrosinase assay, for the evaluate tyrosianse activity were demonstrated on this platform that provide reliable, low cost, small size, and paralleled processing benefits.

II. EXPERIMENTAL SECTIONS

A. Phototransistor System

There are two key optoelectronic devices in the proposed system, including LED as light source and CMOS compatible phototransistor as detector (Figure 1) to measure the colorimetric absorbance of products from three whitening assays. A narrowband LED with specific wavelength is designed for providing specific wavelength in this study. When light source pass through biochemical materials such as protein products the intensity of light will change CMOS phototransistor detects the light intensity change and acquires consequent data. For absorbance measuring, 10 μl samples quantity are quite enough in our experiment. The governed equation according to the Beer-Lambert Law shows below.

$$A = -\log\left(\frac{I}{I_0}\right) = \epsilon_\lambda \cdot l \cdot c \implies A \propto c$$

In this equation, A represents absorbance, I_0 and I stands for the initial light intensity and the light intensity after passing through the sample, ε_λ is the wavelength-related molar absorptivity in units of $1mol^{-1}cm^{-1}$, l is the length in units of cm, c is the concentration of sample in units of $moll^{-1}$. With a fixed path length and a monochromatic light source, the absorbance would be proportional to sample concentration. For this reason, detecting the signal emitted by the biomedical

Contact author: Yen-Pei Lu is with the Instrument Technology Research Center. 20, R&DRd. VI, Hsinchu, 300, Taiwan, (phone: +886-3-5779911#478 fax: +886-3-5773947; e-mail: **ypl@itrc.org.tw.)*

reagents can quantitatively determine soluble formazan, melanin, and L-dopaquinone in solutions.

B. Methods

MTT assay is a standard colorimetric detective method for measuring viability and proliferation of cells in biology. MTT

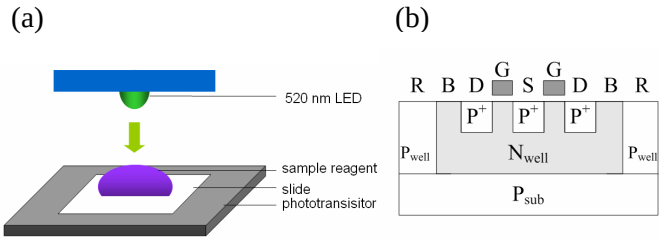

Figure 1. The CMOS optoelectronic platform. (a) CMOS phototransistor device as detector and LED as light source. (b) The structure of CMOS phototransistor.

assay is based on the conversion of yellow 3-(4,5-dimethylthiazol-2-yl)-2,5-diphenyl tetrazolium bromide (MTT) to purple MTT-formazan crystal by mitochondrial enzyme. This reaction is happened in mitochondria and needed to add either dimethyl sulfoxide, an acidified ethanol solution, or detergent sodium dodecyl sulfate diluted in hydrochloric acid to dissolve the insoluble formazan product into a colored solution. The absorbance of colored solution measured between 500 and 600 nm wavelengths can quantify the amount of viable cells [5]. The measurement can be easily preceded in cell cultured plates by using CMOS biosensor.

Cells survival was quantified by a colorimetric MTT assay. This method is previously described with slight modification [6]. Briefly, B16-F10 murine melanoma cells (ATCC: CRL-6475) were cultured in Dulbecco's modified Eagle's medium with 10% heat-inactivated fetal bovine serum, 1.5 g/l sodium bicarbonate, 4.5 g/l glucose, and 1% antibiotics and were seeded at a density of 2×10^5 cells into 6-well plates. The cells were then incubating at 37°C in a humidified atmosphere containing 5% CO_2 for 72 h. MTT was freshly prepared at 1 mg/ml in phosphate-buffered saline (PBS). Add 800 µl MTT solution to each well of cells cultured plate and incubate at 37°C for 4 h. To each well, add 800 µl dimethyl sulfoxide (DMSO) to dissolve MTT-formazan. After incubating at 37°C for 10 min, we measured the density of cells with CMOS biosensor.

Melanin produced by B16-F10 cells was measured using a modification of a previously reported method [7]. Briefly, B16-F10 cells were cultured in 6-well plates at a density of 2×10^5 cells/ml. Cells were divided into three groups as described above. After incubating at 37 °C in 5 % CO_2 for 48 h, cells were digested with a 0.25% (w/v) trypsin-0.52 mM EDTA solution and washed twice with sterilized PBS. The supernatant was discarded and the cell pellets were dissolved in 1 N NaOH at 80 °C for 1 h. Absorbance of melanin content was determined using a spectrophotometer at 450 nm.

In mammalian melanocytes, tyrosinase plays a critical role in the process of melanin because it catalyses the three different melanogenesis steps. They are: 1) hydroxylation of tyrosine to 3,4-dihydroxyphenylalanine (DOPA); 2) the oxidation of DOPA to dopaquinone; and 3) the oxidation of 5,6-dihydroxyindole (DHI) to indole-quinone. Therefore, melanin production is mainly dependent on tyrosinase expression and activation [1, 2]. The spectrophotometric method of tyrosinase activity assay employed in this study depends on melanin from DOPA. Tyrosinase activity assay was determined as previously described with slight modification [8]. This assay is a highly specific and sensitive in cell culture. Briefly, mammalian melanoma B16F10 cells were cultured in 6-well plates at a density of 2×10^5 cells/ml. After incubating at 5% CO_2 37°C incubator for 3 days, cells were digested with 0.25% (w/v) trypsin-0.52 mM EDTA solution (GIBCO) and washed with ice-cold sterilized PBS. Discarded the supernatant, cells were lysed in 150 µl of 0.1 M sodium phosphate buffer (pH6.8) containing 1% Triton X-100 and 0.1 mM PMSF, and then frozen at -20°C for 30 min. After thawing and mixing, cellular extracts were clarified by centrifugation at 12000 rpm for 30 min at 4°C. The 80 µl supernatant and 20 µl of L-DOPA (2 mg/ml) were placed in 96-well plate. Specific activity was defined as the amount of L-dopaquinone formed per cell. Following incubation at 37°C, absorbance was measured for at least 1 h by using CMOS biosensor.

III. CURRENT RESULTS

CMOS-based optoelectronic system is composed of the CMOS phototransistor and the green light emitting diode (LED) light (Fig.1.a). The proposed CMOS phototransistor device was applied as photodetector and manufactured by using the Taiwan Semiconductor Manufacturing Company (TSMC) standard technology. The 0.35 µm CMOS photodiode developed for the present study was designed form an N-well and P-substrate. The cross p-n-p structure of the fabricated CMOS optoelectronic devices were shown in Fig. 1b. The P^+ source placed in the center, polysilicon gate (G) and P^+ drain are surrounded as a ring-shape. The integrated circuit work as a metal-oxide-semiconductor field-effect transistor (MOSFET) with a photodiode connected across the bulk (B) and the square ring (R). In our proposed layout style (Fig.1b), the depletion region of the outer N_{well}/P_{well} ring-shaped photodiode was enlarged and caused a large shift amount of the threshold voltage in order to get a larger photocurrent response, thus increase the sensitivity of the biosensor.

Three biochemical assays including MTT assay, melanin assay, and tyrosinase activity assay that are to represent the effects of skin whitening agents in the melanogenesis pathway were developed using the compact CMOS optoelectronic platform (Fig. 2). The experimental I_d-V_d curves of phototransistor for measuring the MTT, melanin and tyrosinase activity are shown in Figs. 3(a), 4 (a), and 5 (a). From the Beer-Lambert law, the absorbance is reverse propotional to the light intensity, Id. The effects of Kojic acid, one of the skin whitening agents have been reported to inhibit tyrosinase activity and reduce the melanin content without influencing proliferation of B16F10 cells [3]. In figure 3, the results showed that Kojic acid did not affect the viability of B16F10 cells (MTT assay). Hence the results from kojic acid and

control group were the same in MTT assays while using DMSO as blank solvent (Fig.3a). The result from the proposed CMOS-based optoelectronic system was consistent with the commercial microplate reader (Fig.3b). Since kojic acid was reported to inhibit the production of melanin by inhibiting tyrosinase, the key enzyme to generate melanin, we further tested the performance of kojic acid with our optoelectronic system. Fig 4 showed that the amount of melanin was decreased with kojic acid treatment and consistent with the commercial microplate reader. $_{L}$- DOPA is converted to coloured $_{L}$-dopaquinone with the tyrosinase catalysis. Kojic acid inhibited the tyrosinase activity, thus decrease the generation of $_{L}$-dopaquinone. The light intensity (Id) obtained from the CMOS-based optoelectronic system was reverse proportional to the amount of $_{L}$-dopaquinone. In figure 5, the tyrosinase activity was inhibited, and the generation of $_{L}$-dopaquinone was decreased with kojic acid treatment. To sum up, kojic acid did influence the melanogenesis through suppressing tyrosinase activity (tyrosinase activity assay) and reducing content of melanin (melanin assay) at concentration of 500 μg/ml. The control was B16F10 cells only and DMSO, NaOH, and $_{L}$-DOPA representing the reference condition without melanoma cells. The results were comparable to that using by commercial microplate reader (Fig.3-5).

A method combining the modern semiconductor technology and colorimetric absorbance measurement is a popular application for developing the high-trough-put screening platform to screen the candidates of whitening agents in medical cosmetics. In this report, we used the standard CMOS technology and absorption photometry to set up a miniaturized, portable screening device for colorimetric absorbance measurement. The COMS optoelectronic devices were able to evaluate the key assays in the melanogenesis, including MTT assay, melanin content assay, and tyrosinase activity assay. These three assays have been widely used in researches of melanogenesis mechanism, pigmentation dysfunctional diseases, and medical cosmetics. The experimental results revealed that CMOS optoelectronic platform with 520 nm wavelength of LED light source could evaluate the effect of whitening agent kojic acid and the results were matching to that using by traditional micoplate reader.

The system shows the advantages including high sensitivity, low cost, convenient, and expandable. In conclusions, our results indicated that the proposed miniaturized CMOS phototransistor platform can be developed to a high-throughput system for the evaluation of the whitening reagent in the popular cosmetic industry.

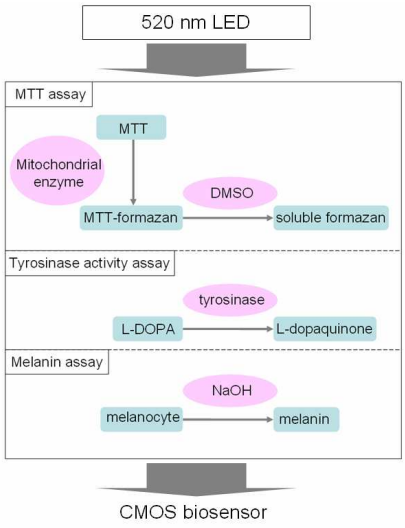

Figure 2. The schematic diagram of three major assays for evaluating whitening agents

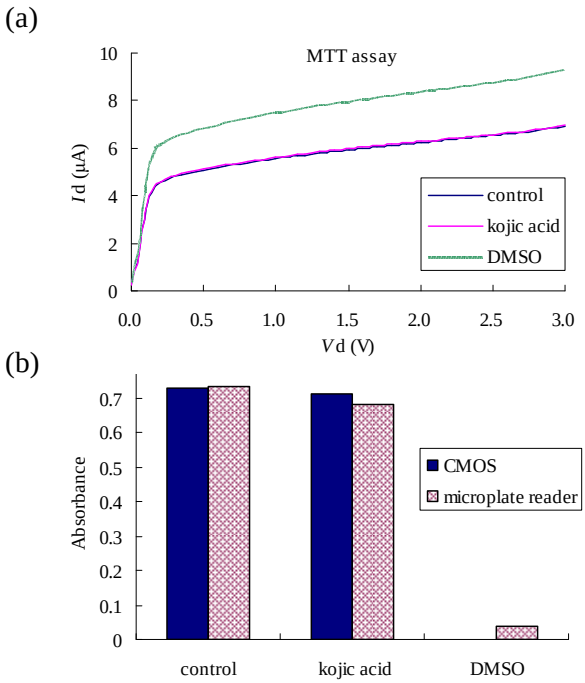

Figure 3. MTT assay. B16F10 cells were treated with 500 μgml kojic acid 0 μg/ml kojic acid (as control group) and DMSO respectively. (a) The measured I_d-V_d curves by CMOS. (b) All samples were determined by CMOS phototransistor system and traditional microplate reader.

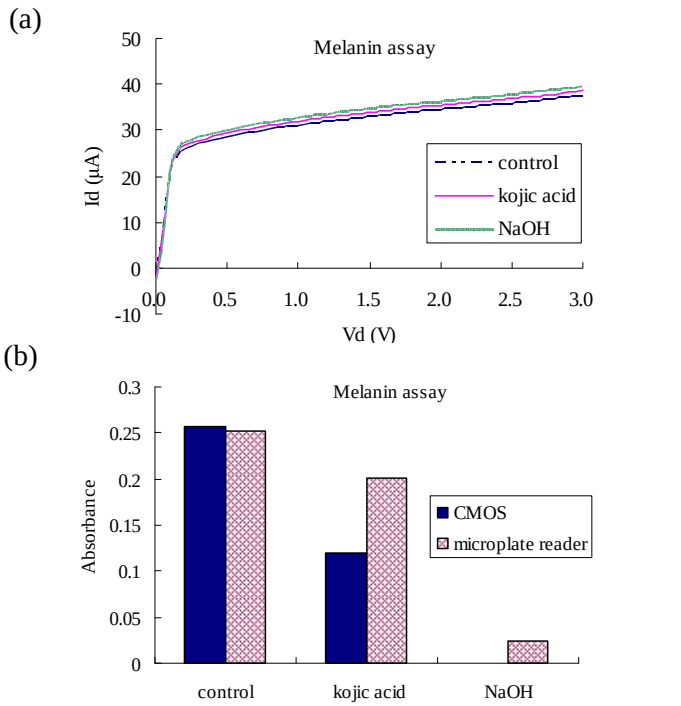

Figure 4. Melanin assay. B16F10 cells were treated with 500 μg/ml kojic acid, 0μg/ml kojic acid (as control group) and NaOH respectively. (a) The measured I_d-V_d curves by CMOS. (b) All samples were determined by CMOS phototransistor system and traditional microplate reader.

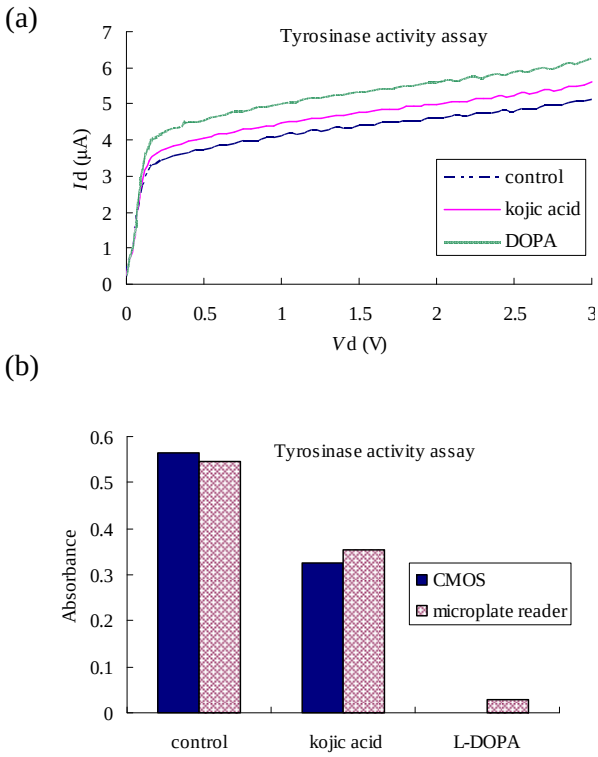

Figure 5. Tyrosinase activity assay. B16F10 cells were treated with 500 μg/ml kojic acid, 0μg/ml kojic acid (as control group) and NaOH respectively. ((a) The measured I_d-V_d curves by CMOS. (b) All samples were determined by CMOS phototransistor system and traditional microplate reader.

REFERENCE

[1] N. Wang and D.N. Hebert, "Tyrosinase maturation through the mammalian secretory pathway: bringing color to life," *Pigment Cell Res*, vol. 19, pp. 3-18, 2006.

[2] M. Tsatmali, J. Ancans, and A.J. Thody, "Melanocyte function and its control by melanocortin peptides", *J Histochem Cytochem*, vol. 50, pp. 125-133, 2002.

[3] F. Solano, S. Briganti, M. Picardo, G. Ghanem, "Hypopigmenting agents: an updated review on biological, chemical and clinical aspects," *Pigment Cell Res*. vol. 19, pp. 550-571, 2006.

[4] K. Sato, H. Takahashi , R. Iraha , and M. Toriyama, "Down-regulation of tyrosinase expression by acetylsalicylic acid in murine B16 melanoma," *Biol Pharm Bull*. vol. 31, pp. 33-37, 2008.

[5] A.H. Cory, T.C. Owen, J.A. Barltrop, and J.G. Cory, "Use of an aqueous soluble tetrazolium/formazan assay for cell growth assays in culture", *Cancer Commun*, vol. 3, pp. 207-212, 1991.

[6] G. Prota, "Progress in the chemistry of melanins and related metabolites", *Med Res Rev*, vol. 8, pp. 525-556, 1988.

[7] Y. Aoki, T. Tanigawa, H. Abe, and Y. Fujiwara, "Melanogenesis Inhibition by an Oolong Tea Extract in B16 Mouse Melanoma Cells and UV-Induced Skin Pigmentation in Brownish Guinea Pigs," *Biosci. Biotechnol. Biochem*., vol. 71, pp. 1879-1885, 2007.

[8] Y.J. Kim, "Antimelanogenic and antioxidant properties of gallic acid", *Bio Pharm Bull*, vol. 30, pp. 1052-1055, 2007.

Using a New Method for Produce the Emulsions by Electrospraying Microfluidic Chip

Meng Hsuan Lee, Chia-Hsien Yeh, and Yu-Cheng Lin

Department of Engineering Science, National Cheng Kung University, Tainan, Taiwan

***Abstract* — In this paper, utilizing the microfluidic cross-junction and high electric field to generate uniform emulsions is reported. Our strategy was based on flow-focusing for the formation of a series emulsions by changing ratio of disperse phase and continuous phase flow rate and by adding the electric field to control the emulsion size decrease. We found the size of the emulsion decreased as the electric filed and the ratio of continuous phase disperse phase flow rate and increased. Experimental data showed that the emulsions were quite uniform with standard deviation less than 10%. When adding the electric field, the Taylor cone is formed and the smaller Na-alginate emulsions are generatee, the size of which is about 10 μm. Using the proposal electrospraying microfluidic chip, the alginate emulsion of smaller size could be obtained compare to the previous cross-junction shape researches.**

Keywords — ***Alginate, Emulsion, Taylor cone, Electrospraying***

I. INTRODUCTION

The technology of emulsion drop generation has a wide application in the food industry and in cosmetics, drug delivery, and ink-jet printing. Microfluidic technology provides a highly controllable means of emulsification. The flow focusing geometry [1, 2] is commonly used to generate droplets whose size is easily controlled by the flow rates. Lin and Lee used an air control system and create a moving-wall structures to generate tiny droplets which about 20 micrometers in diameter [3]. However, there are limits to the smallest droplet size that can be achieved by changing the geometry, the size of the channels, and the properties of the fluids. One potential means of overcoming these limitations is the use of electrospray which is caused by an electric force applied to a liquid surface, and many experiments have been carried out to make smaller droplets using electrospray. Bose reported electrohydrodynamic spraying from an electrified capillary [4].

Na-alginate is used as the dispersed phase which flows through the central channel. Na-alginate is currently gaining a lot of attention for medical applications as well as for the controlled release of drugs [5]. The success of Ca-alginate beads as carriers is due to the following features: (i) they can dissolve poorly soluble drugs and thus increase their bioavailability, (ii) they can stay in the body (in the blood) long enough to provide gradual accumulation in the required area, (iii) their sizes permits them to accumulate in body regions with leaky vasculature, (iv) they can be tailored to achieve targeting or other desired properties by attachment of a specific ligand to the outer surface, (v) they have low toxicity and high loading capacity, as well as minimize drug degradation and loss, and (vi) they can be easily produced in large quantities [6-8].

Applications using the flow behavior of immiscible liquids at the microscale level have been reported. For example, Song et al. [9] presented a microfluidic system that forms aqueous droplets in a continuous flow of a water-immiscible fluid. The droplets act as microreactors, which rapidly mix reagents and transport them with no dispersion. Zhao et al. [10] proposed a strategy to control the flow of immiscible liquids in microchannels by patterning surface free energies, which were applied in the fabrication of a semipermeable membrane. Hisamoto et al. [11] used an immiscible system to develop a new method of performing multi-ion sensing. The proposed immiscible system maintains stable multilayer interfaces for a long distance and completes the ion pair extraction reaction inside the microchannel.

II. MATERIALS & METHOD

Commercial sample of high viscosity Na-alginate was purchased from Sigma Chemical Co. (MO, USA), which was used as the dispersed phase (viscosity 27 cP in 0.5 % solution at 25°C). The sunflower seed oil was used as the continuous phase (viscosity 42 cp) purchased from Uni-President Enterprises Corp. The emulsion is formed due to the hydrodynamic-focusing and electric field effect. Because the disperse phase and continuous phase are not mutually dissolved, the continuous phase has compressed the disperse phase to generate the hydrodynamic-focusing. The parallel electrodes have induced the electric field effect in the cross-junction position, as shown in Fig. 1, and the dimension of the chip was shown in Fig. 2. The backward of the cross-junction position was reduced to width of 50 μm and it would make the electric field effect bigger than the origin shape, for the observation zone is increased to 200 μm and 400 μm. The ANASY® 11 was used to simulate the electric field effect between the different designs. The proposed electrospraying

*Contacting Author: Yu-Cheng Lin, National Cheng Kung University, Department of Engineering Science; University Road, Tainan 701, Taiwan, R.O.C (phone: +886-6-276-2395; fax: +886-6-276-2329; e-mail: yuclin@mail.ncku.edu.tw).

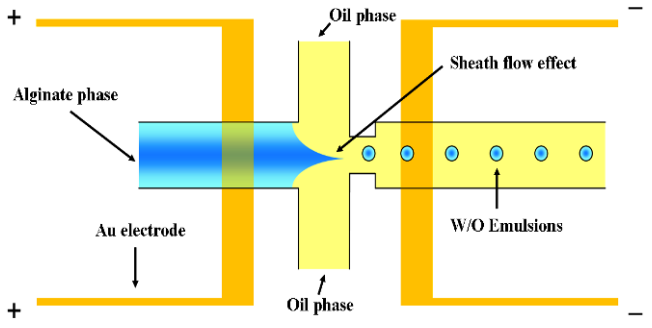

Figure 1. Schematic drawings of Na-alginate emulsions generation system. This method included the cross-junction part and the parallel electrodes.

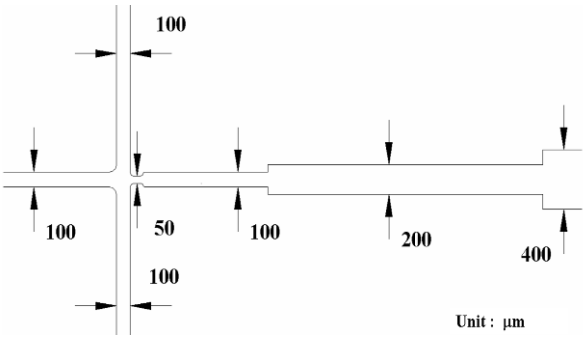

Figure 2. The design dimension of the microfluidic chip, the unit is μm.

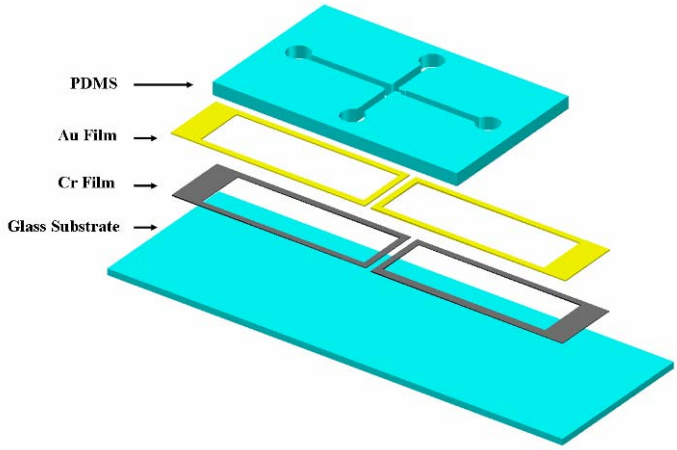

Figure 3. Illustration of microfluidic chip, including glass substrate, Cr film, Au firm and PDMS microstructure fabricated using the MEMS technology.

microfluidic chip consists of two components: the PDMS cross-junction chip and parallel electrodes, as shown in Fig. 3., the Au film and Cr film are made by e-beam evaporation. The thickness of Cr film is 20 nanometer and that of Au film is 200 nanometer, and the role of Cr film is an adhesion layer between Au film and glass substrate. The MEMS technology was used to fabricate the gold/chromium thin film electrodes and PDMS chip. The parallel electrode in the glass was bonded with the PDMS chip by the O_2 plasma machine. Channels were coated by Aquapel (YCC-805) to prevent water droplets from wetting the walls. The coating makes the surfaces more hydrophobic.

The liquid should be slightly conducting to form a Taylor cone. If the liquid has a high conductivity, it cannot form a Taylor cone because there would be no potential difference in the liquid.

The formation of a Taylor cone is necessary to generate very fine droplets. When an electric field is applied, the water-oil interface at the tip is charged and behaves as a capacitor. As the voltage increases, the charges on the interface increase resulting in a higher attraction downstream. The tip of the Taylor cone is stretched to a narrow filament and is broken into tiny droplets due to the Rayleigh instability.

III. RESULT AND DISCUSSION

In the simulation results, we set the scale bar both from 0 V/cm to 220 V/cm, the 50 μm width channel was found to have the bigger electric field (165 V/cm) effect than the 100 μm (105 V/cm) width channel under fixed 100V/cm electric field in the parallel electrode, and as shown in Fig. 4. So the Fig. 4(b) is the better design for electro-spraying microfluidic chip.

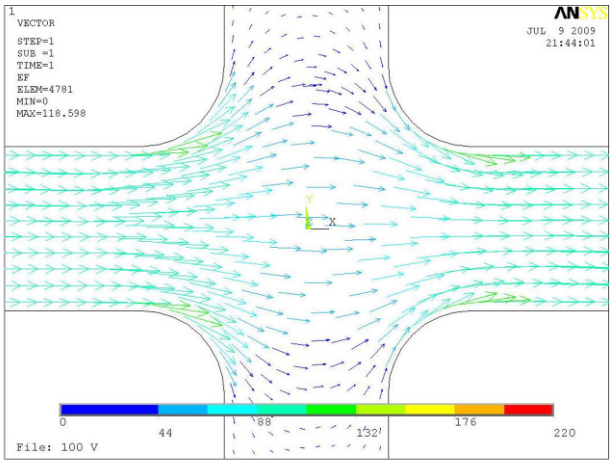

(a)

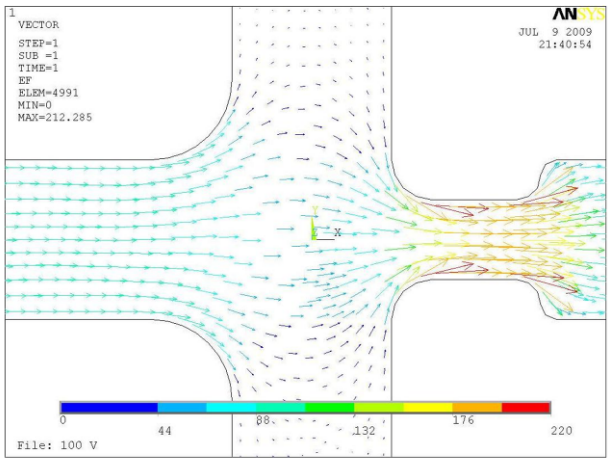

(b)

Figure 4. The electric field of parallel electrodes is simulated in the cross-junction position. (a) The width of channel is 100 μm; (b) the width of channel is 50μm.

The Taylor cone is appeared in cross-junction positions, the new design not only could make the higher electric field increase the electrospraying effect but also increase the sheath force to generate smaller emulsion size. When fixing disperse and continuous phase flow rate, the emulsion size could be decreased by increasing the electric field, as shown in Fig.5. When the electric field is increased to about 500 V/mm, because of the relationship between the mutually exclusive charge, the emulsions from top to bottom show in the channel as shown in Fig. 5 (c), (d).

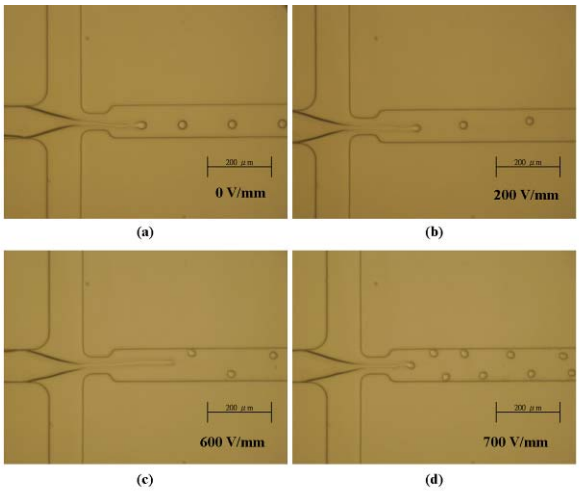

Figure 5. When fixing the flow rate of dispersed phase at 1 μL/min and flow rate of the continuous phase at 5 μL/min, the emulsion size is decreased by increasing the electric field. (a) 0 V/cm, (b) 200 V/cm, (c) 600 V/cm, and (d) 700 V/cm.

The relationship between emulsion size and electric field is shown in Fig.6. Smaller droplet sizes are produced at smaller ratios of flow rates of dispersed fluid to continuous fluid, at the same voltages, the emulsion size can be effectively reduced when increasing the electric field. And the smallest droplet size is less than 10 μm in diameter.

When the electric field is increased to 1000 V / mm or more, it will not be able to generate the uniform emulsion. With a random distribution in the channel, alginate even began to be dissociative, resulting in a number of bubbles, as shown in Fig. 7. The alginate started to solidify due to overheating, when the electric field is more than 1500 V / mm, finally channel will be obstructed by alginate, as shown in Fig. 8

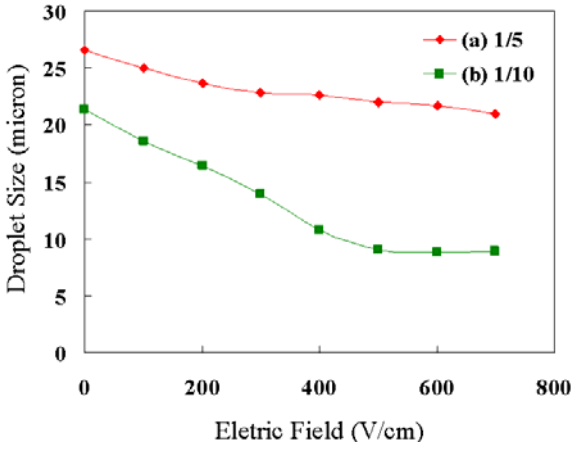

Figure 6. The relationship between droplet size and electric field and fixed the ratio of disperse and continuous phase flow rate. (a) Dispersed phase at 1 μL/min, continuous phase at 5 μL/min; (b) dispersed phase at 1 μL/min, the continuous phase at 10 μL/min.

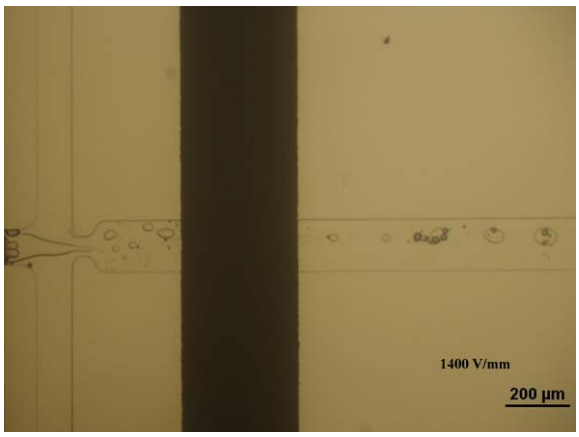

Figure 7. Bubbles generated when the electric field reaches 1400 V/mm

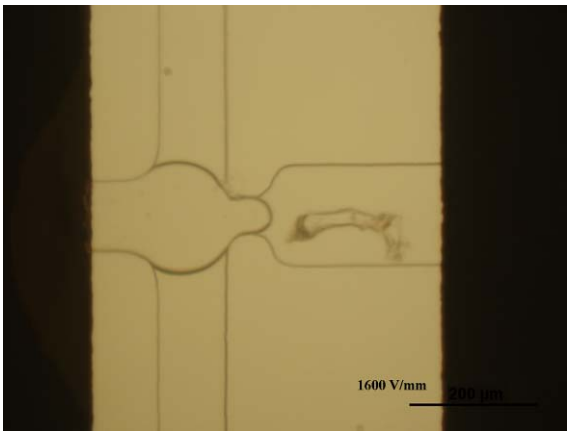

Figure 8. Alginate solidify due to overheating when electric field is1600 V/mm

IV. CONCLUSIONS

We have successfully demonstrated the elecrospraying microfluidic chip to produce the alginate emulsions. In this

method, the electric field and sheath force influences were combined to generate smaller emulsion. The parallel electrode provided the stable electric field to obtain the Taylor cone, which could produce the about 10 μm alginate emulsions with a narrow size distribution (<10%). When increasing the electric field and ratio of disperse and continuous flow rate, emulsions of smaller size could be generated. The approach in manipulation of Na-alginate will provide many potential usages for pharmaceutical applications.

REFERENCES

[1] M. Ganan-Calvo and J. M. Gordillo, "Perfectly Monodisperse microbubbling by capillary flow focusing," Phys. Rev. Lett, vol. 87, pp. 274501, 2001.

[2] S. L. Anna, N. Bontoux and H. A. Stone, "Formation of dispersions using 'flow-focusing' in microchannels", Applied Physics Letter, vol. 82, pp. 364-366, 2003.

[3] S. K. Hsuing, C. T. Chen and G. B. Lee, "Micro-droplet formation utilizingmicrofluidic flow focusing andcontrollable moving-wall chopping techniques," J. Micromech. Microeng, vol. 16, pp. 2403-2410, 2006.

[4] G. Bailey, Electrostatic Spraying of Liquids (Wiley, New York, 1988).

[5] I. W. Sutherland, "Alginates. In Biomaterials: Novel Materials from Biological Sources," Eds: Byrom D. Stockton, pp. 309-331, 1991.

[6] W. R. Gombotz & S. F. Wee, "Protein release from alginate matrices," Adv. Drug Deliv. Rev**,** vol. 31,pp. 267-285, 1998..

[7] R. M. Iskakov, A. Kikuchi & T. Okano, "Timeprogrammed pulsatile release of dextran from calciumalginate gel beads coated with carboxy-n-propylacrylamide copolymers," J. Control. Release, vol. 80, pp. 57-68, 2002.

[8] M. Leonard, A. R. De Boisseson, P. Hubert, F. Dalencon & E. Dellacherie, "Hydrophobically modified alginate hydrogels as protein carriers with specific controlled release properties," J. Control. Release, vol. 98, pp. 395-405, 2004.

[9] Song H, Tice JD, Ismagilov RF (2003) A microfluidic system for controlling reaction networks in time. Angew Chem Int Ed Engl 42:768–772

[10] Zhao B, Viernes NOL, Moore JS, Beebe DJ (2002) Control and applications of immiscible liquids in microchannels. J Am Chem Soc 124:5284–5285

[11] Hisamoto H, Horiuchi T, Uchiyama K, Tokeshi M, Hibara A, Kitamori T (2001) On-chip integration of sequential ion sensing system based on intermittent reagent pumping and formation of two-layer flow. Anal Chem 73:5551–5556

Using Developed Transdermal Delivery Chip To Transfer Drug For Skin Permeation

Zi-Yu Liu, Lin-Tsung Chiou, Chia-Hsien Yeh, and Yu-Cheng Lin*

Department of Engineering Science, National Cheng Kung University, Taiwan

***Abstract*-This study developed a novel transdermal delivery chip system for delivering silver sulfadiazine into rat skin. The chip system was used Micro-Electro-Mechanical-Systems (MEMS) technology to fabricate and electroporation as experimental mechanism. The electrode would generate cell-penetrating electric field in the skin between electrodes when the voltage was applied. Microscope raman spectrometer was used to analyze spectral strength of drug which indicates the drug delivery effect. An excellent transdermal delivery could be obtained and the silver sulfadiazine could be delivered to 200 μm deep in the rat skin when the voltage at 30 V and the frequency at 0.01 Hz were used. Therefore, this chip system could enhance effectively the transdermal delivery and delivery depth.**

Keywords—Transdermal delivery, Electroporation, MEMS, Microscope raman spectrometer

I. INTRODUCTION

The electroporation was the one of the transdermal delivery method, in which the electric field is applied to enhance delivery effect [1-5]. The electroporation was varied with iontophoresis in delivery route [6]. The electroporation was utilized transient electric field to make the skin generate new drug delivery route. The mechanism of electroporation was used high pulse to make the cell membrane generate tiny pore. The cell membrane would generate reversible electric breakdown [7]. These pores were smaller than 10 nm and live time was transient (μsec to sec) that it would make the hydrophile molecule easier passed to cell membrane. The electroporation was used in cell culture generally, genetic transformation and delivery large molecule of drug [8].

The mechanism of transdermal delivery was applied high pulse voltage and made the skin resistance to reduce. It would make the skin barrier to change instantaneously and generate the polarity route in lipid barrier [9]. Therefore, it would reduce the drug delivery limit and make the drug transfer into skin. The large molecule could pass along this route and the cell membrane would recover without electric field. The electroporation research in transdermal delivery was proofed that high and millisecond pulse voltage could make the skin structure to change. The long pulse (100 ms), low voltage (30 V) of drug delivery effect was better than short pulse (1 ms), high voltage (100 V) [10]. The electric pulse voltage and pulse amount would affect the delivery efficiency [11].

The Raman spectrometer could measure the sample arbitrarily by scanning in one point, line and area. The analysis technology of Raman spectrum could analyze organic matter and inorganic matter, scanning the Mannuronic acid and Guluronic acid of alginate [12]. It could analyze the liquid sample that the effect of different concentration to spectrum intensity. And it was discussed the Raman spectrum signal after the sample mixed with gold nanoparticles [13]. The Raman spectrum technique also could analyze the carotenoids and polyacetylenes in the chamomile inflorescence gained on the Raman measurement. In bio-medicine research, the Raman spectrum analytical method was belonged to non-destruction technique. Because it could measure non-invasive and fast, therefore it was usually applied in some research about cell and skin detect. In some researches of cell location, it could find the position of bacterial spores in mixed samples and the low laser power could reduce the cell injury [14]. And it could measure the hydration of hoof membrane and formulation.

After the hoof membrane daubed the drug and measured the spectral intensity of different depth [15]. The purpose of this study was to develop a transdermal delivery chip system for delivering drug into the rat skin. The electroporation chip was utilized MEMS technique to fabricate and used ANSYS software to analyze. The primary object of the chip analysis was knew the electric field of electrode. We put the skin on the chip to do transdermal experiment. Finally, we used the Raman spectrometer to measure the drug within the skin and analyzed the spectral intensity as the rule of transdermal effect.

II. MATERAL & METHOD

A. Design of the Transdermal Delivery Chip

The chip was designed using the AutoCAD® 2008 software, the size of which was shown in fig. 1. In order to decrease the pulse voltage, the chip is designed in the interdigitated electrode.

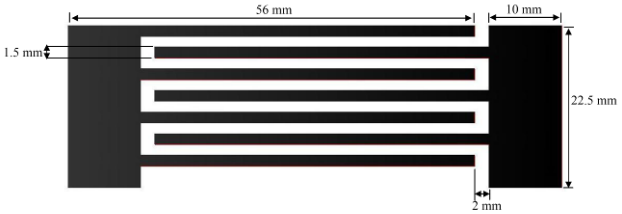

Figure 1. The dimensions of transdermal delivery chip. The chip was designed by using AutoCAD software

Contact author: Y.C. Lin, National Cheng Kung University, Department of Engineering Science, 1 University Road, Tainan 701, Taiwan. Tel: +886-6-276-2395; Fax: +886-6-276-2329; E-mail:* ***yuclin@mail.ncku.edu.tw*

B. Simulation of the Transdermal Delivery Chip

The ANSYS 9.0 software was utilized to analyze the electric field of each electrode gap. We were analyzed the horizontal and perpendicular of chip plane, because the form of electrode was symmetrical that could analyze the region of chip plane. We want to know the distribution and intensity of the voltage and electrical felid, using the voltage variable of element in simulation. PLANE 67 is electrical-thermal-fluid coupled-field. There are voltage variable of temperature and electrical felid in every point. But the thermal produced by electrode is really small to this research influence. We only aim at the chip architecture the electric field distribution to carry on the analysis in fig. 2.

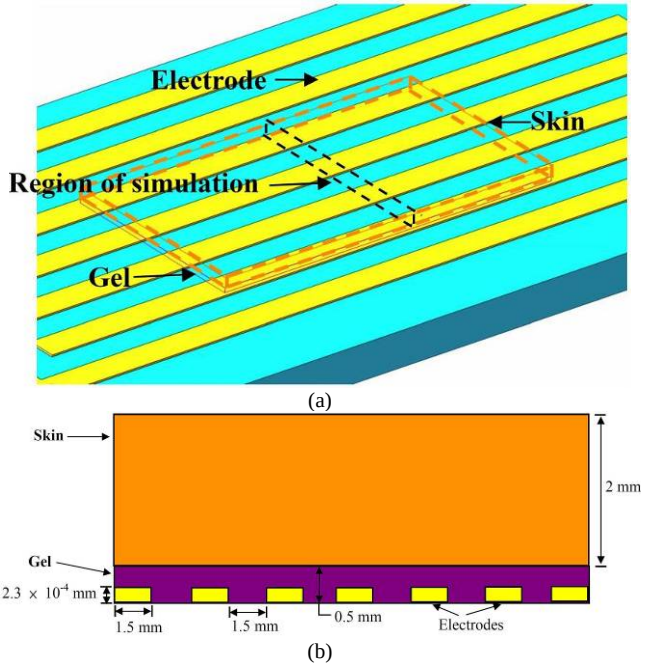

Figure 2. Simulation of chip. (a) Three-dimensional model. (b)The size of simulation area

C. Manufacture of the Electroporation Chip

Figure 3 is the schematic drawing of the transdermal delivery chip which used glass as substrate, Au as electrode, and Cr as adhesive by MEMS fabrication process. Point discharge generated by the interdigitated electrode could enhance the electric field, resulting in the feasibility to reduce the work voltage. It could avoid the risk of thermal injury by reducing the work voltage.

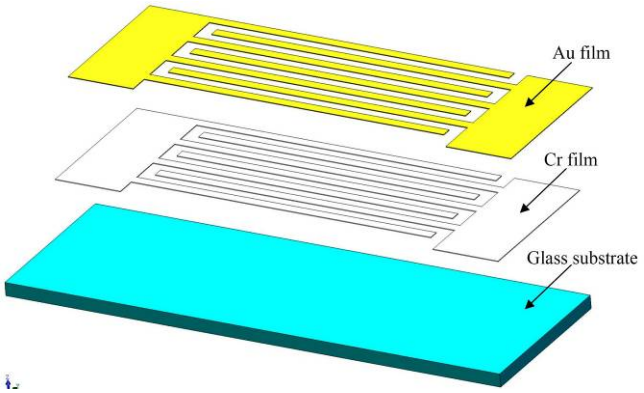

Figure 3. Schematic drawing of the transdermal delivery chip. Au and Cr were evaporated on the glass substrate. The interdigitated electrode array was used to promote the electric field strength and reduce the work voltage

D. Raman Microscope Spectrometer

In this experiment, we used the Raman spectrometer (Renishaw plc 662810 In Via Raman Microscope) to analyze and combined with confocal microscope. We used Renishaw's 785 nm HeNe laser to supply the incident light and utilized the Leica DM/IRB inverted microscope (10 X, 20 X, and 40 X) to focus. After the sample was measured and gained the spectrum, it could use the analysis software of spectrum (WiRE 2.0) to analyze the spectral intensity of sample. Before the analysis of Raman spectrum, all the spectra were needed to erase the cosmic radiation and smoothed by 5th degreed average filtering that used the WiRE 2.0 software.

E. Transdermal Delivery Experiment

Figure 4 was showed that mechanism of transdermal delivery chip system which used electroporation method to delivery the drug into skin. Electric theorem was employed to perform the electroporation with the electric field was generated between the electrode gap and drug were driven into the skin barrier. The electrode would generate point discharge and make the skin barrier create new pathways into the epidermis. The new pathways of the skin would open and recover in a short time during when the electric field was took place. Thus we were used this mechanism to design the transdermal delivery chip system and achieve the goal for enhancing the efficiency of drug delivery.

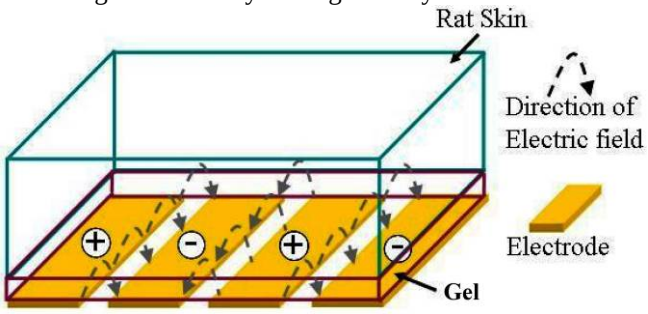

Figure 4. Schematic drawing of the mechanism of transdermal delivery chip system. The electric force was used to drive gel into the skin. The gel permeability was enhanced by increasing the strength of electric fields

F. Experiment procedure

The chip was placed on the PMMA platform which was made by a CO_2 laser micro-machining process. Placed on the platform and was locked by screws, the skin was obtained from the 6-8 weeks old rat. We took the back skin of the rat and stored it in container in the -20°C refrigerator. We were imported three types of pulse voltage (10 V, 20 V, and 30 V) and four types of pulse frequency (1 kHz, 10 Hz, 1 Hz and 0.01 Hz) in fixed experimental time (1 hour). After the experiment was finished, we could pick the skin in gold substrate to measure the spectrum by Raman spectrometer.

III. RESULTS AND DISCUSSION

A. Electric Field Analysis of Chip Structure

We would need to discuss the electric field relation with gap. Figure 5 was the sketch of analysis plane. It was discussed the skin, gel and electrode when it was applied 10 V pulse voltage. We were got the electrode surface (line 3), the bottom of the surface skin between gel surface (line 4) and 0.5 mm a step from bottom of surface skin to top of surface skin (line 8).

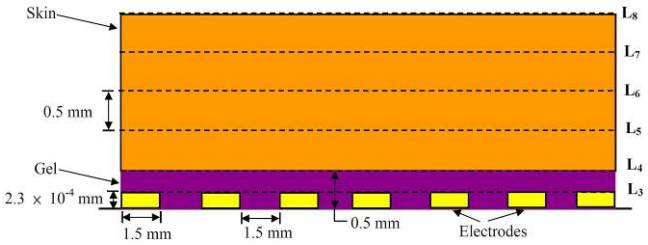

Figure 5. The diagram of analysis chip plane was composed of skin, gel and electrode

Figure 6(a) was showed that had the point discharge obviously in the electrode between gel of the boundary and the maximum electric field was 161.7296 V/cm. And it could find that the gel between the skin of electric field was still remained 386.5993 V/cm in the fig. 7(b). The electrode in the extremity of electric field was higher than the middle electrode. Because the equipotential surface was compact that would make the electric field to increase acutely. The nearly materials would ionize to generate the discharge that it was called electrical discharge. The point discharge was one of the electrical discharges that made the maximum electric field always occur in the end on electrode. The tendency of the point discharge would increase obviously with applied voltage that made the gradient of electric field appear the hollow distribution of the tendency.

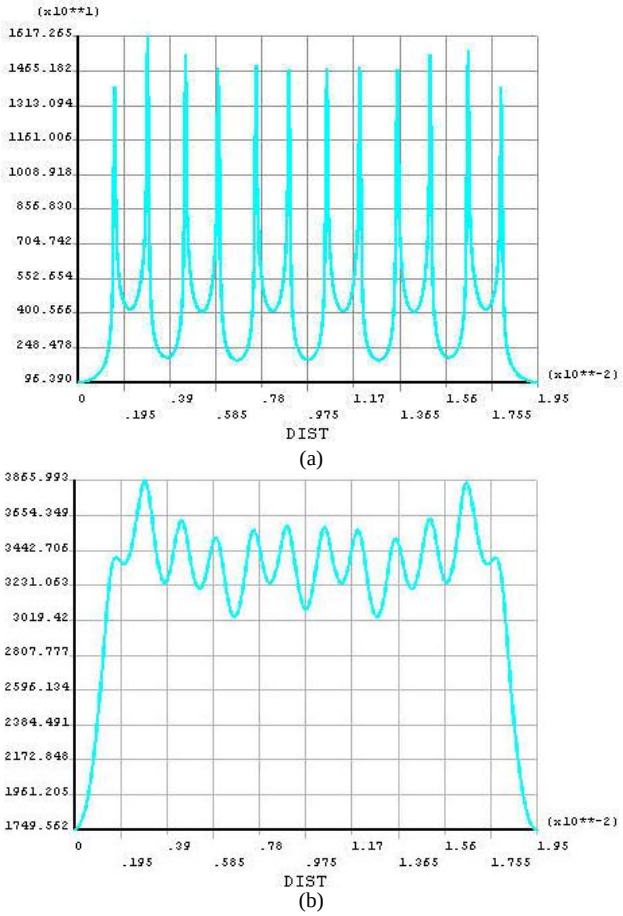

Figure 6. Diagram of the electric field distribution in pulse voltage (10 V). (a) The distribution of electric field (L_3). (b) The distribution of electric field (L_4) was 386.6 V/cm

B. Results of Raman Experiment

We were measured the sample in the same surface skin by taking five points random and averaging from the samples. It would use the average intensity as the basis of delivery effect. Figure 7 could find that the high pulse frequency (1 kHz) of delivery effect was better than low frequency (0.01 Hz) and the maximum delivery depth was approximate 100 μm. From the Fig. 8 and Fig. 9, it could find that the spectral intensity in 20 V and 30 V were obvious decreased separately in 200 μm and 250 μm. So the maximum delivery depth was separately approximated 150 μm and 200 μm in the pulse voltage (20 V and 30 V). And it could find that the maximum spectral intensity was measured in low frequency. Therefore, we were known that the high voltage and low frequency could gain the better drug delivery effect by using this chip system.

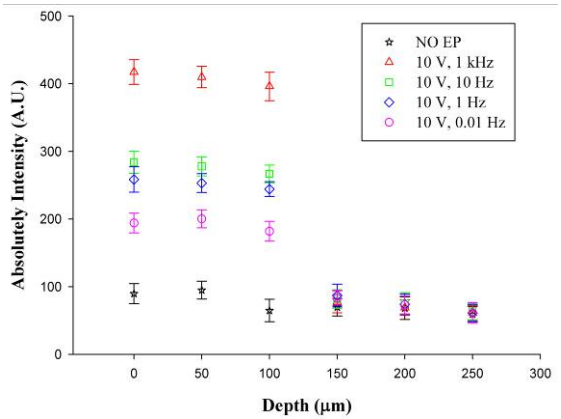

Figure 7. In fixed pulse voltage (10 V), different pulse frequency (1 kHz, 10 Hz, 1 Hz, 0.01 Hz) and experimental time (1 hour)

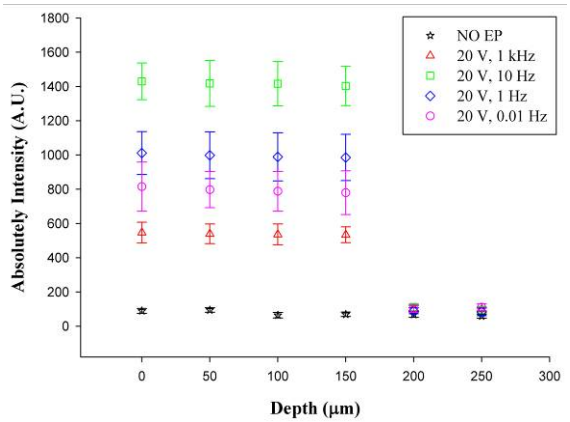

Figure 8. In fixed pulse voltage (10 V), different pulse frequency (1 kHz, 10 Hz, 1 Hz, 0.01 Hz) and experimental time (1 hour)

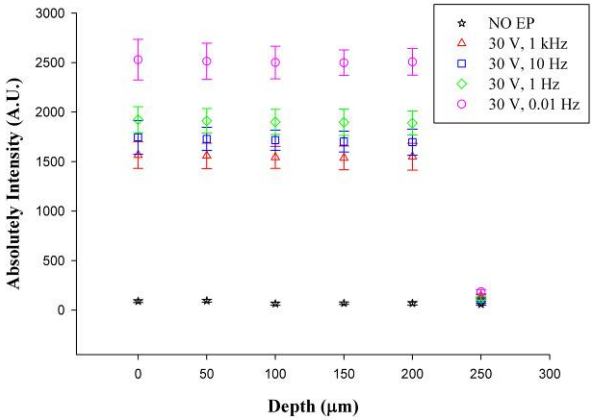

Figure 9. In fixed pulse voltage (10 V), different pulse frequency (1 kHz, 10 Hz, 1 Hz, 0.01 Hz) and experimental time (1 hour)

IV. CONCLUTION

The chip was used the ANSYS software to analyze the electric field. It was designed in the form of interdigitated and fabricated using MEMS technology. This transdermal chip system was successfully delivery the drug into the skin and the delivery effect was better than passive diffusion. It could use the low voltage (10 V) to delivery the drug alike the transdermal effect. We also used the microscope Raman spectrometer to analyze the experimental skin and measured the drug within the skin after the transdermal experiment. We were used the spectral intensity as the basis of transdermal delivery effect. It was found that the high voltage (30 V) and low frequency (0.01 Hz) could gain the better delivery effect and the maximum delivery depth was in 200 μm. Therefore, this transdermal chip system will provide many usages for drug transdermal delivery and target cancer therapies in the future development.

REFERENCES

[1] T. W. Wong, C. H. Chen, C. C. Huang, C. D. Lin and S. W. Hui, "Painless electroporation with a new needle-free microelectrode array to enhance transdermal drug," Journal of Controlled Release, vol. 110,pp. 557-565, 2006.

[2] R. Vanbever, G. Langers, S. Montmayeur and V. Preat, "Transdermal delivery of fentanyl-rapid onset of analgesia using skin electroporation," Journal of Controlled Release, vol. 50, pp. 225-235, 1998.

[3] A. T. Prechtel, N. M. Turza, A. A. Theodoridis, M. Kummer and A. Steinkasserer, "Small interfering RNA (siRNA) delivery into monocyte-derived dendritic cells by electroporation," Journal of Immunological Methods, vol. 311, pp. 139-152, 2006.

[4] Y. L. Zhao, S. N. Murthy, M. H. Manjili, L. J. Guan, A. Sen and S. W. Hui, "Induction of cytotoxic T-lymphocytes by electroporation-enhanced needle-free skin immunization," Vaccine, vol. 24, pp. 1282-1290, 2006.

[5] M. Boudes, S. Pieraut, J. Valmier, P. Carroll and F. Scamps, "Single-cell electroporation of adult sensory neurons for gene screening with RNA interference mechanism," Journal of Neuroscience Methods, vol. 170, pp.204-211, 2008.

[6] Y. Wang, R. Thakur, Q. Fan and B. Michniak, "Transdermal iontophoresis: combination strategies to improve transdermal iontophoretic drug delivery," European Journal of Pharmaceutics and Biopharmaceutics, vol. 60, pp. 179-191, 2005.

[7] S. W. Hui, "Low voltage electroporation of the skin, or is it iontophoresis," Biophysical Society, vol. 74, pp. 679-680, 1998.

[8] D. M. Soden, J. O. Larkin, C. G. Collins, M. Tangney, S. Aarons, J. Piggott, A. Morrissey, C. Dunne and G. C. O'Sullivan, "Successful application of targeted electrochemotherapy using novel flexible electrodes and low dose bleomycin to solid tumours," Cancer Letters, vol. 232, pp. 300-310, 2006.

[9] L. Lauer, S. Ingebrandt, M. Scholl and A. Offenhausser, "Aligned microcontact printing of biomolecules on microelectronic device surfaces," IEEE Transaction on Biomedical Engineering, vol. 48, pp. 838-842, 2002.

[10] A. R. Denet, R. Vanbever and V. Pre'at, "Skin electroporation for transdermal and topical delivery," Advanced Drug Delivery Reviews, vol. 56, pp. 659-674, 2004.

[11] R. Vanbever, E. L. Boulenge and V. Pre'at, "Transdermal delivery of fentanyl by electroporation. I. influence of electrical factors," Pharmaceutical Research, vol. 13, pp. 559-565, 1996.

[12] T. Salomonsen, H. M. Jensen, D. Stenbaek and S. B. Engelsen, "Chemometric prediction of alginate monomer composition a comparative spectroscopic study using IR, Raman, NIR and NMR," Carbohydrate Polymers, vol. 72, pp. 730-739, 2008.

[13] T. L. Wang, H. K. Chiang and H. H. Lu, "Semi-quantitative surface enhanced Raman scattering spectroscopic creatinine measurement in human urine samples," Optical and Quantum Electronics, vol. 37, pp. 1415-1422, 2005.

[14] J. W. Chan, A. P. Esposito, C. E. Talley, C. W. Hollars, S. M. Lane, and T. Huser, "Reagentless identification of single bacterial spores in aqueous solution by confocal laser tweezers Raman spectroscopy," Analytical Chemistry, vol. 76(3), pp. 599-603, 2004.

[15] B. Gotter, W. Faubel and R. H. H. Neubert, "Optical methods for measurement of skin penetration," Skin Pharmacology and Physiology, vol. 21, pp. 156-165, 2008.

Synthesis of Mono-Dispersion Mesoporous Silica Vesicles and Spheres in 50–200 nm by Using Cationic-Anionic Binary Surfactant as Mesostructural Template

Ying-Min Gu[1], Mei-Yun Tsai[1], Yi-Hua Tsai[1], Guan-Tsen Liu[1], Kai-Wen Chang[1], Hong-Ping Lin[1,2]* Chih-Yuan Tang[3] Ching-Yen Lin[3]

[1] *Department of Chemistry, National Cheng Kung University, Tainan, Taiwan 701*

[2] *Center for Micro/Nano Science and Technology, National Cheng Kung University, Tainan, Taiwan 106.*

[3] *Instrumentation Center, National Taiwan University, Taipei, Taiwan*

e-mail: hplin@mail.ncku.edu.tw ; TEL: +886-6-2757575 ext. 65342

***Abstract* — The mesoporous silica vesicles and spheres with high surface area, large pore size and pore volume have been conveniently synthesized by using cationic-anionic binary surfactant system as template. The size of the mesoporous silica vesicles and sphere is uniform and ranged from 50–200 nm. In addition, these mesoporous silica nanoparticles possess the autofluoresce. The morphology and mesostructure are dependent on the pH value of the reaction solution.**

Keywords — ***Mesoporous silica, Vesicles, Spheres, Surfactant, Organic template***

I. INTRODUCTION

Controlled-release systems increase the overall therapeutic efficiency of the drug by maintaining at a proper concentration in the body within the optimum therapeutic range but under the toxicity threshold [1]. Up to now, a wide range of particulate-delivery systems have been designed [2,3]. The optimal particles size of the drug carriers depends both on the route of administration and the targeted organ or cells. Organic liposomes and micelles suffer from essentially poor chemical stability that limits both their route of administration and shelf life [1]. In contrast to organic carries, inorganic porous materials have large pore volume, high chemical stability and modifiable and hydrophilic surface should be considered as the new drug-delivery system. Therefore, synthesis of novel nanomaterials with well-tailored properties is a major challenge in biomedical applications for drug delivery carriers, diagnostic agents, sensing probes, and tracking labels [4,5].

In particular, biocompatible silica nanoparticles have been extensively used due to easy formation and a convenient surface modification procedure. Because of the monodispersity, large surface area, and high drug loading efficiency, and hollow nanostructures, mesoporous silicas in nanometer size have been prepared and tested as a drug delivery system. Moreover, the silica materials are biologically nontoxic and high chemically stabile under conditions where leaching and oxidation is unfeasible. In the previous literatures, it was discovered that surface-functionalized mesoporous silica nanoparticles materials can be readily internalized by animal and plant cells without posing any cytotoxicity issue in vitro. Therefore, these new silica materials render the possibility of designing a new generation of drug/gene delivery systems, and imaging applications.

It is known that aqueous mixtures of oppositely charged single-tailed cationic and anionic surfactants produce a very rich variety of aggregate mesostructures (e.g., spherical and vesicles) even at high dilution that can serve as organic template for the synthesis of the mesoporous silica in a desired dimension and morphologies [6]. With a well control on the silica-surfactant assembling kinetics, the mesoporous silica in various mesostructures and morphologies should be conveniently prepared [7–9]. Herein, we have used a tetradecyltrimethylammonium bromide (C_{14}TMAB)-sodium dodecyl sulfate (SDS) binary surfactant system as the organic template to prepare the mesoporous silica spheres and vesicles in tens to few hundreds nanometer size. The diameter of the mesoporous silica vesicles and spheres is uniform and the deviation of the particle size is less than 15 %.

II. SYNTHESIS

A. Materials

Silica source is tetraethyl orthosilicate (TEOS, Acrôs). The templating agents are tetradecyltrimethylammonium bromide (C_{14}TMAB) and sodium dodecyl sulfate (SDS) purchased from Acrôs. The sulfuric acid (H_2SO_4) is from Acrôs. All commercial chemicals were used directly without further purification.

B. Synthesis of mesoporous silica spheres and vesicles

The typical synthetic procedure for the mesoporous silica vesicles and spheres is as following: (0.69–1.15) g of C_{14}TMAB and 0.30 g of SDS (i.e. SDS/ C_{14}TMAB molar ratio ≈ 0.3 and 0.5) were was dissolved in 200.0 g of water to form a clear solution at 40°C. Then, the pH value of the surfactant solution was adjusted to a proper pH value. The mesoporous silica vesicles are prepared SDS/ C_{14}TMAB molar ratio ≈ 0.3 and the mesoporous silica spheres are synthesized at SDS/ C_{14}TMAB molar ratio ≈ 0.5. After that, 6.73 g of tetraethyl orthosilicate (TEOS) as silica source was added into the catanionic surfactant solution. After stirring for 1 h, that silica-surfactant solution was kept statically at 40 °C for 3 days. Centrifugation, drying and calcination at 550 °C or

Identify applicable sponsor/s here. *This project was funded by the Chinese National 863 Plan (Project code: 88543) and the US NSF (Project code: AAT543).*

Contact author: for fabrication aspects of this project please contact* ***yctai@sense.caltech.edu.*

#Contact author: for microrobotic aspects of this project please contact ***lnsun@hit.cas.cn.***

450°C for 6h (temperature ramp of 1.5°C per minute) in air gave the surfactant-free mesoporous silica samples.

C. Characterization

Powder X-ray diffraction (XRD) patterns were taken on XRD-6000, SHIMATSU, Japan (CuKα, λ = 0.1541 nm). The N_2 adsorption-desorption isotherms were obtained at 77 K on a Micromeritics ASAP 2010 apparatus. Before the analysis, the sample was outgassed at 200 °C for about 6 h in 10^{-3} torr. The scanning electron microscopy (SEM) and transmission electron micrographs (TEM) were taken on an S-800 (Hitachi) operated at an accelerating voltage of 20 keV and an H-7500 (Hitachi) operated at 100 keV, respectively.

III. RESULTS AND DISCUSSION

A.. Mesoporous silica spheres

Figure 1A show the representative TEM image of the mesoporous silica spheres synthesized at SDS/C_{14}TMAB molar ratio ≈ 0.3. It is clearly seen that the spheres sizes are close to 100 nm, and the particles are distinctly separated. With a higher magnification observation (Figure 2B), we found that the mesoporous silica sphere possess multilayered mesostructure, and the spheres demonstrate a concentric mesostructure. After countering more than 100 particles, the particles size of the mesoporous silica spheres are estimated about 81 ± 12 nm. The deviation of the particle size is less than 15 %.

At low-angle range, the mesoporous silica sphere exhibits two XRD (100) and (200) diffraction peaks that represent the lamellar mesostructure (Figure 1C). The XRD examination is parallel to that of the TEM observation. Different from the individual cationic or anionic surfactant, the cationic-anionic binary surfactant of relatively large hydrophobicity can have a high tendency to form the lamellar mesophase as the template even at low concentration for the formation of the nanospheres silica [6]. Analyzing the N_2 adsorption-desorption isotherms of the calcined silica sample, these mesoporous silica spheres demonstrate the type IV isotherms (Figure 1D), and have capillary condensations at P/P_0 around 0.4–0.5. The average pore size calculated by BJH method is about 5.0–6.0 nm, BET surface is about 500 m^2g^{-1} and pore volume lager than 1.5 cm^3g^{-1}. The existence of an additional capillary condensation at P/P0 ≈ 0.95–1.0, indicting by an arrow, is ascribed to the external adsorption by the large pores (> 20.0 nm) generated form the package of the nanospheres. These results indicate that the mesoporous silica nanospheres in uniform diameter can be conveniently prepared by using the cationic-anionic binary surfactants as organic templates. The mesostructure and pore can be preserved after high-temperature calcination for the removal of surfactant [10–12].

B. Mesoporous silica vesicles

As increasing of the SDS/C_{14}TMAB molar ratio, the charge neutralization extent increases, and the double-layer content in the resulting micelles raises. With the highly hydrophobic double tail, the cationic-anionic micelles should avoid a direct contact between the hydrophobic tail and water [7,8]. Thus, the cationic-anionic surfactant tends to tend form vesicles. Therefore, at the SDS/C_{14}TMAB molar ratio of around 0.5, the mesoporous silica vesicles were synthesized (Figure 2A). One can clearly see the hollow interiors. At higher magnification (Figure 2B), the concentric mesostructure of the silica vesicles were revealed and the layer distance is estimated to around 4.0–5.0 nm. Because the layer number of the lamellar mesostructure is less than 6, the hollow volume of the mesoporous silica vesicles is large. After countering more than 100 particles, the particles size of the vesicles are approximated about 75 ± 10 nm. The particle size is uniform and the deviation is less than 15 %.

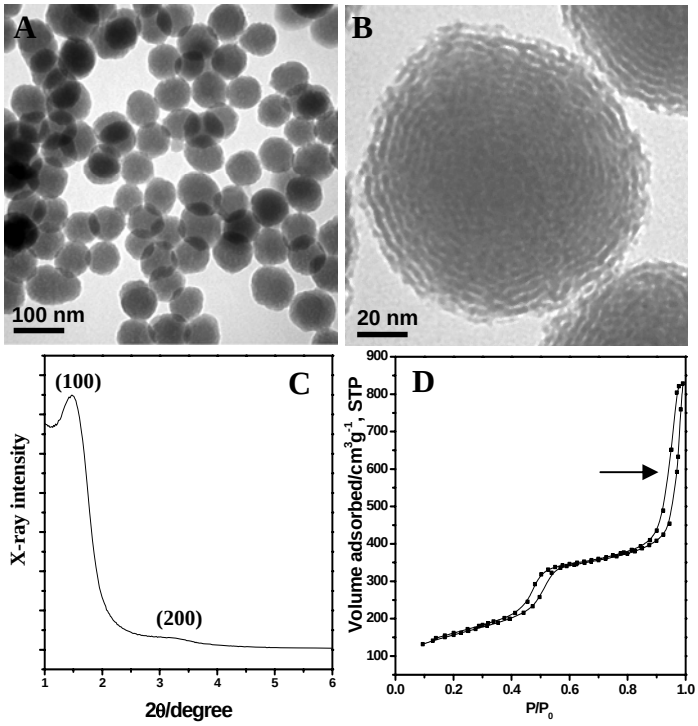

Figure 1. (A); (B) TEM images at different magnifications. (C) Low-angle XRD pattern; (D) N_2 asorption-desorption isotherm of the mesoporous silica spheres templated with C_{14}TMAB-SDS binary surfactant (SDS/C_{14}TMAB molar ratio ≈ 0.3).

From the low-angle XRD pattern, it was found that the mesoporous silica vesicles demonstrate only one broad diffraction peak (the XRD spectrum was not shown here). This is because that the diffraction domain (few layers) in the mesoporous silica vesicles is too small to show high-order diffraction [13,14]. Analyzing the N_2 adsorption-desorption isotherms of the calcined silica sample, these mesoporous silica spheres demonstrate the type IV isotherms (Figure 2C), and have capillary condensations at P/P_0 around 0.5–0.6. The average pore size calculated by BJH method is about 5.0 nm, BET surface is about 458 m^2g^{-1}, and pore volume lager than 1.2 cm^3g^{-1}. The presence of another capillary condensation occurring at P/P_0 ≈ 0.90–1.0, is ascribed to the external adsorption by the hollow interiors of the mesoporous silica

Identify applicable sponsor/s here. *This project was funded by the Chinese National 863 Plan (Project code: 88543) and the US NSF (Project code: AAT543).*

Contact author: for fabrication aspects of this project please contact* ***yctai@sense.caltech.edu.*

#Contact author: for microrobotic aspects of this project please contact ***lnsun@hit.cas.cn.***

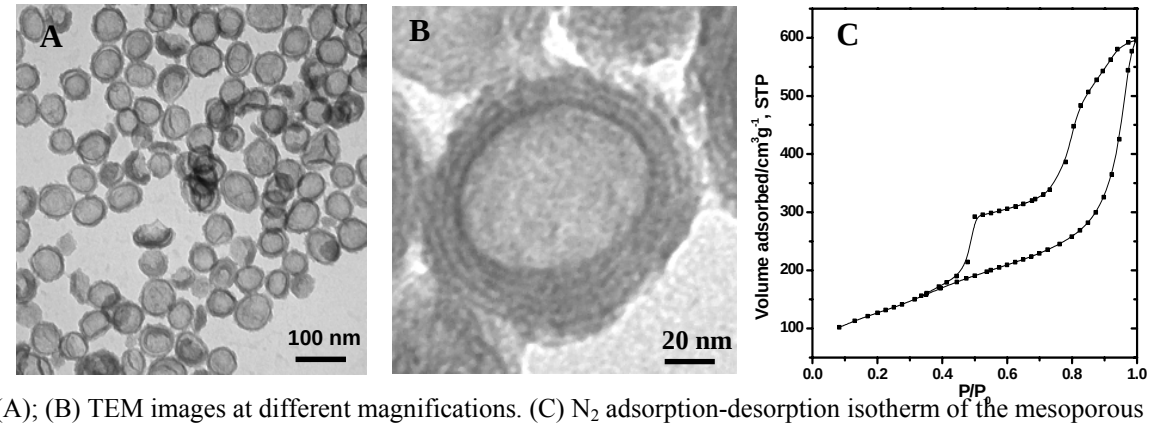

Figure 2. (A); (B) TEM images at different magnifications. (C) N_2 adsorption-desorption isotherm of the mesoporous silica spheres templated with C_{14}TMAB-SDS binary surfactant (SDS/C_{14}TMAB molar ratio ≈ 0.5).

vesicles (pore size > 20.0 nm). According to these examination data, the mesoporous silica vesicles with small particles size deviation can also be prepared just by changing the anionic/cationic ratios. As the mesoporous silica spheres, the thermal stability of the silica vesicles is high. The multilayer-mesostructure can be maintained after 550°C-calcination to remove the surfactant.

In brief, using the cationic-anionic binary surfactant system as the organic template provides a new method to prepare the mesoporous silica spheres and vesicles in uniform size. In addition, the particles size is located within the range of 50–300 nm, which can be considered as the drug delivery used in the blood stream. Because of the spherical geometry, the mutual contact area is smallest between the mesoporous silica spheres and vesicles. Thus, the aggregation extent of the nanometer-sized particles is low even during filtration, drying and calcination procedures. These silica spheres and vesicles can be easily dispersed in the solution.

In additional to using SDS/C_{14}TMAB molar ratio ≈ 0.3 and 0.5, other cationic/anionic surfactant compositions within this range have also been used to synthesize the mesoporous silica samples. We found the mesoporous silica spheres and vesicles with diameter of 100–200 nm can be obtained from the same synthetic procedures as well. As the SDS/C_{14}TMAB molar ratio toward to 0.5, the percentage of the vesicles increases. Because there are many experimental factors affecting the self-assembling kinetics of the surfactant and silica species, the particle size of the mesoporous silica spheres and vesicles can be tuned by changing the pH value, water content, TEOS content and reaction temperature. The particle size of the resulted mesoporous silicas is ranging within 50–200 nm. These systematic controls in the morphologies and particles size will be further investigated in future.

C. Autofluorescence of the mesoporous silicas

In addition to large pore size and volume, the amorphous silica wall of the mesoporous silica vesicles and spheres should possess structural defects (e.g. oxygen vacancies) after a proper calcination process. In the presence of defects, the mesoporous silica vesicles could possess autofluorescence After a 450°C-calcinatioin, the mesoporous silica vesicles show the autofluoresce (Figure 3). The presence of the autofluoresce could be ascribed to the atomic structural defects in the silica wall. When calcination at temperature higher than 500°C the silica condensation extent is almost to complete. The intensity of the autofluorescence from defects decays much. Therefore, with a well control on the surfactant composition and calcination temperature, the mesoporous silica spheres or vesicles in uniform size with autofluoresce can be feasibly prepared. The existence of the autofluorescence can allow the tracking of the silica nanoparticles in real time by luminescence without any treatment of fixing or staining of the specimens.

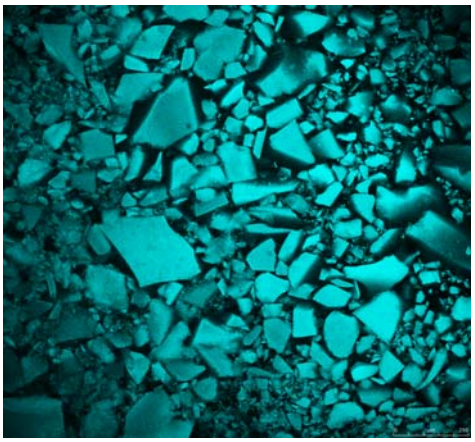

Figure 3 Confocal micrograph of the mesoporous silica vesicles upon excitation at 405 nm.

IV. Conclusion:

Because the surfactant-silica assembly is a form of self-assembly with covalent modification, the morphology and particle size are particularly dependent on factors related to reaction kinetics and micellar behavior, such as the reaction temperature, water content, and pH value of the silicas solution [10]. Thus the advancements in morphology control

and surface functionalization of mesoporous silica nanoparticles have enhanced the biocompatibility or even biodigestibility of these materials with high surface areas and pore volumes as carrier of medicines and proteins. In addition, the previous literatures reported that the surface-functionalized mesoporous silica nanoparticles can be readily internalized by animal and plant cells without posing any cytotoxicity issue in vitro [15–17]. These new developments render the possibility of designing a new generation of drug/gene delivery systems and biosensors for intracellular controlled release and imaging applications.

ACKNOWLEDGMENT

This research is financially supported by National Science Council of Taiwan (NSC95-2113-M-006-011-MY3 and NSC95-2323-B-006-008) and Taiwan Textile Research Institute and Landmark Project from National Cheng Kung University (R017).

REFERENCES

[1] W. Zhao H. Chen , Y. Li, L. Li, M. Lang, and J. Shi, "Uniform Rattle-type Hollow Magnetic Mesoporous Spheres as Drug Delivery Carriers and their Sustained-Release Property," Adv. Funct. Mater, vol.18, pp. 2780–2788, 2008.

[2] N. K. Mal, M. Fujiwara and Y. Tanaka, "Photocontrolled reversible release of guest molecules from coumarinmodified mesoporous silica" Nature, vol 421, January 2003.

[3] N. K. Mal, M. Fujiwara, Y. Tanaka, T. Taguchi, and M. Matsukata, "Photo-Switched Storage and Release of Guest Molecules in the Pore Void of Coumarin-Modified MCM-41" Chem. Mater, vol.15, pp.3385-3394.

[4] Y. Zhu, J. Shi, W. Shen, X. Dong, J. Feng, M. Ruan, and Y. Li, "Stimuli-Responsive Controlled Drug Release from a Hollow Mesoporous Silica Sphere/Polyelectrolyte Multilayer Core–Shell Structure" Angew. Chem. Int. Ed., vol. 44, pp.5083 –5087.

[5] X. Li, L. Zhang, X. Dong, J. Liang, J. Shi, "Preparation of mesoporous calcium doped silica spheres with narrow size dispersion and their drug loading and degradation behavior" Microporous and Mesoporous Materials, vol.102, pp. 151–158, January 2007.

[6] D. Lootens, C. Vautrin, H. Van Damme and T. Zemb, "Facetted hollow silica vesicles made by templating catanionic surfactant vesicles," J. Mater. Chem., vol. 13, pp.2072–2074, July 2003.

[7] S. Pevzner, O. Regev, A. Lind, and M. Linde´n, "Evidence for Vesicle Formation during the Synthesis of Catanionic Templated Mesoscopically Ordered Silica as Studied by Cryo-TEM" J. Am. Chem. Soc., vol. 125, pp.652-653 October 14, 2002.

[8] A. Lind, B. Spliethoff, and M. Linde´n, "Unusual, Vesicle-like Patterned, Mesoscopically Ordered Silica," Chem. Mater, vol. 15, pp. 813-818, 2003.

[9] H.-P. Hentze, S. R. Raghavan, C. A. McKelvey, and E. W. Kaler, "Silica Hollow Spheres by Templating of Catanionic Vesicles," Langmuir, vol. 19 ,pp. 1069-1074, 2003.

[10] R. K. Iler, "The Chemistry of Silica: Solubility, Polymerization, Colloid and Surface Properties, and Biochemistry," Wiley, New York (1979).

[11] C. T. Kresge, M. E. Leonowicz, W. J. Roth, J. C. Vartuli and J. S.Beck"Ordered mesoporous molecular sieves synthesized by a liquid-crystal template mechanism" Nature vol. 359, pp. 710 - 712 , October 1992.

[12] D. Zhao, J. Feng, Q. Huo, N. Melosh, G. H. Fredrickson, B. F. Chmelka, and G. D. Stucky "Triblock Copolymer Syntheses of Mesoporous Silica with Periodic 50 to 300 Angstrom Pores," Science, Vol. 279, no. 5350, pp. 548 – 552, January 1998.

[13] J. Y. Ying, C. P. Mehnex, and M. S. Wong, "Synthesis and Applications of Supramolecular-Templated Mesoporous Materials," Angew. Chem. Int. , vol. 38, pp. 56-57. 1999.

[14] H.-P. Lin and C.-Y. Mou, "Structural and morphological control of cationic surfactant-templated mesoporous silica," Acc. Chem. Res, Vol. 35 pp. 927-935 , November 2002.

[15] I. Slowing, B. G. Trewyn, S. Giri,, and V. S.-Y Lin, "Mesoporous silica nanoparticles for drug delivery and biosensing applications" Adv. Func. Mater., vol. 17, pp. 1225-1236 , May 21 2007

[16] D. R. Radu, C.-Y. Lai, K. Jeftinija, E. W. Rowe, S. Jeftinija, and V. S. Y. Lin, "A Polyamidoamine Dendrimer-Capped Mesoporous Silica Nanosphere-Based Gene Transfection Reagent," J. Am. Chem. Soc., vol. 126 , pp. 13216-13217, Oct 20, 2004.

[17] I. Slowing, B. G. Trewyn, and V. S.-Y. Lin*,"Effect of Surface Functionalization of MCM-41-Type Mesoporous Silica Nanoparticles on the Endocytosis by Human Cancer Cells," J. Am. Chem. Soc. , vol.128 pp.14792-14793 . Nov 22 2006.

Evolution of Microstructure and Nanomechanical Behavior of Diamond-Like Carbon Films at High Temperature Annealing

B. H. Wu[1,*], C. K. Chung[1, 2] and C. W. Lai[2]

[1] *Center for Micro/Nano Science and Technology, National Cheng Kung University, Tainan, Taiwan*
[2] *Department of Mechanical Engineering, National Cheng Kung University, Tainan, Taiwan*
E-mail: kennywu@mail.mina.ncku.edu.tw, Tel: +886-6-2757575-31385, Fax: +886-6-2080103

Abstract — **The microstructure and nanomechanical behavior of diamond like carbon (DLC) films has been investigated at high temperature annealing. The DLC films with 250 nm thickness were deposited on the crystalline silicon (c-Si) substrate using ultra-high-vacuum ion beam sputtering and post thermal annealing at high temperature up to 900 °C for 0.5-1.5 hours. Raman spectra showed that the as-deposited DLC film contained tetrahedral amorphous carbon (ta-C) state and presence of increased sp^2 bonds after annealing at 900 °C. GIXRD spectra obtained for the DLC films indicated the absence of diffraction peaks at room temperature (RT) and varied vacuum annealing conditions. It indicates that the above DLC films are still amorphous at high thermal stability despite the change of bonding behaviour from primary sp^3 to more sp^2 bonding. The nanohardness and elastic modulus of the DLC films measured by continuous stiffness measurement technique in the nanoindentation decreased significantly from 29.6 and 351.2 GPa at RT to 17.5 and 150 GPa at 900 °C, respectively which has been attributed to the graphitization of DLC films at high temperature.**

Keywords —DLC; thermal stability; nanoindentation; ultra-high-vacuum ion beam sputtering.

I. INTRODUCTION

Microstructure and nanomechanical behavior impacts the reliability of microelectromechanical systems/ nanoelectro-mechanical systems (MEMS/NEMS) applications. It is essential to study the microstructure and nanomechanical properties of the materials that are commonly used in high temperature applications. The thermal stability of DLC films is a major problem in achieving high temperature applications. It is required that DLC films should endure at least up to 500 °C or more for the high temperature coating materials applied to molds and forming industries [1]. DLC thin films exhibits unique properties such as high nanohardness, surface smoothness, low friction coefficient and high wear resistance [2–3]. Many studies have been carried out to understand the high temperature behavior of DLC films, most of the studies have dealt with their thermal stability in a vacuum or inert gas conditions [1, 4–5]. In this paper, another technique of ultrahigh vacuum ion beam sputtering (UHV IBS) was used to prepare of DLC film on the single crystalline Si substrate using pure target of C at a base pressure of 10^{-7}–10^{-8} Pa. In comparison with films deposited by other PVD or CVD techniques, the oxygen and hydrogen contamination in UHV IBS is expected to be very low.

The nanohardness and thermal stability of DLC films are two important issues in the application of wear and cutting, and are affected by the internal stress and the amount of sp^3 bonding [6] in the films. In view of practical applications for MEMS/NEMS, it should be took into account that the micro/nano-scaled DLC thin films will be subjected to various temperatures, and they must cause considerable influence on DLC microstructures that contribute to properties of DLC. In the present study, we investigate the microstructure and nanomechanical behavior of DLC films at high temperature annealing up to 900 °C.

II. EXPERIMENTAL DETAILS

The diamond-like carbon films with 250 nm thickness were deposited onto single crystalline Si(100) substrates at room temperature (RT) using targets of C (99.999% purity) in the ultra high vacuum ion beam sputtering (UHV-IBS) system (IBS-2000, ULVAC, Japan) with an electron cyclotron resonance (ECR) microwave plasma beam source. The deposition rates of DLC thin film was about 1.3 nm/ min. It was calculated from film thickness divided by deposition time. The flow rate of Ar process gas was fixed at 8 sccm (standard cubic centimeter per minute). The ion beam with output current of about 100 mA was generated and accelerated by external voltage of 1.0-2.0 kV, current of 20-23.5 mA, and analog/digital voltage of 0.5-1.0 kV, current of 1.2-1.8 mA. The base pressure and the working pressure during deposition were about 10^{-7}-10^{-8} Pa and 4.5 x 10^{-2} Pa, respectively. The substrate was rotated at 10 rpm (revolution per minute) to improve the deposition uniformity. The distance between the substrate and the target was about 115 mm. The related deposition conditions of the DLC films are listed in table 1. The post high vacuum annealing was performed at 10^{-4} Pa at temperatures of 900 ºC for 0.5- 1.5 hours to study the microstructure and nanomechanical behavior of DLC films at high temperature annealing.

The reaction and bonding behavior of DLC films was characterized by Raman spectroscopy (Labram HR, France) with high sensitivity for carbon and its compound in the variation of graphite peak (G-peak), disorder-induced peak (D-peak) at specific wavenumber shifts. The phase formation of DLC films was identified by grazing incidence X-ray

**Corresponding author:* Tel: +886-6-2757575-31385,
Fax: +886-6-2080103.
E-mail: kennywu@mail.mina.ncku.edu.tw

diffractometer (GIXRD, RIGAKU-D/MAX2500, Japan) using Cu Kα radiation of 0.15418 nm with a scanning 2θ angle of 20-80°. The nanomechanical properties of the films were investigated using a MTS Nano Indenter® with continuous stiffness measurement (CSM) technique in XP mode and a high resolution DCM (dynamical contact module) head, and using a Berkovich indenter. A frequency of 45 Hz was used to avoid the sensitivity to thermal drift [7] and the loading resolution was 50 nN. The loading process was controlled by a constant strain rate of 0.05 s^{-1}. Six indentations were done in each sample and averaged for the results with a deviation. Nanohardness is defined as the indentation load divided by the projected contact area of the indentation. It is the mean pressure under the indenter [8]:

$$H = \frac{P_{\max}}{A} \quad \text{.....(1)}$$

where P_{max} is the maximum applied force and obtained directly from the force-displacement curve; A is the projected contact area of indenter tip with the material. A geometry independent relation involving contact stiffness, contact area, and reduced elastic modulus can be derived by Sneddon [9] as follows:

$$S = 2\beta\sqrt{\frac{A}{\pi}}E_r \quad \text{.....(2)}$$

where β is a constant which depends on the geometry of the indenter (β = 1.034 for a Berkovich indenter), and E_r is the reduced elastic modulus which accounts for the fact that elastic deformation occurs in both the sample and the indenter. E_r is given by [8]

$$\frac{1}{E_r} = \frac{1-\upsilon_f^{\,2}}{E_f} + \frac{1-\upsilon_{id}^{\,2}}{E_{id}} \quad \text{.....(3)}$$

where E and υ represent the elastic modulus and Poisson ratio, respectively, and the subscript f and id represent the film and the indenter, respectively. The indenter properties used in this study's calculations are E_{id}= 1141 GPa and υ_{id}= 0.07 [8], assuming that υ_f= 0.25. The relationship between microstructure and nanomechanical properties of DLC films at RT and high temperature were investigated in this study.

III. CURRENT RESULTS

Figs. 1(a)- (d) show the Raman spectra of the as-deposited DLC films on the c-Si substrate and annealed at 900 °C for 0.5-1.5 hours, respectively. In the region of Raman shift wavenumbers of 1200 to 1800 cm^{-1}, there is a broad asymmetric scattering band, which is a characteristic of the DLC film. The position of the G-peak is at about 1580-1600 cm^{-1} with an integrated intensity I_G while a D-peak is at about 1350 cm^{-1} with an integrated intensity I_D [10, 11]. In the result of our fabricated DLC films, the position of G-peak is at about 1560-1580 cm^{-1} and that of D-peak is at about 1380-1410 cm^{-1}. The integrated intensity ratio (I_D / I_G) in the conventional DLC films can be correlated with the trend of more sp^2 or sp^3 bonding of amorphous carbon (a-C). The higher the I_D / I_G is, the more the sp^2 bonding . The Raman curve in Fig. 1(a) reveals that the as-deposited DLC film is in a tetrahedral amorphous carbon (ta-C) state [12]. It is found that the ratio of integrated intensity ratio I_D/I_G increases with the annealing time i.e. the DLC film with I_D / I_G of 0.90 at RT while annealing temperature achieved 900 °C with I_D / I_G of 1.48 for 0.5 hours increases to about 1.66 for 1.5 hours. In addition, the G-peak position also shifts slightly to higher wavenumbers from RT to the annealing temperature of 900 °C i.e. the DLC film with a Raman shift wavenumber of 1559 cm^{-1} at RT increases to about 1575 cm^{-1} at 900 °C. It indicates that the transition of C-C bonding with more sp^3 into sp^2 bonds in the a-C film at high temperature annealing [13].

Figs. 2 (a)- (d) show the GIXRD spectra of the DLC films deposited on c-Si substrates at RT and when annealed at 900 °C for 0.5-1.5 hours, respectively. There is no diffracted peak from the DLC films at RT and varied vacuum annealing conditions. It indicates that the above DLC films are amorphous which is in agreement with the Raman result. Figs. 3(a)- (b) show the nanoindentation measured hardness and elastic modulus of the DLC films deposited at RT and annealed at varied vacuum conditions as a function of depth. The hardness of DLC films decreases significantly from 29.6 at RT to about 17.5 GPa at 900 °C with the increasing annealing time and its elastic modulus also decrease from 351.2 to about 150 GPa. It is attributed to the graphitization of DLC film at high temperature together with primary sp^3 bonding to a-C state with more sp^2 (or sp^2-sp^3) bonding and increased I_D/I_G ratio as shown in Fig. 1.

The CSM and a high resolution DCM head in the nanoindentation was applied to measure the nanohardness and elastic modulus of the films. The relevant components of the tip measurement setup in CSM dynamic model of the MTS nanoindentation system include the tip attached to the indenter column with the mass *m*, support springs to the indenter frame with spring constant K_s, capacitive displacement gauge with damping constant D_i, load application coil/ magnet to control the force and the load frame with the stiffness K_f, which are the core of the indentation system for the sample testing. The contact stiffness (S) of the sample can be alternatively measured during the loading step of an indentation test. In the CSM dynamic model, the equivalent damping D contains the effects contributed from the damping of the sample (D_s) and the damping of the displacement gauge (D_i) during contact. Both of the measured stiffness S and the damping coefficient D_s of the sample can be expressed in the following equations (4) and (5) [8, 14]:

$$S = \left[\frac{1}{F_0 z_0^{-1}\cos\phi - (K_s - m\omega^2)} - K_f^{-1}\right]^{-1} \quad \text{.....(4)}$$

and

$$D_s\omega = F_0 z_0^{-1}\sin\phi - D_i\omega \quad \text{.....(5)}$$

where z_0, ϕ and ω represent the displacement amplitude, phase angle between the force and displacement, and the excitation frequency of the system, respectively. Since the parameters K_f , *m*, K_s, and D_i of the system are known, the parameters *S* and $D_s\omega$ can be determined under an applied

harmonic excitation $F_0 \sin\phi$. The reduced elastic modulus E_r and elastic modulus E of the sample will be calculated from the measured stiffness S by equations (2) and (3), respectively. Figs. 3(a)- (b) show the nanoindentation measured hardness and elastic modulus of the DLC films deposited at RT and annealed at varied vacuum conditions as a function of depth. Table 3 lists the highest values of hardness and modulus at RT and annealed at varied vacuum conditions. The hardness of DLC films decreases significantly from 29.6 at RT to about 17.5 GPa at 900 °C with the increasing annealing time and its elastic modulus also decrease from 351.2 to about 150 GPa. It is attributed to the graphitization of DLC film at high temperature together with primary sp^3 bonding to a-C state with more sp^2 (or sp^2-sp^3) bonding and increased I_D/I_G ratio as shown in Fig. 1 and table 2.

IV. CONCLUSION

The DLC films were prepared by UHV-IBS at RT and post thermal annealing at high temperature up to 900 °C for 0.5-1.5 hours. Different characterization methods, Raman, GIXRD and nanoindentation are used to investigate the bonding, phase identification and nanomechanical properties of DLC films. The results reveal that DLC films are amorphous at RT and 900 °C annealing while the increased sp^2 bonding is detected while annealing at 900 °C. The nanohardness and elastic modulus of the DLC film by nanoindentation decreases significantly from 29.6 and 351.2 GPa at RT to 17.5 and 150 GPa at 900 °C, respectively. It is attributed to the graphitization of part of DLC film at high temperature together with more sp^2 bonding. It indicates that the above DLC films are still amorphous at high thermal stability although the bonding behavior from primary sp^3 to more sp^2 bonding.

ACKNOWLEDGMENT

We attribute our sincere thanks to Center for Micro/Nano Science and Technology (CMNST) and Center for Precious Instruments in National Cheng Kung University, Tainan, Taiwan, for the access of analysis equipments and technical support.

REFERENCES

[1] J. Choi, S. Nakao, S. Miyagawa, M. Ikeyama, Y. Miyagawa, "The effect of Si incorporation on thermal and tribological properties of DLC films deposited by PBII&D with bipolar pulses," Surf. Coat. Tech. 201, 2007, pp. 8357-8361.

[2] M. Dai, K. Zhou, Z. Yuan, Q. Ding and Z. Fu, "The cuttings performance of diamond and DLC-coated cutting tools," Diam. Relat. Mat. 9, 2000, pp.1753–1757.

[3] H. Voigt, F. Schitthelm, T. Lange, T. Kullick and R. Ferretti, "Diamond-like carbon-gate PH-ISFET," Sens. Actuator B, 1997, pp. 441–445.

[4] D. R. Tallant, J. E. Parmeter, M. P. Siegal, R. L. Simpson, "Thermal stability of diamond-like carbon," Diam. Relat. Mat. 4, 1995, pp.191–199.

[5] W. J. Wu and M. H. Hon, "Thermal stability of diamond-like carbon films with added silicon," Surf. Coat. Tech. 111, 1999, pp. 134–140.

[6] B. K. Gupta and B. Bhushan, "Micromechanical properties of amorphous carbon coatings deposited by different deposition techniques," Thin Solid Films 270, 1995, pp. 391–398.

[7] G. H. Yang, B. Zhao, Y. Gao and F. Pan, "Investigation of nanoindentation on Co/Mo multilayers by the continuous stiffness measurement technique," Surf. Coat. Tech. 191, 2005, pp. 127–133.

[8] W. C. Oliver and G. M. Pharr, "An improved technique for determining hardness and elastic modulus using load and displacement sensing indentation experiments," J. Mater. Res. 7, 1992, pp. 1564–1583.

[9] I. N. Sneddon, "The relation between load and penetration in the axisymmetric boussinesq problem for a punch of arbitrary profile," Int. J. Eng. Sci. 3, 1965, pp. 47-57.

[10] A. C. Ferrari and J. Robertson, "Interpretation of Raman spectra of disordered and amorphous carbon," Phys. Rev. B 61, 2000, pp. 14095-14106.

[11] Y. G. Gogotsi, M. Yoshimura, "Formation of carbon films on carbides under hydrothermal conditions, "Nature 367, 1994, pp. 628-630.

[12] J. Robertson, "Diamond-like amorphous carbon," Mater. Sci. Eng. R37, 2002, pp. 129–281.

[13] R. Vuppuladhadium, H. E. Jackson, R. L. C. Wu, "Raman scattering from hydrogenated amorphous carbon films, "J. Appl. Phys. 77, 1995, pp. 2714-2718.

[14] B. Bhushan and X. Li, "Nanomechanical characterisation of solid surfaces and thin films," Int. Mater. Rev. 48, 2003, pp. 125–164.

Table 1. Deposition conditions of DLC films by IBS under UHV.

Base pressure (Pa)	10^{-7}-10^{-8}
Working pressure (Pa)	4.5×10^{-2}
Substrate's temperature	R.T.
Sputtering distance (mm)	115
Substrate's rotation (rpm)	10
Ar flow (sccm)	8
Output current (mA)	100
External voltage (kV) / current (mA)	1.0-2.0/ 20-23.5
Analog-digital voltage (kV) / current (mA)	0.5-1.0/ 1.2-1.8

Table 2. The comparison of the Raman data of DLC films with the Raman shift position (ω_D, ω_G) and the full width at half maximum (FWHM-Γ_D, Γ_G) of both D-peak and G-peak, and the ratio of integrated intensity ratio, I_D / I_G.

	D-peak		**G-peak**		
Samples	Position-$\grave{u}_D$ (cm^{-1})	FWHM-$\tilde{A}_D$ (cm^{-1})	Position-$\grave{u}_G$ (cm^{-1})	FWHM-$\tilde{A}_G$ (cm^{-1})	I_D / I_G
RT	1409	199	1559	151	0.90
900°C-0.5hr	1383	192	1576	116	1.48
900°C-1.0hr	1379	194	1574	122	1.51
900°C-1.5hr	1381	197	1575	120	1.66

Table 3. Hardness (H) and elastic modulus (E) properties of the DLC films deposited at RT and annealed at varied conditions measured by MTS nanoindentation system using CSM with a DCM technique.

Serial numbers	RT	900°C -0.5h	900°C -1.0h	900°C -1.5h
H (GPa)	29.6 ± 0.3	17.5 ± 1.1	17.2 ± 0.4	17.9 ± 0.8
E (GPa)	351.2 ± 1.0	152.1 ± 2.7	148.3 ± 1.8	150.3 ± 1.2

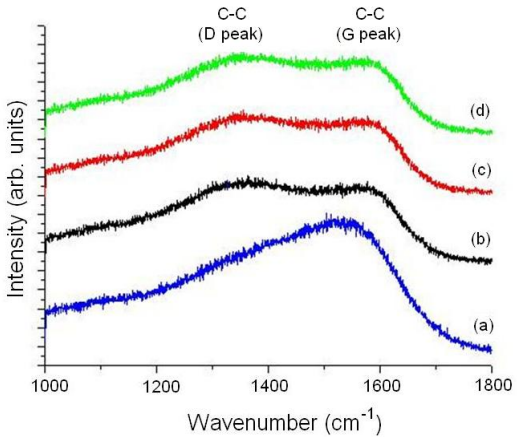

Fig. 1. The Raman spectra of DLC films: (a) as-deposited at RT, and annealed under high vacuum at 900 °C for (b) 0.5, (c) 1.0 and (d) 1.5 hours, respectively.

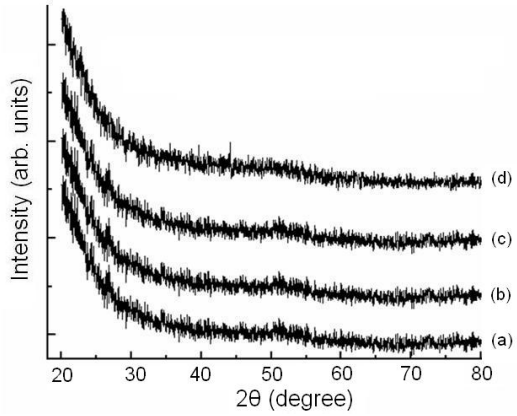

Fig. 2. GIXRD spectra of DLC films: (a) as-deposited at RT, and annealed at 900 °C for (b) 0.5, (c) 1.0 and (d) 1.5 hours, respectively.

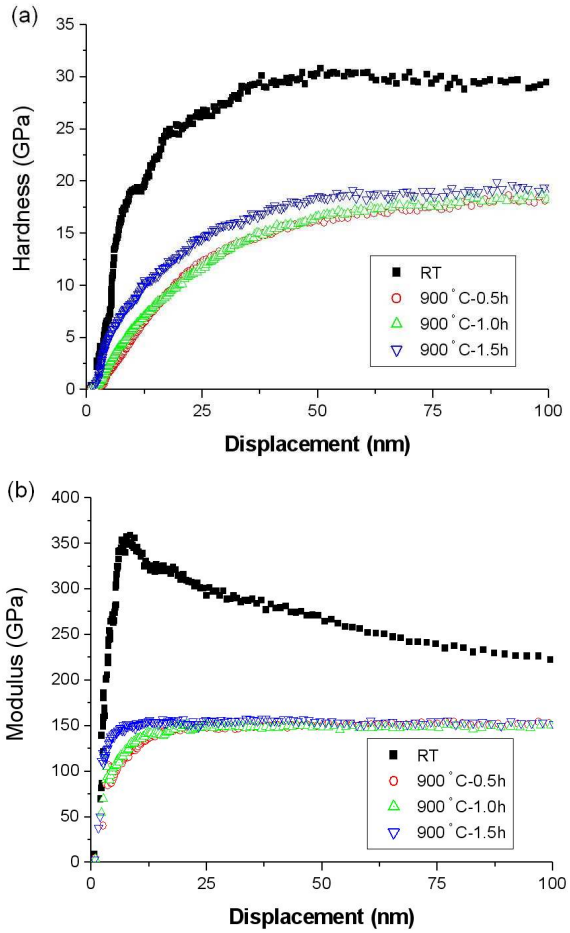

Fig. 3. (a) Hardness and (b) modulus as measured by CSM with DCM technique during nanoindentation of the DLC films at RT and annealed at varied vacuum conditions.

P42

Structure Variation and Annealing Effect on Mechanical Properties of Single Carbon Films

C.W. Lai[1], B.H. Wu[2], S.T. Hung[1] and C.K. Chung[1, 2]

[1] Dep't of Mechanical Engineering, National Cheng Kung University, Tainan, Taiwan, ROC

[2] Center for Micro/Nano Science and Technology, National Cheng Kung University, Tainan, Taiwan, ROC

Abstract — The aim of this study is to investigate the effect of thickness variation, rapid thermal annealing and silicon layer addition on mechanical property of single carbon film by using nanoindentation. From the results, Raman spectra showed that I_D/I_G ratio decreased with increasing carbon film thickness on single-layer structure at room temperature (RT). The higher the I_D/I_G, the more the sp^2 bonds are. The evolution of both hardness and Young's modulus of films had the inverse trend as the formation of sp^2 bond. Therefore, it is noted that less sp^2 bond formation was beneficial to enhance the hardness and Young's modulus of single carbon layer structure. Compared with single-layer structure, hardness and Young's modulus of C/Si two-layer decreased through Si addition. Under thermal treatment process, it can be found that hardness and Young's modulus decreased at 750 °C due to graphitization then the SiC was formed at higher annealing temperature on the surface of two-layer structure lead to hardness enhancement.

Keywords — mechanical property, carbon, annealing, ion beam sputtering,

I. INTRODUCTION

Amorphous carbon (a-C) thin films were used in a wide range of technological and industrial applications, such as in the microelectronic, optical and biomedical fields. The performance of mechanical properties of amorphous carbon films has been concerned for protective coating in the mechanical and tribological application. On the other hand, because of good thermal stability, mechanical properties and chemical inertness of silicon carbide (SiC), SiC has been used as a coating material for high temperature applications. Chung and Han [1] reported that the hardness of 3C-SiC thin films deposited by atmospheric pressure chemical vapor deposition (APCVD) could be improved to 28-36 GPa which was related to hydrogen gas content together with microstructure. The synthesis of SiC films were usually by means of physical vapor deposition (PVD) [2,3] or chemical vapor deposition (CVD) [4,5] in high vacuum at a base pressure of ~10^{-4} Pa. However, the formation of SiC through direct reaction of carbon (C) and silicon (Si) or their precursors may be influenced by the possible ambient contamination of oxygen or hydrogen from the CVD precursors into the films during deposition. The conventional CVD crystalline SiC (c-SiC) film was formed at 1200 °C or more [5-7] while the PVD deposited SiC film was amorphous at lower temperature. Chung and Wu [8] reported that post-annealing three-layer a-Si/C/a-Si structure could reduce the formation temperature of c-SiC together with C and Si to 900 ºC. The high-temperature deposition of film on the Si substrate may change the microstructure. Here, we discussed the relationship on mechanical properties of single carbon films with structure variation and annealing effect.

II. EXPERIMENTAL

The boron-doped single crystalline p-Si(100) wafers were initially cleaned in a solution of H_2SO_4 and H_2O_2 in the ratio of 3:1. Single carbon film was deposited on the Si (100) substrate by ultra-high-vacuum ion beam sputtering (IBS-2000, ULVAC, Japan) with an electron cyclotron resonance (ECR) microwave plasma beam source. The sputtering target were C (99.999% purity) and Si (99.999% purity). The experimental parameters such as ion energy, Ar gas flow rate, and substrate heating can be controlled independently. The Ar process gas was fixed at a flow rate of 8 sccm. The base pressure and the working pressure were about 10^{-7}-10^{-8} Pa and 4.5 x 10^{-2} Pa, respectively. The ion beam was generated with output current of about 100 mA at controllable external voltages and currents. The substrate was rotated at 10 rpm to get the deposition uniform and kept at room temperature. The distance from substrate to the target was about 115 mm. Both types of single-layer films with thickness of 10 nm (sample [A]), 50 nm (sample [B]) and 100 nm (sample [C]) and two-layer C/a-Si films with thickness of 100/10 nm/nm (sample [D]) were investigated in this study as showed in Fig. 1. Sample [C] and [D]were annealed at 750 °C and 900 °C by Rapid thermal annealing (RTA). The morphology and microstructure analysis of nanocomposite films were examined by high resolution field emission scanning electron microscopy (HR-FESEM, JSM- 7000F, JEOL, Japan). The reaction and bonding behavior of C and Si were characterized by Raman spectroscopy (Labram HR, France) with high sensitivity for carbon and its compound in the variation of graphite peak (G-peak), disorder-induced peak (D-peak) and Si-C peak at specific wavenumber shifts.

III. RESULTS AND DISCUSSION

Fig. 1 showed the SEM micrographs of sample [A], [B], [C] and [D] deposited on the Si(100) substrate at room temperature (RT), respectively. It can be seen that the surface of each sample is smooth with increasing the carbon thickness or adding the silicon layer. Fig. 2 showed the curve-fitting curves of Raman spectra of the sample [A]-[C] single carbon films deposited on the Si substrate. In the region of Raman shift wavenumbers of 1200 to 1800 cm^{-1}, there is a broad asymmetric scattering band, which is a characteristic of the DLC film. This asymmetric band can be deconvoluted into G

(graphite) and D (disorder) peaks of C-C bonding by auto curve-fitting of Gaussian functions to get the peak position and the integrated intensity. The position of the G-peak is at about 1580-1600 cm^{-1} with an integrated intensity I_G while a D-peak is at about 1350 cm^{-1} with an integrated intensity I_D [9,10]. The integrated intensity ratio (I_D/I_G) in the conventional DLC films were suggested to be correlated with the trend of more sp^2 or sp^3 bonding of amorphous carbon (a-C). The higher the I_D/I_G is, the more the sp^2 bonding is. Table 2 listed the hardness and Young's modulus of sample [A]-[C] single carbon film deposited at room temperature. Fig. 3 revealed the relation between the hardness and I_D/I_G ratio at different thickness of single carbon film deposited at room temperature. From the Table 2 and Fig. 3, it indicated that I_D/I_G ratio decreased with increasing single carbon film thickness at room temperature (RT). The evolution of both hardness and Young's modulus of films had the inverse trend as the formation of sp^2 bond. Therefore, it is noted that less sp^2 bond formation was beneficial to enhance the hardness and Young's modulus of single carbon layer structure. Compared with single-layer structure, hardness and Young's modulus of C/Si two-layer composite film deposited at room temperature decreased through Si layer addition as showed in Table 3.

Fig. 4 showed the Raman spectra with overlapping fitted curves at wavenumbers in the region of 800-1800 cm^{-1} of single-layer carbon films with thickness of 100 nm annealed at 750 °C and 900 °C. Crystalline Si-C bonding in the longitudinal optical mode appeared in the region of 950-1000 cm^{-1} [11–13]. The peak attributed to Si–C bonding in SiC is superimposed on the c-Si–Si peak to form an asymmetric peak, as shown in Fig. 4. Crystalline SiC is formed at 750 °C annealing for 1 min. When the annealing temperature is increased to 900 °C, the reaction is enhanced and the intensities of crystalline Si-C peaks increased much more. We concluded that the grain boundaries of polycrystalline Si transformed from single crystalline Si under high annealing process could enhance the interdiffusion and reaction between C and Si and form a SiC nanocomposite structure.

For two-layer structure analysis under annealing process, Fig. 5 showed the SEM micrographs of sample [D] with C/a-Si (100/10 nm/nm) films deposited on the Si(100) substrate post-annealed at 750 and 900 °C for 1 min, respectively. The wrinkled surface with close islands at random distribution is found at 750 °C annealing and many SiC nanoparticles (np-SiCs) are formed on the surface of films at 900 °C annealing. It indicates that rapid thermal annealing at high enough temperature of 900 °C is beneficial for the formation of np-SiCs on the surface of two-layer C/Si on the Si(100) substrate compared to lower temperature annealing. From the Raman spectra, it can be found that the I_D/I_G ratio increased which means more sp^2 bonding formed at 750 °C annealing. Then C-C bonding disappeared totally while Si-C bonding appeared around 950-1000 cm^{-1} at 900 °C annealing as showed in Fig. 6. Fig. 7 revealed the relation between the hardness and annealing temperature at sample [D]. Compared with Raman spectra and mechanical property measurements, we supposed that hardness and Young's modulus decreased at 750 °C due to graphitization then the SiC was formed at higher annealing temperature on the surface of two-layer structure lead to hardness enhancement.

IV. Conclusions

In this study, the mechanical properties of single layer carbon (C) and two-layer carbon/silicon (C/Si) composite structure deposited by ultra-high-vacuum ion beam sputtering (UHV-IBS) have been investigated using nanoindentation measurement technique. It was noted that the I_D/I_G ratio decreased with increasing carbon film thickness on single-layer structure at room temperature (RT) lead to hardness enhancement. Compared with single-layer structure, hardness of C/Si two-layer structure decreased due to silicon layer addition. Under thermal treatment process, the grain boundaries of polycrystalline Si transformed from single crystalline Si for the interdiffusion reaction between carbon and silicon elements and SiC was formed at 750 °C. Under two-layer structure case, it can be found that hardness of film decreased at 750 °C due to graphitization then the SiC was formed at 900 °C on the surface of carbon/silicon (C/Si) structure lead to hardness enhancement.

V. Acknowledgements

This work is partially sponsored by National Science Council under grant No. NSC 96-2628-E-006-080-MY3. We pay our great thanks to the Center for Micro/Nano Science and Technology (CMNST) in National Cheng Kung University for the access of process and analysis equipments.

VI. References

1. G. S. Chung and K. B. Han, J. Microelectronics 39, pp. 1413-1415, 2008.
2. N. Kikuchi, E. Kusano, T. Tanaka, A. Kinbara and H. Nanto, Surf. Coat. Technol. 149, pp.76-81, 2002.
3. M. Xu, V. M. Ng, S. Y. Huang, J. D. Long, and S. Xu, IEEE Transactions on Plasma Science 33, pp.242-243, 2005.
4. M. Mejregany and C. A. Zorman, Thin Solid Films 355-356, pp.518-524, 1999.
5. K. Kametani, K. Sudoh and H. Iwasaki, Thin Solid Films 467, pp.50-53, 2004.
6. P. M. Sarro, Sens. Actuators 82, pp.210-218, 2000.
7. B.G. Kim, Y.W. Lee, J.W. Lee, and Y. Choi, Surf. Coat. Technol. 151-152, pp.26-30, 2002.
8. C. K. Chung and B. H. Wu, Thin Solid Films 515, pp. 1985-1991, 2006.
9. A.C. Ferrari, J. Robertson, Phys. Rev., B 61, pp. 14095-14107, 2000.
10. Y.G. Gogotsi, M. Yoshimura, Nature 367, p. 628, 1994.
11. A. Kailer, K.G. Nickel1, Y.G. Gogotsi, J. Raman Spectrosc. 30, p. 939, 1999.
12. J. Liu, Y.K. Vohra, Phys. Rev. Lett. 27, pp. 4105-4108, 1994.
13. H. Nienhaus, T.U. Kampen, W. Monch, Surf. Rev. Lett. 324 , p. 328, 1995.

Table 1. Illustration of each specimen structure

Specimen	Structure
[A]	C (10 nm) / Si wafer
[B]	C (50 nm) / Si wafer
[C]	C (100 nm) / Si wafer
[D]	C (100 nm) / a-Si (10 nm) / Si wafer

Table 2. Hardness and Young's modulus of single carbon film deposited at room temperature

	RT	
Specimen	H(GPa)	E(GPa)
[A] C-10 (nm)	8.32	176.56
[B] C-50 (nm)	14.17	184.72
[C] C-100 (nm)	25.63	210.67

Table 3. Hardness and Young's modulus of sample [C] and [D] deposited at room temperature and annealed at 750 °C and 900 °C

Specimens	[C]-RT	[C]-750 °C	[C]-900 °C
H (GPa)	25.63	12.18	14.73
E (GPa)	210.67	163.26	175.15
Specimens	[D]-RT	[D]-750 °C	[D]-900 °C
H (GPa)	24.15	11.52	12.58
E (GPa)	208.29	158.47	164.73

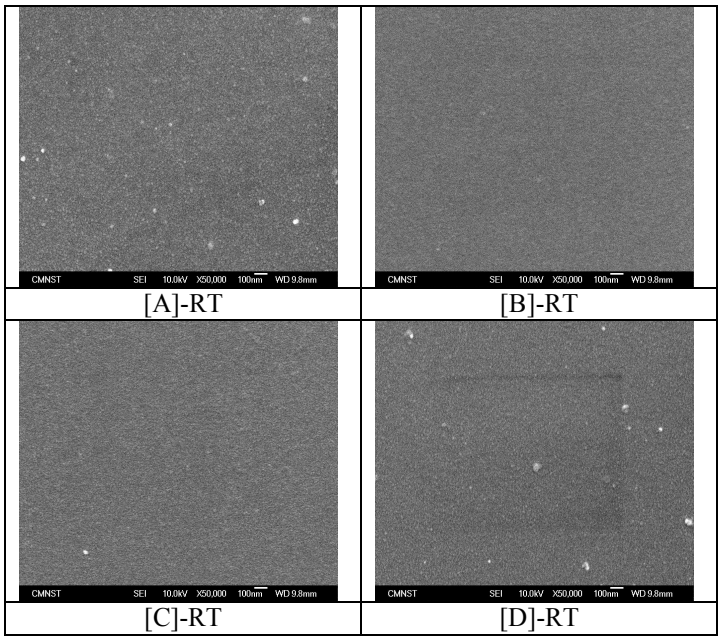

Figure 1. SEM image of single and two-layer composite film deposited on Si substrates at room temperature

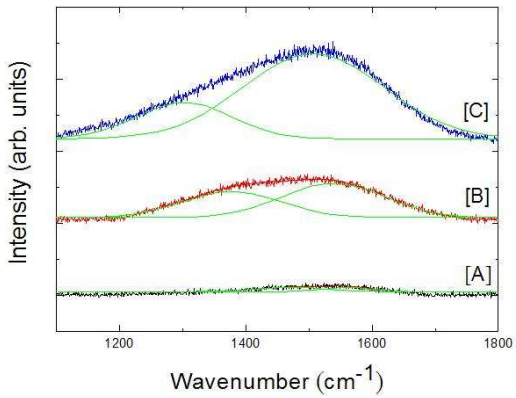

Figure 2. Raman spectra of single carbon films deposited at room temperature with thickness of: [A] 10 nm, [B] 50 nm and [C] 100 nm

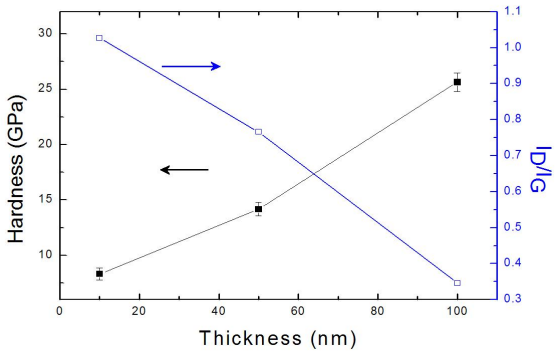

Figure 3. The relation between the hardness and I_D/I_G ratio at different thickness of single carbon film deposited at room temperature.

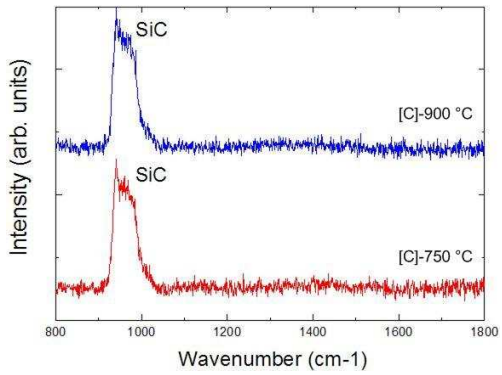

Figure 4. Raman spectra of [C] two-layer composite film deposited on Si substrates at annealing temperature of 750 °C and 900 °C

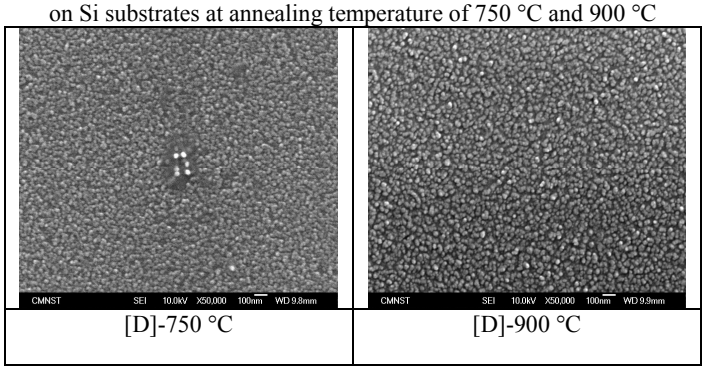

Figure 5. SEM image of sample [D] deposited on Si substrates at annealing temperature of 750 °C and 900 °C

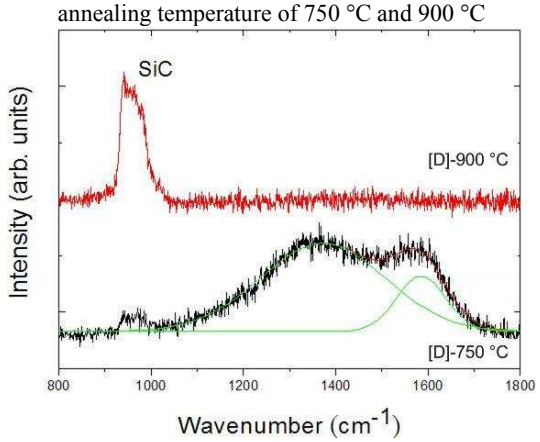

Figure 6. Raman spectra of [D] two-layer composite film deposited on Si substrates at annealing temperature of 750 °C and 900 °C

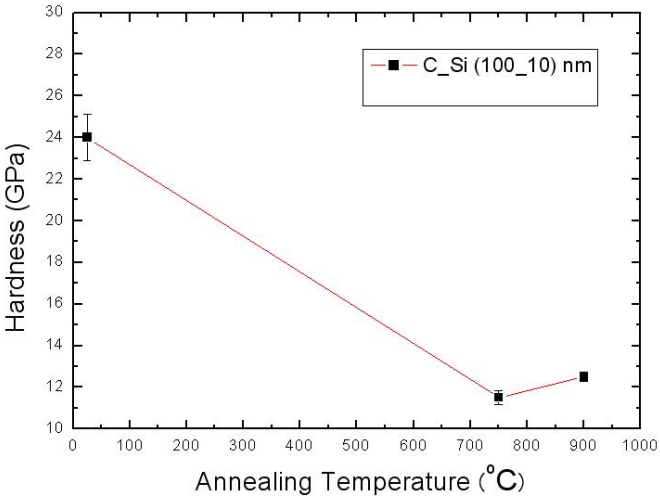

Figure 7. The relation between the hardness and annealing temperature at sample [D]

Investigation of Scratching Nano Grooves on Aluminum Film

C. Y. Huang[1], C. H. Hsieh[2], Junz J. J. Wang [3], C. T. Hsu[3]

[1]Center for Micro/Nano Science and Technology, National Cheng Kung University, Taiwan
[2]National Synchrotron Radiation Research Center, Taiwan
[3]Department of Mechanical Engineering, National Cheng Kung University, Taiwan

***Abstract* — A mechanical machining method, scratch, is used to fabricate nano grooves in this investigation. The nanoindentation instrument with a lateral force module, which has high resolution three dimensional displacement and force sensors and actuators, is utilized to conduct the scratch tests. A Berkovich indenter with a sharp triangular pyramid diamond tip, whose tip radius is less than 50 nm, is used as a scriber to scratch aluminum film in these tests. To shape grooves, successful generation of chips to efficiently remove the material is crucial, and is affected by both scratch direction and depth. It is found that scratch the material by single face of the tip is the best direction to efficiently generate the chips. Moreover, the chips are usually attached to the end of the grooves and still needed to be removed. UV curing material is coated on the scratched sample, and is then separated from the sample after UV curing process. It is shown to be a good method to separate the chips from the sample.**

Keywords — ***Nanofabricatin, Nanogroove, Scratch***

Ⅰ. Introduction

Nano technology utilizes the nano structure to enhance the chemical, physical and mechanical properties of the materials, and has been widely applied in many areas including optical, electronic, energy, biomedicine areas. However, presently most equipments for generating nano structures, such as electron-beam or ion-beam lithography equipments, are quite expensive. How to decrease the cost of the nano products plays an important role on commercialization of nano technology. Some researchers tried to use atomic force microscopy, a relative cheaper instrument, to produce nano structures by the methods of DPN (Dip Pen Nanolithography) or LON (Local Oxidation Nanolithography) [1]. Yan [2] tried to directly scratch the nano patterns on the copper film by AFM. However, the AFM tips are usually made of silicon and are easily worn in the scanning process, which is hard to mass produce the nano structures. Moreover, AFM tips have high flexible cantilever-beam structures and thus can not well control its machining dimension. Compared with the characteristics of low hardness and high flexible structure of the AFM tips, the nanoindentation tips, which are made of diamond, have high hardness, stiffness, and wear resistance. These diamond tips are allowed to scratch in larger areas, and are more suitable to mass produce the nano structures. As a result, utilizing diamond tips to scratch the nano structures could be a potential method to mass produce the nano structures with low cost.

The studies about scratch focus on the measurement of the surface properties of the materials [3, 4], and not much research discusses the machining properties of scratch. There are some studies trying to construct the model of the scratch behavior. Goddard and Wilman [5] suggested and analytical models for predicting the plowing behavior and the apparent friction coefficient of the scratch process. The studies [6-7] proposed the three-dimensional models of the plowing behavior as scratch a rigid plastic material by a pyramid tips. Bucaille et al. [8] studied the influence of the rheology on the geometries of the grooves [8], and found that the material is easily pushed beside of the tip and forms burrs for the material with high rheological factor, but is hard removed for the material with low rheological factor, which is caused by highly elastic recovery.

The purpose of this paper is to investigate the machining properties of scratch. This paper focuses on the discussions of the two issues below: 1. How to efficiently generate chips? 2. How to remove the chips? Several scratch experiments are conducted to study these issues.

Ⅱ. Experimental Equipments

The aluminum film with thickness of 450 nm was deposited on silicon wafer by electron beam evaporator where the chamfer pressure is 9×10^{-6} torr and the deposition rate was1 Å/sec. The aluminum film has high plasticity, and thus can avoid too much elastic recovery after scratch. Moreover, its material properties are isotropic. Thus there's no need to identify the material orientation before scratch.

The nanoindentation equipment (MTS Nanoindentation system & Nanomechanical microscopy XP) is utilized in this study and its option, lateral force measurement (LFM) is adopted to conduct the scratch experiments.

A Berkovich tip with a triangular pyramid shape, as sketched in Fig. 1, with an equivalent radius less than 50 nm is used as the scriber in the scratch tests.

Ⅲ. Experiments and Analysis

The ideal scratch behavior for machining has the two characteristics: 1. the scratched material should have high plasticity. (The elastic deformation can only make material

This work has been granted by the Center for Frontier Material and Nano/Micro Science and Technology, National Cheng Kung University, Taiwan. (D97-2007)

Contact Author: Chao-Yu Huang, Center for Micro/Nano Science and Technology, National Cheng Kung University, No.1, University Road, Tainan City 701, Taiwan; (phone: +886-6-275-7575 ext. 31385; fax: +886-6-208-0103; email:cyhuang@mail.mina.ncku.edu.tw).

have instant deformation, but will not leave any mark after elastically recovery.) 2. The scratched material should be removed as the form of the chips. (The chips are more easily removed from the machined surface than the burrs). The scratch which has the above two characteristics can be considered to have high scratch efficiency.

To test the scratch efficiency in different directions, two directions, which are face-forward and edge-forward directions as shown in Fig. 2, are utilized in the experiments. The normal loads, as illustrated in Fig. 3, continuously varied from 0 mN to 10mN in the scratch distance of 100 um. The residual groove profiles are shown in Fig. 4. By comparing the Figs. 4(a) and Fig. 4(c), it is found that there are burrs attached beside the grooves as scratch in the edge-forward direction. Moreover, by comparing the Figs. 4(b) and 4(d), it is found that much material attached in the end of the grooves as scratch in the face-forward direction. The morphologies of the grooves are examined by utilizing the scanning electron microscopy, SEM. SEM image in Fig. 5(a) clearly shows that there are burrs beside the grooves after scratch in the edge-forward direction. SEM image in Fig. 5(a) indicates that the material attached in the end of the grooves becomes chips after scratch in the face-forward direction. According to the experimental results in Figs. 4 and 5, it can be concluded that 1. as scratch in the edge-forward direction, most material in the grooves is pushed to the sides the grooves to form burrs. 2. as scratch in the face-forward direction, most material is pushed to end the grooves to form chips. As a result, the face-forward direction, which is easier to generate chips, has better scratch efficiency.

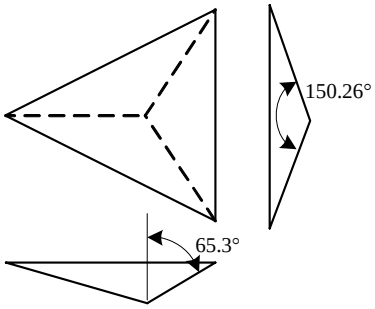

Figure 1 Geometry of Berkovich tip

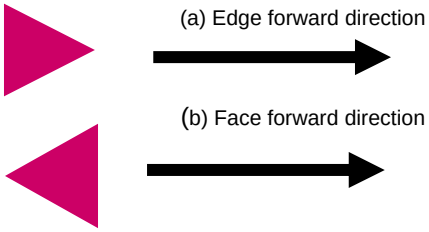

Figure 2 Illustration of the scratch directions (a)edge-forward direction (b)face-forward direction

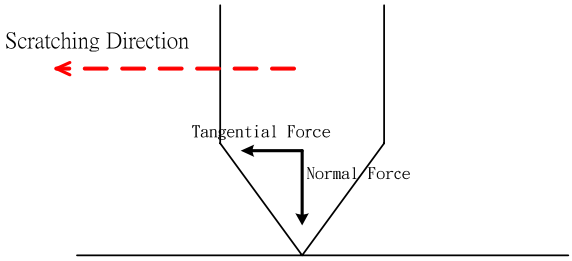

Figure 3 Illustration of the scratch force directions

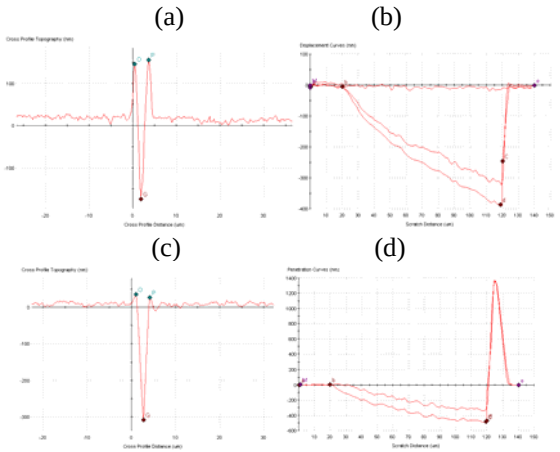

Figure 4 Residual profiles of the grooves: (a)lateral and (b)longitudinal cross sections of the groove scratched in the edge-forward direction; (c)lateral and (d)longitudinal cross sections of the groove scratched in the face-forward direction

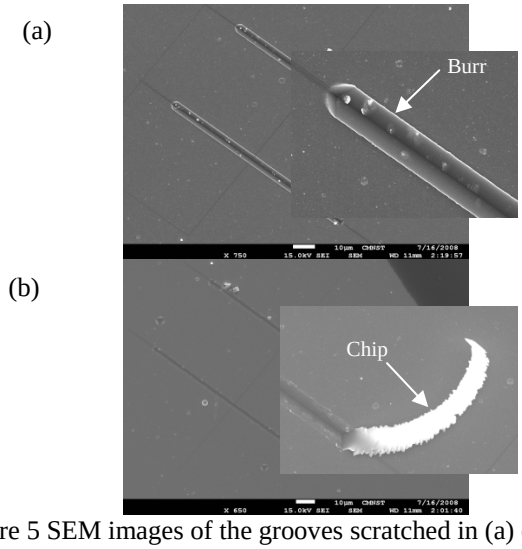

Figure 5 SEM images of the grooves scratched in (a) edge forward direction and (b) face forward direction.

As the scratch depth varies from low to high (or the scratch force from small to large), the scratch experiences three regions: elastic, plowing and cutting regions, as sown in Fig. 6. In the elastic region, all of the scratched material elastically recoveries, and doesn't leave any scratched mark, as shown in Fig. 6(a). In the plowing region, the material is pushed to the sides of grooves to be burrs, as shown in Fig. 6(b), In the cutting region, the scratched material is become chips to be take away, as shown in Fig. 6(c). Even though the scratch in the face-forward direction is easier to generate chips, it still will experience these three regions. To examine the critical force of the cutting region, different scratch forces are used in the following experiments and then observe the occurrence of the chips. The experimental results are listed in the Table 1. Table 1 indicates that the chips are generated as the normal force is greater than 4 mN, which also implies the critical load of the plowing and cutting regions should be between 2mN and 4mN.

The relations between the scratch conditions and the groove geometries are discussed in the following analysis. The curves of normal load versus scratch depth for both of face- and edge- forward scratches shown in Fig. 7. Fig. 8 shows that the normal force of the edge-forward scratch can be well fitted by the function, $F = cD^2$ with a constant of $c = 7.96\times10^{-5}$ [mN/nm^2], where F is the normal load and D is the scratch depth In addition, the curve of face-forward scratch is shown to be very close to that of edge-forward scratch as F is small, but these two curves starts to separate as F is greater than 2.2mN. As the experiments shown in the Table 1, the critical load of the plowing and cutting regions should be between 2mN and 4mN in face-forward scratch. As a result, 2.2mN should be this critical load of the cutting region. The force-forward scratch as F is less than 2.2mN and the edge forward scratch both belong to plowing behaviors, and their force curves are fitting by the $F= cD^2$. Therefore, Fig. 7 also implies that the force curves in the plowing region can be expressed to be proportional to the square of the scratch depths. Moreover, we try to fit the force curve in the cutting region of face-forward scratch, and find that it can be well fitted by

$$F=c_1D+c_2D^2 \quad (1)$$

where c_1=6.06 $\times10^{-5}$ [mN/nm], and c_2=3.93 $\times10^{-3}$ [mN/nm^2]., as shown in Fig. 9.

The chips attached on the end of grooves are still need to be removed. This study tries to use UV adhesive to remove chips. Coat the UV adhesive on the scratched material, and expose the UV adhesive to UV light and make it curing. Finally, remove UV adhesives. Because the chips pastes on the cured UV adhesive, removing the UV adhesive can also remove the chips at the same time. Fig. 10 shows the SEM image of the groove whose chip had been removed by the above way. Fig. 10(b) shows the chip no longer exits on the sample, and indicates that this way can successfully remove the chips. However, Fig. 10(b) also shows there are still some burrs beside the groove.

Table 1 Status of chip formation in different normal loads

Load (mN)	2	4	6	8	10	12
Chip formation	No	Yes	Yes	Yes	Yes	Yes

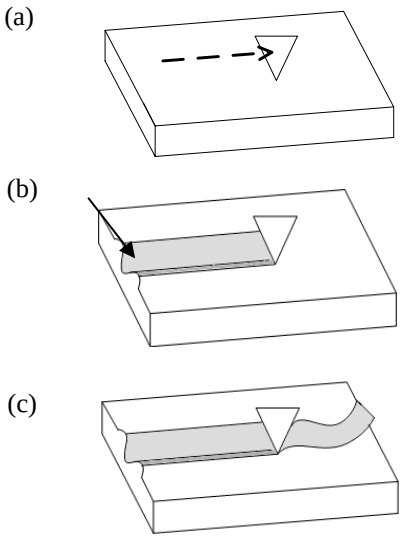

Figure 6 Different scratch regions. (a)elastic, (b)plowing and (c)cutting regions.

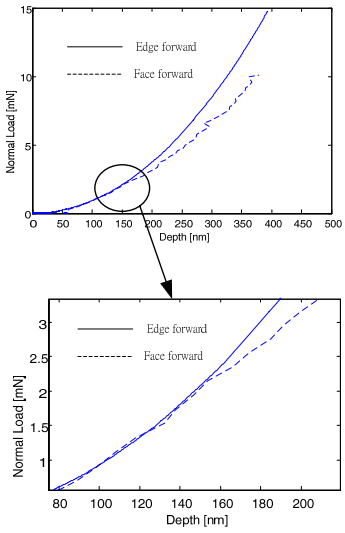

Figure 7 Normal load versus scratch depth for the face-forward and edge-forward scratches

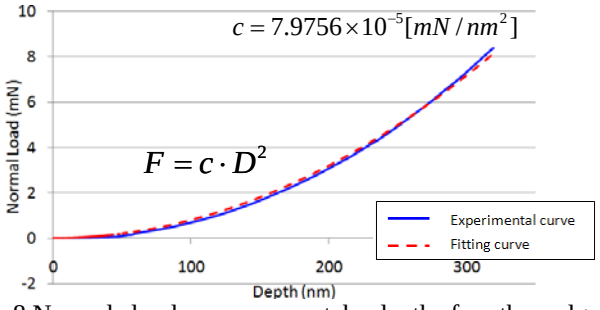

Figure 8 Normal load versus scratch depth for the edge-forward scratch

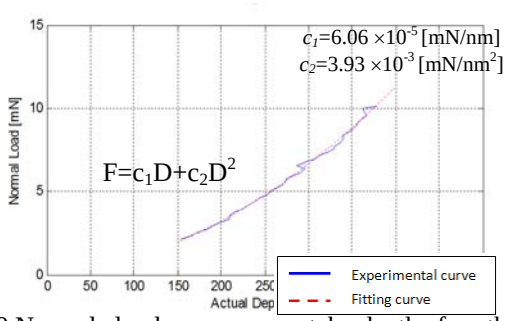

Figure 9 Normal load versus scratch depth for the face-forward scratch in the cutting region

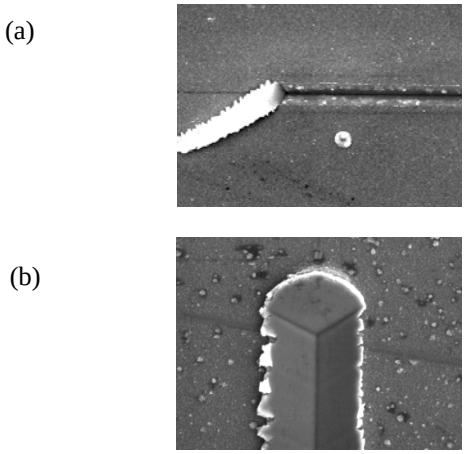

Figure10 Using UV adhesives to remove chips. (a) the groove whose chips haven't been removed; (b) the groove whose chips have been removed by UV adhesive.

IV. Conclusion

This study investigated the characteristics of scratching the nano grooves. As shaping the grooves, successful generation of chips to efficiently remove the material is crucial, which is affected by scratch directions and depth. It is found that scratch in the face-forward direction is the better direction to efficiently generate the chips, and the critical force to generate the chips is 2.2mN. Several experiments were conducted to investigate the relation between the groove depth and the scratch force. Moreover, this study tried to use UV curing material to remove the chips, and found this is a good method to separate the chips from the sample.

Acknowledgment

This work has been granted by the Center for Frontier Material and Nano/Micro Science and Technology, National Cheng Kung University, Taiwan. (D97-2007)

References

[1] R. Garcia, R. V. Martinez, J. Martinez, "Nano Chemistry and Scanning Probe Nanolithographies," Chemical Society Reviews, Vol. 35, pp. 29-38, 2006.

[2] Y. D. Yan, "Investigation on AFM Based Micro/Nano CNC Machining System," International Journal of Machine Tools and Manufacture, Vol. 47, No. 11, pp. 1651-1659, 2007.

[3] Brookes C.A., Some Observations on Scratch and Indentation Hardness Measurements, J. Physics D: Applied Physics, Vol. 5, pp. 1284-1293, 1972.

[4] T. H. C. Childs, "The sliding of rigid cones over metals in high adhesion conditions." Int. J. Mech. Sci. Vol. 12, pp. 393–403, 1970.

[5] J. Goddard and H. Wilman, "A theory of friction and wear during the abrasion of metals." Wear Vol. 5, pp. 114–135. 1962.

[6] P. Gilormini and E. Felder, "Theoretical and experimental study of the ploughing of rigid plastic semi-infinite body by a rigid pyramidal indenter." Wear, Vol. 88 , pp. 195–206. 1983.

[7] M. De Vathaire, F. Delamare and E. Felder, "An upper bound model of ploughing by a pyramidal indenter." Wear, Vol. 66, pp. 55–64. 1981.

[8] J. L. Bucaille, E. Felder and G. Hochstetter, "Mechanical analysis of the scratch test on elastic and perfectly plastic materials with the three-dimensional finite element modeling." Wear, Vol. 249, pp. 422–432, 2001.

Nanoindentation Response and Microstructure of Single-Crystal Silicon under Different Loads

Woei-Shyan Lee [1,*], Tao-Hsing Chen[2] and Shuo-Ling Chang [1]

[1] Department of Mechanical Engineering, National Cheng Kung University, Tainan 701, Taiwan
[2] Center for Micro/Nano Science and Technology, National Cheng Kung University, Tainan 701, Taiwan

***Abstract* —Nanoindentation tests are performed on single-crystal silicon wafers using a Berkovich indenter and maximum indentation loads of 30 mN, 40 mN, and 70 mN, respectively. The microstructural evolutions of the indented specimens are examined using transmission electron microscopy and selected area diffraction techniques. The results show that the unloading curve of the specimen indented to a maximum load of 30 mN has a smooth profile, whereas those of the specimens indented to 40 mN or 70 mN have a pop-out feature. The hardness and Young's modulus of the silicon specimens reduce with an increasing indentation load, and have values of 15.8 GPa and 182 GPa, respectively, under the highest indentation load of 70 mN. A completely amorphous phase is induced within the indentation zone in the specimen indented to a maximum load of 30 mN, whereas a mixed structure comprising amorphous phase and nanocrystalline phase is found in the indentation zones in the specimens loaded to 40 mN and 70 mN, respectively.**

Keywords ***—Nanoindentation, Silicon, Microstructural evolution, Load***

I. INTRODUCTION

Silicon has excellent semiconducting properties and is therefore widely used as a substrate material for many applications in the microelectronics and optoelectronics industries. The mechanical properties of the silicon substrate affect not only the mechanical performance of the device, but also its electrical and / or optical performance. Typically, silicon substrates are coated with a thin layer of silicon nitride or polyimide in order to protect the circuitry from the effects of the ambient environment, to relieve the stress induced during the flip-chip bonding process, to render the device more robust toward the effects of wear and tear, and so on [1-3]. The presence of these thin films has a profound effect on the mechanical properties of the substrate, and thus many experimental studies have been performed to evaluate the properties of various thin films coated on a silicon substrate [4-8]. However, the mechanical properties and nanoindented microstructures of silicon substrates under different loads are not yet fully clear. Therefore, further investigation is required into the effects of load on the nanoindentation response and microstructural evolution of silicon in order to establish the loading conditions which avoid the onset of plastic deformation and therefore improve the reliability of the device. Since the mechanical response and phase transformation of a silicon substrate depend strongly on the magnitude of the applied load, a comprehensive study regarding the effects of load on the indentation behaviour and microstructural change is required. Accordingly, the present study utilises a nanoindentation technique to determine the loading-unloading characteristics of silicon substrates under different indentation loads in the range 30~70 mN. The microstructural evolutions of the indented specimens are then observed using transmission electron microscopy and selected area diffraction techniques.

II. EXPERIMENTAL PROCEDURE

The nanoindentation tests were performed using device grade p-type single-crystal silicon wafers with a (100) orientation. The wafers were 0.725 mm in thickness and were acquired with chemomechanical polished finishes. The nanoindentation tests were performed at room temperature in air using an MTS Nanoindenter XP system fitted with a Berkovich diamond pyramid tip with a radius of 20 nm. The specimens were indented to three different maximum loads, namely 30 mN, 40 mN and 70 mN. The loading-unloading procedure involved the following steps: (1) impressing the indenter until the pre-specified value of the maximum load was attained, (2) holding the indenter in this position for 1 s; and (3) smoothly withdrawing the indenter from the specimen over a period of 10 s. Five indentation tests were performed under each experimental condition, and the corresponding hardness and Young's modulus values of the silicon specimen were then calculated from the load-displacement curves using the Oliver and Pharr method [9]. Following the nanoindentation tests, thin

The authors gratefully acknowledge the financial support provided to this study by the National Science Council (NSC) of Taiwan under contract no. NSC 97-2221-E-006-047.

Contact author:wslee@mail.ncku.edu.tw***

foil specimens for TEM inspection were prepared using an FEI Nova 200 focused ion beam (FIB) milling system with a Ga^+ ion beam and an operating voltage of 30KeV. The cross-sectional microstructures of the various specimens were then observed using a Philips Tecnai F30 Field Emission Gun Transmission Microscope operated at 300 KeV.

III. Results and Discussion

Figure 1 presents typical loading-unloading curves obtained when indenting the silicon specimens to maximum loads of 30 mN, 40 mN and 70 mN, respectively. It is observed that for each curve, the loading region has a smooth, continuous profile with no pop-in events. However, notably different features are observed in the unloading regions of the three curves. For example, for a maximum indentation load of 30 mN, the unloading curve contains a slight elbow (i.e. a gradual change in slope), which indicates a transformation from the original diamond cubic structure to an amorphous structure [10]. By contrast, for maximum indentation loads of 40 mN and 70 mN, respectively, a well-defined pop-out feature is observed in the unloading region of each load-displacement curve. n other words, the critical load for the occurrence of pop-out is around 40 mN for the current silicon specimens. The pop-out features observed in nanoindentation tests have been attributed to many different factors [10-12]. In the present single-crystal silicon specimens, the pop-out feature is thought to be the result of a phase transformation within the indentation-affected zone. Applying the Oliver and Pharr method to the experimental data presented in Fig. 1, it is found that both the hardness and the Young's modulus decrease slightly as the maximum indentation load is increased from 30 mN to 70 mN (i.e. from 16.63 GPa to 15.70 GPa (hardness) and from 192.40 GPa to 182 GPa (Young's modulus), see Table 1).

Figure 2 presents a bright field cross-sectional TEM micrograph of the silicon specimen indented to a maximum load of 30 mN. It can be seen that the indentation-affected zone (indicated by the dotted line) has a uniform microstructure and is separated from the surrounding area of the silicon specimen by a clear boundary. (Note that the long stripes in the region of the specimen outside of the nanoindentation-affected zone are simply interference fringes caused by a bending of the TEM sample during the FIB preparation process.)

Figure 3presents a cross-sectional TEM micrograph of the silicon specimen indented to a maximum load of 40 mN. It can be seen that the indented microstructure changes from a fully amorphous state to a mixed amorphous / nanocrystalline state as the maximum indentation load is increased from 30 mN to 40 mN. This microstructural change is thought to be responsible for the pop-out event in the unloading region of the corresponding load-displacement curve shown in Fig. 1. It is also observed in Fig. 3 that a crack extends from the bottom of the phase transformation region into the silicon substrate, indicating that the critical load for micro-fracture initiation has been exceeded.

Figure 4 presents a cross-sectional TEM micrograph of the silicon specimen indented to a maximum load of 70 mN. The indentation-affected zone contains a mixed structure of amorphous phase and nanocrystalline phase. Comparing Figs. 3 and 4, it is observed that while both microstructures contain a mixture of amorphous phase and nanocrystalline phase in the nanoindentation-affected area, the density of the nanocrystalline phase in the specimen indented to a maximum load of 70 mN (i.e. Fig. 4) is significantly higher than that in the specimen indented to a lower maximum load of 40 mN (i.e. Fig. 3).

IV. Conclusions

This study has evaluated the nano-mechanical properties of single-crystal silicon substrates indented to maximum loads of 30 mN, 40 mN and 70 mN, respectively. The effects of the load on the microstructural changes induced within the indented specimens have been characterised using transmission electron microscopy. For a maximum load of 40 mN or more, a well-defined pop-out feature is observed in the unloading region of the load-displacement curve. Both the hardness and the Young's modulus reduce slightly as the indentation load is increased. A small indentation load of 30 mN prompts the formation of a completely amorphous structure, whereas a higher load (i.e. > 40 mN) gives rise to a mixed amorphous / nanocrystalline structure.

TABLE 1 HARDNESS AND YOUNG'S MODULUS VALUES OF SILICON SPECIMENS INDENTED TO DIFFERENT MAXIMUM LOADS.

	Load		
	30mN	40mN	70mN
Hardness (GPa)	16.63	16.14	15.70
Young's Modulus (GPa)	192.40	187.69	182

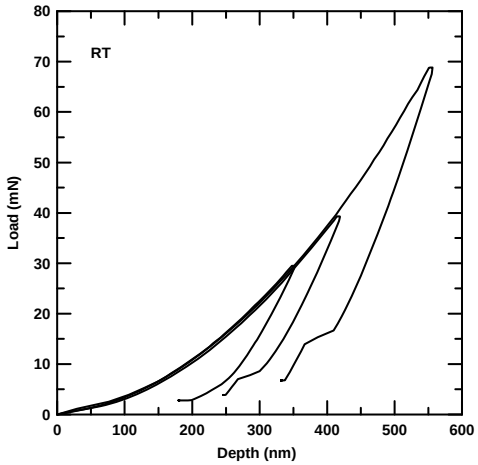

Figure1. Typical load-displacement curves obtained during indentation to maximum loads of 30 mN, 40 mN and 70 mN, respectively.

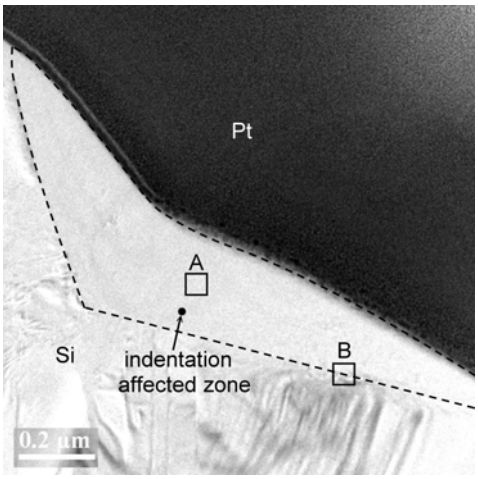

Figure 2. Cross-sectional TEM micrograph of specimen indented to maximum load of 30 mN.

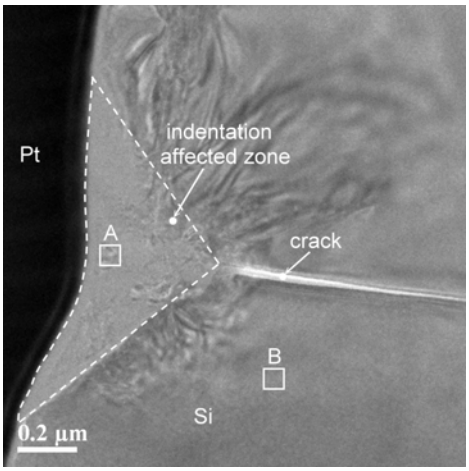

Figure 3. Cross-sectional TEM micrograph of specimen indented to maximum load of 40 mN.

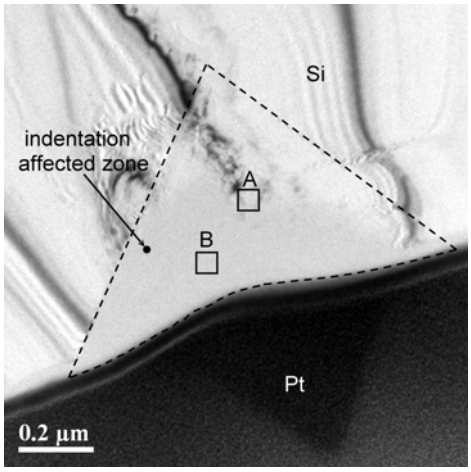

Figure 4. Cross-sectional TEM micrograph of specimen indented to maximum load of 70 mN.

ACKNOWLEDGMENT

The authors gratefully acknowledge the financial support provided to this study by the National Science Council (NSC) of Taiwan under contract no. NSC 97-2221-E-006-047.

REFERENCES

[1] J. L. Wang, “Underfill of flip chip on organic substrate: viscosity, surface tension, and contact angle”, Microelectron. Reliab, vol. 42, pp. 293-299, 2002.

[2] L. Liu, S. Yi, L. S. Ong, and K. S. Chian, “Finite element analysis for microwave cure of underfill in flip chip packaging”, Thin Solid Films, vol. 462, pp. 436–445, 2004.

[3] T. H. Fang, W. J. Chang, and C. M. Lin, “Nanoindentation and Nanoscratch Characteristics of Si and GaAs”, Microelectron. Eng. vol. 77, pp. 389-398, 2005.

[4] R. Saha and W.D. Nix, “Effects of the substrate on the determination of thin film mechanical properties by nanoindentation”, Acta Mater., vol. 50, pp. 23-38, 2002.

[5] W. S. Lee and T. Y. Liu, “The effect of annealing temperature on the microstructure of nanoindented Au/Cr/Si thin films”, Nanotechnology, vol. 18, 335701, 2007.

[6] H. Pelletier, J. Krier, and P. Mille, “characterization of mechanical properties of thin films using nanoindentation test”, Mech. Mater., vol. 38, pp. 1182-1198, 2006.

[7] W. S. Lee and F. J. Fong, “Microstructural study of annealed gold-silicon thin films under nanoindentation”, Mater. Sci. Eng. A, vol. 475, pp. 319-326, 2008.

[8] S. Ruffell, J. E. Bradby, and J. S. Williams, “Annealing kinetics of nanoindentation-induced polycrystalline high pressure phases in crystalline silicon”, Appl. Phys. Lett., vol. 90, 131901, 2007.

[9] W. C. Oliver and G. M. pharr, “Improved technique for determining hardness and elastic modulus using load and

displacement sensing indentation experiments", J. Mater. Res., vol. 7, pp. 1564-1580, 1992.

[10] V. Domnich, Y. Gogotsi, and S. Dub, "Effect of phase transformations on the shape of the unloading curve in the nanoindentation of silicon", Appl. Phys. Lett., vol. 76, pp. 2214-2216, 2000.

[11] J. Jang, M. J. Lance, S. Wen, T. Y. Tsui, and G. M. Pharr, "Indentation-induced phase transformations in silicon: influences of load, rate and indenter angle on the transformation behavior", Acta Mater., vol. 53, pp. 1759-1770, 2005.

[12] W. S. Lee and F. J. Fong, "Eutectic and amorphous phase formation at Au/Cr/Si thin film interface by nanoindentation and annealing", Mater. Trans., vol. 48, pp. 2650-2658, 2007.

Effect of Annealing Temperature on Nanoindented Microstructure of Cu/Si Thin Films

Woei-Shyan Lee [1,*], Tao-Hsing Chen[2] and Yu-Liang Chuang [1]

[1] Department of Mechanical Engineering, National Cheng Kung University, Tainan 701, Taiwan
[2] Center for Micro/Nano Science and Technology, National Cheng Kung University, Tainan 701, Taiwan

Abstract **—The nano-mechanical properties of as-deposited Cu/Si thin films indented to a depth of 2000 nm are investigated using a nanoindentation technique. The nanoindented specimens are annealed at a temperature of either 160℃ or 210℃, respectively. The microstructures of the as-deposited and annealed samples are then examined via transmission electron microscopy (TEM). The results show that both the loading and the unloading regions of the load-displacement curve are smooth and continuous. The hardness and Young's modulus of the Cu/Si thin films are found to vary with the nanoindentation depth, and have maximum values of 2.8 GPa and 143 GPa, respectively, at the maximum indentation depth of 2000 nm. In the case of the as-deposited specimens, the indentation pressure induces a completely amorphous phase within the indentation zone. For the specimens annealed at a temperature of 160℃, the amorphous nature of the microstructure within the indented zone is maintained. However, for the specimens annealed at a higher temperature of 210℃, the indentation affected zone consists of a mixture of amorphous phase and nanocrystalline phase. Copper silicide (η-Cu_3Si) precipitates are observed in all of the annealed specimens.**

Keywords ***—Naonindentation, Silicon, microstructural evolution, Annealing temperture***

I. INTRODUCTION

As micro-electro-mechanical systems (MEMS) techniques continue to mature, the fabrication of thin-film structures has become commonplace in the microelectronics and optoelectronics fields [1-3]. It is well known that the mechanical properties and microstructural characteristics of thin-film materials differ quite significantly from those of bulk materials, and generally vary in accordance with the fabrication process [4], the substrate effect [5, 6], the film thickness [7, 8], the interface structure [9, 10], and so on.

Amongst all the face-centered cubic (fcc) materials, copper (Cu) tends to be one of the most commonly used for the coating of silicon substrates in the fabrication of modern electronic devices dues to its high chemical stability, low resistivity, good patterning ability, good reliability, ready availability, and low cost [11, 12]. Various physical and chemical methods have been proposed for the fabrication of Cu/Si systems with coherent layers [13-16]. It is known that the bonding strength of the Cu/Si system is enhanced via the precipitation of copper silicide particles via a solid state reaction when the interface between the thin Cu film and the Si substrate is heated to a sufficient temperature. Accordingly, this study investigates the nano-mechanical properties of as-deposited Cu/Si samples indented to a depth of 2000 nm and then anneals the indented samples at temperatures of either 160℃ or 210℃, respectively. Thereafter, the microstructures of the as-deposited and annealed samples are examined via transmission electron microscopy (TEM) in order to examine the effects of the annealing temperature on the microstructural evolution of the indented specimens and the degree of copper silicide formation.

II. EXPERIMENTAL PROCEDURE

The Cu/Si thin-film specimens were fabricated by depositing a Cu film with a thickness of approximately 800 nm on a Si (100) substrate using an evaporation deposition technique. The nanoindentation tests were performed using an MTS Nanoindenter XP system fitted with a Berkovich diamond pyramid tip. The loading-unloading procedure involved the following steps: (1) impressing the indenter into the Cu/Si system until the position of maximum indentation was achieved (2000 nm); (2) holding the indenter in this position for 10 s; and (3) smoothly withdrawing the indenter from the specimen over a period of 30 s. The corresponding load-displacement data were then used to determine the hardness and Young's modulus of the Cu/Si thin film in accordance with the method proposed by Oliver and Pharr [17].

Following the nanoindentation tests, the specimens were annealed at a temperature of either 160℃ or 210℃ for 2 min in a rapid thermal annealing (RTA) system. Thin foil specimens

The authors gratefully acknowledge the financial support provided to this study by the National Science Council (NSC) of Taiwan under contract no. NSC 97-2221-E-006-047.

Contact author:wslee@mail.ncku.edu.tw***

of both the as-deposited samples and the annealed samples were prepared using an FEI Nova 200 focused ion beam (FIB) milling system with a Ga^+ ion beam and an operating voltage of 30 keV. The cross-sectional microstructures of the various specimens were then observed using a Philips Tecnai F30 Field Emission Gun Transmission Microscope operated at 300 keV.

III. Results and Discussion

Figure 1 presents the loading-unloading curve for the as-deposited Cu/Si thin film when indented to a depth of 2000 nm. It can be seen that both the loading and the unloading regions of the curve are smooth and continuous, which suggests that no debonding or cracking occurs during the indentation process. The slight elbow feature in the final portion of the unloading curve suggests that the silicon substrate transforms from a diamond cubic like structure to an amorphous structure in the indentation affected zone. Appling the Oliver and Pharr method to the experimental data presented in Fig. 1, it is found that both the hardness and the Young's modulus have maximum values of 2.8 GPa and 143 GPa, respectively, at the maximum indentation depth of 2000nm.

Figure 2 presents a cross-sectional TEM image of an as-deposited, indented specimen. The insets in the upper-right and upper-left corners of Figure 2 show the TEM diffraction patterns of the regions of the specimen indicated by the white squares A and B, respectively. The results show that in the as-deposited condition, the indentation affected zone of the Cu/Si system has an amorphous phrase, while the silicon substrate has a diamond cubic structure.

Figure 3 presents a TEM micrograph of the indented microstructure of a Cu/Si specimen annealed at a temperature of 160℃ for 2 min. It can be seen that following the annealing process, the microstructure of the indentation affected zone is still composed entirely of amorphous phase. Figure 4 presents a high-magnification TEM micrograph of the indentation affected zone and shows that the annealing temperature of 160℃ prompts the uniform precipitation of copper silicide (η-Cu_3Si) particles in the upper region of the indented zone (as indicated by arrow in Fig. 3). The lattice spacing of the η-Cu_3Si precipitates is found to be 2.01±0.02Å, which is in good agreement with the results reported by Bouayadi et al. [18], and is close to the value of the {110} plane spacing given in the literature (i.e. 2.02Å [19]).

Figure 5 presents TEM micrograph of the indentation affected zone in a specimen annealed at a higher temperature of 210℃. It is observed that the indentation affected zone has a mixed structure comprising amorphous phase, copper silicide η-Cu_3Si phase and nanocrystalline phase. Figure 6 presents a high-magnification TEM micrograph of the microstructure in the upper region of the indented zone (as indicated by arrow in Figure 5). The micrograph clearly shows the presence of copper silicide η-Cu_3Si precipitates within the indented region. From inspection, the η-Cu_3Si phases are found to have a lattice spacing of 2.01±0.02Å. Meanwhile, the Si matrix microstructure has a lattice spacing of 3.10±0.04Å, which is similar to that of a bulk Si (100) substrate (i.e. 3.129Å [20]).

IV. Conclusions

The results have shown that the loading and unloading regions of the load-displacement curves obtained in the nanoindentation tests have a smooth and continuous profile. Moreover, it has been shown that the present Cu/Si thin films have a maximum hardness and Young's modulus of 2.8 GPa and 143 GPa, respectively. The TEM observations have shown that for both the as-deposited specimens and the specimens annealed at a temperature of 160℃, the indentation process prompts a change in the microstructure within the indentation affected zone from a diamond cubic structure to an amorphous phase. However, at a higher annealing temperature of 210℃, the microstructure of the indentation affected zone contains a mixture of amorphous phase and nanocrystalline phase. The TEM observations have also shown that both annealed specimens contain copper silicide (η-Cu_3Si) phases. The density of these phases increases as the annealing temperature is increased.

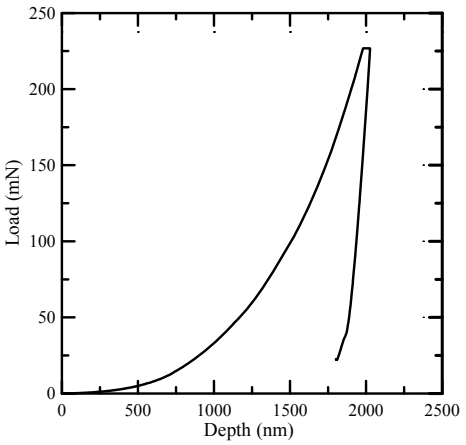

Figure 1. Typical load-displacement curve obtained in nanoindentation test performed to depth of 2000 nm

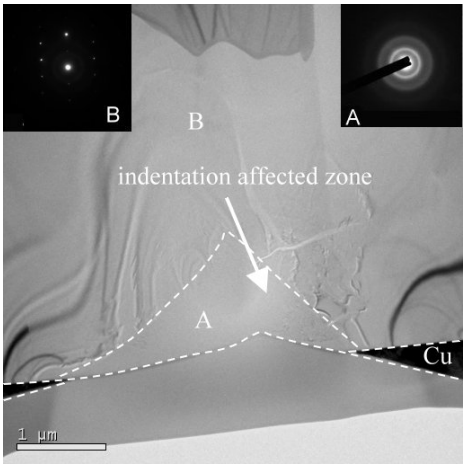

Figure 2. Bright field TEM micrograph of as-deposited indented specimen

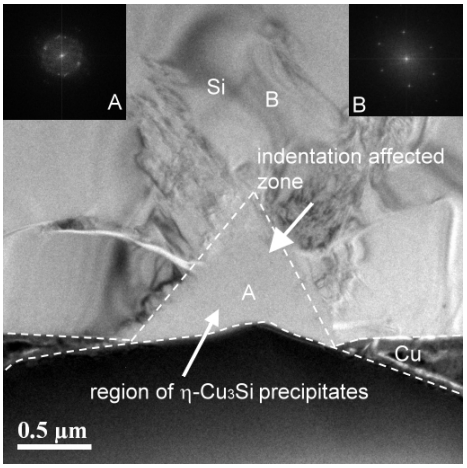

Figure 5 Bright field TEM micrograph of indented specimen annealed at 210℃

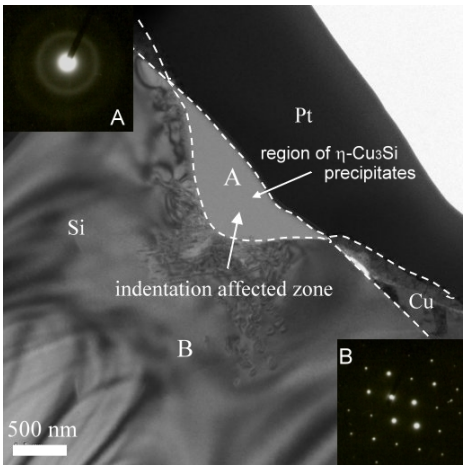

Figure 3. Bright field TEM micrograph of indented specimen annealed at 160℃

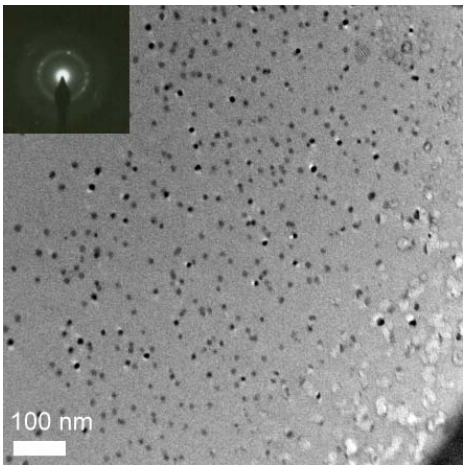

Figure 6. TEM micrograph of copper silicide η-Cu_3Si precipitates within indentation affected zone in specimen annealed at 210℃.

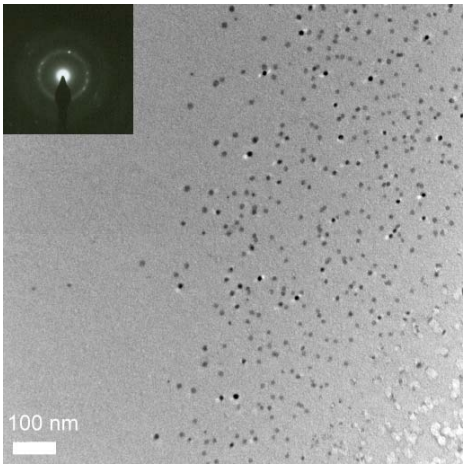

Figure 4. TEM micrograph of copper silicide η-Cu_3Si precipitates within indentation affected zone in specimen annealed at 160℃.

.

ACKNOWLEDGMENT

The authors gratefully acknowledge the financial support provided to this study by the National Science Council (NSC) of Taiwan under contract no. NSC 97-2221-E-006-047.

REFERENCES

[1] S. Majumder, N. E. McGruer, G. G. Adams, P. M. Zavracky, R. H. Morrison, and J. Krinm, "Study of contacts in an electrostatically actuated microswitch", Sens. Actuators A: Phys., vol. 93, pp. 19-26, 2001.

[2] Y. Cao, C. Kim, S. R. Forrest, and W. O. Soboyejo, "Effects of dust particles and layer properties on organic electronic devices fabricated by stamping", J. Appl. Phys., vol. 98, p. 033713-1, 2005.

[3] J. Plummer, M. Deal, and P. Griffin, Silicon VLSI Technology: Fundamental, Practice and Modeling, Prentice Hall, Upper Saddle River, NJ, 2000.

[4] M. Gadelkak, The MEMS Handbook, CRC Press, New York, 2002.

[5] T. H. Wang, T. H. Fang, and Y. C. Lin, "Analysis of the substrate effects of strain-hardening thin films on silicon under nanoindentation", Appl. Phys. A, vol. 86, pp. 335-341, 2007.

[6] R. Saha and W. D. Nix, "Effect of the substrate on the determination of thin film mechanical properties by nanoindentation", Acta Mater., vol. 50, pp. 23-38, 2002.

[7] S. H. Hong, K. S. Kim, Y. M. Kim, J. H. Hahn, C. S. Lee, and J. H. Park, "Characterization of elastic moduli of Cu thin films using nanoindentation technique", Composites Sci. and Technology, vol. 65, pp. 1401-1408, 2005.

[8] Y. Cao, S. Allameh, D. Nankivil, S. Sethiaraj, T. Otiti and W. Soboyejo, "Nanoindentation measurements of the mechanical properties of polycrystalline Au and Ag thin films on silicon Substrates: Effects of grain size and film thickness", Mater. Sci. Eng. A, vol. 427, pp. 232-240, 2006.

[9] P. S. Pizani, R. G. Jasinevicius, and A. R. Zanatta, "Effect of the initial structure of silicon surface on the generation of multiple structural phases by cyclic microindentation", Appl. Phys. Lett., vol. 89, 031917, 2006.

[10] W. S. Lee and F. J. Fong, "Eutectic and amorphous phase formation at Au/Cr/Si thin film interface by nanoindentation and annealing", Mater. Trans., vol. 48, pp. 2650-2658, 2007.

[11] A. Cros, M. O. Aboelfotoh, and K. N. Tu, "Formation, oxidation, electronic, and electrical properties of copper silicides", J. Appl. Phys. vol. 67, 3328, 1990.

[12] Ronald J. Gutmann, T. Paul Chow, Alain E. Kaloyeros, William A. Lanford, and Shyam P. Muraka, "Thermal stability of on-chip copper interconnect structures", vol. 262, pp. 177-186, 1995.

[13] M. Y. Park, J. H. Son, and S. W. Rhee, "chemical vapor deposition of copper thin films with (hexafluoroacetylacetonate) Cu (allyltrimethylsilane)", Electrochem. Solid State Lett., vol. 1, pp. 32-33, 1998.

[14] D. K. Kwak, H. B. Lee, J. W. Han, and S. W. Kang, "Metalorganic chemical vapor deposition of copper on ruthenium thin film", Electrochem. Solid State Lett., vol. 9, pp. C171-C173, 2006.

[15] O. Azzaroni, M. Fonticelli, P. L. Schilardi, G. Benitez, I. Caretti, J. M. Albella, R. Gago, L. Vazquez, and R. C. salvarezza, "Surface nano patterning of metal thin films by physical vapour deposition onto surface-modified silicon nanodots", Nanotechnology, vol. 15, S197-S200, 2004.

[16] M. F. sharin, A. Razak, and Z. Zainal, "Electrophoretic deposition and characterization of copper selenide thin films", The Malaysian Journal of Analytical Science, vol. 11, pp. 324-330, 2007.

[17] W. C. Oliver and G. M. Pharr, "Improved technique for determine hardness and elastic modulus using load and displacement sensing indentation experiments", J. Mater. Res., vol. 7, pp. 1564-1580, 1992.

[18] R. E. Bouayadi, G. Regula, B. Pichaud, M. Lancin, C. Dubois, and E. Ntsoenzok, "Gettering of diffused Au and of Cu and Ni contamination in silicon by cavities induced by high energy He implantation", Phys. Stat. Sol., vol. 222, pp. 319-326, 2000.

[19] J. Wang-Leung, E. Nygren, and J. S. Williams, "Gettering of Au to dislocations and cavities in silicon", Appl. Phys. Lett., vol. 67, pp. 416-418, 1995.

[20] D. Ge, V. Domnich, and Y. Gogotsi, "Thermal stability of metastable silicon phases produced by nanoindentation", J. Appl. Phys., vol. 95, pp. 2725-2731, 2004.

Design and Fabrication of a Three Modules Micro Smart qPCR System

Jian Qin [1], Hao Tian [2], Shilei Guo [3], Taihong Wang[1], Zewen Liu [3*]

[1]*School of Physics and Microelectronics Science, Hunan University, China*

[2]*School of Mechanical Engineering, Dalian University of Technology, China*

[3]*Institute of Microelectronics, Tsinghua University, China*

***Abstract* — A concept of three modules micro smart quantitative polymerase chain reaction (3M^{2}sqPCR) is proposed and designed. The main design philosophy is to meet the ever increasing challenge of low cost, light-weighted, portable and real-time sensitive detection PCR system. The system consists of three modules: the micro-heater module, the reaction cell module and the electrochemical detection module. Experiments have been done to test performance of each module of the prototyped device. The test results reveal that the modules are sensitive and reliable, so the total 3M^{2}sqPCR system is promising realized and suitable to perform further total analysis trials.**

*Keywords — **3M^{2}sqPCR, three-module, micro-heater, micro-eletrode, electrochemical, methylene blue***

I. INTRODUCTION

The concept of Micro-Total-Analysis-System (μ-TAS), also known as "lab-on-a-chip", was proposed in the early 1990s [1]. A lot of research groups who wishing to construct various analytical systems [1-6] have expended much effort on it. Besides the significant feature of miniaturization both in size and portability, integrated μ-TAS platforms have several remarkable advantages compared to conventional methods, such as low cost, high speed, enhanced sensitivity and automation of nearly all key processes ranging from sample preparation to outcome of analysis results [1].

The development of micro-analytical devices has brought revolutionary change to the field of deoxyribonucleic acid (DNA) assays [7]. DNA analysis techniques have become a significant set of tools for many important applications. Besides the frequent molecular diagnosis of diseases and assessments of therapies in clinics and hospitals, they are also broadly applied in environment surveillances, food processing industry, agricultural researches, and forensic identifications [8]. DNA amplification by the polymerase chain reaction (PCR) is an indispensable tool in routine DNA assays, particularly when rare targets are being tested. In order to improve the speed and efficiency of amplification, a lot of studies have been carried out by several groups to fabricate micro-PCR systems and have made significant achievements [9-12]. However, the current micro-PCR designs are mainly aimed on integration of all the devices including the heating, fluidic, and detection parts into a single chip. It brought problem that this single chip will be very complex and expensive, so it is very difficult to be used as a low cost dispensable device, and will limit its application in the large scales.

Besides, in the detection aspect, several methods could be introduced to detect the products of PCR. But the most common detection scheme nowadays is still based on fluorescence markers [13-15]. Although fluorescence-based detection technique is sensitive and reliable in traditional PCR, optical methods are very difficult to be miniaturized and integrated onto a microchip, because of the considerable size and complex composition of optical detection systems. Electrochemistry-based detection methods, on the other hand, could be used as an alternative method for portable instruments. Because compared to laser-induced fluorescence detection methods, electrochemical detection also have amount of advantages, such as excellent sensitivity and selectivity, inherent miniaturization and portability, the independence from the optical path length and sample turbidity, extremely low-cost, low-power requirements, especially the compatibility with micro fabrication technology, and so on[8, 16-18].

Several electrochemical methods could be introduced to detect the products of PCR. But most detection methods need to make asymmetric PCR and make chemical modification, which is complicated and frustrating to control [1]. Methylene blue (MB) which has been widely used as an electrochemical active intercalator of DNA can be utilized for electrochemical signal measurements in the presence of PCR reagent components. The electrochemical signal due to MB is attributed to the adsorption of phenothiazine ring of MB on bare electrode. But MB has different affinity for ssDNA (single-strand DNA) and dsDNA (double-strand DNA), and the MB molecules which intercalated into dsDNA will lose their electrochemical activity. As the PCR proceeds, MB molecules intercalate into the PCR amplified dsDNA, hence there is a reduction of free MB molecules in the PCR solution. As a result, the redox current of the free MB molecules decreases in proportion to the increase of PCR amplicons [8].

In this paper, a concept of 3M^{2}sqPCR system is proposed. The 3M^{2}sqPCR system is set up by clamshell aligned technique as shown in Figure1, which enables the integration of the three separated modules including heating, microfluidic and electrochemical detection modules to form a functional system. MCU (microcontroller unit) system is employed for the control of PCR reaction process, and PCR products analysis. And through the USB interface, test results are able to be uploaded to the computer to display in real-time. Note that the microfluidic module only consists of reaction cell array and mainly made of SU8. The manufacture of this module is simple

This project was funded by National Basic Research Program of China (973 Program, Grant No. 2007CB310500).

Contact author: for the design of this total system please contact* ***liuzw@tsinghua.edu.cn*

and can be produced in batches, so it could service as "disposable part", but the whole systems can be used repeatedly. In this way, the system could be made low cost, and avoiding the complexity for rinsing microfluidic systems.

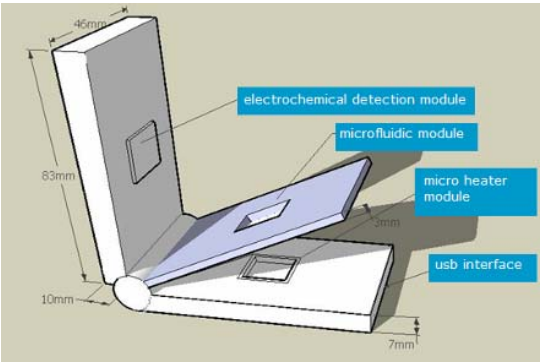

Figure1. Schematic design of the 3M^{2}sqPCR system

II. EXPERIMENTAL SECTION

A. *Device Design and Fabrication*

The micro system consists of three separated modules: the heating module, the microfluidic module and the electrochemical detection module, which all fabricated with MEMS (Microelectromechanical Systems) techniques.

The heating module consists of micro-heaters and RTD (Resistance Temperature Device) micro-sensors, which both fabricated on the silicon wafer substrate with 500nm-thick thermally oxidized silicon layer. Firstly, the wires which made of 80um-wide and 300nm-thick gold with 25nm-thick titanium as adhesion layer are fabricated on the substrate. Then, a 300nm-thick silicon dioxide layer is made using low-pressure chemical vapor deposition (LPCVD), coating on wires as an electric insulation layer between wires and micro-heaters. After fabrication, Pt/Ti (300/25nm thickness, 30um width) is used to build the micro-heaters and temperature micro-sensors, which connected with wires via through holes of silicon dioxide layer (as in Figure 4 (a)).

The microfluidic module which consists of reaction cell array is made of SU-8 material and about 100um thick. As SU-8 material is a kind of negative photoresist, we can make the advantage of it to fabricate by the method of lithography after spin coating and soft baking.

The detection module is an electrochemical (EC) three-electrode system. The electrodes are also fabricated on a silicon wafer covered with 500nm-thick thermally oxidized silicon layer. Au/Ti (300/25nm thickness) is used for the working electrode (WE) material, and Pt/Ti (300/25nm thickness) is used to fabricate the counter electrode (CE) and reference electrode (RE) (Figure2 (a)). A 3um-thick polydimethylsiloxane (PDMS) layer is covered on the surface with leaving the three-electrode exposed by the method of dry-etching [19] (Figure2 (b)), which insulates the wires of microelectrodes and makes the contact between detection module and microfluidic module airtight.

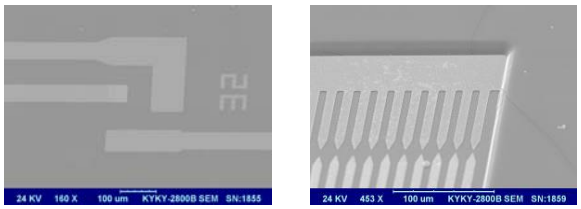

(a) (b)

Figure2. SEM images of the EC three-electrode system
(a) A group without PDMS. The one in the middle of the image is WE, the upper one is CE and another one is RE. (b) A group with PDMS. The brush structure electrode aims to investigate new methods for DNA detection, and the details are not described in this paper.

B. *Device Test*

It is of great importance that the performance of each module could reach the requirement. So calibration and performance tests are done to judge whether the each module fully matches the designed requirement.

In order to determine the real-time temperature of the micro-heater and the feedback performance of RTD micro-sensors, resistance calibration of the micro-sensor Pt wire is done in a furnace. The resistance of the Pt wire, which is measured and recorded by high precision intelligent digital multi-meter (UT71C, UNI-T) connected to a computer, is considered as the average temperature change of the micro-sensor and synchronizing with the change of internal environment temperature of the furnace. After the calibration, a series of experiments on the performances of the micro-heaters have proceed using an infrared camera (Fluke, Ti series) to pick up the real-time temperature (as in Figure4 (b)) of the micro-heaters under the condition of DC (direct current) 5 volt drive and an ambient temperature of 25℃.

In the test of electrochemical detection module performance, MB is utilized for investigating the sensitivity, reliability and repeatability of micro three-electrode systems. There is a MB sample (Sinopharm Chemical Reagent Co. Ltd.) in 0.10M PBS (phosphate buffer solution, PH 7.40) with the concentration of 80μM and the volume of 40μl dropped in the reservoir. And a group of three-electrode is connected to the electrochemical workstation (CHI660C, Shanghai Chenhua Corp.), which connected to a computer with the controlling software. Then, titrating experiments are made using DNA sample with the concentration of 116.5nM, and gives 2μl sample each time. At the same time, we detect the electrochemical signal of MB with the method of Differential Pulse Voltammetry (DPV) to examine the current response with the increasing of DNA concentration in the solution, and the scanning range is from 0V to -0.30V with amplitude of 0.05V. The DNA sample (A1-9176HA) is provided by Institute of Microbiology Chinese Academy of Science, and the concentration of it is 97.5ng/μl and the strand is about 1300 base pairs.

III. RESULTS AND DISCUSSION

As have done some experiments to examine each module, and we get some results reflecting to the performance of the device.

From the scanning electron microscope (SEM) picture (Figure4(a)) of the microfluidic module, we can see that the SU-8 layer, which made through lithography method and used for PCR reaction chamber, has very good depth-width ratio and sealing quality when it contacts with the heating module.

A. The Test Result of Microheaters

The precision and sensitivity of the temperature control of the PCR reaction chamber is chiefly dependent on the accuracy in establishing the sensor's resistance-temperature correlation curve:

$$R = R_0(1 + \alpha(T - T_0))$$

Where R and R_0 are resistances of the temperature sensor at temperature T and T_0 (reference temperature), and α is the temperature coefficient of resistance (TCR) [20]. This equation sets up connections between the voltage reading (from the signal conditioning board that provides a constant excited current of 1mA to the temperature sensors it connected to) and the temperature reading [7].

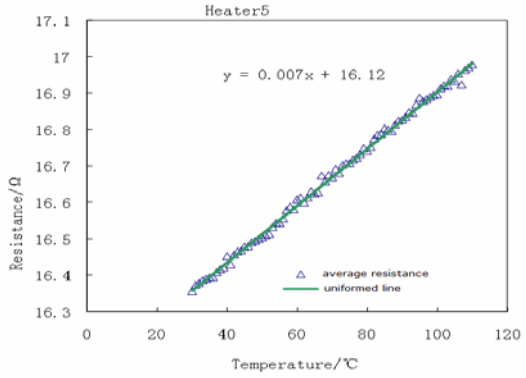

Figure3. Resistance change as a function of temperature for sensor

Dozens of experiments have been done under the condition of previously discussed (in chapter II) and the temperature-resistance curve of the sensor can be obtained (as in Figure 3). From the fitted curve of the line, we can see that the resistance has a relatively linear relationship with the temperature ranging from 20℃ to 120℃. The slope of this line is 0.007, which means that the resulted TCR of this sensor is 7 $\times 10^{-3}$℃$^{-1}$. Thus, with a well-calibrated temperature sensor, we can precisely control the real-time temperature of heaters through MCU by inputting desired impulse current power quantitatively.

In order to examine the performance of micro-heaters, we drop one drop of water (about 50μl) on the heater unit which connected to a DC voltage source, and then heat under the voltage of 5V. At the same time, we examine and record the heat distribution of the water using an infrared camera. We can see from the infrared picture (Figure4(b)) taken at the interval of one second that the heat is well-distributed in the drop of water and the heating rate and cooling rate of the heater are both at approximately 1℃/s (as in Figure 5).

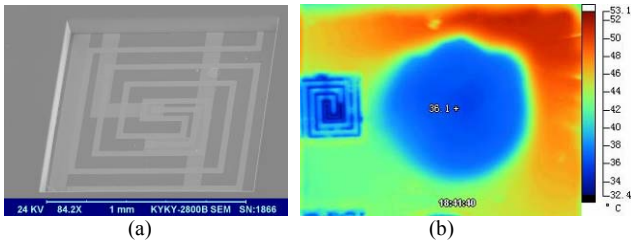

(a) (b)

Figure4. (a) SEM picture of a single micro heater unit (b) an infrared picture of a single micro heater unit with a water drop, the heater is connected to a DC volt source for 1 sec@5V

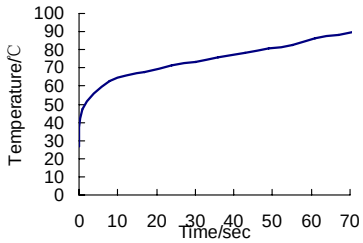

Figure5. Schematic for heater No.5 on temperature change in accordance with time @ DC 5V

B. The Test Result of Microelectrodes

Series of electrochemical experiments have proceeded to investigate the performance of micro-electrodes.

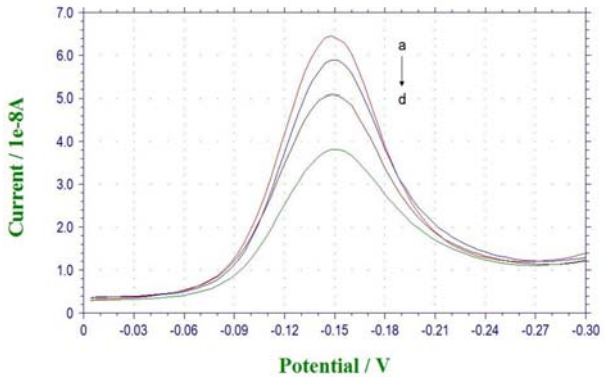

Figure6. Differential pulse voltammetries of 80μM MB titrated with different volumes of 116.5nM A1-9176HA DNA sample. DNA sample volume: (a) 2μl; (b) 4μl; (c) 8μl; (d) 16μl. Differential pulse voltammetries are collected from 0V to -0.30V with amplitude of 5mV.

The curves of a, b, c, d in figure 6 are obtained under the same experimental condition but titrated by DNA sample with different volumes of 2μl, 4μl, 8μl, 16μl, respectively. And the concentrations of DNA sample that we used are the same. The amount of DNA added into the detection system is double than the one previously aims to simulate the initial condition before PCR, in this way it could simulate the amount of DNA that doubles after one cycle. From the differential pulse voltammetries, it can be observed that the peak current (Ip) decrease proportionally with the increase of DNA sample solution. The difference value ΔIp(d-c) is almost two times of ΔIp(c-b), and the situation is same for the relationship between

ΔIp(c-b) and ΔIp(b-a). This well-match along with the amount relation between two adjacent times that DNA sample was added into detection system.

The curve in figure 7 demonstrates the relationship (in fitting curve) between peak current and DNA concentration, and the experimental data of which is collected from the values in figure 6 and the repeated experiments under the same condition (note that the values have taken the influence of volume changing into account). The current response shows excellent correlation with the target DNA concentration ranging from 1×10^{-9} M to 3×10^{-8} M. The equation of this fitting curve is Ip (nA) = 60.76 − 0.89C (nM) (r =−0.9977). A detection limit of 6.9×10^{-10} M for the target DNA can be estimated using 3σ (where σ is the standard deviation of the blank solution, n=12). Considering the extremely small surface area of working electrode ($3\times10^{-9}m^2$), the sensitivity of the detection module is very excellent.

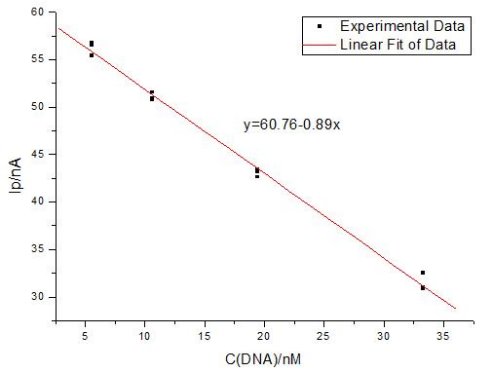

Figure7. The relationship of peak current Ip (nA) and DNA sample concentration C (DNA) (nM).

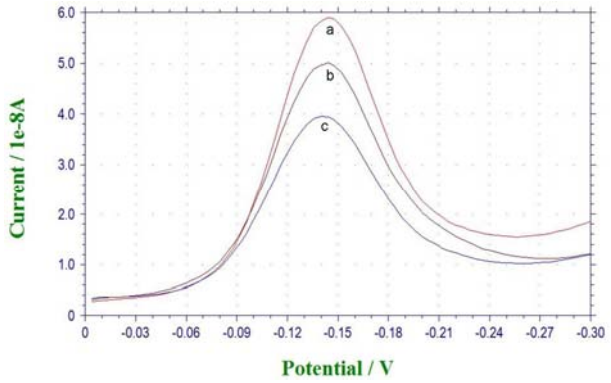

Figure8. Differential pulse voltammetries of 80μM MB solution and the MB solutions added same volume deionized water and DNA sample. (a) 40μl MB solution added nothing; (b) 40μl MB solution added 16μl deionized water; (c) 40μl MB solution added 16μl DNA sample. Differential pulse voltammetries are collected from 0V to -0.30V with amplitude of 5mV.

In order to exclude the influence of volume changing, which brings from adding DNA solution sample into the detecting solution, another group of experiments have been done in a way that add the same volumes of deionized water without DNA into the detecting solution under the same condition of DNA titrating experiments. The curve (a) in figure 8 is obtained without adding anything into the detecting solution and the curve (b) and (c) is obtained from adding 16μl deionized water and 16μl DNA solution respectively, which selected as a contrast example. From the comparison of curve (a) and curve (b), we can see that the dilution influence of adding 16μl deionized water into 40μl solution cannot be ignored, but it can neither cover up the role of DNA when we consider curve (c) in the figure. Consequently we know that DNA plays a major role in reducing the concentration of MB solution through absorption.

IV. CONCLUSION

Using the MEMS technologies, a $3M^2$sqPCR system is designed and fabricated, and the performance of each module is tested. The micro-heater performance of the heating module has reached the requirement of PCR, and the TCR could be used as an indicator of the heater's temperature. The microelectrodes of electrochemical detection module are also tested and the results show that they could be used to measure the PCR product with the MB method. Combining with the controlling circuit，a low cost, light-weighted, portable and real-time detection smart quantitative PCR can be further realized based on the three modules.

ACKNOWLEDGMENT

This work was jointly supported by the National Basic Research Program of China (973 Program, Grant No. 2007CB310500). And the authors also express gratitude to George Fu Gao's group in Institute of Microbiology Chinese Academy of Science for providing DNA samples.

REFERENCES

[1] L. Chen, A. Manza and P. J. R. Day, "Total nucleic acid analysis integrated on microfluidic devices," Lab on a Chip, vol. 7, pp. 1413–1423, August 2007.

[2] D. R. Reyes, D. Lossifidis, P. A. Auroux, and A. Manz, "Micro total analysis systems. 1. introduction, theory, and technology," Anal. Chem, vol. 74, pp. 2623–2636, June 2002.

[3] P. A. Auroux, D. Lossifidis, D. R. Reyes and A. Manz, "Micro total analysis systems. 2. analytical standard operations and applications," Anal. Chem, vol. 74, pp. 2637–2652, June 2002.

[4] T. Vilkner, D. Janasek and A. Manz, "Micro total analysis systems. Recent development," Anal. Chem, vol. 76, pp. 3373–3386, June 2004.

[5] P. S. Dittrich, K. Tachikawa and A. Manz, "Micro total analysis systems. Latest advancements and trends," Anal. Chem, vol. 78, pp. 3887–3907, June 2006.

[6] K. M. Horsman, J. M. Bienvenue, K. R. Blasier and J. P. Landers, "Forensic DNA analysis on microfluidic divices: a review," J. Forensic Sci., vol. 52, pp. 784–799, June 2007.

[7] T. M. Lee, M. C. Carles and I. M. Hsing, "Microfabricated PCR-electrochemical device for simultaneous DNA amplification and detection," Lab on a Chip, vol. 3, pp. 100–105, April 2003.

[8] T. H. Fang, N. Ramalingam, X. D. Dong, T. S. Ngin, X. Zeng, H. Q. Gong, et al., "Real-time PCR microfluidic devices with concurrent electrochemical detection," Biosensors and Bioelectronics, vol. 24, pp. 2131–2136, November 2008.

[9] M. A. Northrup, "A miniature analytical instrument for nucleic acids based on micromachined silicon reaction chambers," Anal. Chem, vol. 70, pp. 918–922, March 1998.

[10] M. U. Kopp, A. J. de Mello and A Manz, "Chemical amplification: continuous-flow PCR on a chip," Science, vol. 280, pp. 1046–1048, May 1998.

[11] C. Zhang, J. Xu, W. Ma and W. Zheng, "PCR microfluidic devices for DNA amplification," Biotechnology Advances, vol. 24, pp. 243-284, December 2006.

[12] C. Zhang, D. Xing and Y. Li, "Micropumps, microvalves, and micromixers within PCR microfluidic chips: advances and trends," Biotechnology Advances, vol. 25, pp. 483-514, May 2007.

[13] L. Chen, J. West, P. A. Auroux, A. Manz and P. J. R. Day, "Ultrasensitive PCR and real-time detection from human genomic samples using a bidirectional flow microreactor," Anal. Chem, vol. 79, pp. 9185–9190, December 2007.

[14] T. C. Chao, and A. Ros, "Microfluidic single-cell analysis of intracellular compounds," J. R. Soc. Interface, vol. 5, pp. S139-S150, August 2008.

[15] G. V. Kaigala, V. N. Hoang, A. Stickel, J. Lauzon, D. Manage, L. M. Pilarski and C. J. Backhouse, "An inexpensive and portable microchip-based platform for integrated RT-PCR and capillary electrophoresis," Analyst, vol. 133, pp. 331–338, January 2008.

[16] A. Sassolas, B. D. Leca-Bouvier, and L. J. Blum, "DNA biosensors and microarrays," Chem. Rev, vol. 108, pp. 109–139, December 2008.

[17] F. R. R. Teles, and L. P. Fonseca, "Trends in DNA biosensors," Talanta, vol. 77, pp. 606-623, July 2008.

[18] A. E. Muniz, A. Ambrosi and A. Merkoci, "Electrochemical analysis with nanoparticle-based biosystems," Trends in Analytical Chemistry, vol. 27, pp. 568-584, May 2008.

[19] J. Garra, T. Long, J. Currie, T. Schneider, R. White and M. Paranjape, "Dry etching of polydimethylsiloxane for microfluidic systems," J. Vac. Sci. Technol. A, vol. 20, pp. 975-982, May/June 2002.

[20] J. F. Creemer, D. Briand, H.W. Zandbergen, W.van der Vlist, C.R.de Boer, N.F.de Rooij and P.M.Sarro, "Microhotplates with TiN heaters," *Sensors and Actuators A: Physical*, vol. 148, pp. 416-421, 2008.

Investigation on High-temperature Decomposition Characteristic of Hydroxyapatite

Chunyan Wang[1,*] , Renfu Quan[2], Hongbin Wang[1], Xicheng Wei[1], Zhijun Zhao[1]

[1]*School of Materials Science and Engineering, Shanghai University, Shanghai 200072, China*

[2] *Department of Orthopaedics, Xiaoshan Traditional Chinese Medical Hospital, Hangzhou, Zhejiang 311201, China*

Abstract **— Hydroxyapatite (HA) has been widely used in clinical field because of its excellent biocompatibility. However, its poor thermal stability limits its application. In present paper, the decomposition characteristics of both nano-sized HA powder prepared by precipitation method and its sinters at the temperature from room temperature to 1500 ℃ in the air were studied. X-ray diffractometer (XRD), High-temperature Raman spectroscopy, High-temperature differential scanning calorimeter (DSC) and Cell culture work were used to investigate their decomposition characteristics. The results show that HA gradually releases its OH^- ions from 1000 ℃ and decomposes into β-tricalcium phosphate (TCP) and tetracalcium phosphate (TTCP) when the heating temperature is higher than 1350℃. β-TCP changes into α-TCP at about 1450 ℃, which remains until the sinter cools to the room temperature. The decomposed sinter reconstitutes to HA again under a slow cooling rate and in a specific atmosphere. The osteoblast on the surface of decomposed sinter is less than that on the undecomposed one.**

Keywords **—** Hydroxyapatite; sinter; decomposition; high-temperature

1. Introduction

Hydroxyapatite (HA, $Ca_{10}(PO_4)_6(OH)_2$) is the main mineral constituent of human bone. It has been developed and made available for experimental or clinical application because of its excellent biocompatibility, faster bone regeneration and direct bonding to regenerated bone without intermediate connective tissue [1-3]. However, the thermal stability and mechanical properties of HA are not ideal [4,5]. In order to improve its mechanical properties, many researchers have developed HA surface coatings by spraying and composite materials. However, the preparing temperature of these materials is usually higher than the decomposition temperature of HA. Wen et al. deposited HA coatings by plasma spray techniques and found it transforms to tricalcium phosphate ($Ca_3(PO_4)_2$, TCP) and oxyhydroxyapatite ($Ca_{10}(PO_4)_6(OH)_{2-x}O_x\square_x$, OHA) [6]. Li et al. reported that the temperature attained by HA powders during the plasma spraying was up to 2850 ℃ [7]. Zhang et al. used pressure-less sintering method and prepared the ZrO_2/HA composite ceramics at 1600℃ and the decomposition phase on the surface was TCP and tetracalcium phosphate ($Ca_4P_2O_9$, TTCP) [8]. The decomposition of HA at high temperature have restricted the large scale applications of the HA coatings or composite materials prepared by the above method.

Therefore, to investigate the decomposition characteristics of HA becomes a meaningful work. Also, it can lay a foundation for the reconstruction study later. Liao et al studied the thermal decomposition and reconstitution of hydroxyapatite powder and found the decomposition temperature of HA powder [9]. Also, the reconstitution behavior of the quenched HA powder was studied by Lin et al [10]. They found that the quenched HA powder could be partly transformed to HA in the air again. According to the above study, few researchers have studied the decomposition of the HA block and sinters and their differences from HA powder. In this paper, the difference of them will be preliminary studied to introduce the preparing techniques of HA block and its composition and to promote the application of HA.

2. Materials and Preparing Methods

$Ca(NO_3)_2{\cdot}4H_2O$ and $(NH_4)_3PO_4{\cdot}3H_2O$, as raw materials, were used to prepare nano-HA powder by the method of

This project was funded by the High-land Project of Shanghai Education Commission, the Ministry of Education and the Ministry of Finance

Contact author: **wcy@shu.edu.cn*

precipitation [11]. Fig. 1 (a) shows that the HA powder with less than 100 nm in length is rod-shaped under a high resolution transmission electron microscope (JEM-2010F, TEM). No clear conglobation can be seen. Nano-HA power was drying for least 3 hours at 110 ℃ in the DHG-9070 drying cabinet before used.

The HA block was pressed by employing the CMT-530 type universal tester under the pressure of 100 MPa and at room temperature. The loading speed rate was 200N/s. The specimen was kept for 180 s under the maximum pressure. And then, the block was put into YFA12/16G-Y chamber electric resistance furnace and sintered at different temperatures in the air. Fig. 1 (b) shows the HA block and its sinter. The diameter of the HA block is 18.9 mm and it shrinked to 13.4 mm after sintered. The shrinkage rate was about 29 %.

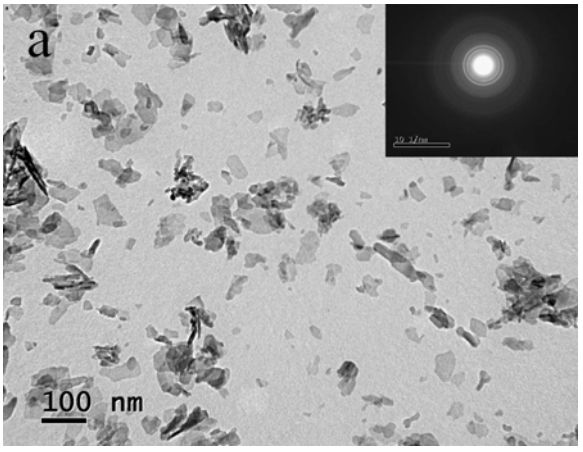

Fig.1 (a) TEM micrograph and diffraction pattern of HA powder; (b) HA block(left) and sinter(right)

D\max-2550 X-ray diffractometer (XRD) with CuKα radiation was used to detect the crystalline structure of HA power and its sinters. The range of scanning angle was from 20° to 40° with a speed of 4°/min. The Raman spectrum at 400℃, 700℃, 750℃, 800℃, 900℃, 1000℃, 1100℃, 1200℃, 1300℃, 1350℃ was recorded using HR LabRAM800 high temperature Raman spectroscopy to evaluate the functional group of HA. NETZSCH DSC 404C High Temperature Differential Scanning Calorimeter (DSC) was used to study the thermal behavior of HA. The scanning temperature was from room temperature up to 1550° with a heating rate of 10°/min and the gas flow rate of 50 ml/min. The undecomposed and decomposed HA blocks prepared according to above preparing methods were used for the cell culture work. After tested, those samples were cut into flake which was observed to identify the typical osteoblast on the different kind of sinters under Cambridge Stereoscan 260.

3. Results and discussion

3.1. X-ray diffraction

Fig. 2 shows the XRD patterns of nano-HA powder and its sinters at different temperatures. The peaks of the original HA powder was not clear. However, with the increase of temperature, the nano-HA powder crystallized better [12]. It can be easily found that the powder heated at 1300℃ was also HA structure. A little β-TCP was found in the pattern, which was the impurity from the preparing process. A departure of the peaks can be seen from the XRD patterns of the powder and the sinter which were sintered at 1300℃. This may be caused by the preparing pressure during the block forming process. The possible reason was that the crystal structure of HA was distorted under the high pressure, which directly caused the departure of their diffraction peaks.

According to the chemical equation：

$$Ca_{10}(PO_4)_6(OH)_2 \rightarrow 2Ca_3(PO_4)_2+Ca_4P_2O_9+H_2O \quad (1)$$

The decomposition product of HA should be TCP, TTCP and H_2O. The peaks of the sinter at 1500℃ show that there are no HA anymore. Contrasted with the JCPDS 09-0348 and 11-0232, the products were actually α-TCP and TTCP. No other calcium phosphate phases were found in the XRD pattern. The result fits the chemical equation.

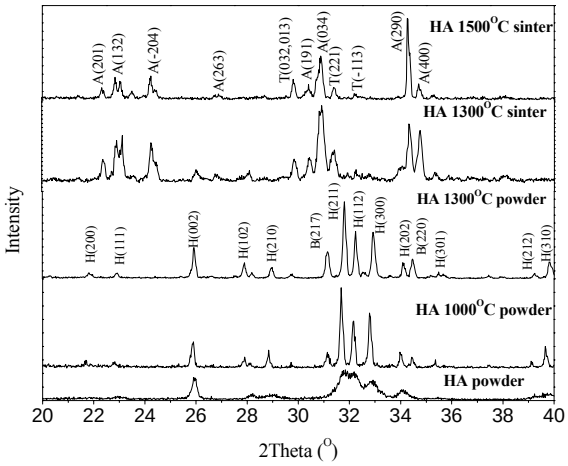

Fig.2. XRD pattern of nano-HA powder and sinters after heated at different temperatures (A: α-TCP, B:β-TCP, T: TTCP, H: HA)

3.2. Raman spectra

Fig. 3 is the Raman spectrum of HA from room temperature to 1350℃. The mode of the band at 433.7 cm^{-1} in Fig 3 (a) was associated to the vibration assigned to ν_2 (O-P-O). The mode ν_4 (O-P-O) was shown at the band of 593.5 cm^{-1}. The mode ν_1 (O-P-O), the shoulder at 962.5 cm^{-1}, was very intense and it was the characteristic vibration of HA [13]. The band at 1047.2 cm^{-1} was associated to vibration ν_3 (P-O). Contrasted with the Raman modes of HA and commercial HA showed in Table 1, the location of the HA shoulder in this study was correct. The shoulders normally shifted to left with a right proportion. Upon heat treatment from 400℃ to 1000℃, the bands of the respective vibration modes were narrowed, with an increased intensity. Combined with the results of XRD, the increment can be explained by the crystallization process. The destroyed atom long-range ordering led the weakened peaks from 1000℃ to 1350℃, which registered as the decrease of the intensity and the stretch of the shoulder.

In Fig. 3 (b), the mode at 3569.4 cm-1 was associated to vibration assigned to OH-. The shoulder regularly disappeared after 1000℃ [9]. It was reported that the decomposition temperature of HA was usually higher than 1000 ℃, especially the HA prepared by the method of precipitation, was 1300-1400℃ [12]. As shown in Fig. 3 (a), the HA structure remained until 1350℃. It has been reported by Liao et al. [9], the decomposition temperature of the HA prepared by the method of precipitation was 1360℃. HA didn't dehydrate completely before decomposition. It was also reported that HA gradually released its OH^- at 1000℃ and transformed to OHA. However, it is difficult to observe HA transform to OHA because OHA originates from HA. Their

Table I. Raman modes of HA and α-TCP

	HA[13-15]	HA-COM[13-14]	α-TCP[16-17]
ν_2（O-P-O）	432, 447	432, 445	420
ν_4（O-P-O）	580, 593, 608	577, 590, 608	567
ν_1（P-O-P）	948, 962	959	938
ν_3（P-O）	1028,1053,1061, 1075	1029,1046, 1072	1017
OH^-	3571	3571	

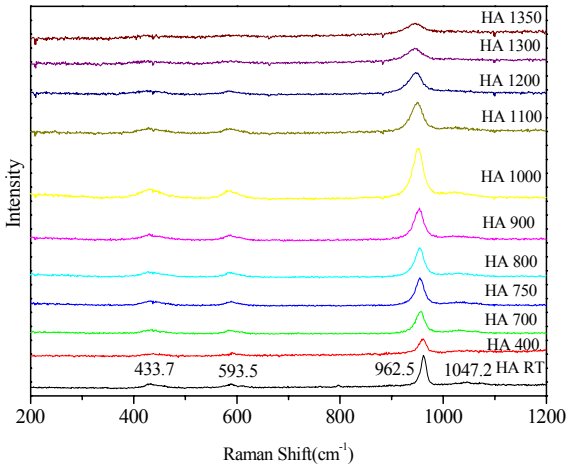

(a) Low wave number

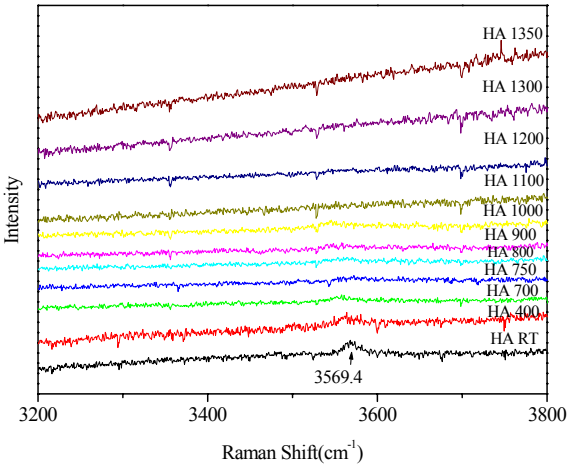

(b) High wave number

Fig.3 Raman spectra of HA samples at different temperatures

characteristic modes overlap one another. So is the XRD pattern.

HA gradually dehydrates, which lead to the release of OH^- ion. The HA dehydration does not occur instantly but over a wide temperature range, which has been reported to mainly depend on the partial H_2O pressure during heating [18]. HA loses its OH^- ion at a lower temperature, about 850℃, in vacuum. If HA is heated in a H_2O stream, the structure of HA preserved up to 1100℃. The HA with a lower cooling rate, such as cooling in the furnace, may reconstitute in air atmosphere [19].

TTCP and TCP converted to HA by a series of hydrolytic reactions:

$$3Ca_4P_2O_9 + 3H_2O \rightarrow Ca_{10}(PO_4)_6(OH)_2 + 2Ca(OH)_2 \quad (2)$$

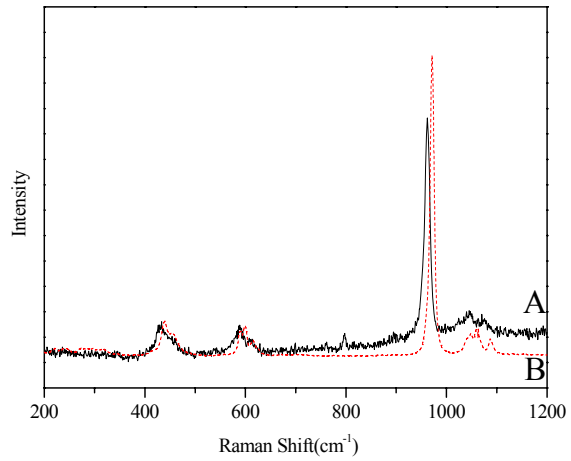

(a) Low wave number

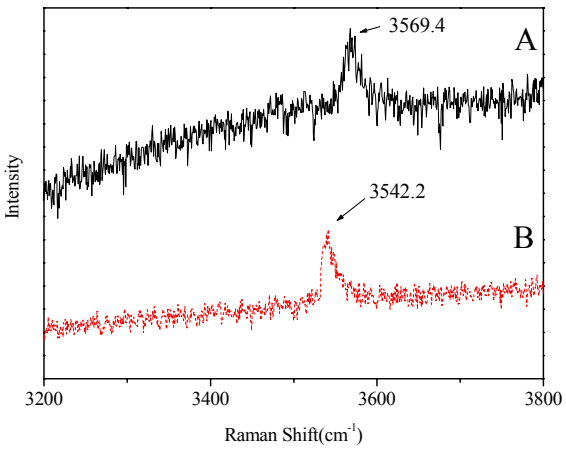

(b) High wave number

Fig 4 Raman spectra of HA(A: room temperature; B: cooled from 1500℃

and

$$10Ca_3(PO_4)_3 + 6H_2O \rightarrow 3Ca_{10}(PO_4)_6(OH)_2 + 2H_3PO_4 \quad (3)$$

and

$$3Ca_3(PO_4)_2 + Ca(OH)_2 \rightarrow Ca_{10}(PO_4)_6(OH)_2 \quad (4)$$

For the HA which cooled to the room temperature in the furnace, the intensity of the peaks changed because of its reconstitution. A little excursion of the main peak can be seen in Fig. 4 (a), and the intensity was higher than the one at room temperature. The OH^- ion which disappeared after heated at more than 1000℃ appeared again, with some excursion and low intensity. As we can seen in Table I, despite the little deviation of the modes, the OH^- ion is the obvious difference between of HA and TCP. The existence of the OH^- ion at 3542.2 cm^{-1} proved the reconstitution of HA under the condition of slow cooling.

3.3. Differential scanning calorimetry

Fig. 5 is the DSC curve of HA. The different peaks can be seen from Fig 5. As known，there are two kinds of water in HA structure which was prepared by the method of precipitation，the absorbed and crystallization water. The absorbed water was lost at the temperature of 50℃-200℃. Then, between 200℃-400℃, the loss of crystallization water happened. The exothermic peak at about 720℃ and 901℃ may be caused by the crystallization process [12, 20].

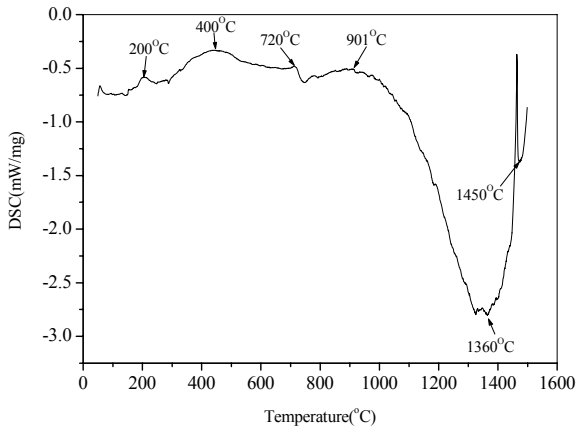

Fig 5 DSC curve of HA

The huge endothermic peak explained the loss of OH^- ion and the decomposition of HA. It is believed when the

endothermic peak reached the maximum at the temperature of 1360℃, HA dehydrates completely and really decomposes. The crystal phase transformation from β-TCP into α-TCP caused the last peak at about 1450℃ [12]. The higher decomposition temperature may delay the crystal phase transformation .The results of XRD and Raman have also been well proved by the DSC curve.

3.4. The cell culture work

The typical SEM osteoblast micrographs on the surface of different sinters are exhibited in Fig. 6. The red region in Fig. 6 is the osteoblast. It was found that the cells had attached on the sample surface after cell culture. As can been seen in Fig. 6 (a), for the undecomposed HA sinter, the osteoblast developed around the HA well. However, Fig. 6 (b) shows that there was a small quantity of osteoblast on the surface of decomposed HA sinters. The decomposition of HA reduced the cellular activity.

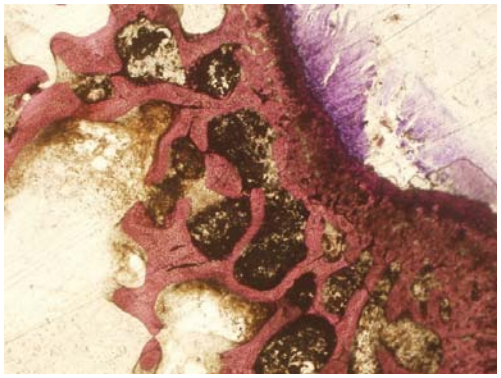

(a) undecomposed HA sinter

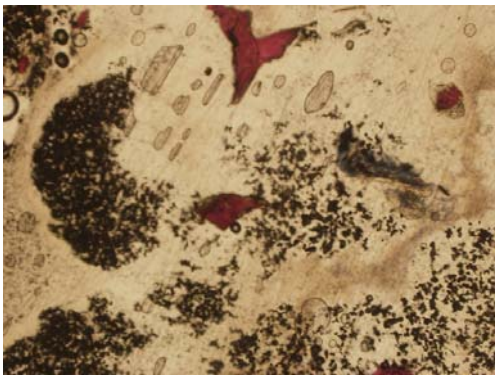

(b) decomposed HA sinter

Fig.6 The Cell Culture work on the undecomposed and decomposed HA sinters

Obviously, it is the HA sinter as bone substitute materials, not powder. The present research on the decomposition and reconstitution of HA and its sinter was not enough. How to reconstitute the HA sinters becomes the key problem to enhance the proliferation and differentiation of osteoblast. We have already done some study on it and got some results. It will be reported later.

4. Conclusions

On the basis of the study on the decomposition characteristics of both nano-sized HA powder and its sinters, The conclusions can be obtained as follows:

(1) HA gradually releases its OH^- ions from 1000 ℃ and decomposes into β-TCP and TTCP when the heating temperature higher than 1350℃.

(2) At about 1450℃, β-TCP changes into α-TCP which remains until the sinter cools to the room temperature.

(3) When the HA sinter slowly cools to room temperature under a suitable atmosphere, the decomposed HA reconstitutes to HA.

(4) The decomposition of HA due to high temperature deteriorates its biocompatibility.

Acknowledgment

This work was partly supported by the highland projects of Shanghai Education Commission, the Ministry of Education and the Ministry of Finance.

References

[1] M. Jarcho, “Calcium phospahte ceramics as hard tissue prosthetics,” *Clin. Orthop Rel. Res.*, 1981, pp. 259-278.

[2] H. Aoki, “Medical Application of Hydroxayapatite,” *Ishiyaku Euro America Inc.*, St. Louis:Takayama Press, 1994.

[3] K. de Groot, “Bioceramics of Calcium Phospahte,” *CRC Press*, 1993.

[4] C. F. Li, “Crystalline behaviors of hydroxyapatite in the neutralized reaction with different citrate additions,” *Powder Technol.* 2009, pp.1-5.

[5] M.H. Fathi, and E. Mohammadi Zahrani, “Fabrication and Characterization of fluoridated hydroxyapatite nanopowders via mechanical alloying,” *J. Alloys Compd.*, 2009, pp.408-414.

[6] J. Wen, Y. Leng, J. Y. Chen, and C. G. Zhang, "Chemical gradient in plasma-sprayed HA coatings," *Biomaterials*, 2000, pp. 1339-1343.

[7] G.M. Wu, W.D. Hsiao, and S.F. Kung, "Investigation of hydroxyapatite coated polyether ether ketone composites by gas plasma sprays," *Surf. Coat. Technol.*, 2009, pp. 2755-2758.

[8] M. Zhang, H. B. Wang, R. F. Quan, and X. C. Wu, "Preparation and biocompatibility of hydroxylapatite-zirconia biocomposite," *Acta Mater. Compos. Sinica*, 2006, pp. 115-121.

[9] C. J. Liao, F. H. Lin, K. S. Chen, and J. S. Sun, "Thermal Decomposition and Reconstitution of Hydroxyapatite in Air Atmosphere," *Biomaterials*, 1999, pp. 1807-1813

[10] F. H. Lin, C. J. Liao, K. S. Chen, and J. S. Sun, "Thermal reconstruction behavior of the quenched hydroxyapatite powder during reheating in air," *Mater. Sci. Eng. C*, 2000, pp.97-104

[11] X. J. Wang, and Y. B. Li, "Study on Bionic Composite of Nano-HA Needle-like Crystals and Polyamide," *High Tech. Lett.*, 2001, pp.1-5.

[12] Y.J. Song, S. L. Wen, M. S. Li, Q. C. Su, Qinghui Jiang, "Preparationg and Physicochemical Process of Nanosized Hydroxyapatite Powders with High Purity," *J. Inorg. Mater.*, 2002, pp. 985-991.

[13] A. F. L. Almeida, P.B.A. Fechine, J.M. Sasaki, A.P. Ayala, J.C. Goes, D. L.Pontes, and et al., "Optical and electrical properties of barium titanate-hydroxyapatite composite screen-printed thick films," *Solid State Sci.*, 2004, pp. 267-278.

[14] C.C. Silva, A.G. Pinheiro, M.A.R. Miranda, J.C. Goes, and A.S.B. Somra, "Structural properties of hydroxyapatite otained by mechanosynthesis," *Solid State Sci.*, 2005, pp.553-558.

[15] J.L. Xu, and K.A. Khor, "Chemical analysis of silica doped hydroxyapatite iomaterials consolidated by a spark plasma sintering method", *J. Inorg. Biochem.*, 2007, pp.187-195.

[16] H. Li, B.S. Ng, K.A. Khor, P. Cheang, and T.W. Clyne, "Raman spectroscopy determination of phases within thermal sprayed hydroxyapatite splats and subsequent in vitro dissolution examination," *Acta Mater.*, 2004, pp. 445-453.

[17] L. J. Ruan, and X. R. Wang. "Raman Spectra Study of $\alpha_L \leftrightharpoons \alpha$ Phase Transition in the Trocalcium Phosphate $Ca_3(PO_4)_2$," *J. WH Uni. Technol.*, 1993, pp.38-41

[18] B. Locardi, U. E. Pazzaglia, C. Gabbi, and B. Profilo. "Thermal behaviour of hydroxyapatite intended for medical applications," *Biomaterials*, 1993, pp.437-41

[19] P. Ducheyne, and G. W. Hastings. "Metal ceramic biomaterials", vol. II: strength and surface. *Boca Raton, FL: CRC Press*, 1984.

[20] D.P. Wang, L. Wang, and W. H. Huang, "Effect of PH Value on Nanosized Hydroxyapatite Synthesized through Precipitation Process," *J. TJ Uni. (Natural Science)*, 2005, pp. 93-98

Microfabrication of Asymmetric Planar Electrodes for Long-term Glucose Monitoring

Chih-Hsiu Yin[1], Shaw-Hwa Parng[1]*, Jui-Tse Chen[1], Kun-Feng Lee[1], Chu-Hsuan Chen[1], Tsung-Che Chou[2], Yun-Ju Chuang[2], Horn-Chin Lee[2], and Yuh-Jiuan Lin[1]

[1]*Medical Electronics and Device Technology Center, Industrial Technology Research Institute, Taiwan.*
[2]*Micro-System Technology Center, Industrial Technology Research Institute, Taiwan.*

***Abstract* — In the present study, we proposed a design of asymmetric planar electrodes for long-term monitoring of glucose level at body temperature. The asymmetric planar electrodes were fabricated by thin film technology on glass and cut as chip sensor. The glass-based chip sensor was further immobilized with glucose oxidase for glucose measuring. To investigate the stability of the glass-based chip sensor, we performed a long-term study and compared with a commercial polymer sensor. All of the experiments were carried out in phosphate buffer solution at 37°C. The result indicated that the glass-based chip senor was more stable in background signal than a commercial polymer sensor during a 18 days of study. The chip senor immobilized with glucose oxidase showed fast response time and broad detection range for glucose measurement. The present study demonstrated that our design of asymmetric planar electrodes was suitable for developing a glucose sensor with long-term stability.**

Keywords — ***Asymmetric planar electrode; glucose sensor; long-term monitoring; microfabrication.***

I. INTRODUCTION

Diabetes is a global chronic disease that is caused by a syndrome of disordered metabolism and results in high blood glucose level. Diabetic patients who examine and control their blood glucose level regularly can reduce complications, such as high blood pressure, blindness, heart disease, stroke, neurological disorders, and kidney failure. Today, using a portable glucose meter with "finger pricking" of blood sampling is still a popular method for diabetic patients to monitor their blood glucose level. However, this blood sampling is uncomfortable and not convenient due to it requires several tests per day. The patients who perform blood glucose monitoring more than once daily is estimated that lower than 30% [1]. To this end, a continuous, low-invasive even non-invasive blood glucose monitoring technique for home care could improve diabetic patients to maintain their blood glucose in normal level and warn to against developing hypoglycemia.

Glucose oxidase-based biosensor has been mostly used in glucose sensor for diabetic patients. Previous studies concentrated mainly on enzyme immobilization on electrodes by cross-linking with glutaraldehyde. However, this procedure was complex. Immobilization of glucose oxidase into an electrochemically conducting or nonconducting polymer is interesting because of simple preparation, high reproducibility, and low cost [2, 3]. Compared with conducting polymers, nonconducting polymers usually have a highly selective response to glucose, which is important for eliminating the interference of other electroactive species in practice [4, 5]. The electrochemical polymerization of hydrobenzene and aminobenzene derivatives can produce corresponding polymers, which are good candidates in constructing a glucose sensor by simple electrochemical oxidation in the presence of glucose oxidase [6, 7].

Although glucose oxidase-based glucose sensor shows highly specific detection to blood glucose, signal decay of sensor is still a problem. Therefore, the patients who use continuous glucose meter can not avoid calibration by traditional portable glucose meter several times per day. In the present study, we developed a novel chip sensor with asymmetric planar electrodes that consisted of a larger surface area of counter electrode and a smaller surface area of working electrode for glucose measurement. We evaluated the background stability of the chip sensor by electrochemical measurement in phosphate buffer solution. The chip senor was also immobilized with glucose oxidase as glucose sensor. The glucose sensor measured glucose level in phosphate buffer solution showed fast response time and broad detection range.

II. ELECTRODE FABRICATION AND EXPERIMENTAL SETUP

A. Sensor fabrication

The glass-based chip sensor was fabricated by thin film technology has been described in detail elsewhere [8, 9]. Fig. 1 shows the microfabrication process. At first, the electrode pattern on the substrate was performed by a lift-off process. A sacrificial material such as photoresist was first deposited and patterned on the substrate. The electrode layer of Ti/Pt (50 nm/200 nm) was then deposited on top and the sacrificial material was subsequently removed through exposure to solvent soaking and spraying, leaving behind only the material deposited directly on the substrate. After that, the pattern of the Pt film was covered using the positive photoresist and 200 nm thick Ag film was sputtered. The Pt and Ag electrode was then formed using lift-off process. Acetone was used to remove the photoresist. The Ag electrode was dipped into 0.1 M HCl for one minute with 0.5 V power applied. Finally, the chip was insulated by polyimide separating the working electrode of the sensor from the external contact pad.

*Contact author: for fabrication aspects of this project, please contact ***antonio@itri.org.tw***

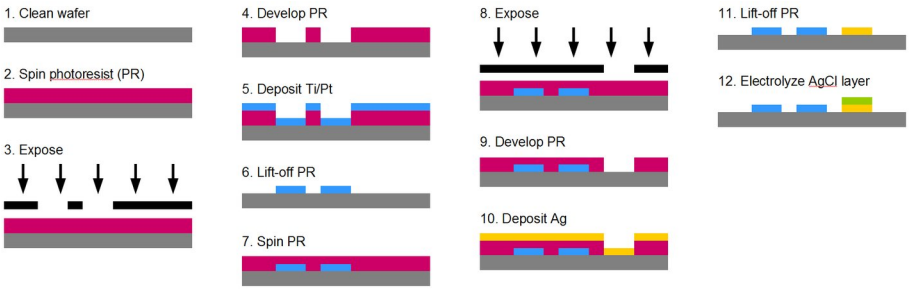

Figure 1. Microfabrication process of glass-based chip sensor.

B. Solution preparation

To examine the performance of electrodes, all experiments were carried out in a phosphate buffer environment. The phosphate buffer was consisted of 25 mM KH_2PO_4 (Riedel-de Haen, USA) and 41 mM Na_2HPO_4 (Riedel-de Haen), pH 7.0. Known amount glucose may be added in the same phosphate buffer for investigating the response of glucose sensor. Glucose sensor was prepared before each examination. Glucose oxidase (Sigma, USA) was dissolved in distilled water with a concentration of 600 unit/ml for coating of electrodes.

C. Apparatus and measurement

All electrochemical experiments were carried out with a CHI 440 electrochemical workstation (CH Instruments Inc., USA.). A three electrode set consisting of a 2.0-mm-diameter Pt disk working electrode, a Ag/AgCl reference electrode, and a Pt wire counter electrode was immersed in a small glass vial through holes drilled into a threaded plastic cap. Prior to the experiment, the working electrode was polished with a small amount of 0.05-micron alumina powder on a felt polishing pad and rinsed thoroughly with distilled water to remove alumina adhered to the electrode surface.

III. Results and Discussion

BioMEMS has a highly impact to *in vivo* as well as *in vitro* biomedical markets. Especially both fields of implantable miniaturized systems and low cost analysis chips are preferred markets for micro systems. However, the main challenges are not only arising from micro technology, but also from the interface between biological and technical systems.

Glucose oxidase has been mostly used in biological applications as biosensor, biocatalyst or drug-delivery systems. Some specific examples include the synthesis of glucose-sensitive hydrogels that could be used to deliver insulin to diabetic patients using an internal pH trigger [10]. The immobilization and stability of glucose oxidase on novel substrates have therefore continued to attract attention by scientists working in relative fields.

The diagnosis and management of diabetes require a tight monitoring of blood glucose levels. Millions of diabetics test their blood glucose levels daily, making glucose the most commonly tested analysis. Indeed, glucose biosensors account for about 85% of the entire biosensor market [11]. Such huge market size makes diabetes as a model disease for developing new biosensing techniques. Amperometric enzyme electrodes, based on glucose oxidase, have played a leading role in the move to simple easy-to-use blood glucose testing and are expected to play a important role in the move toward continuous glucose monitoring.

In the present study, we attempted to prepare a glucose sensor by MEMS technique. The glass-based chip sensor was fabricated on a glass substrate. The glass-based chip sensor consisted of a Ti/Pt working electrode, a Ag/AgCl reference electrode, and a Ti/Pt counter electrode with geometric area of each electrode of 3.85, 0.133, and 5.81 mm^2, respectively. The conducting wires were constructed on glass substrate and the remaining sheathed was carefully covered with polyimide. Fig. 2 shows the glass-based chip sensor. The chip sensor was inserted directly into a sensor housing. To examine the performance of the glass-based chip sensor, we used a standard three electrode set that consisted of a 2 mm-diameter Pt disk working electrode, a Ag/AgCl reference electrode, and a Pt wire counter electrode as control study as shown in Fig. 3a. The glass-based chip sensor that inserted into a sensor housing was connected to the measurement system by wire welded bonding as shown in Fig. 3b. Both sensors were immersed in a container with phosphate buffer for cyclic voltammetry study. Fig. 4 shows the cyclic voltammetry of both sensors and indicates the stable signal property. The signal of the chip sensor showed stronger than the standard three electrode set due to that the reaction distance of electrodes on the chip sensor was shorter.

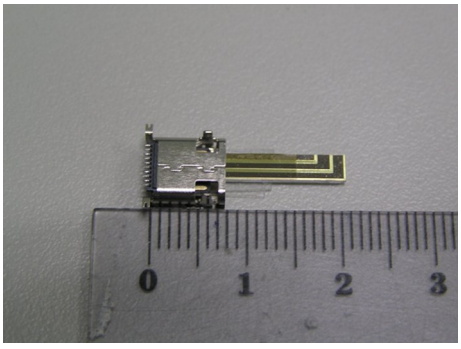

Figure 2. The glass-based chip sensor connected with a holder.

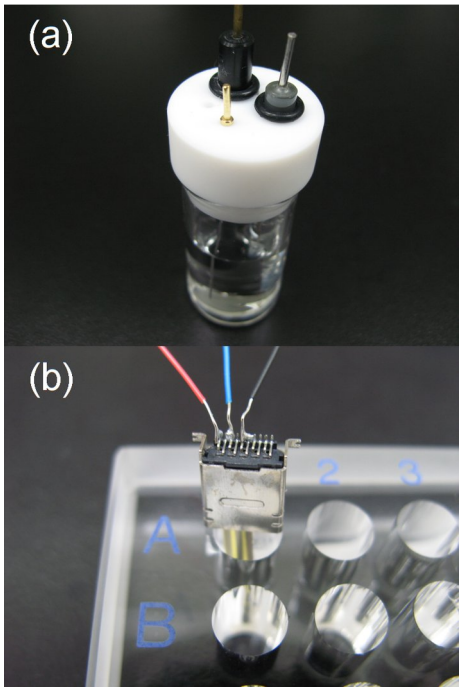

Figure 3. Two electrochemical sensors were examined their cyclic voltammetry profile: (a) standard three electrode set (model CHI630, CH Instrument, USA); (b) glass-based chip sensor connected by a holder and dipped in a quartz 96-well plate.

For long-term study, we investigated the stability of the glass-based chip sensor and compared with a commercial polymer sensor. Both sensors were incubated in phosphate buffer at 37°C and examined by measuring cyclic voltammetry. As can be seen in Fig. 5a, the commercial polymer sensor expresses variable current in the range of 0.2 V to 0.8 V during the 19 days study. This result indicated that the standard deviation of the current variation greatly. Therefore, the polymer sensor could not maintain the stability over 19 days. In contrast, the activity of the glass-based chip sensor remained virtually constant current during the 18 days study as shown in Fig. 5b. This result indicated the excellent long-term stability of the glass-based chip sensor at 37°C.

The glass-based chip sensor was also examined the ability of glucose measurement. Before use, glucose oxidase was immobilized on electrode of the chip sensors. During the preparation of a glucose sensor, immobilization of glucose oxidase on electrode surface was a key step in fabricating a high performance glucose sensor. The glucose sensor was immersed in phosphate buffer with different concentration of glucose. It could reach the steady-state current within 10 s, which was much faster than previous reports that 50 s on pure silica matrix [12], and 20 s on silica sol–gel composite film [13, 14]. The current of the glucose sensor expressed linear property in the detection range of 50 to 300 mg/dl glucose as shown in Fig. 6. The error bar on output current at each glucose level showed that the lot-to-lot reproducibility given by standard deviation. The error bar of the glucose sensor was relatively small that only 6% of coefficient of variation for the output current at the glucose concentration of 100 and 150 mg/dl. In contrast, the glucose sensor showed larger at low and high glucose concentration with 12% of coefficient of variation for the current response.

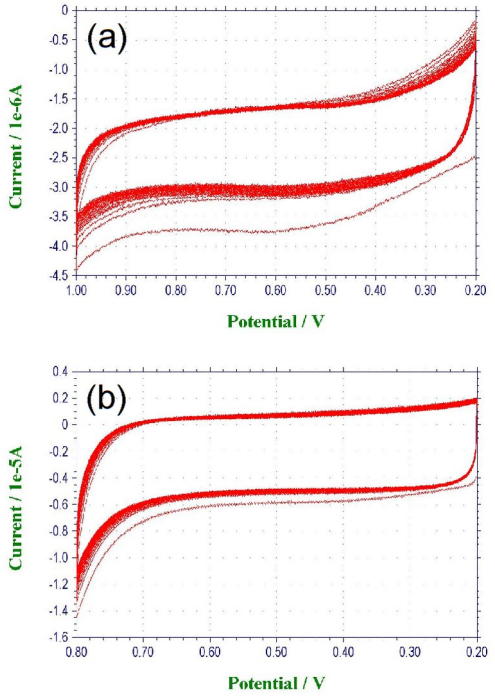

Figure 4. The cyclic voltammetry profile of two electrochemical sensors dipped in phosphate buffer solution (pH 7.0): (a) standard three electrode set; (b) glass-based chip sensor.

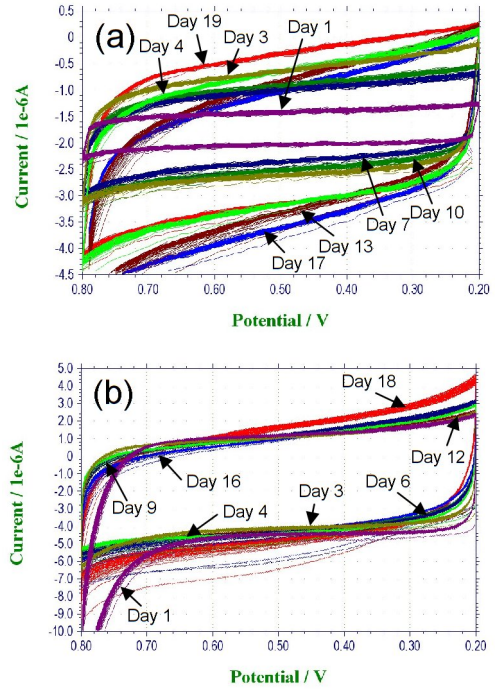

Figure 5. The cyclic voltammetry profile of two electrochemical sensors dipped in phosphate buffer solution (pH 7.0) for long-term study: (a) commercial polymer sensor; (b) glass-based chip sensor.

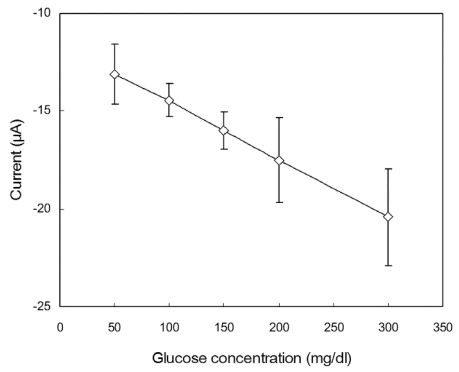

Figure 6. Calibration curve of the glass-based chip sensor for glucose measurement.

IV. CONCLUSION

The present study was to prepare MEMS based electrodes for glucose long-term monitoring. In order to miniaturize the whole sensor and incorporate it into a hypodermic needle, the electrodes of the glucose sensor were made by MEMS technique. We evaluated the background stability of the glass-based chip sensor by electrochemical measurement in a phosphate buffer to simulate in-vivo environment. Glucose oxidase activity was measured as a function of response time in order to find the stability of glucose oxidase when it was immobilized on the electrodes. Data showed that a highly sensitive, stable, and long-term glucose microsensor had been successfully fabricated on a glass-based substrate. The glass-based chip sensor showed stable background signal performance at 37°C during a 18 days experiment. After immobilizing glucose oxidase, the glucose sensor revealed fast response time that current could reach to steady-state within 10 s. The glucose detection range of the glucose sensor was 50 to 300 mg/dl with good reproducibility. This research discusses the operation parameters of electrochemical glucose MEMS biosensors. The major strategies for enhancing the chip performance, and outlines key challenges and opportunities in their further development and use. Emphasis is given to fundamental advances of glucose sensing environment and related materials.

REFERENCE

[1] Z. T. Bloomgarden, "Treatment issues in type 1 diabetes," Diab. Care, 2002, vol. 25, pp. 230-236.

[2] D. Belanger, J. Nadreau, and G. Fortier, "Feature Article Rotating ring disk electrode studies of polypyrrole–glucose oxidase biosensors," Electroanalysis, 1992, vol. 4, pp. 933-940.

[3] Z. Zhang, H. Liu, and J. Deng, "A glucose biosensor based on immobilization of glucose oxidase in electropolymerized o-Aminophenol film on platinized glassy carbon electrode," Analy. Chem., 1996, vol. 68, pp. 1632-1638.

[4] J. P. Lowy, K. McAteer, S. S. E. Atrash, A. Duff, and R. D. O'Neill, "Characterization of glucose oxidase-modified poly(phenylenediamine)-coated electrodes in vitro and in vivo: homogeneous interference by ascorbic acid in hydrogen peroxide detection," Anal. Chem., 1994, vol. 66, pp. 1754-1761.

[5] D. Centonze, C. Malitesta, F. Palmisano, and P. G. Zambonin, "Permeation of solutes through an electropolymerized ultrathin poly-o-phenylenediamine film used as an enzyme-entrapping membrane," Electroanalysis, 1994, vol. 6, pp. 423-429.

[6] P. N. Bartlett and D. J. Caruana, "Electrochemical immobilization of enzymes. Part V. microelectrodes for the detection of glucose based on glucose oxidase immobilized in a poly(phenol) film," Analyst, 1992, vol. 117, pp. 1287-1292.

[7] E. Ekinci, A. A. Karagozler, and A. E. Karagozler, "The preparation and sensor application of poly (p-Aminophenol)," Electroanalysis, 1996, vol. 8, pp. 571-574.

[8] G. Jobst, I. Moser, M. Varahram, P. Svasek, E. Aschauer, Z. Trajanoski, et al, "Thin-film microbiosensors for glucose-lactate monitoring," Anal. Chem., 1996, vol. 68, pp. 3173-3179.

[9] I. Moser, G. Jobst, and G. A. Urban, "Biosensor arrays for simultaneous measurement of glucose, lactate, glutamate, and glutamine," Biosens. Bioelectron., 2002, vol. 17, pp. 297-302.

[10] C. M. Hassan, F. J. Doyle, and N. A. Peppas, "Dynamic behavior of glucose-responsive poly(methacrylic acid-g-ethylene glycol) hydrogels," Macromolecules, 1997, vol. 30, pp. 6166-6173.

[11] W. Joseph, "Electrochemical glucose biosensors," Chemical Reviews, 2008, vol. 108, pp. 814-825.

[12] J. Li, L. S. Chia, N. K. Goh, and S. N. Tan, "Silica sol–gel immobilized amperometric biosensor for the determination of phenolic compounds," Anal. Chim. Acta, 1998, vol. 362, pp. 203–211.

[13] J. Wang, P. V. A. Pamidi, and D. S. Park, "Sol-gel-derived metal-dispersed carbon composite amperometic biosensors," Electroanalysis, 1997, vol. 9, pp. 52-55.

[14] U. Narang, P. N. Prasad, F. V. Bright, K. Ramanathan, N. D. Kumar, B. D. Malhotra, et al., "Glucose biosensor based on a sol-gel derived platform," Analy. Chem., 1994, vol. 66, pp. 3139-3144.

Study on Nanoscale Bombardment Dynamics Using Molecular Dynamics

Y. L. Yeh[3], B. H. Chen[1]*, Chao-Ho Lan[1] , Jie-Ren Ku[1], Chung-Wei Cheng[2], Shing Cheng Chang[4], Cha'o-Kuang Chen[4], M. J. Jang[3], C. C. Wang[5]

[1] *Industrial Technology Research Institute, Energy and Environment Laboratories, B. H. Chen, Tainan, Taiwan.*
[1]*Industrial Technology Research Institute, Energy and Environment Laboratories, Chao-Ho Lan, Tainan, Taiwan.*
[1]*Industrial Technology Research Institute, Energy and Environment Laboratories, Jie-Ren Ku, Tainan, Taiwan.*
[2]*Industrial Technology Research Institute, ITRI South, Chung-Wei Cheng, Tainan, Taiwan.*
[3]*Department of Automation and Control Engineering, Far East University, Y. L. Yeh, Tainan, Taiwan.*
[4]*Department of Mechanical Engineering, University of National Cheng-Kung, Shing Cheng Chang, Tainan, Taiwan.*
[4]*Department of Mechanical Engineering, University of National Cheng-Kung, Cha'o-Kuang Chen, Tainan, Taiwan.*
[3]*Department of Automation and Control Engineering, Far East University, M. J. Jang, Tainan, Taiwan.*
[5]*Department of Mechanical Engineering, Far East University, C. C. Wang, Tainan, Taiwan.*

***Abstract* — The present study has investigated the cluster deposition process of thin film formation. MD simulation has been employed to study the morphology of the collision system and to investigate the transient behavior, which occurred between the atoms of the deposited cluster and the substrate. The substrate relaxation process and the influence of the incident energy were also discussed. A traveling condition of the cluster for random incidences was applied in the simulations, and the ratio of translational and total kinetic energy of clusters were varied to observe their influence on the cluster's diffusivity. It was found that the system's reconstruction phenomena tended to recover the lattice structure, which was disordered by the impact cluster. After thermal equilibrium, the partial wetting behaviors or cluster embedded morphology were observed according to different incident energy. In the "impact process", the high local temperature and high heat transfer rate were observed due to the high compressibility of the impact zone. By changing the ratio of translational and total kinetic energy of clusters, the simulation results indicated that translational kinetic energy of cluster contributed to the local temperature raising and the interpenetration of cluster atoms, while the vibrational energy benefited the spreading behaviors of cluster.**

Keywords ***—Molecular Dynamics, Cluster impact dynamics, Thin film***

I. INTRODUCTION

In the recent years, there are a lot of interests in the cluster deposition method, which has wider applications than the atomic deposition [1]. Beams of large clusters, which are composed of many weakly bound atoms or molecules, can be generated in supersonic expansions of gas into vacuum through a nozzle. The cluster bombardment process is a convenient technology to build the nanoscale materials, such as separate nanoislands on substrate and various thin films for different applications. It is also used for shallow implantation and surface smoothing by the clusters with high impact energy.

The simulation methods usually adopted to investigate the transient phenomena of thin film deposition process are Monte Carlo (MC) simulation and Molecular Dynamics (MD) simulation. The present study adopts MD simulation since it is a fundamental method which provides an insight into the atomic processes involved in the formation of the PVD-film structure. By MD simulation, Hou et al. [2] modeled the low-energy cluster beam deposition (LECBD) of Au clusters on Au (111) surfaces. The simulated morphology of the thin film was in excellent agreement with their experimental measurements [3]. A further model, which combined molecular dynamic method and metropolis Monte Carlo method, of LECBD was performed to investigate the thermodynamic and structure properties of bimetallic cluster assembled materials at the atomic scale [4]. It revealed that the cluster impact induces significant chemical disorder but the clusters assembled film keep their initial identities.

During the thin film growth, three principal regions were observed in the two-phase system, i.e. a crystal bulk region, a fluid bulk region and an interfacial region containing the absorption layer [5]. The latter region can be regarded as a sheet of atomic thickness, whose structural and dynamics properties differ from those of both the fluid bulk and the crystal bulk regions. Smith and Srolovitz [6] then indicated that the void volume fraction and the surface roughness of the film structure increase as the substrate temperature and incident energy decrease. Yasumatsu and Kondow [7] focused a review on several representative collision systems and identified the two energy-transmission steps of the cluster-impact processes, which involve the "impulsive compression" on the constituent molecules of the cluster and cause the high temperature and pressure locally and temporally. First, the collision energy is transmitted impulsively to the cluster and the surface atoms involved in the collision, namely the collision system, at the moment of the collision due to ultrafast deformation of the impacted cluster. Subsequently, the energy deposited in the

Identify applicable sponsor/s here. *This project was funded by the National Science Council of Taiwan under Grant Nos. NSC 98-2221-E-269 - 016.*

Contact author: for fabrication aspects of this project please contact* ***bhchen@itri.org.tw***.**

specific modes is redistributed among other internal degrees of freedom by interaction among the constituent molecules of the collision system. Because the properties of a cluster are associated with the number of constituent molecules, the features of the cluster-impact processes change specifically with the collision energy and the cluster size.

In the present study, MD simulations of the low energy cluster beam deposition were performed and the physical behaviors of the atoms were observed by calculating the atom diffusivity. The clusters passing through the vacuum to the substrate with a velocity of center of mass were used here. To investigate the effect of the intracluster interaction on the cluster bombardment on a substrate, the cluster's temperature was assigned to be higher than the translational temperature to have an enough internal kinetic energy, namely vibrational and rotational temperature. In other words, the influence of the ratio of translational energy and total kinetic energy on the cluster-impact process was investigated. The object of the present paper is to study the transient atom diffusion ability at non-equilibrium conditions for the cluster-impact process by varying the velocity or temperature of incident cluster. The results presented in the current study possess a qualitative relevance to solid-vapor interface systems.

II. SIMULATION MODEL

Fig. 1 presents a schematic representation of the model used in the present study to investigate the cluster-impact process on the solid surface. The Morse potential adopted in the present paper has successfully applied in the investigation of thin films defect formation, film density variation, surface roughness, and in the qualitative analysis of the influence of various working parameters, namely substrate temperature, incident energy and particle deposition rate [6], [8]–[10]. This model is a representative potential pair type, with a function form shown bellow:

$$U(r_{ij}) = D\left[e^{-2\alpha(r_{ij}-r_0)} - 2e^{-\alpha(r_{ij}-r_0)}\right] \quad (1)$$

Where r_{ij} is the distance between atom i and j .The parameters r_0 , D, and α corresponding to the nearest atomic distance at equilibrium, the cohesion energy and the value fitted to the bulk elastic module, are respectively 2.6260 $\mathring{A}$, 0.3429 eV and 1.3588 $\mathring{A}^{-1}$ related to the interaction of copper atoms [10]. The velocity Verlet algorithm [11] was used to calculate the trajectories of the atoms according to the classical Newton's mechanics and statistical mechanics with the time step of 1 fs.

We considered the deposition of a cupper cluster on an fcc (100) copper surface. To avoid any interaction between the solid surface and the incident cluster prior to the bombardment, the present study assigned the initial position of the cluster to be at distance of about 10 times the atomic diameter from the upper layer of the substrate in the perpendicular direction of the surface. This traveling condition fulfils the statistical randomization of the impact position of deposition clusters more than the non-traveling cases with the same initial condition except for the position of cluster placed at a given distance, which is small than the truncated distance from the substrate or clusters deposited previously [2], [12]. Furthermore, there existed a non-zero initial potential energy between the cluster and the substrate in the non-traveling cases, and would cause some incorrect phenomena in the simulation. But for a distance far from substrate enough, i.e. with the traveling condition, it approximates to zero. This traveling condition of incident particles was often used in the MD simulation of sputter-deposited film growth for each incident atom[10].

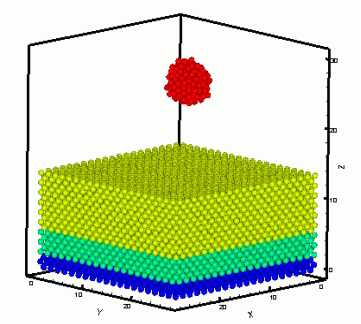

Figure 1. The model of molecular dynamics simulation.

The isolated cluster in the vacuum was described with the microcanonical ensemble (NVE), whose temperature fluctuated at a "certain" value, 2000K, and moved in the z direction with a "certain" velocity of center of mass, 300 m/s. The isolated cluster of 256 atoms was constructed initially by 4 × 4 × 4 atomic cells of fcc structures and lasted for 50 ps to perform the velocity and temperature requested. The translational and total kinetic energy were 7.598eV and 66.272 eV respectively. The single crystal substrate was composed of a fcc box of 20 × 20 × 10 atomic cells with 16000 atoms, i.e. the substrate had the size of 7.4 nm × 7.4 nm × 3.7 nm. To prevent the substrate atoms from shifting, the bottom layers were fixed. Instead of fixing the bottom monolayer [10], several bottom layers should be fixed to avoid the incorrect boundary effects on the non-fixed layers due to the truncated potential method. Three bottom layers fixed were enough in the present study because the truncated distance here was 2.5 times the atomic diameter in the simulations. Above the fixed layers were five thermal control layers, which were assumed to be an ideal heat sink, maintained a constant substrate temperature, 300 K. In other words, the thermal layers were described with the canonical ensemble (NVT) and the velocities of the atoms in the thermal layers was rescaled at each time step according to the substrate temperature in the simulation [13] to follow the Maxwell velocity distribution. This reflected the physical sputtering process, in which the substrate was kept at a constant temperature by means of a power supply controller. The energy imparted to the substrate by the impact of the incident atoms was absorbed by the large number of atoms within the substrate [10], [14]. The rest of the layers were treated by free motion to reflect the corresponding responses of atoms in the impact process and prevent from the thermal layers being spoiled by incident clusters. Periodic boundary conditions were applied in the x and y directions, while an open boundary were applied in the z direction. The substrate, as the cluster, was in the thermal equilibrium after 50 ps evolution before the impact process started.

III. RESULTS AND DISCUSSION

MD simulations of the phase transitions occurring at the solid-vapor interface were carried out in order to investigate the structural and thermophysical properties of the interface. From a structural point of view, the simulation took the surface relaxation and reconstruction phenomena into account.

The cluster bombardment process can be taken into the combination of two processes. At the earlier stage, the "impacting process", which depends on the velocity of impact cluster, was accomplished with the exchanges of atoms, the energy transportation and absorption, and the propagation of the shock wave into the surface. This process was also regarded as the elimination process of the high compression phenomena. After the cluster was stopped on the substrate, the system tended towards thermal equilibrium via the kinetic energy removing by the heat sink, and the lattice structure was also reconstructed. Such trajectories variation in the phase space of the atoms of the system performed a tendency of system to reach the minimum entropy, and was viewed as the "relaxation process". This process was similar to the surface wetting behavior by liquid nanodroplets [15]–[17].

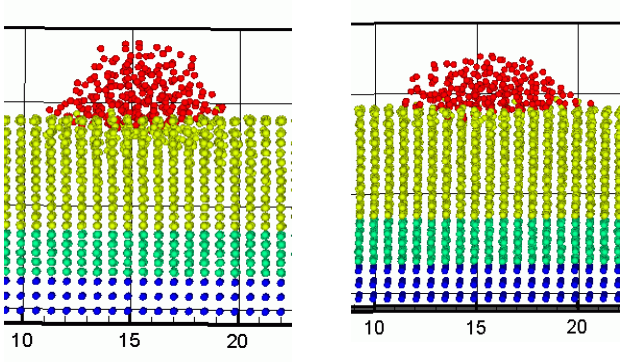

(a) (b)

Figure 2. (a) The instant snapshots of the collision system and (b) that after 1 ps.

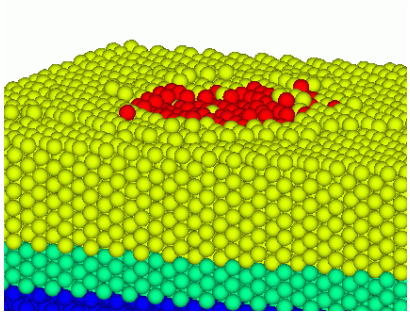

Figure 3. The morphology of the collision system in the high energy impact case.

III-I The result and discussion

III-I-I The atomic diffusion

Fig. 2 showed the transition morphology of the collision system in a short time of 1 ps. It was noted that the atoms of cluster and substrate exchanged, as shown in Fig. 2 (a). The upper layers of the substrate were impacted by cluster atoms and become disorder for the stress relaxation phenomena, which enabled the substrate to release the energy rapidly stored in the impact zone. Fig. 2 (b) showed the structure after 1 ps , and indicated that the atoms of collision system soon tended to return to the original sites of equilibrium by the elastic recovering force after transferring the unnecessary energy to the heat sink. However, the substrate structure was damaged by the interpenetrating of cluster atoms, i.e. some plastic deformation were produced in the cluster impact process. The plastic deformation of substrate would increase as the energy of impact cluster rises, as shown in Fig. 3. A crater, and also a flat surface morphology, was caused by the bombardment, called the high energy case later, of the cluster with high translational energy, 2600 eV, and high total kinetic energy, 2650 eV. Actually, a supersonic shock wave was found to propagate through the crystal and the cluster can be fully planted into the substrate at an ultra-fast velocity, such as 10 km/s, whereas some molecules of the cluster were outside of the solid surface when the impact velocity is reduced to 2 km/s [18].

III-I-II The energy and momentum transmission

During the bombardment process, the velocity of the cluster was accelerated by the attractive force between the cluster and substrate, and then decelerated rapidly by the high rebounding force due to the impulsive compression, as seen in Fig. 4. Finally, the atoms of the cluster were in the equilibrium position with thermal vibrations as the atoms of the substrate. Therefore, the cluster had a fluctuating velocity around zero. Fig. 5 showed the variations of total kinetic energy of the cluster during the first 15 ps, and also that of cluster center of mass. The energy difference between them was observed in the figure. It revealed that the temperature increases of the cluster in the impact duration resulted not only from the acceleration behaviors but also the compression heating. After heating, the cluster was stopped on the substrate with the atoms vibrating with a local high temperature, 3000 K, as shown in Fig. 6. As a result of the high temperature in the collision zone, a distinct quasi-fluid behavior was evident on the substrate. As the cooling of substrate, the cluster finally reached to the thermal equilibrium with the substrate in 300 K.

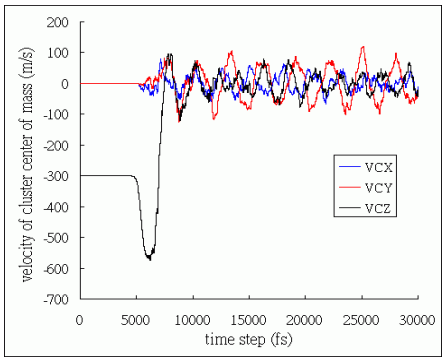

Figure 4. The variation of velocities of the impact cluster during simulation process.

In the high energy impact case, a clear look at the energy transmission direction was observed in the impacting duration of 0.6 ps, as shown in Fig. 7. It revealed that the (111) surface of the crystal exhibited rapid momentum transmission mechanism. This is because the activation energy in the closed packed (111) surface is so small that the barrier for diffusion is very low [19].

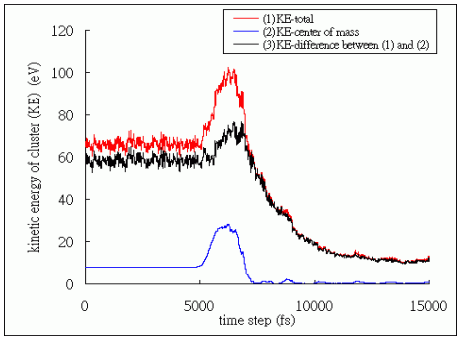

Figure 5. The variation of kinetic energy of the cluster during simulation process.

III-II Thermal equilibrium

III-II-I The surface wetting behaviors

After thermal equilibrium, the velocities of the atoms of cluster and substrate followed the Maxwell–Boltzmann distribution, as shown in Fig. 8 Fig. 9 (a) and (b) showed that the atoms of the collision system were epitaxial with the structure after the thermal equilibrium in 300 K, which is maintained by the thermal layers. The partial wetting behaviors [16] of the Cu-Cu interface with a contact angle were achieved in this case rather than the flat complete wetting. This is the determinant of the qualities of the thin films from the clusters deposition, because the large vacancies could rise due to certain of fabrication parameters, e.g. low substrate temperature, low incident energy, rapid cooling rate, etc. As shown in Fig. 3, a more flat coverage was produced as the impact energy increased. However, large damage would produced on the surface at the same time by the over high energy, and this might not good for some applications. Fig. 10 showed the displacement of moveable substrate atoms after the simulation finished in the high energy case. It was found that atomic diffusion away from the original lattice site had occurred in almost each layer, whereas in the low energy case only atoms of the top two layers hopped to the other lattice sites through the cluster's collision.

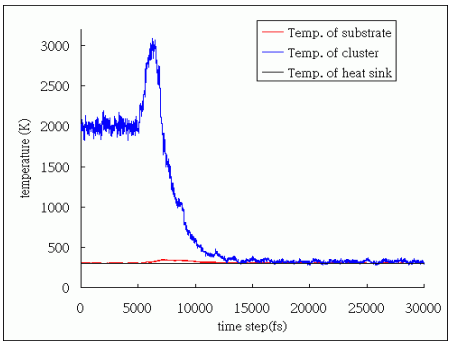

Figure 6. The temperature curves of the substrate and cluster.

It is obviously that low energy clusters are needed for the deposition of porous thin films, which are desired for retaining peculiar properties of the clusters or for larger reaction areas in the chemical processes. On the other hand, an energetic cluster impact process is used for the deposition of thin films which present high density and good mechanical properties. Furthermore, for the surface smoothing process [20] by ion cluster beams, the clusters with ultra-high energy are required.

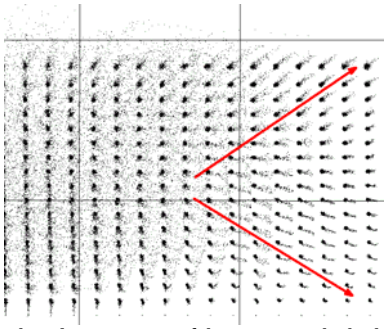

Figure 7. The right side trajectories of the system in the high energy impact process for the impacting duration of 0.6 ps

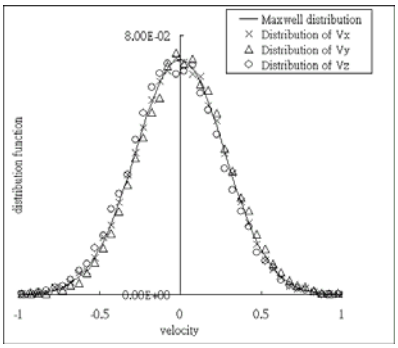

Figure 8. The velocity distribution of system atoms.

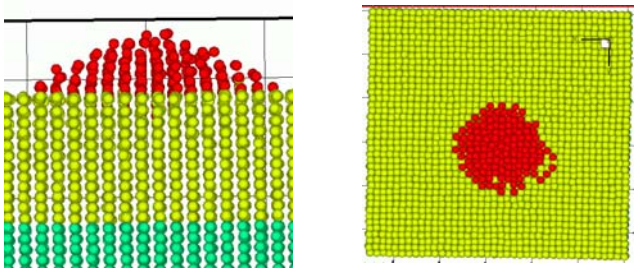

(a) (b)

Figure 9. The morphology of the collision system in thermal equilibrium. (a) side view, (b) top view.

III-II-II Thermal hysteresis

As shown in Fig. 6, thermal hysteresis occurs when the incident energy of the deposited atoms during the transient deposition process exceeds the substrate heat transfer rate. An exponential decay of temperature of cluster was observed and the relaxation time of the system is about 6 ps in this case. If the mean free time of each incident cluster in the thin film growth process exceeds the time required by the deposited atoms to attain a thermal equilibrium state, i.e. , the influence of the incident clusters upon the substrate is diminished. However, an increase in the deposition rate reduces the mean free time, and increases the influence of the incident clusters. Therefore, the deposition rate of incident clusters should be chosen with the consideration for the heat transfer efficiency of the substrate. Anyway, an over high cooling rate of the substrate to attain thermal equilibrium rapidly is not suggested.

It would reduce the migration ability of the cluster atoms, which is beneficial to the formation of a smoother and higher density thin film surface.

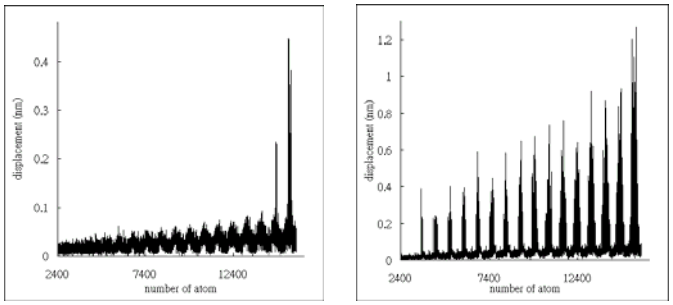

(a) (b)

Figure 10. The displacement of moveable substrate atoms in (a) low energy and (b) high energy impact process.

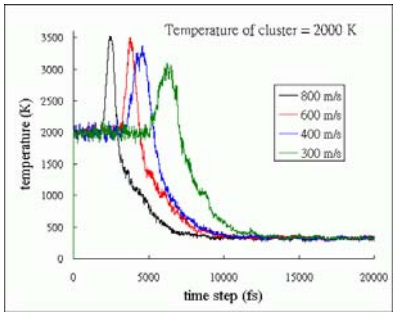

Figure 11. The cluster's temperature variations of the different simulation cases

III-III Effect of the proportion of cluster energy

The effects with reference to the proportion of the translational kinetic energy to the total kinetic energy of clusters were investigated by the cases of different velocity of cluster, namely 400 m/s, 600m/s and 800m/s, in the same temperature, 2000 K. It was found that higher local temperature was generated as the velocity of cluster increased, and this might be preferred in some processes, which required the chemical reactions of the impact cluster and substrate atoms. As shown in Fig. 11, the maximum temperature in the case of 800 m/s was 500 K higher than that of 300 m/s, even though the impact energy of cluster were the same in the two cases. Comparing the time needed for the substrate to estimate the local high temperature due to impacting compression, it was obviously that the high velocity case had the shorter time. It revealed that higher incident velocity caused higher heat transfer rate in the incident direction, which was perpendicular to the surface here and had the shortest distance for the energy transmission from the surface atoms deep into the heat sink.

To study the dependence of the surface diffusivity in these cases, the spreading index [21] was calculated, which is defined as the mean-square transverse positions of the cluster atoms relative to the cluster center of mass and can be written as

$$\eta(t) = \sum_{i=1}^{N} \left\{ \left[x_i(t) - x_{c.m.}(t) \right]^2 + \left[y_i(t) - y_{c.m.}(t) \right]^2 \right\} \quad (2)$$

where N is number of cluster atoms. Fig. 12 showed that the atoms of cluster with high incident velocities had less diffusive ability in lateral plane, since they tended to interpenetrate into the surface. On the other hand, the lower translational velocity meant the higher vibrational energy in the cases of the same total kinetic energy, or namely temperature, of clusters. It was clearly that internal vibrational energy of cluster contributed to the lateral spreading behaviors much than the translational energy. That is, increasing the vibrational energy of the non-dissociation cluster as possible is helpful for the formation of flat thin film. Fig. 12 also showed the results of the cases with the same velocity, 300 m/s, but different temperature, 300 K, 800 K, and 1500 K.

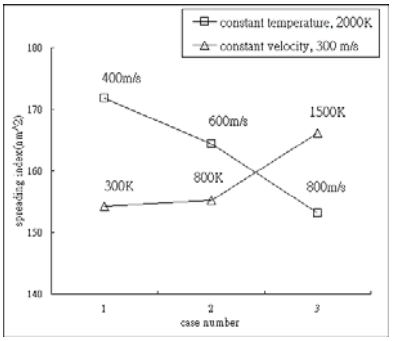

Figure 12. The spreading index of different simulation cases.

IV. Conclusions

In the present study, MD simulation has been employed to study the transient behaviors, relaxation process and morphology of the collision system. The mass, momentum, and energy transfer phenomena in the "impact process" and "relaxation process" were observed. It was found that the (111) surface of the crystal exhibited rapid momentum and energy transmission mechanism.

The influence of the incident energy on the cluster's diffusivity was also investigated by changing the ratio of translational and total kinetic energy of clusters. The numerical simulation results indicated that translational kinetic energy of cluster contributed to the local temperature raising and the interpenetration of cluster atoms; nevertheless, the vibrational energy benefited the spreading behaviors of cluster.

References

[1] Jensen, P., "Growth of nanostructures by cluster deposition: Experiments and simple models," Reviews of Modern physics, 71, 1999, pp. 1695-1735.

[2] Hou, Q., Hou, M., Bardotti, L., Prevel, B., Melinon, P. and Perez, A., "Deposition of clusters on Au (111) surfaces." I. Atomic-scale modeling, Physical Review B, 62, 2000, pp. 2825-2834.

[3] Bardotti, L., Prevel, B., Melinon, P., Perez, A., Hou, Q. and Hou, M., "Deposition of clusters on Au (111) surfaces." II. Experimental results and comparison with simulation, 62, 2000, pp. 2835-2842.

[4] Hou, M., Kharlamov, V. S. and Zhurkin, E. E., "Atomic-scale modeling of cluster-assembled thin films," Physical Review B, 66 , 2002, pp. 195408.

[5] Gilmer, G. H., Grabow, M. H. and Bakker, A. F., "Modelling of epitaxial growth," Materials Science and Engineering B, 6, 1990, pp. 101-112.

[6] Smith, R. W. and Srolovitz, D. J., "Void formation during film growth: A molecular dynamics simulation study," J. Applied Physics, 79, 1996, pp. 1448-1457.

[7] Yasumatsu, H. and Kondow, T., "Reactive scattering of clusters and cluster ions from solid surfaces, Reports on Progress in Physics, 66, 2003, pp. 1783-1832.

[8] Dong, L., Smith, R. W. and Srolovitz, D. J., "A two-dimensional molecular dynamics simulation of thin film growth by oblique deposition," J. Applied Physics, 80, 1996, pp. 5682-5690.

[9] Lugscheider, E. and von Hayn, G., "Simulation of the film growth and film–substrate mixing during the sputter deposition process," Surface and Coatings Technology, 116-119, 1999, pp. 568-572.

[10] Ju, S. P., Weng , C. I, Chang, J.G. and Hwang, C.C., "Topographic study of sputter-deposited film with different process parameters," J. Applied Physics, 89, 2001, pp. 7825-7832.

[11] Allen, M. P. and Tildesley, D. J., "Computer Simulation of Liquids," Oxford, 1987,New York.

[12] Haberland, H., Insepov, Z. and Moseler, M., "Molecular-dynamics of thin film growth by energetic cluster impact," Physical Review B, 51, 1995, pp. 11061-11067.

[13] Haile, J. M., "Molecular Dynamic Simulation,"John Wiley and Sons, Inc., 1992, New York.

[14] Phan, L. K., Cock, L., Nguyen, H. L. and Than, D. H., "The influence of tantalum content in relation to substrate temperature on magnetic and structural properties of Co–Cr–Ta thin films," J. Magnetism and Magnetic Materials, 193, 1999, pp. 117-120.

[15] Kubo, A., Makino, T., Sugiyama, D. and Tanaka, S. I., "Molecular dynamics analysis of the wetting front structure in metal / metal systems, "J. of Materials science, 40, 2005, pp. 2395-2400.

[16] Tartaglino, U., Zykova-Timana, T., Ercolessib, F. and Tosattia, E., "Melting and nonmelting of solid surfaces and nanosystems," Physics Reports, 411, 2005,, pp. 291-321.

[17] Webb, E. B., Hoyt, J. J., Grest, G. S. and Heine, D. R., "Atomistic simulations of reactive wetting in metallic systems, " J. of Materials science, 40, 2005, pp. 2281-2286.

[18] Ma, X. L. and Yang, W., "Supersonic wave propagation in Cu under high speed cluster impact," Nanotechnology, 15, 2004, pp. 449-456.

[19] Hansen, L., Stoltze, P., Jacobsen, K. W. and Nørskov, J. K., "Self-diffusion on copper surfaces," Physical Review B, 44, 1991, pp. 6523-6526.

[20] Muramoto, T., "Itabasi, K. and Yamamura, Y., MD simulation of surface smoothing due to cluster impact: estimation of radiation damage," Nuclear Instruments and Methods in Physics Research B, 228, 2005, pp. 1–8.

[21] Kwon, I., Biswas, R., Grest, G. S. and Soukoulis, C. M., "Molecular-dynamics simulation of amorphous and epitaxial Si film grown on Si (111)," Physical Review B, 41, 1990, pp.3678-3687.